



THE UNIVERSITY OF QUEENSLAND
A U S T R A L I A

**Trajectory Optimisation of a Partially-Reusable
Rocket-Scramjet-Rocket Small Satellite Launch System**

Sholto O. Forbes-Spyratos

B.Eng. (Mechanical and Aerospace) (Hons. I) & B.Sc. (Physics)

A thesis submitted for the degree of Doctor of Philosophy at
The University of Queensland in 2018

School of Mechanical Engineering

Centre for Hypersonics

Abstract

The small satellite industry is expanding rapidly, driving a need for dedicated and cost effective small satellite launchers. These small satellite launchers are currently designed to be single-use and low-cost, however, significant improvements in cost effectiveness and responsiveness may be achieved via the introduction of reusability. Unfortunately, the inclusion of reusability into small launch system designs is significantly more challenging than for larger launchers, and novel design methods may be necessary to achieve reliable and efficient re-use. One possibility for accomplishing reusability in a small launch system is the inclusion of airbreathing propulsion systems.

Airbreathing propulsion systems are extremely efficient, and do not require oxidiser to be carried on-board a launch system, bringing considerable operational and design advantages. However, airbreathing engines also add complexity to a launch system, with intricate subsystems and limited flight regimes. Because of this complexity, and the relative immaturity of airbreathing engine development, airbreathing launch systems are still in the early stages of design, with various configurations being investigated. Of these configurations, multi-stage systems are likely to be the most applicable to small launch systems, due to the favourable effects of stage separation with the restricted mass margins of small launchers. However, a multi-stage design compounds on the complexity of airbreathing launch systems, and the efficiency trade-offs between the stages of multi-stage airbreathing launch systems, particularly for three-stage systems with a fly-back component, are not well understood. This work aims to aid in the development of multi-stage airbreathing launch systems by developing and studying optimal payload-to-orbit trajectories for a three-stage airbreathing launcher, in order to understand the capabilities of the system and analyse the performance trade-offs between the stages during flight of a maximum payload-to-orbit trajectory with a fly-back of the airbreathing stage.

A representative launch system is developed, consisting of two rocket stages and scramjet-powered accelerator stage. This launch system is based on the SPARTAN scramjet-powered accelerator, being developed by the University of Queensland and Hypersonix, with a first stage based on the Falcon-1e, and a bespoke third stage. These stages are designed to the detail required for preliminary analysis, along with aerodynamic, mass and propulsive models. During the launch of this system, there are complex trade-offs between the performance of each stage that must be accounted for, requiring a robust and accurate trajectory optimisation methodology. A package is developed to calculate the maximum payload-to-orbit trajectory of the representative launch system, designated LODESTAR, which uses optimal control theory to design flight paths. LODESTAR utilises GPOPS-2, a pseudospectral method optimal control software, configured to calculate maximum payload-to-orbit trajectory profiles. Along with the configuration of GPOPS-2, LODESTAR provides a 3 degree-of-freedom simulation of each stage, and tools to verify and examine the optimised solutions produced by GPOPS-2.

Launch trajectories are initially simulated assuming that the scramjet accelerator lands at some position downrange. A launch trajectory is simulated in which the scramjet accelerator flies at maximum dynamic pressure as a reference and verification case, as flight at this limit during airbreathing engine operation is often assumed in previous studies to produce a maximum efficiency trajectory. This trajectory achieves a payload-to-orbit of 98.3kg, launching to sun synchronous orbit. The maximum payload-to-orbit trajectory of the launch system is calculated, and is found to differ significantly from the trajectory in which the scramjet accelerator is constrained to constant dynamic pressure. The scramjet accelerator is found to deviate from its maximum dynamic pressure at both stage separation points, and for a segment in the middle of its trajectory. The higher separation points result in the efficiency of the scramjet accelerator reducing, but increase the efficiency of the rocket stages, improving the overall efficiency of the system. Additionally, an altitude raising manoeuvre is performed in a region where the specific impulse of the scramjet engines is relatively homogeneous with varied flight conditions, resulting in a further small performance increase. Overall, flying an optimal trajectory increases the payload-to-orbit of the system launching to sun synchronous orbit to 156.4kg, an increase of 59.1% compared to a trajectory in which the scramjet accelerator flies at maximum dynamic pressure.

Next, the fly-back of the scramjet accelerator is included within the trajectory optimisation, and simulated to produce a non-intuitive maximum payload-to-orbit flight profile. It is found that the scramjet accelerator is able to achieve fly-back, but that it must ignite its scramjet engines during its return flight, causing the fly-back to become an important consideration in the optimal trajectory design. When the fly-back is included, the first stage pitches easterly, rather than northerly. The scramjet accelerator banks heavily throughout its acceleration to manoeuvre to polar inclination, decreasing the performance of the scramjet accelerator, but also reducing the amount of fuel used during fly-back, for a net performance gain. The fly-back is found to exhibit multiple ‘skipping’ manoeuvres, which serve to increase the range of the scramjet accelerator, minimising the fuel necessary during the return flight. In addition, the scramjet engines are powered on at the troughs of the first three skips, corresponding to the points of highest possible specific impulse. This optimal trajectory for the launch system is able to deliver 132.1kg of payload to sun synchronous orbit while successfully returning the scramjet accelerator to its initial launch site.

Finally, a study is conducted to quantify the sensitivity of the launch system to variations in key design parameters. The sensitivities of coupled design parameters are compared, to quantify their relative impacts on the performance of the launch system. The magnitudes of these relative impacts are assessed, and the behaviour of the maximum payload-to-orbit trajectory is investigated as the physical characteristics of the launch system are modified, to provide insights into both the optimised trajectory and the launch vehicle design.

Declaration by author

This thesis is composed of my original work, and contains no material previously published or written by another person except where due reference has been made in the text. I have clearly stated the contribution by others to jointly-authored works that I have included in my thesis.

I have clearly stated the contribution of others to my thesis as a whole, including statistical assistance, survey design, data analysis, significant technical procedures, professional editorial advice, and any other original research work used or reported in my thesis. The content of my thesis is the result of work I have carried out since the commencement of my research higher degree candidature and does not include a substantial part of work that has been submitted to qualify for the award of any other degree or diploma in any university or other tertiary institution. I have clearly stated which parts of my thesis, if any, have been submitted to qualify for another award.

I acknowledge that an electronic copy of my thesis must be lodged with the University Library and, subject to the policy and procedures of The University of Queensland, the thesis be made available for research and study in accordance with the Copyright Act 1968 unless a period of embargo has been approved by the Dean of the Graduate School.

I acknowledge that copyright of all material contained in my thesis resides with the copyright holder(s) of that material. Where appropriate I have obtained copyright permission from the copyright holder to reproduce material in this thesis.

Publications During Candidature

Journal papers

S. O. Forbes-Spyratos, M. P. Kearney, M. K. Smart, and I. H. Jahn. “Trajectory Design of a Rocket-Scramjet-Rocket Multi-Stage Launch System”. In: *Journal of Spacecraft and Rockets* (2018). DOI: [10.2514/1.A34107](https://doi.org/10.2514/1.A34107)

Conference papers

S. Forbes-Spyratos, M. Kearney, M. Smart, and I. Jahn. “Trajectory design of a rocket-scramjet-rocket multi-stage launch system”. In: *21st AIAA International Space Planes and Hypersonics Technologies Conference, Hypersonics 2017*. Xiamen, China, 2017. ISBN: 9781624104633

S. O. Forbes-Spyratos, M. P. Kearney, M. K. Smart, and I. H. Jahn. “Fly-back of a scramjet-powered accelerator”. In: *AIAA Scitech, 2018*. Orlando, FL, 2018. ISBN: 9781624105241. DOI: [10.2514/6.2018-2177](https://doi.org/10.2514/6.2018-2177)

J. Chai, M. Smart, S. Forbes-Spyratos, and M. Kearney. “Fly Back Booster Design for Mach 5 Scramjet Launch”. In: *68th International Astronautical Congress*. Aelaide, Australia, 2017

Publications Included in This Thesis

This thesis comprises partly of publications, as allowed by University of Queensland Policy PPL 4.60.07. The papers that have been included have all been published in peer reviewed journals at the time of submission.

S. O. Forbes-Spyratos, M. P. Kearney, M. K. Smart, and I. H. Jahn. “Trajectory Design of a Rocket-Scramjet-Rocket Multi-Stage Launch System”. In: *Journal of Spacecraft and Rockets* (2018). DOI: [10.2514/1.A34107](https://doi.org/10.2514/1.A34107)

Contributor	Contribution
Sholto O. Forbes-Spyratos	Conception and Design (85%) Performed simulations (100%) Analysis of results (90%) Wrote and edited paper (85%)
Ingo H. Jahn	Conception and Design (5%) Analysis of results (5%) Wrote and edited paper (7.5%)
Michael P. Kearney	Conception and Design (5%) Wrote and edited paper (7.5%)
Michael K. Smart	Conception and Design (5%) Analysis of results (5%) Wrote and edited paper (5%)

Contributions by Others to the Thesis

The model of the Baseline SPARTAN was provided for this work by Dr. Dawid Preller and Mr. Joseph Chai, including mass properties, dimensions, and CAD models. The CRESTM10 scramjet engine database was provided for this study by Prof. Michael Smart, consisting of tabulated performance data over a range of inlet conditions. The viscous correction incorporated into the SPARTAN's aerodynamic calculations was performed by Mr. Alexander Ward, and provided for this study in the form of a tabulated aerodynamic database.

Manuscripts included in this thesis

No manuscripts included.

Research involving Human or Animal Subjects

No animal or human subjects were involved in this research.

**Statement of Parts of the Thesis Submitted to Qualify for the Award
of Another Degree**

None.

Financial Support

This research was supported by an Australian Government Research Training Program Scholarship and a University of Queensland Candidate Development Award.

Acknowledgements

For Kaitlin, with love to my family and friends, and utmost gratitude to my advisors; Ingo Jahn, Michael Kearney, and Michael Smart.

Keywords

airbreathing propulsion, scramjets, hypersonics, access-to-space, small satellite launchers, airbreathing launch systems

Australian and New Zealand Standard Research Classification (ANZSRC)

ANZSRC code: 090107 Hypersonic Propulsion and Hypersonic Aerodynamics, 20%

ANZSRC code: 090106 Flight Dynamics, 10%

ANZSRC code: 090108, Satellite, Space Vehicle and Missile Design and Testing, 25%

ANZSRC code: 090104 Aircraft Performance and Flight Control Systems, 15%

ANZSRC code: 010303 Optimisation, 30%

Fields of Research (FoR) Classification

FoR code: 0901, Aerospace Engineering, 100%

CONTENTS

List of figures	xxvi
List of tables	xxix
Nomenclature	xxx
1 Introduction	1
1.1 Research Goals	5
1.2 Thesis Outline and Contributions	7
2 Background	11
2.1 Small Satellite Launchers	13
2.2 Scramjets	15
2.3 The Launch System Design Process	17
3 Literature review	21
3.1 Hypersonic Airbreathing Launch Systems and Trajectories	22
3.1.1 Single Stage Airbreathing Launch Systems	23
3.1.2 Two-Stage Launch Systems	30
3.1.3 Three-Stage Launch Systems	42
3.2 Hypersonic Vehicle Return and Glide Trajectories	45
3.3 The SPARTAN	48
3.4 Optimal Control	52
3.4.1 Shooting Methods	54
3.4.2 Collocation Methods	55
3.5 Available Optimal Control Solvers	59

CONTENTS

3.6	Aerodynamic Analysis	60
3.6.1	Cart3D	62
3.7	Summary	62
4	Launch System Design and Modelling	65
4.1	The Second Stage Scramjet Accelerator	67
4.1.1	The Scramjet Accelerator	67
4.1.2	Thermal Protection	69
4.1.3	Propulsion	69
4.1.4	Aerodynamics	73
4.1.5	Trimmed Aerodynamic Database of the Scramjet Accelerator with Engine-On	83
4.1.6	Trimmed Aerodynamic Database of the Scramjet Accelerator with Engine-Off	83
4.2	The First Stage Rocket	85
4.2.1	The Aerodynamics of the First Stage Rocket and Scramjet Accelerator . . .	87
4.3	The Third Stage Rocket	89
4.3.1	Geometry	91
4.3.2	Fuel Tank Sizing	92
4.3.3	Heat Shield Sizing	92
4.3.4	Propulsion	93
4.3.5	Aerodynamics	96
4.3.6	Thrust Vectoring	96
4.4	Modelling and Design Simplifications	98
4.4.1	Control	98
4.4.2	Staging Effects	100
4.4.3	Mass Model Simplifications	101
4.5	Summary	102
5	Trajectory Modelling and Optimisation	103
5.1	Mission Definition	104
5.2	Vehicle Simulation	105
5.2.1	Equations of Motion	106
5.3	Optimal Control Problem Structure	107
5.3.1	Trajectory Connection Points	109
5.3.2	I. First Stage Vertical Ascent	110
5.3.3	II. First Stage Pitching Ascent	111
5.3.4	III. Second Stage Ascent Trajectory	112
5.3.5	IV. Second Stage Return Trajectory	114
5.3.6	V. Third Stage Powered Ascent	115

5.3.7	VI. Third Stage Unpowered Ascent	116
5.3.8	VII. Third Stage Hohmann Transfer	116
5.4	Optimal Solution Analysis	118
5.5	The Optimisation Process in LODESTAR	120
5.6	Trajectory and Performance Analysis	122
5.7	Summary	123
6	Optimised Ascent Trajectory	125
6.1	Case 1: Constant Dynamic Pressure Trajectory	127
6.2	Case 2: Optimised Ascent Trajectory	130
6.3	Case 2: Modelling of Uncertainties	139
6.4	Energy Usage Analysis	140
6.5	Sensitivity Analysis	143
6.5.1	Case 3: Maximum Dynamic Pressure Sensitivity	143
6.5.2	Case 4: Scramjet Accelerator Drag Sensitivity	145
6.5.3	Case 5: C-REST Specific Impulse Sensitivity	146
6.5.4	Case 6: Scramjet Accelerator Mass Sensitivity	147
6.5.5	Case 7: Scramjet Accelerator Fuel Mass Sensitivity	149
6.5.6	Case 8: Third Stage Mass Sensitivity	150
6.5.7	Case 9: Third Stage Specific Impulse Sensitivity	151
6.5.8	Case 10: Third Stage Drag Sensitivity	153
6.6	Comparison of Design Parameters	153
6.7	Summary	156
7	Optimised Trajectory Including Fly-Back	159
7.1	Case 11: Optimised Ascent Trajectory with Scramjet Accelerator Return	160
7.2	Ascent Trajectory	161
7.3	Fly-Back Trajectory	167
7.4	Case 11: Modelling of Uncertainties	169
7.5	Case 11: Aero thermal Heating Analysis	169
7.6	Energy Usage Analysis	169
7.7	Design Sensitivity Analysis	171
7.7.1	Case 12: Maximum Dynamic Pressure Sensitivity with Fly-Back	172
7.7.2	Case 13: Scramjet Accelerator Drag Sensitivity with Fly-Back	174
7.7.3	Case 14: C-REST Specific Impulse Sensitivity with Fly-Back	175
7.7.4	Case 15: Scramjet Accelerator Mass Sensitivity with Fly-Back	176
7.7.5	Case 16: Scramjet Accelerator Fuel Mass Sensitivity with Fly-Back	177
7.7.6	Case 17: Third Stage Mass Sensitivity with Fly-Back	178

CONTENTS

7.7.7	Case 18: Third Stage Specific Impulse Sensitivity with Fly-Back	179
7.8	Comparison of Design Parameters with Fly-Back	180
7.9	Summary	182
8	Conclusions	187
9	Recommendations for future work	193
References		195
Glossary of Key Terms		215
A	Thermal Analysis	221
A.1	Heat Transfer Calculation	221
A.2	Transient Thermal Analysis and Boundary Conditions	223
A.3	Thermal Analysis of the Optimised Trajectory With Fly-Back	224
A.4	Thermal Protection Exploration	228
A.4.1	Scramjet Accelerator TPS Design Exploration	228
A.4.2	Heating limited Trajectory	229
A.4.3	Third Stage Heat Shielding Design Exploration	232
A.4.4	The Effects of a Pull-Up on the Third Stage Heat Shield Design	232
A.5	Summary	233
B	Modelling Uncertainties	235
B.1	Aerodynamic and Propulsion Simulation Uncertainties	236
B.1.1	Aerodynamic Uncertainty	236
B.1.2	Propulsion System Uncertainties	239
B.1.3	Quantification of Aerodynamic and Propulsion Uncertainty Effects	240
B.2	Atmospheric Variations	241
B.2.1	Seasonal and Solar Cycle Based Variations	241
B.2.2	Localised Variability	243
C	Examples and Verification	245
C.1	Example - Brachistochrone Problem	245
C.2	Example - Space Shuttle Reentry	246
C.2.1	Problem Formulation	247
C.2.2	Unconstrained Result	248
C.2.3	Heating Rate Limited Result	250
C.3	Optimised Trajectory Analysis	251

C.3.1	Mesh History	251
C.3.2	Verification	252
D	Modelling and Simulation	257
D.1	Propulsion Interpolation Scheme	257
D.2	Scramjet Accelerator Flow Results	258
D.3	Cart3D Mesh	259
D.4	Performance of the Scramjet Accelerator During Fly-Back	260
E	Alternate Trajectory Cases	263
E.1	Trajectory With Variation in Return Drag	263
E.2	Maximum Payload-To-Orbit Trajectory With Dynamic Pressure Constraint	263
E.3	Constant Dynamic Pressure Trajectory with Fly-Back	264
E.4	Sonic Boom Ground Effects	267
E.5	Alternate Launch Location	268
F	Trajectory Plot Comparisons	275
F.1	Optimised Ascent Trajectory Comparisons With No Fly-Back	276
F.1.1	Case 3: Maximum Dynamic Pressure Sensitivity Comparison	276
F.1.2	Case 4: Scramjet Accelerator Drag Sensitivity Comparison	278
F.1.3	Case 5: Scramjet Accelerator Specific Impulse Sensitivity Comparison	280
F.1.4	Case 6: Scramjet Accelerator Mass Sensitivity Comparison	282
F.1.5	Case 7: Scramjet Accelerator Fuel Mass Sensitivity Comparison	284
F.1.6	Case 8: Third Stage Mass Sensitivity Comparison	286
F.1.7	Case 9: Third Stage Specific Impulse Sensitivity Comparison	288
F.1.8	Case 10:Third Stage Drag Sensitivity Comparison	290
F.2	Optimised Ascent Trajectory Comparisons With Fly-Back	292
F.2.1	Case 12: Dynamic Pressure Sensitivity Comparison	292
F.2.2	Case 13: Scramjet Accelerator Drag Sensitivity Comparison	295
F.2.3	Case 14:scramjet accelerator Specific Impulse Sensitivity Comparison	298
F.2.4	Case 15: Scramjet Accelerator Mass Sensitivity Comparison	301
F.2.5	Case 16: Scramjet Accelerator Fuel Mass Sensitivity Comparison	304
F.2.6	Case 17: Third Stage Mass Sensitivity Comparison	307
F.2.7	Case 18: Third Stage Specific Impulse Sensitivity Comparison	310
G	Viscous Drag Variation	313

LIST OF FIGURES

1.1	The SPARTAN scramjet-powered accelerator[35].	4
2.1	Comparison of Blue Origin and SpaceX partially-reusable launch systems with existing and historic launch systems[38].	11
2.2	The trajectory of the Falcon Heavy[39].	12
2.3	The trajectory of the Ariane featuring Adeline[44].	13
2.4	A simple schematic of a scramjet engine[67].	16
2.5	Characteristic performance for airbreathing and rocket engines with Mach number[68].	16
2.6	The general design process flow for a launch vehicle, adapted from Blair et al[72] . .	18
3.1	An example airbreathing flight corridor of an airbreathing launch vehicle[69].	23
3.2	An illustration of the optimised maximum range trajectory of a hypersonic vehicle[88].	47
3.3	The elevons of the SPARTAN[12].	49
3.4	The scramjet accelerator of the SPARTAN, as designed by Preller[32].	49
3.5	The flight trajectory of the SPARTAN. a) shows the physical trajectory and b) shows the forces on the vehicle and performance indicators.	50
3.6	The third stage rocket of the rocket-scramjet-rocket launch system[12].	51
3.7	The third stage trajectory of the SPARTAN launch system[32].	52
3.8	A comparison of single shooting and multiple shooting[97].	55
3.9	Examples of h and p collocation methods[97].	56
3.10	Comparison of optimisation techniques[88]. A hypersonic vehicle is optimised for maximum range. The hp-adaptive method can be observed to have produced the most optimal result.	58
3.11	The Skylon spaceplane, simulated using Cart3D at $Mach\ 12.189$, $\alpha = 7.512^\circ$ [148]. Cell distribution produced by mesh adaptation is shown.	63

LIST OF FIGURES

4.1	The launch process of the rocket-scramjet-rocket launch system, presented in simplified form.	66
4.2	The representative launch system, top view, showing the scramjet accelerator and first stage.	67
4.3	The representative launch system, side view, showing the scramjet accelerator and fuel tanks, along with the third and first stages.	67
4.4	The external features of the scramjet accelerator.	68
4.5	The locations of conditions relevant to C-REST engine simulation.	70
4.6	Flow conditions after the conical shock generated by the vehicle nose cone as a function of flight Mach number and angle of attack. Figure a) shows the Mach number, b) shows the pressure ratio, and c) shows the temperature ratio following the conical shock, at the engine inlet.	71
4.7	Specific impulse of the C-REST engines with input temperature and Mach number. Available data points are indicated. M_1 and T_1 are the inlet Mach number and temperature, as shown in Figure 4.5.	72
4.8	Operable equivalence ratio of the C-REST engines with input temperature and Mach number. Available data points are indicated.	73
4.9	Fuel mass flow rate with varying flight conditions. Conditions are shown only up to 50kPa dynamic pressure.	74
4.10	The process for generating aerodynamic databases.	75
4.11	Surface triangulation of the scramjet accelerator, generated using Pointwise[156].	76
4.12	The convergence of a Cart3D simulation of the scramjet accelerator at Mach 6, 2° angle of attack.	77
4.13	View of the scramjet accelerator surface triangulation showing engine outlet boundaries.	78
4.14	The total thrust output of the scramjet accelerator, including the CRESTM10 database, and Cart3D nozzle and boat tail simulations.	79
4.15	The specific impulse of the scramjet accelerator, including the C-rest database, and Cart3D nozzle and boat tail simulations.	80
4.16	Viscous drag coefficient across various Mach numbers.	81
4.17	Centre of gravity positions for various flight conditions.	82
4.18	The forces on the scramjet accelerator during flight.	82
4.19	Scramjet accelerator model showing control surfaces.	83
4.20	Flap deflection required for trim of the scramjet accelerator. Negative is flap up.	84
4.21	Engine-on Cart3D simulation at Mach 6, 2° angle of attack, and 25km altitude.	85
4.22	The aerodynamic coefficients of the scramjet accelerator with the C-REST engines powered-on at 30km altitude. Coefficients correspond to a reference area of 62.77m ² and a centre of gravity of 15.24m (full of fuel, with third stage).	86

4.23	Cart3D flow result for the scramjet accelerator with engine off, at Mach 6, 2° angle of attack.	87
4.24	Aerodynamic Characteristics of the scramjet accelerator with C-REST engine powered-off at an altitude of 30km. Coefficients correspond to a reference area of 62.77m ² and a centre of gravity of 15.16m (no third stage, no fuel).	88
4.25	Unstarted scramjet engines at mach 3, 2° angle of attack.	89
4.26	Cart3D result for the scramjet accelerator and first stage vehicles at Mach 2, -1° angle of attack.	89
4.27	The aerodynamic characteristics of the first and second stage stack. Coefficients correspond to a reference area of 62.77m ² .	90
4.28	Thrust vector moment balancing of the first stage.	91
4.29	The third stage rocket, showing major internal features.	91
4.30	Variation in thrust coefficient of thrust with area ratio[167].	96
4.31	Aerodynamic characteristics of the third stage rocket, for a reference area of 0.95m ² .	97
4.32	Thrust vector moment balancing of the third stage.	98
5.1	Sun synchronous orbit illustration, passing over the equator at the same time each day[181].	104
5.2	Approximate location of the ELA launch site. Image from Google maps.	105
5.3	The Earth-fixed components of the geodetic rotational coordinate system.	107
5.4	Illustration of the phases of the launch profile. Controlled and uncontrolled phases are distinguished.	109
5.5	The Hohmann transfer manoeuvre. ΔV indicates a velocity change due to a burn.	117
5.6	The process of the rocket-scramjet-rocket trajectory optimisation. Relevant sections are indicated in square brackets at each process step.	121
6.1	Maximum payload-to-orbit trajectory path with the scramjet accelerator flying at constant dynamic pressure (Case 1). Initial heading angle 91.4°.	127
6.2	The first stage trajectory of the launch system, with the scramjet accelerator constrained to flight at constant dynamic pressure (Case 1).	129
6.3	The constant dynamic pressure flight path of the scramjet accelerator (Case 1).	131
6.4	The third stage trajectory of the launch system, with the scramjet accelerator constrained to flight at constant dynamic pressure (Case 1).	132
6.5	The optimised maximum payload-to-orbit trajectory of the launch system (Case 2).	133
6.6	The optimised maximum payload-to-orbit trajectory of the launch system under power of the first stage rocket (Case 2).	134
6.7	The optimised maximum payload-to-orbit trajectory of the scramjet accelerator (Case 2). XXX Change no of DP in all traj figures	136

LIST OF FIGURES

6.8	Net I_{sp} contours for the scramjet accelerator at Mach numbers from 5-9, showing flight conditions for an optimised trajectory with no constraints (Case 2) and a constant dynamic pressure trajectory (Case 1).	137
6.9	The specific impulse of the C-REST engines, plotted for inlet temperature (T_1) and inlet Mach number (M_1). Data points are shown in black.	137
6.10	The third stage trajectory of the launch system flying the maximum payload-to-orbit trajectory (Case 2).	138
6.11	The sensitivity of the key design parameters of the launch system.	154
7.1	Maximum payload-to-orbit trajectory path with the inclusion of scramjet accelerator fly-back (Case 11).	160
7.2	The first stage of the optimised maximum payload-to-orbit trajectory with scramjet accelerator fly-back (Case 11).	162
7.3	The acceleration of the scramjet accelerator flying an optimised maximum payload-to-orbit trajectory with scramjet accelerator fly-back (Case 11).	163
7.4	Net I_{sp} contours for the scramjet accelerator at Mach numbers between 5.5 and 8.5, showing the optimised trajectory path (Case 11).	164
7.5	The third stage trajectory of an optimised maximum payload-to-orbit trajectory with scramjet accelerator fly-back (Case 11).	165
7.6	The fly-back trajectory of the scramjet accelerator flying an optimised maximum payload-to-orbit trajectory (Case 11).	166
7.7	The sensitivity of the key design parameters of the launch system, including scramjet accelerator fly-back. Red and green coloured areas indicate decreases or increases in the magnitude of sensitivity respectively, compared to the sensitivity study without scramjet accelerator fly-back in Section 6.6.	181
A.1	The locations chosen for thermal analysis, selected for the potential of high heat loading.	222
A.2	Temperature time histories on the scramjet accelerator.	225
A.3	Temperature time histories on the third stage rocket with time.	226
A.4	Comparison of scramjet accelerator trajectories with varying stagnation point heating limits.	231
B.1	The probability density distribution of optimised payload-to-orbit values over the range of LHC determined samples.	241
B.2	Variation in temperature and density in the 1976 U.S Standard Atmosphere Model[154]. Arrows indicate lowest and highest mean monthly values obtained at any location, and dashed lines indicate one-percent extremes.	242
C.1	The solution to the Brachistochrone problem, solved in GPOPS-2[120].	246

C.2	The maximum crossrange trajectory solution of the unconstrained shuttle reentry problem.	249
C.3	The control and heating solution of the unconstrained shuttle reentry problem.	249
C.4	The maximum crossrange trajectory solution of the constrained shuttle reentry problem.	250
C.5	The control and heating solution of the constrained shuttle reentry problem.	251
C.6	The mesh history of each phase of the optimised, maximum payload-to-orbit trajectory with scramjet accelerator fly-back (Case 11). The phases are shown as follows: a) first stage rocket, b) scramjet accelerator acceleration, c) scramjet accelerator fly-back and d) third stage.	252
C.7	The Hamiltonian time history of each phase of the maximum payload-to-orbit optimised trajectory, with scramjet accelerator fly-back (Case 11).	253
C.8	The error between the integrated dynamics of the system, and the solution states of each phase of the maximum payload-to-orbit optimised trajectory, with scramjet accelerator fly-back (Case 11). Normalised to the range of each state.	254
C.9	The error between the forward simulated states, and the solution states of each phase of the maximum payload-to-orbit optimised trajectory, with scramjet accelerator fly-back (Case 11). Normalised to the range of each state.	255
D.1	The transformation to a normalised interpolation scheme.	257
D.2	CART3D flow result for the scramjet accelerator, at Mach 1.1, 6° angle of attack.	258
D.3	CART3D flow result for the scramjet accelerator, at Mach 3, 6° angle of attack.	259
D.4	Adapted mesh of the scramjet accelerator at Mach 6 3° angle of attack.	259
D.5	Adapted mesh around the scramjet accelerator and first stage vehicles, flying at Mach 2, -1° angle of attack.	260
D.6	The performance of the scramjet accelerator during the boost phase. Light blue indicates that the scramjet engines are turned on.	261
E.1	The first stage trajectory of the representative launch system flying a maximum payload-to-orbit trajectory, constrained to 50kPa between Mach numbers 6 to 8.	265
E.4	The ground track of a payload-to-orbit optimised trajectory including scramjet accelerator return flight, with the scramjet accelerator constrained to 50kPa dynamic pressure during ascent.	265
E.5	The payload-to-orbit optimised third stage trajectory including scramjet accelerator return flight, with the scramjet accelerator constrained to 50kPa dynamic pressure during ascent.	266
E.2	The scramjet accelerator trajectory of the representative launch system flying a maximum payload-to-orbit trajectory, constrained to 50kPa between Mach numbers 6 to 8.	270

LIST OF FIGURES

E.3	The third stage trajectory of the launch system flying a maximum payload-to-orbit trajectory, constrained to 50kPa between Mach numbers 6 to 8.	271
E.6	The level of population annoyance with increasing overpressure.	272
E.7	The sonic boom overpressure on the ground, for the optimised trajectory path (Case 11).	272
E.8	The optimised maximum payload-to-orbit trajectory of the launch system launching onto a southerly orbit, from Streaky Bay.	273
F.1	Comparison of scramjet stage ascent trajectories with variation in the maximum dynamic pressure of the representative launch system.	276
F.2	Comparison of third stage rocket ascent trajectories with variation in the maximum dynamic pressure of the representative launch system.	277
F.3	Comparison of scramjet stage ascent trajectories with variation in the drag of the scramjet accelerator.	278
F.4	Comparison of third stage rocket ascent trajectories with variation in the drag of the Scramjet Accelerator.	279
F.5	Comparison of scramjet accelerator ascent trajectories with variation in the specific impulse of the scramjet accelerator.	280
F.6	Comparison of third stage rocket ascent trajectories with variation in the specific impulse of the scramjet accelerator.	281
F.7	Comparison of scramjet accelerator ascent trajectories with variation in the mass of the scramjet accelerator.	282
F.8	Comparison of third stage rocket ascent trajectories with variation in the mass of the scramjet accelerator.	283
F.9	Comparison of scramjet accelerator ascent trajectories with variation in the fuel mass of the scramjet accelerator.	284
F.10	Comparison of third stage rocket ascent trajectories with variation in the fuel mass of the scramjet accelerator.	285
F.11	Comparison of scramjet accelerator ascent trajectories with variation in the mass of the third stage.	286
F.12	Comparison of third stage rocket ascent trajectories with variation in the mass of the third stage.	287
F.13	Comparison of scramjet accelerator ascent trajectories with variation in the specific impulse of the third stage.	288
F.14	Comparison of third stage rocket ascent trajectories with variation in the specific impulse of the third stage.	289

F.15 Comparison of scramjet accelerator ascent trajectories with variation in the drag of the third stage.	290
F.16 Comparison of third stage rocket ascent trajectories with variation in the drag of the third stage.	291
F.17 Comparison of scramjet accelerator ascent trajectories with variation in the maximum dynamic pressure of the scramjet accelerator.	292
F.18 Comparison of third stage rocket ascent trajectories with variation in the maximum dynamic pressure of the scramjet accelerator.	293
F.19 Comparison of scramjet accelerator return trajectories with variation in the maximum dynamic pressure of the scramjet accelerator.	294
F.20 Comparison of scramjet accelerator ascent trajectories with variation in the drag of the scramjet accelerator.	295
F.21 Comparison of third stage rocket ascent trajectories with variation in the drag of the scramjet accelerator.	296
F.22 Comparison of scramjet accelerator return trajectories with variation in the drag of the scramjet accelerator.	297
F.23 Comparison of scramjet accelerator ascent trajectories with variation in the specific impulse of the scramjet accelerator.	298
F.24 Comparison of third stage rocket ascent trajectories with variation in the specific impulse of the scramjet accelerator.	299
F.25 Comparison of scramjet accelerator return trajectories with variation in the specific impulse of the scramjet accelerator.	300
F.26 Comparison of scramjet accelerator ascent trajectories with variation in the mass of the scramjet accelerator.	301
F.27 Comparison of third stage rocket ascent trajectories with variation in the mass of the scramjet accelerator.	302
F.28 Comparison of scramjet accelerator return trajectories with variation in the mass of the scramjet accelerator.	303
F.29 Comparison of scramjet accelerator ascent trajectories with variation in the fuel mass of the scramjet accelerator.	304
F.30 Comparison of third stage rocket ascent trajectories with variation in the fuel mass of the scramjet accelerator.	305
F.31 Comparison of scramjet accelerator return trajectories with variation in the fuel mass of the scramjet accelerator.	306
F.32 Comparison of scramjet accelerator ascent trajectories with variation in the mass of the third stage.	307

LIST OF FIGURES

F.33 Comparison of third stage rocket ascent trajectories with variation in the mass of the third stage.	308
F.34 Comparison of scramjet accelerator return trajectories with variation in the mass of the third stage.	309
F.35 Comparison of scramjet accelerator ascent trajectories with variation in the specific impulse of the third stage.	310
F.36 Comparison of third stage rocket ascent trajectories with variation in the specific impulse of the third stage.	311
F.37 Comparison of scramjet accelerator return trajectories with variation in the specific impulse of the third stage.	312
G.1 Comparison of scramjet accelerator ascent trajectories with variation in the viscous drag of the scramjet accelerator.	315
G.2 Comparison of third stage ascent trajectories with variation in the viscous drag of the scramjet accelerator.	316
G.3 Comparison of scramjet accelerator return trajectories with variation in the viscous drag of the scramjet accelerator.	317

LIST OF TABLES

2.1	A selection of the small satellite launchers which are operational or in development	14
3.1	Single-stage airbreathing launch systems.	25
3.2	Two-stage airbreathing launch systems.	39
3.3	Three-stage airbreathing launch systems.	44
3.4	Summary of programs capable of pseudospectral optimisation.	60
4.1	Mass breakdown of the modified scramjet accelerator vehicle.	68
4.2	First Stage Engine Properties[165].	86
4.3	Mass breakdown of the third stage rocket.	92
4.4	Third stage fuel distribution.	92
4.5	Third stage heat shield properties.	93
4.6	Comparison of upper stage rocket engines, sourced primarily from the Encyclopedia Astronautica reference website[165].	94
5.1	Segment coupling conditions for combined trajectory optimisation.	111
5.2	Optimisation setup of the first stage phase.	112
5.3	Optimisation setup of the second stage ascent. * This is only used in the constant dynamic pressure simulation.	113
5.4	Optimisation setup of the second stage return.	114
5.5	Optimisation setup of the third stage powered ascent.	115
6.1	Summary of the key results from a maximum payload-to-orbit trajectory with the scramjet accelerator constrained to 50kPa (Case 1).	128
6.2	A summary of key results from the maximum payload-to-orbit trajectory (Case 2). .	135

LIST OF TABLES

6.3	The uncertainty margins associated with the aerodynamic and propulsive modelling (copy of Table B.1, see Appendix 6.3 for details).	140
6.4	An energy usage breakdown of the ascent trajectories, both with, and without, the scramjet accelerator constrained to constant dynamic pressure (Cases 1 & 2). The energy expenditures of each phase are shown, with blue indicating a 'productive' energy usage, whereas red indicates energy 'wastage'.	141
6.5	Comparison of key trajectory parameters with variation in the maximum dynamic pressure of the scramjet accelerator (Case 3).	144
6.6	Comparison of key trajectory parameters with variation in the drag of the scramjet accelerator (Case 4).	145
6.7	Comparison of key trajectory parameters with variations in the specific impulse of the C-REST engines (Case 5).	146
6.8	Comparison of key trajectory parameters with variation in the structural mass of the scramjet accelerator (Case 6).	148
6.9	Comparison of key trajectory parameters with variation in the fuel mass of the scramjet accelerator (Case 7).	149
6.10	Comparison of key trajectory parameters with variation in the mass of the third stage (Case 8).	150
6.11	Comparison of key trajectory parameters with variation in the third stage specific impulse (Case 9).	152
6.12	Comparison of key trajectory parameters with variation in the drag of the third stage (Case 10).	153
7.1	Selected trajectory conditions for a maximum payload-to-orbit trajectory including scramjet accelerator fly-back (Case 11).	161
7.2	An energy usage breakdown of the ascent trajectories, both with, and without, scramjet accelerator fly-back (Cases 11 & 2). Blue indicates a 'productive' energy usage, whereas red indicates energy 'wastage'. Negative energy indicates energy being supplied.	170
7.3	Comparison of key trajectory parameters with variation in the maximum dynamic pressure of the scramjet accelerator, with fly-back (Case 12).	173
7.4	Comparison of key trajectory parameters with variation in the drag of the scramjet accelerator, with fly-back (Case 13).	174
7.5	Comparison of key trajectory parameters with variation in the specific impulse of the C-REST engines, with fly-back (Case 14).	175
7.6	Comparison of key trajectory parameters with variation in the structural mass of the scramjet accelerator, with fly-back (Case 15).	177

7.7	Comparison of key trajectory parameters with variation in the fuel mass of the scramjet accelerator, with fly-back (Case 16).	178
7.8	Comparison of key trajectory parameters with variation in the mass of the third stage, with fly-back (Case 17).	179
7.9	Comparison of key trajectory parameters with variation in the specific impulse of the third stage, with fly-back (Case 18).	180
A.1	Inner surface temperatures in kelvin on the shroud of the scramjet accelerator with variations in heat shielding properties.	229
A.2	Maximum inner surface temperature with a constant rate of heat transfer away from the inner surface of the shroud.	229
A.3	Scramjet stage stagnation point heating limited trajectories, optimised for maximum payload-to-orbit with stagnation point heating calculated using a cold wall approximation.	230
A.4	Inner face temperatures in kelvin with variations in third stage heat shielding properties.	232
A.5	Summary of a payload-to-orbit optimised trajectory with a 46.2kg third stage heat shield.	232
B.1	The uncertainty margins associated with the aerodynamic and propulsive modelling of the representative launch system in this study. Values are shown to the significant figure accuracy reported by their source.	240
B.2	Optimised trajectory properties with atmospheric uncertainty variations.	243
C.1	Optimisation setup of the Brachistochrone problem.	246
E.1	A summary of key results from the maximum payload-to-orbit trajectory, constrained to 50kPa between Mach numbers 6 to 8.	264
E.2	A summary of key trajectory parameters of the maximum payload-to-orbit trajectory launched in a southerly direction.	269
G.1	Summary of key trajectory parameters with scramjet accelerator viscous drag variation.	314

Nomenclature

XXXX Format, put in alphabetical order, add space before subscripts t = Time (s)

\mathbf{x}	=	State Variables	\mathbf{u}	=	Control Variables
q	=	Dynamic Pressure (Pa)	H	=	Hamiltonian
λ	=	Costate Variables	ψ	=	Equality Constraint Function
b	=	Bound Constraint Values	λ	=	Inequality Constraint Function
J	=	Total Cost Functional	I_{sp}	=	Specific Impulse (s)
M	=	Mach Number & Endpoint Cost Function	P	=	Pressure (Pa)
F	=	Force (N)	ρ	=	Density (kg/m^2)
R	=	Gas Constant ($8.314 \text{ JK}^{-1}\text{mol}^{-1}$)	D	=	Drag (N)
L	=	Lift (N) & Integrated Cost Function	C_L, C_D	=	Aerodynamic Coefficients
ξ	=	Longitude (rad)	ϕ	=	Latitude (rad) & Equivalence Ratio
ζ	=	Heading Angle (rad)	v	=	Speed (m/s)
A	=	Reference Area (m^2)	g	=	Gravitational Acceleration at Earth's Surface (m/s^2)
r	=	Radius from Earth Centre (m)	γ	=	flight path angle (rad)
ω	=	Angular Velocity (rad/s)	a	=	Acceleration (m/s^2)
m	=	Mass (kg)	T	=	Thrust (N) & Temperature (K)
w_{cap}	=	Capture Width	α	=	Angle of Attack (rad)
η	=	Efficiency	KE	=	Kinetic Energy (J)
PE	=	Potential Energy (J)			
<i>Subscripts</i>					
E	=	Earth	1	=	1 st Stage Rocket
2	=	2 nd Stage Scramjet Vehicle	3	=	3 rd Stage Rocket
\rightarrow	=	Stage Transition	0	=	Initial
f	=	Final	a, b	=	Nominal Stage Numbers
LOX	=	Liquid Oxygen	LH2	=	Liquid Hydrogen
AoA	=	Angle of Attack	e	=	Exit
SL	=	Sea Level	atm	=	Atmospheric
vac	=	Vacuum	LEO	=	Low Earth Orbit
r	=	Radial	t	=	Tangential
p	=	Propulsive	I-VII	=	Trajectory Phases

CHAPTER 1

INTRODUCTION

XXX check velocity vs speed while im reading, and before oral

XXX put all table labels above

In recent years, the space sector has seen a significant shift in the paradigm of space launch system design. The sector has moved towards privatisation, with new and innovative launch systems competing to offer the most cost-efficient and reliable launches. The sector has also seen a split between those who produce large satellite launchers and those who produce small satellite launchers. For large payload launchers, reusability is a major focus in the design of new launch systems, with the purpose of making a launch system cost efficient over multiple launches[5]. For small payload launchers, reusability is more complex than for large launchers, as the additional systems necessary for reusability add a larger fraction of system mass, and require a proportionally larger fuel mass. Consequently, the focus of small launch system design is currently on producing expendable launch systems as cheaply and efficiently as possible, using state of the art technologies such as 3D printing to expedite the process and minimise cost[6]. However, if reusability is able to be successfully integrated into small launch system design, it has the potential to increase the cost efficiency and launch flexibility, potentially opening up the small satellite market significantly.

A potential candidate for integrating reusability into small satellite launch systems is the use of airbreathing engines[7, 8]. Airbreathing engines produce higher specific impulse than rockets, and do not require oxidiser to be carried on-board a launch vehicle[9]. The higher efficiency and reduced propellant mass of airbreathing vehicles allows the additional mass of the systems necessary for reusability to be mitigated[10]. An airbreathing vehicle can be designed in a similar fashion to a conventional aircraft, with wings, stabilisers and ailerons[11, 12]. A vehicle designed in this fashion has a high lift-to-drag ratio, and good manoeuvrability, allowing for a return flight and landing on a conventional landing strip[12]. This style of return removes the need for transport, enabling a fast turn-around and cost-efficient re-use.

CHAPTER 1. INTRODUCTION

The primary airbreathing engines in consideration for launch vehicles are ramjet and scramjet engines, and rocket-based combined cycle engines that combine multiple engine cycles for operation over a wider range of flight conditions[13, 14]. These engines offer good efficiency and have operational regimes that allow them to effectively accelerate a launch vehicle over a range of Mach numbers. Ramjets and scramjets rely on the high speed of the aircraft to compress the flow of air entering the engine before combustion. Ramjets slow the air to subsonic speeds before combustion and are limited to operation at low Mach numbers, whereas scramjets keep the flow supersonic throughout, and operate within the hypersonic regime, above Mach 5. These engines have limited operational regimes, and require atmospheric flight in order to take oxidiser from the air. These operational constraints mean that a launch system cannot be solely powered by airbreathing engines. Rocket power is necessary for at least the exoatmospheric portion of the trajectory. As a result, the designs of airbreathing launch systems require rocket stages to reach orbit[7], and if high-speed airbreathing engines are used in the launch system, rocket power is also desirable for accelerating scramjet accelerator to minimum operational speed, as the alternative is using different types of lower-speed airbreathing engines sequentially[7], which is weight and cost intensive.

These various propulsion systems may all be integrated into a single stage-to-orbit spaceplane that is capable of launching, placing payload in orbit, reentering, and returning to a suitable landing site[15–22]. Alternatively, they may be separated into multiple stages, similarly to typical, fully rocket-based launch systems[23–32]. Single stage-to-orbit launch vehicles are fully-reusable, and have the potential to be extremely cost-efficient, if they are able to be reused for many missions[33]. However, their development cost is likely to be very high, and they are generally suited for launching large amounts of payload-to-orbit[15–22], a market which is now extremely competitive thanks to the relatively recent advent of large, partially reusable, rocket-based launch systems. Multi-stage airbreathing launch systems, however, have the potential to bring cost-efficient reusability to small payload launchers[12], particularly if they are able to stage at high speeds[33]. Airbreathing systems scale more efficiently than rockets, meaning that the systems needed for reusability in a small launcher do not require the launcher system to be dramatically increased in size, one of the primary limitations on reusability in small rocket-based launch systems. For this reason, partially-reusable two and three-stage airbreathing launch systems are being investigated for small satellite launch[12]. To date, two-stage launch systems have primarily been studied over three-stage launch systems, however, three stage launchers have recently been espoused as potentially offering advantages in reusable mass and mass-to-orbit efficiency[12].

There are as of yet no airbreathing launch systems that have progressed past the research and very early design stages[15–32]. The development and analysis of trajectories is a crucial part of this early design process, and is a complex task for an airbreathing launch system to ensure that the launch system is able to survive launch and fly with maximum efficacy. A trajectory must be calculated that allows the launch system to achieve its objective of placing the maximum payload into orbit, while

recovering any reusable stages and adhering to the structural, thermal and propulsive limitations of the vehicle[34]. In order to maximise the efficiency of the launch system, and thus the payload-to-orbit, there are complex trade-offs in the performance of the launch system that must be taken into account: the airbreathing engines of a ramjet or scramjet-powered stage require high dynamic pressure to operate effectively, and airbreathing stages are generally designed for high lift-to-drag. Conversely, rocket-powered stages operate more efficiently at higher altitude, and are generally designed for weight and cost efficiency. For airbreathing launch systems, the various distinct operation modes and phases involved during launch require trade-offs in engine efficiency and thrust generation, stage mass, and vehicle aerodynamics. These factors result in a complex flight path that does not follow simple design rules for optimal efficiency, requiring advanced trajectory studies to ensure that the launch vehicle is operating effectively.

For single-stage-to-orbit airbreathing launch systems, trajectories have been developed and studied in detail[15–22], in particular due to a multitude of studies in the 1980s and 90s, the most prominent of which was the National Aerospace Plane (NASP), which led, in part, to the Hyper-X program and the X-43 flight experiment[33]. These studies show complex trade-offs that occur in a maximum efficiency airbreathing vehicle trajectory, including trade-offs between the operational efficiencies of the various engine modes. These trajectories often show flight at maximum dynamic pressure or maximum thermal loading, to maximise the efficiency of the airbreathing engines, before a pull-up to orbit, sometimes initially under airbreathing power. These trajectory analyses generally assume that return is possible, due to the high speed and manoeuvrability of the vehicles allowing flexible reentry, and their on-board low-speed engines allowing propulsion and cruise in-atmosphere.

Compared to single-stage airbreathing systems, multi-stage airbreathing launch system trajectories are far more complex, with even more complex trade-offs between the operational modes due to these modes being separated into mechanically distinct stages[34]. The trajectories of two-stage-to-orbit airbreathing launch systems that have been studied generally exhibit constant dynamic pressure flight to maximise the operation of the airbreathing engines, and a pull-up at the end of the airbreathing trajectory. The return trajectories of two-stage-to-orbit launch systems are generally performed under cruise power, utilising turbojet, or sometimes ramjet engines[23, 25, 29, 30], or land at a point downrange[26]. There is considerable disparity between studies over whether constant dynamic pressure flight is optimal, and if a pull-up under airbreathing power is optimal[23–32]. No studies have attempted a detailed investigation into the trade-offs between the stages, and the optimal trajectory is not well understood. For three-stage-to-orbit launch systems the launch trajectory is more complex again, due to there being two separation points at which to consider trade-offs, and each stage generally only having a single engine type. Three-stage-to-orbit systems are by far the least studied of the airbreathing launcher configurations, and have to this point only been designed around prescribed trajectory shapes that constrain the hypersonic airbreathing stages to constant dynamic pressure[31, 32]. It is currently unknown what the optimal trajectory shape for a three-stage launcher is, whether

it is possible to return the second stage of a launch system of this type to its initial launch location, and how the design of the launch system may affect the trajectory shape. The presence of a first-second stage separation, high second-third stage separation speeds, lack of low speed engines on the second stage, and small third stage rocket make the calculation of an optimal trajectory shape for a three-stage airbreathing launcher a unique problem, with extremely complex trade-offs. The study of two-stage-to-orbit trajectories is somewhat useful in this regard, however, the disparity between the various studies that have been conducted, and the absence of inquiry into the performance of the launch system stages, means that detailed investigation of the trajectories of multi-stage vehicles is needed.



Figure 1.1: The SPARTAN scramjet-powered accelerator[35].

This work aims to expand our knowledge on the operation of airbreathing launch systems by developing and analysing optimal trajectories for a partially-reusable rocket-scramjet-rocket small satellite launch system. For this study a representative launch system is produced, based on the design of the SPARTAN launch system under development by The University of Queensland and Hypersonix[12]. Optimised trajectories are developed using modern and robust optimal control theory techniques that are able to calculate the optimised trajectory profile for a launch vehicle in a robust and computationally efficient manner, allowing a trajectory to be calculated in which the flight path of each individual stage is considered simultaneously to produce a maximum-payload trajectory[36]. Optimal control is able to produce an optimised trajectory that satisfies the specific structural and flight constraints of the vehicle being simulated, allowing the physical limitations of the vehicle, such as heating and structural loading limits, to be imposed[36]. This work gives insights into the trade-offs between the rocket and airbreathing stages that are unique to this type of launch system. This manner of optimal trajectory analysis allows for generalities to be made about the nature of the trajectory shape, and for the performance of the launch system to be investigated in order for the understanding of this type of launch system to be improved. This trajectory analysis is intended to both aid in the ongoing design process of multi-stage launchers, by characterising the performance needs of a rocket-scramjet-rocket launch system throughout its trajectory, as well as to stand on its

own merit by indicating the best possible trajectory shape for this type of launch system.

1.1 Research Goals

The aim of this work is to expand the knowledge and understanding of airbreathing launch systems and their operation, through the development and analysis of optimised trajectories for a three-stage airbreathing launch system.

XXXX This is an important part to check with ingo, and compare with my intros to the various sections (thermal particularly)

This aim will be achieved by addressing the following research goals:

1. *Generate new knowledge in regards to the optimal trajectory shape of a three-stage airbreathing launch system flying to space, through the development of a robust and representative maximum efficiency trajectory.*

A representative launch system design will be developed, along with a robust vehicle simulation and trajectory optimisation toolkit. Maximum efficiency trajectories will be produced, and investigated in detail to provide insights into the optimal operation of a three-stage airbreathing launch system.

2. *Improve the understanding of the viability of reusability in airbreathing launch systems, through an investigation of the impact of airbreathing stage fly-back on the optimised trajectory for a three-stage airbreathing launch system.*

The vehicle simulation and optimisation toolkit will be expanded to include the capability to fly-back. Maximum efficiency trajectories will be generated with fly-back included, and these will be compared and contrasted to the trajectories without fly-back. A thermal analysis will be conducted to improve the understanding of the aerothermal effects of the maximum efficiency trajectory on the launch system.

3. *Expand the understanding of how design affects the performance of airbreathing launch systems.*

Key design parameters will be varied, and maximum efficiency trajectories produced for each design variation. The performance effects will be studies and compared, to give insights into the relative magnitude effects of the key design parameters studied.

CHAPTER 1. INTRODUCTION

4. *Explore the effects of design variations on the maximum efficiency trajectories of airbreathing launch systems, including stage-stage interactions.*

The maximum efficiency trajectories generated for the key design parameter variations will be studied and compared, to analyse the sensitivity of the optimised trajectories and investigate the stage-stage interaction phenomena under design variations.

1.2 Thesis Outline and Contributions

Chapter 2 - Background

Contextual background is presented to frame the objectives of this work. To inform on the current developments in the industry, details are provided on the current state of space launch systems, with a particular focus on small satellite launchers. An overview of scramjet engines is provided to illustrate their potential advantages, followed by an outline of the launch system design process to position this work within the conceptual and preliminary design space.

Chapter 3 - Literature Review

A review of literature related to the various aspects of this study is presented. A review of the designs and trajectories of partially-airbreathing launch systems is presented, comparing various single-stage, two-stage and three-stage conceptual vehicles. It is determined that the optimal flight path for a multi-stage airbreathing launch system has not been well defined, and that for three-stage vehicles the optimal flight path has not been investigated. The SPARTAN launch vehicle is presented in detail, as the most well defined three-stage airbreathing launch system design. The fly-backs and maximum-range trajectories of multiple hypersonic launch systems and gliders are investigated to determine the feasibility of return and the possible trajectory characteristics. To facilitate the development of an optimised trajectory, an overview of optimal control techniques is presented, with particular emphasis on the pseudospectral method of solving optimal control problems, which is employed within this study. Lastly, the available methods of aerodynamic analysis are analysed, and details of Cart3D, the fluid dynamics analysis tool that is used in this study, are presented.

Chapter 4 - Modelling of Launch System Dynamics

The design of a representative three-stage launch system is presented, and the aerodynamics and engine models of all three stages are detailed. The scramjet accelerator stage based on the SPARTAN is presented first, followed by the first and third stages. The design of each stage is shown, along with sizing and mass breakdowns. The propulsion model used for each stage is detailed, along with the modelling and interpolation schemes used. The aerodynamic characteristics and simulation methodology of each stage is presented, and the process for trimming each vehicle is specified. Finally, the modelling simplifications present in the design are discussed.

Chapter 5 - Trajectory Modelling and Optimisation

The method used for the simulation and optimisation of the trajectory is presented, including the details of the trajectory analysis program, LODESTAR, that has been developed for this study. The specifics of the optimal control methodology are presented. The simulation methodology is detailed, along with the construction of the optimal control simulation for the mission used in this study. The specific set-up of the optimal control program is detailed for each trajectory stage, specifying the costs and constraints that drive the optimal control solver. Finally, the methods for analysing and validating the final solutions are specified.

Chapter 6 - Optimised Ascent Trajectory

Maximum payload-to-orbit optimised trajectories for the representative launch system, calculated using LODESTAR, are presented. These trajectories represent the first optimised trajectories that have been developed for a three-stage airbreathing launch system. A trajectory is designed in which the scramjet accelerator is constrained to flight at a constant dynamic pressure, for comparison to prior work. Next, a maximum payload-to-orbit trajectory is created and it is found that an increase in altitude at the stage separation points significantly improves payload-to-orbit. This trajectory is compared and contrasted to the constant dynamic pressure trajectory to determine the sources of the performance increase. Crucial performance parameters are analysed, including the energy usage of each stage of the launch system, the first time that a multi-stage airbreathing launch system trajectory has been analysed to this level of detail. Key vehicle design parameters are varied, and the trends in maximised payload-to-orbit and trajectory shape are analysed to study the relative impact of the design parameters on the performance of the launch system.

Chapter 7 - Optimised Trajectory Including Fly-Back

The trajectory of the launch system is optimised for maximum payload-to-orbit, including the fly-back of the scramjet accelerator to its initial launch location. This trajectory represents the first time that the fly-back of a stage under scramjet power has been modelled, and the first time that the optimised trajectories of a three-stage system have included fly-back. It is found to be necessary to reignite the scramjet engines during the return flight, and the scramjet accelerator is found to bank during acceleration to lessen the fuel consumed during fly-back. The trajectories with, and without, fly-back are compared to determine the impact of scramjet accelerator fly-back on the performance of the launch system, along with key performance parameters. In a similar fashion to Chapter 5, the effects of vehicle parameters on the optimised trajectory are studied. The sensitivity of the optimised trajectory and payload-to-orbit are analysed, with emphasis on how the fly-back trajectory is affected by the varied vehicle parameters.

Conclusions and Recommendations

The body of this thesis concludes by summarising the most significant findings from this work. Recommendations for future work are made.

CHAPTER 2

BACKGROUND

The progress of launch system technologies over the last 60 years has been rapid. From the early vehicles based on intercontinental ballistic missile technology such as the Thor based launch systems, capable of launching 40-400kg to LEO in the 1950s, to the more modern Atlas V based systems of the 2000s capable of launching 9750-18500kg to LEO[37]. The materials, propulsion technology,

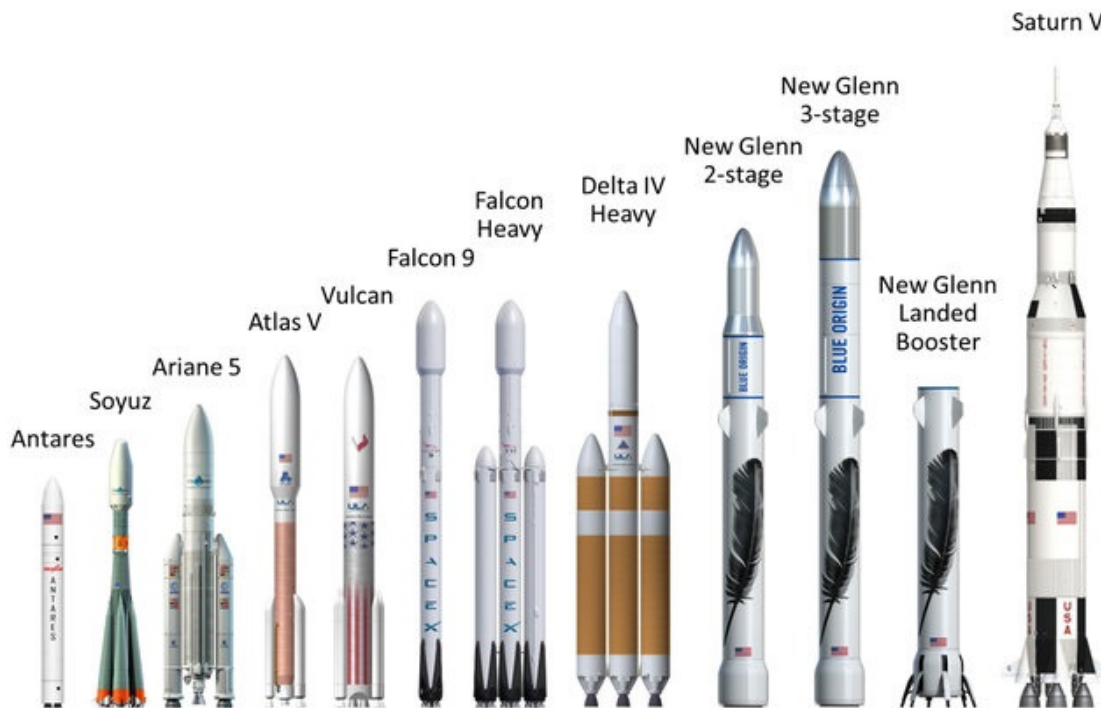


Figure 2.1: Comparison of Blue Origin and SpaceX partially-reusable launch systems with existing and historic launch systems[38].

aerodynamics and guidance algorithms have all improved significantly, enabling rockets to become

CHAPTER 2. BACKGROUND

more efficient, cheaper to produce, and more reliable. As the demand for satellite launches grows, and the cost of development of launchers becomes cheaper, the potential for profiting from space launches increases. This has driven a large portion of the space flight industry to move towards privatisation, with a heavy focus on reusable technology.

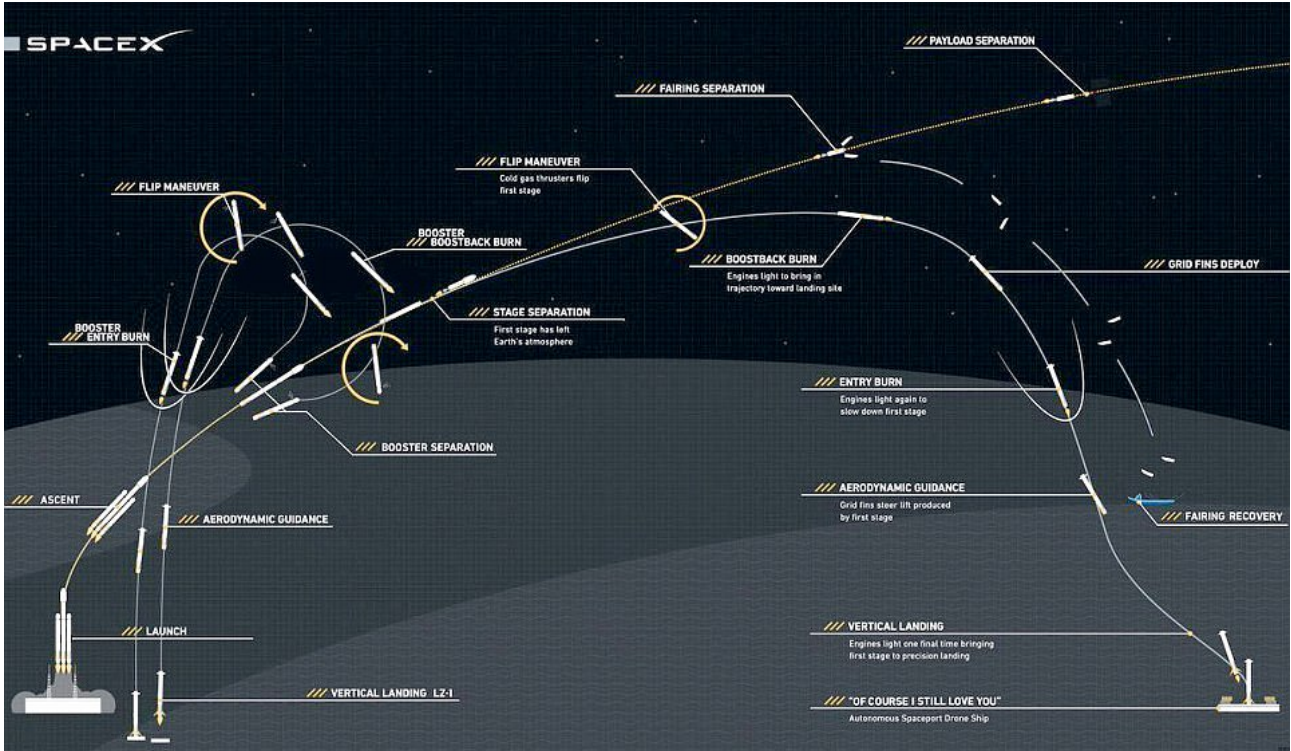


Figure 2.2: The trajectory of the Falcon Heavy[39].

Reusable launch technology has been possible for many years, in the form of the space shuttle. However, the space shuttle was weighed down by large launch costs and operational complexity, and was not a commercial success[40]. Recently, reusable launchers have become the focus of many of the largest private launch companies, as reusability becomes more achievable due to technological advances[41, 42]. The SpaceX Falcon 9 and Falcon Heavy have been demonstrated on multiple occasions, landing booster stages successfully, and re-flying reused boosters multiple times[41]. In the near future the Blue Origin New Glenn is planned[41], with potentially the Airbus Adeline to follow (to be used on the Ariane 6)[43]. The Falcon and New Glenn launchers are large rockets, and are shown in Figure 2.1 in a size comparison with other, expendable rocket systems, including the Ariane 5, which is projected to be similarly sized to the Ariane 6.

The purpose of reusing launch vehicles is to reduce the cost-over-time of the reused components drastically, which subsequently allows the cost of individual launches to be reduced[45]. Reducing costs lowers the barrier of entry for space launches, potentially improving the diversity of space-based enterprises. Reusing launch system components also allows faster turnaround times for launches, as refurbishment of stages is much faster than manufacturing stages from scratch. Reduced turnaround

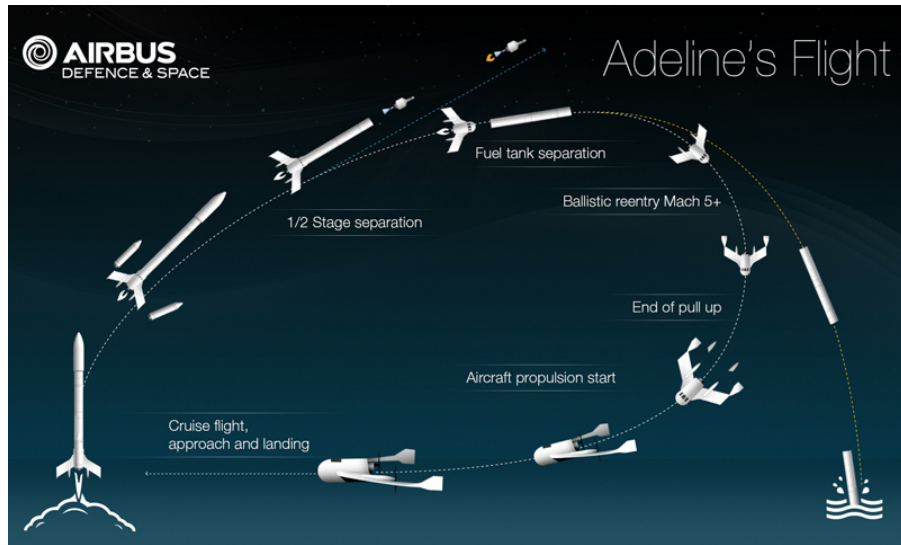


Figure 2.3: The trajectory of the Ariane featuring Adeline[44].

times are key for improving mission scheduling, allowing satellites to be launched more rapidly, on a more flexible time frame. For a launch vehicle to be reusable, it must necessarily have the ability to come back to Earth safely, without damage to major system components. In addition, it is preferable for the vehicle to return to its initial launch site, to reduce the cost and time necessary for transport. The trajectories of the Falcon Heavy and Adeline are shown in Figures 2.2 and 2.3, illustrating two radically different approaches to reusability; the exoatmospheric manoeuvre and booster-deceleration of the Falcon; and the in-atmospheric fly-back of the Adeline, which only recovers the engine component of the system. While these reusability approaches use different technologies, they are aiming to achieve the same thing: the recovery of a significant portion of the launch system, with as much of the launch system as possible returned to the initial launch location. These return flights require the addition of system components, which allow the reusable stage to fly to a specified landing point. Control surfaces[46], structural components[47], additional fuel[47], and in the case of the Adeline, additional engines[43], must be incorporated within the reusable launch vehicle designs. The additional weight that these components contribute further increases the fuel and structural mass necessary to initially accelerate the reusable stage. The impact of reusability on the mass and cost of the vehicle is minimised when the velocity at the initiation of the return trajectory is decreased. Because of this mass increase on any stage which is to be designed to be reusable, most current reusable launch vehicle designs include only reusable first stages, with later stages being expendable.

2.1 Small Satellite Launchers

The vast improvements in computational technologies in recent years have allowed satellites to decrease in size and cost to a large degree. These factors have lowered the barrier of entry into small

Launcher	Company	Country	Payload Capacity	Cost/Kg (USD)	Availability	Stages & Propulsion	Reusability
Electron[49]	RocketLab	NZ/USA	150Kg to SSO	\$32,600	Available	Rocket-rocket	No
Bloostar[50]	Zero2Infinity	Spain	100kg to SSO	\$40,000	-	Balloon-rocket-rocket-rocket	No - Partial Planned
Eris[48]	Gilmour Space Technologies	Aus/SG	380kg to LEO	\$23,000-38,000	Q4 2020		No
Intrepid-1[51]	Rocket Crafters	USA	376kg to SSO	\$23,936	Q1 2019	Rocket-rocket	No
KZ-1A[52]	CASIC	China	250kg to SSO	-	-	Rocket-rocket	No
Vector-H[53]	Vector Space Systems	USA	160kg to LEO	\$21,875	2018	Rocket-Rocket-(Third rocket optional)	No
SMILE[54]	NLR	EU	50kg	<\$50,000	-	-	-
Firefly α [55]	Firefly Aerospace	USA	630kg to SSO	-	2019	Rocket-Rocket	No
LauncherOne[56]	Virgin Orbit	UK	300kg to SSO	\$33,000	-	Aircraft-rocket-rocket	Aircraft
XS-1[57]	Boeing	USA	-	-	-	-	First Stage
500R[58]	Orbital Access	UK	500kg to SSO	-	-	Aircraft-Rocket	Fully Reusable

Table 2.1: A selection of the small satellite launchers which are operational or in development.

satellite manufacturing significantly, driving a surge in the demand for small satellite launches. Many private and public companies are currently developing small satellite launchers, that will allow small satellites to be launched into bespoke orbits on schedules determined by the customer[5]. The details of a selection of the most promising or innovative of the small satellite launchers currently in active development is shown in Table 2.1. Many of these launchers are projected to be available within the next few years, and will offer cost-per-kg comparable to piggybacking on larger launches. These small satellite launch systems are mostly expendable, aiming to reduce costs by creating a launch system which is as cost-efficient as possible to produce and launch[6]. This often entails making use of conventional, well-tested designs, combined with state of the art manufacturing techniques, such as 3-D printing[6, 48]. This method allows for rapid development, although it has an intrinsic cost limit due to the requirement of manufacturing a new launch system for each launch.

If small satellite launch systems are able to be designed to be reusable, the cost of launch would be able to be brought down further. However, designing a small satellite for reusability is more complex than for a larger rocket system. The systems used to manoeuvre exoatmospherically and decelerate like the Falcon or New Glenn, or fly-back like the Adeline, take up a relatively higher mass margin as the size of the launcher decreases. This in turn increases the mass of the launcher, including the structural mass as well as the fuel and oxidiser mass, relative to other launchers that are targeting the same payload mass range. If a mass and cost efficient, design for a reusable small satellite launcher is to be produced, it is likely that a technology must be developed that is specifically geared towards small satellite launch. One of the most promising technologies currently under development that may enable reusable small satellite launch systems is high speed airbreathing engines[59], in particular the hypersonic scramjet engine. These engines produce high fuel efficiency and utilise atmospheric oxygen as oxidiser, potentially mitigating the mass inefficiencies caused by the reusability-enabling systems in small launch systems.

2.2 Scramjets

A Scramjet, or supersonic combustion ramjet, is an airbreathing engine design that combusts air at supersonic speeds and is capable of high Mach number operation. Across their operating range, scramjets offer much higher specific impulse than rockets, and require significantly less propellant mass[60, 61]. Scramjets compress air without moving parts, using geometry changes within the engine[62], as well as on the forebody of the vehicle to create inlet shocks which provide the compression required for combustion[63]. After combustion, the combustion products are expanded through a thrust nozzle, schematically shown in Figure 2.4. This is similar in operation to a ramjet engine, though a scramjet does not generate a normal shock, allowing supersonic air to enter the combustor. Maintaining supersonic speeds throughout the engine allows scramjets to operate efficiently at Mach numbers of 5 and greater. Scramjets were proposed in the 1940's[64] and found to be capable of positive net thrust

in 1993[65], but have yet to be developed to a level which would allow for commercial application. Though scramjets are still in-development, the potential advantages which they offer over rockets for certain applications are driving their development in a number of institutions[66].

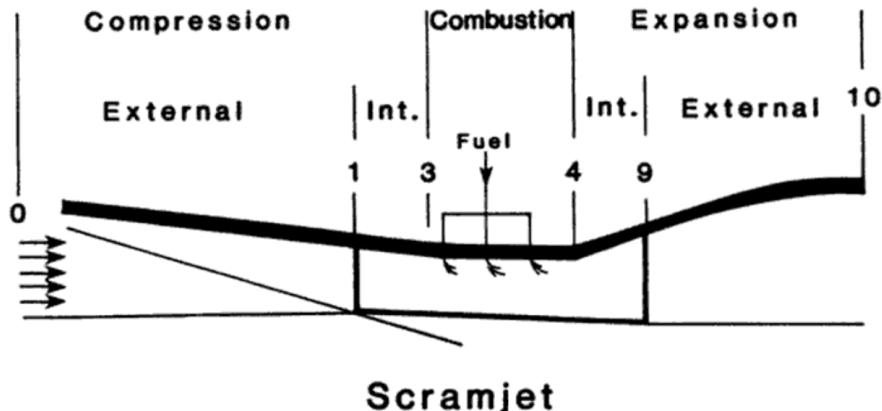


Figure 2.4: A simple schematic of a scramjet engine[67].

Scramjet engines are suitable for a number of applications where sustained flight or acceleration is desired at high Mach numbers. The high efficiency of scramjet engines, and the lack of needing to carry oxidiser on-board, means that significantly less propellant is used during flight compared to rocket engines, and consequently, that a much smaller fraction of a scramjet-powered vehicle consists of propellant mass[10]. The smaller fuel mass fraction of a vehicle powered by scramjet engines mitigates the mass of the vehicle systems, allowing features such as wings, control surfaces, landing gear, and passenger transport capabilities to be included in the vehicle design[10].

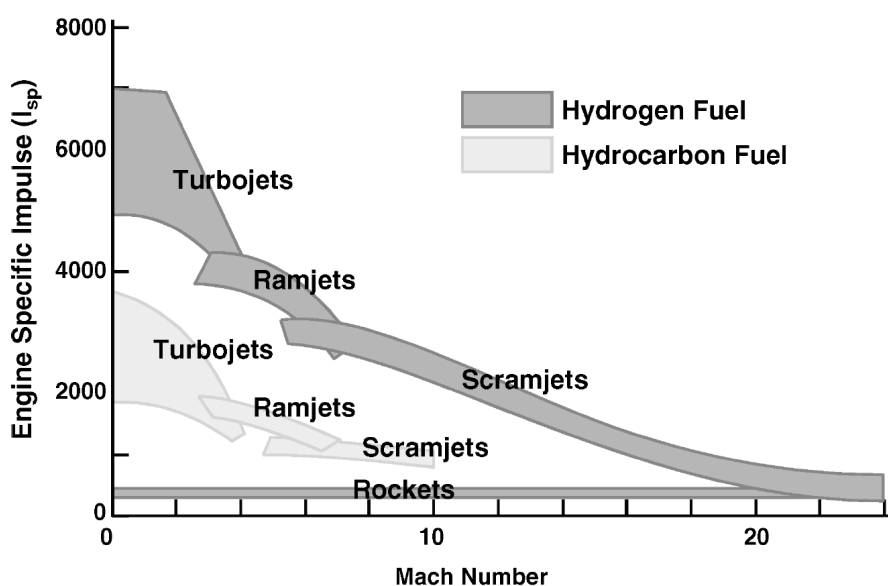


Figure 2.5: Characteristic performance for airbreathing and rocket engines with Mach number[68].

Theoretically, the operable range of scramjets is wide[69]. Scramjets are operable at hypersonic speeds around Mach 5, and the specific impulse of a scramjet decreases with speed until it is equal to rockets around Mach 19[68], as shown in Figure 2.5. However, in practical designs, the operating range for a scramjet engine is far more limited. For a fixed geometry scramjet, the operable region is constrained by the geometries of the forebody of the vehicle, the inlet, and the combustor of the scramjet engine[9]. The Mach number range of a scramjet engine varies by design, but Mach number ranges of 5-10[12], 7-11[70] and 6-10[21] have been suggested as appropriate operable regimes for scramjet-powered launch vehicles. The operable range of scramjet engines can be improved with mechanisms to vary the geometry of the inlet during flight[71]. However, the systems necessary for variable geometry inlets add weight and complexity to the scramjet engine, and can be detrimental to overall system performance[9].

The inclusion of scramjet engines for high efficiency operation in the hypersonic regime may be considerably advantageous for small satellite launch systems. However, the incorporation of these engines within a launch vehicle requires significant additional design complexity over traditional all-rocket systems, due to their unique operational constraint; the requirement to fly in-atmosphere for long periods, at hypersonic speeds. This is a significantly different design philosophy when compared to traditional all-rocket launch systems, which generally want to exit the atmosphere as quickly as possible, and minimise drag losses while doing so. Because of this significant difference in operation, the designs of airbreathing launch vehicles are likely to be radically different from traditional rocket systems. Novel designs must be developed for airbreathing launch systems, that take advantage of the unique advantages offered by airbreathing engines, while overcoming the challenges that they introduce. Currently, the knowledge of how to design launchers incorporating high-speed airbreathing engines is limited, with particular limitations in the understanding of the coupling of the design and the associated trajectory to orbit.

2.3 The Launch System Design Process

The design of any launch system is a complex, multi-faceted process, that involves many areas of engineering and scientific expertise. This work aims to expand the understanding of airbreathing launch system operation through optimal trajectory analysis. Understanding the maximum efficiency trajectory of a launch system and how this interacts with the design is an integral step in the early launch vehicle design. The analysis of a launch system's trajectory enables the designers to understand the performance characteristics and design-trajectory coupling of the launch system, and drives design decisions that are made throughout the development process.

Figure 2.6 illustrates the general design process flow for a launch system as defined by NASA[72], in which the design stages involve a repeated iterative process between the overall launch system de-

sign and compartmentalised design tasks. This compartmentalisation takes place firstly by separating the launch system into its hardware and software subsystems, and then into general areas that define the specifications of the subsystem design (design functions). These areas include;

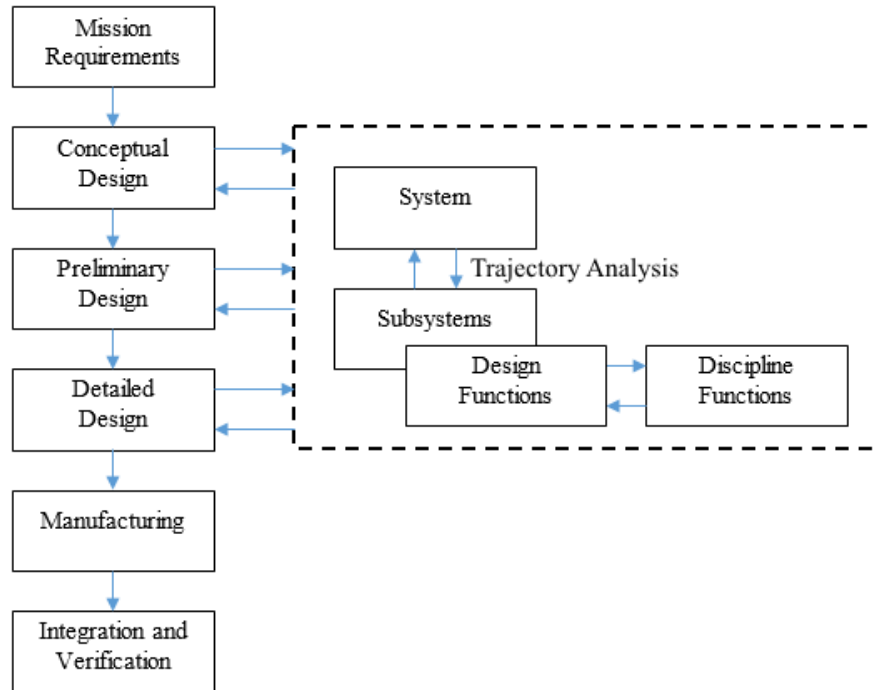


Figure 2.6: The general design process flow for a launch vehicle, adapted from Blair et al[72]

- aerodynamics;
- trajectory, guidance and navigation;
- control;
- structures;
- thermal;
- propulsion;
- avionics;
- materials;
- and manufacturing,

among others[72]. The design is then further compartmentalised into pertinent areas of specific speciality and expertise (discipline functions) that defines the problems that must be solved, and skills that are necessary for low level design

The design of a traditional all-rocket launch system may be compartmentalised relatively easily, and the general shape of rocket launch system trajectories are well-known and relatively easily understood. The primary goals of the trajectory of a rocket-powered launch system are to minimise drag while not exceeding structural and thermal limits, and in general this results in a vertically-launched pitching trajectory, that exits the atmosphere as rapidly as possible while managing velocity at points of maximum structural and thermal stress. The design and design-trajectory coupling of an all-rocket launch system is well understood, and thus the design process for a rocket-powered launch system is able to be separated into independent stages or subsystems relatively easily, with clear design goals.

For an airbreathing launch system, this compartmentalisation is much more difficult, because the design of an airbreathing launch system is much more complex, with significant inter-stage design coupling, and heavy dependencies and trade-offs between the way in which an airbreathing launch system is flown, and its optimal design and performance characteristics. Atmospheric flight of airbreathing stages requires aircraft-style designs for control and stability, and results in complex trade-offs between the performance of the airbreathing engines, and the structural and thermal limitations of each stage. In addition, there is trade-offs between the performance of the various engines that are utilised by airbreathing launch systems, which generally mix airbreathing and rocket engines that have significantly different performance regimes. These trade-offs are specific to the types of engines and number of stages being employed by the launch system, and are closely coupled to the trajectory being flown. The investigation of the ideal launch trajectory of an airbreathing launch system, utilising subsystem models of appropriate fidelities, is an integral step in the early design process. Early trajectory analysis is important for the design of the launcher and its subsystems to be investigated, and for significant performance drivers to be identified early on. This is particularly true because many of the subsystems and technologies necessary to achieve airbreathing space access are in development at an academic level, and advances are necessary in multiple fields before the flight of an airbreathing launch vehicle becomes a reality. The investigation of the trajectory of an airbreathing launch system gives key insights into the design requirements of the launcher and its subsystems, and can drive academic study on the subsystems of airbreathing launchers, such as their propulsion and thermal protection systems, as well as their overall designs. This can be used by designers to inform early designs, and to reduce the number of iterative cycles required during the design process.

CHAPTER 3

LITERATURE REVIEW

The study of airbreathing access-to-space systems has been undertaken in some form since the early days of space flight. The prospect of the efficient, cost effective, and reusable space access that airbreathing launch may provide is enticing, and many man-hours and billions of dollars has been expended researching airbreathing launch vehicles. However, airbreathing launch is yet to be realised, due to the large scientific and engineering challenges involved in sending an object to space using airbreathing propulsion. Research is ongoing across many fields and disciplines to develop the designs of airbreathing launch vehicles, including the designs of subsystems such as engines, thermal protection systems, and control systems that can cope with the unique requirements of sustained hypersonic flight. The design of an airbreathing launch system must be determined with careful consideration of the trajectory that the launch system flies to orbit, because the trajectory of a launch system determines the structural and heating loads that are experienced, as well as the necessary control strategy that must be employed to achieve orbit. Accurate trajectory models are required to elucidate the performance metrics of the launch system, and these initial flight paths are used to guide the design of the launch system.

This section covers the literature available in the areas that are key to developing and analysing the trajectory for a rocket-scramjet-rocket launch system. Firstly, a study is conducted on the airbreathing launch systems that have previously been designed and analysed, along with an analysis of the trajectories of these launch systems that may offer valuable insights into the operations of rocket-scramjet-rocket launch systems. Of particular interest are the trajectories of multi-stage airbreathing launch systems, that give insights into the trajectory features that arise from effects of stage separations. After this, an overview is given of the optimal control methods that may be used to develop efficient trajectories, along with their applicability to launch vehicle trajectories. Lastly, a discussion is presented on the methods of aerodynamic modelling that may be used to develop dynamic models of the launch system, along with a focussed discussion on the Cart3D program, that is used in this

work.

3.1 Hypersonic Airbreathing Launch Systems and Trajectories

Airbreathing access-to-space systems have been investigated in various forms including single-stage, two-stage, and three-stage designs. Of these design forms, single-stage and two-stage designs are by far the most common, with very few three-stage designs having been considered to date. This is partly due to the fact that nearly all of the airbreathing launch systems that have been designed are large launchers, designed to launch payloads of the order of thousands of kilograms to orbit. In large launchers, the additional structural mass that results from the addition of engines or subsystems can be mitigated more effectively than for small launcher form factors. For small satellite launchers, the mass penalties of the systems necessary for airbreathing launch and reusability become more significant, likely necessitating the division of the launcher into separate stages. For dedicated small satellite launch, which has become economically feasible only in recent years, a three-stage rocket-scramjet-rocket launcher system has been suggested as a feasible form factor[12].

For any airbreathing launch system, the design of a trajectory during the early design phases is particularly important. Airbreathing launch systems are typically designed using a combination of rocket and airbreathing engines, that have very different requirements for operation. Rocket engines in general perform well from atmospheric to vacuum conditions, while airbreathing engines require relatively high density air and sustained atmospheric flight for operation, which can cause the structural and thermal limits of the vehicle to come into play[12]. Figure 3.1 shows an example flight corridor for an airbreathing launch vehicle, illustrating the upper limits of dynamic pressure at which the structural limits of the launch vehicle are met, and the lower limit of dynamic pressure at which the airbreathing engines are no longer capable of operation. This brings unique complications, as sustained flight in-atmosphere requires a high lift/drag ratio and results in high structural and thermal loading over long periods, that must be considered during trajectory analysis. In addition, there are a number of interdependent design factors that must be considered during trajectory design including;

- the requirement for the airbreathing stages to fly in-atmosphere;
- the variable efficiency of the airbreathing engines;
- the relative efficiency of the different types of engines within the system;
- the aerodynamic performance of each vehicle or engine-mode of the system;
- and the structural limitations of the system.

These factors cause trade-offs between the stages of the launch system[73], and limit the operational regime of the launch system. These trade-offs are particularly important for a reusable vehicle, where

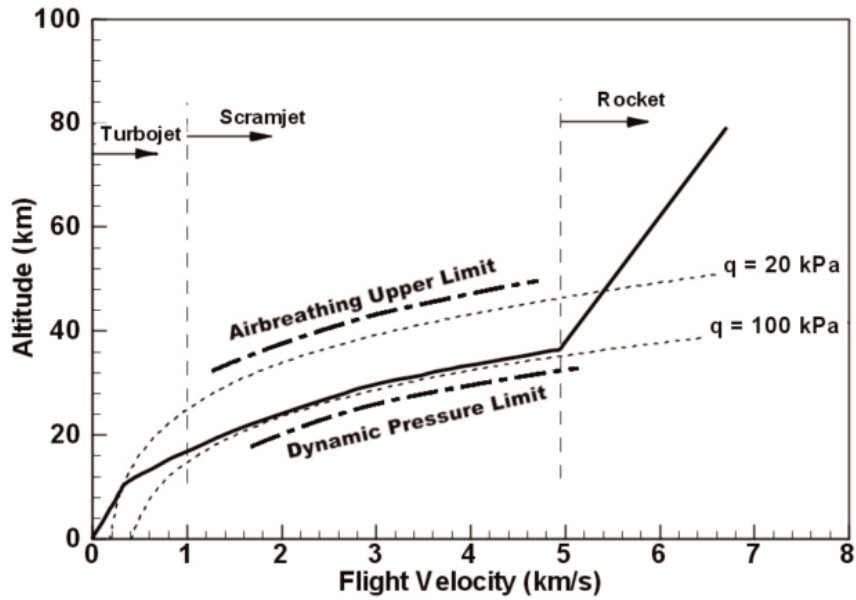


Figure 3.1: An example airbreathing flight corridor of an airbreathing launch vehicle[69].

the viability of returning the vehicle to a suitable landing location must be determined, and the impact of the return trajectory on the launch flight profile must be established. The fly-back can be a high-impact design driver, with the performance of the vehicle relying significantly on an efficient return flight[74, 75].

This study aims to understand the optimal trajectory of a rocket-scramjet-rocket multi-stage launch system, that may be considerably different to other configurations of airbreathing launchers. To this end, this section investigates the designs of all forms of airbreathing launch systems that have been developed, along with their trajectories. The manner in which the design and number of stages of the launch systems influences their trajectories is studied, allowing for some key features of airbreathing launch system trajectories to be identified.

3.1.1 Single Stage Airbreathing Launch Systems

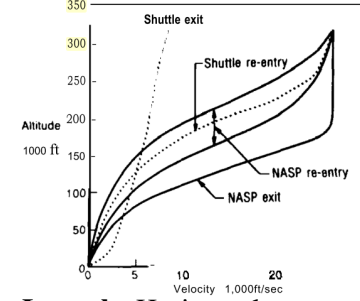
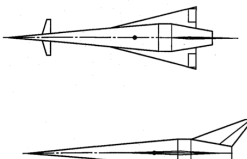
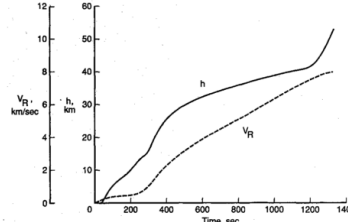
A single stage launch system design aims to achieve space launch with only one vehicle, and generally no separation of mass until payload deployment. Table 3.1 summarises the recent single-stage-to-orbit airbreathing launchers that have been developed as detailed designs, along with their key design and trajectory features.

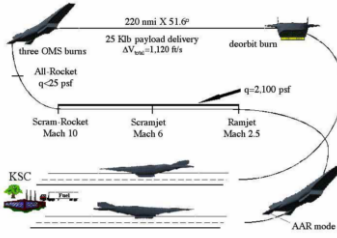
All of the single stage-to-orbit (SSTO) airbreathing launch vehicles that have been studied are designed to be fully reusable. Being fully reusable is the primary attraction of the SSTO spaceplane, and indeed is likely to be the only way in which a system of this type is able to be financially viable. The single-stage form factor is in general convenient for reusability, as the additional structural and sub-

system complexity necessary to facilitate return is mitigated by having only one large vehicle. SSTO vehicles also have the advantage of not needing to stage, saving on the additional system weight and complexity required when staging in atmosphere. However, SSTO launch vehicles are required to accelerate the entire launch system to orbital or near-orbital speeds, and exit the atmosphere completely. This introduces significant complexity to the return flight and reuse of SSTO systems, which are required to re-enter the atmosphere at orbital speeds[76]. This reentry poses significant challenges to the thermal and structural protection and control subsystems of SSTO vehicles, particularly when a primary design driver is cost efficiency. Accelerating an entire launch system to orbit also results in a significant amount of 'dead-weight', ie. subsystems that are designed for use only in a specific part of a launch, that must nonetheless be transported to orbit and back. In particular for airbreathing SSTO systems, this 'dead-weight' derives from the need to carry multiple engines that are switched between during flight. This means that airbreathing SSTO launch systems are generally highly fuel efficient at all stages of flight, but carry heavy engines that are not used in all flight regimes. To mitigate this 'dead-weight', SSTO vehicles are generally powered by rocket-based combined cycle (RBCC) engines which are capable of operating in various airbreathing or air-assisted rocket modes using common engine components, sometimes augmented by turbojet engines for efficient power during launch or return flight. Despite this mitigation measure, the many subsystems required by SSTO launch systems are complex and heavy, and are likely to also be extremely costly. For this reason, all of the SSTO airbreathing launchers that have been investigated are designed for medium-to-large payload launch, and are large, heavy vehicles, with design profiles incorporating many aircraft-like features such as wings, tails and aerodynamic control surfaces.

The ascent trajectories of SSTO airbreathing launch vehicles are significantly different from all-rocket launch systems, due to their airbreathing engines requiring atmosphere to operate, necessitating the launch vehicle spending a large amount of time flying close to horizontal. Most SSTO airbreathing systems are designed to be horizontally launched, under turbojet or rocket-assisted power. The exception to this is the GTX, which launches vertically under rocket power[17, 18]. All of the SSTO vehicles examined follow a constant dynamic pressure trajectory during the majority of airbreathing hypersonic flight, at a low trajectory angle, to allow the efficient operation of their airbreathing engines. Constant dynamic pressure flight is advantageous for an airbreathing accelerator due to the trade-off between structural loading and engine performance[77]. As dynamic pressure increases so does the structural loading on the vehicle, however the performance of a ramjet or scramjet engine is directly reliant on dynamic pressure[77]. A constant dynamic pressure trajectory is viewed as being an acceptable compromise between these two factors when designing a launch vehicle, operating at the dynamic pressure limit of the launch vehicle. Although a constant dynamic pressure trajectory is likely to produce high efficiency flight for the high speed airbreathing portion of an ascent trajectory, there are a variety of factors that must be considered in designing the trajectory of a launch system. For example, a constant dynamic pressure flight may produce suboptimal conditions for the switch

Table 3.1: Single-stage airbreathing launch systems.

Launcher	Design	Trajectory
X-30 (NASP) [76]	<p>Conceived as a technology demonstrator for the NASP program, the X-30 would have been the first airbreathing launch system to be operationally demonstrated, but its program was cancelled prematurely. Many important aspects of the X-30 have not been made public[76] and so details on this vehicle are incomplete.</p>  <ul style="list-style-type: none"> Mass: Designs studied with a range of around 200,000lbs-300,000lbs[76] (90,718.5 - 136,077.7kg). Propulsion: Powered by scramjets with reusable rocket engines or RBCC engines. 	 <ul style="list-style-type: none"> Launch: Horizontal.
Langley Accelerator (NASP) [16, 79, 80]	<p>Developed as a standardised vehicle for single-stage-to-orbit airbreathing launcher studies, the Langley Accelerator was not intended to be an operational concept. The version developed by Powell et al.[16] is presented here.</p>  <ul style="list-style-type: none"> Mass: 136,079kg. Length: 61m. Propulsion: Fully airbreathing in-atmosphere, rockets for circularisation. 	 <ul style="list-style-type: none"> Launch: Horizontal. Trajectory: Maximum dynamic pressure reached as rapidly as possible, and flown until pull-up is performed under the power of the scramjet engines. Return: Coast phase after scramjet shutdown until circularisation by rocket engines.

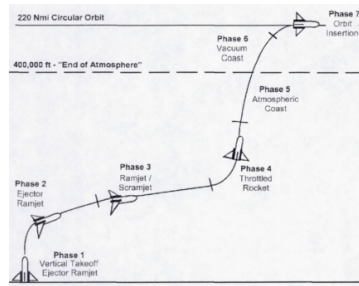
<p>HOTOL[27]</p> <p>The British HOTOL concept was a single-stage-to-orbit spaceplane developed initially as a proof-of-concept study in 1982, but later courted to the ESA as a major project and refused. Funding was withdrawn in 1982 before development could commence.</p>	 <ul style="list-style-type: none"> Payload: 7-10t. Length: 62m. Propulsion: Four Swallow engines, operating in airbreathing mode until 26km altitude, and rocket mode thereafter. 	<ul style="list-style-type: none"> Trajectory: No detailed trajectory information is readily available.
<p>ABLV-GT (Hyper-X)[21, 81]</p> <p>The ABLV-GT was developed by Georgia Tech Space Systems Design Lab as an extension of the ABLV (airbreathing launch vehicle) design study performed by NASA, aiming to develop a conceptual design for a realistic launch vehicle. This vehicle has strong links to the Next Generation Launch Technology Program, a successor to the NASP program, which produced the X-43 test vehicle, the first demonstrator of scramjet operation in free-flight.</p>	 <ul style="list-style-type: none"> Note: X-43A shown as a representative vehicle shape. Mass: 13,520,000lbs Length: 190.5ft. Propulsion: Powered by turboramjet & RBCC engines. 	 <ul style="list-style-type: none"> Launch: Horizontal. Trajectory: Maximum dynamic pressure flight during majority of ram/scramjet operation followed by a pull-up under rocket-augmented scramjet power.

GTx (Trailblazer)[17, 18]

The GTx (formerly Trailblazer) was another offshoot of the ABLV program.



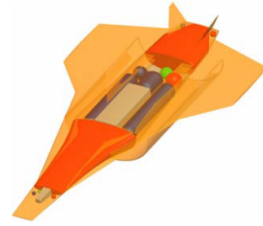
- **Payload:** 25,000lbs.
- **Mass:** 1,252,617lbs.
- **Length:** 263.5ft.
- **Propulsion:** Ramjet-scramjet-rocket propulsion.



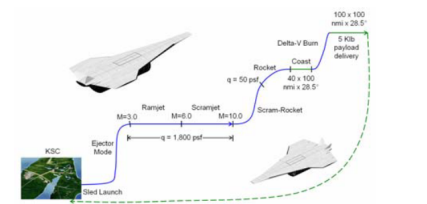
- **Launch:** Vertical.
- **Trajectory:** Flight at maximum dynamic pressure of 2,000psfa (95.76kPa) followed by a pull-up under scramjet power, when the maximum Mach limit of the scramjet is reached. Rocket power is used to accelerate to orbit.
- **Return Trajectory:** Not considered.

Lazarus[20]

The Lazarus concept was developed at the Georgia Institute of Technology Space Systems Design Lab, as an SSTO concept for medium size payload launch, with a secondary purpose of use as a global strike platform.



- **Payload:** 5,000lbs (2,268.0kg)..
- **Mass:** 180,000lbs (81,646.6kg).
- **Length:** 102.8ft (31.3m).
- **Propulsion:** RBCC engines with high energy density material fuel. A sled is used for takeoff, that provides fuel to the RBCC engines.



· **Launch:** Horizontal using sled.

· **Trajectory:** Maximum dynamic pressure flight during airbreathing operation at 1,800psf (86.2kPa). At Mach 10 a pull-up is initiated using combined scramjet-rocket propulsion. At the maximum operable altitude of the scramjet engines, the rocket takes over to accelerate to orbit.

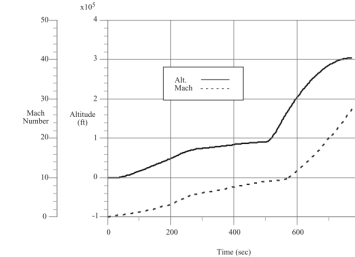
· **Return Trajectory:** Not considered.

Hyperion[22]

The Hyperion was developed by Georgia Tech Space Systems Design Lab, as an assessment of the 'Vision Vehicle' design class, solicited by NASA as part of the Advanced Reusable Technologies Program. Hyperion was conceptualised to assess whether RBCC propulsion and other advanced technologies can significantly reduce the cost of space access.



- **Payload:** 20,000lbs (9,071.8kg) to LEO.
- **Mass:** 800,700lbs (363,191.4kg).
- **Length:** 179ft (54.6m).
- **Propulsion:** Powered by 5 RBCC engines, with return flight supplemented by low-thrust H2 ducted fans.



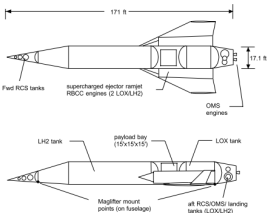
· **Launch:** Horizontal.

· **Trajectory:** Flight at maximum dynamic pressure of 2,000psf (95.76kPa) during airbreathing operation. Pull-up during scramjet operation, with transition to rocket mode during pull-up.

· **Return:** No Return trajectory considered.

Argus[15]

The Argus was a conceptual design intended to be investigated and compared to other classes of launchers to determine cost effective long term solutions to space access.



Payload: 20,000lbs (9071.8kg).

Mass: 597,250lbs (270,908.0kg).

Length: 171ft (52.1m).

Propulsion: Initially accelerated along a maglifter track. Afterwards powered by two RBCC ejector-ramjet engines, with OMS thrusters used for circularisation and manoeuvring on-orbit.

Launch: Horizontal on maglifter track.

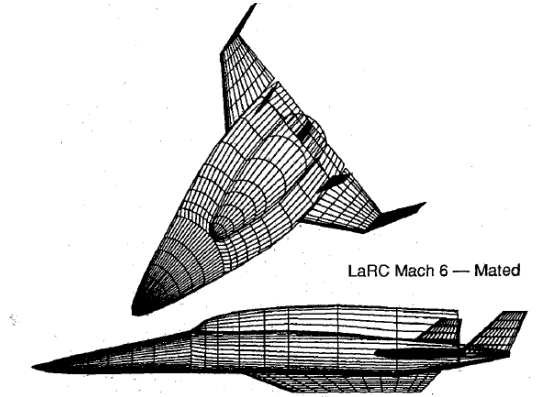
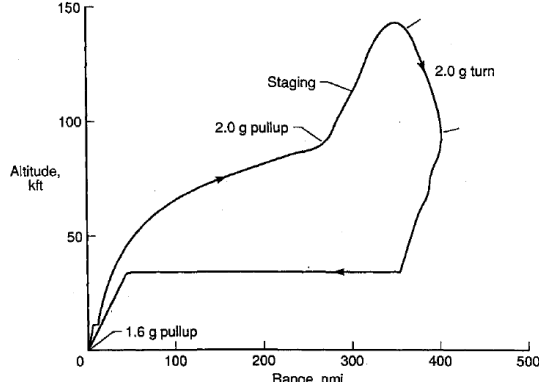
Trajectory: After launch, accelerated using ejector ramjet so that maximum dynamic pressure of 1500psf (71.8kPa) is reached at transition to fan-ramjet mode. At Mach 6, transition to rocket mode occurs for acceleration to parking orbit.

from airbreathing engines to rocket power for exoatmospheric flight. For this reason, most of the vehicles studied then perform a pull-up manoeuvre during airbreathing operation, before or during the transition to rocket-power. At the end of airbreathing operation it is often more optimal for the vehicle to fly at less than maximum dynamic pressure for a time during airbreathing engine operation, allowing the trajectory angle and altitude to be raised before the rocket engines are powered-on. This trajectory shape trades off the performance of the airbreathing engines for altitude before the rocket engines are powered on fully, and has been shown to be the optimal trajectory throughout the studies of the vehicles covered in Table 3.1[15–22], as well as for generic trajectory optimisation studies that do not develop a detailed vehicle design[19, 78, 79]. A pull-up was found to be optimal for vehicles where the rocket engines are not ignited until circularization altitude[16, 79], vehicles where the rocket engine is ignited immediately after airbreathing engine cut-off[17–19] as well as for vehicles that operate in combined scramjet-rocket mode[20, 21]. For SSTO vehicles a pull-up manoeuvre is a trade-off between the altitude at airbreathing engine cut-off and the velocity achievable at cut-off. Due to the entire vehicle being lifted into orbit, this generally becomes a relatively simple problem of engine efficiency. The airbreathing engine is used for its high efficiency, until the dynamic pressure drops below the operable limit of the airbreathing engine, or until the efficiency of the airbreathing engine drops to a level where the use of rocket engines is preferable.

While the SSTO launch systems and trajectory shapes that have been studied have indicated that horizontal flight at close to maximum dynamic pressure, with a period of flight at off-maximum dynamic pressure at some points during the trajectory to trade-off efficiency between flight modes, these analyses of SSTO vehicles can only be indirectly applied to multi-stage vehicles. SSTO vehicles must necessarily carry their whole mass to orbit, due to a lack of stage transitions, and as such may not behave in the same manner as multi-stage vehicles, and may be designed considerably differently. For this reason, the designs and trajectories of multi-stage airbreathing launch systems must be primarily used to inform decisions on the design and optimal flight paths of new multi-stage designs.

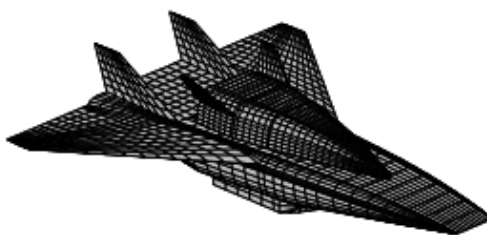
3.1.2 Two-Stage Launch Systems

The most studied alternative to single-stage-to-orbit for an airbreathing launch vehicle is the two-stage-to-orbit configuration. Table 3.2 provides a summary of the TSTO airbreathing launch systems that have gone through a detailed design process, along with their key design and trajectory features. The TSTO configuration generally separates the launch system into an airbreathing or airbreathing/rocket-powered ‘booster’ stage, and a rocket-powered ‘orbiter’ stage. This configuration allows for the separation of the booster stage after the airbreathing engines have ceased to be used. This separation removes a large fraction of the system mass, because airbreathing engines are generally complex and heavy systems. As a consequence of this mass reduction, the rocket engines

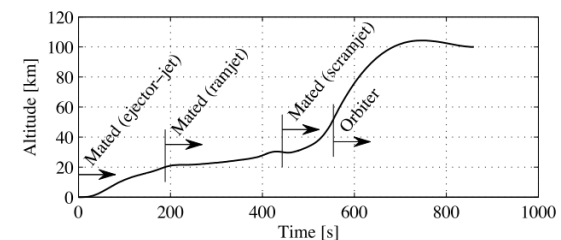
Launcher	Design	Trajectory
<p>LaRC Turboramjet[23]</p> <p>The LaRC boosters were developed by Wilhite et al.[23] in order to test the effects of staging Mach number on a two-stage system. These boosters were studied as part of the NASP program, and were intended only to be used as a representative vehicle for research purposes.</p>	 <p>LaRC Mach 6 — Mated</p> <ul style="list-style-type: none"> Reusability: Fully reusable. Mass: Nominal gross takeoff weight of approximately 360klb (160Mg), although this varies with staging Mach number. Payload: 10,000lbs (4535.9kg) to LEO. Propulsion: First stage propulsion is rocket-turboramjet, second stage propulsion is rocket. 	 <p>Altitude, kft</p> <p>Range, nmi</p> <ul style="list-style-type: none"> Launch: Horizontal. Airbreathing Trajectory: Constrained to maximum dynamic pressure of 1,000psf (47.9kPa) until the staging Mach number of 5.6 or 7 is reached. A pull-up occurs at nominal staging Mach number under ramjet power, to reach the prescribed staging dynamic pressure of 300psf (14.4kPa). Pull-up occurs at a 2g constrained rate. Orbiter Trajectory: Undefined. Return Trajectory: Unpowered turn and deceleration, followed by a turbojet powered cruiseback.

JAXA TSTO Spaceplane[24]

Fujikawa et al.[24] have developed a spaceplane as a feasibility study on TSTO fully-reusable launch for JAXA.



- **Reusability:** Fully-reusable.
- **Propulsion:** First stage RBCC, second stage rocket.
- **Payload:** 800kg.
- **Mass:** Booster 533.8t, orbiter 47.1t.
- **Length:** Booster 38.4m, orbiter 18.8m.



· **Launch:** Horizontal.

· **Airbreathing Trajectory:** Majority of flight is at less than maximum dynamic pressure in order to improve the performance of the RBCC engines due to external nozzle effects. A pull-up is performed during scramjet operation, explained as part of the RBCC performance improvement.

· **Return Trajectory:** Not considered.

NASA Ames TSTO Spaceplane[25]

A TSTO spaceplane was conceptualised by Mehta and Bowles[25], based on a '93 design for the NASP program. This concept was designed to be economically viable launcher, with built-in growth potential.



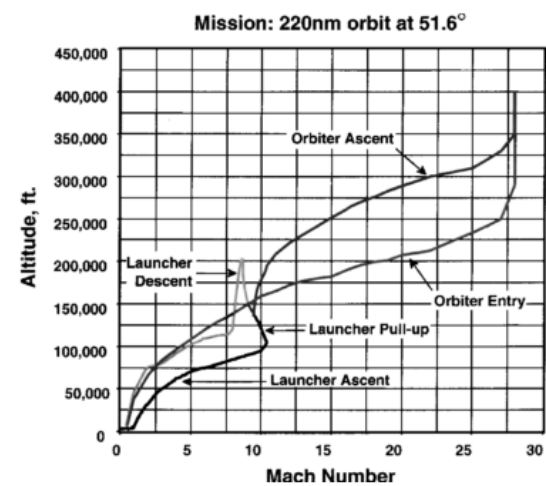
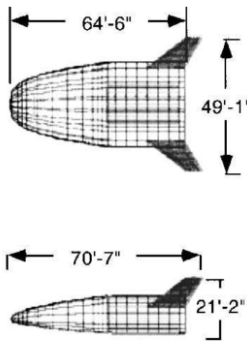
Reusability: Fully reusable.

Payload: 25,000lbs (11,339.8kg).

Propulsion: Booster propulsion system is tubojet/ramjet/scramjet while orbiter has standard LOX/H₂ rocket propulsion.

Mass: Booster: 602,300lbs (27,3198kg), Orbiter: 19,9301lbs (90,401kg).

Length: Booster: 224ft (68.3m), Orbiter: 64.5ft (19.7m).



Launch: Horizontal.

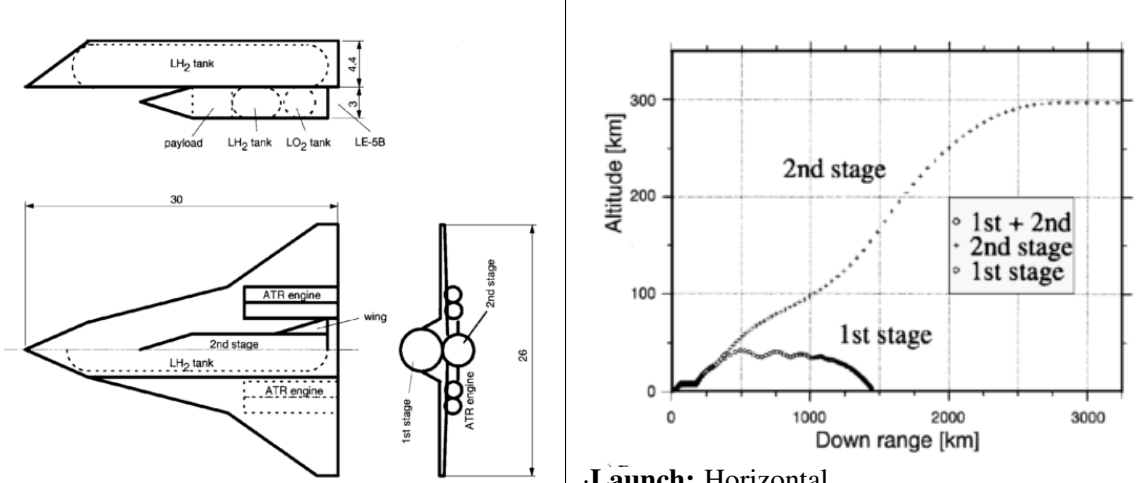
Airbreathing Trajectory: Acceleration before the hypersonic regime is achieved steadily, with an increase in altitude at the transonic 'pinch point' to reduce dynamic pressure. During the hypersonic regime, a constant dynamic pressure of 2100lb/ft² (100.5kPa) until Mach 10. At Mach 10, a 2g pull-up is initiated, to lower the dynamic pressure to 300lb/ft² (14.4kPa) for separation, and to improve the flight path angle at separation. The scramjet engines are cut off at the start of this pull-up.

Orbiter Trajectory: Ascent under rocket power.

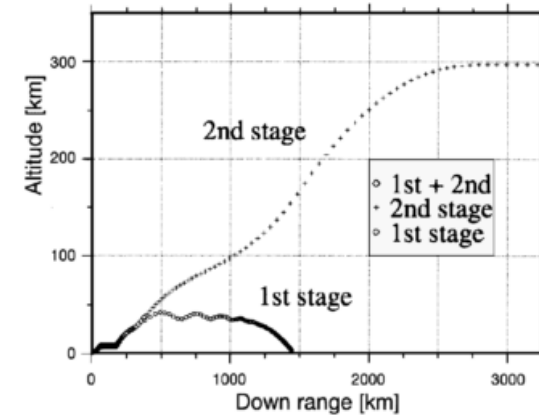
Return Trajectory: The booster initiates a turn, and cruises back under turbojet power. The orbiter reenters and returns unpowered.

Tohoku University TSTO Launcher[26]

Developed by Takahashi et al.[26], a conceptual TSTO system was designed to investigate acceptable launch, landing and abort sites along the coast of the Japanese islands.



- **Reusability:** Partially reusable, first stage only.
- **Payload:** 2,000kg to LEO.
- **Mass:** Booster: 75.0ton, Orbiter: 19.7ton.
- **Length:** Booster: 30m, Orbiter: 19m.
- **Propulsion:** The booster uses the air-turbo-ramjet engine developed at Japan's Institute for Space and Astronautical Science. The orbiter uses the LE-5B rocket engine.



- **Launch:** Horizontal.
- **Airbreathing Trajectory:** Flight at a maximum dynamic pressure of 50kpa.
- **Orbiter Trajectory:** Separation at Mach 6 and 50kPa dynamic pressure, followed by a pull-up to orbit under rocket power.
- **Return Trajectory:** Glide to a landing site downrange.

Sänger (Saenger)^[27]

The Sänger was a German TSTO alternative to the HOTOL. Sänger was intended to drive studies and technology development within the German Hypersonic Technology Program (HTP).



·**Reusability:** First stage reusable. Two alternative upper stages; a reusable, manned version for a crew of four and 3t payload, and an expendable cargo version for carrying 7-8t payload to LEO.

·**Mass:** Booster: 405t.

·**Length:** Booster: 82.5m.

·**Propulsion:** First stage powered by tubojets and ramjets, with upper stages powered by conventional LOX/LH₂ rockets.

·**Trajectory:** No detailed trajectory information available beyond separation to second stage at Mach 6.6.

·**Return Trajectory:** Not considered.

Dassault Aviation Star-H / HERMES [27]

Developed by Dassault, the STAR-H was the French study that sought to mirror the HOTOL and Sänger with the design of an aerospace plane capable of servicing the ISS. The STAR-H incorporates the Hermes, a European manned launcher concept, as 'payload' making it essentially a two-and-a-half stage vehicle.



Reusability: Reusable first stage, expendable orbiter, 'payload' of a small spaceplane glider is also reusable.

Mass: Booster 299t, orbiter 101t.

Propulsion: First stage powered by five combined cycle engines, second stage rocket powered.

Airbreathing Trajectory: No detailed trajectory information is available beyond separation to second stage at Mach 6.

Return Trajectory: Not considered.

Starsaber[28]

Starsaber was a conceptual design produced by the Georgia Institute of Technology Space Systems Design Lab, with the collaboration of NASA's Marshall Space Flight Centre. Starsaber was intended to investigate the feasibility of RBCC engines for small payload class missions.



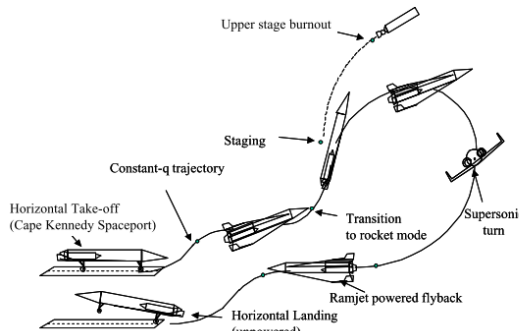
Reusability: Partially reusable. First stage reusable, second stage expendable.

Payload: 300lbs (136kg).

Mass: Booster: 79,150lbs (35,902kg), Orbiter: 3,400lbs (1542kg).

Length: Booster: 77ft (23.5m), Orbiter 13.1ft (4.0m).

Propulsion: The booster is powered by two RBCC (ejector-ramjet/ramjet/rocket) engines, while the orbiter is powered by rocket engines.



Launch: Horizontal.

Airbreathing Trajectory: Takeoff occurs in ejector-ramjet mode, accelerating to the maximum dynamic pressure boundary of 1,500psf (71.8kPa), at which point transition to ramjet mode occurs. Constant dynamic pressure is maintained throughout ramjet operation, before transition to all-rocket mode. The vehicle pulls-up in all-rocket mode, and separates the orbiter when the dynamic pressure falls below 1psf (0.05kPa).

Orbiter Trajectory: Ascent under rocket power.

Return Trajectory: Return to the launch site under ramjet power, choosing the altitude at which lift equals weight for a constant angle of attack.

QuickSat[29]

Quicksat was designed by SpaceWorks Engineering and the Air Force Research Lab as a conceptual exploration of combined cycle propulsion systems for reusable space access. Quicksat was developed in support of a U.S. military initiative to investigate responsive space access for national security purposes. Quicksat is capable of both the orbital delivery of a Space Manoeuvre Vehicle, as well as hypersonic strike.



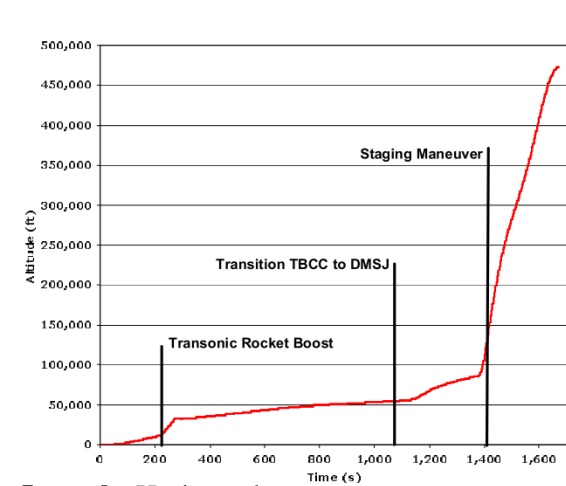
Reusability: Fully reusable.

Payload: 500lbs (226.8kg).

Mass: Booster 77,125 (34,983kg) and is 52.2ft (15.9m), Orbiter: 13,090lbs (5937kg).

Length: Booster: 52.2ft (15.9m), Orbiter: 27.5ft (8.4m).

Propulsion: The booster is powered by turbojets, dual-mode scramjets, and rockets, while the orbiter is rocket powered.



Launch: Horizontal.

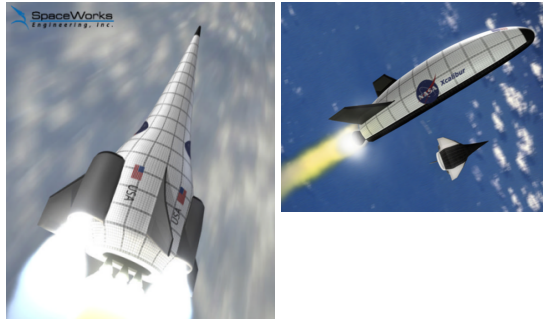
Booster Trajectory: Turbojets initially used, with transition to rockets throughout the transonic regime. Turbojets are again used supersonically, maintaining a dynamic pressure of 1,600psf (76.6kPa). At Mach 3.75, the vehicle transitions to ramjet power, and flies at maximum dynamic pressure of 2,000psf (95.7kPa), transitioning to scramjet power when necessary. At Mach 8, a pull-up is initiated, and the vehicle transitions to rocket power before staging at 250,000ft

Orbiter Trajectory: Circularisation under rocket power.

Return Trajectory: The booster reenters, decelerates, and returns under turbojet power.

XCALIBUR[30]

XCALIBUR was designed by SpaceWorks Engineering in support of NASA Marshall Space Flight Centers Advanced Space Transportation Program (ASTP). The XCALIBUR design was intended to investigate the viability of RBCC engines for future reusable launch vehicles.



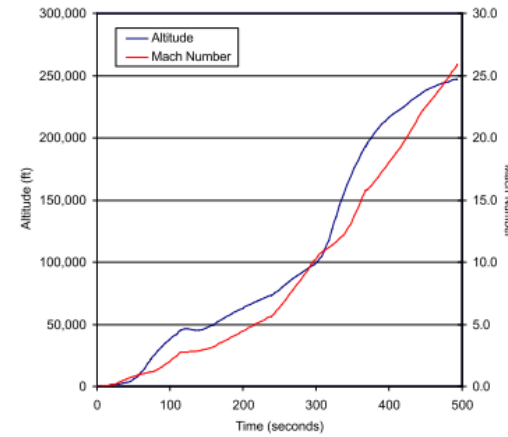
Reusability: Fully reusable.

Propulsion: The booster stage is powered by four RBCC engines, while the orbiter is HEDM rocket powered.

Payload: 20,000lbs (9,071kg).

Mass: Booster: 89,7790lbs (407,231kg), Orbiter: 103,710lbs (47042kg).

Length: Booster: 181.7ft (55.4m), Orbiter: 42.4ft (12.9m).



Launch: Vertical.

Airbreathing Trajectory: Flight at the maximum dynamic pressure of 1,800psf (86.2kPa) during ramjet and scramjet operation, for maximum engine performance. At Mach 10, pull-up occurs under scram-rocket power, reaching staging conditions of 95psf (4.5kPa) dynamic pressure. It is stated that under pure scramjet power, flight would be at maximum dynamic pressure.

Orbiter Trajectory: Injection into orbit using rocket boosters.

Return Trajectory: Not considered.

XXXX remove dots next to bolded words

Table 3.2: Two-stage airbreathing launch systems.

used for the final acceleration to orbit may be considerably smaller, and therefore cheaper and lighter, while the inefficient mass scaling of the airbreathing engine systems may be mitigated. A variety of engine architectures can be observed in the TSTO vehicles shown in Table 3.2. The booster stages are universally powered, at least in part, by airbreathing engines. RBCC engines are common, however some designs eschew the use of rocket engines in the booster stage altogether. This is possible due to the lessened emphasis on mass efficiency, enabling the use of multiple efficient, but relatively low-speed engines. The separation of the booster stage in multi-stage launch systems also allows for a relatively simpler return and landing of the booster stage, when compared to single-stage launch systems. The booster stage is separated at significantly less than orbital velocity, decreasing the structural and heating loads that it experiences during return flight. This lessens the weight of the TPS systems necessary for the booster vehicle, and simplifies the return process. However, the opposite is true for the orbiter stage. The much smaller size of the orbiter stage means that if it is reusable, the systems for its return will require a larger mass fraction of the orbiter vehicle, and the high speed entry and return will require significant TPS and control system complexity. For this reason, some of the TSTO systems shown in Table 3.2 opt for partial reusability, where the booster stage is reused, but the orbiter stage is discarded. This allows for the largest, most costly, and most easily reused portion of the launch system to be returned, while the orbiter stage may be designed to be low-cost and disposable, and in general designed to be more akin to a traditional rocket, and less like a 'spaceplane'.

The trajectories of TSTO airbreathing launch systems, where available, are relatively similar to those of SSTO launch systems. However, the trajectory features that are observed between trajectories, either resulting from optimisation, or being considered optimal, are inconsistent between studies. As shown in Table 3.2, all of the TSTO systems that have gone through detailed design are launched horizontally, and most fly at the maximum dynamic pressure boundary for the majority of the duration of hypersonic airbreathing flight. The exception to this is the JAXA TSTO launcher, which flies at a higher altitude to increase the performance of its particular airbreathing engines. The flight at maximum dynamic pressure is often followed by a pull-up near the end of airbreathing operation, similarly to the pull-up observed in SSTO launchers. However, these features that are observed in the studies of TSTO launch systems are inconsistent, occurring to significantly different extents and for distinctly different reasons.

The pull-up is a significant departure from the maximum dynamic pressure trajectory that offers the greatest thrust from hypersonic airbreathing engines. For a multi-stage vehicle, the pull-up that defines the location of the staging point is determined by a multitude of factors stemming from the design and configuration of the launch system. The optimal separation point is determined by a trade-off between;

- the high efficiency of the scramjet engines;
- the thrust produced by the scramjet engines;

3.1. HYPERSONIC AIRBREATHING LAUNCH SYSTEMS AND TRAJECTORIES

- the potential thrust of the rocket engines;
- the energy necessary to increase the altitude of the scramjet stage;
- and the aerodynamic efficiency when performing the required direction change.

All of these factors must be considered for the pull-up, along with the performance of the launch system during airbreathing acceleration, in order to generate an optimal trajectory.

The optimal trajectory shape for a two-stage airbreathing launch system is still unclear, and differs between studies and designs. In the launch vehicles that have been studied, maximum dynamic pressure flight followed by a pull-up under airbreathing operation is sometimes considered the 'optimal' flight path[24, 25, 34]. However, this pull-up and the reasoning behind it is inconsistent between studies. The optimal trajectory of a TSTO spaceplane has been investigated in isolation by Bulirsch and Chudej[34], who indicate that a small pull-up under airbreathing power maximises payload-to-orbit, but also that flight at constant dynamic pressure is not payload-optimal at any point of the airbreathing trajectory. Similarly, in the study of the JAXA TSTO Spaceplane[24], a pull-up is indicated to be optimal, again after flight at off-maximum dynamic pressure. However, in this case it is indicated that the pull-up may be performed in order to improve the performance of the airbreathing engines, which is not usually the result of off- maximum dynamic pressure flight. Mehta & Bowles[25] prescribe a 2g pull-up off of maximum dynamic pressure in order to "lower dynamic pressures and to achieve the optimal launching flight path angle for the orbiter vehicle". This prescribed manoeuvre indicates that a pull-up before airbreathing-rocket transition is considered the optimal trajectory in isolation, however, this pull-up is also specifically done to reduce the maximum dynamic pressure of the orbiter stage (reaching the maximum allowable dynamic pressure for the orbiter stage at separation), and the specific optimal conditions are not investigated.

The antithesis to the consideration of a pull-up under airbreathing operation as optimal is presented by launcher studies that do not perform a pull-up, where the maximum dynamic pressure flight for the entire duration of airbreathing operation of a TSTO launch system is considered to produce maximum efficiency. This is the case for the Tohoku University Launcher[26], as well as the Starsaber[28] and the XCALIBUR[30]. The Tohoku University Launcher maintains constant dynamic pressure until separation, after which the rocket-powered upper stage performs the pull-up to orbit under its own power, while the Starsaber and XCALIBUR transition to rocket mode during constant dynamic pressure flight, and pull up under rocket and scram-rocket power respectively. These studies may indicate that it is preferable for the booster vehicle to stay close to maximum dynamic pressure during airbreathing operation, when it is able to do so, or when maximum dynamic pressure flight is optimal. This is supported by a study by Staufenbiel[73], which investigated the effects of staging conditions on a second stage rocket in isolation, and concluded that "higher Mach numbers are preferable to increasing the flight-path angle above values of a few degrees". However, this study did not include

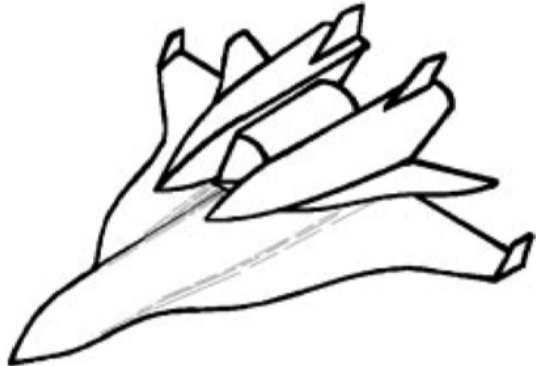
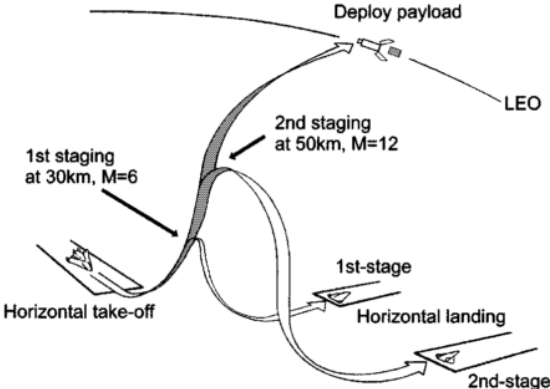
an airbreathing stage optimisation, and specifically stated that the airbreathing stage must be included to determine optimal separation conditions[73].

For many of the vehicles studied, a pull-up at the end of airbreathing operation is driven by the structural or thermal requirements of the launch system, particularly of the upper-stage, limiting the staging point. If the upper-stage is not designed to withstand significant dynamic pressures or thermal loads, then a separation in low-density air is necessary. There has been a number of studies that have identified a pull-up manoeuvre under airbreathing operation as being advantageous for a multi-stage system in order to decrease the dynamic pressure of the vehicle at airbreathing-rocket stage separation[23, 25, 82]. In the studies by Tsuchiya et al.[82] and Wilhite et al.[23], decreased dynamic pressure is necessary for the successful operation of the orbital rocket stages. In these studies the airbreathing stages pull-up to reduce the dynamic pressure to the operable limit of the rocket-powered orbital stages. When the orbital stages are able to operate, stage separation occurs. These pull-up manoeuvres demonstrate the advantages of a pull-up for the operation of the orbital stages, allowing the aerodynamic and thermal loading on the vehicle to be reduced. However, the dynamic pressure limitation on the trajectory shape makes the trajectories that are produced heavily dependent on the vehicle designs, and not generally indicative of maximum efficiency trajectories.

Clearly there is significant disparity in the designs of the two-stage airbreathing launch systems that have previously been studied, and there is also significant differences in the trajectories that are flown and that are considered optimal for the various designs investigated. In particular, there is disparity between whether acceleration at maximum dynamic pressure followed by a pull-up is considered optimal for a two-stage launch system, or if flight at maximum dynamic pressure for the entirety of airbreathing operation is more efficient. It is certain that the trajectory and the design of multi-stage launch systems are heavily coupled, and that both must be understood well before a detailed design is able to be achieved. However, there has been no detailed studies that have thoroughly investigated the trajectory shapes or inter-stage trade-offs unique to multi-stage systems.

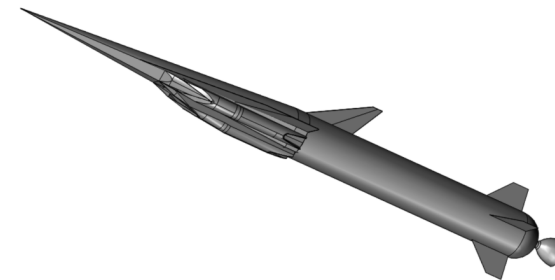
3.1.3 Three-Stage Launch Systems

In addition to two-stage airbreathing launch systems, Three-stage-to-orbit (3STO) airbreathing launch systems have recently been advocated as an efficient configuration for dedicated small satellite launch, a payload profile that has lately garnered a large amount of interest. A three-stage configuration allows for cost-efficient partial-reusability in small launchers, enabling the acceleration of a small, disposable third stage, with reusable first and second stages. Three-stage systems are likely to be most applicable to smaller launch systems, where any 'dead' weight from unused propulsion systems at hypersonic speeds carries relatively larger mass penalties when compared to more massive systems. Three-stage systems allow the propulsion systems to be segmented further than two-stage systems,

Launcher	Design	Trajectory
<p>Tohoku University 3STO[31]</p> <p>Kimura and Sawada investigate a three-stage-to-orbit launch system with an expendable upper stage for responsive LEO launch from multiple launch locations.</p>	 <ul style="list-style-type: none"> Payload: 2t to LEO. Mass: First stage 123.42t, second stage 61.89t, third stage 11.27t. Length: First stage 50m, second stage 26m, third stage 16m. Propulsion: First stage four air-turboramjets, second stage scramjet, third stage rocket. 	 <ul style="list-style-type: none"> Launch: Horizontal. First Stage Trajectory: Flight at a constant dynamic pressure of 20kPa, before staging at 30km altitude, at Mach 5-6. Airbreathing Trajectory: Ascent under scramjet power along a predefined trajectory that is designed to avoid violating maximum heating constraints, at a low trajectory angle, before staging at 50km altitude, at Mach 11-12. Third Stage Trajectory: Ascent under rocket power. Return Trajectory: The first and second stage land at a site downrange. The first stage cruises under turbojet power, while the second stage glides.

SPARTAN[32]

The SPARTAN is a three stage, partially reusable, access to space system under development at The University of Queensland[32, 83] and Hypersonix[84]. The SPARTAN is designed for affordable small payload launch from a variety of launch locations.

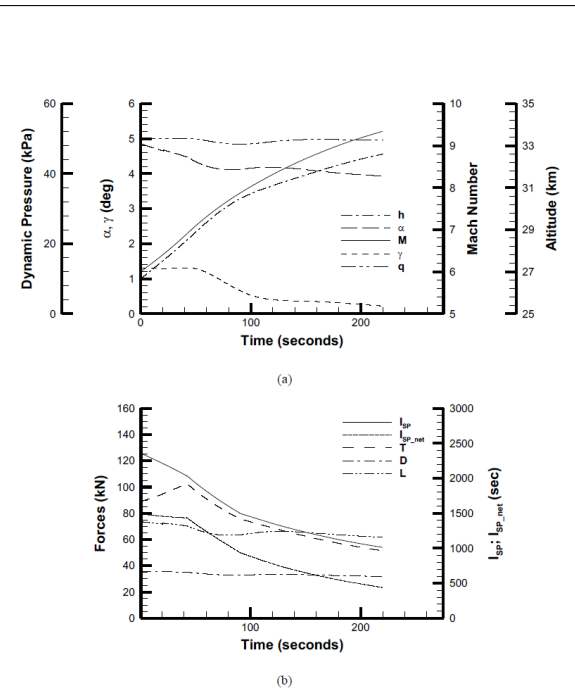


- Payload:** 279.8kg

- Mass:** First stage 11957.6kg, second stage 5905.1kg, third stage 2850kg.

- Length:** Second stage 22.94m, third stage 11.8m.

- Propulsion:** First stage rocket, second stage scramjet, third stage rocket.



- Launch:** Vertical.

- First Stage Trajectory:** Gravity turn.

- Airbreathing Trajectory:** Trajectory constrained to scramjet stage flying a constant dynamic pressure of 50kPa.

- Third Stage Trajectory:** Ascent under rocket power, held at 10° angle of attack.

- Return Trajectory:** Return trajectory undefined.

Table 3.3: Three-stage airbreathing launch systems.

allowing separation between flight regimes and the mass-efficient utilisation of each engine mode[12].

The three-stage airbreathing launchers that have been or are being investigated are summarised in Table 3.3. Only two such systems have been identified; the Tohoku University 3STO launch system investigated by Kimura and Sawada in 1999[31], and the SPARTAN, a rocket-scramjet-rocket launch system currently under development by the University of Queensland and Hypersonix. Both of these systems are designed to be a cost effective near-term solution to airbreathing access to space, using a disposable third stage rocket along with reusable first and second stages. Both systems use second stages powered by scramjets, with the SPARTAN utilising a rocket-powered first stage along with vertical launch for a low complexity and relatively high technology readiness level (TRL) first stage design, while the Tohoku University launcher utilises turboramjets along with a horizontal launch and a large, winged first stage.

The flight paths developed so far for both of these launch systems are predefined, and designed around the physical limits of the launch systems and maximising the efficiency of the airbreathing engines. Both the Tohoku University launcher and the SPARTAN fly close to the maximum limits of the vehicle during airbreathing operation to maximise airbreathing engine performance. While this is believed to be the most optimal or representative trajectory for these launch systems, no analysis has been undertaken to indicate that these trajectories are in fact the most efficient way of flying to orbit. This is particularly true for the SPARTAN, because the fly-back of the scramjet stage has not been modelled, even though it is integral to the cost effectiveness of the launch system. The vertical launch of the SPARTAN is considerably different to other multi-stage launch systems, and it remains to be seen whether a constant dynamic pressure airbreathing trajectory is in-fact the optimal way in which to constrain the system during launch. At the end of the airbreathing trajectory, when compared to the trajectories flown by two-stage-to-orbit airbreathing launch systems, it is evident that a pull-up during airbreathing operation, before the release of the third stage, may possibly improve the efficiency of a rocket-scramjet-rocket launch system. Although the extent of this pull-up, or indeed whether a pull-up is necessary at all, cannot be estimated from the studies of airbreathing launch systems analysed in the preceding sections. The current work seeks to model the optimal trajectory of a rocket scramjet-rocket launch system, utilising a modified version of the SPARTAN launch system in order to gain insights into the most efficient way to fly a launch system of this type.

3.2 Hypersonic Vehicle Return and Glide Trajectories

A significant mission segment of an airbreathing launch system is the return of some or all of its stages, either to a landing site downrange, or to the initial launch location. The trajectory and manner of this return have a large impact on the viability of future airbreathing launchers, as the return and re-use of these launchers is a particular benefit of their design[12]. The most efficient method of returning airbreathing launcher systems must be studied, ideally in concert with the ascent trajectory,

in order to develop an optimal mission plan.

There are three main methods that have been studied for potential hypersonic vehicle return; glide-back, cruise-back and boost-back. Glide-back involves the hypersonic vehicle returning to base and landing entirely using its aerodynamics. This requires a sufficient lift-to-drag ratio to sustain the hypersonic vehicle over the entire return range, as well as the controllability to land the hypersonic vehicle in level flight. For a hypersonic trajectory a fully glide-back return flight is most likely unobtainable. This is due to the large downrange distance flown, and the large initial velocity at the beginning of the fly-back trajectory, when the vehicle is oriented away from the landing site. Multiple studies have investigated the maximum staging velocity allowable for the glide-back flight of a booster, and have found that the maximum separation velocity for glide-back to be feasible is between Mach 3-4 at 30km-120km downrange distance, with higher initial velocities or longer downrange distances requiring fly-back under power[74, 75].

Cruise-back involves the inclusion of subsonic engines, which are used to power the fly-back of the hypersonic vehicle until landing similar to a conventional aircraft. These engines may be included solely for the fly-back[75], or used in the acceleration phase for low velocity acceleration[23, 25, 74]. The addition of subsonic engines powering a constant velocity cruise-back phase allows the accelerator to return to base with a similar trajectory to that of traditional aircraft, allowing the velocity and altitude of the accelerator to be precisely controlled. However, the addition of subsonic engines necessary for cruise-back increases the mass of the vehicle significantly, leading to decreased mass efficiency and increased design complexity[75].

Another mode of powered fly-back is to use the existing hypersonic airbreathing engines during the return trajectory in a boost-back trajectory. Using the existing airbreathing engines allows for range to be added when compared to a glide-only return trajectory, without the inclusion of additional engines, **saving on mass and space within the vehicle, and reducing the complexity of the design**. The hypersonic airbreathing engines can be operated at appropriate times during the fly-back, when they will be most impactful on the return trajectory range. However, the hypersonic airbreathing engines may only be used within their operating region, and vary in thrust and efficiency dependent on flight conditions. Hypersonic airbreathing engines have maximum efficiency at low Mach numbers[12], with the thrust produced depending on the dynamic pressure and inlet conditions, which vary with the trajectory path and angle of attack of the vehicle. The possibility of an airbreathing vehicle reigniting high speed airbreathing engines for short periods has been investigated by Tsuchiya and Mori[82], as described in Table 3.2. Tsuchiya and Mori investigate two conceptual launch vehicles; a vehicle powered solely by airbreathing propulsion returning after separation of an orbital stage at Mach 5.1, and an airbreathing/rocket vehicle returning after a separation at Mach 6.8[82]. Both vehicles use the high speed airbreathing engines during return flight. Both vehicles ignite the airbreathing engines at around Mach 3.5 for “several tens of seconds” to extend the range of the fly-back manoeuvres. After this, the vehicles descend and land at the launch site. These boosters fly to a downrange distance of

3.2. HYPERSONIC VEHICLE RETURN AND GLIDE TRAJECTORIES

600-625km from the launch site prior to return, and less than 5% of the vehicles initial propellant was required to return the vehicles to the initial launch sites[82]. These boost-back trajectories were initiated at lower than Mach 7, and their feasibility at higher separation velocities is not clear. Even at relatively low separation speeds it is evident that the additional fuel weight used during the return phase may significantly affect the performance of a launch system. As such it is important to assess the effects of the fly-back of high-speed staging on the efficiency of a launch system, and to determine the functional implications of mandating return-to-launch-site capabilities.

In addition to investigating the trajectories of airbreathing launch vehicles, the maximum-range, minimum-fuel trajectories of hypersonic vehicles and lifting bodies that are not necessarily launch vehicles can also allow a better understanding of the maximum efficiency return trajectory shape. The maximum range trajectory of a hypersonic vehicle operating at high altitudes is often a ‘skipping’ trajectory, where the altitude of the vehicle is repeatedly raised and lowered to take advantage of the most efficient angle of attack of a vehicle while travelling through high density air[85–89]. A skipping trajectory has been shown to be range optimal for hypersonic gliding vehicles when range is desired to be maximised, from a wide range of release points and vehicle configurations[74, 85–87, 89, 90]. A skipping trajectory has also been shown to be optimal for an airbreathing hypersonic vehicle thrusting throughout the trajectory[88, 91], as shown in Figure 3.2. The range optimal operation of the scramjet engine is shown to be repeated ignitions at the trough of each skip[88]. The scramjets are ignited as the vehicle climbs after the trough, as the Mach number decreases to the minimum operable conditions of the scramjet engines[88]. Minimising the Mach number during operation in this way maximises the efficiency of the scramjet engines[88].

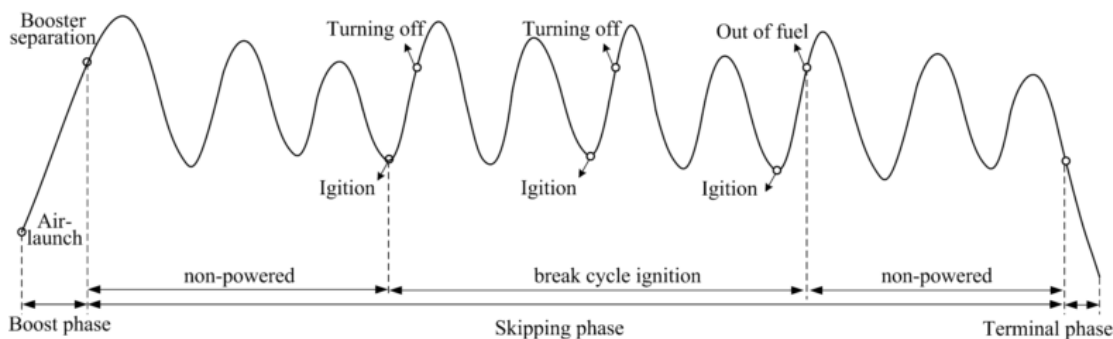


Figure 3.2: An illustration of the optimised maximum range trajectory of a hypersonic vehicle[88].

The complexity of the optimal return and maximum range trajectories for hypersonic vehicles require good aerodynamics and manoeuvrability to carry out properly, as well as potentially requiring multiple restarts from the airbreathing engines. A coupling of the ascent and return during trajectory design is clearly important, because there is a complex trade-off between both phases to produce an overall fuel-optimal trajectory, particularly if it is necessary for the airbreathing engines to be reignited during the return flight.

3.3 The SPARTAN

In order to investigate the optimal launch trajectory of a three stage, airbreathing launch system, a representative system design must be used to provide a general configuration, sizing, and design for an analysis. Only two three-stage launch systems were identified in Section 3.1.3; the Tohoku University 3STO launcher, and the SPARTAN launch system. For this study, the SPARTAN launch system is chosen as the basis for a representative launch system, for multiple reasons:

- The SPARTAN is a small, partially returnable launch system, seeking to fill a reusability niche that cannot be satisfied by current rocket-powered launch system designs.
- The SPARTAN’s design is relatively mature, having undergone significant study over the past years, and is still being actively developed.
- The SPARTAN is designed to utilise the REST engines, which are some of the most well validated scramjet engines together with airframe integration. Capturing the performance of the engines correctly is integral to developing a deeper understanding of the performance of airbreathing launch systems.

For these reasons the SPARTAN is assessed as an up-to-date design of a future rocket-scramjet-rocket launch system that is likely to be representative of future space launch systems of this type. Because of this, it is likely that a trajectory analysis performed on a SPARTAN-like launch system will be generally applicable to future rocket-scramjet-rocket launchers, and will progress the development of airbreathing launch systems as a whole.

The SPARTAN launch system is currently undergoing research and design, and is in the preliminary design phase. The SPARTAN has undergone an iterative design process over a number of years[12, 83] with a significant amount of resources dedicated to it by the University of Queensland’s Centre for Hypersonics. The SPARTAN’s design is based around the scramjet accelerator stage of the launch system (designated the SPARTAN in previous works, although this nomenclature has since changed). This scramjet accelerator is the stage that has been designed in the most detail[12, 83], because the development and performance of the scramjet accelerator are likely to be the most critical aspects of the launch system design.

The scramjet accelerator stage of the SPARTAN was first designed by Jazra, Preller and Smart[83, 92], based on the winged-cone vehicle developed by Shaughnessy et al. as part of the NASP program[11]. The scramjet accelerator has been sized to be 22.94m long, with an 8.90m wingspan, and is powered by four rectangular-to-elliptical shape transition (REST) scramjet engines, developed at The University of Queensland, specifically designed to integrate smoothly with the conical forebody

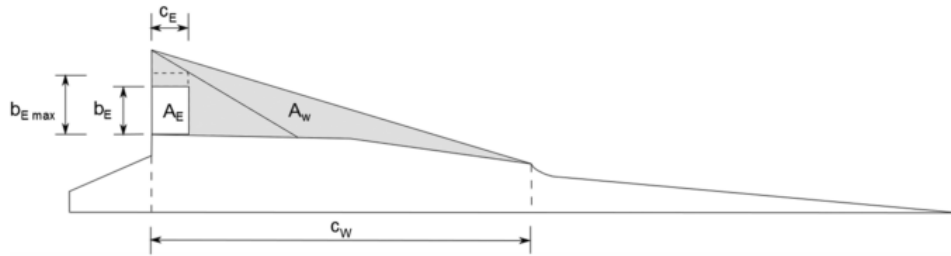


Figure 3.3: The elevons of the SPARTAN[12].

of the scramjet accelerator. Elevons are included on the wings of the scramjet accelerator for primary control, shown in Figure 3.3. These elevons were sized through variation of the width, b_E , to have an area equal to 15% of the area of the wing, and to have a cord length, c_E , of 15% of the chord length of the wing[32]. Three retractable landing gear assemblies are included on the scramjet accelerator, shown in Figure 3.4, so that the scramjet stage may be returned and landed in the same manner as a traditional aircraft; horizontally on a specially purposed runway.

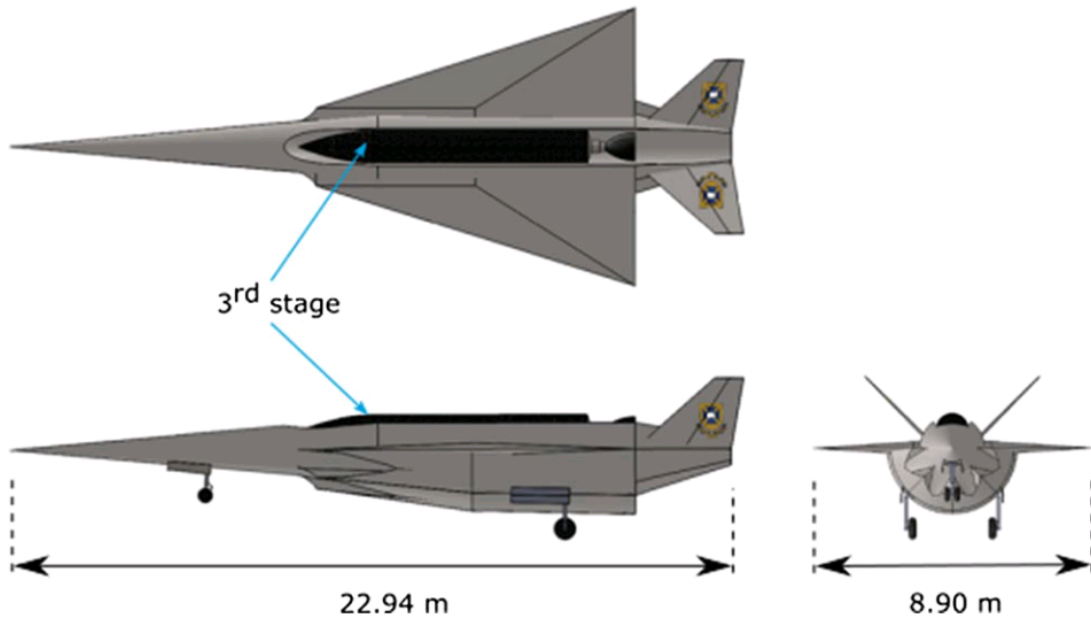


Figure 3.4: The scramjet accelerator of the SPARTAN, as designed by Preller[32].

To date, studies of the SPARTAN have assumed that the most efficient launch trajectory is achieved when the scramjet accelerator stage is constrained to fly at a constant dynamic pressure[12, 32]. Figure 3.5 shows the trajectory of the scramjet accelerator, simulated in three degrees of freedom to fly close to a constant 50kPa dynamic pressure, using a pole-placement angle of attack controller[12]. The ascent trajectory of the SPARTAN begins at Mach 6, and terminates at Mach 9.34, when the hydrogen fuel is exhausted[32]. The net specific impulse of the SPARTAN varies from 1492s at the

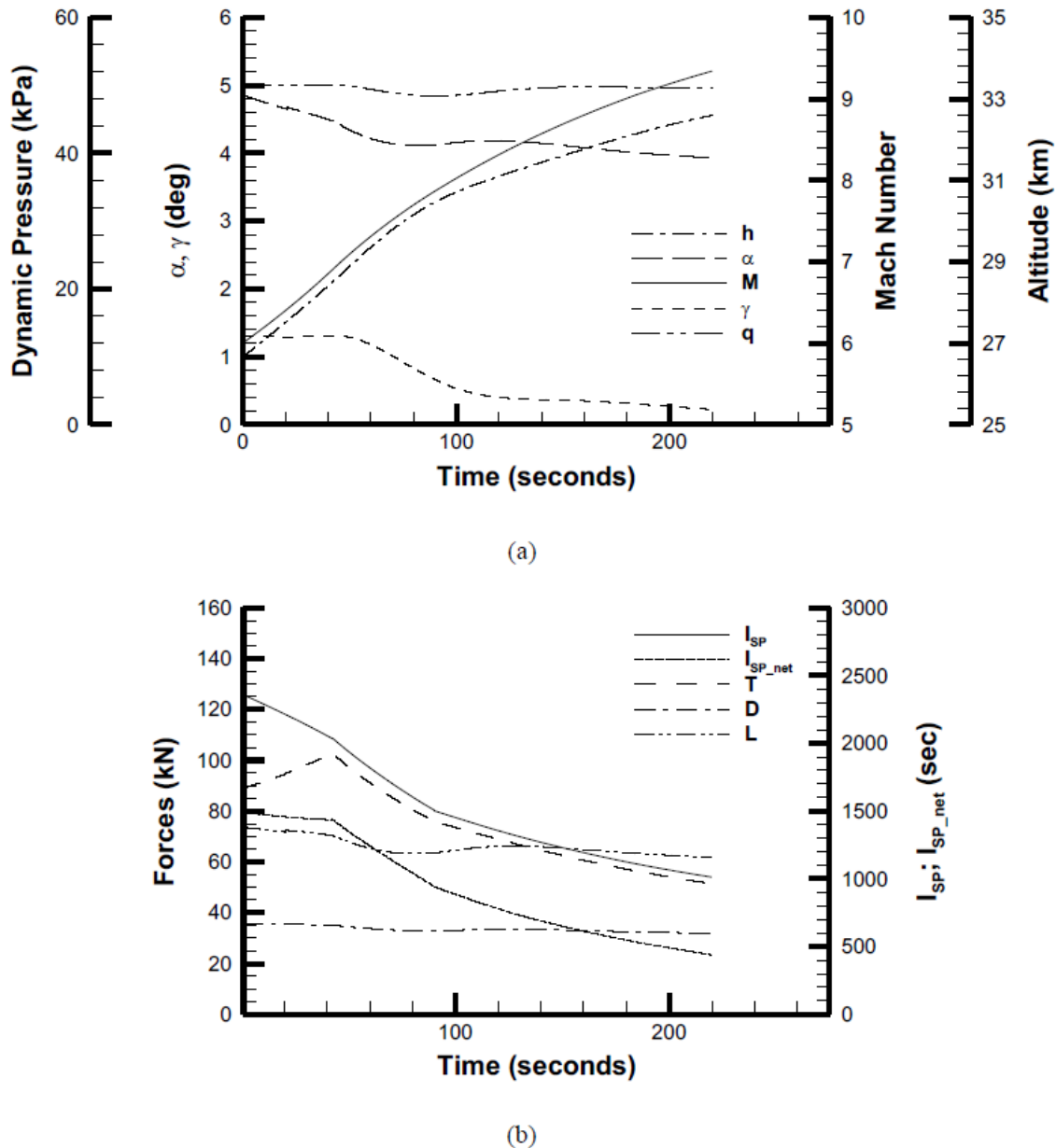


Figure 3.5: The flight trajectory of the SPARTAN. a) shows the physical trajectory and b) shows the forces on the vehicle and performance indicators.

beginning of the trajectory, to 439s by the time the fuel is depleted[12]. The SPARTAN is trimmed throughout the trajectory by elevons on the wing, shown in Figure 3.3. Over the flight of the SPARTAN, the flap deflection changes from 10.6° to 12.2° [32]. The drag contribution of the flap varies from 14.3% to 14.5%, and the lift contribution from 18.8% to 21.0%[32]. However, this is calculated without a detailed analysis of the centre of gravity location, which is assumed to be located at a position that bisects the planform area. Past studies of the scramjet accelerator vehicle have assumed that a fly-back to launch site is possible after third stage separation[12, 32]. However, this fly-back has

not yet been simulated.

The first stage rocket of the SPARTAN is launched vertically, accelerating the scramjet accelerator to its minimum operable Mach number. The first stage has not yet been modelled in detail, with only very representative aerodynamic models used for an analysis of a representative first stage rocket. It is eventually intended that the first stage of the SPARTAN be returnable to launch site under cruise-back power for reuse, however, a first stage capable of return flight has not been designed or modelled for a full scale SPARTAN system[12, 32]. Some preliminary work has been carried out, exploring the reuse of the first stage boosters of the SPARTAN [4] for a modified, reduced size SPARTAN concept, however this work is still in its infancy, and the basic design of the booster or boosters is still to be determined[12, 32].

The third stage of the SPARTAN is an expendable rocket system, that consists of a rocket motor, fuel tanks, structure, payload and a thermal protection system[12], shown in Figure 3.6. The third stage has to this point been designed to be powered by the Pratt & Whitney RL-10-3A[12], and has exhibited good performance when powered by this engine. However, the RL-10-3A is a pump-fed engine, and is likely to be prohibitively expensive for a small launch system. Initially, the third stage

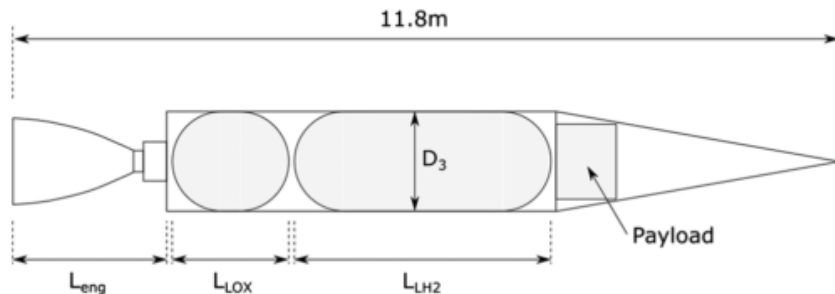


Figure 3.6: The third stage rocket of the rocket-scramjet-rocket launch system[12].

was designed to be situated within the fuselage of the SPARTAN's scramjet accelerator, in the nose cone[83]. This design was changed by Preller[12, 32], so that the rocket was situated in 'piggyback' position at the top of the fuselage as shown in Figure 3.4. Rather than being situated entirely within the fuselage, the third stage was designed to fit into a recess into the back of the vehicle, to aid in high dynamic pressure separation. However, the effect of this recess on the aerodynamics of the scramjet accelerator after separation has not been considered[12, 32]. It is likely that this recess would have a large effect on the aerodynamics and controllability of the vehicle, particularly at high Mach numbers, where large areas of separation and recirculation are likely to be present.

The trajectory of the third stage has to date been constrained to the scramjet accelerator flying a constant dynamic pressure trajectory, releasing the third stage into a high dynamic pressure environment. This trajectory, shown in Figure 3.7, uses a constant, untrimmed, 10° angle of attack throughout, enabling the third stage to pull-up out of the atmosphere. Once the density of the atmosphere is low enough, the thermal protection system separates from the vehicle for mass efficiency,

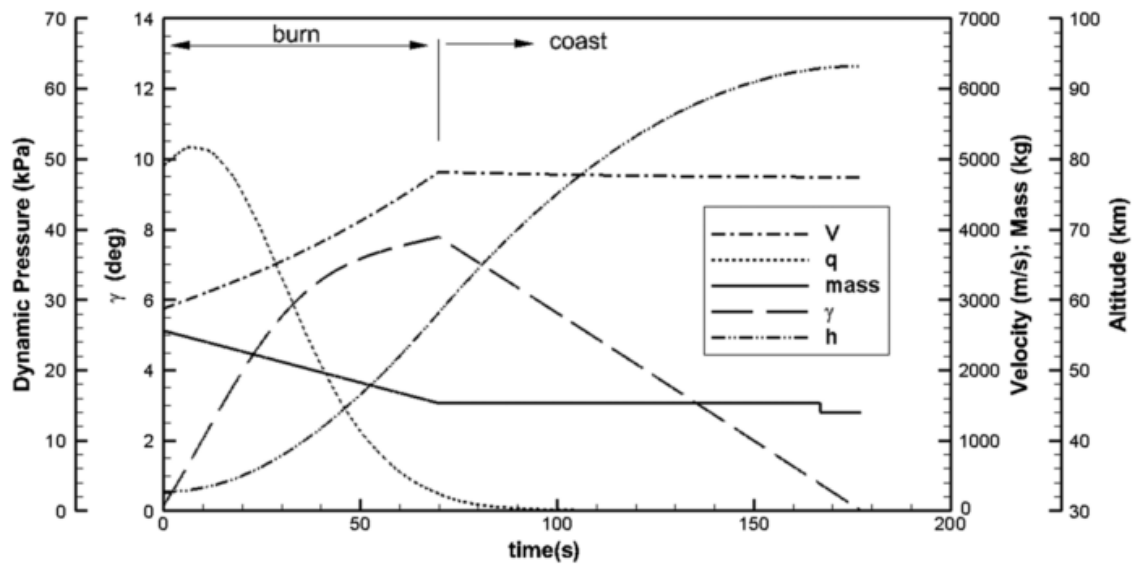


Figure 3.7: The third stage trajectory of the SPARTAN launch system[32].

and once exoatmospheric, the third stage performs a Hohmann transfer to reach the desired orbit. This trajectory enables the delivery of 279.8kg[32] of payload to sun synchronous orbit when using a third stage powered by a Pratt & Whitney RL-10-3A[32].

Whilst the SPARTAN launch system is the most studied 3STO airbreathing system, it is evident that there is significant portions of the system left to design in detail, and significant design challenges to overcome. It is also apparent that the trajectory analysis of the SPARTAN, like all 3STO launch systems, and many 2STO launch systems, makes significant assumptions as to the most optimal flight path, notably constraining the scramjet accelerator to constant dynamic pressure flight. As previous studies have indicated[12], if the performance and designs of this launch system and 3STO airbreathing launch systems in general are to be improved, the development and analysis of an optimal launch trajectory is necessary.

3.4 Optimal Control

To investigate the best possible way of flying a rocket-scramjet-rocket launch system to orbit, a simulation must be developed that will calculate the optimal flight path, taking into account the trajectory of all of three stages of the launch system, including ascent trajectories, as well as the return to base of the scramjet accelerator stage, along with all necessary performance constraints. Calculating an optimal trajectory that combines all phases of a partially reusable, partially airbreathing, three-stage launch system is a complex task, that has not been carried out to-date. Defining the trajectory of a launch system with multiple stages and multiple modes of propulsion purely from an a priori vehicle analysis is unlikely to yield a trajectory that maximises the performance of the system, due to

the highly nonlinear performance of a multi-stage, multi-propulsion mode launch system, and the complex trade-offs that are present between the stages. The effects of these trade-offs are extremely difficult to predict, particularly because of the high sensitivity of airbreathing engines to flight conditions, and the complex aerodynamics of an airbreathing launch system. A method of determining the optimal flight path is required, that is able to maximise the performance of the launch system with very few assumptions as to the shape of the trajectory, in order for the trajectory shape to be analysed and for the trajectory-design coupling to be investigated.

Optimal control theory is used in situations where a control sequence must be found to produce an optimal trajectory with little prior knowledge of the form that the optimal trajectory will take. Optimal control theory is a general term for the mathematics of optimising a time variant dynamic system, that can be controlled. Optimal control theory is distinct from control theory in that it does not necessarily attempt to match a set reference or goal, as is generally the case for trajectories developed using control theory methods such as feedback control. Rather, a single global objective function is minimised by determining optimised control actions across the trajectory, subject to a set of user defined constraints. Optimal control theory has been widely used in aerospace applications, and has been successfully used to optimise the launch of airbreathing hypersonic launch vehicles[16–20, 79], including some of the trajectories detailed in Section 3.1.

For an optimisation of a complex trajectory there are a variety of optimal control methods that are useful for specific problem types. These are separated into two categories: direct and indirect solution methods[36]. Indirect methods are based on the calculus of variations or minimum principle model, and generally result in high accuracy solutions to optimisation problems[93]. However indirect models suffer from the drawbacks of small radii of convergence and the fact that the equations to be solved often exhibit strong nonlinearity and discontinuities. This means that indirect methods will not be solvable unless the problem is very well defined with a minimum of nonlinearity, making indirect methods unsuitable for many complex optimisation problems, such as aerospace vehicle simulations, which can exhibit strong nonlinear behaviour and have a wide solution space.

Direct methods transform an optimisation problem into a nonlinear programming (NLP) problem, which can be solved computationally[94]. NLP solvers solve the optimisation problem defined as[95]:

$$\text{Minimise} \quad f(x) \quad (3.1)$$

$$\text{Subject to} \quad g_i(x) \leq 0 \quad \text{for } i = 1, \dots, m \quad (3.2)$$

$$\text{and} \quad h_j(x) = 0 \quad \text{for } j = 1, \dots, n \quad (3.3)$$

An optimisation problem that has been discretised in this form can thus be solved using any of a variety of NLP solvers. One of the most effective methods of solving twice differentiable NLP problems is sequential quadratic programming (SQP)[96] for which there is a variety of commercial solvers available such as NPSOL, SNOPT, and packages within MATLAB.

In order for these packages to solve an optimisation problem it must be presented in discretised form, and as such must be transformed using transcription techniques[97]. The task of transcribing a continuous optimisation problem into discrete NLP solvable form is not simple. SQP solvers can very easily run into convergence issues when provided with an optimisation problem which has not been well defined. Also, any transcription must be carried out with care that the accuracy of the solution is not compromised. There are multiple ways to approximate a continuous optimisation problem directly as an NLP problem, the most common of which are shooting and collocation methods. The choice of discretisation method can affect the stability and accuracy of the solution as well as the solution time of the problem.

3.4.1 Shooting Methods

Shooting methods in optimal control are forward-time methods of discretisation[97]. Shooting methods explicitly enforce the dynamics of the system, and update the free conditions and system controls to move towards an optimal solution from an initial guess[97]. Shooting methods are generally simple to apply, and require little specialised knowledge to use once they have been implemented.

The Single Shooting Method

The oldest and simplest method of approximating continuous optimisation problems as NLP problems is the direct single shooting method. Direct single shooting discretises the control function over the solution space, and solves this directly as an NLP by integrating the vehicle dynamics, or state variables, along the trajectory at each trajectory guess[36, 97–99]. **Figure 3.8 illustrates the single shooting method, with green points indicating the start and end points, and red dots indicating the discretisation of the trajectory path. The vehicle dynamics are solved over these discretised time points directly, with controls modified to minimise an end target.** Single shooting is simple to apply and has been used since the 1970s for rocket trajectory optimisation[100]. **Single shooting methods have also been used for the analysis of airbreathing launch trajectories, with some degree of success[16, 21, 22, 24, 30]. However,** single shooting methods suffer from nonlinearity problems, ie. an optimisation problem solved using the single shooting method will potentially struggle to solve if the problem exhibits even small nonlinearities, due to being unable to converge to an optimal solution. This makes the single shooting method unsuitable **for the in-depth trajectory analysis of complex problems such as a scramjet model, as there are many nonlinear factors inherent in atmosphere and airbreathing engine modelling. For this reason single shooting is not commonly used at the current time for the trajectory analysis of complex launch vehicles.**

The Multiple Shooting Method

Direct multiple shooting solves some of the instabilities of the single shooting method by splitting the trajectory into multiple shooting arcs, and collocating these at specific time points[36, 97–99]. This creates a system of discontinuities, illustrated in Figure 3.8, which are gradually minimised by the solver algorithm until the trajectory is continuous. These discontinuities allow greater flexibility for the solver than is afforded by the single shooting method.

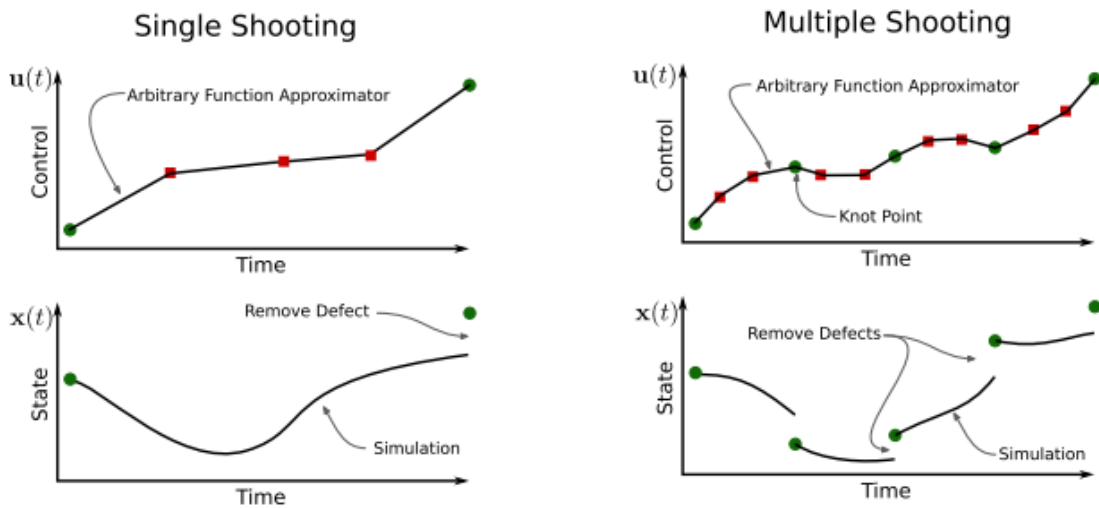


Figure 3.8: A comparison of single shooting and multiple shooting[97].

The multiple shooting method has greatly improved convergence compared to the single shooting method, removing much of the susceptibility to instabilities resulting from nonlinear effects. For this reason, multiple shooting has been used successfully in a variety of applications, including the trajectory optimisation of reusable space vehicles[101]. However, the multiple shooting approach still suffers from a relatively small radius of convergence and slow computation times[99]. Radius of convergence is extremely important to this study as the optimal solution cannot be approximated to a great degree of accuracy. As such it is desirable to use a method with a large radius of convergence for the complex trajectory optimisation problem being considered, to improve the robustness of the solution process.

3.4.2 Collocation Methods

Collocation methods are arguably the most powerful methods for solving optimal control problems[98]. Collocation methods are simultaneous methods, where both the states and controls are approximated using a specific form of functional[97, 98]. In these methods, the dynamics of the system are not explicitly enforced, but instead are constrained at specified points along the trajectory,

called collocation points, or nodes[97], with the trajectory often divided into multiple segments at specific nodes, called 'knot' points. These nodes and knot points are illustrated for a pseudospectral method of collocation in Figure 3.9, showing the relationship between the segments and nodes used, and the orthogonal polynomials that approximate the states and controls of the system being optimised. Constraining the dynamics in this way means that the derivative of the state functions become a constraint within the NLP, being equated to the polynomial approximation functions by the solver algorithm. Collocation methods provide larger radius of convergence, greater robustness, and smaller computational times compared to multiple shooting[99]. However, the solution accuracy of collocation methods is less than that of multiple shooting methods[99], although this can be improved through the choice of basis functions used for collocation[98].

Collocation methods can be represented in two ways; h and p schemes[97]. p schemes, or global methods, represent the entire trajectory as high order polynomials, and converge by increasing the order of these polynomial[97]. This method works well if the underlying solution is smooth, however, if there are discontinuities present, a p scheme will fail[97]. h schemes separate the trajectory into a series of medium order polynomials, stitched together at knot points using defect constraints, similarly to the multiple shooting method[97, 98, 102]. These joining points are called knot points[97, 102]. A comparison between h and p methods is shown in Figure 3.9.

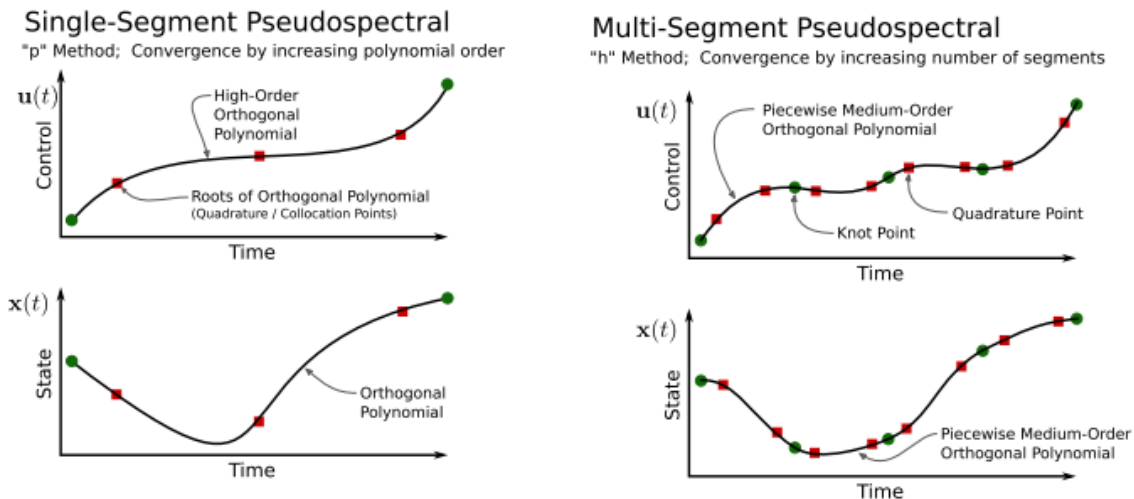


Figure 3.9: Examples of h and p collocation methods[97].

The Pseudospectral Method

The most accurate and effective type of collocation methods use orthogonal polynomials to approximate the state and control functionals[103]. In trajectory optimisation, this type of collocation is referred to as the pseudospectral method[97]. The pseudospectral method was first introduced in 1972 by Kreiss & Oliiger[104] as an efficient way to compute meteorology and oceanography prob-

lems. The pseudospectral method has recently garnered a large amount of attention for its ability to rapidly and accurately solve a wide variety of optimal control problems. When a solution is well behaved and smooth, the pseudospectral method converges at an exponential rate, with a high accuracy known as spectral accuracy[102, 105].

The pseudospectral method employs the use of orthogonal polynomials such as Legendre or Chebychev polynomials to approximate the state and control functions. This approximation is used to transcribe the optimal control problem into a nonlinear programming problem (NLP) through collocation. This process involves mapping the time domain of the system to the time interval $[-1, +1]$, and discretising the approximated dynamics at a specific set of points, obtained from Gaussian quadrature[97, 98, 103, 106, 107]. There are multiple types of pseudospectral methods, distinguished by the polynomial and collocation points used. Usually, these polynomials are Chebyshev or Lagrange polynomials[98, 103], and the collocation points are the roots of a Legendre polynomial[108]. Chebyshev polynomials have been used since the introduction of pseudospectral methods in optimal control, but have been superseded in many cases by Lagrange polynomials, which offer simpler collocation conditions[98]. There are many possible types of collocation nodes, although there are three most commonly used sets; Legendre-Gauss (LG); Legendre-Gauss-Radau (LGR); and Legendre-Gauss-Lobatto (LGL)[98, 108]. The choice of collocation type determines how the roots of the problem are calculated, and changes the formulation of the problem slightly[108]. Practically, there is very little difference between these node sets[108]. Further information on the pseudospectral information may be found in Reference [106].

The pseudospectral method is usually employed as a p method, where a global polynomial is used, and convergence is achieved by increasing the order of this polynomial[98]. Recently, hp -adaptive pseudospectral methods have been introduced, which segment the mesh using an h method, whilst also having a variable polynomial degree, as in the p method[105]. These hp methods converge by varying the degree of the approximating polynomial as well as the number of segments simultaneously. Utilising both h and p methods improves the accuracy and robustness of the solution, as illustrated in Figure 3.10, from a study by Chai et al.[88] comparing the single shooting method to non-adaptive and hp -adaptive pseudospectral methods. **This figure illustrates a comparison of a boost-skip hypersonic vehicle optimised for maximum range. All trajectories are relatively similar, however the hp -adaptive method is able to achieve slightly more range by redistributing nodes effectively. The hp -adaptive method also exhibits higher solution accuracy; in this problem the scramjet is limited to ignite at less than 1500m/s, and the hp -adaptive method ignites the scramjet at exactly 1500m/s, while the non-adaptive method ignited at 1499.256m/s, and the direct shooting at 1499.548m/s. This is a slight difference, but illustrates the improved capability of the hp -adaptive method to converge to specific optimal points. In addition to improved robustness and accuracy, the hp -adaptive method exhibits greater computational efficiency than the other methods, taking 5.3s in total to run this optimisation, compared to 12.7s for a non-adaptive method, and 268.2s for the direct shooting approach.**

In general the hp-adaptive method decreases the computational effort and memory usage necessary during the solution process by converging more rapidly to an optimal result[88, 105].

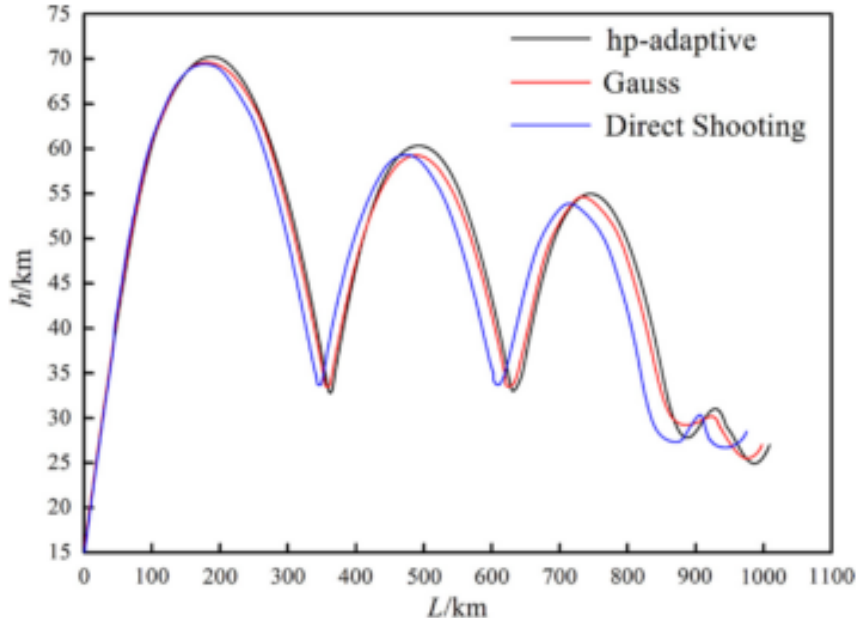


Figure 3.10: Comparison of optimisation techniques[88]. A hypersonic vehicle is optimised for maximum range. The hp-adaptive method can be observed to have produced the most optimal result.

A secondary usability advantage of the pseudospectral method is the ability to generate Hamiltonian and costate values easily[98, 109, 110]. The Hamiltonian and costate values allow a solution to easily and quickly be checked to determine if some of the necessary conditions for optimality are being met. This is useful to determine if the optimal solution calculated by the pseudospectral solver is valid.

The pseudospectral method has been proven to be extremely effective for simulations in aerospace applications and has been proven in flight applications such as the zero propellant manoeuvre of the International Space Station in 2007, where the ISS was rotated 180 degrees without any propellant used following a pseudospectral method solution[111]. The pseudospectral method has been used successfully in a multitude of studies for the trajectory analysis of hypersonic vehicles[85, 86, 88, 112–118], and has proved an extremely effective tool for solving the highly nonlinear trajectory optimisation problems that arise from complex aerodynamics. These successful use cases indicate that the pseudospectral method is robust for complex, nonlinear systems, and that the pseudospectral method can be used to solve problems with many state variables and phases, such as is required by the aerodynamics and multi-stage nature of the launch system being considered in this work.

3.5 Available Optimal Control Solvers

There are a number of optimal control solvers available, both commercially and open source, that represent well tested implementations of state of the art pseudospectral methods. A summary of the most prominent available solvers is shown in Table 3.4. These programs are mostly general solvers, and must be configured specifically in order to solve a particular optimal control problem. The exception is ASTOS[119], which is a standalone program designed for aerospace trajectory optimisation.

Functionally, most of the available solvers are similar in operation. The states and controls of the optimal control problem are defined to the program by the user, along with any constraints; continuous or endpoint. The cost function of the problem is input, and dynamic model of the system is defined. An initial guess is provided, and once activated, the solver will move toward an optimal solution from this initial guess. The most significant practical difference between the solvers lies in the robustness of the optimal solution, ie. how easily a particular solver is able to converge to the optimal solution. For a simple and continuous optimisation problem all solvers will be able to approach the same solution (though with varying efficiency). However, for a complex and nonlinear optimisation problem, some solvers will converge much more easily and rapidly than others. Generally, this stems from the underlying transcription method used. The most common form of discretisation used by these solvers is the pseudospectral method, although other forms of collocation, as well as multiple shooting, are also used. Of the methods used, hp-adaptive pseudospectral methods exhibit the best convergence and accuracy properties[88]. The readily available packages which utilise hp-adaptive pseudospectral methods are GPOPS-2[120] and ICLOCS2[121]. Both ICLOCS2 and GPOPS-2 uses IPOPT[122], a widely used open source nonlinear optimisation package which utilises an interior point line search filter method.

ICLOCS2 is a software package in the alpha stages of development, which is based upon ICLOCS, a multiple shooting solver[121]. ICLOCS2 is able to implement a range of transcription methods, including a hp-adaptive Legendre-Gauss Pseudospectral method[121]. As ICLOCS2 is relatively new at the time of writing, it has not yet been implemented in any published works and documentation is limited.

GPOPS-2 is a proprietary hp-adaptive pseudospectral method solver developed by RP Optimization Research LLC, which implements a variety of hp-adaptive pseudospectral methods, so that the best method may be chosen for a given problem[120]. GPOPS-2 is specifically designed to be as flexible as possible, to accommodate for a wide range of problem formulations[120]. GPOPS-2 is well proven in aerospace applications, and has been used for spacecraft orbit optimisation as well as in-atmosphere trajectory optimisation[116, 123]. GPOPS-2 is well suited to solving multi-phase optimal control problems, which is necessary for efficient multi-stage launch optimisation[120]. GPOPS-2 represents the state of the art in trajectory optimisation software, and as such is used by a number of institutions around the world.

Software	Publisher	Platform	Optimisation Type
DIDO[124]	Elissar Global	MATLAB	Chebychev Pseudospectral
GPOPS II[120]	RP Optimization Research	MATLAB	hp-Adaptive Legendre-Gauss-Radau Pseudospectral
PROPT (IPOPT)[125]	TOMLAB	MATLAB	Legendre-Gauss Pseudospectral
ICLOCS2[121]	Imperial College	MATLAB	Multiple Shooting / hp-adaptive Legendre-Gauss Pseudospectral
POST2[126]	NASA	FORTRAN	Direct Shooting
OTIS[127]	NASA	Fortran	Pseudospectral + Various
TRANSWORHP[128]	ESA	Fortran/C++	Full Discretisation
ASTOS[119]	Astos Solutions	Standalone	Multiple Shooting/Collocation
ACADO[129]	Open Source	C++	Direct
JModelica[130]	Modelon AB, Open Source	Modelica/Python	Collocation/ Pseudospectral

Table 3.4: Summary of programs capable of pseudospectral optimisation.

Although many of these optimisation packages are relatively similar, and are appropriate for highly nonlinear hypersonic launch problems, GPOPS-2 is the most readily available package that utilises a very high robustness and accuracy transcription method. However, GPOPS-2 is only a generic solver, requiring significant configuration to solve a launch problem. This configuration includes launch vehicle modelling, and design of the optimal control problem, so that a solution maybe achieved. These are no small tasks, as the configuration of an optimal control problem for a complex launch vehicle requires deep knowledge of both the vehicle design and performance, as well as the underlying optimal control processes.

3.6 Aerodynamic Analysis

Optimising the trajectory of a space access vehicle using optimal control methods requires the development of a dynamic model of the launch vehicle. This dynamic model requires the aerodynamics of each stage of the launch system to be characterised at every flight condition experienced during launch. This is usually achieved either analytically for simple vehicle designs, or through the generation of large aerodynamic coefficient databases that cover the operable region of the vehicle. The generation of databases is generally necessary when it is desired to capture more complex and non-linear aerodynamics that must be pre-computed for efficiency.

There are a variety of tools available to calculate the aerodynamics of aerospace vehicles. These tools are primarily designed towards either accuracy or efficiency, as more accurate methods require more computational power, longer computational times and, usually, more man-hours to produce a solution. This trade off means a tool must be selected which best suits the requirements of a given problem. For a preliminary vehicle design, it is often desirable to select a tool which is as computationally efficient as possible, as the design of the vehicle is liable to change often. Whereas for more advanced stages of vehicle design, an accurate tool is desirable, to assess the design of the vehicle in detail.

The lowest fidelity, and highest efficiency methods include packages that use empirical relations derived from databases of existing vehicles, such as Missile Datcom[131], as well as panel method codes such as HYPAERO[12], cbaero[132] and HOTSOSE[133]. Low fidelity methods offer rapid solutions, with highly variable accuracy. For simple, standard vehicle shapes, low fidelity methods may be relatively accurate, as low fidelity solutions are usually calibrated to higher fidelity simulations or experiments. However, for complex vehicle geometries, for example geometries involving engine flow-paths, the accuracy of low fidelity models diminishes significantly[134] unless calibrated by experiment or high-fidelity models. **In addition, the determination of control surface aerodynamics in these models is not particularly sophisticated unless pre-calibrated.** Despite this, low-fidelity codes are usually taken as being appropriate for preliminary design analysis, and are used in the analysis of all of the multi-stage airbreathing launch vehicles studies in Sections 3.1.2 & 3.1.3 where aerodynamic analysis is presented[23–26, 28–32].

Medium fidelity methods consist of inviscid Euler solvers such as Cart3D[135] and FUN3D[136], which are able to provide reasonable accuracy, with medium run times, by neglecting viscous effects within the solution. These solvers are often used in the later stages of preliminary design, or when higher fidelity is necessary due to design features, but rapid solutions are still desired. Neglecting the viscous effects in the fluid flow means that the solution obtained from an inviscid solver will only be an approximation of the real flow, and that the accuracy of the solution varies depending on the type of problem being solved. For problems such as lift on a thin airfoil, inviscid Euler methods may be quite accurate, however for a problem such as boundary growth on a flat plate these methods will not accurately model the solution[137]. A particular advantage that many inviscid Euler codes provide is automatic adjoint mesh adaptation, the ability for the mesh to be automatically and rapidly generated, and updated sequentially throughout the solution process, refining areas of complex geometry or flow. This enables multiple solutions to be easily computed, without the need to regenerate meshes manually. In the early stages of vehicle design, inviscid-flow Euler CFD solvers are used extensively across industry and academia[138], as they are often able to capture **the trends in the aerodynamics of a launch vehicle sufficiently well for preliminary design purposes, while having relatively short run times that make the generation of aerodynamic databases practicable.** However, inviscid solvers naturally do not capture the aerodynamic forces on a vehicle due to viscous effects. This deficiency

can be corrected using an approximation of the viscous forces, to improve the accuracy of the solution generated by an inviscid solver, while retaining the computational advantages of inviscid CFD[139].

High fidelity methods consist of Navier-Stokes CFD solvers such as Eilmer3/4[140], Fluent[141], CFX[142], COMSOL[143], TAU[144], and OpenFOAM[145]. These solvers will resolve the fluid flow and aerodynamic forces to a high level of accuracy, including viscous effects. However, bespoke high quality meshes for the problem must be generated prior to the calculation of the solution, which increases the working time significantly. Additionally, the computation times are much longer, and require more computational resources than lower fidelity methods. These factors make the generation of an aerodynamic database using high fidelity CFD an extremely time consuming process. As such, high fidelity CFD is suited for use on mature vehicle designs, or when accurate flow simulation is judged to be necessary to **capture the behaviour of all or part of a vehicle. This is generally applied when the behaviour of the flow is particularly complex, or when the accurate calculation of the flow properties is necessary to assess aerodynamics or engine performance.**

3.6.1 Cart3D

Cart3D is an inviscid Euler solver CFD package, designed for use during preliminary vehicle design and analysis[138]. Cart3D is computationally efficient and requires only a surface triangulation of the vehicle being analysed to initiate a simulation. Cart3D is utilised in this study due to its balance of efficiency and ease of use, along with its reasonable accuracy for hypersonic flow calculations[139, 146, 147]. Cart3D features adjoint mesh adaptation, and uses cartesian ‘cut-cells’ that intersect the surface, allowing complex geometries to be analysed automatically. The mesh automatically refines as the simulation progresses, adaptively reducing error. The absence of a requirement for a user generated mesh allows Cart3D to be easily applied to complex launch vehicle designs, as well as allowing for simple modification of control surface deflections and flight conditions. Cart3D has been used extensively for aerodynamic simulations in preliminary design, including analysis of the plumes of the Skylon spaceplane[148], HIFiRE-5[149], and in low sonic boom shape optimisations[150]. Cart3D has shown fair agreement when compared to experimental and high-fidelity CFD results[139, 146, 147], particularly in the hypersonic regime. Cart3D’s comparative performance is analysed in detail in Appendix B.1, utilising previous studies that compare Cart3D with experimental data and high fidelity CFD computations.

3.7 Summary

XXXX Get into to have a look at this This section provided a review of available literature pertaining to the design and trajectory optimisation of a rocket-scramjet-rocket launch system. Previous

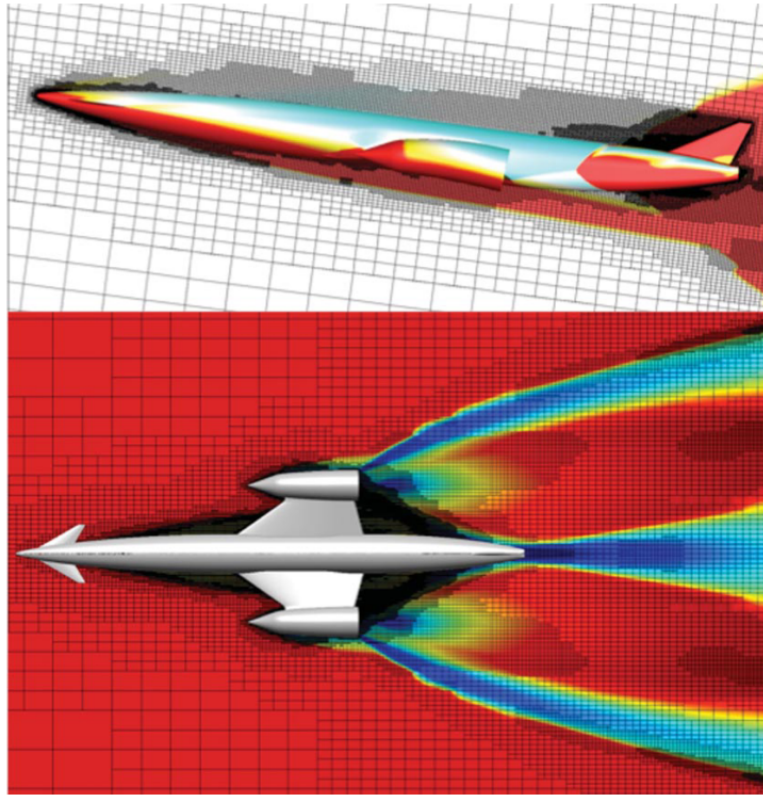


Figure 3.11: The Skylon spaceplane, simulated using Cart3D at Mach 12.189, $\alpha = 7.512^\circ$ [148]. Cell distribution produced by mesh adaptation is shown.

works on the design of airbreathing launch systems were detailed, separated into single, two-stage, and three-stage systems, and the launch trajectories of these systems were assessed. For single-stage systems it has generally been shown that flight at maximum dynamic pressure under airbreathing operation, followed by a pull-up before transition to rocket power until orbit was considered the optimal trajectory. For two-stage launchers, the optimal trajectory to orbit is unclear, differing significantly between the various launch systems and studies that have been performed. Studies of some two-stage launchers showed flight at maximum dynamic pressure followed by pull-ups for various reasons, as well as trajectories that flew at off-maximum dynamic pressure conditions for the majority of airbreathing engine operation, or did not leave maximum dynamic pressure at all. Only two three-stage systems were identified, both following a prescribed maximum dynamic pressure flight path for the entirety of airbreathing engine operation. In general, there were no in-depth studies of the optimal trajectories of multi-stage airbreathing launch systems, and the disparity in the trajectory shapes of previous studies was due to strong trajectory-design coupling, as well as differences in the assumed optimal flight paths of the launch systems studied. In particular, it was evident that the trajectory paths of three-stage airbreathing launch systems to date have not been analysed in sufficient detail to provide insight into the coupling between the efficient operation of each stage, and that optimal trajectory development is warranted.

Due to being the most mature three-stage airbreathing concept; the SPARTAN rocket-scramjet-rocket launch system being developed by The University of Queensland and Hypersonix was investigated in detail for use as a basis of a launch vehicle design in this study. To assist ascent and return trajectory coupling, the return and maximum range trajectories of prior hypersonic vehicles were investigated, indicating that the return of a vehicle separated at hypersonic speeds is likely not possible without the operation of on-board engines. However, performing a ‘skipping’ manoeuvre may assist in maximising the glide range. To facilitate the development of optimal trajectories, the background of optimal control theory was outlined, and the specific optimal control techniques that are most applicable to trajectory optimisation were detailed, along with a survey of existing optimal control solvers and their use-cases. This survey indicated that a pseudospectral method was likely to offer the robustness and accuracy required by the complex optimal control problem of a three-stage airbreathing launch system trajectory. For vehicle aerodynamic modelling, a survey into CFD solvers was conducted, with Cart3D being identified as a medium-fidelity solver that balances accuracy with computational efficiency to a level that is useful for conceptual vehicle design and analysis.

CHAPTER 4

LAUNCH SYSTEM DESIGN AND MODELLING

This work aims to study the optimised trajectory and performance of a rocket-scramjet-rocket launch system. In order to produce this trajectory, the launch system must be modelled in some detail. This chapter presents the design and modelling of a representative rocket-scramjet-rocket launch system, in which the scramjet stage is reusable for multiple launches. This rocket-scramjet-rocket launch system is designed to launch small satellites to a 567km altitude sun-synchronous orbit and is based on the SPARTAN launch system concept, originally designed by Jazra, Preller & Smart[12, 83], and now being developed by The University of Queensland and Hypersonix. The SPARTAN launch system is used as the basis for a representative launch system within this study because it is the only rocket-scramjet-rocket launch system undergoing design, and because it is up-to-date technologically, as it is currently undergoing research and development. In addition, the SPARTAN is relatively mature when compared to other small, multi-stage systems, with multiple studies dedicated to its design. This design is based on the use of a set of four REST scramjet engines, a relatively mature scramjet engine design that has been experimentally tested and thoroughly modelled. The rocket-scramjet-rocket launch system described in this chapter is used as a representative model for a partially-airbreathing, partially-reusable, three-stage small satellite launcher. The optimal trajectory results and performance analysis produced are expected to be directly applicable to future iterations of the SPARTAN, as well as generally applicable, at least in part, to other multi-stage airbreathing launch systems that use a 'space-plane' type design.

Figure 4.1 shows a simplified representation of the launch trajectory for the vehicle simulated in this study. The launch system is launched vertically under rocket power, from a traditional small rocket launch facility. The scramjet accelerator is mounted to the front of the first stage rocket allowing the scramjet accelerator to take the brunt of the aerodynamic forces and heating, as well as allowing the use of the control surfaces of the scramjet accelerator. During first stage rocket operation, the launch system pitches rapidly, reaching close to horizontal flight to allow the scramjet accelerator

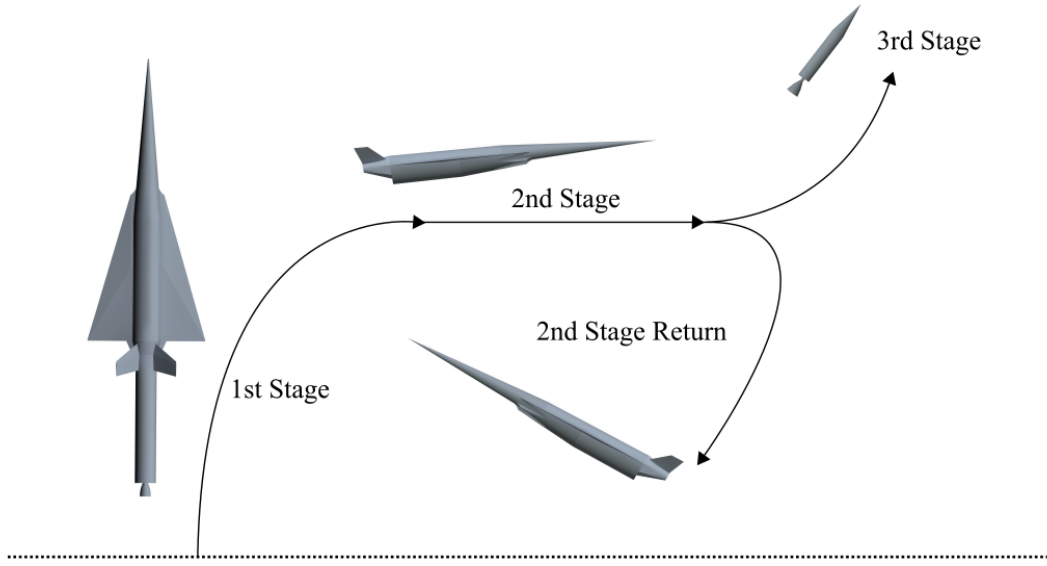


Figure 4.1: The launch process of the rocket-scramjet-rocket launch system, presented in simplified form.

to be released into high dynamic pressure conditions. The scramjet accelerator is accelerated to its minimum operating speed of approximately Mach 5, at which point separation occurs. The scramjet accelerator's four scramjet engines are ignited, and the scramjet accelerator is accelerated through the atmosphere, reaching approximately Mach 9. At this point, the specific impulse of the scramjet engines, and thus the efficiency of the scramjet accelerator, have decreased, and the third stage rocket is separated. The third stage rocket accelerates and performs a pull-up, before cutting its engine and coasting out of the atmosphere. Once the rocket is exoatmospheric, the engine is reignited, performing first a circularisation burn, and then a Hohmann transfer to the intended orbit. Meanwhile, the scramjet accelerator banks and executes a fly-back manoeuvre to return to its initial launch site. The scramjet accelerator extends landing gear, and lands on a traditional runway in the style of a conventional aircraft. The scramjet accelerator is able to be rapidly refurbished and remounted for further launches. To fulfil the requirements of this trajectory, the scramjet accelerator must be able to fly and manoeuvre from speeds greater than Mach 9 to landing, as well as being able to withstand high structural and heating loads without significant deterioration.

The launch configuration of the representative launch system is shown in Figures 4.2 & 4.3. The size and external design of the scramjet accelerator are used exactly as defined for the Baseline vehicle designed by Preller & Smart[12]. Both the first and third stage rockets are designed in this study, and are sized around the Baseline vehicle. The first stage rocket has not previously been designed, and as such is created for this study, while the third stage is redesigned to use a SpaceX Kestrel en-

gine. This third stage design replaces the third stage used within previous iterations of the SPARTAN concept, which was powered by a Pratt & Whitney RL-10-3A engine[12]. The pump-fed RL-10-3A engine was deemed too costly, and it has been replaced by a significantly cheaper pressure-fed Kestrel engine in this study. The internal layout of the scramjet accelerator has been reconfigured around this redesigned third stage. This launch system weighs a total of 28,355kg, and is 32.44m long.

The following sections present the detailed design of the launch system, along with the aerodynamic and propulsion modelling of each stage. The scramjet accelerator design is presented first, as the design of the scramjet accelerator drives the operational requirements and sizing of the launch system, and thus the design of the first and third stage rockets.

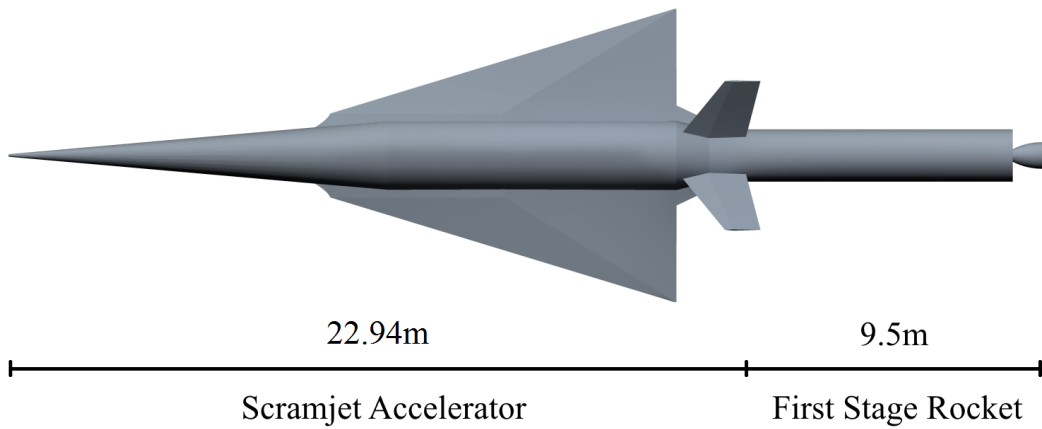


Figure 4.2: The representative launch system, top view, showing the scramjet accelerator and first stage.



Figure 4.3: The representative launch system, side view, showing the scramjet accelerator and fuel tanks, along with the third and first stages.

4.1 The Second Stage Scramjet Accelerator

4.1.1 The Scramjet Accelerator

The **representative scramjet-powered accelerator vehicle used in this study**, shown in Figure 4.4, is based closely on the Baseline vehicle designed by Preller & Smart[12]. **The external geometry of the**

scramjet accelerator is unchanged in this study, and is used to provide a baseline scale to the launch system. The scramjet accelerator is 22.94m long, with a frontal cone half angle of 5° [12]. A mass

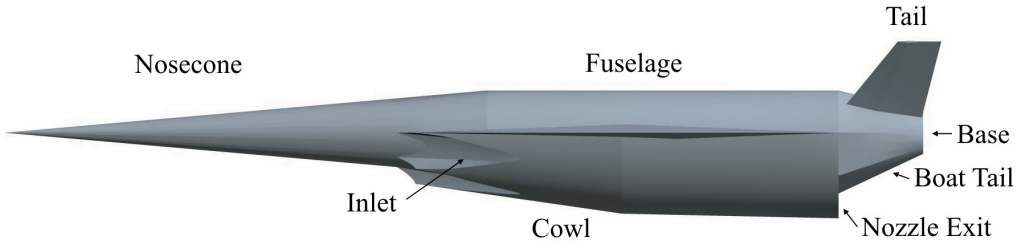


Figure 4.4: The external features of the scramjet accelerator.

breakdown of the scramjet accelerator is shown in Table 4.1, adapted from previous work by Preller & Smart[12]. The fuel mass of the scramjet accelerator has been modified for the representative launch system in this work, as the fuel tank sizes and total fuel mass are sized to accommodate the Kestrel-powered third stage, described in Section 4.3. This study assumes that the third stage is stored within

Part	Total	Fuselage	Wings	Tanks	Systems	Landing Gear	Scramjets	Fuel
Mass (kg)	6519.1	2861.6	350.7	179.4	707.5	188.9	669.0	1562.0

Table 4.1: Mass breakdown of the modified scramjet accelerator vehicle.

the fuselage of the scramjet accelerator for simplicity. It is assumed that the release mechanism for the third stage is able to be situated within the available space surrounding the third stage, however the release mechanism, as well as the change in the aerodynamics of the vehicle during staging, is not considered further in this study (see Section 4.4 for a discussion of the major simplifications within the launch system model).

The fuel tanks are sized to fit around the kestrel-powered third stage, as shown in Figure 4.3. There are three fuel tanks; two cylindrical tanks situated underneath the third stage; and a truncated conical tank in the nose. The conical fuel tank is designed to fit immediately forward of the third stage. This fuel tank is 8m long, leaving 1.47m^3 of space in the nose for cooling systems, frontal landing gear, and any additional systems or sensors which are necessary in the nose cone. The cylindrical tanks are positioned underneath and slightly to either side of the third stage, leaving space underneath for vehicle systems. The cylindrical fuel tanks are designed to be 8.5m long, with diameters of 0.87m, sized to give a nominal total tank volume of 22m^3 . The resized fuel tanks hold a total of 1562kg of LH₂ fuel. This assumes an LH₂ density of 71kg/m^3 , slightly denser than LH₂ at phase transition point at 1 atm. The mass of the fuel tanks is scaled, by surface area, from Dawid Preller's Baseline vehicle model[12], giving a total fuel tank mass of 179.4kg.

4.1.2 Thermal Protection

For this study the thermal protection system has been adapted from the thermal protection system used by Preller[32]. The scramjet accelerator is thermally protected by a 11.3mm thick Carbon-Carbon aeroshell, with an alumina-borosilicate mat/ stainless steel multilayer insulator at the connection points between the aeroshell and the aluminium internal structure[32]. The nose of the scramjet accelerator is protected by 40mm thick tungsten tip, weighing 92kg, to provide rapid heat dissipation and sink in the area of greatest heating. For the purposes of this work it is assumed that the external shell is not connected to the internal structure close to points of large heating such as leading edges, and is structurally independent in these regions. In previous studies, a similar heat shielding has been assumed to provide adequate protection for the scramjet accelerator flying along a constant dynamic pressure trajectory[32], and this assumption is used in the main body of this work. The thermal protection system (TPS) sizing and performance of the launch system are investigated further in Section 7.3 and Appendix A.

4.1.3 Propulsion

The scramjet accelerator is powered by four underslung scramjet engines, fuelled by liquid hydrogen. These engines are Rectangular To Elliptical Shape Transition (REST) engines, configured to allow for a conical forebody (C-REST). REST engines have a rectangular to elliptical shape transition inlet, and an elliptical combustor, offering simplicity in design as well as reduced thermal loading and viscous drag compared to scramjets with planar geometries[151]. REST engines are also specifically designed to operate over a wide range of Mach numbers, and at off design conditions, making them particularly applicable to use on scramjet accelerator vehicles. REST engines have been shown experimentally to operate successfully at off design conditions[152, 153], and have shown good agreements with numerical CFD models[153]

Propulsion Modelling

Before the flow enters the engine, it is affected by the conical shock generated by the forebody of the scramjet accelerator. Figure 4.5 shows the locations of the flow properties, which are necessary to calculate engine performance. The ambient atmospheric conditions (the free stream conditions illustrated in Figure 4.5) are calculated by interpolation using the 1976 NASA Atmospheric properties[154]. The flow properties at the inlet of the engines (the post-shock conditions illustrated in Figure 4.5) are calculated using the Taylor-Maccoll analysis method for conical shocks[155]. This calculation is performed in part utilising the cone_shock program provided for this study by Prof. Michael Smart. The flow conditions as a function of flight conditions following the conical shock are

shown in Figure 4.6.

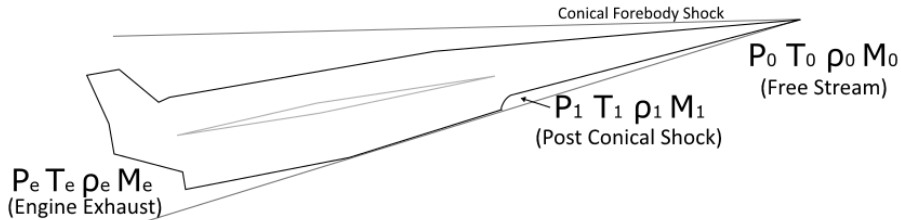


Figure 4.5: The locations of conditions relevant to C-REST engine simulation.

The C-REST engines that the scramjet accelerator uses have been configured to fly between Mach 5 and 10. This type of engine is known as a C-RESTM10 engine[12]. A CRESTM10 propulsion database has been used in previous studies to model the scramjet engines of the scramjet accelerator[12]. A modified version of this database is used in this study. The specific impulse profile of the C-RESTM10 engine, taken from the CRESTM10 propulsion database, is shown in Figure 4.7. This database has been created through separate modelling of the compression within the inlet, combustion within the combustor, and expansion through the internal nozzle[32, 92]. The inlet compression was modelled by performance curves based on a set of CFD solutions[32, 92]. These performance curves are used to obtain the flow conditions at the end of the inlet. The combustor is modelled using quasi-one-dimensional cycle analysis, assuming a combustion efficiency of 80%[32, 92]. Lastly, the properties at the end of the combustor are expanded assuming a nozzle efficiency of 90%[32]. The C-RESTM10 is designed for operation at $M_0 = 10$, and the contraction ratio and combustor divergence are not optimal for operation at low Mach numbers. At low Mach numbers, an equivalence ratio of 1 may cause the flow to choke and unstart. Consequently, an equivalence ratio of less than 1 is set at low Mach numbers, in order to avoid unstart[32]. At these Mach numbers, the C-REST engines are operating in dual-mode[32].

The CRESTM10 database provides data points of engine performance over inlet conditions within the operational range, at 50kPa dynamic pressure equivalent conditions. The specific impulse data set is shown in Figure 4.7. This data is interpolated for the given inlet conditions, to calculate specific impulse produced by the engine. As the data points of the CRESTM10 database are unevenly distributed for inlet Mach and temperature, care must be taken in order to interpolate smoothly to allow the optimal control solver to converge successfully. To ensure that smooth interpolation is achieved, the CRESTM10 database is first interpolated using linear interpolation, for each ‘set’ of four nodes which form a square. A uniform grid is created using this linear interpolation, on which a cubic spline interpolation is applied using Matlab’s griddedInterpolant function. This is explained in detail in Appendix D. During flight the C-REST inlet conditions generally stay within the region bounded by the available data. However, for the purposes of the trajectory optimisation, it is necessary to provide data for a wide range of inlet conditions (T_1, M_1). To calculate I_{SP} and equivalence ratios

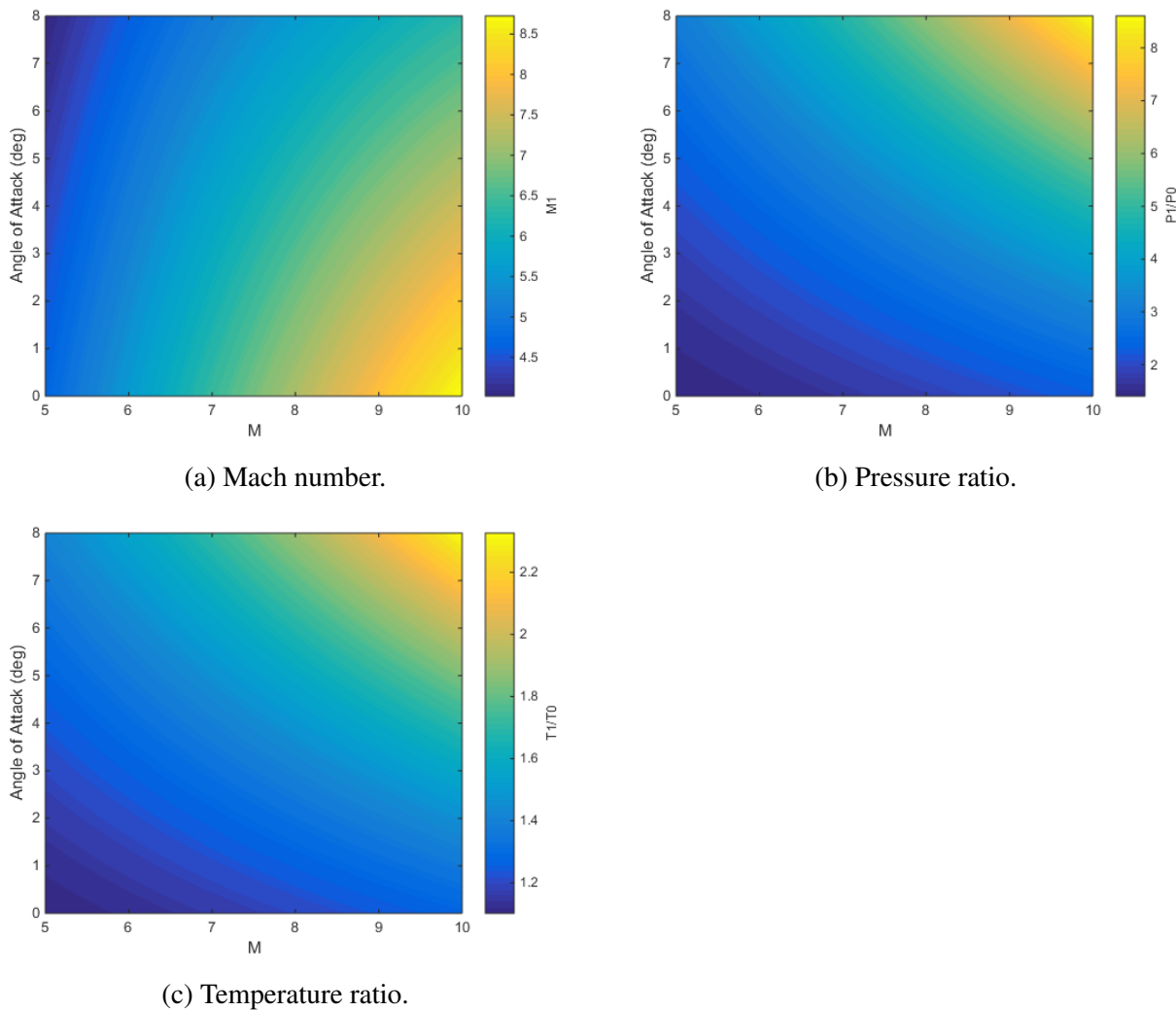


Figure 4.6: Flow conditions after the conical shock generated by the vehicle nose cone as a function of flight Mach number and angle of attack. Figure a) shows the Mach number, b) shows the pressure ratio, and c) shows the temperature ratio following the conical shock, at the engine inlet.

outside of the modelled range of inlet conditions, the existing data is extrapolated. This extrapolation is performed in the same manner as the interpolation, a linear extrapolation, followed by a cubic spline interpolation of the extrapolated points. This allows for smooth continuity between the interpolated and extrapolated points, while ensuring that the extrapolated regions provide reasonable values. This smooth and reasonable extrapolation is critical for the trajectory optimisation process, even though the final trajectory conditions are not expected to fall significantly outside of the bounds of the CRESTM10 database. Allowing the optimiser to extrapolate data in turn allows for a full exploration of the solution space, ensuring that the search space is not unnecessarily limited, and assisting robust convergence on an optimal solution.

For operation at high Mach numbers, the fuel mass flow rate is assumed to be stoichiometric, so that $m_f = 0.0291m_{air}$. This ensures that the scramjet engines are performing at high efficiency

throughout the acceleration of the scramjet stage. However, the C-REST engine is a fixed geome-

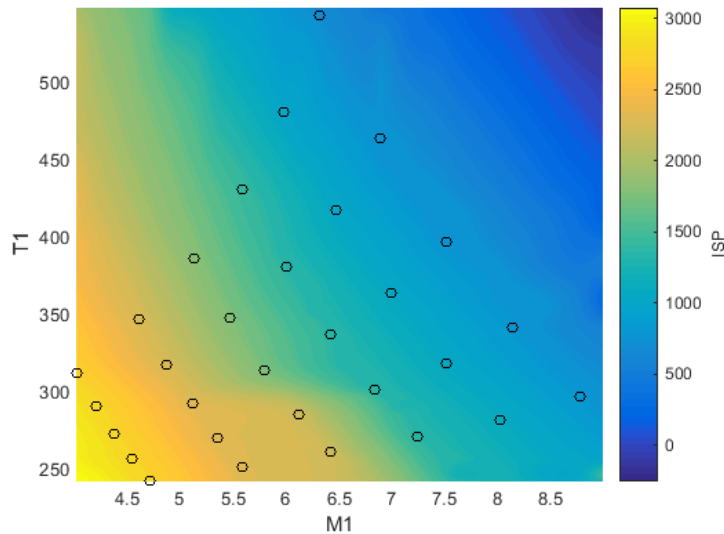


Figure 4.7: Specific impulse of the C-REST engines with input temperature and Mach number. Available data points are indicated. M_1 and T_1 are the inlet Mach number and temperature, as shown in Figure 4.5.

try engine, primarily designed for operability at high Mach numbers[12]. At lower Mach numbers, the addition of excessive fuel may cause the engine to choke and unstart, resulting in total loss of thrust[12]. To avoid unstart, an equivalence ratio (ϕ) of less than 1 is necessary at low Mach numbers. In this region the equivalence ratio is set to the maximum value which does not cause the engine to unstart. These maximum equivalence ratios were determined during the modelling of the engines throughout the creation of the CRESTM10 database. The equivalence ratio interpolation is linear, as the number of data points available for interpolation is low. The prescribed equivalence ratio over the range of scramjet engine operation is shown in Figure 4.8. The mass flow rate into the engine is determined through a set of empirical relationships within the CRESTM10 database, that determine the air captured by the inlet. These empirical relationships take into account the manner in which apparent intake area is affected as angle of attack is varied, as well as the mass spillage due to the complex inlet shape. The fuel mass flow rate is then determined from the captured air flow rate as follows;

$$\dot{m}_{fuel} = \left(\frac{m_{fuel}}{m_{ox}} \right)_{st} \phi \dot{m}_{air}. \quad (4.1)$$

The fuel mass flow rates across flight conditions are shown in Figure 4.9, including the effects of the reduced equivalence ratio at low Mach numbers.

The thrust for each engine, T , is then obtained by the inclusion of the interpolated specific impulse, ie.

$$T = g_0 \dot{m} I_{sp}. \quad (4.2)$$

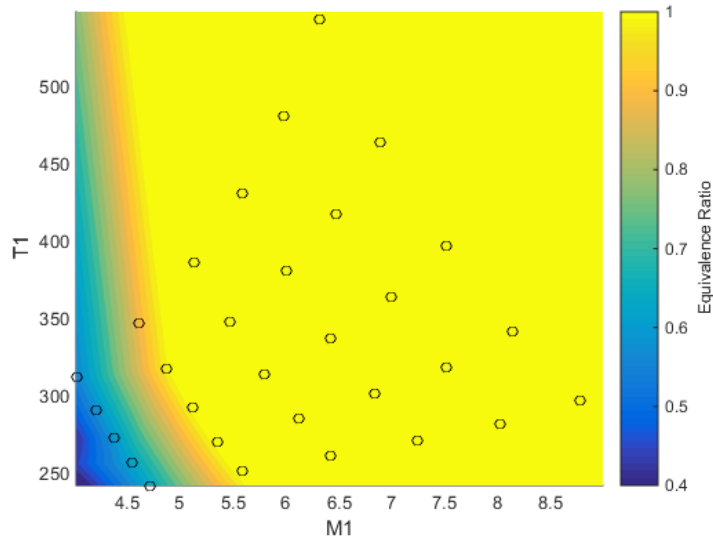


Figure 4.8: Operable equivalence ratio of the C-REST engines with input temperature and Mach number. Available data points are indicated.

The available database uses a C-REST engine with a nozzle exit area of 0.56m^2 . For the scramjet vehicle modelled in this work, this is further expanded to 0.97m^2 . Additional thrust is obtained from the additional nozzle segment, and the specific impulse of the C-REST engines will be higher than calculated from the CRESTM10 database. The modelling of this additional nozzle segment and the thrust obtained are detailed in Section 4.1.4.

4.1.4 Aerodynamics

In order for the trajectory of the scramjet accelerator to be successfully simulated and optimised, the aerodynamics of the scramjet accelerator must be calculated for the large range of flight conditions experienced during its acceleration and return flights. The aerodynamics of the scramjet accelerator are calculated at set flight conditions (alt, Mach, AoA) covering the breadth of necessary conditions, and the results are tabulated as non-dimensional coefficients in databases. During trajectory simulations, the aerodynamics of the scramjet accelerator are determined by interpolation over the aerodynamic databases using bivariate splines, and the drag and lift produced are calculated using the standard definition of the aerodynamic coefficients:

$$F_d = \frac{1}{2}\rho C_D v^2 A, \quad (4.3)$$

$$F_L = \frac{1}{2}\rho C_L v^2 A. \quad (4.4)$$

The trimmed aerodynamic databases of the scramjet accelerator are generated in full prior to

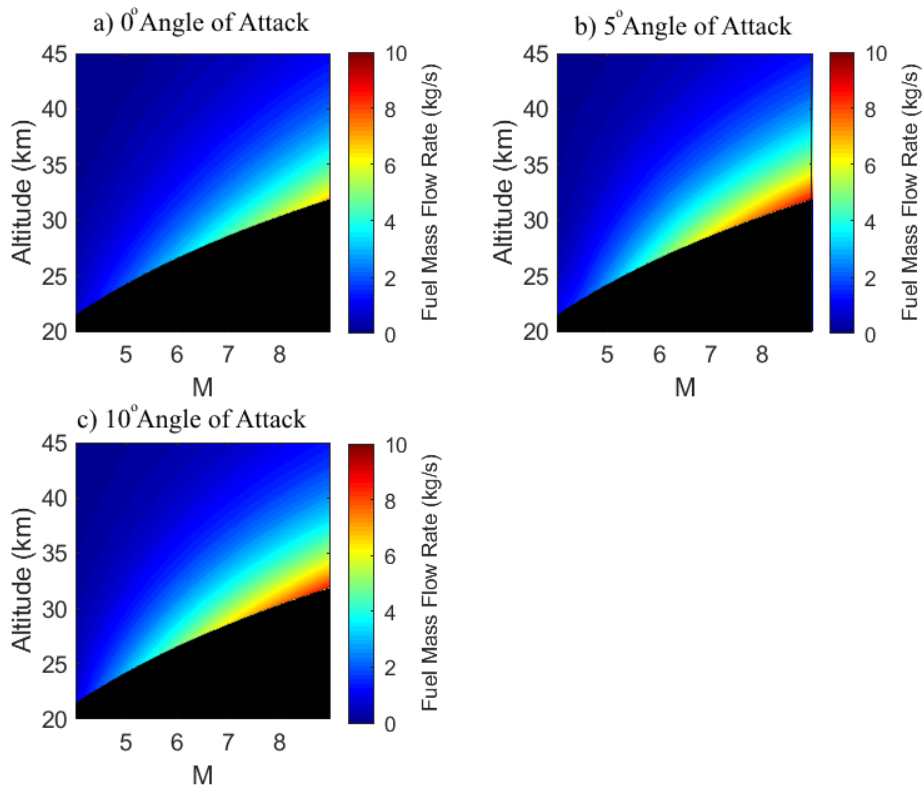


Figure 4.9: Fuel mass flow rate with varying flight conditions. Conditions are shown only up to 50kPa dynamic pressure.

trajectory simulation to improve the computational efficiency of the simulation. The aerodynamic coefficients of lift, drag and moment are tabulated, and these tables are interpolated during simulation. The aerodynamics are calculated for Mach numbers between 0-10, angles of attack between 0° and 10° , and for altitudes between 0-40km. Separate aerodynamic simulations are performed for engine-on and engine-off conditions, as the operation of the scramjet engines changes the aerodynamic characteristics of the scramjet accelerator significantly. When the engines are powered-on, the engines are generating thrust on the internal nozzle, as well as on the boat tail and base. When the scramjet engines are not operational air flows through the engine flowpath without fuel injection, generating a large amount of drag.

The process for generating the aerodynamic databases is shown in Figure 4.10. First, a CAD model of the scramjet accelerator is developed, providing the centre of gravity of the scramjet accelerator (shown in Figure 4.17), as well as a geometry database which is used to create triangulated surface meshes (shown in Figure 4.11). These surface meshes are then imported into the inviscid CFD solver Cart3D[135], which calculates flow solutions to determine the aerodynamics of the scramjet accelerator at various flight conditions. CFD solutions are generated for the scramjet accelerator with the scramjet engines turned off, with the scramjet engines operational, and for a range of flap deflec-

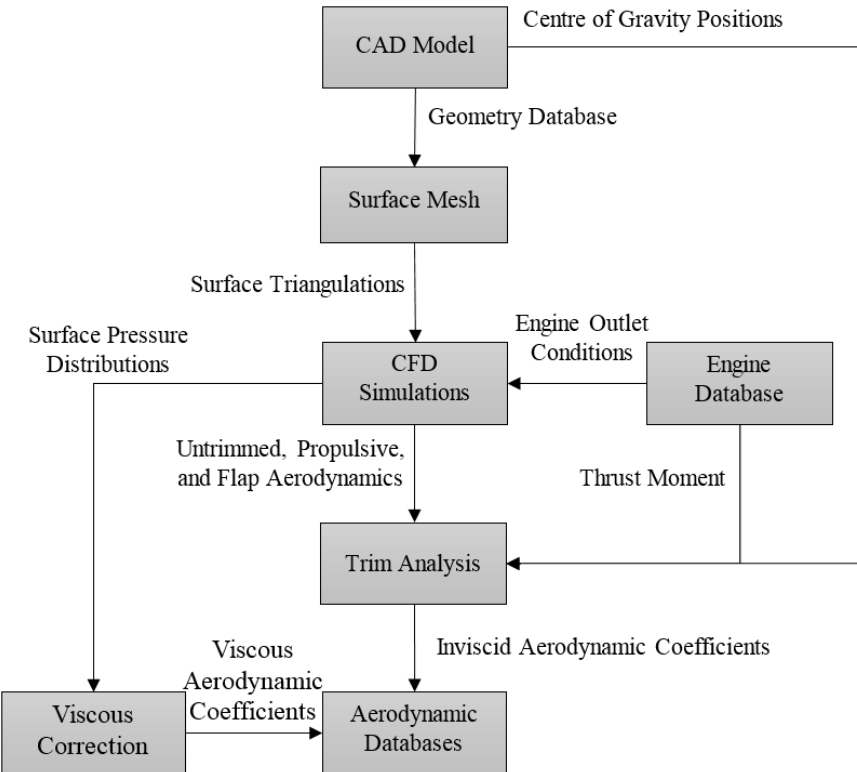


Figure 4.10: The process for generating aerodynamic databases.

tions. The flap deflections necessary to trim the vehicle are calculated at every flight condition, by balancing the aerodynamic moment of the scramjet accelerator and the moment caused by the off-axis thrust alignment of the scramjet engines, with the aerodynamic moment generated by the flaps. The additional lift and drag generated by the flaps are then added to the untrimmed aerodynamics to create a trimmed database. Finally, the viscous contributions to the aerodynamics of the scramjet accelerator are calculated, and added to the aerodynamic database as additions to the non-dimensional inviscid lift and drag coefficients. These processes are described in detail in the following sections.

Cart3D Simulations

The aerodynamics of the scramjet accelerator have been calculated using Cart3D, an inviscid CFD package used in the preliminary design of aerospace vehicles. Cart3D utilises adjoint mesh adaption with a Cartesian cut-cells approach to produce an iteratively refined mesh to fit a flow solution. Cart3D is used to generate the aerodynamic database of the scramjet accelerator due to its applicability in all regimes, and its robustness across multiple flow solutions[139, 147, 150, 157–160]. Cart3D has previously been used to analyse hypersonic vehicles, and has shown fair agreement with experimental data across multiple studies[139, 146, 147], as described in Appendix B.1.

Initially, a surface triangulation of the scramjet accelerator is created in Pointwise, shown in Figure

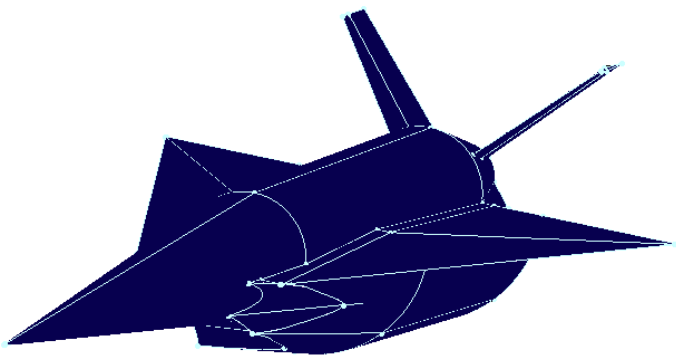


Figure 4.11: Surface triangulation of the scramjet accelerator, generated using Pointwise[156].

4.11. This is then imported into CART3D as a watertight surface. The Cart3D Meshes are then initiated with an outer boundary distance of 40 times the vehicle length. This boundary distance has been observed to produce suitable free stream conditions and good mesh convergence. Nine mesh adaption levels are used. Nine levels have been observed to generally produce good convergence, with moderate computation times of 1-3 hours per simulation. The convergence of the residuals and forces are investigated to ascertain if a solution has converged. Figure 4.12 shows an example of solution validation for Mach 6, 2° angle of attack, engine-on conditions. Good convergence can be observed in the force functionals, with a corresponding decrease in the error estimate of the functional indicating solution convergence.

Following simulation in CART3D over the required flight conditions, the aerodynamic coefficients are extracted. The simulation files are processed using Clic, a subprogram of CART3D used to calculate aerodynamic forces and moments, given surface pressure distributions. For engine-off aerodynamics, the aerodynamic coefficients of the entire scramjet accelerator are extracted. However, for the engine-on aerodynamics of the scramjet accelerator, the engine flowpath, boat tail and base of the scramjet accelerator are removed when the aerodynamic coefficients are extracted. The flowpath of the scramjet engines is assumed to be replaced by the conditions given by the CRESTM10 engine database, and a separate Cart3D simulation is used to calculate the aerodynamic forces on the boat tail and base.

Engine Exhaust Contributions

When the scramjet engines are turned on, the exhaust exits the nozzle of the engines and expands onto the boat tail of the scramjet accelerator. This changes the aerodynamics of the boat tail significantly, necessitating separate Cart3D simulations to calculate the varied aerodynamic coefficients of the boat tail. In addition, the scaled engine modelled in the CRESTM10 propulsion analysis has an exit area of 0.5586m^2 , smaller than the nozzle exit area on the scramjet accelerator, of 0.9719m^2 . The larger

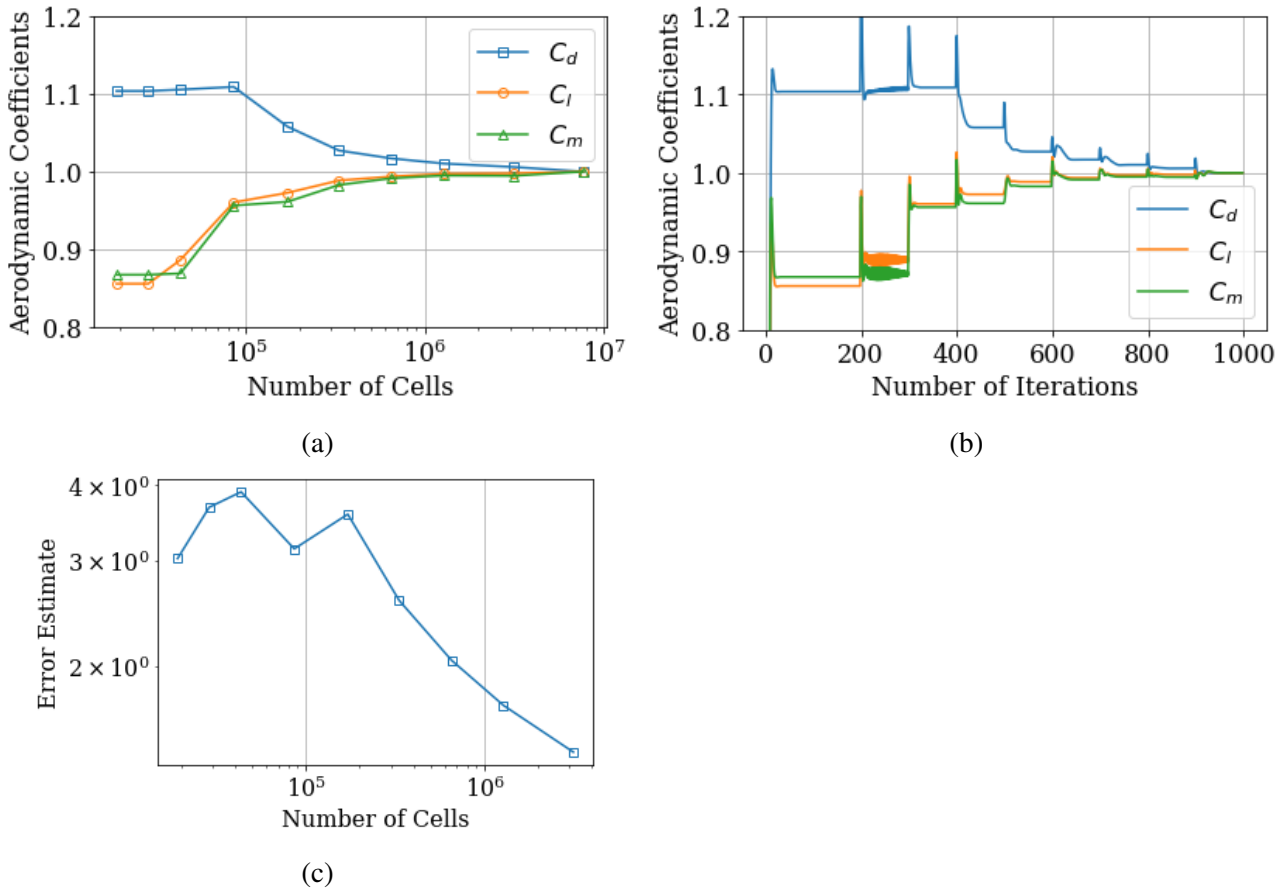


Figure 4.12: The convergence of a Cart3D simulation of the scramjet accelerator at Mach 6, 2° angle of attack.

nozzle exit of the scramjet accelerator provides additional expansion area, and additional thrust, which is modelled using Cart3D.

The exhaust of the C-REST engines is simulated using CART3D, using SurfBC boundary conditions, which produce outflow and inflow conditions at the inlet and exit of the scramjet engines[161]. The exit conditions calculated by the CRESTM10 database, as defined in Section 4.1.1, are set as the inflow conditions for the Cart3D surface. The inflow surfaces are positioned inside the nozzle on the scramjet accelerator model, scaled to match the exit area of the engines simulated for the CRESTM10 database, 0.5586m^2 . The surface triangulation of the scramjet accelerator with outflow surfaces is shown in Figure 4.13. Cart3D performs simulations nondimensionally, and requires the outflow conditions of a boundary to be normalised. The outflow conditions of P_e , ρ_e and M_e given by the CRESTM10 propulsion model are normalised to Cart3D nondimensionalised variables as follows[162, 163];

$$P_e^* = P_e / (\gamma_0 P_0), \quad (4.5)$$

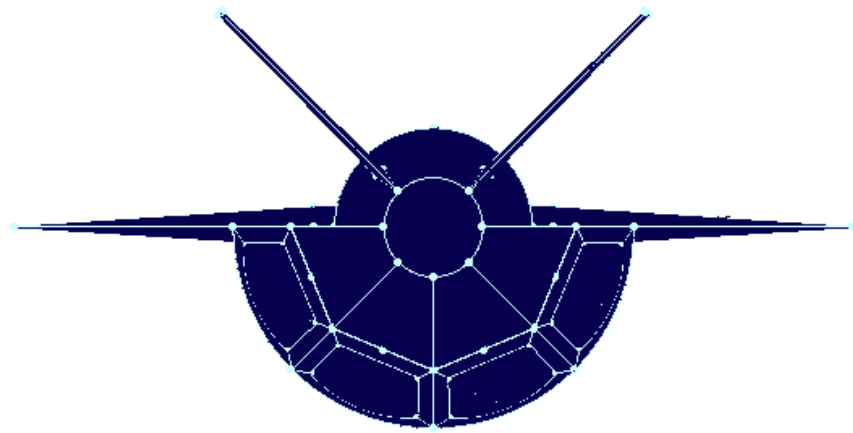


Figure 4.13: View of the scramjet accelerator surface triangulation showing engine outlet boundaries.

$$\rho_e^* = \rho_e / \rho_0, \quad (4.6)$$

$$M_e^* = \sqrt{\gamma_e / \gamma_0} (M_e \sqrt{P_e^* / \rho_e^*})^2. \quad (4.7)$$

Where $*$ indicates the nondimensionalised input to Cart3D. This nondimensionalisation includes a correction on the Mach number to account for variation in the specific heat ratio present in the combustion products, which is not possible to include directly in Cart3D[148]. The exhaust of the scramjet engines expands through the additional area of the scramjet accelerator's nozzle, and is further expanded onto the boat tail on the rear of the scramjet accelerator fuselage. This expansion causes significant force on the boat tail of the scramjet accelerator, generating additional lift, thrust, and moment forces. The total thrust generated by the scramjet accelerator, including the thrust generated by the additional nozzle expansion, and the forces on the boat tail, are shown in Figure 4.14, with the corresponding specific impulse shown in Figure 4.15.

Viscous Correction

As Cart3D is an inviscid solver, the aerodynamic database generated by Cart3D lacks the forces generated by skin friction drag. In order for the aerodynamic model to more closely approximate realistic dynamics, a correction for the viscous forces on the scramjet accelerator is calculated, using the viscous correction solver VC3D[139]. VC3D utilises flat plate correlations for skin friction on each surface cell, employing a simplified running length based on the Euclidean distance to the respective stagnation feature. Further details of this solver can be found in Reference[139]. This method has been shown to significantly improve upon the accuracy of the aerodynamic coefficients calculated by Cart3D for multiple test vehicles[139]. The viscous drag coefficients are generated for

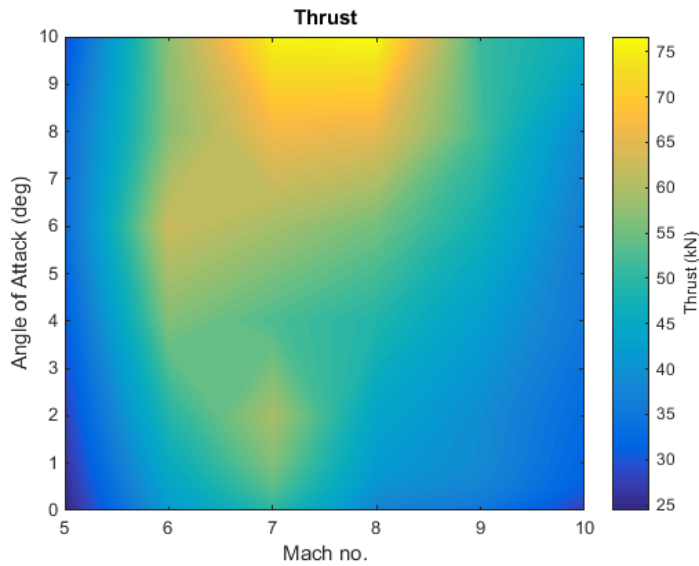


Figure 4.14: The total thrust output of the scramjet accelerator, including the CRESTM10 database, and Cart3D nozzle and boat tail simulations.

the scramjet accelerator at every Mach number and angle of attack which are simulated in Cart3D. Viscous databases are generated for both engine-on and engine-off cases, for altitudes of 20-45km and 0-60km respectively. The viscous drag coefficients for selected flight conditions are shown in Figure 4.16.

Centre of Gravity Analysis

The centre of gravity locations of the scramjet accelerator are calculated using CREO. For simplicity, it is assumed that structural, systems and landing gear masses are homogeneously distributed throughout the centre fuselage of the scramjet accelerator. The calculated centre of gravity for the scramjet accelerator full of fuel and including the third stage rocket is **15.24m** along the body length. The centre of gravity varies as fuel is depleted throughout the acceleration phase, and at third stage release, changing the flap deflections required for trim. **These centre of gravity variations are shown in Figure 4.17.** The cylindrical fuel tanks (**shown underneath the third stage in Figure 4.3**) are depleted first, in order to shift the centre of gravity forward, and improve the aerodynamic stability of the scramjet accelerator during the majority of flight. Depleting fuel from the cylindrical fuel tanks first is likely to also serve to reduce fuel slosh during flight, although the fuel slosh is not modelled in this study, and it is assumed that the centre of gravity of each individual tank remains constant. After the cylindrical tanks have been depleted, the fuel in the conical tank within the nose is used. After third stage release at the end of acceleration, and the centre of gravity changes significantly. When the third stage is released there is still fuel stored in the conical tank for flyback, during which centre of gravity change must also be modelled. Consequently, trimmed aerodynamic databases are created

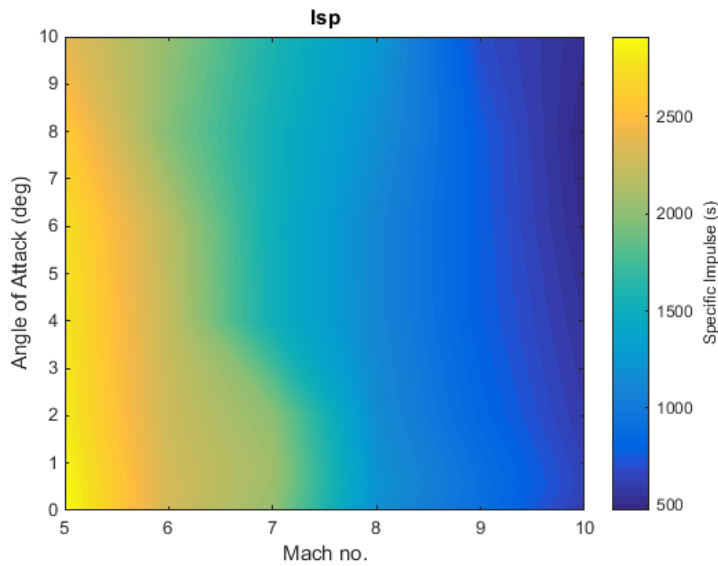


Figure 4.15: The specific impulse of the scramjet accelerator, including the C-rest database, and Cart3D nozzle and boat tail simulations.

for the five discrete configurations shown in Figure 4.17. Centre of gravity for partially full tanks are calculated using a tank fuel fraction-based weighted average of the respective full and empty tank configurations.

Calculation of Trimmed Flap Deflections

The scramjet accelerator as designed by Preller[12] is trimmed using control surfaces on the wings, shown in figure 4.18. The flaps of the scramjet accelerator are modelled at deflected states of -20° , -10° , 10° , and 20° , following the same process as described for the entire vehicle in Section 4.1.4. The scramjet accelerator is modelled in CREO with the flaps at each of these deflected states, and a surface mesh is created in Pointwise. Cart3D is used to simulate each of these flap deflected states, and Clic is used to extract the aerodynamic coefficients, for Mach numbers between 0.2 and 10, with angle of attack held at 0° . These aerodynamic coefficients are tabulated, and interpolation splines fitted, so that the flight Mach number and the moment generated by the flaps can be used to interpolate for the flap deflection, ie. $\theta_{Flaps} = f(M, M_{Flaps})$. Trim is determined by calculating the aerodynamic moment coefficient with zero flap deflection, then calculating the flap deflection necessary to balance the aerodynamic moments to zero. The moments generated by the untrimmed scramjet accelerator, including the aerodynamic moment as well as the thrust moments on the engines and boat tail when the C-REST engines are powered-on, are balanced by the moment generated by the flaps, so that:

$$M_{Flap} = -M_{Untrimmed} \quad (4.8)$$

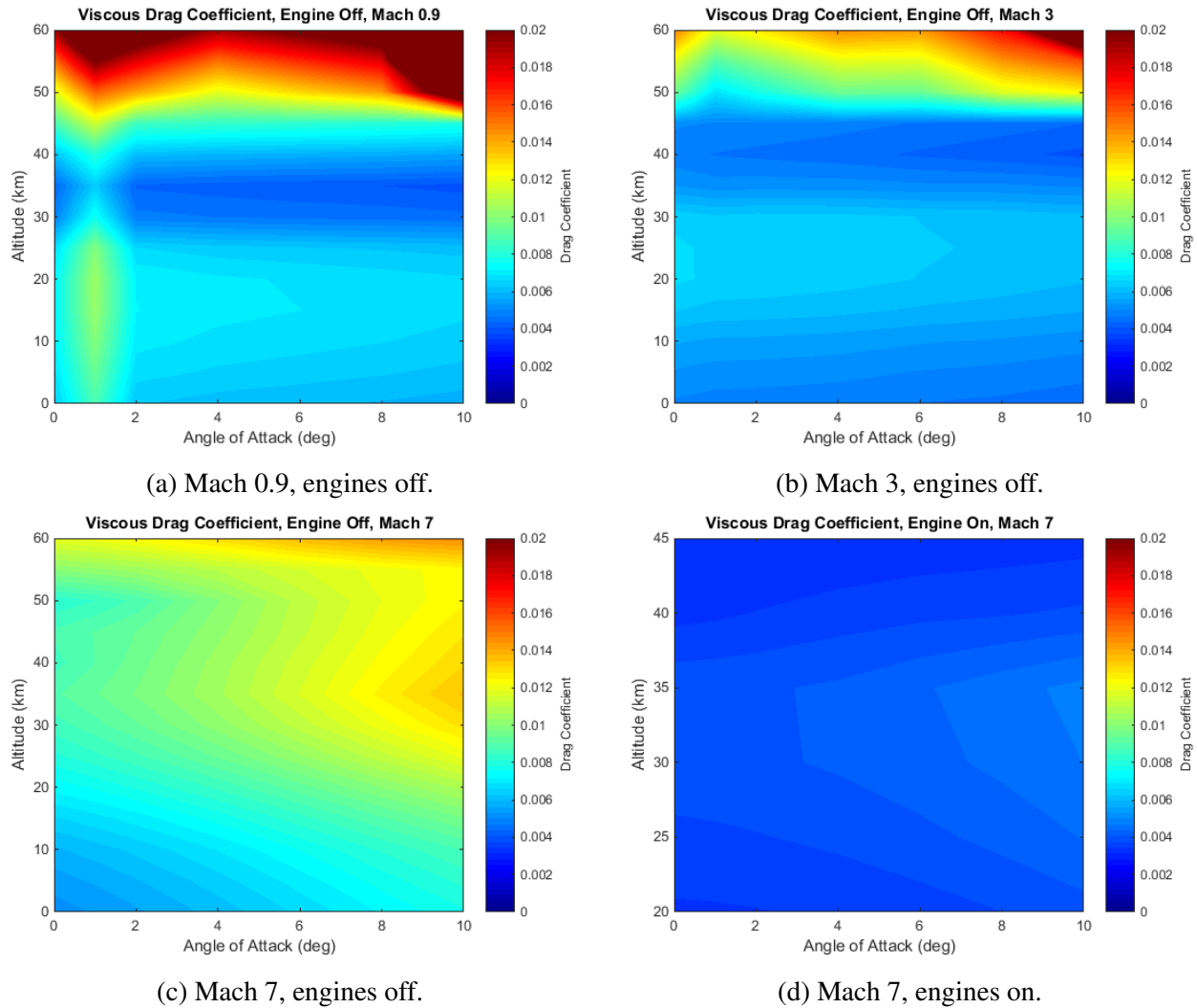


Figure 4.16: Viscous drag coefficient across various Mach numbers.

The flap deflections necessary for trim at the discrete conditions shown in Figure 4.17 are shown in Figure 4.20, calculated for Mach numbers between 0.2 and 10, and at angles of attack from 0° to 10° . Engine-on flap deflections are shown at centre of gravity locations corresponding to full-fuel, full conical tank, and empty conditions with the third stage included, and engine-off flap deflections are shown at the centre of gravity corresponding to a fuel-empty condition after third stage release. The flap deflections are designated as negative up. Negative flap deflection necessary for trim indicates that the centre of pressure is aft of the centre of gravity, and that the vehicle has positive static margin. It can be observed that while the cylindrical fuel tanks are being used, the scramjet accelerator is generally stable at low angles of attack, and the static margin is close to 0, requiring only small flap deflections for trim. As the fuel in the conical tank is depleted, the centre of gravity moves aft, and the scramjet accelerator develops a negative static margin, requiring larger flap deflections to trim at high Mach numbers. These large flap deflections indicate that the scramjet accelerator

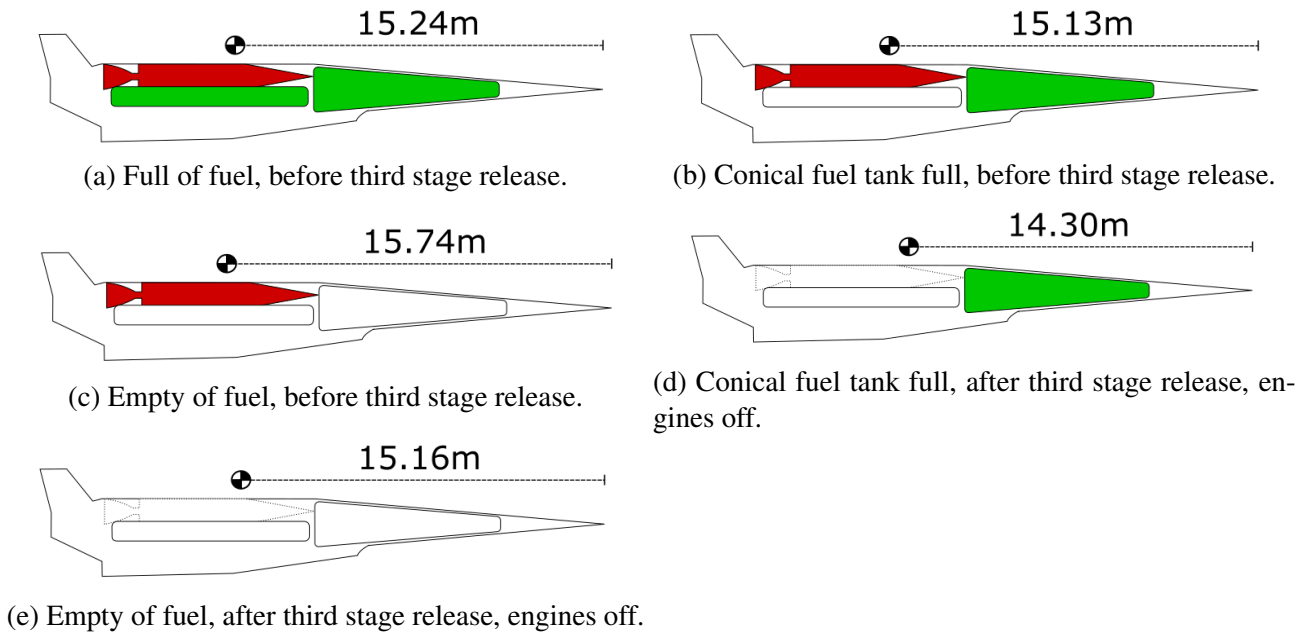


Figure 4.17: Centre of gravity positions for various flight conditions.

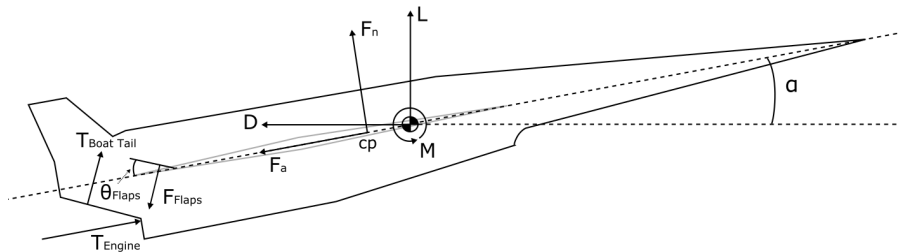


Figure 4.18: The forces on the scramjet accelerator during flight.

may experience instability issues at the end of its acceleration. Determining the controllability of the scramjet accelerator is outside the scope of this study, although this is a key area for investigation in future detailed designs.

Once the flap deflections necessary to trim the scramjet accelerator are calculated, the additional lift and drag produced by the flaps are added to the aerodynamic database, along with additional viscous force components from flap deflections calculated using mean skin friction coefficient. This ensures that the scramjet accelerator is trimmed at every flight condition. Trimmed aerodynamic databases are calculated for engine on and engine off conditions, as well as at all centre of gravity locations listed previously.

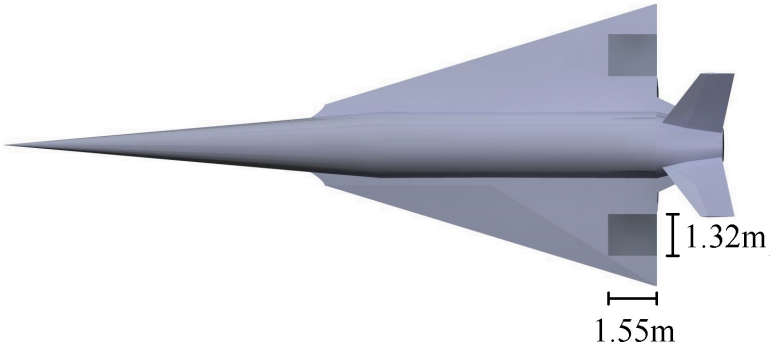


Figure 4.19: Scramjet accelerator model showing control surfaces.

4.1.5 Trimmed Aerodynamic Database of the Scramjet Accelerator with Engine-On

The process described in the preceding sections are used to generate aerodynamics for the scramjet accelerator with the scramjet engines turned on. An example of a Cart3D solution of the nozzle exit and boat tail with the scramjet engines powered-on is shown in Figure 4.21, and the aerodynamics of the scramjet accelerator with engines powered-on are shown in Figure 4.22. The uncertainty margins associated with these aerodynamics are detailed in Appendix B.1. The engine-on aerodynamics of the scramjet accelerator are used during the simulation of the acceleration phase, when the C-REST engines are operational at all times, as well as during the fly-back phase, when the engines are operational for a short time to aid the scramjet accelerator in returning to its initial launch site.

4.1.6 Trimmed Aerodynamic Database of the Scramjet Accelerator with Engine-Off

While the engines are not powered-on air flows through the flowpath without fuel injection, generating a large amount of drag. To model this, geometry of the scramjet accelerator including the flow paths is modelled and triangulated in the same manner as described in Section 4.1.4, and the aerodynamics calculated in the manner described in the preceding sections, save that the modelling of the exhaust of the engine is not necessary. The aerodynamics of the scramjet accelerator are calculated using Cart3D for Mach numbers from 0.2 to 10, and angle of attack values from 0° to 10° to cover the range of flight conditions experienced during the fly-back of the scramjet accelerator. An example Cart3D solution is shown for a Mach 6 engine off condition in Figure 4.23, showing some phenomena shared between powered and unpowered flight, as well as phenomena specific to unpowered flight. **As observed for powered flight, a strong bow shock can be observed, as well as a large shock from the underside of the vehicle, generated by the engine cowl. It can be observed that the aerodynamic pressure is extremely**

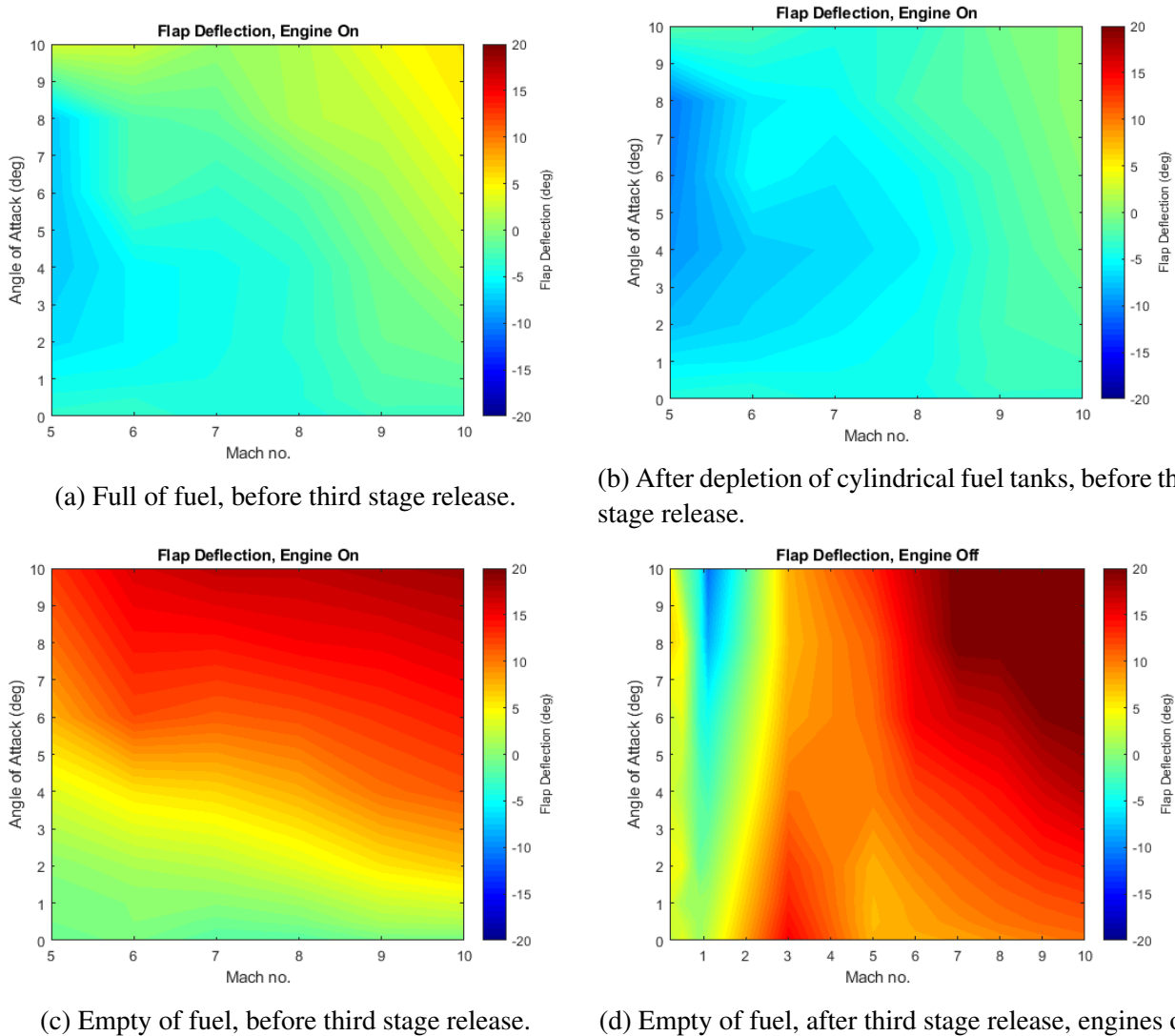


Figure 4.20: Flap deflection required for trim of the scramjet accelerator. Negative is flap up.

high on the angled portion of the engine cowl, due to its high incident angle to the incoming flow. Significantly high pressure is also experienced by the nose cone and cowl underside, as well as on a section of the tail, where a small shock generated by the wings is incident on the tail.

Figure 4.24 shows the engine off aerodynamic characteristics of the scramjet accelerator vehicle over the range of Mach numbers and angle of attack values analysed. Associated uncertainty margins are detailed in Appendix B.1. These results show a distinct maximum region in the L/D of the scramjet accelerator at high Mach numbers, within the hypersonic regime. Below Mach 5, the L/D of the scramjet accelerator decreases sharply. This is caused by the scramjet engines unstarting, generating significant extra drag. The unstarted scramjet engines are shown in Figure 4.25, where shocks within the inlet of the engine are evident, causing high pressures. Below Mach 3, the L/D shows a trend of general increase, except at very low angle of attack, as the effects of the unstarted engine lessen.

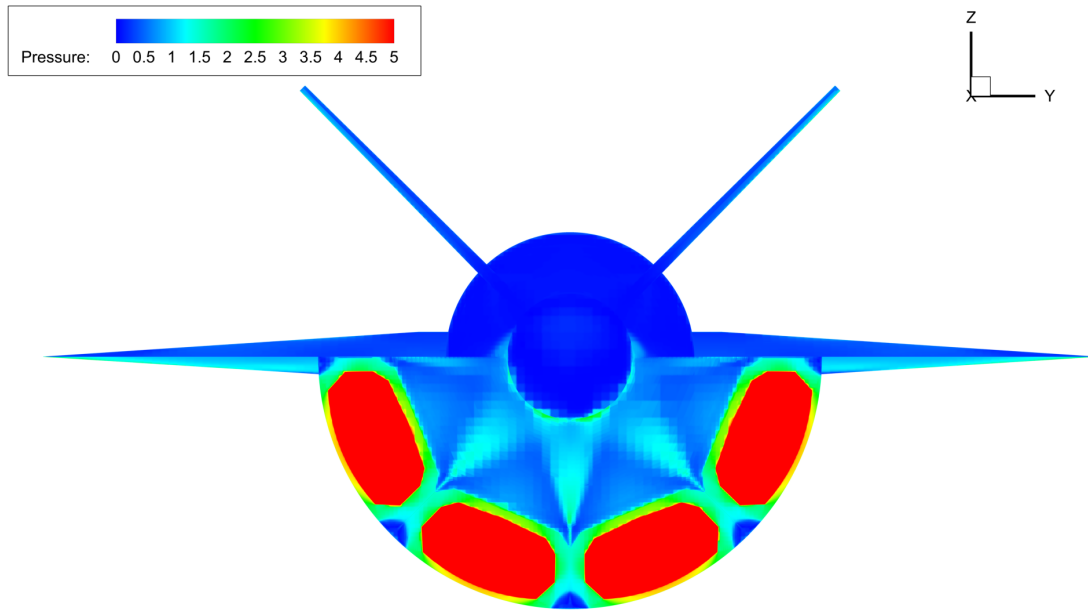


Figure 4.21: Engine-on Cart3D simulation at Mach 6, 2° angle of attack, and 25km altitude.

Below Mach 1 the L/D of the scramjet accelerator increases significantly, in part due to not having the significant drag induced from the engines unstarting, as observed in the supersonic regime.

4.2 The First Stage Rocket

The first stage rocket is required to deliver the second stage to near horizontal flight at Mach 5.1 flight conditions, after which it is discarded. The representative first stage rocket in this study has been modelled as a Falcon-1e first stage scaled down lengthwise to 9.5m and to a mass of 1800kg, keeping the original diameter of 1.67m[164]. This length scaling was performed based off a first principles design of the first stage mass and performance necessary to reach the minimum operating conditions of the scramjet accelerator, performed by Preller & Smart[12]. In this study the first stage length is further tuned, to improve the sizing of the first stage through the use of higher fidelity simulations than were previously utilised. The Falcon-1e has been chosen due to its appropriate scale, and the proven flightworthiness of the Falcon-1. The first stage is attached to the rear of the scramjet second stage and is powered by a single LOX-kerosene Merlin 1-C engine. A connecting cowl has been modelled between the first stage rocket and the scramjet accelerator to improve the aerodynamic profile. The first stage has a structural mass of 820.5kg, determined by scaling of the structural mass of the Falcon-1e. The engine mass of the Merlin 1-C is kept constant during scaling at 630kg[165]. The mass of the fuel in the first stage is scaled as part of the optimisation routine, as the dynamics of the vehicle, and its ability to reach a given separation point, are very closely coupled to the available fuel mass.

The thrust and specific impulse of the Merlin 1-C are determined by interpolation between the sea

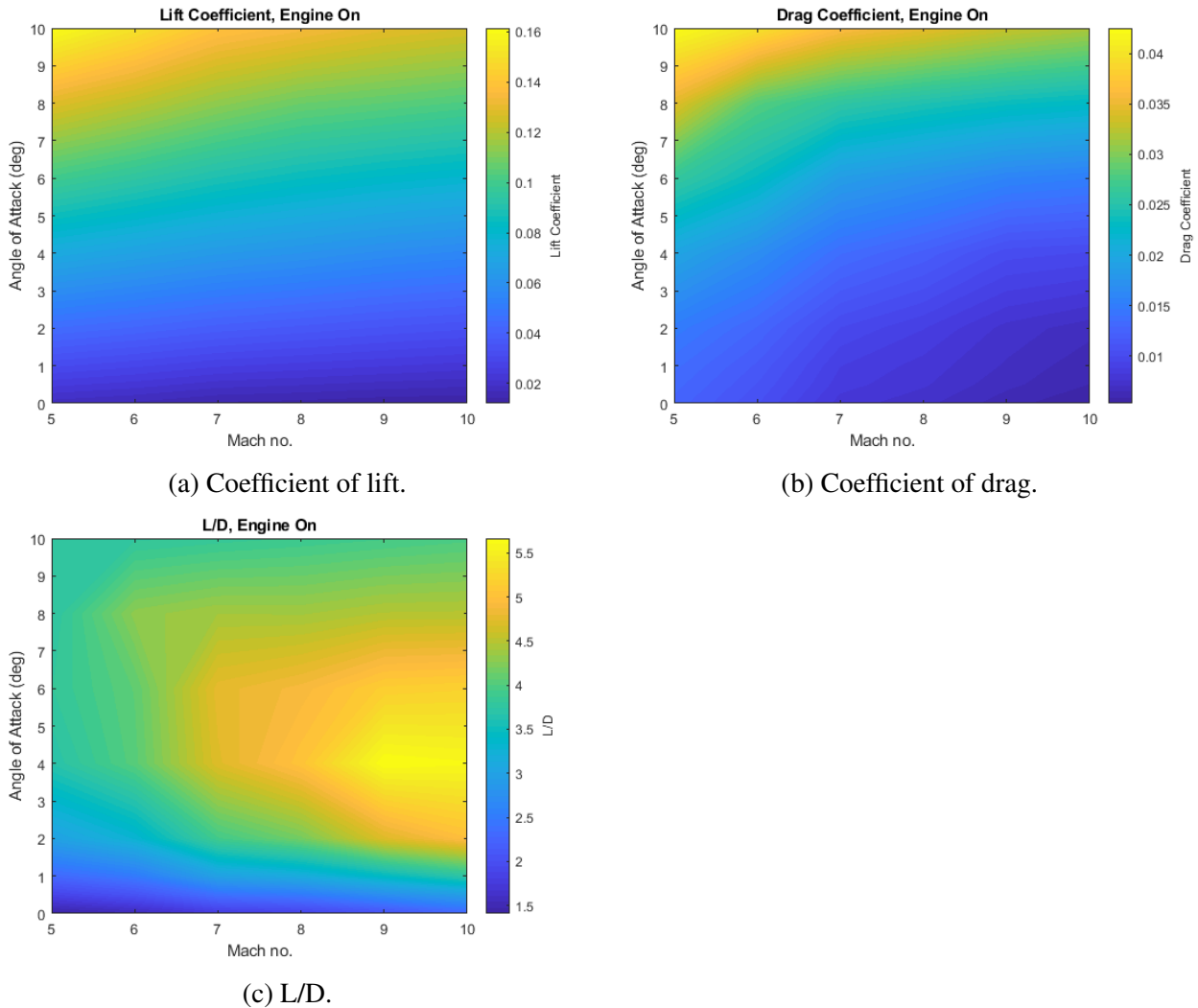


Figure 4.22: The aerodynamic coefficients of the scramjet accelerator with the C-REST engines powered-on at 30km altitude. Coefficients correspond to a reference area of 62.77m^2 and a centre of gravity of **15.24m** (full of fuel, with third stage).

$I_{SP_{SL}}$	275s
$I_{SP_{vac}}$	304s
T_{SL}	555.9kN
A_e	0.552m^2

Table 4.2: First Stage Engine Properties[165].

level and vacuum specific impulse of the Merlin 1-C, shown in Table 4.2, based on ambient pressure. Thrust scaling is determined by linear pressure scaling using nozzle exit area, $T = T_{SL} + (p_e - p_{SL})A_e$. The Merlin 1-C is throttled between 70% and 100%[166].

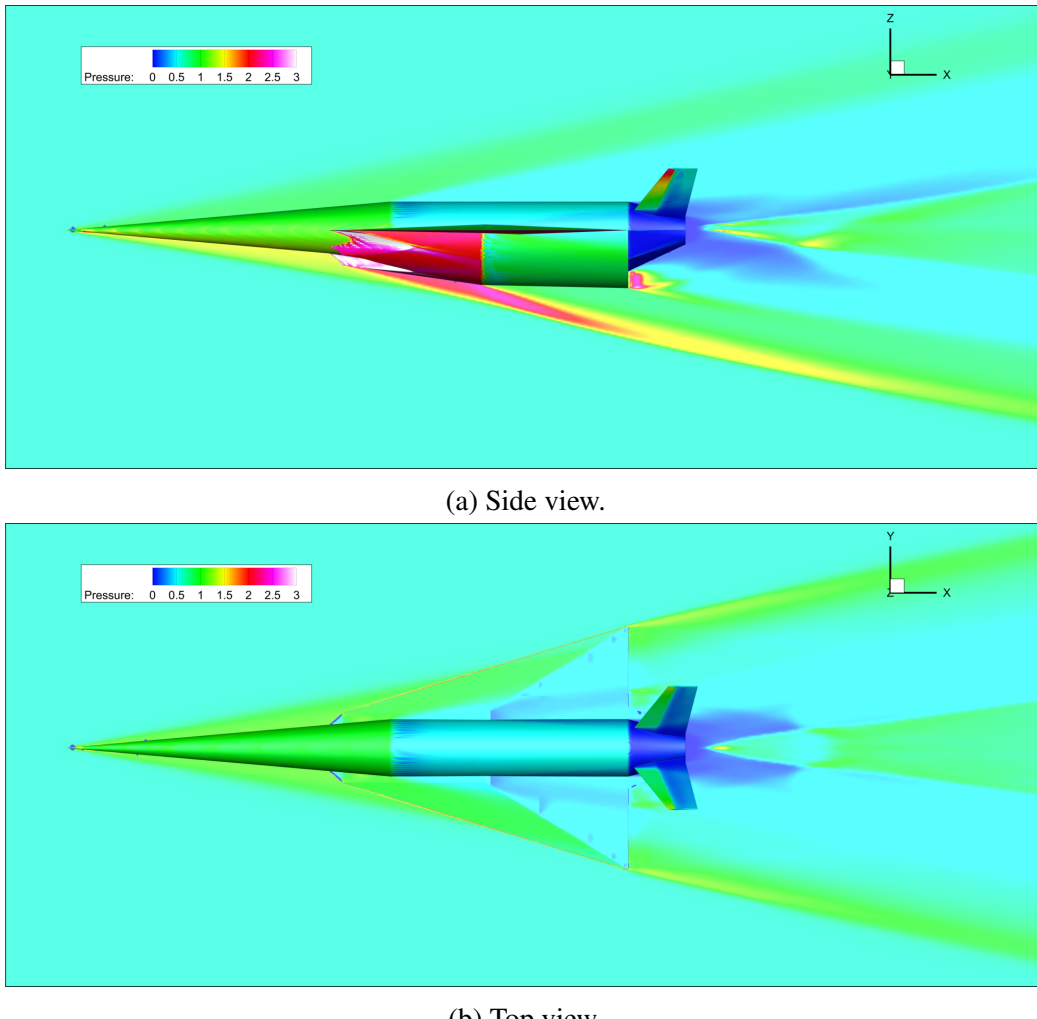
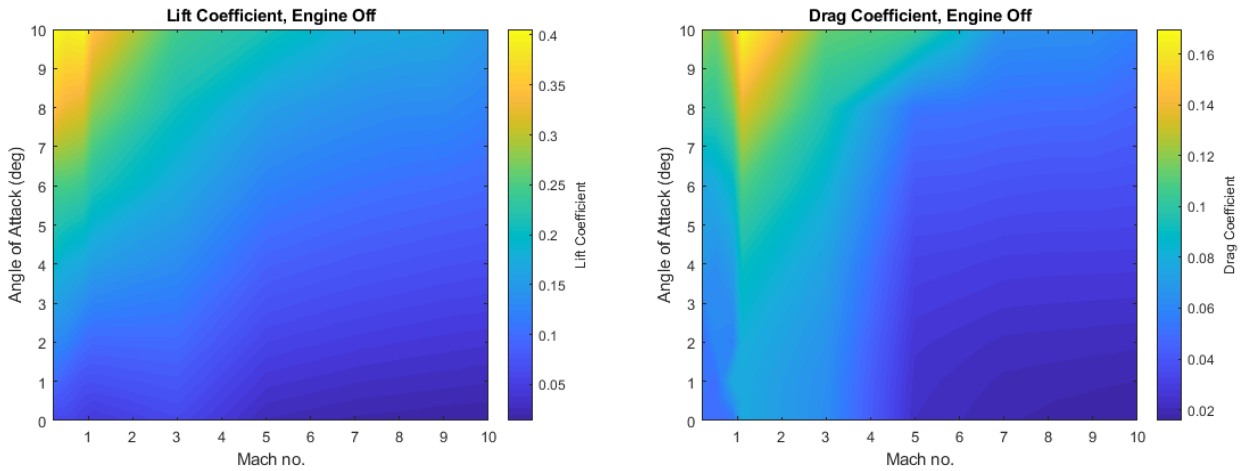


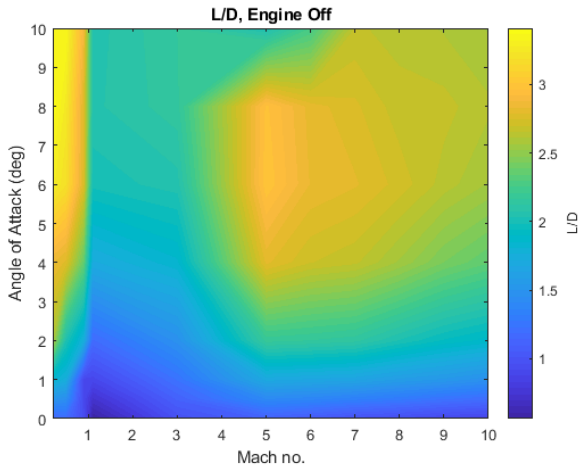
Figure 4.23: Cart3D flow result for the scramjet accelerator with engine off, at Mach 6, 2° angle of attack.

4.2.1 The Aerodynamics of the First Stage Rocket and Scramjet Accelerator

The aerodynamics of the launch system during first stage flight are calculated in a similar manner to those of the scramjet accelerator without the first stage rocket, as detailed in Section 4.1.4. The aerodynamics of the scramjet accelerator and first stage rocket are shown in Figure 4.27, and are calculated using Cart3D and corrected for viscous effects. The first stage aerodynamics are modelled between angles of attack of 0° to -5° , as the first stage will be flying at negative angle of attack to induce faster pitch-over. Mach numbers from 0.2 to 5.1 (second stage separation speed) are simulated. Figure 4.26 shows an example Cart3D simulation case, at Mach 2, -1° angle of attack. The coefficient of lift, drag and aerodynamic moment are tabulated for each simulation. Figure 4.27 shows the lift and drag coefficients of the first stage, as well as the lift-over-drag, across the simulated Mach Numbers and angles of attack ranges. Above -1° angle of attack, the L/D of the first stage is generally greater than 0, meaning that lift is being gained in the positive vertical direction, and that the angle of attack



(a) Coefficients of lift of the scramjet accelerator, calculated using Cart3D. (b) Coefficients of drag of the scramjet accelerator, calculated using Cart3D.



(c) L/D of the scramjet accelerator.

Figure 4.24: Aerodynamic Characteristics of the scramjet accelerator with C-REST engine powered-off at an altitude of 30km. Coefficients correspond to a reference area of 62.77m^2 and a centre of gravity of 15.16m (no third stage, no fuel).

must be lower than 1° to assist pitching. At Mach numbers over Mach 2, the absolute magnitude of the L/D generally increases as the Mach number increases. This is caused by the decreased effects of the scramjet engines unstarting, in turn reducing the drag of the engines at higher Mach numbers, as observed in the aerodynamics of the scramjet accelerator in Section 4.1. Note that absolute magnitude is the metric used for ‘good’ L/D, as the angles of attack are negative.

The First stage is trimmed using thrust vectoring of the Merlin 1-C engine during flight. The centre of gravity of the launch system varies from 23.8m to 16.8m along the vehicle, as the fuel of the first stage is depleted. The thrust vector angle of the first stage engine is adjusted so that the moment caused by the rocket engine is equal and opposite to the moment caused by the aerodynamics of the vehicle, as illustrated in Figure 4.28, ie. $M_T = -M_{Fn}$. This thrust vector angle is calculated as the

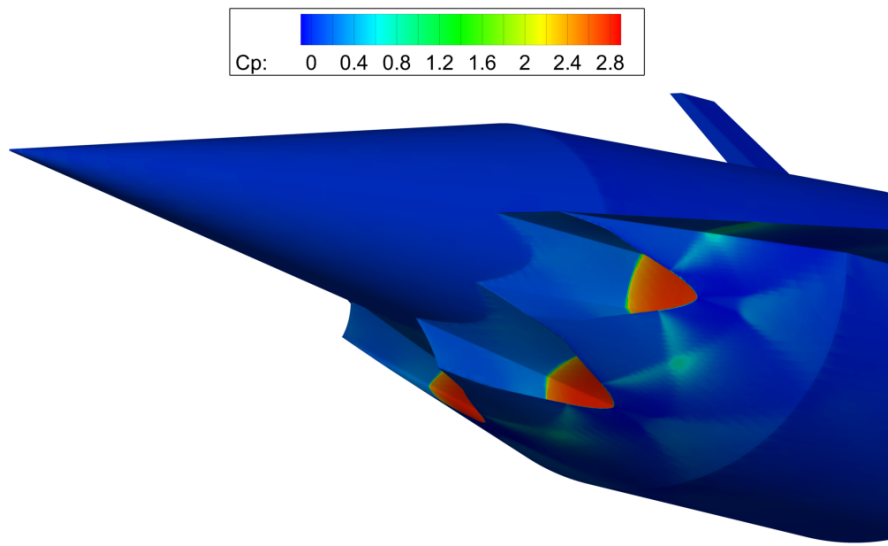


Figure 4.25: Unstarted scramjet engines at mach 3, 2° angle of attack.

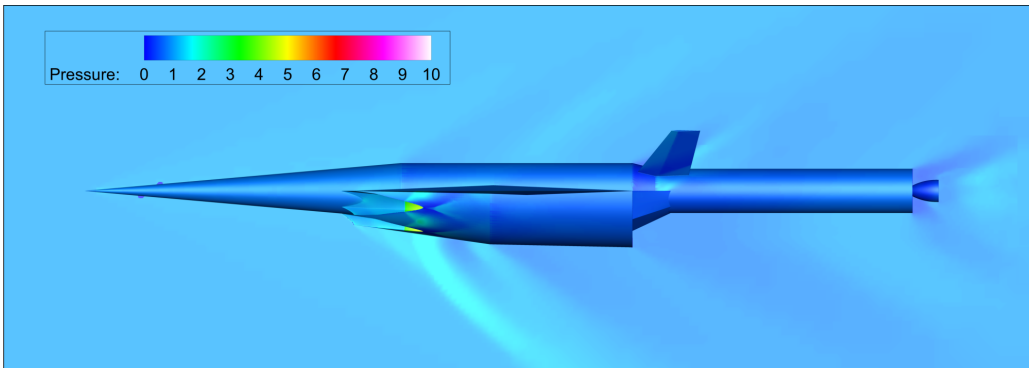


Figure 4.26: Cart3D result for the scramjet accelerator and first stage vehicles at Mach 2, -1° angle of attack.

trajectory is simulated, at every flight condition.

4.3 The Third Stage Rocket

The third stage rocket is an expendable portion of the launch system, tasked with delivering the payload to its final orbital position. The third stage is released from the scramjet accelerator at a flight speed of approximately Mach 9, after which it must fly within the atmosphere for a time, performing a significant altitude raising manoeuvre to achieve orbital flight[12]. In previous studies, the third stage of the SPARTAN was designed around a pump-fed RL-10-3A engine[12], and was designed to fit into a cavity on the back of the fuselage of the vehicle[12]. For the representative launch vehicle in this work a new third stage is designed, to reduce cost, and to integrate within the fuselage of the

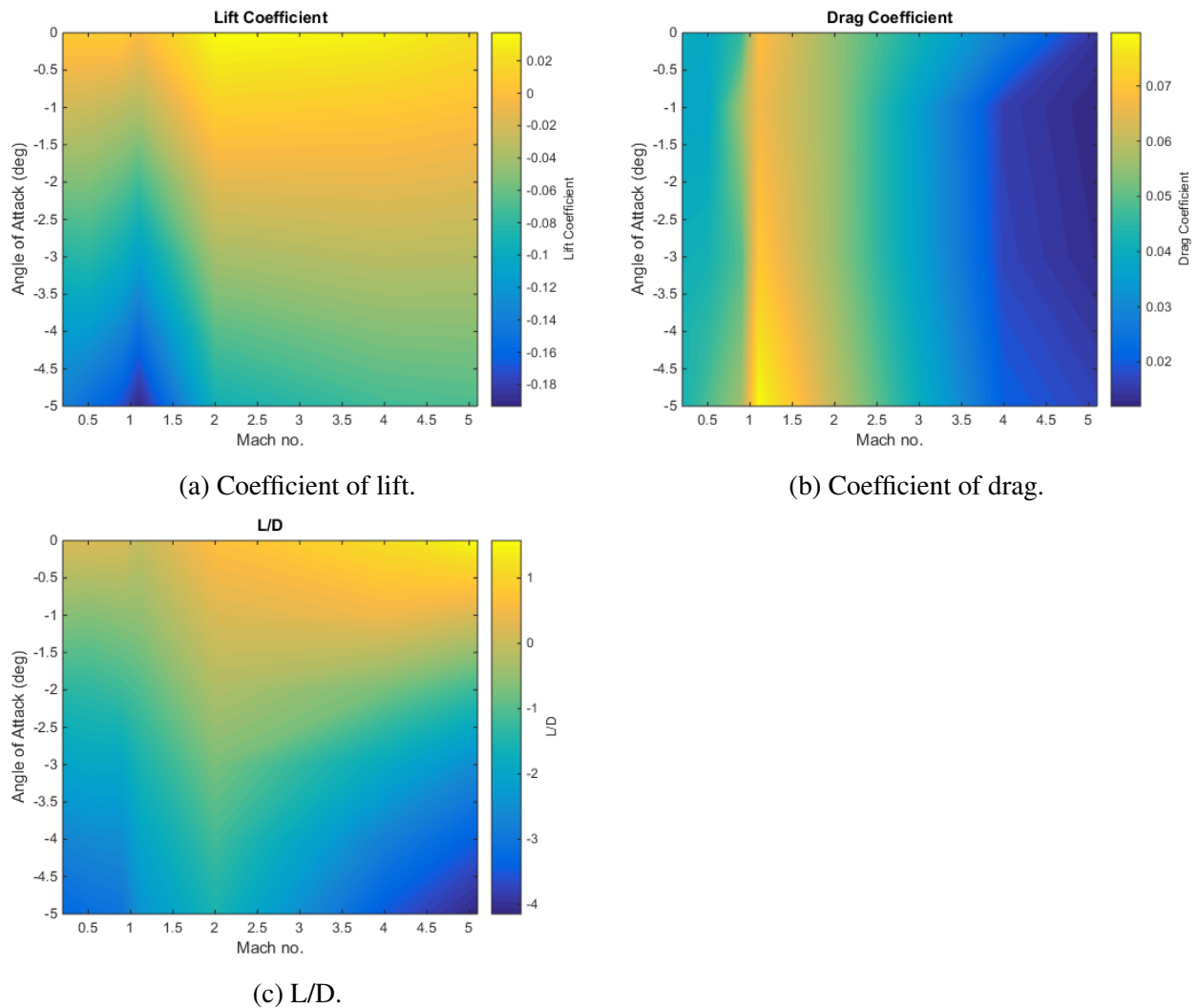


Figure 4.27: The aerodynamic characteristics of the first and second stage stack. Coefficients correspond to a reference area of 62.77m^2 .

scramjet accelerator.

The third stage rocket in this study is designed around a modified version of the SpaceX Kestrel engine. The Kestrel is a pressure-fed engine, designed for launching small satellites to orbit as part of the now retired Falcon-1. The Kestrel is chosen primarily for its low cost, to ensure that the representative launch system in this study closely approximates a cost-effective future launch system.

The third stage internals have been designed to weigh a total of 3300kg. This has been chosen as a nominal design weight, to satisfy the fuel necessary to achieve orbit with an acceptable payload, while also allowing for ample payload volume. The internal layout of the third stage rocket is shown in Figure 4.29, and a mass breakdown is given in Table 4.3. The third stage has a structural mass fraction of 0.079, to match the Falcon 1 second stage without the Kestrel engine or fairing included[164]. This

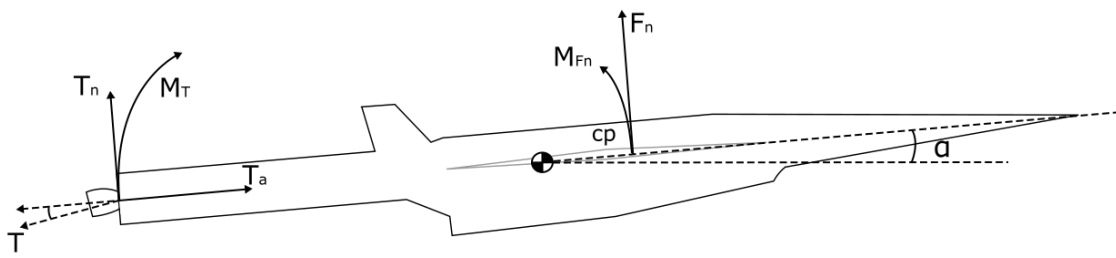


Figure 4.28: Thrust vector moment balancing of the first stage.



Figure 4.29: The third stage rocket, showing major internal features.

gives a total structural mass of 236.3kg, without heat shield or engine.

4.3.1 Geometry

The third stage rocket in this study has a total length of 8.7m, and is sized so that it is able to fit within the main cylindrical fuselage section of the scramjet accelerator's geometry. This is done to reduce the heat loads present on the third stage during the second stage acceleration, as well as to improve the aerodynamics of the scramjet accelerator during ascent and fly-back (see Section 4.4.2). While the release mechanism of the third stage is not considered in this study, it is assumed that the release process will be simplified if the release mechanism is constrained to the cylindrical fuselage of the scramjet accelerator, rather than involving geometric variation of the nose cone of the scramjet accelerator, which receives a large amount of aerodynamic force as illustrated in Figure 4.23b. The third stage nose length is set at 2.7m, for a similar nose geometry to the third stage designed for previous analysis of the scramjet accelerator[12]. The tip of the nose has been rounded with a hemispherical diameter of 0.07m, for aerothermodynamic performance. The third stage centrebody length has been set to 4.5m, giving a total length of 8.7m, with the 1.9m long Kestrel engine[164] protruding 1.5m from the centrebody. The diameter of the third stage has been set to 1.1m including heat shield, to match the diameter of the Kestrel engine, and to be close to half the diameter of the scramjet accelerator, a scale used to fix the third stage width of the RL-10-3A powered third stage[12].

Part	Total	Structural	Heat Shield	Engine	Fuel (est)	Payload (est)
Mass (kg)	3300.0	236.3	124.6	78.0	2761.1	100.0

Table 4.3: Mass breakdown of the third stage rocket.

4.3.2 Fuel Tank Sizing

The internal design of the third stage is allowed to be slightly variable as the trajectory is optimised. The third stage mass is fixed at 3300kg, and the calculated payload-to-orbit varies by exchanging leftover fuel mass for effective payload mass. The Kestrel engine utilises LOX/RP-1 propellants, with an oxidiser-to-fuel mixture ratio 2.56[167] and a density of 813kg/m³[168]. To calculate the dynamics of the third stage, the fuel tanks have been approximately sized, assuming 100kg of payload-to-orbit. Realistically the exchange between fuel and payload mass would cause the fuel tanks to be resized slightly, however, for the purposes of this study the fuel tanks are assumed to be of constant weight for simplicity. Currently this is a reasonable assumption as the internals of the rocket are very simplified, and the changes in the total fuel used are relatively small. With an assumed payload mass of 100kg, the third stage carries a total propellant mass of 2761.1kg. Table 4.4 shows the component breakdown of the LOX oxidiser and RP1 for this fuel weight. The total mass and volumes of these fuels will change slightly as the trajectory of the launch system is optimised, and fuel is traded for payload mass. However, the ratio between the fuel and oxidiser will stay constant.

	LOX	RP1
Ratio	2.56[167]	1
Density	1141kg/m ³	813kg/m ³ [168]
Volume	1.740m ³	0.954m ³
Mass	1985.5 kg	775.6 kg

Table 4.4: Third stage fuel distribution.

4.3.3 Heat Shield Sizing

The third stage rocket is separated from the scramjet accelerator at a high dynamic pressure, after which it spends some time accelerating in-atmosphere before reaching exoatmospheric conditions. During the time spent within a high dynamic pressure environment the third stage experiences a significant heat load. The heat shielding must be capable of withstanding the extremely high heat and structural loading necessary to protect the third stage rocket internals and payload, as well as being lightweight, as the payload-to-orbit is extremely sensitive to the mass of the third stage, and cost effective, as increasing the cost of the third stage directly increases launch cost due to it being expendable.

The heat shield used to protect the third stage is constructed from a tungsten nose tip, a reinforced carbon-carbon nose cone, and a phenolic cork cylinder, weighing 124.6kg in total. This heat shield is designed to match the materials and thicknesses used by previous studies[12]. A mass breakdown is shown in Table 4.5. Tungsten is used at the tip of the nose cone, the area of maximum heat loading. Tungsten has extremely high heat capacity, and a very low coefficient of thermal expansion[169]. However, tungsten is costly and heavy, and conducts heat well, and so is only used on the very tip of the nose where it is absolutely necessary **to resist and distribute the large amount of heat generated by the stagnation region**. Reinforced carbon-carbon is used for the conical section of the heat shield, as this is an area that will be subject to high heat and structural loading. Carbon-carbon is able to withstand high temperatures, as well as being thermal shock resistant and having a low coefficient of thermal expansion[170]. Carbon-carbon is used in rocket and missile nose cones, as well as on aircraft leading edges due to its good heat resistant properties[170]. However, carbon-carbon is expensive, and is used only on the conical section of the heat shield to minimise cost. For the cylindrical section of the heat shield protecting the main body of the third stage, phenolic cork is used. Phenolic cork is a composite of ground cork and phenolic binders which is light and relatively cheap, with good heat resistivity. Phenolic cork has lower tensile strength and heat resistivity than carbon-carbon[170, 171], but is cheaper and lighter, making it appropriate for use on section of the heat shield which experiences lower heating and structural loads.

Part	Density	Geometry	mass
Tungsten Nose	$\rho_{Tungsten} = 19250 \text{ kg/m}^3$	142mm diameter, 20mm thick	10.0kg
C-C Cone	$\rho_{CC} = 1593 \text{ kg/m}^3$	10.8mm thick	89.7kg
Phenolic Cork Body	$\rho_{PhenolicCork} = 512 \text{ kg/m}^3$	3.1mm thick	24.9kg

Table 4.5: Third stage heat shield properties.

4.3.4 Propulsion

The propulsion system for the third stage rocket in previous studies has been modelled after the RL-10-3A[32]. However, the RL-10-3A is expensive, and for the expendable upper stage of a small launch system a cheap engine will be required, as the cost of this engine will have a large bearing on the cost efficiency of the launch system as a whole. The following section outlines the redesign of the third stage rocket, so that it is more cost effective, and uses a more modern engine.

Exoatmospheric Rocket Engine Survey

The third stage requires a rocket engine with sufficient thrust to accelerate out of the atmosphere, and a diameter small enough to allow the rocket to fit within the fuselage of the scramjet accelerator. The major factors when choosing a rocket engine are efficiency and thrust-to-weight ratio, as well as

Engine	Fuel Supply	Fuel	Thrust	Isp	Mass	Diameter	Length	Thrust Vector Capability
R1-10A-3A	Pump-Fed	LOX/LH2	73.4kN	444s	141kg	1.01m	1.78m	Yes, Unknown limits
Aestus II	Pump-fed	MMH/NTO	46kN	337.5s	148	-	2.2m	6°
RS-72	Pump-fed	MMH/NTO	55.4kN	338s	154kg	-	2.286	6°
ATE	Pump-fed	MMH/NTO	20kN	345s	57.9kg	0.38m	1.4m	15°
Rutherford [172]	Pump-fed	LOX/RP-1	24kN	343s	35kg	-	-	-
AJ10-118K	Pressure-fed	A-50/NTO	43.3kN	320.5s	124.5kg	1.53m	2.7m	Fixed
Kestrel [164]	Pressure-fed	LOX/RP-1	30.7kN	317s	52kg	1.1m	1.9m	Yes, Unknown limits
Aestus	Pressure-fed	MMH/NTO	27.5kN	320s	110kg	1.27m	2.2m	4° & 4° by mechanical adjustment
OMS	Pressure-fed	MMH/NTO	26.7kN	316s	118kg	1.168m	1.956m	8°

Table 4.6: Comparison of upper stage rocket engines, sourced primarily from the Encyclopedia Astronautica reference website[165].

cost. It is desirable to use a rocket engine that has already been developed and flight tested, to reduce the costs and potential complications of engine development. Table 4.6 shows a comparison study of small sized upper stage rocket engines which are currently in use, or have been used, for commercial space flight. The pump-fed motors have significantly higher specific impulse than pressure fed motors, and while the masses of pressure-fed engines appear low compared to turbopump engines, this mass is generally made up for by the additional mass required by the pressurised propellant and pressurant tanks of pressure-fed engines, mitigating this mass advantage. However, while the cost of these engines is not generally published, pressure fed engines cost significantly less than pump-fed engines, due to the cost of the turbopump and the associated complexity of a pump-fed system. As such, it is desirable to use a pressure-fed rocket engine for a small satellite launch system if possible. Of the pressure-fed engines, the SpaceX Kestrel exhibits a significantly higher thrust/mass ratio than the other engines, with comparable specific impulse and size. Additionally, the Kestrel has been designed for a low cost, small satellite launcher, making the Kestrel engine likely to be fit-for-purpose for powering the third stage rocket.

Kestrel Propulsion System Modelling

The Kestrel engine which powers the third stage is modified to have 50% increased propellant mass flow rate, giving a mass flow rate of 14.8kg/s. This is done to assist the rocket in exiting the atmosphere, as it was found during analysis that the third stage has difficulty exiting the atmosphere when powered by a standard Kestrel engine. A 50% increase in mass flow rate provides additional thrust such that the trajectory angle of the third stage does not decrease significantly after release from the scramjet accelerator flying a constant dynamic pressure trajectory. This was chosen as the indicative factor that the third stage is successfully able to pull-up out of the atmosphere. It is likely that this mass flow increase will necessitate a heavier combustion chamber as well as more heavy duty piping and valves, more or larger injectors, and a heavier nozzle and structure to transmit the higher thrust forces[167, 173]. To compensate for these factors, the mass of the Kestrel is increased by 50%, from 52kg[165] to 78kg, to approximate an increase in mass of the the thrust chamber as well as all feed systems, cooling systems, and the thrust transmission structure. This is estimated to be slightly conservative, as the surface area of the combustion chamber, and thus the mass and the cooling necessary, will not vary linearly with the increase in volume necessary to maintain a constant characteristic length as mass flow rate in increased[167, 173]. However, as the mass of the relative components of the Kestrel are not published, a conservative approach to mass modelling of the engine is most appropriate. The need to modify the Kestrel engine for this study highlights the potential necessity for the design of a cheap rocket engine with higher thrust than the Kestrel, Aestus or OMS, if a rocket-scramjet-rocket system is to be practical and cost-effective.

The nozzle exit diameter of the Kestrel engine has been kept constant at 1.1m. An increase in

mass flow necessitates a corresponding increase in throat area. This increase in throat area decreases the area ratio of the nozzle. The initial area ratio is 60, measured from schematics in the Falcon-1 Users Guide. A 50% mass flow increase corresponds to a 50% throat area increase, causing the area ratio to decrease to 40. This decrease in area ratio results in a 2% loss of efficiency from the nozzle, measured from the thrust coefficient relationships shown in Figure 4.30[167]. The modified specific impulse of the 50% up-sized Kestrel engine is 310.7s.

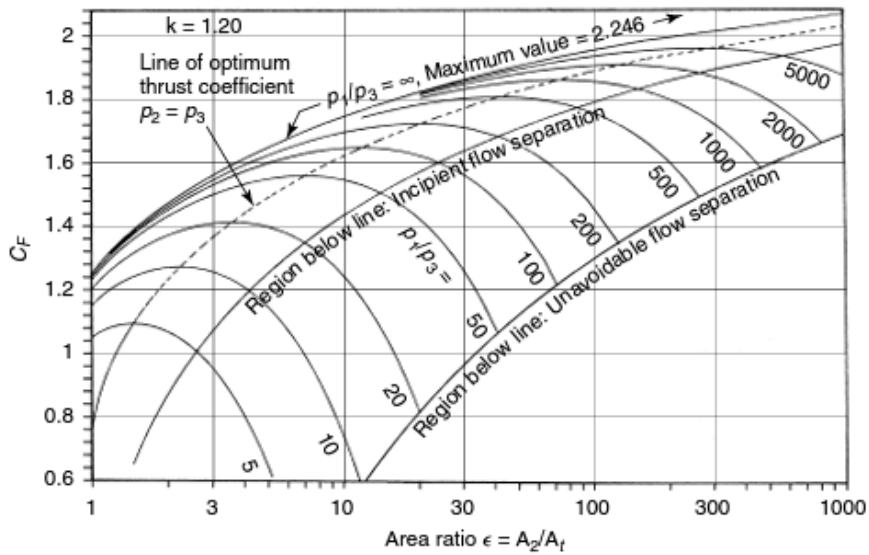


Figure 4.30: Variation in thrust coefficient of thrust with area ratio[167].

4.3.5 Aerodynamics

The third stage aerodynamics have been calculated using Cart3D, in the same manner as for the scramjet accelerator and first stage, with a modification for viscous effects using VC3D. The aerodynamic coefficients of the third stage rocket are shown in Figure 4.31. These do not show any particular complexity, as is expected for a simple rocket shape, and the highest L/D is exhibited at the maximum angle of attack.

4.3.6 Thrust Vectoring

The third stage rocket is controlled via thrust vectoring. The aerodynamic moment is calculated using Cart3D's Clic program, and the thrust vector is set so that the moment generated by the engine matches the aerodynamic moment, as shown in Figure 4.32, ie $M_T = -M_{F_n}$. This thrust vector is calculated at each flight condition during the trajectory simulations. The maximum thrust vector limit has been set to 8° . As no data on the maximum thrust vectoring capabilities of the kestrel engine

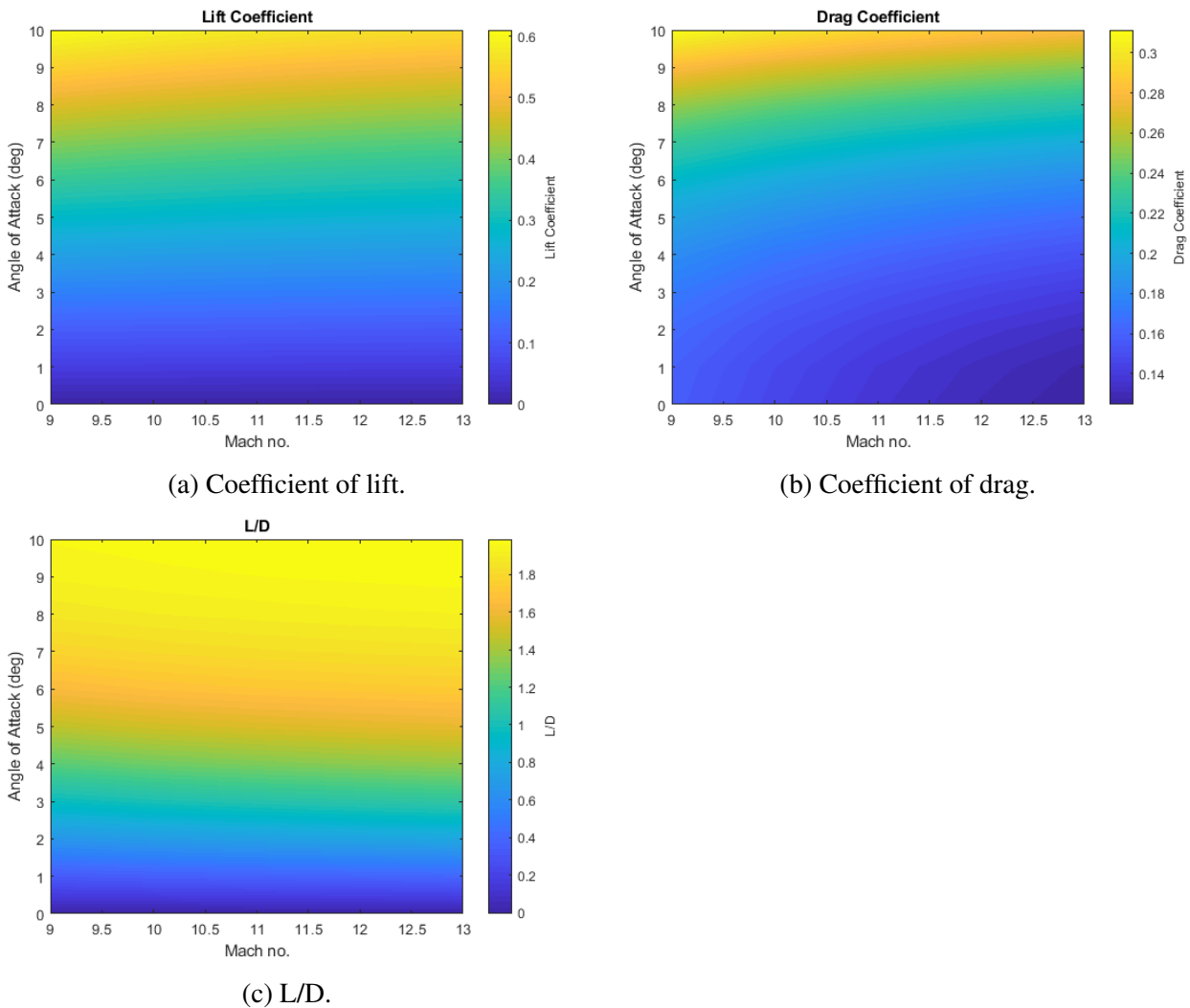


Figure 4.31: Aerodynamic characteristics of the third stage rocket, for a reference area of 0.95m^2 .

was able to be found, this was set to the maximum gimbal range of the Aestus engine and Orbital Manoeuvring Engine (OME), which are similarly sized pressure-fed engines[165].

The centre of gravity is determined using CREO by creating a three dimensional model of the rocket with representative densities, illustrated in Figure 4.29. It is assumed that the mass of the structure of the rocket (excluding fuel tanks, heat shielding, engine and payload) is distributed homogeneously for simplicity. The Mass Properties tool within CREO is used to calculate the centre of gravity, which is located at 4.33m from the nose when the rocket is full of fuel, and 4.04m from the nose when the rocket is completely empty. The centre of gravity is interpolated linearly from these values as the fuel mass within the rocket decreases. These centre of gravity calculations are performed with the heat shield on, as the thrust vectoring is only calculated while the rocket is in-atmosphere, with the engine on.

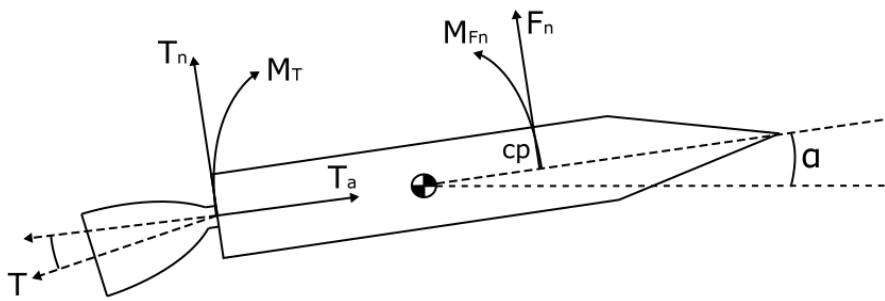


Figure 4.32: Thrust vector moment balancing of the third stage.

4.4 Modelling and Design Simplifications

The representative rocket-scramjet-rocket launch system in this study is based on the SPARTAN[12], as it is the most mature concept for a small satellite launch system using scramjets in the public domain. However, the system is still at the preliminary design phase, meaning that the design, as well as system and sub-system models still incorporate significant simplifications and have not been fully developed. These simplified models and design methodologies are necessary and appropriate for preliminary system and trajectory analysis, allowing the trajectories in this work to be developed and a wide range of launch system parameters to be investigated. However, the effects of these simplifications within this analysis must be acknowledged. The modelling and design simplifications have been considered in two parts; the simplifications in the performance modelling producing the uncertainties captured in the sensitivity study carried out in Sections 6.5 and 7.7; and the design related simplifications that particularly affect the control, staging, and mass modelling of the launch system, which are considered here. The effects of the simplifications in this section are not quantified, but the sensitivity studies give an indication as to the implications of variations of the effected performance and design parameters. The following sections address the effects of the currently open design choices and simplifications present in this study, and how they may affect the findings from the current work.

4.4.1 Control

Control Surface Design

The control surfaces of the second stage of the representative launch system in this study are based on the previously developed SPARTAN[12], and are modelled as large rectangular flaps. These flaps trim the vehicle during flight, and deflect significantly. These flaps experience large forces, and will need strong and resilient actuators to be able to hold deflection for long periods of time. In future iterations of a launch systems of this type, it may be necessary to design any aerodynamically controlled stages so that the necessary deflections of the control surfaces are minimised, through careful design of the aerodynamic profile and centre of gravity location.

In addition to the possible limitations arising from the actuation mechanism, the control surfaces of the vehicle may experience design limitations due to the design and placement of the control surface. A control surface deflected in a supersonic flow acts as a compression ramp, with an incidence angle that changes rapidly at the flap hinge. Depending on the flow conditions, wall temperature adverse pressure gradient and boundary layer stability, the shock at the flap may cause the boundary layer to separate, causing a recirculation bubble, along with a separation shock that reattaches on the control surface[174]. This recirculation bubble decreases the pressure in the region that it is present on the control surface, while the separation shock increases the shear stress directly downstream of its reattachment[174]. These effects may reduce the effectiveness of the control surfaces at higher deflection angles, changing the deflection necessary to achieve trim and potentially increasing drag significantly. In addition, the reattachment of the shock will cause a high temperature region on the control surface, that may need to be accounted for during the design of the thermal protection system of the control surface. These effects are currently not included.

Likely impacts on design:

- Decreased aerodynamic performance due to increased drag because of additional viscous drag or additional necessary deflection.
- Increased actuator strength necessary resulting in increased weight. If limitations on control surface deflection are imposed, they would limit the flight regime of the vehicle.
- Adverse heating is present on the control surfaces, necessitating redesign or repositioning of the control surfaces. This would result in a change in the behaviour of the control surfaces, and possibly increased weight if additional thermal protection is necessary.

Control Modelling

In order to effectively apply the Pseudospectral method of optimal control for the purposes of this work, a point mass model is used in all phases of simulation, with the control surface deflections of the scramjet accelerator and thrust vectoring of the first and third stages modified throughout the trajectory to trim the vehicle, assuming that the entire aerodynamics performance is known prior to flight. However, all three stages of the representative launch system designed in this study are aerodynamically unstable for portions of their trajectories. Sections 6.1, 6.2 and 7.1 identify the end of the first stage and scramjet stage trajectories as unstable, as well as the majority of fly-back and third stage trajectories. For the purposes of this study, the design of the representative launch system as presented is regarded to be sufficient for a preliminary trajectory analysis. This is appropriate for an early trajectory analysis that is meant as an initial analysis of optimal fight paths. However, it is likely that in the future a highly detailed study of a three-stage airbreathing launch system's design and control strategy must be undertaken, to determine the practicality of controlling this launch system during flight, and in particular the viability of thrust vector control. The controllability will be

heavily interdependent on the vehicle design, and the trajectory will be limited by the controllability of the launch system. In particular, the portions of the trajectory during which the vehicles of the launch system have been determined to be aerodynamically unstable may be difficult to control in a practical manner, and should be considered carefully for future designs of launch systems of this type. Exploring this further is one of the items identified under future work.

Likely impacts on design:

- Necessity for a vehicle geometry redesign if the control authority or stability of the vehicle is insufficient to adequately fly a nominal trajectory, with follow-on effects to vehicle aerodynamic performance and mass properties.

4.4.2 Staging Effects

A particular challenge inherent to multi-stage airbreathing launch systems is the dynamics of the stage separation itself. This stage separation often occurs in-atmosphere, at relatively low trajectory angles. This separation is a key factor in the design of each stage, particularly the time when the upper stage engine must be ignited to ensure appropriate control and speed after separation. This separation also results in vehicle-vehicle aerodynamic interactions between the stages of the launch system as they separate. These stage separations may induce aerodynamic forces and moments on the stages of the launch system that are significantly different to the nominal flight regime of each stage, and will need to be carefully studied and mitigated for a launch system of this type to be feasible[175, 176]. These separation effects are not generally taken into account in the early stages of launch vehicle conceptualisation, as they can be considered as secondary to an overall trajectory-based design, sizing, and optimisation in the early stages of design. However these separation effects are likely to be significant to a detailed vehicle design, and a multi-stage vehicle must be analysed in the later stages of vehicle design using CFD and experimental analysis, along with an iterative design process, to ensure that appropriate control authority can be maintained during and after separation[175].

During the first-second stage separation of the representative launch system the first stage and cowling will require separation while flying at low trajectory angles, at high dynamic pressure. For the first and second stages to separate cleanly, the first stage and cowling must decelerate more rapidly than the second stage scramjet. This manoeuvre must be executed in a controlled manner, because there must be no risk of adverse contact between the stages. Clean separation may be challenging, and may require the ignition of the scramjet engines prior to the release of the first stage, if deemed possible by further study and analysis.

The separation of the third stage rocket is likely to be particularly challenging, requiring separating the third stage from the scramjet-powered accelerator while retaining control authority over both vehicles, and ensuring that there is no significant risk of contact between the vehicles. The configuration of the vehicles during launch is particularly important for separation, and will need to be

investigated thoroughly in the future, when detailed designs of three-stage airbreathing launch systems are progressed. The current work assumes that the third stage is contained within the airbreathing stage, similar to some previous designs of the SPARTAN launch system[83] and the Starsaber[28]. However, other design strategies of multi-stage airbreathing launchers support the upper stage on top of[82, 177] or below[26] the airbreathing stage, or contain upper stages within a cavity on the back of the vehicle[12, 23, 25]. Each of these methods has positives as well as drawbacks, that must be considered throughout the design process. The storage of the third stage within the main body of the scramjet-powered accelerator during the ascent phase, as is done in this study, with a cowl covering the third stage storage area, necessitates a release mechanism such as retractable panels or a hinged fuselage section. This method of release is also likely to require an ejection mechanism, to impart a force onto the third stage and create separation between the stages. Additionally, it is possible that it would be necessary to ignite the third stage before it is fully released from the scramjet accelerator, due to the lack of a control mechanism for the third stage without the rocket engine ignited. The alternative of storing the third stage outside the body of the airbreathing stage would necessitate the third stage being designed for additional thermal protection and possibly structural strength, and would likely reduce the aerodynamic performance of the airbreathing stage. Storing the upper stage in an uncovered cavity on the back of the airbreathing vehicle mitigates some of the aerodynamic and thermal drawbacks, but introduces complications during fly-back, when the cavity on the upper side of the airbreathing vehicle is open. This cavity may have significant impact on the aerodynamics of the vehicle during fly-back, potentially increasing the drag and changing the aerodynamic moments of the vehicle significantly. The methods of staging of a launch system of this type must be considered carefully in future design studies, taking into account the controllability of the launch system, along with the aerodynamic and aerothermal properties of each stage.

Likely impacts on design:

- Increased mass if complex separation mechanisms are necessary.
- Variation of scramjet stage fuel mass depending on the internal volume of separation mechanisms.
- Changed aerodynamic performance if the third stage is stored externally, or in a cavity.

4.4.3 Mass Model Simplifications

This study uses a simplified mass model of the representative launch system, utilising design studies of the SPARTAN vehicle[12] that are based on statistical models and models of a representative winged-cone vehicle[178], and a scaled model of the Falcon 1e[164]. In addition, the mass model distribution of the launch system in this study assumes a homogeneous distribution of subsystem and structural masses when calculating centre of gravity, and the rotational inertia of the launch system are not modelled. Simplified mass models are the norm for preliminary system analysis[15–26, 28–32],

however, these mass models do carry with them some uncertainty margin. These uncertainty margins are not directly estimated in this work due to the lack of data or reference studies available for launch systems of this type and size. In future design studies, the subsystems of the vehicles and interface mechanisms will need to be modelled in detail, and positioned so that accurate mass distribution and control characteristics are obtained. The relationship between the control characteristics of the vehicle and its internal design will need to be investigated, and this will be thoroughly coupled with the separation dynamics of the launch system.

Likely impacts on design:

- Variation in the mass and mass distribution of the launch system as detailed models are developed.

4.5 Summary

In this chapter, the design and simulation approaches for the representative rocket-scramjet-rocket launch system were presented, based around a modified version of the scramjet accelerator of the SPARTAN launch system. The design of the first stage is based on the first stage of the Falcon-1e, scaled down to **9.5m**, while the third stage is designed around the use of a modified SpaceX Kestrel engine, with the fuel tanks of the scramjet accelerator resized from the baseline SPARTAN design to accommodate for the new third stage size. Mass breakdowns and key design features have been detailed for all three stages, including fuel ratios and structural mass fractions. The aerodynamic databases of all three stages were presented and analysed, and the processes for generating these databases were detailed. The CFD simulations of each stage in Cart3D have been presented, including the process of verifying the convergence of each solution. The propulsion modelling of the C-REST scramjet engines was presented, along with the schemes used to generate smooth, second order continuous interpolations of the engine data, an important aspect of vehicle modelling for trajectory optimisation. The processes for determining the trim characteristics of each stage were presented, including the process for generating the trimmed aerodynamic databases for the scramjet accelerator, the thrust vectoring of the first and third stages, and the calculation of the variable centre of gravity of all three stages. Finally, the simplifications and approximations that have been made throughout the modelling and design were discussed, along with their possible impacts on the performance of the launch system.

CHAPTER 5

TRAJECTORY MODELLING AND OPTIMISATION

XXXX Need to add in path constraint of how thermal effects are handled after adding as a chapter
XXXX put table labels above

This chapter presents the LODESTAR (Launch Optimisation and Data Evaluation for Scramjet Trajectory Analysis Research) tool, which has been developed specifically to calculate the optimal trajectories of partially airbreathing satellite launch systems, as a general tool for this purpose is not currently widely available. LODESTAR has the capability to calculate optimal mission profiles for systems consisting of various combinations of rocket and airbreathing stages, using **accurate and robust** optimisation techniques. LODESTAR optimises a trajectory towards a user-defined objective function, such as maximum payload-to-orbit, subject to constraints that ensure that the launch system does not exceed its aerodynamic, thermal, or structural limitations. LODESTAR calculates an optimal trajectory by simulating the dynamics of the launch system, and configuring an optimal control solver to define the launch trajectory optimisation problem being solved. The dynamics of the launch system are calculated in **three** degrees of freedom, with the performance of each vehicle calculated from aerodynamic and propulsion databases using precalculated interpolations, as described in Chapter 4. These interpolations are designed to be smooth and continuous in order to improve the robustness of the optimal control solver. LODESTAR separates a launch trajectory into multiple segments, to assist the solution process within the optimal control solver, improving robustness and accuracy. Once the solution has been calculated, LODESTAR possesses the capability to verify the optimal control solution, an integral step when calculating an optimised trajectory with complex vehicle dynamics. LODESTAR is developed in MATLAB, and utilises GPOPS-2[179] as an optimal control solver. GPOPS-2 is a proprietary pseudospectral method optimisation package, which is based on an hp-adaptive version of the Radau pseudospectral method, described in further detail in Section 3.5.

Within this chapter, the structure of LODESTAR is presented, as well as the set-up of LODESTAR for trajectory optimisation, and the verification methods used to determine if a solution has converged

correctly. The configuration of LODESTAR presented in this chapter is designed specifically to calculate the maximum payload-to-orbit trajectory of a rocket-scramjet-rocket launch system, delivering a small satellite to sun synchronous orbit.

5.1 Mission Definition

The configuration of LODESTAR must be tailored towards the specific vehicle and mission profile which are being optimised. For this study, LODESTAR has been configured to simulate and optimise the launch of the representative rocket-scramjet-rocket launch system, detailed in Chapter 4, for maximum payload-to-orbit. The nominal mission of the rocket-scramjet-rocket is presented here in order to provide a suitable reference for the configuration specifications, which are detailed in the following sections.

The mission chosen for the optimal trajectory calculation is a launch to sun synchronous orbit. A satellite in sun synchronous orbit is at close to polar inclination, regressing so that it keeps its orbital alignment to the sun. The sun synchronous orbit is one of the most commonly used types of orbit for space science missions, as it has many useful properties[180]. A sun synchronous orbit allows for global coverage, passing over each latitude at the same time each day, illustrated in Figure 5.1. It also allows for a satellite to either have full sun and have consistent power generation, or alternatively, allows for a satellite to have a consistent ‘dark side’ each day to alleviate thermal issues[180]. A sun synchronous orbit at 566km has been used in previous studies as the target orbit[12], and this orbit is also used for the current work.

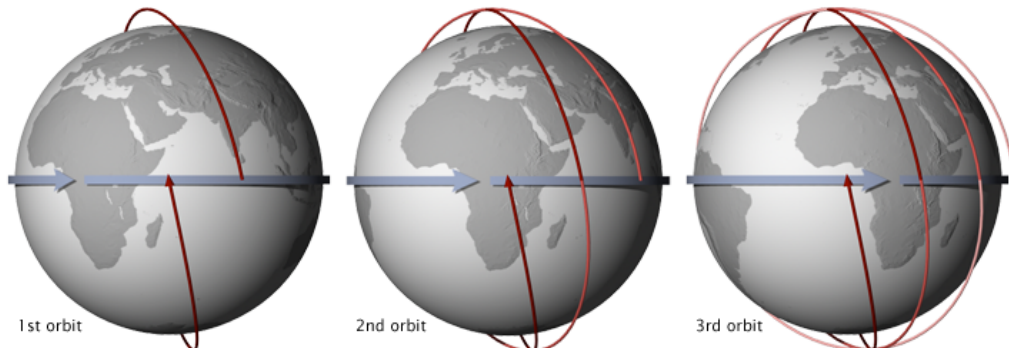


Figure 5.1: Sun synchronous orbit illustration, passing over the equator at the same time each day[181].

The launch site selected for the simulation is the proposed Equatorial Launch Australia launch site near Nhulunbuy in the Northern Territory, Australia[182]. This proposed launch site looks to take advantage of the remoteness of northern Australia, as well as its close proximity to the equator. While the proximity to the equator of this launch site is slightly disadvantageous for launch to sun synchronous orbits, the possibility of other launch directions from this location, and its active

development, make it an appropriate choice as a practical launch location within Australia. The site is ‘about 30km south of Nhulunbuy’[182] which places it within the approximate region indicated in Figure 5.2.



Figure 5.2: Approximate location of the ELA launch site. Image from Google maps.

5.2 Vehicle Simulation

LODESTAR simulates each of the vehicles within the rocket-scramjet-rocket launch system by establishing a set of dynamic equations that fully describe the motion of the vehicle in terms of the time, states (\mathbf{x}), and controls (\mathbf{u}) of the system;

$$\dot{\mathbf{x}}(t) = f[t, \mathbf{x}(t), \mathbf{u}(t)]. \quad (5.1)$$

The states and controls are the variables that define the time dependent physical characteristics of the system. The state variables are dependent on the controls and the system dynamics, while the control variables drive the behaviour of the system and can be varied independently [94]. The state variables are defined by the coordinate system, and the outputs of each vehicle model [98]. These are nonlinear functions, that depend on the interpolation of data sets which supply the atmospheric, aerodynamic, and propulsion characteristics of each vehicle. The methods used to interpolate these

data sets must be as smooth and continuous as possible, and cover the entire possible operational range of the vehicle. Even if the optimal solution is well within the range of all input data sets, the optimal control solver will potentially explore all regions within the user-defined bounds. If there are large discontinuities or inaccurate extrapolation effects within the possible solution space of a particular vehicle, the solver may be unable to converge, or converge to a physically invalid solution. Discontinuities within the aerodynamics or engine properties of a particular vehicle must be mitigated through the careful application of interpolation techniques, discussed further in Appendix D.1. Discontinuities that are unable to be mitigated, such as stage separations, must be separated into distinct phases within the optimal control solution and connected by linkage constraints [36], as discussed further in Section 5.3.

5.2.1 Equations of Motion

The dynamics of the launch system are calculated in three degrees of freedom, in a geodetic rotational reference frame, illustrated in Figure 5.3. The Earth is modelled as an oblate spheroid using the World Geodetic System 1984[183] (WGS-84) shape and gravity model. In this reference frame, the dynamics of each vehicle are expressed in terms of the angle of attack α , bank angle η , radius from centre of Earth r , longitude ξ , latitude ϕ , flight path angle γ , speed (velocity magnitude) v and heading angle ζ . The equations of motion are given by[184, 185]:

$$\dot{r} = v \sin \gamma \quad (5.2)$$

$$\dot{\xi} = \frac{v \cos \gamma \cos \zeta}{r \cos \phi} \quad (5.3)$$

$$\dot{\phi} = \frac{v \cos \gamma \sin \zeta}{r} \quad (5.4)$$

$$\begin{aligned} \dot{\gamma} &= \frac{(L + T \sin \alpha) \cos \eta}{mv} + \left(\frac{v}{r} - \frac{g_r}{v} \right) \cos \gamma - \frac{g_t}{v} \sin \gamma \cos \zeta \\ &\quad + \cos \phi \left[2\omega_E \cos \zeta + \frac{\omega_E^2 r}{v} (\cos \phi \cos \gamma + \sin \phi \sin \gamma \sin \zeta) \right] \end{aligned} \quad (5.5)$$

$$\dot{v} = \frac{T \cos \alpha - D}{m} - g_r \sin \gamma + g_t \cos \gamma \cos \zeta + \omega_E^2 r \cos \phi (\cos \phi \sin \gamma - \sin \phi \cos \gamma \sin \zeta) \quad (5.6)$$

$$\begin{aligned} \dot{\zeta} &= \frac{(L + T \sin \alpha) \sin \eta}{mv \cos \gamma} - \frac{v}{r} \tan \phi \cos \gamma \cos \zeta + 2\omega_E \cos \phi \tan \gamma \sin \zeta \\ &\quad - \frac{\omega_E^2 r}{v \cos \gamma} \sin \gamma \cos \phi \cos \zeta - 2\omega_E \sin \phi - g_t \sin \zeta \end{aligned} \quad (5.7)$$

Where ω_E is the angular velocity of the Earth, and g_r and g_t are the gravity of the Earth in the

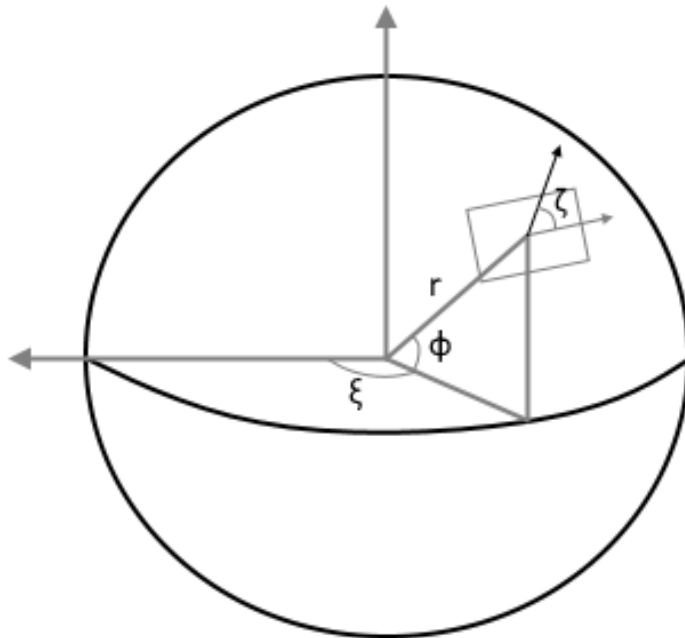


Figure 5.3: The Earth-fixed components of the geodetic rotational coordinate system.

radial and transverse directions. These dynamics are used as the dynamic constraints of the launch system, as shown in Equation 5.1, with each dynamic parameter implemented as a state variable (\mathbf{x}). As described in Chapter 4; the lift (L) and drag (D) forces are interpolated from each flight condition using aerodynamic databases, and include trim.

5.3 Optimal Control Problem Structure

One of the primary functions of LODESTAR is to interface with the optimal control solver GPOPS-2. GPOPS-2 is a generic optimal control solver that utilises the pseudospectral method of optimal control, as well as the IPOPT nonlinear optimisation package. GPOPS-2 is described in Section 3.5. Practically, the implementation of optimal control involves the specification of the dynamics of the system to be optimised, as well as the set of constraints and objectives that define the optimisation problem, described as follows:

Cost Function

The cost function, J , defines the target of the optimisation problem. This cost function may be any function which is defined by the states or controls of the optimisation problem. The cost function is

defined as follows:

$$J(t, \mathbf{x}(t), \mathbf{u}(t)) = M[t, \mathbf{x}(t_f), \mathbf{u}(t_f)] + \int_{t_0}^{t_f} L[\mathbf{x}(t), \mathbf{u}(t)] dt, \quad t \in [t_0, t_f], \quad (5.8)$$

where M is the terminal cost function and L is the time integrated cost.

Dynamic Constraints

The optimisation problem is subject to a set of dynamic constraints, which describe the behaviour of the system over the solution space:

$$\dot{\mathbf{x}}(t) - f[t, \mathbf{x}(t), \mathbf{u}(t)] = 0, \quad t \in [t_0, t_f]. \quad (5.9)$$

These dynamic constraints ensure that the polynomial approximations of the state variables, as described in Section 3.4.2, match the physical dynamics of the system. Implementing the dynamics as constraints in the manner of the pseudospectral method allows each state variable to be approximated separately, and gives the optimiser some freedom to explore each state variable independently, greatly increasing the robustness of the optimal control problem.

Bounds and Path Constraints

Inequality constraints define the bounds of each state, as well as any path constraints. The bounds directly confine the state and control variables to prescribed values. This serves the purpose of limiting the search space to the physically possible (eg. constraining altitude to be greater than ground level), constraining the vehicle within its performance limits (eg. limiting the angle of attack), and improving computational efficiency by ensuring that the optimiser is constrained to a reasonable solution space:

$$\mathbf{b}_{min} \leq \mathbf{x}(t), \mathbf{u}(t) \leq \mathbf{b}_{max}, \quad t \in [t_0, t_f]. \quad (5.10)$$

The path constraints are inequality constraints which consist of functions based on the states and controls of the system. Path constraints place adaptive bounds on the system, which vary over time with the state of the system:

$$\lambda[t, \mathbf{x}(t), \mathbf{u}(t)] \leq \mathbf{0}, \quad t \in [t_0, t_f]. \quad (5.11)$$

Path constraints are used by LODESTAR to impose physical limitations on the system such as structural, aerothermodynamic, pathing, and control limits.

Event Constraints

The event constraints constrain the states at the start and end points of a trajectory or phase:

$$\psi_0[\mathbf{x}(t_0), t_0] = \mathbf{0}, \quad (5.12)$$

$$\psi_f[\mathbf{x}(t_f), t_f] = \mathbf{0}. \quad (5.13)$$

These constraints determine the initial and terminal conditions of the optimisation problem, such as the initial location and velocity, and the starting fuel mass.

Together, these objectives, constraints, and variables describe the optimal control problem being solved, and form the inputs which LODESTAR provides to GPOPS-2. GPOPS-2 uses these inputs, along with a pseudospectral method transcription, to form the constrained optimisation problem that is solved using IPOPT.

5.3.1 Trajectory Connection Points

The optimisation of a large, multi-vehicle launch trajectory requires that the optimal control problem be broken down into multiple segments, or phases[179]. These phases are joined by event constraints, which couple the states and time of each phase to the preceding and following phases as follows:

$$\mathbf{x}_{f,1} - \mathbf{x}_{0,2} = 0, \quad (5.14)$$

$$\mathbf{t}_{f,1} - \mathbf{t}_{0,2} = 0. \quad (5.15)$$

This segmentation is performed in order to assist the convergence of the optimal control solver, by ensuring that the dynamics of the underlying model are as smooth and continuous as possible across each segment.

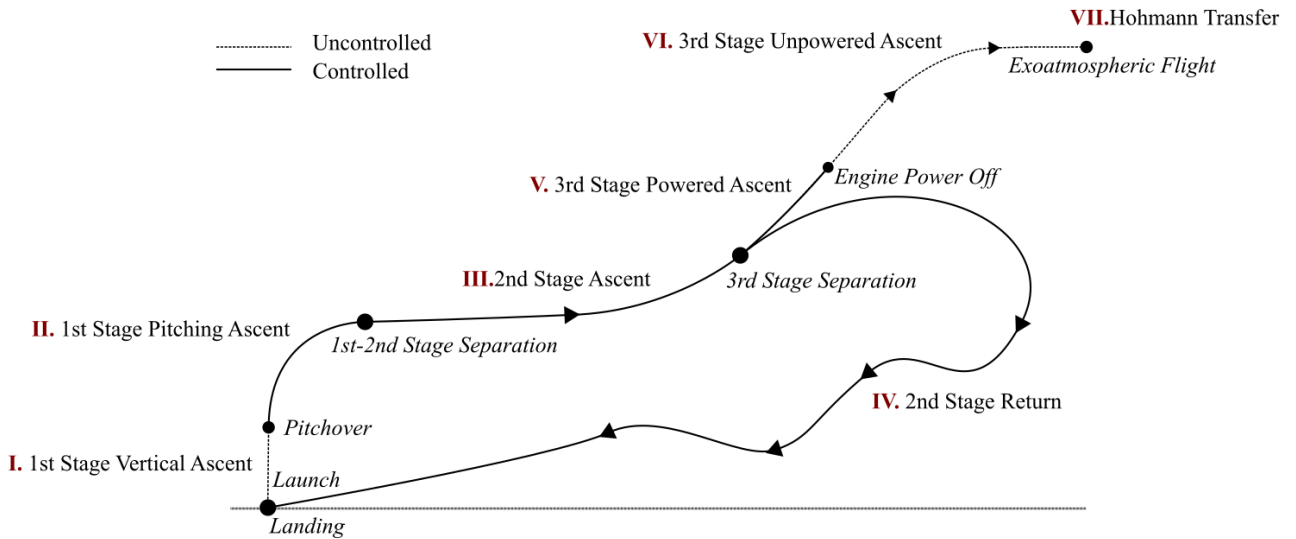


Figure 5.4: Illustration of the phases of the launch profile. Controlled and uncontrolled phases are distinguished.

For a launch system, discontinuities in the system dynamics generally arise when the aerodynam-

ics, mass or propulsion mode of a launch vehicle change significantly between stages or flight modes. If a vehicle model with large discontinuities is implemented directly into a single phase application of the pseudospectral method, it is likely to cause significant convergence issues, as the system dynamics will be unable to be approximated by the underlying polynomial of the pseudospectral method across these transition points[186].

To allow the trajectory profile to be formulated as an optimal control problem, the trajectory of the rocket-scramjet-rocket launch system is broken down into the seven segments shown in Figure 5.4. The segments are separated into two groups; controlled segments which take the form of phases within the optimal control problem; and segments without control which are either forward simulated at each iteration of the optimiser, or simulated externally to the optimal control problem. For example, the unpowered segments of the third stage are simulated within the optimiser, and are included as a terminal cost, as described in Equation 5.8.

Segments II-V are controlled by various combinations of angle of attack, bank angle and throttle, and are implemented as the phases of the optimisation problem. These phases are: II, the 1st stage pitching ascent; III, the 2nd stage ascent; IV, the 2nd stage return flight; and V, the 3rd stage powered ascent. Segments I, VI and VII are segments without direct control, which are simulated using forward time stepping methods. These phases are: the pre-pitch segment of the first stage, the unpowered section of the third stage ascent, and the final Hohmann transfer to orbit. Each segment is connected through a set of continuity constraints. The optimal control problem phases are connected through the use of initial and end discontinuity constraints (Equations 5.14 and 5.15), while the forward simulated segments are simply initiated and terminated at set conditions. The segment coupling conditions are described in Table 5.1.

The following sections describe the setup of each individual phase of the optimal control problem, including the variables and constraints for the optimised phases. The bounds on the state dynamics are chosen to encompass the solution space, while not being overly expansive, to assist with the convergence and scaling of the optimal control solver. Across all optimised phases, the bounds on the latitude and longitude are chosen to cover the possible solution space, and are kept consistent across each phase to ensure that the position of the vehicle is not being unreasonably constrained between segments. The speed constraints are chosen to cover the possible solution space, with the lower bound of 10m/s chosen to ensure that the speed does not approach 0m/s, as this produces singularities within the system dynamics.

5.3.2 I. First Stage Vertical Ascent

LODESTAR optimises the ascent of the first stage rocket in two segments; pre and post-pitchover. The aerodynamics of flight during these segments are simulated using spline interpolation of the databases generated using the method described in Section 4.2.1, and the engine properties are determined using

Section	Initial Conditions	End Conditions	Controlled
I: 1 st Stage Vertical Ascent	Launches from rest, at the predefined launch site.	Fly until pitchover conditions are met.	no
II: 1 st Stage Pitching Ascent	Start at pitchover conditions	Terminates at end of fuel.	yes
III: 2 nd Stage Ascent	Must begin at 1 st stage pitching ascent end conditions.	Terminates at end of ascent fuel.	yes
IV: 2 nd Stage Return	Must begin at 2 nd stage ascent end conditions.	Must approach landing conditions at the initial launch site.	yes
V: 3 rd Stage Powered Ascent	Must begin at 2 nd stage ascent end conditions.	Must produce exoatmospheric flight at the termination of stage VI.	yes
VI: 3 rd Stage Unpowered Ascent	Must begin at 3 rd stage powered ascent end conditions.	Terminates when flight is parallel with Earth's surface.	no
VII: 3 rd Stage Hohmann Transfer	Must begin at 3 rd stage unpowered ascent end conditions.	Must attain prescribed orbit.	no

Table 5.1: Segment coupling conditions for combined trajectory optimisation.

linear pressure scaling as described in Section 4.2.

The pre-pitchover phase is the segment of flight immediately after vertical launch. During this phase, the launch system continues vertically for a short time in order to clear the launch tower and stabilise the vehicle, and to allow the dynamics of the system to be calculated appropriately during the pitching ascent. A single simulation was performed with a reference vehicle, resulting in a terminal condition of 30m altitude and a speed of 15m/s. During the vertical launch the rocket is assumed to need no control, and is held at 0° angle of attack.

5.3.3 II. First Stage Pitching Ascent

At 30m altitude and a speed of 15m/s, pitchover occurs. The pitchover is a very minor amount of instantaneous pitching (0.01°) which is introduced in order to begin the pitching ascent, allowing the optimised initial heading angle of the vehicle to be resolved correctly. The first stage pitching ascent trajectory is an angle of attack controlled phase in the optimisation routine, which is simulated from pitchover until second stage separation. Table 5.2 shows the optimisation setup of this phase. During this phase, the launch system is allowed to fly at negative angles of attack, to assist in pitching. **The controls for this phase are the second derivative of angle of attack and the throttle change rate, which are chosen as the control variables to assist in mitigating the first stage's sensitivities to angle of attack**

Variable Group	Associated Variables	Value/Range
Initial Constraints	Altitude (z) Speed (v) Trajectory Angle (γ) Latitude (ϕ) Longitude (ξ) Angle of Attack (α)	30m 15m/s 89.9° -12.16° 136.75° 0°
Terminal Constraints	$\mathbf{x}_{f,\text{II}} - \mathbf{x}_{0,\text{III}}$ $t_{f,\text{II}} - t_{0,\text{III}}$	0 0
Path Constraints	Dynamic Pressure (q)	0kPa - 50kPa
Control Variables	$\ddot{\alpha}$ \dot{T}	$\pm 0.029^\circ/s^2$ $\pm 0.05/s$
State Variables	Altitude (z) Speed (v) Trajectory Angle (γ) Latitude (ϕ) Longitude (ξ) Heading Angle (ζ) Total Mass (m) Angle of Attack (α) $\dot{\alpha}$ Throttle (T)	0 - 30km 10 - 3000m/s $-5.7^\circ - 89.9^\circ$ $\pm 28.6^\circ$ $114.6^\circ - 171.9^\circ$ $\pm 360^\circ$ 11453 - 29388kg $-5^\circ - 0^\circ$ $\pm 5.7^\circ/s$ 0.7 - 1

Table 5.2: Optimisation setup of the first stage phase.

and throttle, ie. when the trajectory angle is near 90° and at low velocities, the effects of changes in the aerodynamics and throttle on the dynamics of the system are very large. This sensitivity can cause convergence issues, which are mitigated by using the second derivative of angle of attack and the first derivative of the throttle as the control variables. The initial fuel mass of the first stage rocket is not fixed, as variations in the initial fuel mass can have an important effect on the capabilities of the first stage. The fuel mass can influence the velocity achievable at first to second stage separation, as well as the rate at which the rocket is able to pitch, and consequentially, the altitude and flight path angle range of the first stage. Allowing the initial fuel mass to vary increases the flexibility of the optimal control solver, and enables the optimal sizing of the first stage to be investigated.

5.3.4 III. Second Stage Ascent Trajectory

The second stage ascent phase consists of the acceleration of the scramjet accelerator, controlled using angle of attack and bank angle. The optimisation setup of this phase is detailed in Table 5.3. The propulsion, lift, and drag of the vehicle are obtained from interpolation of the C-RESTM10 and trimmed aerodynamics databases described in Sections 4.1.3, 4.1.5, and 4.1.6. During the ascent, the engines are assumed to be operating at maximum thrust, corresponding to the maximum equivalence

Variable Group	Associated Variables	Value/Range
Initial Constraints	Fuel Mass (m_F)	1562kg
Terminal Constraints	$\mathbf{x}_{f,\text{II}} - \mathbf{x}_{0,\text{III}}$	0
	$t_{f,\text{II}} - t_{0,\text{III}}$	0
Terminal Constraints	Altitude (z)	0 - 45km
	Trajectory Angle (γ)	0 - 20°
	Bank Angle (η)	0°
	$\mathbf{x}_{f,\text{III}} - \mathbf{x}_{0,\text{IV}}$	0
	$t_{f,\text{III}} - t_{0,\text{IV}}$	0
	$\mathbf{x}_{f,\text{III}} - \mathbf{x}_{0,\text{V}}$	0
	$t_{f,\text{III}} - t_{0,\text{V}}$	0
Path Constraints	Dynamic Pressure	0 - 50kPa
Target Cost (Optional)	Dynamic Pressure*	$(q - 50000)^2 / 50000$
Control Variables	$\dot{\alpha}$	±0.5°/s
	$\dot{\eta}$	±1°/s
State Variables	Altitude (z)	0 - 50km
	Speed (v)	10 - 3000m/s
	Trajectory Angle (γ)	-10° - 20°
	Latitude (ϕ)	±28.6°
	Longitude (ξ)	114.6° - 171.9°
	Heading Angle (ζ)	-240° - 360°
	Fuel Mass (m_F)	0 - 1562kg
	Angle of Attack (α)	0° - 10°
	Bank Angle η	-1° - 90°

Table 5.3: Optimisation setup of the second stage ascent. * This is only used in the constant dynamic pressure simulation.

ratio at all times. This equivalence ratio is 1 in most sections of the trajectory, except at low Mach numbers where the possibility of unstart and choking necessitates a reduction in equivalence ratio as discussed in Section 4.1.1. This trajectory is constrained by a maximum dynamic pressure of 50kPa, corresponding to the maximum structural limits of the vehicle. The control variables are set as the rate of change of angle of attack, and the rate of change of bank angle. Using the derivatives of the angle of attack and bank angle as the control variables serves to smooth the angle of attack and bank angle by constraining the change rates. The angle of attack is constrained to 10°, approximated as a reasonable upper bound to the angle of attack, and conforming to previous studies of the SPARTAN. The bank angle is constrained to a maximum of 90°, as it is assumed that the scramjet accelerator is not able to invert. The bank angle is also constrained to positive values only (ie. the heading angle may only increase) as the scramjet accelerator is launched from the ELA launch site at Nhulunbuy, and it is preferable to launch to the northeast or east to avoid overflying populated areas.

An integrated cost function component (L in Equation 5.8) can be included during this phase, shown in Table 5.3, when flying a constant dynamic pressure trajectory is desired. This cost function

is smooth and approaches 0 at the target dynamic pressure, allowing the third stage cost function of payload mass to still be active, while prioritising flying at constant dynamic pressure.

5.3.5 IV. Second Stage Return Trajectory

Variable Group	Associated Variables	Value/Range
Initial Constraints	Bank Angle (η)	0°
	$\mathbf{x}_{f,\text{III}} - \mathbf{x}_{0,\text{IV}}$	0
	$t_{f,\text{III}} - t_{0,\text{IV}}$	0
Terminal Constraints	Altitude (z)	0 - 1km
	Speed (v)	0 - 20m/s
	Latitude (ϕ)	-12.16°
	Longitude (ξ)	136.75°
Path Constraints	Dynamic Pressure (q)	0 - 50kPa
Control Variables	$\dot{\alpha}$	$\pm 0.5^\circ/\text{s}$
	$\dot{\eta}$	$\pm 1^\circ/\text{s}$
	Throttle	$\pm 0.2/\text{s}$
State Variables	Altitude (z)	0 - 70km
	Speed (v)	10 - 5000m/s
	Trajectory Angle (γ)	$\pm 80^\circ$
	Latitude (ϕ)	$\pm 28.6^\circ$
	Longitude (ξ)	114.6° - 171.9°
	Heading Angle (ζ)	60° - 500°
	Fuel Mass (m_F)	0kg - 500kg
	Angle of Attack (α)	0° - 10°
	Bank Angle (η)	0° - 90°
	Throttle	0 - 1

Table 5.4: Optimisation setup of the second stage return.

After releasing the third stage rocket, the scramjet-powered second stage must return back to the initial launch site. During this return flight, the scramjet accelerator is able to use its engines if necessary to ensure that it is able to return successfully. During the fly-back, the scramjet accelerator cannot exceed its dynamic pressure limit of 50kPa. The end state is constrained to a minimum of -20° trajectory angle, which is assumed to be an appropriate lower bound on the trajectory angle for approach to a landing strip. The altitude is constrained to less than 1km at the end point to ensure that the scramjet accelerator is approaching landing altitude. The velocity at the termination of the return trajectory is left variable. Constraining the end velocity may over-constrain the optimisation problem, and it is assumed that for a payload-to-orbit optimised trajectory the scramjet accelerator will end its return at a low speed, so that the energy necessary for return is minimised.

The aerodynamics of the scramjet accelerator during fly-back are determined by interpolation of

the engine-on and engine-off trimmed data sets described in Section 4.1.4. During the return, the C-REST engines are able to be throttled on and off. As the scramjet engines are throttled on, the aerodynamics are assumed to vary linearly between the aerodynamics calculated by the engine-off and engine-on datasets. The throttle setting is defined as a state variable, with range between 0 and 1, where 1 represents the maximum equivalence ratio at that point. The corresponding fuel mass flow rate is scaled linearly with the throttle:

$$\dot{m}_{fuel} = \dot{m}_{fuel,max} \text{throttle}, \quad (5.16)$$

and the thrust of the engine is assumed to scale linearly with the fuel mass flow rate. A control variable of throttle change rate is added, to smooth the throttle in the same way as angle of attack and bank angle.

5.3.6 V. Third Stage Powered Ascent

Variable Group	Associated Variables	Value/Range
Initial Constraints	Total Mass (m)	3300kg
	$\mathbf{x}_{f,III} - \mathbf{x}_{0,V}$	0
	$t_{f,III} - t_{0,V}$	0
Terminal Constraints	$Alt_{f,VI}$	$\geq 90\text{km}$
	Heading Angle (ζ) VI	97.64°
	Angle of Attack (α)	0°
Path Constraints	Thrust Vector Angle	$\pm 8^\circ$
	Normal Force F_N	$0 - F_{N,10^\circ,50kPa}$
Target Cost	Payload-to-Orbit	Payload Calculated in Phase VII
Control Variables	$\dot{\alpha}$	$\pm 1^\circ/\text{s}$
State Variables	Altitude (z)	30 - 84km
	Speed (v)	10 - 8000m/s
	Trajectory Angle (γ)	$-5^\circ - 30^\circ$
	Latitude (ϕ)	$\pm 28.6^\circ$
	Heading Angle (ζ)	$80^\circ - 120^\circ$
	Total Mass (m)	0kg - 3300kg
	Angle of Attack (α)	$0^\circ - 10^\circ$

Table 5.5: Optimisation setup of the third stage powered ascent.

The trajectory of the third stage rocket is separated into the powered and unpowered phases of ascent. During the powered ascent phase, the third stage is manoeuvred out of the atmosphere using one continuous burn of the Kestrel engine. The powered ascent is an optimised phase, with optimisation properties described in Table 5.5. The powered phase is controlled using angle of attack, and trimmed using thrust vectoring of the engine, as described in Section 4.3.6. The aerodynamics of the third stage

are determined using interpolation of the aerodynamic dataset developed as described in Section 4.3.5.

The third stage rocket is constrained to an angle of attack of less than 10° . This is assumed to be the maximum controllable angle of attack possible for the third stage rocket. Additionally, the normal force is limited to the normal force observed at 10° angle of attack, and 50kPa[12] dynamic pressure, which is assumed to be the maximum allowable normal force on the third stage rocket. This normal force is calculated at the third stage release conditions, and imposed as a path constraint.

The final angle of attack is constrained to 0° , as the angle of attack will not be able to be controlled during the unpowered ascent. The other terminal constraints of this phase correspond to end constraints imposed after the third stage unpowered ascent has been simulated, but are taken into account in the set up of this phase because the unpowered ascent is not implemented as a phase in GPOPS-2. The altitude at the end of the unpowered ascent (Phase VI) is constrained to a lower limit of 90km, in order to ensure that the rocket is exoatmospheric. The final heading angle is also constrained at this point, so that the orbit of the third stage attains the correct inclination for sun synchronous orbit.

5.3.7 VI. Third Stage Unpowered Ascent

After the burn of the Kestrel engine is complete, at the end of phase V, the engine is cut and the third stage coasts to exoatmospheric conditions. The unpowered phase of the ascent is not controlled. After the engine is cut, the third stage does not have sufficient aerodynamic control to manoeuvre, and the trajectory of the third stage is a coast at 0° angle of attack. The trajectory of the third stage rocket is only directly optimised during the powered section of its trajectory, the unpowered section of the trajectory is simulated from the end of the controlled section of the trajectory, using a second order Taylor series approximation. This integration ceases when the flight path angle reaches 0° . During this phase, the heat shield is released once the rocket has reached a dynamic pressure of 10Pa, where it is assumed that atmospheric effects will have ceased to have a major thermal effect. As the third stage is required to deliver the payload into heliosynchronous orbit, the third stage must achieve an inclination of 97.63° at the end of this phase[180]. These terminal constraints are implemented in Phase V.

5.3.8 VII. Third Stage Hohmann Transfer

After the rocket has attained exoatmospheric flight parallel to the Earth's surface, a circularisation burn is performed. This circularisation burn takes the third stage rocket into low orbit around the Earth. However, in order to reach a heliosynchronous orbit of 567km, the orbit of the third stage rocket must be raised. To this end, the final manoeuvre performed by the third stage rocket is a Hohmann transfer. A Hohmann transfer is the most fuel efficient way to raise a spacecraft from one circular orbit to another[187]. The orbit of the third stage is first circularised into a low orbit through

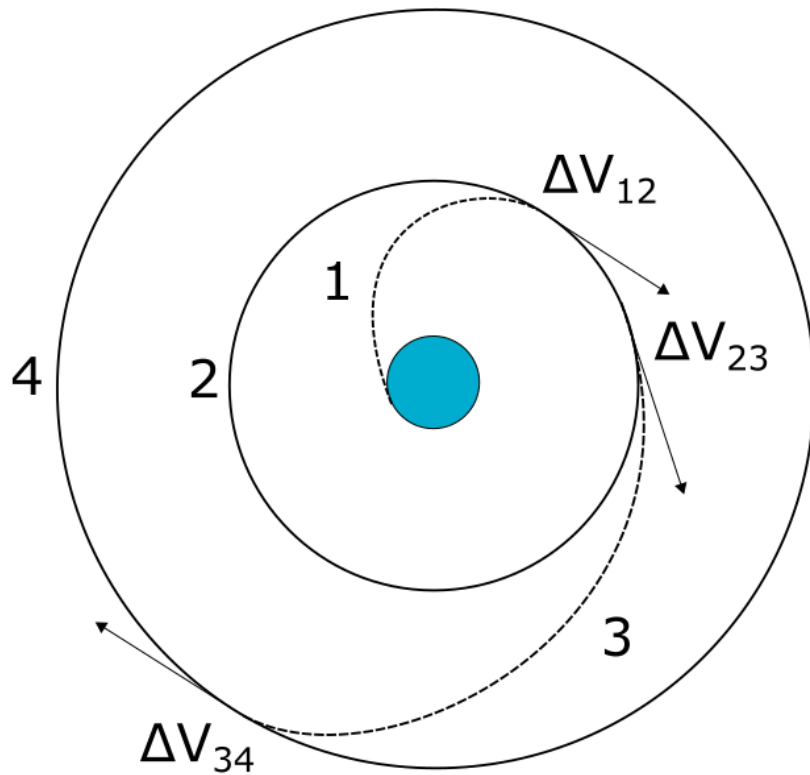


Figure 5.5: The Hohmann transfer manoeuvre. ΔV indicates a velocity change due to a burn.

a velocity change due to a burn, ΔV_{12} :

$$\Delta V_{12} = \sqrt{\frac{\mu}{r_2}} - v_1, \quad (5.17)$$

where μ is the standard gravitational parameter, r is the distance from the centre of the Earth, and v_1 is the velocity before circularisation. Following circularisation, the third stage engine is reignited (or remains ignited) and the third stage manoeuvres into an appropriate elliptical orbit:

$$\Delta V_{23} = \sqrt{\frac{\mu}{r_2}} \left(\sqrt{\frac{2r_4}{r_2 + r_4}} - 1 \right). \quad (5.18)$$

At the apogee of the transfer orbit, corresponding to the desired orbital radius, an insertion burn is performed, and the orbit is circularised:

$$\Delta V_{34} = \sqrt{\frac{\mu}{r_4}} \left(1 - \sqrt{\frac{2r_2}{r_2 + r_4}} \right). \quad (5.19)$$

At this point, the payload is separated from the third stage rocket.

The mass of the third stage rocket after each burn is calculated using the Tsiolkovsky rocket

equation:

$$m_2 = \frac{m_{1f}}{\exp^{\frac{v_{12}}{I_{SP} \cdot g_0}}} \quad (5.20)$$

$$m_3 = \frac{m_2}{\exp^{\frac{v_{23}}{I_{SP} \cdot g_0}}} \quad (5.21)$$

$$m_4 = \frac{m_3}{\exp^{\frac{v_{34}}{I_{SP} \cdot g_0}}} \quad (5.22)$$

Finally, the payload-to-orbit is determined by removing the structural mass from the total mass of the vehicle at the end of the Hohmann transfer. The remaining mass is taken to be the payload-to-orbit capability of the vehicle.

$$m_{payload} = m_4 - m_{struct} \quad (5.23)$$

5.4 Optimal Solution Analysis

Due to the nature of the pseudospectral method, it is possible that GPOPS-2 will not be able to converge to a physically valid or optimal solution. LODESTAR provides the capacity to analyse the optimal solution provided by the pseudospectral method solver to assist in determining whether the pseudospectral method solver has converged close to an optimal solution of the nonlinear programming problem. It is particularly useful to verify that the optimality and constraint tolerances that have been chosen are sufficiently small, or to check whether the pseudospectral method solver has approached an optimal solution in the case that the defined tolerances are not able to be reached. Checking the solution is achieved through the examination of five key parameters: the IPOPT constraint violation, and dual infeasibility parameters; the Hamiltonian necessary condition for optimality; the state derivatives; and finally, a forward simulation.

The first two metrics to be checked are the IPOPT constraint violation (*inf-pr*) and dual infeasibility parameter (*inf-du*)[188]. The constraint violation parameter is a measure of the infinity-norm (*L_∞-norm*) of the constraints of the problem[188]. This factor must be suitably small in order to indicate that the constraints of the problem have been met. While the permissible magnitude of this factor changes with each individual problem, it is always desirable for this factor to be as small as possible. The dual infeasibility provides an indication of the optimality of the solution. A low dual infeasibility indicates that the solution is dual feasible and is likely to have approached an optimal solution. A dual feasible solution indicates that the dual problem is at least a lower bound on the optimal solution, $p^* \geq g(\lambda, v)$. For more details on duality see Reference[189]. Again, the magnitude of this value is variable with each problem, though as a problem becomes more complex, the ability to converge towards an optimal solution diminishes. It should generally be observable that the *inf-du* term is decreasing by multiple orders of magnitude and is stable at the completion of optimisation for

a solution to be approaching optimality.

The Hamiltonian of the optimal control problem is defined as:

$$H(x(t), u(t), \lambda(t), t) = \lambda^T(t) f(x(t), u(t)) + L(x(t), u(t)). \quad (5.24)$$

The Hamiltonian of the optimal control problem is calculated using LODESTAR, and investigated as a partial verification that the first order necessary conditions hold. Due to the unconstrained end time of the trajectory problems, the Hamiltonian necessary condition for an optimal solution is $H = 0$ [190]. A sufficiently small Hamiltonian indicates that the end solution is likely to have approached an optimal solution.

The pseudospectral method considers the dynamics of the system as constraints on the optimal control problem, and solves across the entire trajectory simultaneously. This causes the physical system dynamics to have an associated margin of error, ie. $\dot{x} = f(x)$ will only hold to a certain degree of accuracy. For a well-converged solution, this margin of error will be negligibly small, and the dynamics of the system will be consistent with the vehicle dynamics. However, when the problem has not converged, the dynamics of the system may have a large error. A check is performed on each state (dynamic variable) to affirm that the derivative of the approximated state is equal to the derivative supplied by the vehicle model. This checks that the solver has converged to a solution which satisfies the vehicle dynamics at each individual node (discretised time point). The state feasibility of the solution is checked through a verification of the state derivatives of each phase, $\dot{x} = f(x, u)$. \dot{x} is first determined through numerical differentiation of the state variables over the solution time, differentiated at the node points created by GPOPS-2. Then $f(x, u)$ is determined using the dynamics of the system and vehicle model, in the same way that $f(x, u)$ is input to the pseudospectral solver. Examination of the error between the ‘expected’ state derivatives, and the numerical approximation of the derivatives, $\dot{x} - f(x, u)$, allows the accuracy of the system dynamics to be assessed.

The final verification check is performing a full forward simulation. This forward simulation starts at the initial conditions of the optimal control problem, and propagates the dynamics of the system forward in time using the Runge-Kutta method, through Matlab’s ODE45 function. The forward simulation uses the optimised control variables as the only input. This checks that the flight path will follow the path computed by GPOPS-2, using only the calculated control inputs. This is the most complete test of the constraints of the optimal solution. However, in some cases calculating a forward solution may be problematic. The pseudospectral method has a limited number of nodes, potentially spread across relatively large time steps. Due to the high accuracy of the polynomial approximation, the pseudospectral method is able to maintain accuracy over large time steps[102, 105]. However, a forward simulation necessarily has less accuracy than the spectral method, and may interpolate differently when applied to the optimal solution, causing minor deviations. These variations are usually negligibly small, however, this is problematic during the return phase, due to the way the

throttling of the engines is modelled, ie. the specific impulse of the engines is set to 0 under Mach 5 or 20kPa inlet conditions during the optimisation process. As the engines are often throttled close to the minimum operable conditions, these restrictions can intensify the effects of otherwise minor deviations in the forward simulation. For this reason, the forward simulation of the return stage is split into three segments, with divisions at 1/6th and 1/3rd of the total trajectory length, chosen to separate the first major ‘skip’ and bank, and split the ‘skipping’ section of the trajectory. A forward simulation is initiated at each of these segments, mitigating some of the effects of the engines throttling on and off in the forward simulation. Splitting the forward simulation allows the forward simulation of the return stage to be assessed without the effects of the throttle model having an unreasonably large effect.

5.5 The Optimisation Process in LODESTAR

Figure 5.6 shows an illustration of the optimal control routine within LODESTAR. Each of the processes shown is described in more detail in the preceding sections, which are indicated in Figure 5.6. Initially, LODESTAR provides the initial guess and problem setup, configuring GPOPS-2 and defining the optimal control problem being solved. The iterative process begins with GPOPS-2 providing the current iteration of the trajectory solution to LODESTAR, along with a mesh of nodes that define the points in time at which the dynamics of the system are approximated. LODESTAR then calculates the aerodynamic and engine performance of the launch system at each node along the trajectory, as well as atmospheric and flight conditions. The system dynamics are calculated, and provided to GPOPS-2 which implements these as per Equation 5.1. LODESTAR evaluates the trajectory, and simulates the unpowered third stage ascent and Hohmann transfer as forward simulations. LODESTAR uses the mass of the third stage fuel remaining at the end of its trajectory to calculate the payload-to-orbit, and passes this to GPOPS-2 as an endpoint cost function. The vehicle dynamics and payload-to-orbit are evaluated by GPOPS-2, which utilises the IPOPT nonlinear programming solver[122] to update the guess of the trajectory solution via an interior point method, at which point this updated guess is passed through to LODESTAR once more. The solution is evaluated by GPOPS-2 at each iteration to compute the feasibility and optimality of the solution. This process repeats until either a predefined tolerance of optimality, or a predefined number of iterations, is reached. The process repeats for a number of mesh iterations defined by the user, which further refine the trajectory. To aid robustness, GPOPS-2 is initiated from four separate initial guesses, with the final altitude guess varied by 1km between each initial trajectory. These iterations of GPOPS-2 are run in parallel, using Matlab’s Parfor function. After all the iterations of GPOPS-2 have completed, the solutions are evaluated, and the ‘best’ solution is chosen as the solution with the most accurately modelled dynamics. This process is parallelised within LODESTAR, with green and red arrows in Figure 5.6 indicating the initiation and termination of the parallel loop respectively.

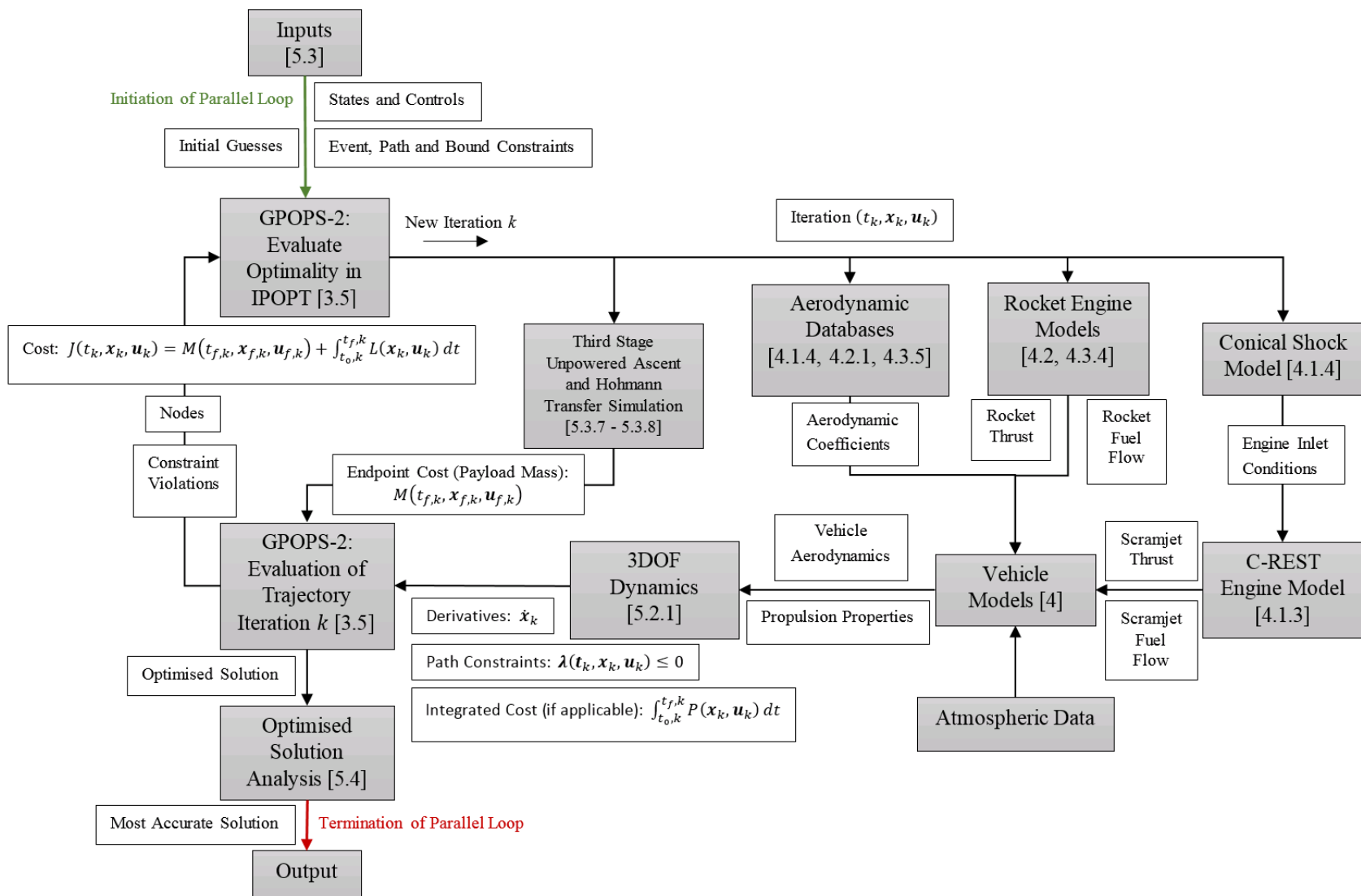


Figure 5.6: The process of the rocket-scramjet-rocket trajectory optimisation. Relevant sections are indicated in square brackets at each process step.

5.6 Trajectory and Performance Analysis

LODESTAR provides a range of plotting tools, which present the optimised trajectory graphically, along with various performance indicators of each vehicle, including L/D, net specific impulse, and control time histories. LODESTAR also possesses the capability to graphically show the aerodynamic and engine performance of the vehicle over the range of possible flight conditions, with overlays of the optimised trajectory path. These tools can be used to identify the performance region in which the vehicle is flying, in order to distinguish trends and trade-offs in the optimal flight path. In addition to graphical tools, LODESTAR also calculates an energy usage analysis of the launch system. This includes calculating the exergy efficiency of each vehicle, and the overall launch system, as well as individual sources of energy losses within each stage.

Exergy expresses how much useful work is available to a system, and exergy efficiency quantifies how well a system utilises the available work. Exergy efficiency can show how well each stage is using its available energy, and assist with quantifying the efficiency trade-offs between the stages. Exergy efficiency is an important parameter for analysing launch vehicles, allowing the relative efficiencies of each stage to be compared when the design or trajectory of a launch system is varied[191]. The exergy efficiency of a stage of a launch system is expressed as the fraction of the fuel combustion energy which is turned into ‘useful’ kinetic and potential energy during flight:

$$\eta_{exergy,stage} = 1 - \frac{\Delta m_{fuel}H_{fuel} - \Delta KE - \Delta PE + \Delta KE_{discarded} + \Delta PE_{discarded}}{\Delta m_{fuel}H_{fuel}}, \quad (5.25)$$

where H_{fuel} is the heating value of the fuel, ΔKE is the change in the kinetic energy of the stage, ΔPE is the change in the potential energy of the stage over its trajectory, and $\Delta KE_{discarded} + \Delta PE_{discarded}$ is the energy imparted to the mass discarded at staging. This exergy efficiency expresses how efficiently each stage utilises its available fuel over each individual trajectory. However, this stage-based exergy efficiency does not account for the effects of the unused mass of the successive stages on the performance of the launch system, ie. the exergy efficiency of each stage is a measure of how well it accelerates the next stage. The total exergy efficiency of the launch system is calculated as the fraction of the total available energy which goes directly into placing the payload into orbit:

$$\eta_{exergy} = \frac{\Delta KE_{payload} + \Delta PE_{payload}}{\sum_{stage} \Delta m_{fuel}H_{fuel}}. \quad (5.26)$$

This exergy efficiency expresses how efficiently the launch system as a whole is able to accelerate the payload to orbit. Within this work, exergy efficiency is expressed as the percentage of total exergy utilised, $\% \eta$, ie. $\eta_{exergy} \times 100$.

5.7 Summary

This chapter described the implementation of a tool for optimising the trajectory of multi-stage launch systems, designated LODESTAR. LODESTAR simulates each stage of a launch system, and interfaces with the optimal control solver GPOPS-2 to generate an optimised trajectory solution. The set-up of LODESTAR for the launch of a rocket-scramjet-rocket launch system, delivering a small satellite to sun synchronous orbit, has been detailed. Each stage of the launch system is simulated individually within LODESTAR, either as a separate phase of the optimal control problem, connected by event constraints, or as a forward simulation. The bounds of each stage have been chosen so as to provide suitable limits to the dynamics of the system, and the payload-to-orbit capability of the system has been set as the end cost function of the optimal control problem. The state and control variables of each stage were detailed, along with the state, event and path constraints. The capability of LODESTAR to verify the optimised solution was presented, including analysis using the necessary conditions of optimality, as well as forward simulation comparisons. Finally, the trajectory and performance analysis capabilities of LODESTAR were presented, including graphical tools and exergy efficiency calculations.

CHAPTER 6

OPTIMISED ASCENT TRAJECTORY

XXX Think about the formatting of the figure labels, ie Case :

This chapter presents a maximum payload-to-orbit trajectory optimisation for the representative launch system described in Chapter 4. This launch system is simulated as being launched from the Equatorial Launch Australia launch site in East Arnhem Land (Detailed in Section 5.1), and delivers a small satellite into sun synchronous orbit. LODESTAR is used to calculate the maximum payload-to-orbit trajectory solutions for this launch system. First, a trajectory solution is calculated in which the scramjet accelerator flies at constant dynamic pressure of 50kPa. This trajectory is calculated to serve as a baseline for comparisons, as previous studies have assumed that flying the scramjet accelerator at its maximum allowable dynamic pressure would produce the best overall system performance[12]. Next, an optimal payload-to-orbit trajectory is developed, and the trajectory shape compared and contrasted to the constant dynamic pressure trajectory. Lastly, a sensitivity study is performed, by varying key performance parameters of the launch system and investigating the effects of each parameter on the performance of the launch system.

XXX I should maybe change these first two to be clearer - they are both optimised for payload to orbit, but 1 is constrained and 1 isn't. Perhaps I should make a remark beforehand than ALL of these are optimised for payload to orbit, im just changinf constraints / parameters. I should make a special note that the unconstrained case is referref to as the 'maximum payload-to-orbit trajectory'
The following trajectories are developed:

- Case 1: 50kPa fixed dynamic pressure scramjet accelerator trajectory.
→ This trajectory provides a baseline trajectory for comparison purposes.
- Case 2: Trajectory optimised for payload-to-orbit, $q_{max} = 50\text{kPa}$.
→ This trajectory demonstrates improved performance through trajectory optimisation.

- Case 3: Variation of maximum allowable dynamic pressure between $q_{max} = 45\text{kPa}$ & $q_{max} = 55\text{kPa}$.
→ Comparison of optimised trajectories allows the influence of the scramjet accelerator's ability to withstand aerodynamic forces on the launch system performance to be investigated.
- Case 4: Variation of the coefficient of drag of the scramjet accelerator between $C_d = 90\%$ & $C_d = 110\%$.
→ Comparison of optimised trajectories allows the effects of the scramjet accelerator's aerodynamic design on the launch system performance to be investigated.
- Case 5: Variation of the specific impulse of the scramjet accelerator's C-REST engines between $I_{SP} = 90\%$ & $I_{SP} = 110\%$.
→ Comparison of optimised trajectories allows the effects of the efficiency of the C-REST engines on the launch system performance to be investigated.
- Case 6: Variation of the mass of the scramjet accelerator between $m_2 = 90\%$ & $m_2 = 110\%$.
→ Comparison of optimised trajectories allows the effects of the internal design of the scramjet accelerator on the launch system performance to be investigated.
- Case 7: Variation of the fuel mass of the scramjet accelerator between $m_{fuel} = 90\%$ & $m_{fuel} = 110\%$.
→ Comparison of optimised trajectories allows the effects of the amount of fuel which the scramjet accelerator is able to carry on the launch system performance to be investigated.
- Case 8: Variation of the mass of the third stage rocket between $m_3 = 90\%$ & $m_3 = 110\%$.
→ Comparison of optimised trajectories allows the effects of the third stage internal design on the launch system performance to be investigated.
- Case 9: Variation of the specific impulse of the third stage rocket between $I_{SP,3} = 90\%$ & $I_{SP,3} = 110\%$.
→ Comparison of optimised trajectories allows the effects of the efficiency of the third stage engine on the launch system performance to be investigated.
- Case 10: Variation of the coefficient of drag of the third stage rocket between $C_d = 90\%$ & $C_d = 110\%$.
→ Comparison of optimised trajectories allows the effects of the aerodynamic design of the third stage on the launch system performance to be investigated.

These optimised trajectory cases allow the benefits of flying an optimised trajectory to be quantified, and allow the impact of key design parameters on the performance of the launch system to be characterised.

These optimised trajectories are presented in the following sections, along with key performance indicators and their sensitivities. These are presented to a number of significant figures judged necessary to adequately present the trajectory results and sensitivities to the accuracy of the trajectory simulation, with the caveat that the launch system modelling carries with it significant uncertainties as described in Appendix B.

6.1 Case 1: Constant Dynamic Pressure Trajectory

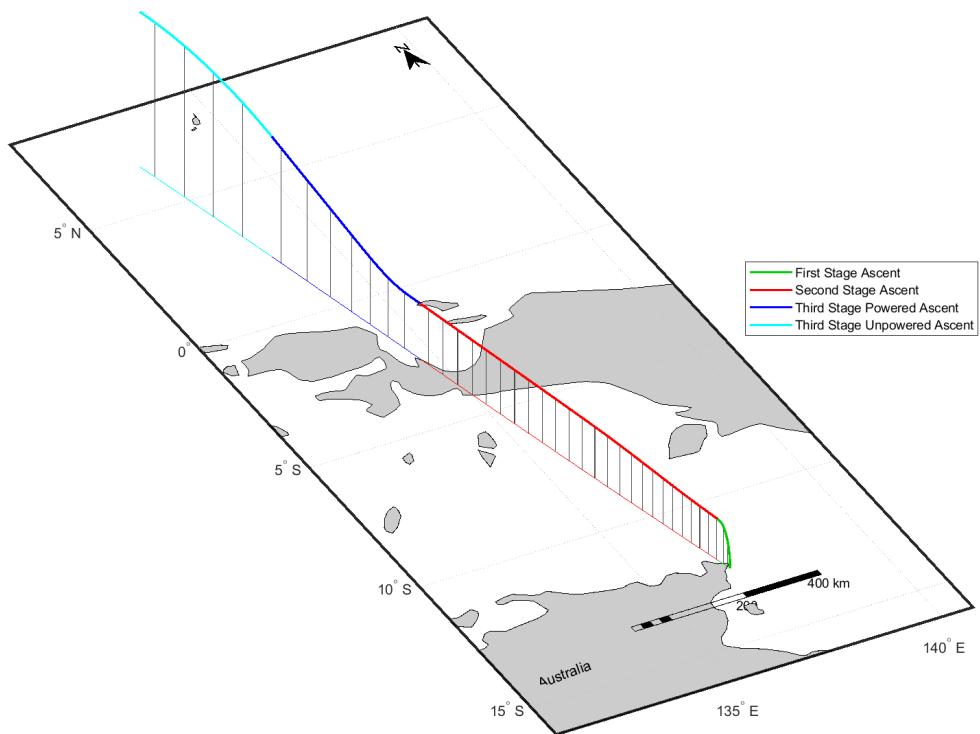


Figure 6.1: Maximum payload-to-orbit trajectory path with the scramjet accelerator flying at constant dynamic pressure (Case 1). Initial heading angle 91.4° .

The first trajectory that is produced using LODESTAR is a maximum payload-to-orbit trajectory in which the scramjet accelerator flies a constant dynamic pressure path, at its maximum allowable dynamic pressure of 50kPa. In order to drive the scramjet accelerator towards a constant dynamic

pressure path, the cost function detailed in Table 5.3 is utilised. In addition to the dynamic pressure cost function, the maximum payload-to-orbit cost function is also active on the third stage phase, so that once the scramjet accelerator flies close to 50kPa, the third stage will fly a maximum payload-to-orbit trajectory from the termination of the scramjet accelerator's constant dynamic pressure path. Previous studies have assumed that flying the scramjet accelerator at constant dynamic pressure will produce the best possible system performance[12]. Because of this assumption, a constant dynamic pressure trajectory is produced to serve as a baseline for comparison with the maximum payload-to-orbit optimised trajectory. Producing a constant dynamic pressure trajectory also serves to verify that LODESTAR is able to calculate a trajectory in which the scramjet accelerator flies at a fixed dynamic pressure for the duration of its flight. In addition, the designs and aerodynamic simulations of each vehicle of the launch system have been improved in this work, compared to previous studies[12]. In this work, the internal design of the scramjet accelerator has been modified (as described in Section 4.1), the third stage design has been modified significantly (as described in Section 4.3), the first stage is included (as described in Section 4.2), and Cart3D[135] is used for aerodynamic calculations (as detailed in Section 4.1.4). Simulating a constant dynamic pressure verifies that the first stage is able to reach the maximum dynamic pressure of the scramjet accelerator, and that the scramjet accelerator is able to fly at its maximum dynamic pressure within its control and aerodynamic limits. This verification ensures that any deviations from the scramjet accelerator's maximum dynamic pressure in subsequent optimised trajectories serve to improve the performance of the system, rather than being a result of the problem setup or design constraints.

Trajectory Condition	Value
Payload to Orbit (kg)	98.3
Total η_{exergy} (%)	1.155
1st Stage η_{exergy} (%)	6.252
Separation Alt, 1→2 (km)	23.84
Separation v, 1→2 (m/s)	1451
Separation γ, 1→2 (deg)	0.7
2nd Stage η_{exergy} (%)	5.120
Separation Alt, 2→3 (km)	32.16
Separation v, 2→3 (m/s)	2785
Separation γ, 2→3 (deg)	0.2
2nd Stage Distance Flown (km)	1084.9
3rd Stage η_{exergy} (%)	9.514
3rd Stage $t, q > 5\text{kpa}$ (s)	112.3
3rd Stage Fuel Mass (kg)	2886.9

Table 6.1: Summary of the key results from a maximum payload-to-orbit trajectory with the scramjet accelerator constrained to 50kPa (Case 1).

LODESTAR successfully computes the trajectory of the rocket-scramjet-rocket system, with the

6.1. CASE 1: CONSTANT DYNAMIC PRESSURE TRAJECTORY

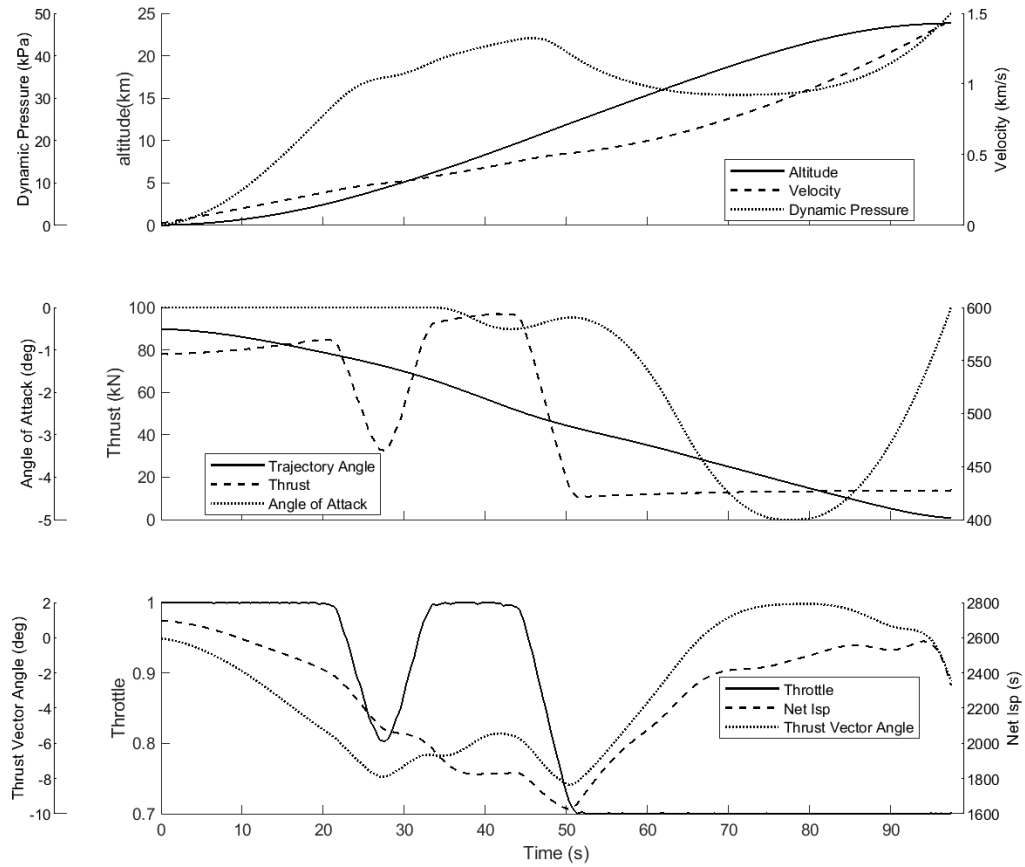


Figure 6.2: The first stage trajectory of the launch system, with the scramjet accelerator constrained to flight at constant dynamic pressure (Case 1).

scramjet accelerator flying at constant dynamic pressure, achieving a payload-to-orbit of 98.3kg. Figure 6.1 shows the optimised trajectory path, Figures 6.2-6.4 show details of the optimised trajectory for each stage, and Table 6.1 provides a summary of the key parameters of the trajectory, including the exergy efficiency of each stage. The rocket-scramjet-rocket system launches vertically, flying a fixed vertical trajectory for 3.9s, after which a pitchover is initiated. Under power of the first stage rocket, the launch system begins pitching, flying north-west, over the Arafura Sea. After pitchover the angle of attack stays constant at 0° for 99.9s, as shown in Figure 6.2. At this point, the angle of attack is reduced, reaching a minimum of -5.0° , before increasing back up to 0° for stage separation. **The first stage is throttled down temporarily at 20.3s flight time, to a minimum of 80.5%.** At 41.9s, the throttle is reduced to its minimum of 70%, and maintained at this for the remainder of flight to assist in pitching. The scramjet accelerator is separated at a trajectory angle of 0.7° at an altitude of 23.84km, at a flight time of 97.4s, with a total ground distance of 37.2km covered under power of the first stage rocket. The first stage rocket achieves an exergy efficiency of $6.252\%\eta$ when separating

the scramjet accelerator onto a constant dynamic pressure trajectory.

The constant dynamic pressure trajectory for the scramjet accelerator stage is shown in Figure 6.3, with key results summarised in Table 6.1. After the separation of the first stage rocket, the scramjet accelerator flies north west over the Arafura Sea, and crosses West Papua before releasing the third stage rocket. Due to the clear objective of a constant dynamic pressure trajectory, any deviations from the target dynamic pressure are readily apparent, allowing the efficacy of the optimiser to be verified. The constant dynamic pressure trajectory shows very close adherence to 50kPa dynamic pressure throughout the trajectory (maximum 0.2% deviation), indicating that scramjet accelerator flight at a constant dynamic pressure is able to be achieved. Over the trajectory, the Mach number increases from **4.88**, the speed increases from 1451m/s to 2785m/s, and the flap deflection increases from **-6.14°** to **a maximum of 3.93° during pull-up**. The angles of attack of the scramjet accelerator are low across the trajectory, generally between **0.6-1.0°**, indicating that the lift of the scramjet accelerator is high for this mission profile. At the beginning of the trajectory the equivalence ratio increases, as the capture limitations are relaxed with increasing Mach number. This causes the net specific impulse ($I_{sp_{net}} = \frac{T-D}{\dot{m}_f g}$) to increase, to a maximum of **1448s**, during the first **180.4s** flight time. After this initial increase, the net specific impulse decreases over the trajectory, as the efficiency of the scramjet engines decreases. Third stage release occurs at **591.4s flight time**, at 32.16km altitude. Immediately before third stage separation, there is a slight increase in the angle of attack and flap deflection of the scramjet accelerator. This is done to increase the trajectory angle and improve the payload-to-orbit slightly, but does not have a significant effect on the performance of the launch system.

Figure 6.4 shows the corresponding third stage atmospheric exit trajectory after release, evaluated as described in Chapter 5. The **flight path of the** third stage released from a constant dynamic pressure trajectory, shown in Figure 6.4, stays close to horizontal for the first **12s** of flight, and then pitches up slowly. This slow ascent leads to the rocket spending a large amount of time at low altitude, in a high drag environment, spending 112.3s at over 5kPa dynamic pressure. The angle of attack increases gradually to a maximum of **10°** at **27.8s** and is then maintained at the maximum **10°** until **111.7s**, when the angle of attack is reduced slightly, increased to the maximum briefly, and finally reduced to **0°** for burnout at **146.2s**. The dynamic pressure of the third stage rocket reduces to 10kPa at **188.2s**, at which point the heat shield is discarded. The rocket coasts to a trajectory angle of **0°**, which is reached at a total flight time of **827.6s**. The trajectory terminates at 90km, the lowest allowable altitude for circularisation. When this altitude is reached, the trajectory is circularised and a Hohmann transfer manoeuvre is performed to reach sun synchronous orbit.

6.2 Case 2: Optimised Ascent Trajectory

This section presents the maximum payload-to-orbit trajectory for the rocket-scramjet-rocket launch system, with the scramjet accelerator able to deviate from its maximum dynamic pressure. The op-

6.2. CASE 2: OPTIMISED ASCENT TRAJECTORY

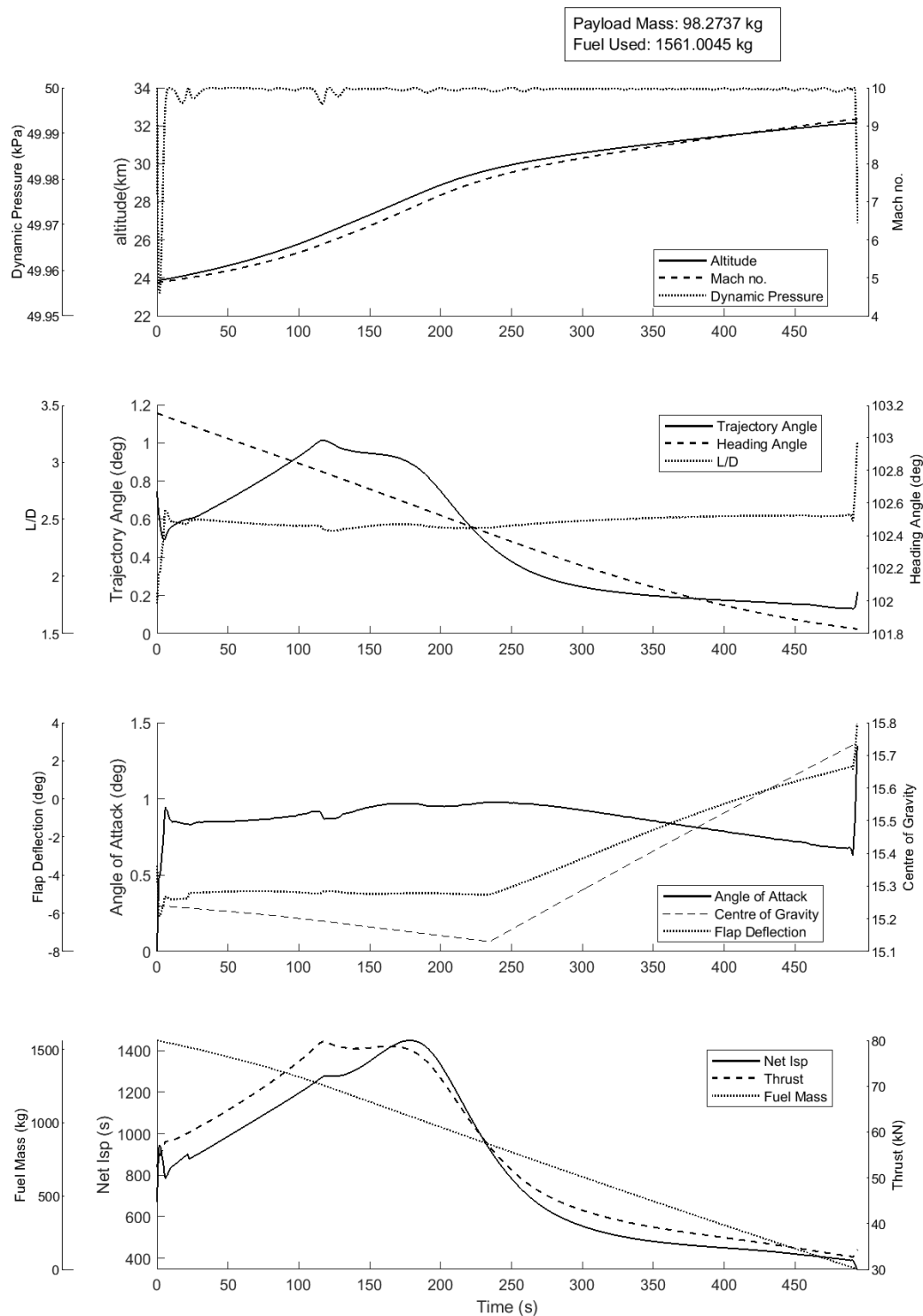


Figure 6.3: The constant dynamic pressure flight path of the scramjet accelerator (Case 1).

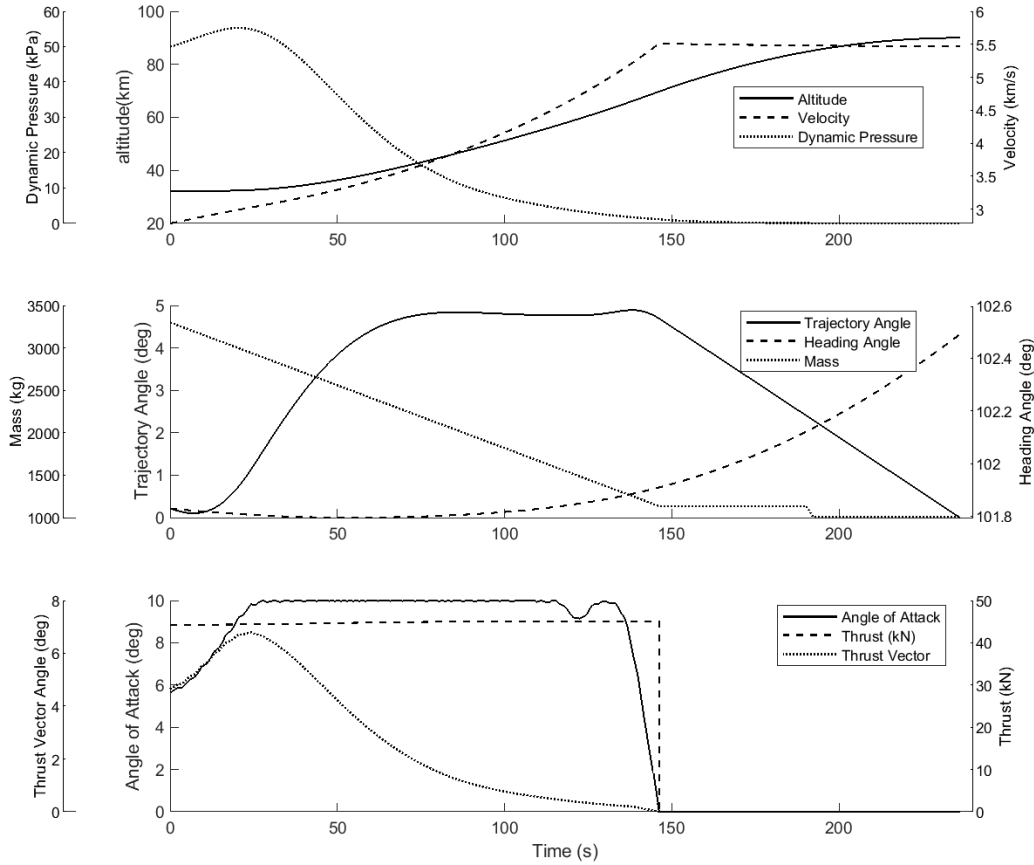


Figure 6.4: The third stage trajectory of the launch system, with the scramjet accelerator constrained to flight at constant dynamic pressure (Case 1).

timal trajectory shape for a 50kPa dynamic pressure limited trajectory is shown in Figure 6.5, with detailed trajectory information for each stage shown in Figures 6.6 - 6.10, and key results summarised in Table 6.2. The maximum payload-to-orbit trajectory shape involves the scramjet accelerator deviating from maximum dynamic pressure at multiple points. These manoeuvres serve either to increase the net specific impulse of the scramjet accelerator, or to trade-off the efficiency of the scramjet accelerator in order to increase the efficiency of the first and third stages. This payload-to-orbit optimised trajectory is able to deliver 156.4kg of payload to heliocentric orbit, an increase of **59.1%** over the constant, 50kPa dynamic pressure result (Case 1).

The first stage, shown in Figure 6.6, **flies a different** trajectory to that of the Case 1, in which the first stage releases the scramjet accelerator onto a constant dynamic pressure trajectory. The trajectory angle at the separation of the scramjet accelerator is 12.3° , rather than the trajectory angle of 0.2° required for the scramjet accelerator to fly a constant dynamic pressure trajectory. Additionally, the altitude at first-second stage separation is raised to 24.52km, an increase of **0.68km** compared to Case

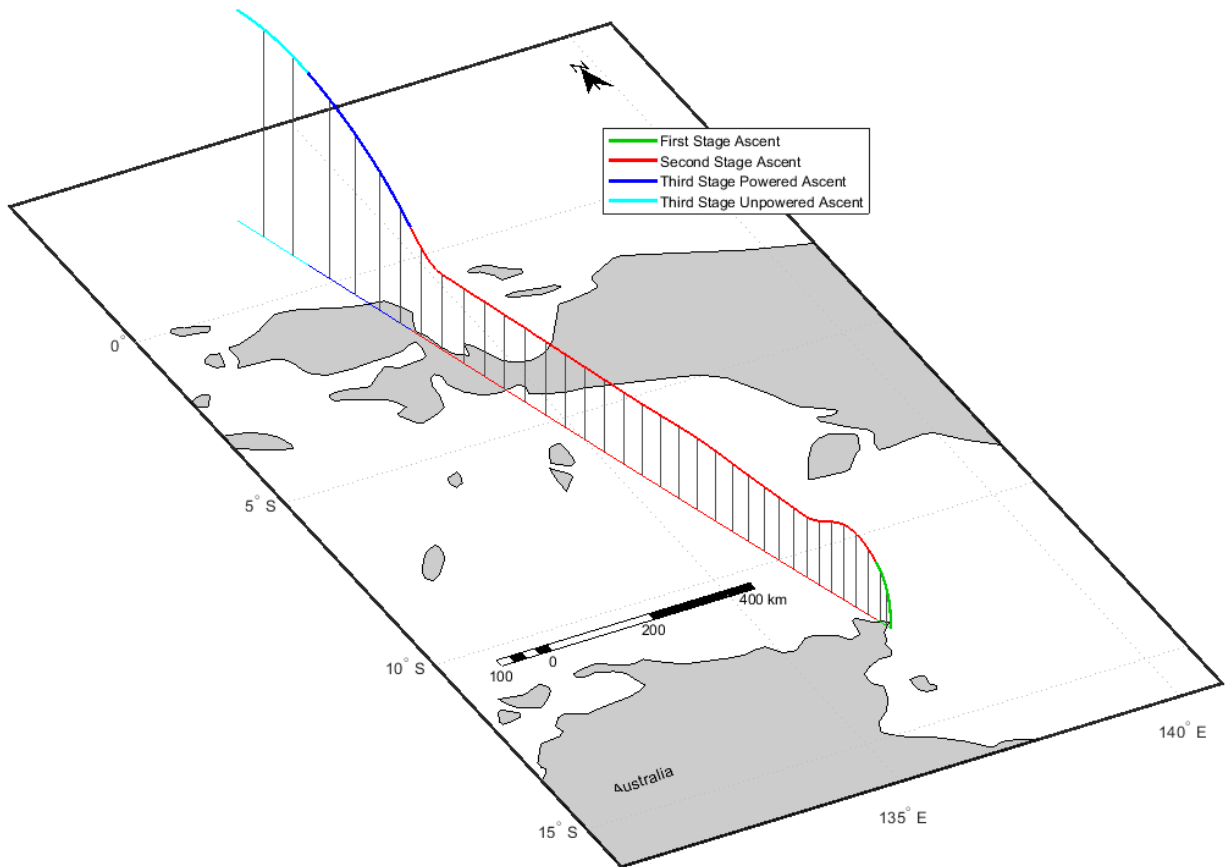


Figure 6.5: The optimised maximum payload-to-orbit trajectory of the launch system (Case 2).

1. This higher release angle and altitude causes the altitude of the scramjet accelerator to initially increase, and consequently for its dynamic pressure to decrease. This increased trajectory angle at separation is the consequence of a trade-off between the efficiency of the scramjet accelerator and the efficiency of the first stage. In particular, while the first stage is still throttled down twice, at 19.7s and 62.7s, it is throttled down for much less total time than the first stage separating onto a constant dynamic pressure trajectory. The exergy efficiency of the first stage is increased to $6.875\%\eta$ due to the increased acceleration that this reduced throttling affords, an overall improvement of $+0.623\%\eta$ ($+9.96\%$) compared to Case 1. During the Case 2, the first stage rocket releases the scramjet accelerator at a speed of 1533m/s, an increase of 5.7% compared to Case 1.

After the initial deviation from the maximum dynamic pressure, the scramjet accelerator returns to 50kPa dynamic pressure for a time. At 184.9 seconds flight time, the altitude of the trajectory is again raised, and the dynamic pressure decreased, to a minimum of 43.0kPa. In this region ($M_0 \approx 7.5$) the net specific impulse of the scramjet accelerator is relatively homogeneous with respect to changes in dynamic pressure, as can be observed in the specific impulse of the C-REST engines in Figure

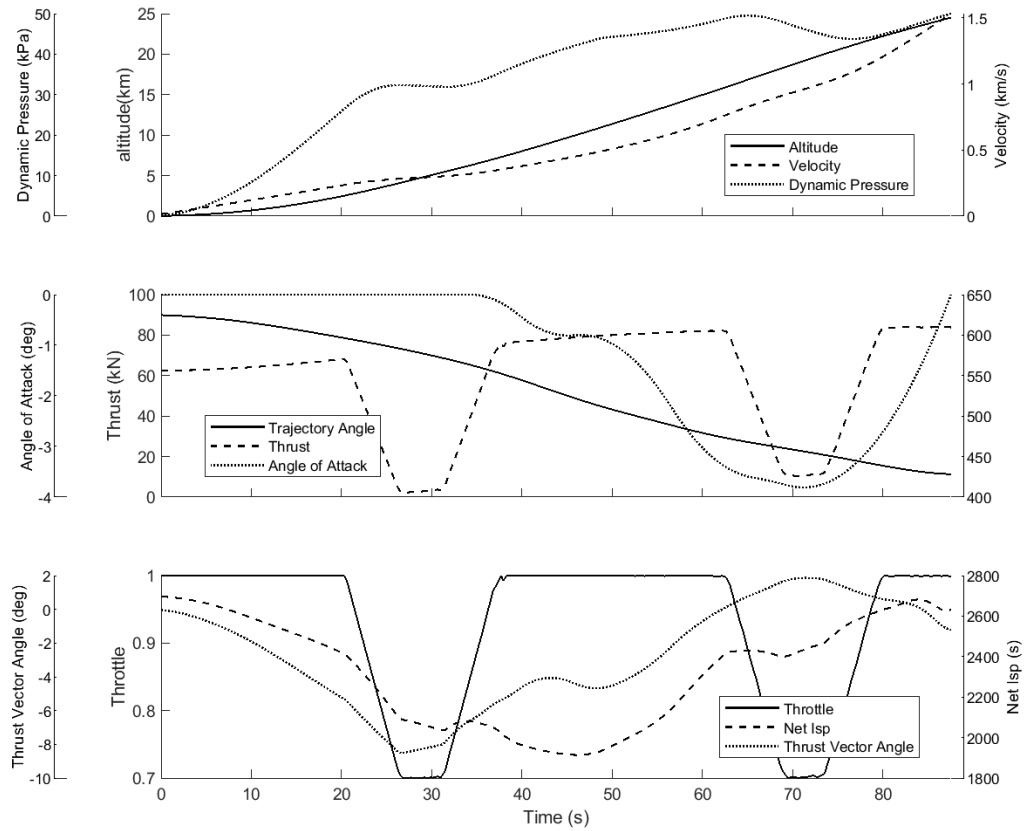


Figure 6.6: The optimised maximum payload-to-orbit trajectory of the launch system under power of the first stage rocket (Case 2).

6.9. The homogeneity between flight conditions means that the variation in engine performance with flight conditions is small and that flying at the maximum dynamic pressure in this region does not maximise the specific impulse from the C-REST engines compared to the drag reductions that can be attained through flight at lower dynamic pressure. Figure 6.8 compared Case 1 and Case 2, and shows that while the optimised trajectory differs significantly from a constant dynamic pressure trajectory, both achieve similar net specific impulses during the acceleration phase of flight, with the exception of the initial trajectory conditions at Mach 5, where the efficiency of the scramjet accelerator is traded for first stage rocket performance. Appendix E.2 details a complementary maximum payload-to-orbit trajectory in which the scramjet accelerator is constrained to 50kPa between Mach 6-8, to prevent the altitude raising manoeuvre from taking place. This constrained trajectory allows for the magnitude of the performance gain from the altitude raising manoeuvre to be quantified. Overall, the altitude raising manoeuvre results in a slight increase in net specific impulse, compared to the trajectory constrained to maximum q , increasing the overall efficiency of the launch system from $1.680\%\eta$ to $1.685\%\eta$. This is a relatively minor variation, and the payload-to-orbit benefits of this altitude

Trajectory Condition	Value
Payload to Orbit (kg)	156.4
Total η_{exergy} (%)	1.685
1st Stage η_{exergy} (%)	6.875
Separation Alt, 1→2 (km)	24.52
Separation v, 1→2 (m/s)	1533
Separation γ, 1→2 (deg)	11.3
2nd Stage η_{exergy} (%)	4.401
Separation Alt, 2→3 (km)	43.81
Separation v, 2→3 (m/s)	2640
Separation γ, 2→3 (deg)	12.3
2nd Stage Distance Flown (km)	1195.6
3rd Stage η_{exergy} (%)	15.53
3rd Stage $t, q > 5\text{kpa}$ (s)	6.8
3rd Stage Fuel Mass (kg)	2828.8

Table 6.2: A summary of key results from the maximum payload-to-orbit trajectory (Case 2).

raising manoeuvre are correspondingly small; Case 2 exhibits a payload-to-orbit increase of 0.5kg compared to Case 1 between Mach 6-8, a difference of only 0.3%. However, it is important to note that, while its benefits are small, the altitude raising manoeuvre is consistently observed in all maximum payload-to-orbit optimised trajectories in which dynamic pressure is unconstrained, and this manoeuvre is similar to the manoeuvres observed by Fujikawa et al.[24] in their study of the Jaxa TSTO Spaceplane, though to a much lesser extent. Also, despite its small benefit to payload-to-orbit, this altitude raising manoeuvre has the added benefit of reducing the heating and structural loading on the scramjet accelerator.

At 319.4s, the scramjet accelerator returns to flight at close to 50kPa dynamic pressure until 511.1s. During this time, a series of four small manoeuvres are performed, increasing the angle of attack of the scramjet accelerator briefly, and then reducing it in succession. These manoeuvres allow for longer periods of flight at lower angles of attack, where the net specific impulse of the scramjet accelerator is improved.

At 511.1s a pull-up manoeuvre is performed, gaining altitude until the third stage rocket is released at 543.7s of scramjet accelerator flight time. The point at which the pull-up manoeuvre begins is the location that takes into account the best combination of speed, altitude and release angle for the trade-off between the scramjet stage performance and the release of the third stage rocket. This pull-up indicates the region at which increasing altitude and release angle becomes more important than extracting maximum thrust from the scramjet (which is generally attained at high q and low flight angle at an equivalence ratio of 1). At high Mach numbers, flight in a lower dynamic pressure environment results in less thrust output from the scramjet engines, as well as an increase in angle of attack and flap deflection angle to compensate for the additional lift required. Due to this, less overall

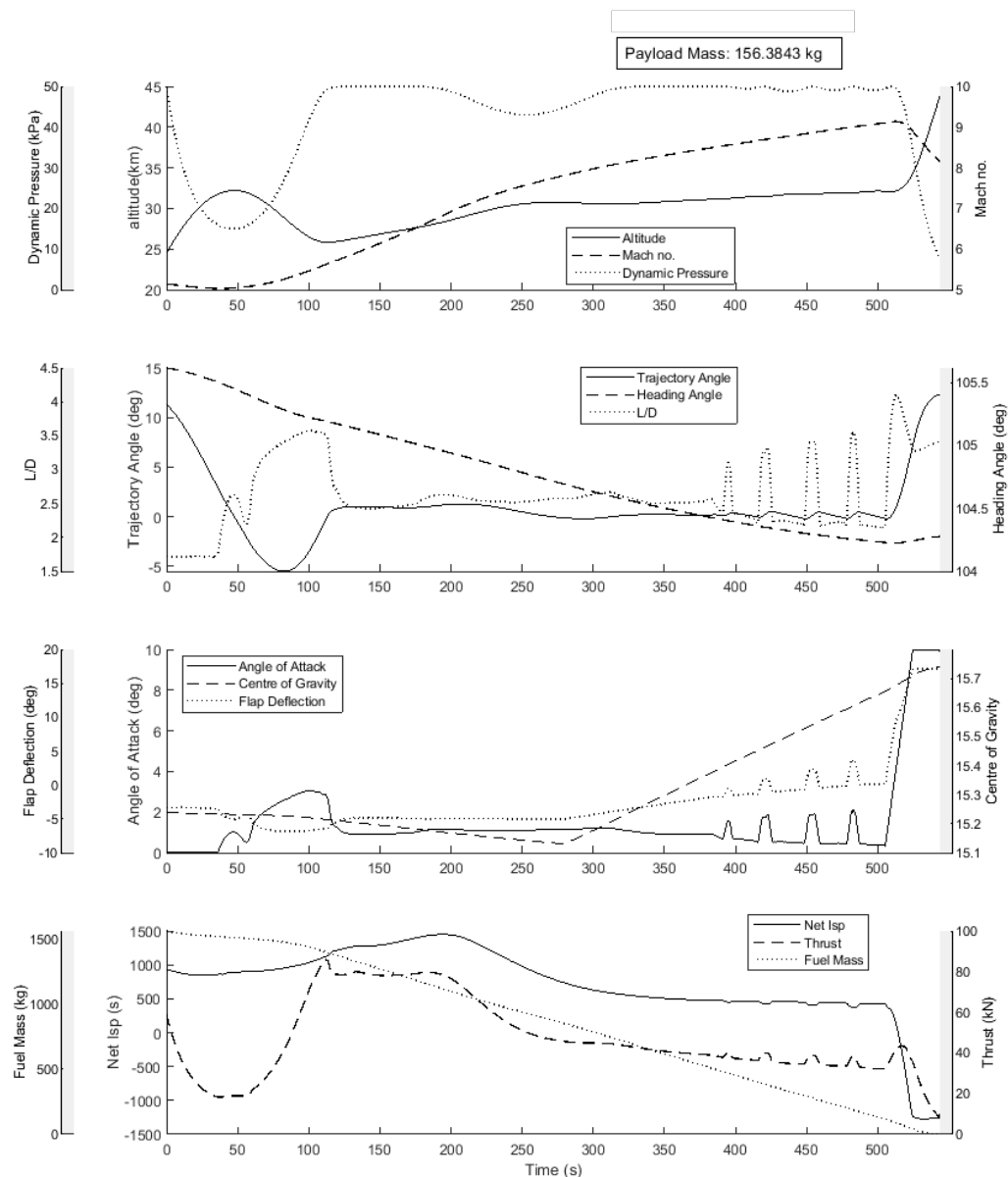


Figure 6.7: The optimised maximum payload-to-orbit trajectory of the scramjet accelerator (Case 2).
 XXX Change no of DP in all traj figures

acceleration is obtained compared to the fixed dynamic pressure result. Separation occurs at a speed of 2640m/s, a decrease of 145.0m/s (-5.2%). However, at the same time separation altitude increases by 11.65km (+36.2%) to 43.81km, resulting in a decrease in separation dynamic pressure to 7.8kPa. The scramjet stage pull-up assists the rocket in manoeuvring to exoatmospheric altitude by increasing the altitude and angle at separation, utilising the superior aerodynamics and manoeuvrability of the scramjet accelerator. The increase in release angle, to the optimal angle of 12.3°, significantly reduces

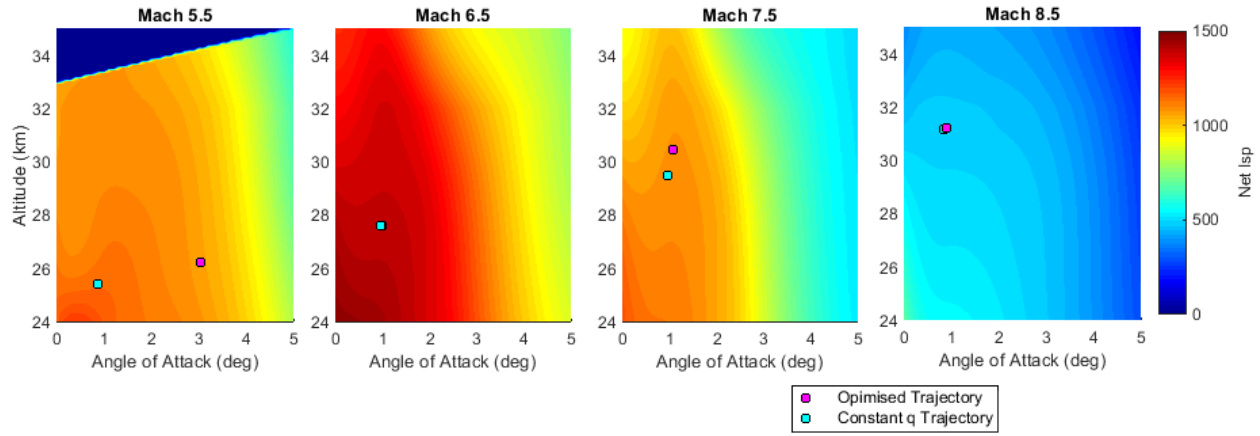


Figure 6.8: Net Isp contours for the scramjet accelerator at Mach numbers from 5-9, showing flight conditions for an optimised trajectory with no constraints (Case 2) and a constant dynamic pressure trajectory (Case 1).

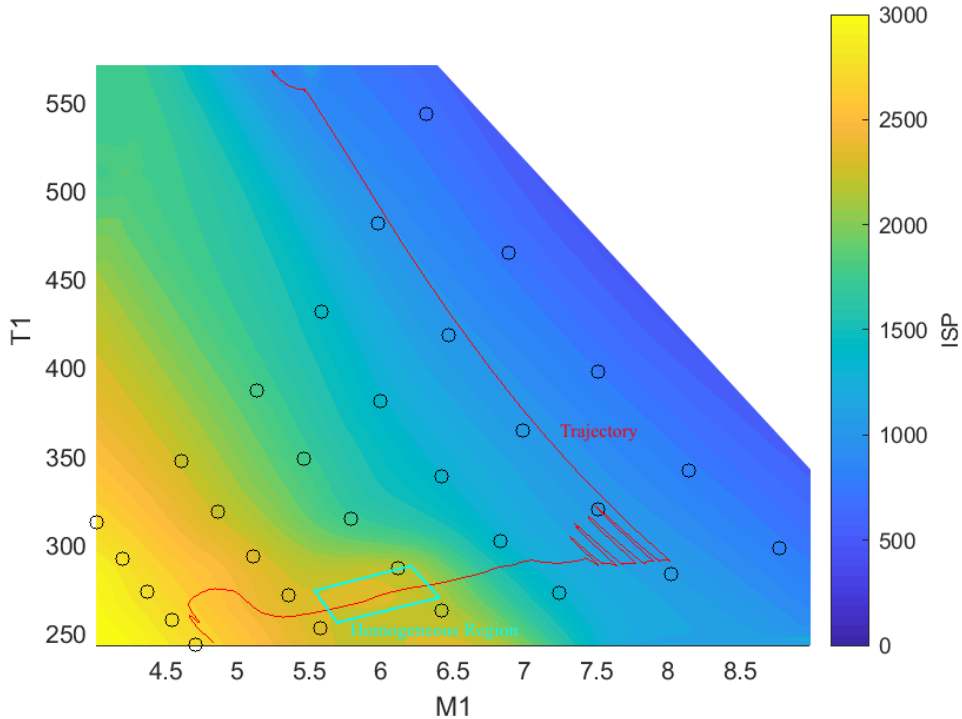


Figure 6.9: The specific impulse of the C-REST engines, plotted for inlet temperature (T_1) and inlet Mach number (M_1). Data points are shown in black.

the turning that is required by the rocket as evident from comparing Fig 6.4 and 6.10. Overall, the altitude raising manoeuvres that the scramjet accelerator performs result in a decrease in the exergy efficiency of the scramjet accelerator to $4.401\%\eta$, a total decrease of $-0.719\%\eta$ (-14.04%) compared

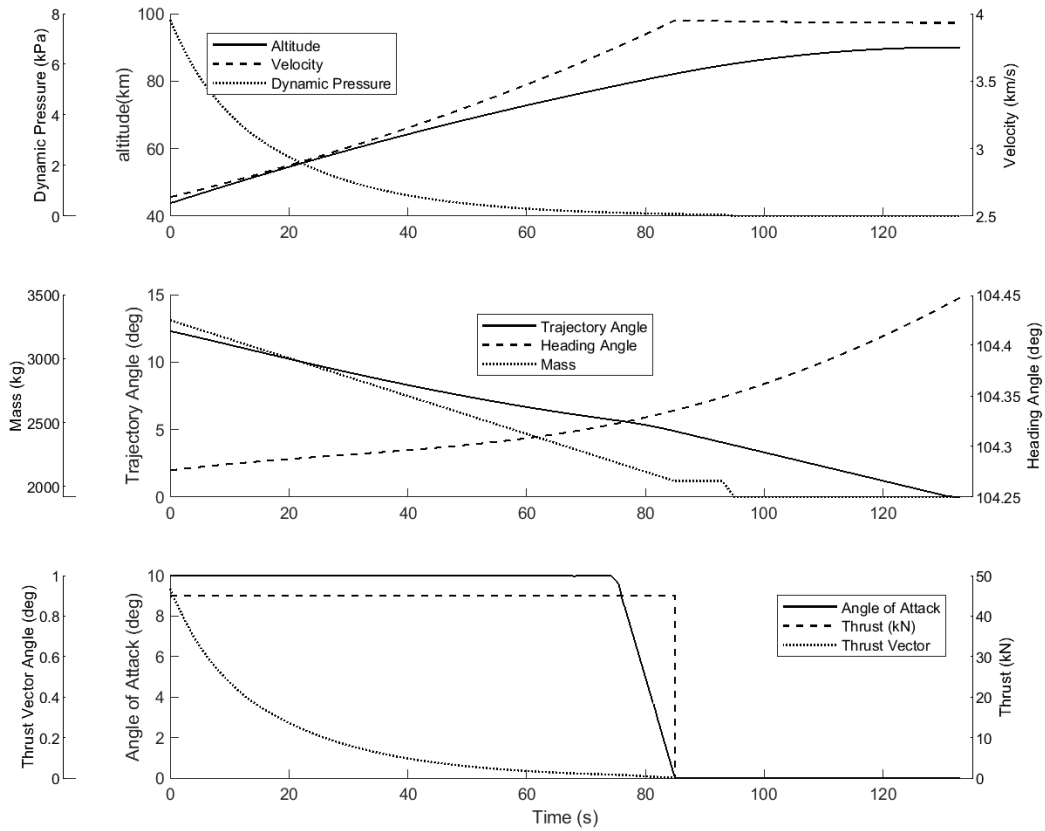


Figure 6.10: The third stage trajectory of the launch system flying the maximum payload-to-orbit trajectory (Case 2).

to Case 1; the scramjet accelerator flying at a constant dynamic pressure. However, Case 2 drastically increases the exergy efficiency of the third stage, to $15.53\%\eta$, an overall increase of **+6.013% η** (**+63.20%**) compared Case 1. Along with the increased efficiency of the first stage, this exergy trade-off leads to the total exergy efficiency of the launch system increasing, from $1.155\%\eta$ to $1.685\%\eta$.

This pull-up, lowering the dynamic pressure from maximum under airbreathing power, is somewhat similar to the pull-ups that were observed in some of the previous studies of multi-stage airbreathing launch systems in Section 3.1.2, namely the LaRC Turboramjet[23], the JAXA TSTO Spaceplane[24], and the XCALIBUR[30]. All of these pull-ups were either performed specifically to lower dynamic pressure for the orbiter stage[23, 30], or to improve the operation of the airbreathing engines[24]. In contrast, the pull-up in this study directly improves the efficiency of the launch system, without improving the performance of the scramjet engines, by trading-off efficiency between the airbreathing and rocket stages. This indicates the aerodynamics of the scramjet-powered stage may be utilised to achieve separation conditions that can directly improve the payload-to-orbit performance of the launch system.

The trajectory of the third stage rocket after release from an optimised scramjet trajectory is shown in Figure 6.10. Release at a higher, more optimal angle, reduces the aerodynamic moment necessary to trim the vehicle. In turn, this reduced moment reduces the necessary thrust vector angle significantly. The third stage rocket is released at a high trajectory angle, and continuously gains altitude, avoiding the close-to-horizontal flight required by Case 1, where it is released at a fixed 50kPa dynamic pressure. Due to the higher altitude and release angle, the third stage rocket is released at a lower dynamic pressure, 7.8kPa compared to 50.0kPa, and spends much less time flying in a high dynamic pressure environment, 7.7s at over 5kPa dynamic pressure rather than 112.3s. The reduced time that the rocket must spend in a high dynamic pressure environment, and the decrease in the maximum dynamic pressure that the rocket stage experiences, may allow the structural mass and heat shielding necessary to achieve exoatmospheric flight to be decreased, and may enable higher payload to orbit. This possible improvement in payload-to-orbit is explored further in Appendix A.4.4. In addition to improved payload-to-orbit, releasing the rocket at lower dynamic pressure reduces the thrust vector angle significantly, to below 1° , compared to the angles of close to 7° required for Case 1, where the third stage is ascending after release at 50kPa dynamic pressure. These reduced thrust vector angles would likely improve the controllability of the third stage rocket considerably, although detailed investigation of the controllability of the third stage rocket is beyond the scope of this study.

6.3 Case 2: Modelling of Uncertainties

The aerodynamic and propulsive properties of the launch system that have been presented in this section are modelled using medium and low fidelity methods essential to allow full system trajectory optimisation to be carried out efficiently. These methods bring with them an associated uncertainty in the values that are calculated for the aerodynamic and propulsive performance of a vehicle, including those presented in Sections 4.1.3-4.1.6, 4.2.1, and 4.3.4-4.3.5. These uncertainties are estimated in Appendix B.1 from previous studies that have compared the medium-to-low fidelity tools used to analyse propulsion and aerodynamics with high fidelity tools and experimental results. Previous error magnitudes are used to estimate the error magnitudes in the current study, with the maximum applicable error magnitude being used. The final values obtained from this study are replicated in Table 6.3. The presence of these uncertainties may mean that the performance of the vehicle is significantly different to expected, producing significantly different payloads-to-orbit to those calculated.

A Monte-Carlo study is conducted in using these uncertainty bounds, with further details available in Appendix B.1.3. For this, the parameters in 6.3 are independently varied according to a Latin Hypercube analysis method to create a series of distinct cases, with each parameter in each regime multiplied by a constant within the uncertainty range, and maximum payload-to-orbit trajectories developed for each perturbed case. Analysis using the percentile method yields a 97.5% confidence

Uncertainty	Subsonic	Transonic	Supersonic/Hypersonic
1 st & 3 rd Stage I_{SP}	1.3%	1.3%	1.3%
Scramjet I_{SP}	-	-	25%
C_L	17%	28.7%	12%
C_D	33%	21%	11%
C_M	23%	67.1%	22.0%

Table 6.3: The uncertainty margins associated with the aerodynamic and propulsive modelling (copy of Table B.1, see Appendix 6.3 for details).

interval for Case 2 of 8.8–238.8kg in payload-to-orbit due to aerodynamic and propulsion modelling uncertainties (probability densities are shown in Figure B.1), illustrating the large uncertainties still present in the modelling of airbreathing launch systems that are to be expected when using low-to-medium fidelity tools, as is the norm in the conceptual design phases, particularly given the general sensitivity of the payload mass in launch systems to variations in the launch system performance. However, this interval also indicates that producing a positive payload-to-orbit is likely to be possible under the current modelling scheme, although it is evident that more detailed analysis of this system is necessary before an accurate payload-to-orbit value is able to be attained. This said, the payload-to-orbit values calculated in this study are only intended as an indication of the performance possible using this launch system. The primary usefulness of these trajectories is in the studies of the optimal trajectory shape and performance trade-offs, which hold under the presence of uncertainty.

6.4 Energy Usage Analysis

An energy usage analysis is conducted on the maximum payload-to-orbit launch trajectories, both with, and without the scramjet accelerator constrained to constant dynamic pressure flight (Cases 1 & 2). This is performed in order to understand the primary sources of energy loss for each stage, and to compare the trajectories optimised with, and without the scramjet accelerator constrained to constant dynamic pressure. An energy usage breakdown of each of each stage is compared in Table 6.4. The energy usage breakdown compares: the energy used to accelerate the payload, $\Delta KE_{payload} + \Delta PE_{payload}$; the energy imparted to the successive stages, $\Delta KE_{nextstage} + \Delta PE_{nextstage}$; the energy used overcoming drag, $\int_{t_0}^{t_f} v D dt$; the energy used imparting energy to the structural mass of each stage, which is separated, $\Delta KE_{discarded} + \Delta PE_{discarded}$; and the availability losses (irreversibilities) which primarily comprise of: 1. The internal cycle and mechanical losses of the vehicle, and 2. The losses in the wake of the vehicle, largely made up of losses due to the energy imparted on to the vehicle exhaust[192, 193]. These availability losses make up a significant part of the losses in all stages, dominating in the first stage and scramjet accelerator, and lessening in the third stage rocket, as expected for multi-stage launch systems[191–193].

The efficiency of the first stage rocket increases when the first-second stage separation altitude and

	Case 1	Case 2
Trajectory	50kpa Constant q	No q Constraint
First Stage Fuel Exergy	201.91 GJ	201.91 GJ
KE + PE of Payload	0.06% (0.13 GJ)	0.11% (0.22 GJ)
KE + PE of 2 nd & 3 rd Stage	6.19% (12.50 GJ)	6.76% (13.66 GJ)
Overcoming Drag	2.76% (5.57 GJ)	2.49% (5.03 GJ)
KE + PE of 1 st Stage Structural Mass	0.92% (1.86 GJ)	1.01% (2.04 GJ)
KE + PE of 1 st Stage Fuel Mass	2.48% (5.00 GJ)	2.67% (5.39 GJ)
Availability Losses	87.58% (176.83 GJ)	86.95% (175.56 GJ)
Scramjet Accelerator Fuel Exergy	187.38 GJ	187.38 GJ
KE + PE of Payload	0.15% (0.28 GJ)	0.21% (0.39 GJ)
KE + PE of 3 rd Stage	4.97% (9.31 GJ)	4.19% (7.85 GJ)
Overcoming Drag	18.68% (35.00 GJ)	20.42% (38.08 GJ)
KE + PE of scramjet accelerator Structural Mass	7.69% (14.41 GJ)	6.61% (12.39 GJ)
KE + PE of scramjet accelerator Fuel Mass	1.33% (2.49 GJ)	1.33% (2.49 GJ)
Availability Losses	67.18% (125.88 GJ)	67.25% (126.01 GJ)
Third Stage		
In-Atmosphere Fuel Exergy	27.78 GJ	16.78 GJ
KE + PE of Payload	4.13% (1.15 GJ)	4.37% (0.73 GJ)
Overcoming Drag	10.75% (2.99 GJ)	0.68% (0.11 GJ)
KE + PE of 3 rd Stage Structural Mass	12.58% (3.49 GJ)	7.96% (1.34 GJ)
KE + PE of 3 rd Stage Fuel Mass	54.63% (15.18 GJ)	55.29% (9.28 GJ)
KE + PE of Heat Shield	10.67% (2.96 GJ)	7.28% (1.22 GJ)
Availability Losses	7.25% (2.01 GJ)	24.42% (4.10 GJ)
Circularisation and Hohman Transfer Fuel Exergy	8.76 GJ	19.06 GJ
KE + PE of Payload	24.94% (2.18 GJ)	24.12% (4.60 GJ)
All Other Energy Losses	75.06% (6.58 GJ)	75.88% (14.46 GJ)

Table 6.4: An energy usage breakdown of the ascent trajectories, both with, and without, the scramjet accelerator constrained to constant dynamic pressure (Cases 1 & 2). The energy expenditures of each phase are shown, with blue indicating a 'productive' energy usage, whereas red indicates energy 'wastage'.

trajectory angle are raised, in the trajectory with no dynamic pressure constraint. This is due to the unconstrained rocket in Case 2 being able to fly higher, reducing drag losses, and increasing its speed (and thus kinetic energy). This additional speed also decreases the availability losses of the first stage rocket due to a decrease in the residual kinetic energy of the exhaust gases, with an associated increase in propulsion efficiency, illustrated by the equation for the propulsive efficiency of a rocket[167]:

$$\eta_P = \frac{2v_0/v_g}{1 + (v_0/v_g)^2}, \quad (6.1)$$

where v_g is the exhaust velocity, and v_0 is the velocity of the vehicle. At higher rocket velocities there is a smaller difference between the flight speed of the vehicle, and the exhaust velocity of the

rocket engine, resulting in higher propulsion efficiencies, and consequently lower availability losses. However, due to the first stage rocket starting from rest, the first stage rocket always loses a large portion of its exergy to irreversible propulsion inefficiency.

The scramjet accelerator loses a large amount of its exergy to overcoming drag, due to the scramjet accelerator accelerating at high speeds within the atmosphere, at high dynamic pressures. The drag losses of the scramjet accelerator flying a trajectory with no dynamic pressure constraint in Case 2 are higher than those of the scramjet accelerator flying a constant dynamic pressure trajectory in Case 1, at 20.42%, compared to 18.68%. This is due to the additional manoeuvring of the scramjet accelerator during the pull-up before third stage release when the dynamic pressure is not constrained, which requires high angles of attack, and increases drag significantly. The energy imparted upon the payload and third stage rocket during the scramjet accelerator's acceleration is decreased significantly when the scramjet accelerator is allowed to deviate from 50kPa dynamic pressure, reducing from 9.31GJ to 7.85GJ, a decrease of -15.7%. This energy is traded-off during the pull-up manoeuvre, by utilising the superior aerodynamics of the scramjet accelerator to manoeuvre into flight conditions that are favourable for the separation of the third stage, improving the efficiency of the third stage ascent. Even though less energy is imparted upon the third stage before separation, a release from the end of a scramjet accelerator pull-up in Case 2 enables the third stage to impart significantly more energy onto the payload, at 5.33GJ, compared to 3.33GJ when released from 50kPa in case 1, an increase of +60.1%, with a significantly increased exergy efficiency of 15.53%.

The additional energy efficiency of the third stage (which is split into in-atmosphere and exo-atmospheric manoeuvres in Table 6.4) comes from less time spent in-atmosphere. This results in a decrease in the energy lost due to drag, as well as a decrease in the energy imparted upon the heat shield. The energy lost from the third stage overcoming drag is dependent on the amount of time that the rocket spends in the atmosphere, and comprises 10.75% of the fuel exergy when released at 50kPa in Case 1, and 0.68% when released after a pull-up of the scramjet accelerator in Case 2. The energy lost accelerating the heat shield is also significantly larger when released from the scramjet accelerator flying a constant dynamic pressure trajectory in Case 1, at 2.96GJ (10.67%) of the fuel exergy, compared to only 1.22GJ (7.28%) when the third stage is released after a pull-up of the scramjet accelerator in Case 2. This is due to the third stage spending considerably more time in a high dynamic pressure environment when released from a constant dynamic pressure trajectory, requiring the heat shield for longer, so that more kinetic and potential energy is imparted upon the heat shield during acceleration. However, the energy losses due to the availability loss of the third stage are higher when released from the end of a scramjet accelerator pull-up, compared to the trajectory constrained to constant dynamic pressure. This is due to the third stage being released at lower speed, from the end of a scramjet accelerator pull-up manoeuvre, resulting in a lower propulsive efficiency as illustrated in Equation 6.1. This indicates that there is a trade-off between the propulsion inefficiencies of the third stage, and the drag and heat shield energy losses.

6.5 Sensitivity Analysis

The launch system studied in this work is intended to be representative of a three stage, rocket-scramjet-rocket, small satellite launch system, to be used to inform future vehicle designs. It is anticipated that the design of the launch system will change significantly before an optimal, or even practically feasible, design is reached. To quantify how variations in the design of a stage or variations in the performance of a stage due to modelling error may affect the performance of the launch system, it is useful to conduct a sensitivity analysis on the launch system, in which selected design parameters of the launch system are varied, and the effects on the optimised maximum payload-to-orbit trajectory of the launch system are investigated. The investigation of the key design parameters of the launch system provides a comparative metric, which is used to quantify the relative impact of the vehicle design on the performance of the launch system. The performance trade-offs between the stages are investigated by studying the variation in the optimised trajectory, particularly the stage separation conditions, as the parameters of the launch system design are changed. Trends are developed for each parameter study, quantifying how much the performance factors of the launch system vary per percentage of variation of each design parameter ($\Delta/\Delta\%$) via a linear approximation. This percentage variation gives a general metric for how much each design parameter effects the performance factors of the launch system, when the parameters are varied from the baseline launch vehicle. The relative performance impacts of correlated design parameter pairs are compared, using normalised variations for comparison so that the absolute magnitude of a one percent variation of each individual design parameter is taken into account. Appendix F shows comparison plots of the scramjet accelerator and third stage trajectories for each parameter variation study, however, the first stage rocket trajectories are very similar and are not compared graphically. Key results including performance factors of each stage and separation conditions are summarised within this section.

In addition to informing future launch system design and control decisions, this sensitivity study serves to verify the ability of LODESTAR to generate optimal trajectories with varied vehicle designs, as well as investigating the robustness of the optimised solution with respect to uncertainties in the vehicle design and performance. When necessary for the trajectory simulations within this section, it is assumed that the scramjet engines are operable at velocities slightly under Mach 5. This assumption is made in order to allow meaningful assessment of parameters which effect the first-second stage separation velocity, without modification of the first stage rocket. All optimised trajectories within this section use the full amount of fuel available to the scramjet accelerator vehicle.

6.5.1 Case 3: Maximum Dynamic Pressure Sensitivity

To investigate the sensitivity of the vehicle to changes in q_{max} , the maximum permissible dynamic pressure is varied by $\pm 10\%$, and the flight trajectory optimised, with results shown in Table 6.5, and comparison plots shown in Appendix F.1.1. The variation in maximum dynamic pressure has

Trajectory Condition	q_{max} :	45kPa	47.5kPa	50kPa	52.5kPa	55kPa	$\Delta/\Delta\%q$
Payload to Orbit (kg)		140.2	153.2	156.4	158.7	160.6	0.9
Total η_{exergy} (%)		1.537	1.656	1.685	1.706	1.724	8×10^{-5}
1st Stage η_{exergy} (%)		6.834	6.859	6.875	6.883	6.888	0.003
Separation Alt, 1→2 (km)		25.11	24.81	24.52	24.24	23.97	-0.06
Separation v, 1→2 (m/s)		1523	1529	1533	1535	1538	0.72
Separation γ, 1→2 (deg)		11.0	11.1	11.3	11.5	11.5	0.03
2nd Stage η_{exergy} (%)		4.469	4.364	4.401	4.422	4.461	-
Separation Alt, 2→3 (km)		38.28	44.16	43.81	43.44	43.58	-
Separation v, 2→3 (m/s)		2672	2630	2640	2647	2655	-
Separation γ, 2→3 (deg)		10.4	12.0	12.3	12.6	12.7	0.1
2nd Stage Flight Time (s)		660.4	645.6	631.2	620.3	608.7	-2.57
2nd Stage Distance Flown (km)		1252.4	1224.7	1195.6	1172.3	1148.5	-5.2
3rd Stage η_{exergy} (%)		13.860	15.210	15.527	15.757	15.950	0.095
3rd Stage t, $q > 5\text{kpa}$ (s)		22.6	6.0	6.8	7.6	7.4	-
3rd Stage Fuel Mass (kg)		2845.0	2832.0	2828.8	2826.5	2824.6	-0.93

Table 6.5: Comparison of key trajectory parameters with variation in the maximum dynamic pressure of the scramjet accelerator (Case 3).

only a small effect on the total exergy efficiency of the system, and hence only a small effect on the payload mass delivered to sun synchronous orbit. Varying the maximum dynamic pressure by $\pm 10\%$ causes a variation of only $+0.039\%\eta$ or $-0.148\%\eta$ in the exergy efficiency of the launch system and a corresponding $+4.2\text{kg}$ ($+2.7\%$) or -16.2kg (-10.4%) variation in the payload to orbit. There are no clear trends in the altitudes or velocities of scramjet stage-third stage separation, although the 45kPa limited case has a significantly lower pull-up than the other cases. However, there is a clear trend in separation angle, from 10.4° at 45kPa, to 12.7° at 55kPa, due to the increased manoeuvrability of the scramjet accelerator stage at higher dynamic pressures. The 45kPa limited case flies for 660.4s, significantly longer than the 55kPa limited case, which flies for 608.7s. As the dynamic pressure decreases, the size of the altitude raising manoeuvre in the middle of the trajectory decreases. This is due to the increased altitude and angle of attack moving the flight conditions into a region where the specific impulse of the C-REST engines is not homogeneous, so that it is beneficial to fly at maximum dynamic pressure.

As the maximum dynamic pressure increases, the exergy efficiencies of both the first and third stages increase. The first stage efficiency increase is slight, and is due to the first stage needing to manoeuvre less when separating at a higher dynamic pressure and a higher trajectory angle. This reduced manoeuvring allows the first stage to be throttled less, so that flight time is reduced, and time in relatively inefficient low altitude, high density conditions is lessened. However, a higher third stage efficiency is the primary benefit of increasing the dynamic pressure limit. This higher third stage efficiency with increasing dynamic pressure limit is due to the higher energy imparted

upon the third stage by the first stage and scramjet accelerator, resulting from the greater efficiency and manoeuvrability of the launch system when able to fly at higher dynamic pressure. When the third stage is separated with more energy, it is generally separated at a higher velocity, improving the propulsive efficiency (illustrated by Equation 6.1). The exception to this is the 45kPa trajectory, where altitude is traded off for velocity at third stage release in order to allow the third stage to achieve orbit. In this case the trade-off of altitude results in the third stage spending significant time in-atmosphere, with high drag losses.

6.5.2 Case 4: Scramjet Accelerator Drag Sensitivity

Trajectory Condition	$C_{d,2}$:	90%	95%	100%	105%	110%	$\Delta/\Delta\%C_{d,2}$
Payload to Orbit (kg)		179.0	165.8	156.4	147.2	137.8	-2
Total η_{exergy} (%)		1.892	1.772	1.685	1.601	1.515	-0.00018
1st Stage η_{exergy} (%)		7.287	7.082	6.875	6.665	6.457	-0.042
Separation Alt, 1→2 (km)		24.94	24.74	24.52	24.30	24.07	-0.04
Separation v, 1→2 (m/s)		1584	1559	1533	1506	1478	-5.3
Separation γ, 1→2 (deg)		11.2	11.2	11.3	11.4	11.5	0.02
2nd Stage η_{exergy} (%)		4.910	4.603	4.401	4.217	4.032	-0.043
Separation Alt, 2→3 (km)		43.20	43.54	43.81	43.51	43.15	-
Separation v, 2→3 (m/s)		2780	2700	2640	2585	2529	-12.38
Separation γ, 2→3 (deg)		11.6	12.0	12.3	12.6	12.9	0.06
2nd Stage Flight Time (s)		629.9	630.4	631.2	637.9	649.3	0.93
2nd Stage Distance Flown (km)		1246.1	1221.5	1195.6	1176.4	1159.3	-4.37
3rd Stage η_{exergy} (%)		17.728	16.447	15.527	14.628	13.706	-0.197
3rd Stage $t, q > 5\text{kpa}$ (s)		9.7	8.1	6.8	6.8	7.5	-
3rd Stage Fuel Mass (kg)		2806.2	2819.4	2828.8	2838.0	2847.4	2.02

Table 6.6: Comparison of key trajectory parameters with variation in the drag of the scramjet accelerator (Case 4).

To investigate the effect of the vehicle design and uncertainty in aerodynamic performance on the optimal trajectory, the drag of the scramjet accelerator is varied by $\pm 10\%$, and an optimised trajectory calculated with dynamic pressure limited to 50kpa. The drag of the scramjet accelerator is varied during both the first stage ascent, as well as the acceleration of the scramjet accelerator. Results are compared to the 100% drag result in Table 6.6 with a trajectory path comparison shown in Appendix F.1.2.

The drag of the scramjet accelerator has a significant effect on the overall exergy efficiency of the system ($+0.207\%\eta$ at 90% drag, and $-0.170\%\eta$ at 110% drag) and correspondingly, on the maximum payload-to-orbit, $+22.6\text{kg}$ at 90% drag, a variation of $+14.5\%$ and -18.6kg at 110% drag, a variation of -11.2% . The exergy efficiencies of the first stage rocket and the scramjet accelerator are decreased significantly as the drag is increased, from $7.287\%\eta$ and $4.910\%\eta$ respectively at 90%

drag, to $6.457\%\eta$ and $4.032\%\eta$ respectively at 110% drag. This reduction in efficiency is due to the increase in energy which must be used to overcome the added drag. The first-second stage separation staging altitude and velocity decrease significantly as the drag is increased, while the trajectory angle increases. This trend is due to the lower and slower trajectory that the first stage flies as drag is increased, as well as the increased penalty of manoeuvring due to decreased L/D.

The scramjet accelerator trajectory results show that when drag is varied, the optimal trajectories do not change shape significantly, and pull-up to similar altitudes. Although as the drag is increased (ie. L/D is decreased), the second stage follows a slightly slower and hence lower flight path, and the scramjet accelerator pulls-up to a higher trajectory angle. The similar shape of the optimal trajectory with variation in the aerodynamics of the scramjet accelerator suggests that sacrificing velocity to increase separation altitude in a pull-up manoeuvre is optimal for multiple vehicle designs, and that the size of this pull-up is consistent with variation in the aerodynamics of the scramjet accelerator.

As the drag of the scramjet accelerator increases, the exergy efficiency of the third stage shows a corresponding decrease, from $17.728\%\eta$ at 90% drag, to $13.706\%\eta$ at 110% drag. This is primarily due to the lower velocity of scramjet accelerator-third stage separation at higher drag, which results in a decreased third stage propulsive efficiency (illustrated by Equation 6.1). This decreased propulsive efficiency in turn increases the availability losses during the operation of the third stage, from 21.19% at $C_D=90\%$, to 26.53% at $C_D=110\%$.

6.5.3 Case 5: C-REST Specific Impulse Sensitivity

Trajectory Condition	$I_{SP,2}$:	90%	95%	100%	105%	110%	$\Delta/\Delta\%I_{SP,2}$
Payload to Orbit (kg)	137.2	146.8	156.4	167.9	181.7	2.2	
Total η_{exergy} (%)	1.510	1.598	1.685	1.790	1.917	0.0002	
1st Stage η_{exergy} (%)	6.872	6.882	6.875	6.882	6.875	-	
Separation Alt, 1→2 (km)	24.52	24.53	24.52	24.53	24.52	-	
Separation v, 1→2 (m/s)	1532	1534	1533	1534	1533	-	
Separation γ, 1→2 (deg)	11.3	11.3	11.3	11.4	11.5	-	
2nd Stage η_{exergy} (%)	3.846	4.122	4.401	4.744	5.159	0.065	
Separation Alt, 2→3 (km)	43.32	43.45	43.81	43.21	43.85	-	
Separation v, 2→3 (m/s)	2520	2582	2640	2716	2799	13.83	
Separation γ, 2→3 (deg)	13.1	12.7	12.3	11.9	11.3	-0.08	
2nd Stage Flight Time (s)	638.9	633.2	631.2	628.7	637.3	-	
2nd Stage Distance Flown (km)	1157.2	1174.4	1195.6	1218.9	1254.6	4.78	
3rd Stage η_{exergy} (%)	13.648	14.593	15.527	16.643	17.981	0.214	
3rd Stage t, q > 5kpa (s)	6.5	6.7	6.8	9.6	8.4	-	
3rd Stage Fuel Mass (kg)	2848.0	2838.4	2828.8	2817.3	2803.5	-2.2	

Table 6.7: Comparison of key trajectory parameters with variations in the specific impulse of the C-REST engines (Case 5).

The specific impulse of the C-REST scramjet engines is varied by $\pm 10\%$ to directly investigate the effects of the efficiency of the scramjet engines on the performance of the launch vehicle. A comparison of key trajectory parameters is shown in Table 6.7, with comparison plots presented in Appendix F.1.3. The maximum payload-to-orbit varies by $+25.3\text{kg}$ ($+16.2\%$) to -19.2kg (-12.3%), and the total exergy efficiency varies by $+0.232\%\eta$ to $-0.175\%\eta$, at $110\% I_{SP}$ and $90\% I_{SP}$ respectively. The increased C-REST specific impulse does not vary the first stage performance significantly, and the first-second stage separation point stays relatively constant for all cases. The lack of a clear trend in the first stage release point indicates that the efficiency trade-off between the first stage and the scramjet accelerator is not significantly affected by the efficiency of the scramjet accelerator, and is primarily driven by the capabilities of the first stage rocket.

Varying the specific impulse of the C-REST engines has a considerable effect on the exergy efficiency of the scramjet accelerator, causing the efficiency to increase by $+0.758\%\eta$ ($+14.7\%$) at $110\% I_{SP}$ and decrease by $-0.555\%\eta$ (-12.6%) at $90\% I_{SP}$. Increasing the specific impulse of the C-REST engines allows the scramjet accelerator to accelerate more over the flight time, increasing the velocity at second-third stage separation significantly. The availability losses of the scramjet accelerator decrease from 69.25% at $90\% I_{SP}$, to 64.84% at $110\% I_{SP}$. However, the drag losses, and the energy needed to accelerate the structural mass of the third stage, increase from 20.01% and 5.78% at $90\% I_{SP}$, to 20.74% and 7.75% of the scramjet accelerator's total exergy at $110\% I_{SP}$, partially offsetting the increased performance. These increased losses are due to the additional velocity at the end of the trajectory causing increased drag, and requiring more kinetic energy to be imparted upon the structural mass of the scramjet accelerator. Varying the specific impulse does not change the optimal second-third stage separation altitude significantly, however the increased velocity allows this altitude to be reached by the scramjet accelerator with less trajectory angle variation during the pull-up. Increasing the specific impulse allows the third stage to successfully reach orbit from a lower trajectory angle release point, as low as 11.3° at $110\% I_{SP}$, while decreasing the specific impulse requires a higher release point, up to 13.1° at $90\% I_{SP}$. The exergy efficiency of the third stage is increased as the specific impulse of the scramjet accelerator increases, increasing by $+2.454\%\eta$ at $110\% I_{SP}$, and decreasing by $-1.879\%\eta$ at $90\% I_{SP}$. This is due to the significantly decreased in-atmosphere availability losses of the third stage when released at a higher velocity, 3.41GJ at $110\% I_{SP}$, compared to 4.59GJ at $90\% I_{SP}$, as well as the decreased kinetic and potential energy required by the third stage.

6.5.4 Case 6: Scramjet Accelerator Mass Sensitivity

The structural mass of the scramjet accelerator is varied by $\pm 10\%$ ($\pm 495.7\text{kg}$), to investigate the effects of the structural, thermal shielding, and system mass of the scramjet accelerator on the performance of the launch system. A summary of the key parameters of each trajectory is detailed in Table 6.8, with comparison plots shown in Appendix F.1.4. Variation in the mass of the scramjet acceler-

Trajectory Condition	m_2 :	90%	95%	100%	105%	110%	$\Delta/\Delta\%q$
Payload to Orbit (kg)		169.7	162.8	156.4	149.7	142.6	-1.3
Total η_{exergy} (%)		1.807	1.744	1.685	1.624	1.559	-0.00012
1st Stage η_{exergy} (%)		7.071	6.976	6.875	6.764	6.651	-0.021
Separation Alt, 1→2 (km)		25.10	24.81	24.52	24.23	23.93	-0.06
Separation v, 1→2 (m/s)		1604	1568	1533	1497	1462	-7.11
Separation γ, 1→2 (deg)		10.8	11.0	11.3	11.6	11.7	0.05
2nd Stage η_{exergy} (%)		4.541	4.459	4.401	4.342	4.270	-0.013
Separation Alt, 2→3 (km)		44.06	43.88	43.81	43.31	43.35	-
Separation v, 2→3 (m/s)		2713	2674	2640	2608	2571	-7.03
Separation γ, 2→3 (deg)		12.1	12.3	12.3	12.3	12.3	0.01
2nd Stage Flight Time (s)		636.6	633.5	631.2	634.9	636.5	-
2nd Stage Distance Flown (km)		1258.0	1226.3	1195.6	1174.5	1141.3	-5.7
3rd Stage η_{exergy} (%)		16.832	16.161	15.527	14.869	14.169	-0.132
3rd Stage $t, q > 5\text{kpa}$ (s)		7.6	7.4	6.8	7.4	7.4	-
3rd Stage Fuel Mass (kg)		2815.5	2822.4	2828.8	2835.5	2842.6	1.35

Table 6.8: Comparison of key trajectory parameters with variation in the structural mass of the scramjet accelerator (Case 6).

ator causes the maximum payload-to-orbit of the launch system to vary by +13.3kg (+8.5%) at 90% structural mass and by -13.8kg (-8.8%) at 110% structural mass. As the mass of the scramjet accelerator increases, the acceleration of the first stage decreases, and the availability losses of the first stage increase, from 86.49% at 90% structural mass to 87.40% at 110% structural mass. The increased availability losses decrease the efficiency of the first stage as the mass of the scramjet accelerator increases.

A higher scramjet accelerator structural mass causes the scramjet accelerator to stay at relatively lower velocities over its trajectory, which results in a higher specific impulse throughout. Varying the structural mass of the scramjet accelerator generally lowers the altitude at the end of the pull-up manoeuvre slightly, so that more optimal L/D can be maintained for longer. In addition, as the mass of the scramjet accelerator is varied, the velocity at scramjet accelerator-third stage separation varies significantly, by +73m/s (+2.8%) at 90% structural mass, and -69m/s (-2.6%) at 110% structural mass due to reduced acceleration.

As the mass of the scramjet accelerator increases, the exergy efficiency of the third stage is decreased, varying by $-1.358\%\eta$ at 110% structural mass, and as the scramjet accelerator mass is decreased, the exergy efficiency of the third stage is increased, varying by $+1.305\%\eta$ at 90% structural mass, primarily due to increased propulsive efficiency from being released at a higher velocity.

Trajectory Condition	$m_{f,2}:$	90%	95%	100%	105%	110%	$\Delta/\Delta\%m_{F,2}$
Payload to Orbit (kg)		148.9	152.6	156.4	160.0	163.7	0.7
Total η_{exergy} (%)		1.692	1.688	1.685	1.681	1.678	-1e-05
1st Stage η_{exergy} (%)		6.937	6.908	6.875	6.845	6.806	-0.006
Separation Alt, 1→2 (km)		24.70	24.61	24.52	24.43	24.34	-0.02
Separation v, 1→2 (m/s)		1555	1544	1533	1522	1510	-2.22
Separation γ, 1→2 (deg)		11.1	11.2	11.3	11.4	11.5	0.02
2nd Stage η_{exergy} (%)		4.576	4.481	4.401	4.319	4.253	-0.016
Separation Alt, 2→3 (km)		43.67	43.79	43.81	43.81	43.59	-
Separation v, 2→3 (m/s)		2593	2616	2640	2663	2687	4.66
Separation γ, 2→3 (deg)		12.6	12.5	12.3	12.2	12.0	-0.03
2nd Stage Flight Time (s)		583.1	607.6	631.2	656.3	682.2	4.94
2nd Stage Distance Flown (km)		1077.1	1137.2	1195.6	1256.3	1319.4	12.07
3rd Stage η_{exergy} (%)		14.802	15.162	15.527	15.883	16.237	0.072
3rd Stage $t, q > 5\text{kpa}$ (s)		6.2	6.3	6.8	6.8	7.7	0.07
3rd Stage Fuel Mass (kg)		2836.3	2832.6	2828.8	2825.2	2821.5	-0.74

Table 6.9: Comparison of key trajectory parameters with variation in the fuel mass of the scramjet accelerator (Case 7).

6.5.5 Case 7: Scramjet Accelerator Fuel Mass Sensitivity

The available fuel mass of the scramjet accelerator is varied by $\pm 10\%$, to investigate the effects of variations of the fuel tank size within the scramjet accelerator. Comparison plots are shown in Appendix F.1.5, with a summary of key trajectory parameters detailed in Table 6.9. The fuel mass causes the maximum payload to orbit to vary by **+7.3kg (+4.67%)** at 110% fuel mass, and by **-7.5kg (-4.80%)** at 90% fuel mass. In every case, the scramjet accelerator utilises the full amount of fuel available to it, so that the addition of extra fuel mass allows the scramjet accelerator to accelerate for longer.

As was observed in Case 6, the addition of extra mass to the scramjet accelerator causes the first stage separation altitude and velocity to decrease, and also for the first stage exergy efficiency to decrease. At 110% fuel mass, the first-second stage separation altitude decreases by **-0.18km (-0.7%)**, the separation velocity decreases by **-23m/s (-1.5%)** and the exergy efficiency of the first stage decreases by **-0.069% η (-1.0%)**, while at 90% fuel mass, the first-second stage separation altitude increases by **+0.18km (+0.7%)**, the separation velocity increases by **+22m/s (+1.4%)** and the exergy efficiency of the first stage increases by **+0.007% η (+0.4%)**. All cases exhibit similar trajectory shapes, with the scramjet accelerator pulling-up to similar altitudes, so that increasing the fuel mass directly increases the velocity at second-third stage separation and requires slightly less pull-up angle. The second-third stage separation velocity is increased by **+47m/s (+1.8%)** and the trajectory angle is decreased by **-0.3° (-2.4%)** at 110% fuel mass, while the velocity is decreased by **-47m/s (-1.8%)** and the trajectory angle is increased by **+0.3° (+2.4%)** at 90% fuel mass. As the increased fuel mass

directly increases the velocity at the end of the scramjet accelerator's trajectory, the beneficial effects of additional fuel exhibit diminishing returns as the velocity at the end of the scramjet accelerator's trajectory increases, and Isp decreases. This diminishing specific impulse causes the exergy efficiency of the scramjet accelerator to decrease by $-0.148\%\eta$ (-3.4%) at 110% fuel mass, and to increase by $+0.175\%\eta$ ($+4.0\%$) at 90% fuel mass. However, the addition of extra fuel mass means that there is more total energy available to the scramjet accelerator (206.1 GJ at 110% fuel mass, compared to 168.6 GJ at 90% fuel mass), and so the scramjet accelerator is able to accelerate more over its trajectory. For this reason, the addition of fuel mass to the scramjet accelerator is beneficial, although the benefits to the payload-to-orbit exhibit diminishing returns. Once again, as the second-third stage release velocity increases, the exergy efficiency of the third stage increases due to increased propulsive efficiency.

6.5.6 Case 8: Third Stage Mass Sensitivity

Trajectory Condition	$m_3:$	90%	95%	100%	105%	110%	$\Delta/\Delta/\%m_3$
Payload to Orbit (kg)		141.9	149.5	156.4	140.5	108.0	-
Total η_{exergy} (%)		1.599	1.645	1.685	1.517	1.200	-
1st Stage η_{exergy} (%)		7.008	6.941	6.875	6.800	6.731	-0.014
Separation Alt, 1→2 (km)	24.91	24.71	24.52	24.32	24.13	-0.04	
Separation v, 1→2 (m/s)	1580	1556	1533	1509	1486	-4.72	
Separation γ, 1→2 (deg)	11.0	11.2	11.3	11.5	11.6	0.03	
2nd Stage η_{exergy} (%)		4.065	4.228	4.401	4.789	5.402	0.065
Separation Alt, 2→3 (km)	43.70	43.64	43.81	36.58	33.15	-	
Separation v, 2→3 (m/s)	2695	2666	2640	2686	2758	-	
Separation γ, 2→3 (deg)	11.9	12.2	12.3	10.0	3.0	-	
2nd Stage Flight Time (s)	635.3	633.3	631.2	627.9	630.5	-	
2nd Stage Distance Flown (km)	1239.0	1217.1	1195.6	1167.6	1154.5	-4.37	
3rd Stage η_{exergy} (%)		15.620	15.607	15.527	13.198	9.521	-0.292
3rd Stage $t, q > 5\text{kpa}$ (s)	7.9	7.1	6.8	28.0	152.2	-	
3rd Stage Fuel Mass (kg)	2539.4	2683.8	2828.8	2996.6	3181.1	31.92	

Table 6.10: Comparison of key trajectory parameters with variation in the mass of the third stage (Case 8).

The total mass of the third stage rocket is varied by $\pm 10\%$, to investigate the effects of changing the internal mass density of the third stage rocket on the performance of the launch system. Table 6.10 details key trajectory parameters, and Appendix F.1.6 presents comparison plots of each trajectory. The mass of the heat shield is unchanged at 124.6kg, and the structural mass is assumed to contribute to 9% of the remaining mass (so that the structural mass varies by $\pm 10\%$). The remaining mass which is varied consists of a flexible combination of fuel and payload mass, in the same manner as all other cases. This mass variation investigates the effects of the third stage internal layout on the trajectory

of the launch system, quantifying the consequences of fitting additional fuel, payload and structure within the available space.

Interestingly, there is a non-linear trend in the overall performance of the launch system with variations in the mass of the third stage, with peak performance at 100% mass. The payload mass and efficiency decrease when third stage mass is decreased, by -14.5kg (-9.3%) at 90% mass, but also decrease when third stage mass is increased, by -48.4kg (-30.9%). The first stage responds in the same manner as the other mass variation cases, with decreased separation altitude and velocity, and increased separation angle as mass increases. The scramjet accelerator stage also exhibits similar trends to other mass variation cases when the mass of the third stage is reduced; pulling up to similar conditions, with the exception of a reduced separation velocity as mass increases. However, when the third stage mass is decreased, the scramjet accelerator-third stage separation altitude is decreased significantly, to 33.15km at 110% third stage mass compared to 43.81km at standard mass, and the velocity is increased to 2758m/s, an increase of 118m/s compared to the standard mass case. In addition, the third stage exhibits nonlinear performance variation, with its exergy efficiency decreasing only slightly ($-0.093\eta\%$) between 90% mass variation and the standard mass, but decreasing very significantly as mass is increased further (by $-6.006\eta\%$ at 110% mass). When the mass is lowered, the third stage is more efficient, due to being separated at a higher velocity, and accelerating faster, however, there is less fuel exergy to use, resulting in an overall less efficient trajectory. When the mass is increased there is a distinct drop-off point in efficiency, due to the thrust of the third stage struggling to lift and accelerate the higher starting mass of the third stage past a certain point. Although the fuel exergy is increased, the reduced performance of the third stage is too poor to achieve the lift required for positive altitude change without being compensated for by the scramjet accelerator, and the overall efficiency is reduced significantly.

This highly nonlinear trend indicates that there is a 'sweet spot' in the design of the third stage rocket in regards to mass and internal density, because of the complex performance trade-offs between the stages of the launch system. Beyond a certain point, adding more fuel (and associated structure) to the third stage causes the scramjet accelerator to perform poorly. This reduced performance is compensated for by the scramjet accelerator flying a more efficient trajectory, causing the third stage efficiency to reduce significantly, and offsetting the additional energy added from the extra fuel itself.

6.5.7 Case 9: Third Stage Specific Impulse Sensitivity

The specific impulse of the third stage rocket is varied by $\pm 10\%$ in order to investigate the effect of the rocket engine efficiency on the payload-to-orbit. Appendix F.1.7 presents comparison plots of the optimised trajectories, and Table 6.11 details key trajectory parameters. The specific impulse variation has a significant effect on the trajectory of the system, and the payload-to-orbit, increasing the payload by +91.6kg (+58.6%) at 110% I_{sp} , and decreasing the payload by -144.0kg (-92.3%) at

Trajectory Condition	$I_{SP,3}$:	90%	95%	100%	105%	110%	$\Delta/\Delta\%I_{SP,3}$
Payload to Orbit (kg)		12.4	92.8	156.4	202.3	248.0	11.6
Total η_{exergy} (%)		0.375	1.105	1.685	2.106	2.524	0.00106
1st Stage η_{exergy} (%)		6.875	6.874	6.875	6.873	6.874	-
Separation Alt, 1→2 (km)		24.52	24.52	24.52	24.52	24.52	-
Separation v, 1→2 (m/s)		1533	1533	1533	1532	1532	-
Separation γ, 1→2 (deg)		11.3	11.3	11.3	11.3	11.3	-
2nd Stage η_{exergy} (%)		5.018	4.588	4.401	4.411	4.435	-
Separation Alt, 2→3 (km)		32.81	36.73	43.81	43.38	43.11	-
Separation v, 2→3 (m/s)		2808	2706	2640	2644	2650	-
Separation γ, 2→3 (deg)		2.1	10.1	12.3	12.2	12.0	-
2nd Stage Flight Time (s)		630.2	623.6	631.2	632.0	630.8	-
2nd Stage Distance Flown (km)		1194.8	1176.9	1195.6	1196.7	1193.6	-
3rd Stage η_{exergy} (%)		1.168	9.007	15.527	20.416	25.428	1.199
3rd Stage $t, q > 5\text{kpa}$ (s)		128.4	28.2	6.8	7.8	8.5	-
3rd Stage Fuel Mass (kg)		2972.8	2892.4	2828.8	2782.9	2737.2	-11.61

Table 6.11: Comparison of key trajectory parameters with variation in the third stage specific impulse (Case 9).

90% I_{sp} .

The third stage specific impulse variation has no direct influence on the trajectory of the first stage rocket, and the first-second stage separation conditions are relatively consistent across the thrust levels simulated. As the specific impulse of the third stage is reduced, the pull-up of the scramjet accelerator becomes much lower and the separation is significantly faster, using a more efficient scramjet accelerator trajectory to impart significantly more energy on the third stage rocket (5.00GJ at 90% I_{SP} compared to 4.19GJ at 100% I_{SP}). However, this is not a linear trend as specific impulse is increased. This nonlinearity is similar to the situation observed when the third stage mass is varied (Case 8), in that the decreased performance of the third stage immediately after separation results in more severe performance effects past a certain point. In this case, as the specific impulse of the third stage is increased, the pull-up manoeuvre of the scramjet accelerator becomes relatively consistent, and the overall performance variation is less significant with variations in the third stage specific impulse. This consistency past a certain point indicates that there is a distinct cutoff of third stage efficiency for the launch system, below which the scramjet accelerator must compensate for reduced third stage performance, and the third stage aerodynamics must be utilised more. This modified staging point indicates that if the performance of the third stage rocket engine is reduced, it may be beneficial to redesign the third stage for greater aerodynamic performance.

Trajectory Condition	$C_{d,3}$:	90%	95%	100%	105%	110%	$\Delta/\Delta\%C_{d,3}$
Payload to Orbit (kg)		156.5	156.4	156.4	156.1	156.0	0
Total η_{exergy} (%)		1.686	1.685	1.685	1.683	1.682	-0.0002
1st Stage η_{exergy} (%)		6.870	6.875	6.875	6.872	6.873	-
Separation Alt, 1→2 (km)		24.52	24.52	24.52	24.52	24.52	-
Separation v, 1→2 (m/s)		1532	1533	1533	1532	1532	-
Separation γ, 1→2 (deg)		11.3	11.3	11.3	11.3	11.3	-
2nd Stage η_{exergy} (%)		4.404	4.398	4.401	4.393	4.398	-
Separation Alt, 2→3 (km)		43.38	43.48	43.81	43.86	43.73	-
Separation v, 2→3 (m/s)		2642	2641	2640	2638	2640	-
Separation γ, 2→3 (deg)		12.3	12.3	12.3	12.3	12.3	-
2nd Stage Flight Time (s)		631.1	632.2	631.2	632.6	632.4	-
2nd Stage Distance Flown (km)		1194.2	1196.8	1195.6	1198.2	1198.0	-
3rd Stage η_{exergy} (%)		15.542	15.525	15.527	15.499	15.488	-
3rd Stage $t, q > 5\text{kpa}$ (s)		8.2	7.6	6.8	7.0	6.8	-
3rd Stage Fuel Mass (kg)		2828.7	2828.8	2828.8	2829.1	2829.2	-

Table 6.12: Comparison of key trajectory parameters with variation in the drag of the third stage (Case 10).

6.5.8 Case 10: Third Stage Drag Sensitivity

The coefficient of drag of the third stage rocket is varied by $\pm 10\%$ to investigate the effects of the third stage design and sizing on the performance of the launch system. Table 6.12 details the key trajectory parameters of each optimised trajectory, and Appendix F.1.8 shows trajectory comparison plots. The third stage drag is found to have only a very small effect on the performance of the launch system, varying the payload to orbit by only +0.1kg at 90% C_d and -0.4kg at 110% C_d . No other parameters show significant variation with variation in the drag of the third stage rocket. While the payload and overall efficiency shows a very small trend, the trade-offs between the stages are inconsistent, with no clear trends in the optimal trajectory. This indicates that the aerodynamic properties of the third stage rocket do not contribute significantly to the performance of the system or the optimal trajectory flown. This is corroborated by the small contributions of the third stage aerodynamic losses to the overall energy losses of the system, as shown for Case 2 in Table 6.4.

6.6 Comparison of Design Parameters

The preceding sections calculate the relative sensitivity of the launch system performance to a variety of design parameters for a nominal dynamic pressure limit of 50kPa. Comparing and contrasting the sensitivity of the launch system to each design parameter allows for the relative impact of each design parameter to be assessed in order to inform future design decisions. Figure 6.11 shows the change in payload mass, normalised to a 1% variation of each design parameter. This change per percentage

Payload Variation (kg) Normalised to a 1% Parameter Variation

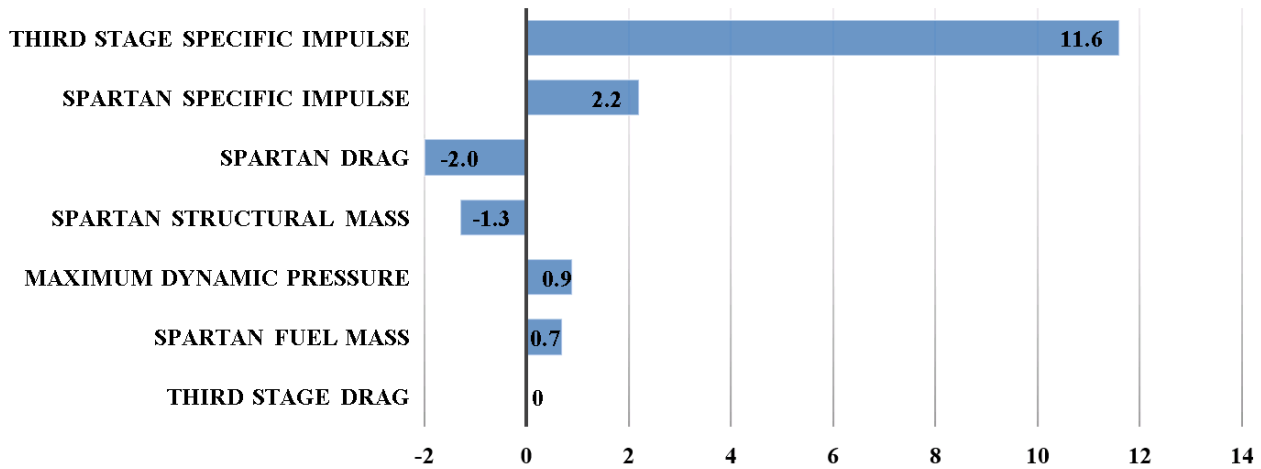


Figure 6.11: The sensitivity of the key design parameters of the launch system.

variation indicates the magnitude by which the payload-to-orbit varies as each design parameter is varied by $\pm 1\%$ (signs are shown for positive parameter variations, with negative signs indicating a decrease in performance), and is measure of the sensitivity of the launch system to variations in each design parameter. However, a 1% variation has a significantly different implication in the context of each individual design parameter, as certain parameters can be adjusted more easily. As such, the change per percentage is most useful when directly assessing each design parameter, and taking into account the associated effects on other, coupled design parameters.

The maximum dynamic pressure of the scramjet accelerator and the scramjet accelerator mass parameter are coupled directly, because the scramjet accelerator's thermal protective properties and structural strength define the maximum dynamic pressure. This means that the low variance in performance with maximum dynamic pressure may be offset by the variation in the mass of the scramjet accelerator, ie. a lower maximum dynamic pressure requires less structural and thermal protection system mass. The relative sensitivities of the launch system to dynamic pressure ($0.9 \frac{\Delta kg}{\Delta \% q_{max}}$), and scramjet accelerator mass ($-1.3 \frac{\Delta kg}{\Delta \% m_{scramjetaccelerator}}$), and their absolute magnitudes (50kPa and 4957kg respectively), allow the sensitivities of these coupled effects to be directly quantified. Comparing these sensitivities implies that so long as decreasing the dynamic pressure by 1kPa allows for a reduction in structural and TPS mass of greater than **-68.6kg**, then operating the scramjet accelerator at lower dynamic pressures may be preferable.

The influence of the fuel mass of the scramjet accelerator on the performance of the launch system is relatively low, per percentage variation. However, the fuel mass is only a fraction of the total mass of the scramjet accelerator. This means that relatively small mass changes, by kg, in fuel mass are still significant. When the fuel mass of the scramjet accelerator is increased, the structural mass of the tanks will require a corresponding increase. Comparing the impact of the fuel mass and structural

mass of the scramjet accelerator along with their relative magnitudes (1562kg of fuel mass and 4957kg of structural mass), the relative impact of each is $0.7 \frac{\Delta kg_{payload}}{\Delta \% m_{scramjetacceleratorfuel}}$ and $-1.3 \frac{\Delta kg_{payload}}{\Delta \% m_{scramjetaccelerator}}$ respectively. This means that so long as fuel mass can be added to the scramjet accelerator with less than 1.7kg of structural mass incorporated for each 1kg of fuel mass, adding additional fuel mass will be beneficial. However, the fuel mass is constrained considerably by the available internal space within the scramjet accelerator, which is likely to be the main limiting factor. If the size of the fuselage of the scramjet accelerator is increased, the aerodynamic performance of the scramjet accelerator will be altered proportionally. The sensitivity of the launch system to the drag of the scramjet accelerator, $-2.0 \frac{\Delta kg}{\Delta \% C_d}$, means that so long as 1kg of fuel can be added to the scramjet accelerator with a drag increase of less than 0.022%, then the maximum payload-to-orbit will increase.

The payload-to-orbit is sensitive to the specific impulse of the C-REST engines, varying at a rate of $2.2 \frac{\Delta kg}{\Delta \% I_{SP}}$. Increasing the specific impulse of the scramjet engines is likely to require the addition of extra systems within the scramjet engines, adding weight to the scramjet accelerator, or a change in the shape of the scramjet engines, adding drag to the scramjet accelerator. The slightly lower sensitivity of the launch system to the scramjet accelerator mass ($-1.3 \frac{\Delta kg}{\Delta \% m_{scramjetaccelerator}}$) compared to the sensitivity to the specific impulse, means that so long as increasing the I_{SP} of the scramjet accelerator by 1% causes a corresponding increase in the structural mass of the scramjet accelerator of less than 83.9kg, the performance of the launch system will improve. The sensitivity of the launch system to variation of the scramjet accelerator drag ($-2.0 \frac{\Delta kg}{\Delta \% C_{d,scramjetaccelerator}}$) is similar in magnitude to the sensitivity to specific impulse. If a variation in the shape of the scramjet engines or forebody increases the I_{SP} of the scramjet accelerator by 1%, while increasing the drag of the scramjet accelerator by less than 1.1%, then the efficiency of the launch system will be improved.

The aerodynamic performance (L/D) of the third stage is shown to have only a very small impact on the performance of the launch system, with a negligible drag sensitivity. This means that for any third stage shape variations, the aerodynamic sensitivity is small. Conversely, the specific impulse of the third stage rocket has the highest percentage payload variation effect on the launch system of any of the design parameters tested, at $11.6 \frac{\Delta kg}{\Delta \% I_{SP,3}}$. Increasing the specific impulse of the third stage is likely to involve modifications to the engine, increasing the pressure within the fuel tanks, or adding a turbopump to assist fuel flow, all of which involve increasing the mass of the third stage rocket. However, the significant nonlinearities in the response of the system to changes in the mass of the third stage mean that there is no simple relationship between these two design parameters, and that modifications to the engine of the third stage must be performed along with consideration of the entire system and its trajectory.

6.7 Summary

In this chapter, LODESTAR was used to design the trajectory of the representative rocket-scramjet-rocket multi-stage launch system based on the SPARTAN. A trajectory was simulated in which the scramjet accelerator stage flies at a constant dynamic pressure, producing 98.3kg of payload-to-orbit. This trajectory served to verify LODESTAR and the simulation of the launch system, as well as providing a baseline trajectory for comparison. A trajectory optimised for maximum payload-to-orbit was then calculated, which increased the payload mass to sun synchronous orbit to 156.4kg (with a 97.5% confidence interval of 8.8-238.8kg), an increase of 59.1% compared to a constant dynamic pressure trajectory similar to those explored in previous studies of the SPARTAN[12]. The optimal flight path indicates that the optimal scramjet flight path for a system transitioning between separate airbreathing and rocket-powered stages involves the scramjet accelerator flying at less than its maximum dynamic pressure at three separate points along the trajectory. Initially, the first-second stage separation occurs at a higher trajectory angle than in the constant dynamic pressure trajectory, causing the scramjet accelerator to fly at lower dynamic pressure, and trading off the exergy efficiency of the scramjet accelerator for an increase in the exergy efficiency and fuel mass of the first stage, for an overall performance gain. The optimal flight path then exhibits an altitude raising manoeuvre in the middle of the trajectory, which improves the exergy efficiency of the scramjet accelerator by a very minor $+0.005\%\eta$ (+0.3%). Finally, the scramjet accelerator executes a pull-up manoeuvre before the second-third stage separation. This optimal pull-up manoeuvre trades off velocity (a decrease of 145.0m/s) for altitude (an increase of 11.65km) and improved flight path angle (an increase of 11.6°). This pull-up manoeuvre, along with the higher first-second stage separation, decreases the exergy efficiency of the scramjet accelerator by $-0.719\%\eta$ (-14.04%) when compared to the constant dynamic pressure case. However, these conditions improve the exergy efficiency of the third stage rocket significantly, by $+6.013\%\eta$, an increase of +63.20% over the third stage released from a constant dynamic pressure trajectory. While a pull-up manoeuvre under airbreathing operation has been identified as beneficial in previous studies[23, 24, 30], these pull-ups were either performed to lower dynamic pressure for the orbiter stage[23, 30], or to improve the operation of the airbreathing engines[24]. This study has shown that a pull-up is directly beneficial to the payload-to-orbit performance of the launch system due to the efficiency trade-offs between the stages of the launch system. Energy efficiency is traded off between the scramjet accelerator and third stage, with the scramjet accelerator becoming significantly less efficient (Imparting 1.46GJ less energy to the third stage and payload) in order to increase the efficiency of the third stage, in particular reducing the third stage energy expended due to drag from 2.99GJ, to 0.11GJ. This performance improvement is in addition to the possible design benefits due to heat shield and structural mass reduction of the third stage, due to the significantly lowered dynamic pressure at separation of 7.8kPa, a decrease of 42.2 kPa compared to a 50kPa constant dynamic pressure trajectory.

A sensitivity study was conducted, to determine the relative effects of key vehicle design parameters on the optimised trajectory. The maximum dynamic pressure, specific impulse, aerodynamic performance, structural mass, and fuel mass of the scramjet accelerator were modified, along with the specific impulse, mass and aerodynamic performance of the third stage, and the magnitudes of their payload-to-orbit sensitivities compared. The specific impulse of the third stage rocket was found to produce the most overall effect on the payload-to-orbit, increasing the payload by +91.7kg (+58.6%) at 110% I_{sp} , and decreasing the payload by -143.9kg (-92.0%) at 95% I_{sp} . However, increasing the specific impulse of the third stage rocket is likely to come at a high cost premium, which may be undesirable as the third stage is non-reusable. The most easily variable design factor, the maximum dynamic pressure of the scramjet accelerator, was found to have a relatively small effect on the payload-to-orbit performance of the launch system, varying the payload-to-orbit by only +4.3kg (+2.7%) at 55kPa and -16.1kg (10.3%) at 45kPa. The negative effect on the payload-to-orbit when flying at 45kPa is likely to be offset by the lower TPS and structural mass required by lower dynamic pressure flight. It was determined that if the TPS and structural mass decrease is greater than -68.6kg for every 1kPa reduction in the maximum dynamic pressure, then flying at lower dynamic pressure is potentially preferable.

CHAPTER 7

OPTIMISED TRAJECTORY INCLUDING FLY-BACK

This chapter presents the maximum payload-to-orbit trajectory of the rocket-scramjet-rocket launch system, with the fly-back of the scramjet accelerator included within the optimal trajectory calculation performed by LODESTAR. Flying back the scramjet accelerator for landing at the initial launch site is one of the primary enabling factors in the cost efficient operation of the launch system. If the scramjet accelerator is launched onto a trajectory from which it is not able to fly-back, it must perform a downrange landing, likely at an Indonesian airfield when launched northerly from north Australia. This would necessitate transporting the scramjet accelerator back to Australia, a costly and time consuming process, and would require for international landing facilities to be available. Flying back the scramjet accelerator during the launch process removes the need for costly transportation from a downrange launch site, and allows for rapid refurbishment and re-use with short turn-around times. In addition, if a launch site is used from which there is no downrange landing site, the scramjet accelerator must necessarily fly-back to the initial launch site.

The fly-back of the scramjet accelerator requires turning-around the scramjet accelerator after third stage separation, covering the necessary ground distance for return, and decelerating to reduce the speed of the scramjet accelerator to landing approach speed, while maintaining a suitable descent angle to allow for a controlled approach. The return of the scramjet accelerator to the initial launch site is included in the optimisation process to assess whether it is possible for the fly-back of the scramjet accelerator to be achieved as a part of the launch process, and to maximise the overall payload-to-orbit efficiency of the launch system. This is compared to the optimised, maximum payload-to-orbit trajectory without fly-back in Case 2 (detailed in Chapter 6) to assess the detrimental effects of the fly-back on the performance of the launch system. A sensitivity analysis is conducted, in a similar fashion to Chapter 6. This sensitivity analysis allows the influence of the fly-back of the scramjet accelerator on the design sensitivities of the launch system to be analysed.

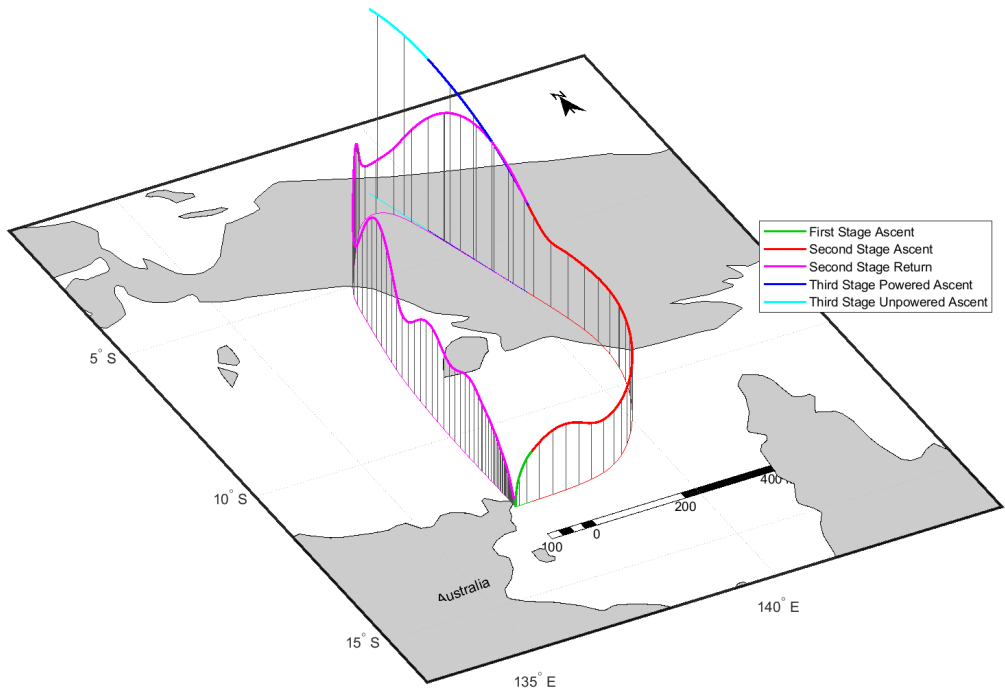


Figure 7.1: Maximum payload-to-orbit trajectory path with the inclusion of scramjet accelerator fly-back (Case 11).

7.1 Case 11: Optimised Ascent Trajectory with Scramjet Accelerator Return

LODESTAR is used to optimise the trajectory of the rocket-scramjet-rocket launch system, including the return of the scramjet accelerator to its initial launch site. The optimised trajectory is shown in Figure 7.1. The rocket-scramjet-rocket launch system is shown to be able to successfully launch a small satellite to sun synchronous orbit, while flying-back the scramjet accelerator to the initial launch site location, and approaching the landing site at appropriately low altitude ($<1\text{km}$) and speed ($<20\text{m/s}$) to allow for landing. The optimised trajectory attains a payload mass to SSO of 132.1kg, a **-24.3kg (-15.5%)** reduction in payload mass compared to the optimised ascent-only trajectory in Case 2, detailed in Chapter 6. The benefits of flying back the scramjet accelerator to its initial launch

Trajectory Condition	Value
Payload to Orbit (kg)	132.1
Total η_{exergy} (%)	1.578
1st Stage η_{exergy} (%)	6.923
Separation Alt, 1→2 (km)	24.57
Separation v, 1→2 (m/s)	1539
Separation γ, 1→2 (deg)	11.1
2nd Stage η_{exergy} (%)	3.758
Separation Alt, 2→3 (km)	42.87
Separation v, 2→3 (m/s)	2506
Separation γ, 2→3 (deg)	12.7
2nd Stage Distance Flown (km)	869.6
2nd Stage Return Fuel (kg)	257.8
2nd Stage Return Distance (km)	1522.3
3rd Stage η_{exergy} (%)	13.14
3rd Stage $t, q > 5\text{kPa}$ (s)	7.7
3rd Stage Fuel Mass (kg)	2853.1

Table 7.1: Selected trajectory conditions for a maximum payload-to-orbit trajectory including scramjet accelerator fly-back (Case 11).

site, compared to the alternative of transporting the scramjet accelerator back to the launch site from a remote landing, are likely to far outweigh this associated reduction in payload.

7.2 Ascent Trajectory

When the fly-back of the scramjet accelerator is included in the trajectory optimisation, the shape of the ascent trajectory of the launch system is altered significantly when compared to the ascent-only trajectory in Case 2, detailed in Chapter 6. The first stage initially pitches towards the east. After pitchover, the angle of attack is maintained at 0° for 35.6s, before it is reduced gradually to -3.9° at 71.9s in order to adjust the altitude and trajectory angle, before increasing back to 0° at first-second stage separation. The scramjet accelerator is released in an easterly direction, at a heading angle of 2.16° , an altitude of 24.57km, and a trajectory angle of 11.1° .

These separation conditions cause an altitude raising manoeuvre to occur at the beginning of the scramjet accelerator trajectory, in the same manner to the optimised ascent-only trajectory in Case 2, detailed in Chapter 6. . The altitude raising manoeuvre after the first stage-scramjet accelerator separation takes the scramjet accelerator to an altitude of 32.3km at 47.1s, and decreases the dynamic pressure of the scramjet accelerator to 14.9kPa, reaching close to the lower limit of operation of the scramjet engines, during which time the bank angle of the scramjet accelerator is increased in order to reduce lift in the vertical direction, minimising the size of the initial altitude raising manoeuvre.

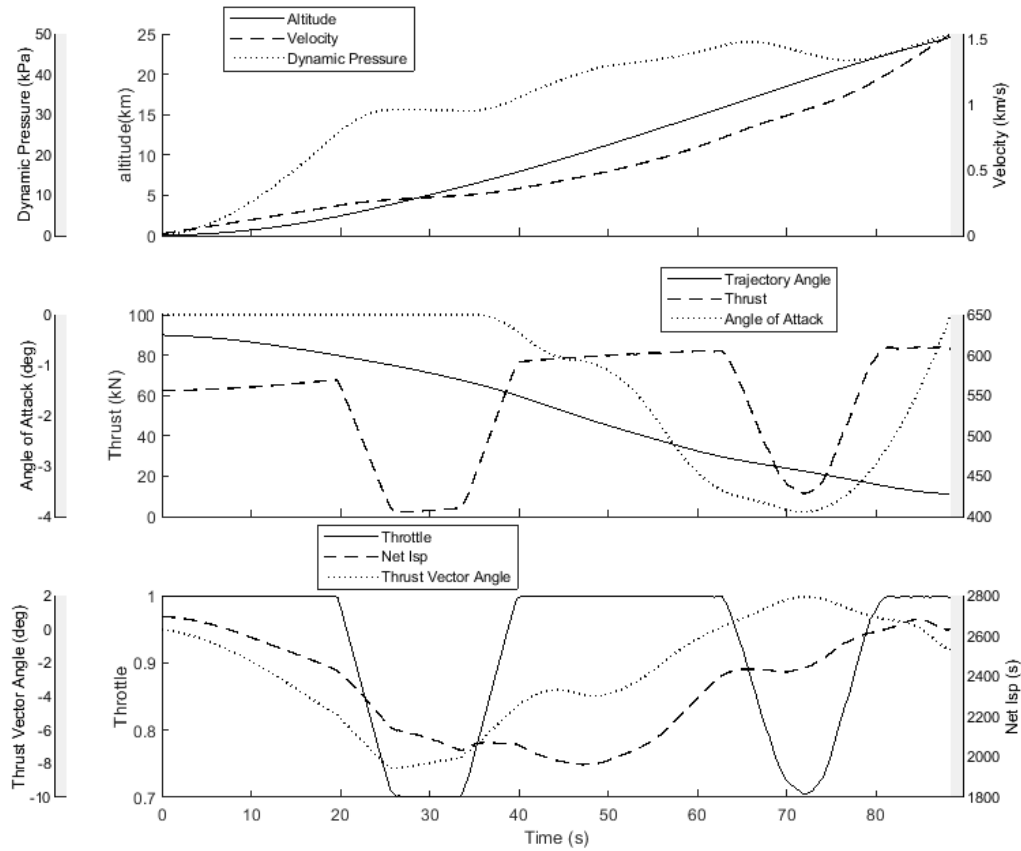


Figure 7.2: The first stage of the optimised maximum payload-to-orbit trajectory with scramjet accelerator fly-back (Case 11).

After the first-second stage separation, the bank angle is increased, at the maximum change rate, to 52.2° , which aids the scramjet accelerator in decreasing its altitude. As the altitude of the scramjet accelerator begins to reduce, the bank angle **reduces** and the angle of attack is raised to 3.9° to increase lift, slowing the descent of the scramjet accelerator so that maximum dynamic pressure is not exceeded. The bank angle then begins to increase once more in order to change the heading angle of the scramjet accelerator, reaching its maximum of 66.2° at 135.0s flight time.

After this point, the bank angle of the scramjet accelerator is maintained between 48.0° and 52.5° , exhibiting higher bank angles towards the latter part of the ascent. At the end of the scramjet accelerator's ascent, the bank angle is reduced to under 2° , so that lift is maximised during the pull-up. The third stage is released at exactly 0° bank angle, defined as a constraint on the end of the trajectory to ensure that the third stage rocket is released in the vertical plane, and is able to manoeuvre to orbit.

The angle of attack of the scramjet accelerator is significantly higher over the trajectory in Case 11, where fly-back is included, compared to maximum payload-to-orbit trajectory with no fly-back in Case 2, detailed in Section 6.2. These significantly higher angles of attack are a result of the high bank

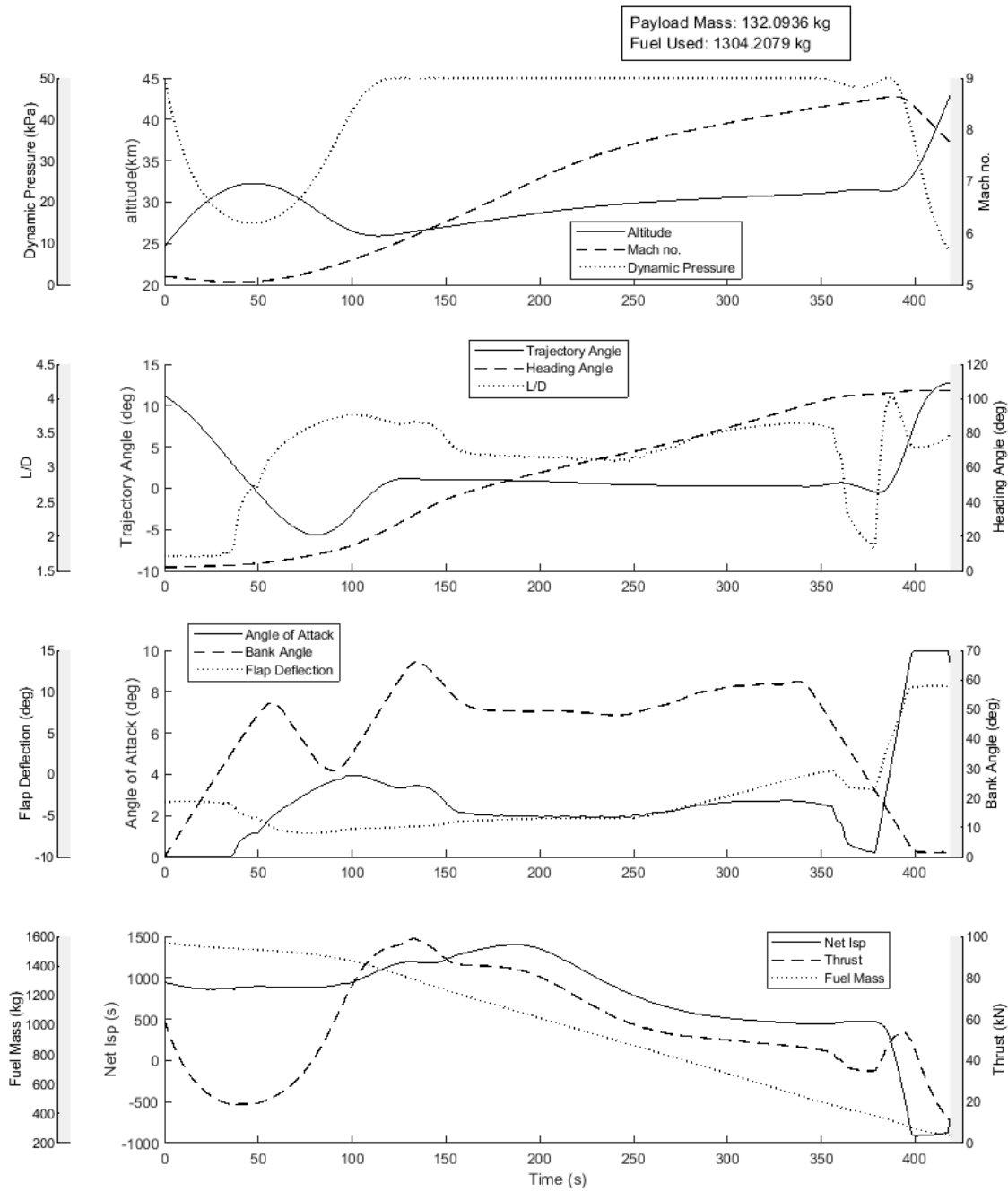


Figure 7.3: The acceleration of the scramjet accelerator flying an optimised maximum payload-to-orbit trajectory with scramjet accelerator fly-back (Case 11).

angle of the scramjet accelerator throughout its trajectory, which cause the lift vector of the scramjet accelerator to be inclined by the bank angle, so that a portion of the lift is used for changing the heading of the scramjet accelerator, rather than providing vertical force. The higher angles of attack

result in the optimal trajectory of the scramjet accelerator following a close to maximum dynamic pressure path for most of the duration of its trajectory, without the altitude raising manoeuvre observed in Section 6.2. The increase in angle of attack means that the scramjet accelerator no longer flies within the homogeneous region of the specific impulse of the C-REST engines. Instead, as shown in Figure 7.4, the flight conditions are close to a region where an increase in angle of attack causes a sharp decrease in specific impulse. This indicates that the angle of attack, and consequently the allowable bank angle, of the scramjet accelerator is being limited by the performance of the C-REST engines. The scramjet accelerator stays close to its maximum dynamic pressure until a pull-up is performed at 386.6s flight time.

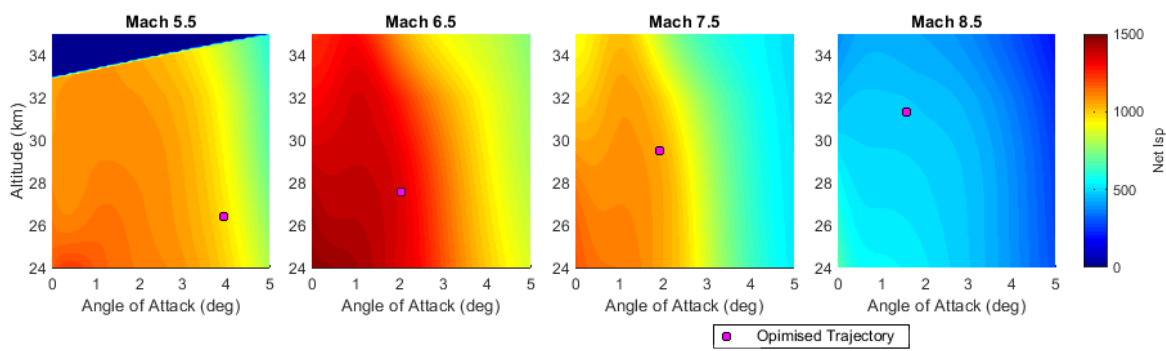


Figure 7.4: Net I_{SP} contours for the scramjet accelerator at Mach numbers between 5.5 and 8.5, showing the optimised trajectory path (Case 11).

The higher angles of attack flown by the scramjet accelerator also have the consequence of decreasing the net specific impulse of the scramjet accelerator during its acceleration, with the maximum specific impulse being decreased by -3.4%. The overall exergy efficiency of the scramjet accelerator is decreased, to $3.758\%\eta$, a decrease of -0.643% η (-14.6%) compared to the maximum payload-to-orbit trajectory with no fly-back. This exergy efficiency decrease is due partially to the decrease in the specific impulse of the scramjet engines, but more significantly is attributed to the fuel necessary for the return flight resulting in less fuel being available for the ascent of the scramjet accelerator, and thus less ‘useful’ work being attained from the total fuel mass. A total fuel mass of 1304.2kg is used during the scramjet accelerator’s acceleration phase, out of a total of 1562kg of available fuel. This reduction in fuel mass used, along with the reduction in net specific impulse due to the higher angle of attack values, reduces the speed at second-third stage separation by -134.0m/s (-5.1%) compared to the maximum payload-to-orbit case with no scramjet accelerator fly-back in Case 2. The scramjet accelerator pulls up to 42.87km altitude and 12.7° trajectory angle before the second-third stage separation, a difference of only -0.94km (-2.1%) and +0.4° (+3.3%) compared to the maximum payload-to-orbit trajectory without fly-back, indicating that the inclusion of fly-back does not have a large effect on the magnitude of the pull-up manoeuvre.

The third stage trajectory, shown in Figure 7.5, is very similar to the third stage trajectory without fly-back in Case 2, shown in Section 6.2, although it is released at a slightly lower altitude and velocity and thus spends a slightly longer time in-atmosphere. The exergy efficiency of the third stage is decreased by $-2.386\% \eta$ (-15.4%) when compared to the maximum payload-to-orbit trajectory with no scramjet accelerator fly-back in Case 2. This lowered efficiency is primarily due to the lower speed of the third stage release, which increases the availability losses of the third stage due to propulsive inefficiencies, as well as the losses due to the additional energy needed to accelerate the increased third stage fuel and structural mass to orbit.

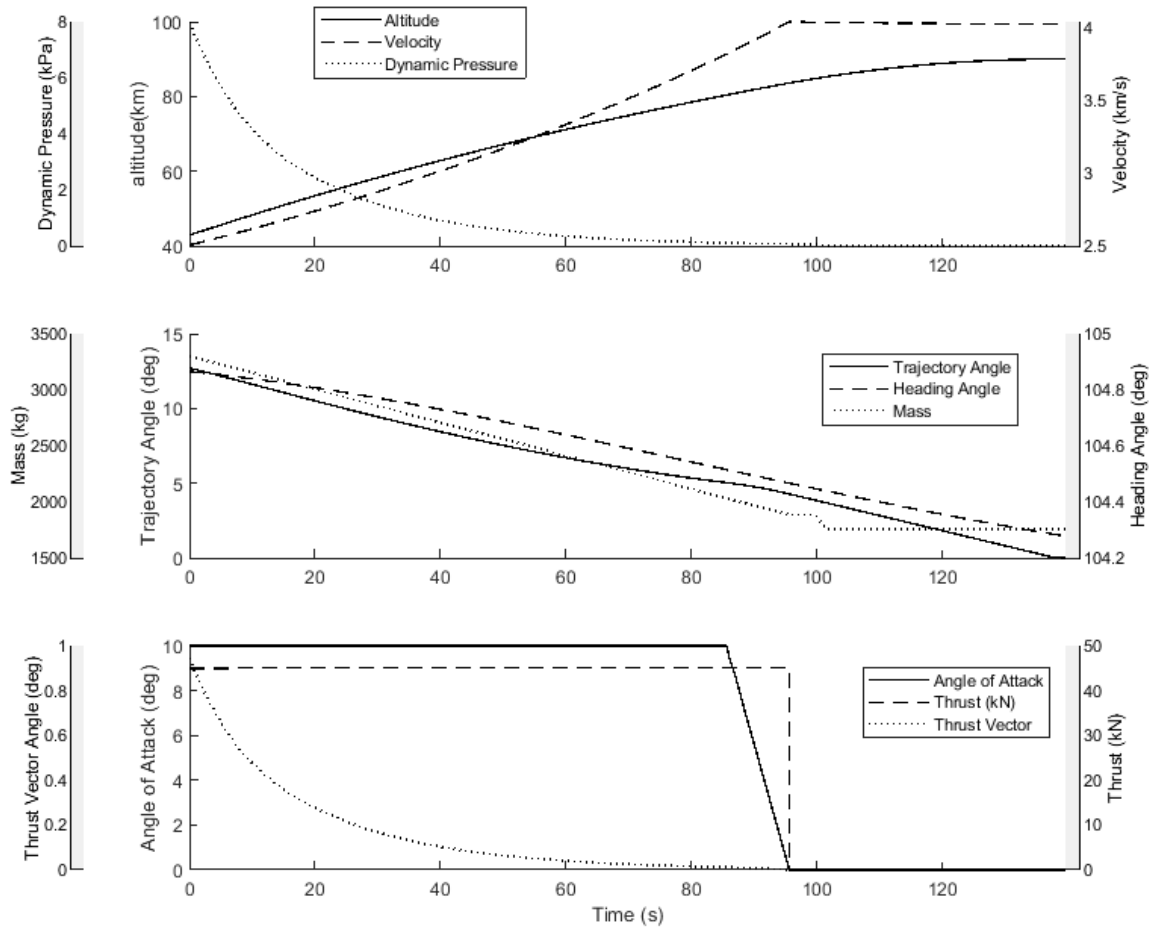


Figure 7.5: The third stage trajectory of an optimised maximum payload-to-orbit trajectory with scramjet accelerator fly-back (Case 11).

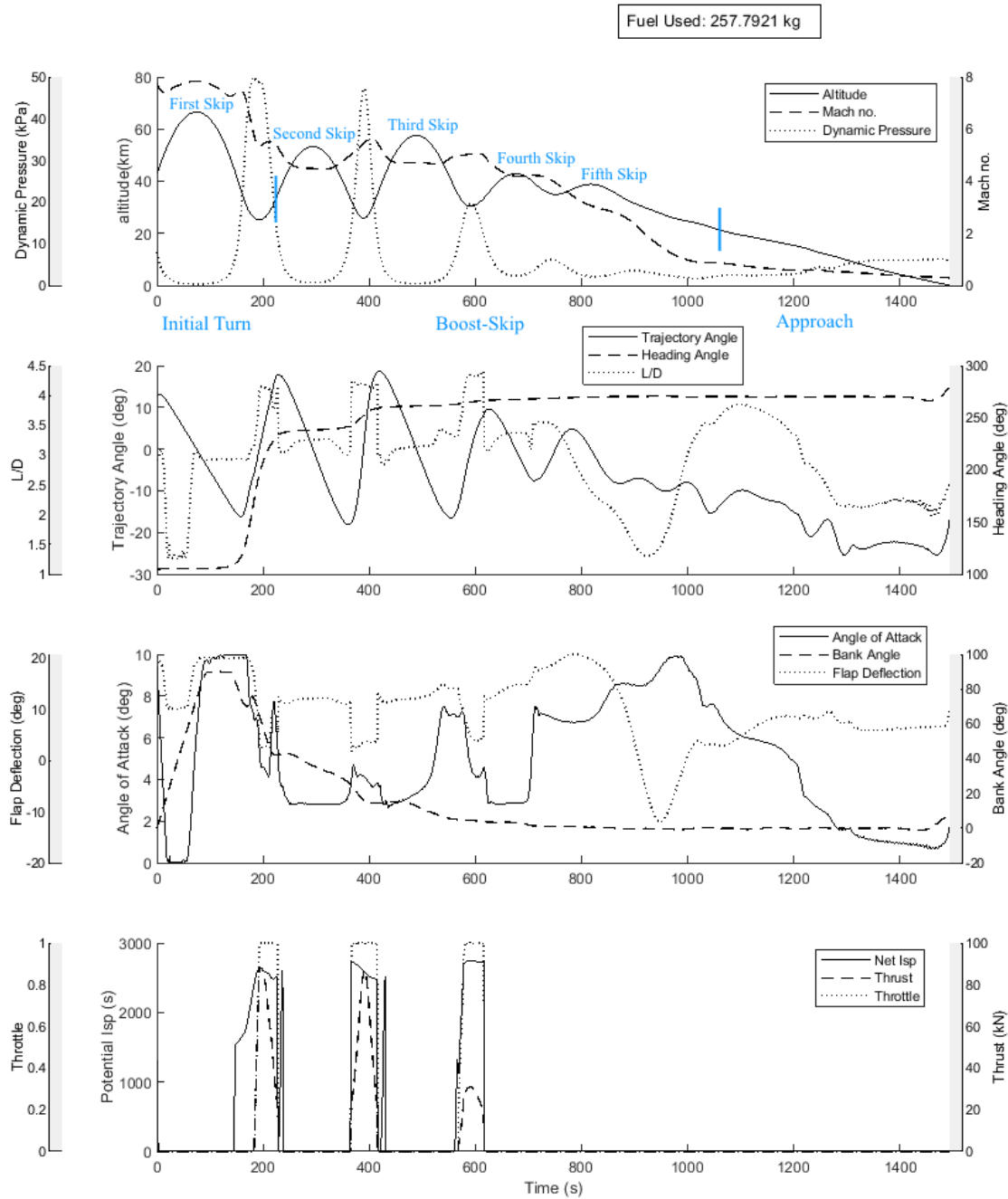


Figure 7.6: The fly-back trajectory of the scramjet accelerator flying an optimised maximum payload-to-orbit trajectory (Case 11).

7.3 Fly-Back Trajectory

The optimised fly-back trajectory for Case 11 is shown in Figure 7.6. The scramjet accelerator is shown to be capable of fly-back, using 257.8kg of fuel, 16.5% of the total fuel. Throughout its fly-back the scramjet accelerator performs distinct skipping manoeuvres, and ignites the scramjet engines a total of three times. These skips are consistent with previous research, which has shown that a periodic skipping trajectory increases the downrange distance achievable by hypersonic vehicles both during powered and unpowered flight[74, 85–88, 90, 91], and serve to reduce the fuel necessary for the return flight.

It is observed that the optimised trajectory exhibits characteristics which can be separated into three distinct segments; 1. initial turn, 2. boost-skip, and 3. approach, as indicated in Figure 7.6.

Initial Turn

The scramjet accelerator separates from the third stage rocket at a bank angle of 0° , and then increases its bank angle at close to the maximum change rate until 94.5s return flight time, at which point the maximum of 90.0° bank angle is reached. This high bank angle initially serves to decrease the lift of the scramjet accelerator, minimising the height of the first skip, with the angle of attack of the scramjet accelerator kept low. As the scramjet accelerator reaches the zenith of its initial skip, at 73.6s flight time and 66.5km altitude, the angle of attack is rapidly increased, up to the maximum of 10.0° , and shortly after the bank angle begins to decrease below its maximum. This increase in angle of attack and decrease in bank angle generates additional lift to slow the descent of the scramjet accelerator into the trough of the first skip, ensuring that the dynamic pressure limit is not exceeded. Although the bank angle is reduced from its maximum, a high bank angle is maintained as the scramjet accelerator descends out of its skip, beginning a sharp change in heading angle as the dynamic pressure increases. This early heading angle change serves to minimise the down-range distance flown, and reduce the fuel necessary for fly-back.

At 194.1s flight time, as the vehicle descends and dynamic pressure increases rapidly, the scramjet engines are ignited. The C-REST engines are powered-on in the trough between the first and second skips, at a point of high potential specific impulse, and initially burn for 33.8s. During the initial burn, the L/D of the scramjet accelerator increases significantly, due to the scramjet engine flow paths of the scramjet accelerator generating thrust, rather than drag. This increase in L/D raises the altitude of the scramjet accelerator and, along with heavy banking, changes the heading of the scramjet accelerator significantly. The burn is limited by the lower inlet dynamic pressure limit of the C-REST engines, of 20kPa, and terminates at 227.9s flight time.

Boost-Skip

After the initial burn ends, the angle of attack of the scramjet accelerator is decreased to 3.2° , and the scramjet accelerator executes its second skip. Once the scramjet accelerator is descending again, and as soon as the dynamic pressure is high enough for C-REST engine operation at **369.0s** return flight time, the scramjet engines are once again ignited. During the second burn, the angle of attack of the scramjet accelerator is increased, to modify the temperature and Mach number at the inlet of the C-REST engines so that the maximum specific impulse is obtained from the C-REST engines during the burn. The angle of attack varies between 4.7° to 3.7° during the second burn, and the L/D is once again raised significantly, initiating the third skip. This skip raises the altitude of the scramjet accelerator to **53.3km**, before it decreases once again. The third and last burn is initiated at **581.7s** and lasts until **615.9s**, when the remaining fuel has been depleted. Before the third burn, the angle of attack is **first increased up to 7.5° , and then decreased at the beginning of the burn, to a minimum of 4.1°** during the burn. The angle of attack values observed are similar to those observed during the second burn, indicating that these angle of attack values obtain a high specific impulse from the C-REST engines, this can be observed in Figure D.6, which shows the specific impulse profile of the return flight during the boost-skip phase.

After the third burn phase, the angle of attack is initially controlled so that the skipping trajectory of the scramjet accelerator is dampened. Immediately after the third burn phase, the angle of attack is reduced, to **2.84°** . This reduction coincides with the ascent portion of the fourth skip, reducing the lift, and the amount of altitude gained. As the zenith of the forth skip is reached, the angle of attack is increased to **7.5°** , increasing the lift, and once again slowing the descent. This high angle of attack is **increased until 984.9s, in stages corresponding with the descent of the last two small skips**. It is notable that the **angle of attack is controlled in this way during the unpowered portion of the trajectory, as it indicates that the skips are being damped**. This implies that some degree of skipping is desirable after the final scramjet burn, but that the angle of attack is being controlled to produce optimally sized skips.

Approach

After the final small skip, at **1046.0s** flight time, the angle of attack is adjusted, so that a gradual, controlled descent is initiated. After the skip phase, as the vehicle is approaching Mach 1, the angle of attack is reduced gradually to bring the scramjet accelerator down below 1km altitude, in a controlled manner. At **1455.0s**, the bank angle is increased, in order to perform a final adjustment of the heading angle, to bring the scramjet accelerator to the desired end location. The scramjet accelerator drops below 1km altitude at **-17.0°** trajectory angle and a speed of **95.2m/s** (Mach 0.28). It is assumed that the scramjet accelerator is able to perform a landing manoeuvre after this point.

7.4 Case 11: Modelling of Uncertainties

A Monte-Carlo study is conducted, using the same uncertainty magnitudes as in Section 6.3, with more detail available in Appendix B.1.3. A confidence interval of 6.8-233.6kg in payload-to-orbit is calculated from this Monte-Carlo study using 97.5% percentile limits. This confidence interval is similar in magnitude to the confidence interval with no fly-back presented in Section 6.3, and similarly illustrates the relatively large uncertainties present due to possible variations in launch system performance. Once again, however, this interval is entirely positive, indicating that it is likely that some payload-to-orbit can be achieved.

7.5 Case 11: Aerothermal Heating Analysis

The aerothermal heating on the scramjet accelerator and third stage rocket during flight has been investigated in Appendix A. On the scramjet accelerator, the temperature on the windward surfaces of the tungsten nose and the Carbon-Carbon wing leading edge reach 2015.1K and 1665.8K respectively. These locations are assumed to have no direct thermal connection to the internal insulation, and the temperatures that have been observed are within the operational regimes of the external heat shielding materials, which for the purposes of this study are considered sufficient for shielding during flight. Various locations on the body of the scramjet accelerator are investigated, with the interior heat shield surfaces of the nose cone reaching a maximum of 1363.1K, the cowl 1384.9K, the wing 1326.4K, and the tail 1142.3K. These temperatures are well within the operational regime of the C-C external heat shielding material, although the internal temperatures are at the limits of the operational regime of the internal multilayer insulation, which is nominally designed for operation in the 900-1100°C (1173-1373K) range. Temperatures on the nose and body of the third stage rocket are investigated and found to be significantly lower than those experienced by the scramjet accelerator. The nose tip of the third stage reaches a maximum inner surface temperature of 953.5K, while the nose cone and body reach maximum temperatures of 475.9K and 779.8K respectively. These relatively low temperatures indicate that the current heat shielding design is likely appropriate for resisting the thermal loading experienced by the third stage rocket.

7.6 Energy Usage Analysis

An energy usage analysis is conducted for Case 11; a maximum payload-to-orbit trajectory, including the fly-back of the scramjet accelerator. This is compared to the energy usage breakdown of Case 2; the optimised trajectory without the fly-back of the scramjet accelerator in Table 7.2. Similarly to Section 6.4, the energy used to accelerate the payload is shown, along with the energy imparted to the successive stages; the energy used overcoming drag; the energy used imparting energy to the structural mass of each stage, which is separated; and the energy lost due to propulsion inefficiency.

	Case 2	Case 11
Trajectory Condition	No Fly-Back	With Fly-Back
First Stage Fuel Exergy	201.91 GJ	201.91 GJ
KE + PE of Payload	0.11% (0.22 GJ)	0.09% (0.19 GJ)
KE + PE of 2 nd & 3 rd Stage	6.76% (13.66 GJ)	6.83% (13.79 GJ)
Overcoming Drag	2.49% (5.03 GJ)	2.41% (4.87 GJ)
KE + PE of 1 st Stage Structural Mass	1.01% (2.04 GJ)	1.02% (2.06 GJ)
KE + PE of 1 st Stage Fuel Mass	2.67% (5.39 GJ)	2.68% (5.41 GJ)
Availability Losses	89.62% (180.95 GJ)	89.64% (181.00 GJ)
Scramjet Accelerator Fuel Exergy	187.38 GJ	156.45 GJ
KE + PE of Payload	0.21% (0.39 GJ)	0.18% (0.28 GJ)
KE + PE of 3 rd Stage	4.19% (7.85 GJ)	4.32% (6.76 GJ)
Overcoming Drag	20.42% (38.26 GJ)	21.45% (33.56 GJ)
KE + PE of Scramjet Accelerator Structural Mass	6.61% (12.39 GJ)	6.76% (10.58 GJ)
KE + PE of scramjet accelerator Fuel Mass	1.33% (2.49 GJ)	1.45% (2.27 GJ)
Propulsion Inefficiency	67.25% (126.01 GJ)	65.84% (103.00 GJ)
Return Fuel Exergy	-	30.92 GJ
KE + PE of Scramjet Accelerator Structural Mass	-	-56.94% (-17.61 GJ)
Overcoming Drag	-	95.30% (29.47 GJ)
KE + PE of scramjet accelerator Fuel Mass	-	-1.65% (-0.51 GJ)
Availability Losses	-	63.29% (19.56 GJ)
Third Stage Fuel Exergy	16.78 GJ	18.69 GJ
KE + PE of Payload	4.37% (0.73 GJ)	3.84% (0.72 GJ)
Overcoming Drag	0.68% (0.11 GJ)	0.62% (0.12 GJ)
KE + PE of 3 rd Stage Structural Mass	7.96% (1.34 GJ)	8.40% (1.57 GJ)
KE + PE of 3 rd Stage Fuel Mass	55.29% (9.28 GJ)	55.12% (10.30 GJ)
KE + PE of Heat Shield	7.28% (1.22 GJ)	7.54% (1.41 GJ)
Availability Losses	24.42% (4.10 GJ)	24.48% (4.58 GJ)
Circularisation and Hohman Transfer Fuel Exergy	19.06 GJ	17.45 GJ
KE + PE of Payload	24.12% (4.60 GJ)	21.96% (3.83 GJ)
All Other Energy Losses	75.88% (14.46 GJ)	78.04% (13.62 GJ)

Table 7.2: An energy usage breakdown of the ascent trajectories, both with, and without, scramjet accelerator fly-back (Cases 11 & 2). Blue indicates a 'productive' energy usage, whereas red indicates energy 'wastage'. Negative energy indicates energy being supplied.

The fly-back of the scramjet accelerator reduces the fuel, and thus the fuel exergy, available to the scramjet accelerator during ascent. This lower exergy, along with the altered manoeuvrability needs of the scramjet accelerator when the fly-back is included, results in a raising of the altitude and trajectory angle at the first-second stage separation. The increased altitude and trajectory angle at separation increases the fuel mass that the first stage rocket is able to use efficiently, and also increases the exergy efficiency of the first stage, partly compensating for the decrease in the efficiency of the scramjet accelerator due to fly-back. Overall, when the fly-back is included in Case 11, more of the exergy of the first stage is utilised imparting energy upon the combination of the payload and the

successive stages, at 6.92% (13.97 GJ), compared to 6.87% (13.87 GJ) without scramjet accelerator fly-back in Case 2. This is due to the rocket flying a more efficient trajectory, with lower drag and higher propulsive efficiency, terminating at a higher altitude and speed.

When flying a trajectory where the scramjet accelerator's fly-back is included, the drag losses during the ascent of the scramjet accelerator consist of a larger percentage of the ascent fuel exergy usage (21.45%, compared to 20.42% without fly-back). This is despite the lower velocity range over which the scramjet accelerator is accelerating when fly-back is included, and is due to the less favourable first-second stage separation conditions, as well as the high banking throughout the acceleration requiring a higher angle of attack to maintain lift. The energy necessary to return the scramjet accelerator to its initial launch location is provided by both the fuel used during the return (30.92 GJ), as well as the kinetic and potential energy imparted upon the scramjet accelerator during its ascent. Significantly more energy is required to overcome drag during the return (29.47 GJ) than is available from the kinetic and potential energy of the scramjet accelerator (17.61 GJ), illustrating the necessity for igniting the scramjet engines during the return flight.

When the fly-back is included, the second-third stage separation occurs at a lower altitude and velocity, and the lower fuel exergy of the scramjet accelerator during its ascent results in less energy being imparted upon the payload and third stage by the scramjet accelerator (7.04 GJ), compared to the trajectory without fly-back (8.24 GJ). The lower, slower separation point when fly-back is included causes the losses of the third stage to increase from all sources, and for more energy to be used exiting the atmosphere.

7.7 Design Sensitivity Analysis

XXX I need to add something in third stage variations that talks generall about energy (see ingos email comments, and conclusion)

It has been shown that the fly-back of the scramjet accelerator has a significant effect on the performance of the rocket-scramjet-rocket launch system, and that the maximum payload-to-orbit optimised trajectory changes significantly to compensate for the additional requirement of successfully returning the scramjet accelerator stage. This section investigates the sensitivity of the launch system to changes in the vehicle design, with the fly-back of the scramjet accelerator included, **in order to investigate the response of the optimised trajectory to variations in the design of the launch system, and to inform future design decisions.** This sensitivity study varies the following parameters by $\pm 10\%$:

- Case 12: Dynamic Pressure,
- Case 13: Specific Impulse,
- Case 14: Scramjet Accelerator Drag,

- Case 15: Scramjet Accelerator Mass,
- Case 16: Scramjet Accelerator Fuel Mass,
- Case 17: Third Stage Mass,
- Case 18: Third Stage Thrust.

As in Section 6.5, the effect of third stage drag is negligible. For this reason, variation in the third stage drag is omitted in this section.

The launch system is able to successfully place a small satellite in orbit for every performance condition that has been tested, while returning the scramjet accelerator to its initial launch location for landing. Every maximum payload-to-orbit optimised trajectory exhibits considerable banking during the scramjet accelerator's ascent trajectory, as well as a pull-up of the scramjet accelerator before third stage release. In every case the optimised return flight path exhibits initial turn, boost-skip and approach phases.

There are two distinct return trajectory shapes for the return trajectory of the scramjet accelerator. The more common return trajectory shape has been shown in the preceding section, and consists of three or more large skips to begin the return trajectory. The second trajectory shape exhibits a small second skip, with the first two burns very closely spaced, or combined into one longer burn. An example of this second type of return trajectory is shown in Figure F.19. During the first two burns, a higher bank angle is maintained when compared to the large skip trajectory shape, however, after the first two burns are completed, the bank angle is reduced more rapidly. During simulations, it was observed that on occasion, the optimal return trajectory type would change as the initial guess or problem setup was altered, with no significant change in the payload-to-orbit capabilities of the launch system. This variability suggests that there is minimal difference between the two shapes of return trajectory, and that both can potentially lead to efficient return flights.

7.7.1 Case 12: Maximum Dynamic Pressure Sensitivity with Fly-Back

The maximum dynamic pressure allowable during flight is varied by $\pm 10\%$ in order to determine the sensitivity of the launch system to the structural and thermal limitations of the scramjet accelerator. Table 7.3 shows a summary of the key parameters of each optimised trajectory, and trajectory comparison plots are shown in Appendix F.2.1. The variation in each trajectory normalised to a one percent variation in the dynamic pressure is shown, if there is a clear trend. The payload-to-orbit of the launch system improves by +5.5kg (+4.2%) at 55kPa, and decreases by -22.2kg (-16.8%) at 45kPa. The overall exergy efficiency of the system increases as the maximum dynamic pressure increases, by +0.049% η at 55kPa, and decreases as the maximum dynamic pressure decreases, by -0.227% η at 45kpa. No significant variation is observed between sensitivity studies with or without the fly-back

Trajectory Condition	q_{max} :	45kPa	47.5kPa	50kPa	52.5kPa	55kPa	$\Delta/\Delta\%q_{max}$
Payload to Orbit (kg)		109.9	118.6	132.1	135.5	137.6	1.4
Total η_{exergy} (%)		1.351	1.458	1.578	1.606	1.627	0.00014
1st Stage η_{exergy} (%)		7.073	6.695	6.923	6.924	6.930	-
Separation Alt, 1→2 (km)		25.90	25.05	24.57	24.28	24.01	-0.09
Separation v, 1→2 (m/s)		1550	1505	1539	1541	1543	-
Separation γ, 1→2 (deg)		16.9	9.9	11.1	11.2	11.4	-
2nd Stage η_{exergy} (%)		3.648	3.517	3.758	3.796	3.815	-
Separation Alt, 2→3 (km)		37.46	41.07	42.87	42.82	42.73	-
Separation v, 2→3 (m/s)		2514	2439	2506	2515	2520	-
Separation γ, 2→3 (deg)		10.9	12.9	12.7	13.0	13.3	-
2nd Stage Flight Time (s)		597.5	552.9	506.9	493.7	483.8	-5.73
2nd Stage Distance Flown (km)		997.7	913.1	869.6	845.0	823.5	-8.33
2nd Stage Return Fuel (kg)		237.2	286.4	257.8	246.7	247.4	-
2nd Stage Return Distance (km)		1461.0	1495.8	1522.3	1507.0	1503.8	-
3rd Stage η_{exergy} (%)		10.883	11.806	13.141	13.480	13.689	0.146
3rd Stage $t, q > 5\text{kPa}$ (s)		24.4	10.3	7.7	6.9	7.7	-
3rd Stage Fuel Mass (kg)		2875.3	2866.6	2853.1	2849.7	2847.6	-1.44

Table 7.3: Comparison of key trajectory parameters with variation in the maximum dynamic pressure of the scramjet accelerator, with fly-back (Case 12).

included in the sensitivity of the launch system to the maximum dynamic pressure of the scramjet accelerator, by percentage.

When fly-back is included, no trends are observed in the exergy efficiencies of the first stage or scramjet accelerator due to maximum dynamic pressure variation. Compared to the sensitivity study with no fly-back in Section 6.5, the trade-offs between the efficiencies of the stages include the manoeuvrability of the scramjet accelerator, which dictates the fuel used during the return flight. This additional factor produces more complicated energy trade-offs, resulting in differing optimal trajectory shapes, with slightly different tradeoffs between the stages as the dynamic pressure is varied due to the nonlinearities in the different engine efficiencies and vehicle performances at each dynamic pressure limit. However, in all cases, increasing the maximum dynamic pressure improves the manoeuvring capabilities of the scramjet accelerator and increases the acceleration rate during ascent, which leads to a reduced flight time (-23.1s at 55kPa, and +90.6s at 45kPa), and less ground coverage (-46.1km at 55kPa, and +128.1km at 45kPa). Increasing the dynamic pressure limit generally allows for a higher scramjet accelerator-third stage release angle due to increased manoeuvrability. In all cases increasing the dynamic pressure limit increases the efficiency of the third stage rocket, also generally reducing the time that the third stage spends flying in greater than 5kPa dynamic pressure.

Trajectory Condition	$C_{d,2}$:	90%	95%	100%	105%	110%	$\Delta/\Delta\%C_{d,2}$
Payload to Orbit (kg)		149.4	140.1	132.1	123.3	113.6	-1.8
Total η_{exergy} (%)		1.733	1.653	1.578	1.490	1.371	-0.00018
1st Stage η_{exergy} (%)		7.291	7.102	6.923	6.739	6.676	-0.032
Separation Alt, 1→2 (km)		25.01	24.77	24.57	24.39	24.66	-
Separation v, 1→2 (m/s)		1584	1561	1539	1515	1505	-4.1
Separation γ, 1→2 (deg)		10.3	10.8	11.1	11.5	15.7	0.23
2nd Stage η_{exergy} (%)		4.107	3.921	3.758	3.580	3.311	-0.039
Separation Alt, 2→3 (km)		43.14	42.99	42.87	42.42	41.89	-0.06
Separation v, 2→3 (m/s)		2612	2557	2506	2452	2385	-11.17
Separation γ, 2→3 (deg)		12.2	12.4	12.7	13.0	13.6	0.07
2nd Stage Flight Time (s)		504.9	505.9	506.9	511.6	586.2	3.37
2nd Stage Distance Flown (km)		910.3	889.1	869.6	849.5	917.7	-
2nd Stage Return Fuel (kg)		228.1	249.0	257.8	253.6	196.5	-
2nd Stage Return Distance (km)		1642.5	1591.5	1522.3	1390.4	1161.2	-23.27
3rd Stage η_{exergy} (%)		14.837	13.929	13.141	12.275	11.327	-0.173
3rd Stage $t, q > 5\text{kpa}$ (s)		8.9	7.6	7.7	7.7	7.5	-
3rd Stage Fuel Mass (kg)		2835.8	2845.1	2853.1	2861.9	2871.6	1.77

Table 7.4: Comparison of key trajectory parameters with variation in the drag of the scramjet accelerator, with fly-back (Case 13).

7.7.2 Case 13: Scramjet Accelerator Drag Sensitivity with Fly-Back

The coefficient of drag is varied by $\pm 10\%$ to investigate the effect of variation in the aerodynamic design of the scramjet accelerator on the performance of the launch system, when the fly-back of the scramjet accelerator is included. Appendix F.2.2 presents trajectory comparison plots, and Table 7.4 compares key parameters of each trajectory. Increasing the drag of the scramjet accelerator by 10% decreases the payload-to-orbit by **-18.5kg (-14.0%)**, while decreasing the drag by 10% increases the payload-to-orbit by **+17.3kg (+13.1%)**. The sensitivity to variations in the scramjet accelerator's aerodynamics is decreased slightly when compared to the sensitivity study with no fly-back, down to **-1.8 $\frac{\Delta\text{kg}}{\Delta\%C_d}$** compared to **-2.0 $\frac{\Delta\text{kg}}{\Delta\%C_d}$** . This is due to the increased drag decreasing the total acceleration, which in turn decreases the ground distance necessary to cover during the fly-back, from 1642.5km at 90% drag, to 1161.2km at 110% drag, partially offsetting the detrimental effects of the increased drag on the performance of the launch system.

The exergy efficiencies of all three stages are decreased significantly as the drag of the scramjet accelerator is increased. This decrease in efficiency is due to the increased drag losses of the first stage and scramjet accelerator, 2.48% and 24.45% respectively at 110% C_D , compared to 2.27% and 19.98% respectively at 90% C_D , and the increased availability losses (due to propulsive inefficiency) of the third stage when released from a lower velocity, 27.78% at 110% C_D , compared to 22.62% at 90% C_D . As was observed in the drag sensitivity study with no fly-back in Section 6.5.2, the second-

third stage separation angle shows an increase as the drag is increased, by $+0.9^\circ$ ($+7.1\%$) at 110% drag, and decreasing by -0.5° (-3.9%) at 90% drag. In addition, the altitude of the second-third stage separation shows a clear trend, decreasing as the drag of the scramjet accelerator is increased, by -0.98km (-2.29%) at 110% drag, and increasing slightly as the drag is decreased, by $+0.27\text{km}$ ($+0.63\%$) at 90% drag. The release altitude and trajectory angle serve to initiate the first skip of the return trajectory in a consistent manner, so that the shape of the initial skip is very similar with drag variation. In all cases the angle of attack is reduced to 0° immediately during return to lessen the size of the initial skip, and is then raised to close to the maximum of 10° to prevent the dynamic pressure limit being exceeded. This consistency indicates that the initial skip of the return flight is driving the conditions at second-third stage release, and that it is primarily the control and structural limitations, rather than the aerodynamics of the scramjet accelerator, which determine the shape of this skip.

7.7.3 Case 14: C-REST Specific Impulse Sensitivity with Fly-Back

Trajectory Condition	$I_{SP,2}$:	90%	95%	100%	105%	110%	$\Delta/\Delta\%I_{SP,2}$
Payload to Orbit (kg)	114.6	123.4	132.1	139.6	148.3	1.7	
Total η_{exergy} (%)	1.414	1.498	1.578	1.651	1.733	0.00016	
1st Stage η_{exergy} (%)	6.927	6.930	6.923	6.899	6.896		-
Separation Alt, 1→2 (km)	24.58	24.58	24.57	24.57	24.56		-
Separation v, 1→2 (m/s)	1539	1540	1539	1536	1535		-
Separation γ, 1→2 (deg)	11.2	11.3	11.1	11.1	11.0		-
2nd Stage η_{exergy} (%)	3.265	3.506	3.758	3.990	4.240	0.049	
Separation Alt, 2→3 (km)	42.62	42.31	42.87	42.68	42.85		-
Separation v, 2→3 (m/s)	2393	2451	2506	2557	2611	10.83	
Separation γ, 2→3 (deg)	13.4	13.1	12.7	12.4	12.1	-0.06	
2nd Stage Flight Time (s)	507.4	507.5	506.9	509.0	509.9		-
2nd Stage Distance Flown (km)	827.4	849.2	869.6	888.6	908.6	4.04	
2nd Stage Return Fuel (kg)	275.2	268.8	257.8	255.6	247.0	-1.39	
2nd Stage Return Distance (km)	1419.2	1476.9	1522.3	1590.0	1645.2	11.3	
3rd Stage η_{exergy} (%)	11.422	12.287	13.141	13.876	14.727	0.164	
3rd Stage $t, q > 5\text{kpa}$ (s)	7.7	7.6	7.7	9.2	9.2		-
3rd Stage Fuel Mass (kg)	2870.6	2861.8	2853.1	2845.6	2836.9	-1.67	

Table 7.5: Comparison of key trajectory parameters with variation in the specific impulse of the C-REST engines, with fly-back (Case 14).

The specific impulse of the scramjet accelerator is varied by $\pm 10\%$ in order to assess the sensitivity of the optimised trajectory to the performance of the scramjet engines. Key parameters of the trajectories are summarised in Table 7.5, and comparison plots are shown in Appendix F.2.3. Raising the specific impulse of the C-REST engines increases the payload-to-orbit, by $+16.2\text{kg}$ ($+12.3\%$) at 110% I_{SP} , while lowering the specific impulse decreases the payload-to-orbit, by -17.5kg (-13.2%) at

90% I_{SP} . This produces a general trend in the payload-to-orbit of $1.7 \frac{\Delta kg}{\Delta \% I_{SP}}$, lower than the trend of $2.2 \frac{\Delta kg}{\Delta \% I_{SP}}$ observed in the sensitivity study without fly-back, in Section 6.5.3. This lowered sensitivity in the payload-to-orbit is due to a correspondingly lowered sensitivity in the exergy efficiency of the scramjet accelerator, of $0.049 \frac{\Delta \% \eta}{\Delta \% I_{SP}}$, compared to $0.065 \frac{\Delta \% \eta}{\Delta \% I_{SP}}$ in the sensitivity study without fly-back. This lowered sensitivity is due to the modified I_{SP} having no effect on the performance of the scramjet accelerator during the unpowered portions of the fly-back trajectory, which serve to offset the overall variation in exergy efficiency.

Similarly to the specific impulse sensitivity study without fly-back conducted in Section 6.5.3, the first-second separation conditions, as well as the exergy efficiency of the first stage, exhibit no clear trends. Following first-second separation, the general shape of the trajectory path of the scramjet accelerator does not change significantly with specific impulse variation, including the the pull-up altitude. As with the optimised trajectories with no fly-back, increasing the specific impulse of the scramjet engines by 10% increases the velocity at separation (by +105m/s, +4.2%) and decreases the trajectory angle (by -0.6°, -4.7%), while decreasing the specific impulse of the scramjet engines by 10% decreases the velocity at second-third stage separation (by -113m/s, -4.5%), and increases the trajectory angle (by 0.7°, +5.5%). The exergy efficiency of the third stage rocket increases as the exergy efficiency of the scramjet accelerator increases. This is in line with the trend which has been observed in all previous cases, that the increased separation velocity increases the propulsive efficiency of the third stage, in turn increasing its overall efficiency.

7.7.4 Case 15: Scramjet Accelerator Mass Sensitivity with Fly-Back

The mass of the scramjet accelerator is varied by ±10% to investigate the sensitivity of the launch system performance to the structural mass of the second stage, with the inclusion of scramjet accelerator fly-back. As in Section 6.5.4, the mass is varied by only ±10% in order to limit the variation in the velocity of the first-second stage separation. Table 7.6 details key parameters of each trajectory, and Appendix F.2.4 shows comparison plots. Varying the structural mass of the scramjet accelerator yields a change in maximum payload-mass to orbit of +12.6kg (+9.5%) at 90% mass, and -14.9kg (-11.3%) at 110% mass.

As observed in Section 6.5.4, increasing the structural mass of the scramjet accelerator generally decreases the altitude of first stage-scramjet accelerator separation, and decreases the velocity and trajectory angle. In addition, increasing the structural mass of the scramjet accelerator decreases the exergy efficiency of the first stage rocket, due to the first stage rocket not accelerating as quickly as the mass of the scramjet accelerator is increased, causing the propulsive efficiency of the first stage to decrease (illustrated by Equation 6.1). As was observed in Section 6.5.4, the lower velocity of first-second separation means that when the scramjet accelerator mass is increased, the velocity range over which the scramjet accelerator is accelerating is lower. This is beneficial for the specific

Trajectory Condition	$m_2:$	90%	95%	100%	105%	110%	$\Delta/\Delta\%m_2$
Payload to Orbit (kg)		144.7	138.4	132.1	124.1	117.2	-1.4
Total η_{exergy} (%)		1.697	1.639	1.578	1.499	1.402	-0.00015
1st Stage η_{exergy} (%)		7.095	7.017	6.923	6.793	6.776	-0.017
Separation Alt, 1→2 (km)		25.23	24.85	24.57	24.48	24.07	-0.05
Separation v, 1→2 (m/s)		1606	1573	1539	1499	1478	-6.64
Separation γ, 1→2 (deg)		10.4	10.9	11.1	11.4	13.0	0.11
2nd Stage η_{exergy} (%)		3.852	3.804	3.758	3.679	3.553	-0.014
Separation Alt, 2→3 (km)		43.29	42.63	42.87	41.92	41.47	-
Separation v, 2→3 (m/s)		2570	2540	2506	2467	2425	-7.26
Separation γ, 2→3 (deg)		12.7	12.7	12.7	12.8	13.0	-
2nd Stage Flight Time (s)		504.8	505.8	506.9	513.6	564.8	2.55
2nd Stage Distance Flown (km)		905.8	888.0	869.6	850.8	897.3	-
2nd Stage Return Fuel (kg)		246.2	253.5	257.8	254.5	186.9	-
2nd Stage Return Distance (km)		1600.1	1555.1	1522.3	1442.2	1203.5	-18.12
3rd Stage η_{exergy} (%)		14.388	13.767	13.141	12.354	11.676	-0.137
3rd Stage $t, q > 5\text{kpa}$ (s)		6.8	8.6	7.7	9.7	9.8	-
3rd Stage Fuel Mass (kg)		2840.5	2846.8	2853.1	2861.1	2868.0	1.39

Table 7.6: Comparison of key trajectory parameters with variation in the structural mass of the scramjet accelerator, with fly-back (Case 15).

impulse of the C-REST engines, which exhibit higher I_{SP} at lower velocities. For this reason, when the scramjet accelerator mass is increased, the net specific impulse of the scramjet accelerator stays high for longer in the main segment of the trajectory, above 500s I_{SP} for 441s of its trajectory at 110% mass, compared to 265s above 500s I_{SP} at 90% mass. However, the higher scramjet accelerator mass decreases the overall acceleration of the scramjet accelerator, in turn decreasing the efficiency of the third stage due to decreased propulsive efficiency.

7.7.5 Case 16: Scramjet Accelerator Fuel Mass Sensitivity with Fly-Back

The fuel mass of the scramjet accelerator is varied by $\pm 10\%$, to investigate the sensitivity of the performance of the launch system to variations in the size of the fuel tanks within the scramjet accelerator. Appendix F.2.5 shows plots comparing each trajectory, and Table 7.7 details comparisons of key trajectory parameters. When the fuel mass within the scramjet accelerator is increased by 10%, the payload to orbit increases by +6.4kg (+4.8%) and when the fuel mass is decreased by 10%, the payload mass reduces by -6.1g (-4.6%). The magnitude of the payload-to-orbit sensitivity is very similar to the sensitivity observed without fly-back, in Section 6.5.5, indicating that the addition of fly-back does not have a significant effect on the sensitivity of the launch system to variations in the fuel mass of the scramjet accelerator.

The first stage shows similar trends in its trajectory when the fuel mass of the scramjet accelerator

Trajectory Condition	$m_{f,2}$:	90%	95%	100%	105%	110%	$\Delta/\Delta\%m_{F,2}$
Payload to Orbit (kg)		126.0	128.5	132.1	134.8	138.5	0.6
Total η_{exergy} (%)		1.597	1.578	1.578	1.565	1.564	-
1st Stage η_{exergy} (%)		6.961	6.936	6.923	6.884	6.866	-0.005
Separation Alt, 1→2 (km)		24.73	24.65	24.57	24.48	24.40	-0.02
Separation v, 1→2 (m/s)		1558	1547	1539	1527	1518	-2.01
Separation γ, 1→2 (deg)		10.8	10.8	11.1	11.1	11.3	-
2nd Stage η_{exergy} (%)		3.917	3.821	3.758	3.690	3.646	-0.013
Separation Alt, 2→3 (km)		42.63	43.01	42.87	43.09	43.04	-
Separation v, 2→3 (m/s)		2466	2482	2506	2524	2549	4.14
Separation γ, 2→3 (deg)		13.0	12.8	12.7	12.6	12.4	-0.03
2nd Stage Flight Time (s)		463.5	483.8	506.9	526.9	551.1	4.37
2nd Stage Distance Flown (km)		773.2	816.0	869.6	914.4	971.2	9.89
2nd Stage Return Fuel (kg)		263.4	252.7	257.8	253.2	250.6	-
2nd Stage Return Distance (km)		1520.8	1477.6	1522.3	1511.8	1526.5	-
3rd Stage η_{exergy} (%)		12.542	12.790	13.141	13.404	13.767	0.061
3rd Stage $t, q > 5\text{kpa}$ (s)		7.6	7.6	7.7	7.7	8.8	0.05
3rd Stage Fuel Mass (kg)		2859.2	2856.7	2853.1	2850.4	2846.7	-0.63

Table 7.7: Comparison of key trajectory parameters with variation in the fuel mass of the scramjet accelerator, with fly-back (Case 16).

is varied to the trends observed with no fly-back in Section 6.5.5. As in Section 6.5.5, increasing the fuel mass of the scramjet accelerator decreases the exergy efficiency of the scramjet accelerator, by $-0.112\%\eta$ (-2.98%) at 110% fuel mass, and decreasing the fuel mass of the scramjet accelerator increases its exergy efficiency, by $+0.159\%\eta$ ($+4.23\%$) at 90% fuel mass. Once again, the overall exergy efficiency of the system shows no distinct trend. As in Section 6.5.5, this is due to the increased period of acceleration causing the specific impulse of the C-REST engines to decrease. However, the overall energy availability is increased by the additional fuel mass, resulting in more overall exergy. This results in the overall energy imparted upon the third stage by the scramjet accelerator increasing, from 6.606GJ at 90% m_f , to 7.516GJ at 110% m_f , in turn increasing the payload-to-orbit.

7.7.6 Case 17: Third Stage Mass Sensitivity with Fly-Back

The mass of the third stage rocket is varied by $\pm 10\%$, to investigate the effects of the internal mass density of the third stage rocket when the fly-back of the scramjet accelerator is included. Table 7.8 details key trajectory parameters, and Appendix F.2.6 shows trajectory comparison plots. As in Section 6.5.6, the varied mass is a combination of the fuel and structural mass of the third stage, and payload mass, representing the density of the components within the third stage. As previously, the heat shield mass is not varied, the structural mass held at 9% of the total, non-heat shield mass, and the remaining mass variation is a combination of fuel and payload mass.

Trajectory Condition	$m_3:$	90%	95%	100%	105%	110%	$\Delta/\Delta\%m_3$
Payload to Orbit (kg)		119.9	126.4	132.1	114.8	86.9	-
Total η_{exergy} (%)		1.506	1.546	1.578	1.377	1.068	-
1st Stage η_{exergy} (%)		7.039	6.978	6.923	6.860	6.798	-0.012
Separation Alt, 1→2 (km)		24.94	24.75	24.57	24.39	24.20	-0.04
Separation v, 1→2 (m/s)		1584	1561	1539	1516	1494	-4.48
Separation γ, 1→2 (deg)		10.6	10.8	11.1	11.4	11.5	0.05
2nd Stage η_{exergy} (%)		3.451	3.605	3.758	4.105	4.744	0.062
Separation Alt, 2→3 (km)		42.92	42.94	42.87	36.67	32.93	-
Separation v, 2→3 (m/s)		2552	2528	2506	2550	2638	-
Separation γ, 2→3 (deg)		12.5	12.6	12.7	10.7	3.3	-
2nd Stage Flight Time (s)		501.8	503.6	506.9	505.2	526.0	-
2nd Stage Distance Flown (km)		886.3	876.0	869.6	853.5	888.2	-
2nd Stage Return Fuel (kg)		254.1	255.2	257.8	240.7	192.8	-
2nd Stage Return Distance (km)		1545.7	1534.4	1522.3	1447.2	1175.0	-16.57
3rd Stage η_{exergy} (%)		13.235	13.226	13.141	10.804	7.683	-0.271
3rd Stage $t, q > 5\text{kpa}$ (s)		9.0	8.0	7.7	28.1	155.4	-
3rd Stage Fuel Mass (kg)		2561.4	2706.9	2853.1	3022.4	3202.2	31.94

Table 7.8: Comparison of key trajectory parameters with variation in the mass of the third stage, with fly-back (Case 17).

As was observed in Section 6.5.6, there is a non-linear payload mass-to-orbit trend with variations in the third stage mass. Once again, when the third stage mass is reduced, the payload mass is reduced, by -12.2kg (-9.2%), and when the third stage mass is increased, the payload mass is also reduced, by a larger -45.2kg (-34.2%). Once again, the pull-up of the scramjet accelerator is relatively consistent when the third stage mass is reduced, but is lowered significantly when the third stage mass is increased, as the second stage must compensate for the additional mass of the third stage. The magnitude of the response is very similar to the sensitivities with no fly-back, indicating that the fly-back does not significantly effect the sensitivity of the launch system performance with variations in the mass of the third stage rocket.

7.7.7 Case 18: Third Stage Specific Impulse Sensitivity with Fly-Back

The specific impulse of the third stage rocket is varied by $\pm 10\%$ to investigate the sensitivity of the launch system to the performance of the third stage rocket, when the fly-back of the scramjet accelerator is included. Table 7.9 shows selected performance indicators, while Appendix F.2.7 shows comparison plots of the maximum payload-to-orbit trajectory at each third stage specific impulse. Negative payload-to-orbit is produced at 90% specific impulse, indicating that it is not possible for the third stage to reach the required orbit at this specific impulse.

The sensitivity of the optimal trajectory to the third stage specific impulse with scramjet accel-

Trajectory Condition	$I_{SP,3}$:	90%	95%	100%	105%	110%	$\Delta/\Delta\%I_{SP,3}$
Payload to Orbit (kg)		-5.6	84.2	132.1	176.8	222.5	11.0
Total η_{exergy} (%)		0.226	1.075	1.578	2.020	2.470	0.00109
1st Stage η_{exergy} (%)		6.921	7.108	6.923	6.904	6.913	-
Separation Alt, 1→2 (km)		24.57	26.34	24.57	24.56	24.56	-
Separation v, 1→2 (m/s)		1538	1552	1539	1536	1537	-
Separation γ, 1→2 (deg)		11.1	18.6	11.1	11.1	11.0	-
2nd Stage η_{exergy} (%)		4.373	3.562	3.758	3.761	3.787	-
Separation Alt, 2→3 (km)		32.53	42.02	42.87	42.06	42.56	-
Separation v, 2→3 (m/s)		2679	2480	2506	2508	2513	-
Separation γ, 2→3 (deg)		2.6	13.3	12.7	12.6	12.5	-
2nd Stage Flight Time (s)		514.0	606.2	506.9	505.5	505.3	-
2nd Stage Distance Flown (km)		892.4	996.8	869.6	863.7	866.5	-
2nd Stage Return Fuel (kg)		225.6	159.1	257.8	258.5	256.4	-
2nd Stage Return Distance (km)		1288.3	1230.9	1522.3	1514.5	1507.9	-
3rd Stage η_{exergy} (%)		-0.532	8.253	13.141	17.868	22.842	1.127
3rd Stage $t, q > 5\text{kpa}$ (s)		132.3	9.3	7.7	8.9	8.0	-
3rd Stage Fuel Mass (kg)		2990.8	2901.0	2853.1	2808.4	2762.7	-10.98

Table 7.9: Comparison of key trajectory parameters with variation in the specific impulse of the third stage, with fly-back (Case 18).

erator fly-back is very similar to that observed in the sensitivity study with no scramjet accelerator fly-back, in Section 6.5.7, with a sensitivity of $11.0 \frac{\Delta m_{payload}}{\Delta\%I_{SP,3}}$ variation in both cases. These similar sensitivities indicate that the fly-back does not considerably effect the sensitivity of the launch system to variations in the third stage specific impulse.

As observed in Section 6.5.7, there is a distinct cutoff as the specific impulse is lowered, at which the third stage no longer has the required performance to raise altitude consistently and exit the atmosphere effectively. Once again, the scramjet accelerator must compensate for the reduced third stage performance by lowering the pull-up at the end of its trajectory, increasing the velocity and decreasing the trajectory angle at separation so that a greater velocity is achieved at separation and the aerodynamics of the third stage are used more extensively.

7.8 Comparison of Design Parameters with Fly-Back

XXX updated prior to 8/1 when discrepancies were found in results. it appears that the mass sensitivity used was wrong, need to redo.

The sensitivities of the performance of the launch system, including the fly-back of the scramjet accelerator, to a variety of design parameters have been presented in the preceding sections. Figure 7.7 shows a relative comparison of the payload-to-orbit sensitivity for each design parameter, normalised to a one percent variation in each respective parameter. The magnitude of each sensitivity is also

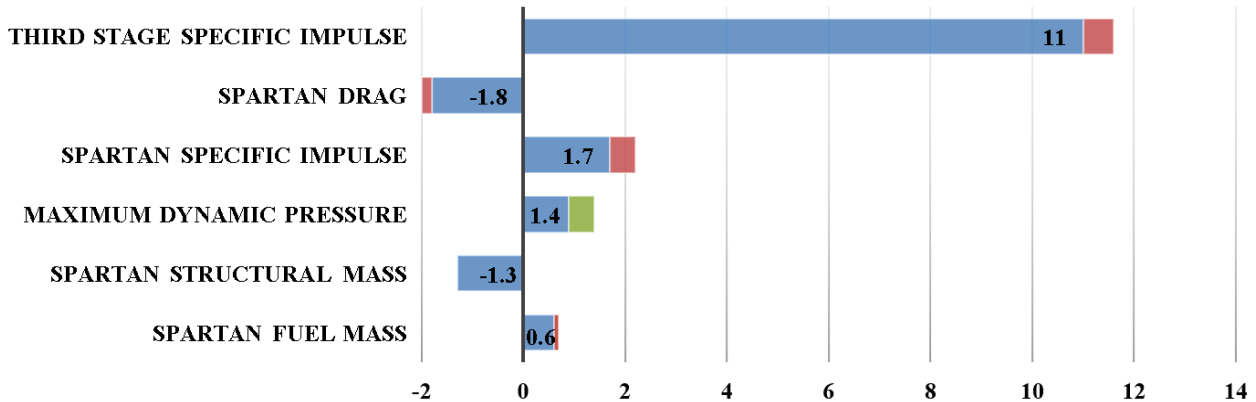
Payload Variation (kg) Normalised to a 1% Parameter Variation


Figure 7.7: The sensitivity of the key design parameters of the launch system, including scramjet accelerator fly-back. Red and green coloured areas indicate decreases or increases in the magnitude of sensitivity respectively, compared to the sensitivity study without scramjet accelerator fly-back in Section 6.6.

compared with the sensitivity of the launch system performance without fly-back, detailed in Section 6.6.

The sensitivity of the launch system to the **structural mass of the scramjet accelerator** is unchanged when fly-back is included. However, the increase in the sensitivity of the launch system to the **maximum allowable dynamic pressure**, to $1.4 \frac{\Delta kg}{\Delta \% q_{max}}$, means that the potential beneficial effects of reducing the maximum dynamic pressure of the scramjet accelerator are increased. So long as the mass of the scramjet accelerator is **increased** by less than 114.4kg for each 1kPa **increase** in the maximum dynamic pressure, the performance of the launch system will improve. The sensitivity of the launch system to the specific impulse of the scramjet accelerator is decreased significantly when the fly-back of the scramjet accelerator is included, to $1.7 \frac{\Delta kg}{\Delta \% I_{SP,scramjetaccelerator}}$, a decrease of $-0.5 \frac{\Delta kg}{\Delta \% I_{SP,scramjetaccelerator}}$ (-22.7%) compared to the sensitivity without fly-back, while the sensitivity of the launch system to the scramjet accelerator's structural mass is unchanged, at $-1.3 \frac{\Delta kg}{\Delta \% m_{scramjetaccelerator}}$. Comparing these sensitivities, it is apparent that if the specific impulse of the scramjet accelerator can be increased by 1% with less than 106.7kg increase in the structural mass of the scramjet accelerator, then the overall performance of the launch system will be improved. Similarly, the sensitivity of the launch system to variation in the drag of the scramjet accelerator is reduced, to $-1.8 \frac{\Delta kg}{\Delta \% C_{d,scramjetaccelerator}}$. Comparing this sensitivity with the sensitivity to the **C-REST specific impulse**, the specific impulse of the C-REST engines must be improved by 1% while increasing the drag of the scramjet accelerator by less than 0.9% due to shape variation, in order for the overall performance change to be beneficial.

The **unchanged** sensitivity of the launch system performance to the structural mass of the scramjet accelerator, along with the decreased fuel mass sensitivity, means that so long as 1kg of fuel mass

can be added with less than 1.5kg of structural mass added, the performance of the launch system will improve. Additionally, the decreased sensitivity of the launch system to the drag of the scramjet accelerator means that so long as 1kg of fuel can be added to the scramjet accelerator, with a drag increase of less than 0.021% due to increased size, then the maximum payload-to-orbit will increase (assuming lift is unchanged).

Once again, the payload variation effect of the third stage specific impulse is very high, at $11.6 \frac{\Delta kg}{\Delta \% I_{SP,3}}$. However the variation of the specific impulse by even small amounts will require modifications to the engine and rocket internals, varying the mass and internal space requirements significantly.

7.9 Summary

In this chapter, the maximum payload-to-orbit trajectory for the representative rocket-scramjet-rocket system has been calculated, with the inclusion of the fly-back of the scramjet accelerator stage. It was found that this launch system is able to deliver 132.1kg of payload to sun synchronous orbit (with a 97.5% confidence interval of 6.8-233.6kg), while successfully returning the scramjet-powered stage to the initial launch site. This return flight decreases the nominal payload-to-orbit by -24.3kg (-15.5%), but removes the need for the costly and time consuming transportation of the scramjet accelerator after launch that would be necessary if landing at a downrange location. During the return flight, the scramjet engines are powered on three times, in total using 257.8kg of fuel for the return flight, 16.5% of the scramjet accelerator's total fuel.

It was found that when the fly-back of the scramjet accelerator is included in the optimal trajectory calculation, the first stage of the launch system pitches in an easterly direction. The launch system exhibits a first-second separation point of 24.57km and a trajectory angle of 11.1°, similar to the maximum payload-to-orbit trajectory with no fly-back. In addition to increasing exergy efficiency of the first stage, when the return flight is included the higher first-second separation point allows the scramjet accelerator time to increase its bank angle, so that when the scramjet accelerator descends to high dynamic pressure it is able to change its heading angle rapidly. The scramjet accelerator maintains a high bank angle throughout its trajectory, executing a banking manoeuvre, and staying close to its maximum dynamic pressure. This banking manoeuvre requires higher angles of attack, increasing the drag of the scramjet accelerator, but also reduces the ground distance necessary for the return of the scramjet accelerator, decreasing the amount of fuel necessary for fly-back and increasing the overall efficiency of the scramjet accelerator. At the end of its acceleration, the scramjet accelerator was found to exhibit a pull-up manoeuvre before the separation of the third stage, in a similar fashion to the maximum payload-to-orbit trajectory with no fly-back.

The fly-back of the scramjet accelerator is found to be separated into three stages; an initial turn, a boost phase, and an approach. The initial turn takes place immediately after separation, and consists of the scramjet accelerator banking heavily in order to manoeuvre the heading angle back towards the

initial launch site. During the boost-skip phase the scramjet accelerator exhibits multiple ‘skipping’ manoeuvres. These skipping manoeuvres have been shown in previous literature to extend the flight range of hypersonic vehicles[74, 85–88, 90, 91], and serve to reduce the amount of fuel used during the fly-back. In addition, the skipping manoeuvres allow the scramjet engines to be powered on at the points where the specific impulse of the C-REST engines are highest, maximising the performance of the scramjet accelerator, and minimising the fuel necessary for return. During the approach phase, the trajectory of the scramjet accelerator is smoothed, and the scramjet accelerator glides to the landing point. The optimal trajectory terminates when scramjet accelerator reaches 0.1km altitude at a velocity of 95.2m/s. After this point, it is assumed that the scramjet accelerator lands on a traditional runway. This result indicates that it is feasible to return a hypersonic launch vehicle separated at a high Mach number to its initial launch site, and that a cost efficient mission profile for a rocket-scramjet-rocket launch system is attainable.

The sensitivity of the launch system to various design parameters has been investigated. The payload-to-orbit sensitivity of the launch system to variations in the specific impulse, drag, structural mass and fuel mass of the scramjet accelerator was found to decrease when fly-back is included, compared to the sensitivity study with no fly-back. This decreased sensitivity indicates that the fly-back of the scramjet accelerator offsets some of the payload-to-orbit variation due to changes in these parameters, particularly due to increased velocity at third stage separation or down-range distance making the return flight of the scramjet accelerator more difficult. However, the sensitivity to the maximum dynamic pressure was found to increase, due to the more rapid fuel use when dynamic pressure is increased lowering the flight time of the scramjet accelerator, in turn reducing the distance flown during return. Decreased performance of the third stage was found to affect the second-third stage separation point significantly, past a certain point. This indicates that when the third stage performs poorly, the performance trade-off between the scramjet accelerator and third stage shifts in favour of the scramjet accelerator, so that the scramjet accelerator prioritises flying a more efficient trajectory, rather than delivering the third stage to a higher release point.

CHAPTER 8

CONCLUSIONS

XXX Add sentence about how when the third stage performance is decreased, the scramjet accelerator compensates

The purpose of this work was to aid in the development of multi-stage airbreathing launch systems by designing and investigating the optimal launch trajectory of a partially-reusable, rocket-scramjet-rocket, small satellite launch system. In order to calculate this trajectory, the design of a representative rocket-scramjet-rocket launch system for small satellite launch was developed, and modelled in sufficient detail to allow insight into three-stage-to-orbit airbreathing launch systems to be generated. This launch system design was based on the SPARTAN scramjet-powered accelerator, in development by The University of Queensland and Hypersonix. The engine performance, aerodynamics, controls, and mass model of the launch system were calculated, and integrated into a software package that was created to simulate and optimise launch system trajectories. This software package was designated LODESTAR, and was based on the generic GPOPS-2 program, a pseudospectral method optimal control solver. LODESTAR was designed to simulate the trajectory of each stage of the launch system in a geodetic rotational reference frame, optimising the entire trajectory of the launch system simultaneously for maximum payload-to-orbit, so that the performance trade-offs between the stages are captured accurately.

Ascent-Only Trajectory

Optimised trajectories were simulated using the representative launch system for maximum payload-to-orbit, achieving the first optimal launch trajectories that have been calculated for an airbreathing three-stage launch system. Using pseudospectral optimisation, LODESTAR was able to calculate trajectories that were non-intuitive, removing the need for trial and error, and allowing insights into the performance of the rocket-scramjet-rocket launch system. The lack of constraints applied at the staging points (as well as a general lack of constraints other than performance limits throughout the trajectory) allowed for a holistic investigation of the optimal trajectory, and in particular for optimal

trade-offs between the stages to be determined. Initially, the trajectory of the launch system was developed with the assumption that the scramjet accelerator lands at a location downrange (see Case 2, Chapter 6). The maximum payload-to-orbit optimal trajectory was compared to a trajectory where the scramjet accelerator was constrained to fly at its maximum of 50kPa dynamic pressure (Case 1, Chapter 6), a common assumption for the maximum efficiency trajectory for airbreathing launch systems. The maximum payload-to-orbit trajectory of the launch system was found to be capable of delivering 156.4kg of payload to sun synchronous orbit (with a 97.5% confidence interval of 8.8-238.8kg), an increase of 59.1% over the simulation with the scramjet accelerator constrained to constant dynamic pressure. For the maximum payload-to-orbit trajectory the scramjet accelerator was still observed to fly close to its maximum dynamic pressure for the majority of scramjet engine operation, however, three key features were observed in the trajectory that were not present in a trajectory constrained to constant dynamic pressure; an altitude raising manoeuvre in the centre of the scramjet accelerator's trajectory, a higher first stage-scramjet accelerator separation point, and a pull-up before scramjet accelerator-third stage separation.

The altitude raising manoeuvre in the centre of the scramjet accelerator's trajectory was observed to occur in a region of relative homogeneity in the performance of the scramjet accelerator, increasing the efficiency of the scramjet accelerator by +0.3%. This indicates that the optimal performance of the scramjet accelerator vehicle may not always be achieved at maximum dynamic pressure. However, the effect of this altitude raising on maximum payload-to-orbit is small, and it is the stage separation points that have the most effect on the performance of the launch system. The higher first stage-scramjet accelerator separation point is unique to a three-stage launch system, and was found to decrease the amount of turning that must be performed by the first stage, reducing the necessary throttling and increasing the efficiency of the first stage. However, this higher separation point initially causes the altitude of the scramjet accelerator to increase, and the scramjet accelerator must manoeuvre itself to its maximum dynamic pressure at the beginning of its trajectory, resulting in decreased aerodynamic performance. This indicates that the result of this higher separation point is an efficiency trade-off between the stages, where the optimal separation point maximises the efficiency of both stages in concert. This trade-off is also present in the final, and most important, manoeuvre; the pull-up before the scramjet accelerator-third stage separation. This manoeuvre decreases the amount of turning which the third stage must perform, and enables the third stage to gain altitude much more rapidly, causing it to spend significantly less flight time at high dynamic pressure. This reduced exposure to high dynamic pressure reduces the energy losses due to the aerodynamic drag of the third stage, as well as reducing the amount of energy imparted upon the heat shield, by allowing it to be jettisoned earlier. This pull-up is similar to the pull-up observed in some two-stage systems, with scramjet-rocket transition occurring at a much lower altitude than was observed in single-stage systems. However, this is the first time that a pull-up under airbreathing operation after a mostly constant dynamic pressure trajectory has been explicitly shown to maximise performance in a multi-stage

launch system.

The manoeuvres at the stage separations were performed in order to utilise the superior aerodynamic performance of the scramjet accelerator stage, and were found to result in the exergy efficiency of the scramjet accelerator decreasing by $-0.719\%\eta$ (-14.04%). However, this reduction in the efficiency of the scramjet accelerator is a trade-off for increases in the exergy efficiencies of the first and third stages, of $+0.623\%\eta$ (+9.96%) and $+6.013\%\eta$ (+63.20%) respectively, resulting in a significantly higher overall efficiency. These deviations from maximum dynamic pressure indicate that it is imperative to design the scramjet engines of a three-stage launch system to be operable at low dynamic pressure, and at high angle of attack, and that the scramjet accelerator vehicle must be designed with manoeuvrability and controllability in mind.

Ascent and Fly-Back Trajectory

The fly-back of the scramjet accelerator to the initial launch site after the separation of the third stage was included in the problem definition, and maximum payload-to-orbit trajectories calculated. It was found that the launch system is capable of delivering 132.1kg of payload to sun synchronous orbit (with a 97.5% confidence interval of 6.8-233.6kg), while successfully returning the scramjet accelerator to its initial launch site. This optimal trajectory generates new knowledge for airbreathing launch systems incorporating fly-back, and shows that it is feasible to return a scramjet-powered accelerator to its initial launch site under only scramjet power, the first time that this has been shown for a multi-stage launch system, with only a relatively small (-15.5%) reduction in the payload mass-to-orbit. The inclusion of the fly-back of the scramjet accelerator was found to alter the shape of the ascent trajectory significantly: Altitude-raising manoeuvres before the stage separations were still performed, of similar magnitudes to the manoeuvres performed with no fly-back, however, a significant heading change was performed during launch to minimise the distance required to fly-back, requiring heavy banking during the operation of the scramjet accelerator. The optimal fly-back of the scramjet accelerator required the ignition of the scramjet engines, and was observed to exhibit three distinct phases, an initial turn, a boost-skip, and an approach. These manoeuvres serve to increase the range of the scramjet accelerator during its return, minimising the fuel necessary for the fly-back by allowing efficient heading changes, improving the specific impulse of the scramjet engines during operation, and enhancing the aerodynamic efficiency during return. In total, 257.8kg of fuel was used during the fly-back, 16.5% of the scramjet accelerator's total fuel mass. The multiple restarts observed during the return trajectory indicate the importance of being able to restart the scramjet engines rapidly, and both the ascent and return trajectories further emphasise the need for the scramjet accelerator stage to be manoeuvrable and controllable.

Design and Performance Investigation

After the optimised trajectories were calculated, eight key design parameters of the launch system were modified, and the sensitivities of the maximum payload-to-orbit trajectory studied in order to assess the sensitivity of the optimised trajectory, and predict how design changes may affect the performance of three-stage airbreathing launch systems, similar to the representative launch system utilised in this study. The parameters varied were; the maximum dynamic pressure of the scramjet accelerator; the drag coefficients of the scramjet accelerator and third stage; the specific impulses of the scramjet accelerator and third stage; and the structural and fuel masses of the scramjet accelerator and the third stage. These parameters were varied for trajectories both with and without scramjet accelerator fly-back. When the fly-back was included, the sensitivity to most design parameters was observed to decrease due to the fly-back distance counteracting some of the effects of the design variations. However, the sensitivity to maximum dynamic pressure was observed to significantly increase, as the complex coupled nature of the ascent and fly-back meant that the maximum dynamic pressure had a more prominent effect on the overall trajectory.

It was found that the ability of the first stage to pitch, determined by the acceleration of the launch system, is the primary driver of the first stage-scramjet accelerator separation conditions. When the efficiency of the scramjet accelerator was increased, the efficiency of the third stage was also observed to increase, and vice versa. The exception to this trend was found when the fuel mass of either stage was varied, resulting in a larger mass and decreased efficiency, but a higher total exergy. When the performance of the third stage was decreased past a certain point, the trade-off between the third stage and the scramjet accelerator was found to shift towards the scramjet accelerator. Third stages with poor performance were separated at a very low and level release point in order to maximise the efficiency of the scramjet accelerator, and thus the energy imparted on the third stage before release. However this additional energy was mostly imparted as kinetic energy, and the third stage was relied upon to use its aerodynamics to pull-up out of the atmosphere. This trade-off resulted in a distinct drop-off in overall performance, indicating that achieving suitable second-third stage performance trade-offs for a pull-up manoeuvre to be feasible is crucial for the efficient operation of a launch system of this type. Comparing the sensitivities of significantly coupled design parameters allowed the effects of the modified design parameters to be quantified, and it was found that the relationship between the maximum dynamic pressure and the structural mass of the scramjet accelerator was of particular interest. The sensitivity of the launch system to the maximum dynamic pressure of the scramjet accelerator was found to be relatively low, indicating that it may be advantageous to design the scramjet accelerator to fly at a lower maximum dynamic pressure in order to reduce heat shielding and structural mass.

The maximum payload-to-orbit trajectory profiles that have been developed are non-intuitive, involving complex trade-offs between the efficiencies of each stage of the launch system, as well as

the fly-back of the scramjet accelerator. The design of these optimised flight paths is made possible through the use of the pseudospectral method of optimal control, coupled with accurate and robust propulsion and aerodynamic modelling. The trajectory profiles and analyses that have been developed in this work can be used to inform and give insight into the flight paths of future launch systems, and can assist in directing future design decisions for airbreathing, multi-stage launch systems.

CHAPTER 9

RECOMMENDATIONS FOR FUTURE WORK

This work was carried out to inform future launch vehicle designs by determining the behaviour and sensitivities of such a launch system. Although a representative launch system for performance assessment was created, it was not the intent of this work to assert that this launch system is anything more than a preliminary design, nor to make significant design modifications based on the optimised trajectory results. As such, a number of improvements to the design of the launch system as well as some outstanding research questions were identified during the course of this work. In order to build upon this work and advance our knowledge of reusable, partially-airbreathing launch systems, the following research directions are suggested:

Design of a fly-back first stage booster.

During this work, the first stage booster is assumed to be expendable, to enable a simple design process. However, in the future it is likely that the first stage of the launch system will be required to be reusable for the launch system to be economically feasible. As such, a first stage booster must be designed and sized to be capable of accelerating the scramjet accelerator to operational speeds, as well as returning to the initial launch site after separation at Mach 5.

Further three-stage launch system design.

The development and characterisation of the maximum payload-to-orbit trajectory of a rocket-scramjet-rocket launch system paves the way for a detailed design optimisation of all three stages concurrently. While some analysis of the potential design impacts of the payload-to-orbit optimised trajectory on the launch system design was carried out in this work, a full redesign and analysis of the representative three-stage launch system was outside the scope of this study. In addition, some of the design approximations used in this study are necessarily simplified. Future studies will need to be conducted that develop detailed launch system designs while making use of the trajectory shapes, interstage performance trade-offs, and design parameter sensitivities that have been investigated in this study.

These future design studies may either be in the form of multidisciplinary design optimisations, or detailed design studies, each of which will use the conclusions of this work differently.

Detailed internal design analysis of all stages.

This study necessarily utilises a simplified model for internal structures. However, this study has also found that it is necessary to fly a multi-stage airbreathing launch system close to its structural and thermal limits during a payload-to-orbit optimised trajectory. To ensure that a launch system of this type is being designed in a realisable manner, it will be necessary for future design studies to model the internals of all stages in detail, including layout, structural connections, and internal thermal management.

Detailed controllability analysis and control system design.

During this work the launch system was modelled in three degrees of freedom, and the angles of attack of the launch system stages were constrained to values that were estimated to represent the realistic control limits of each vehicle. However, it was observed that during the maximum payload-to-orbit, the scramjet accelerator and third stage rocket become aerodynamically unstable. A controllability study and detailed system design of all three stages is necessary to improve the accuracy of the vehicle simulation models, and to ensure that the launch system is able to operate effectively over its trajectory. This analysis and design will necessarily include an investigation of the centre of gravity and aerodynamics of the launch system, a six degree-of-freedom simulation of the launch system throughout its launch trajectory, the application of advanced controller designs, and the analysis and design of physical control systems that are able to satisfy the control requirements of the maximum payload-to-orbit trajectory.

Stage separation analysis and mechanism design.

The representative launch system studied in this work was designed to have the third stage rocket contained within the scramjet accelerator, and was assumed to have instantaneous, controlled separation at both the first-second and second-third stage separation points. Future detailed design studies must necessarily investigate the mechanics of these stage separations, including detailed designs of the mechanisms of the separation, high fidelity analysis of the aerodynamics and control during separation, and analysis of post-separation consequences.

Cost analysis of the launch system.

A primary driver for a realistic launch system is its overall performance, as a function of payload-to-orbit, launch flexibility, and launch cost. In order for three-stage airbreathing launch systems to be properly characterised, a bottom-up cost model estimate is necessary, allowing for the primary cost drivers to be identified down to a subsystem level. This should include an in-depth analysis of the operational needs and economics of running a launch service provider, along with an analysis of projected demand.

REFERENCES

- [1] S. O. Forbes-Spyratos, M. P. Kearney, M. K. Smart, and I. H. Jahn. “Trajectory Design of a Rocket-Scramjet-Rocket Multi-Stage Launch System”. In: *Journal of Spacecraft and Rockets* (2018). DOI: [10.2514/1.A34107](https://doi.org/10.2514/1.A34107).
- [2] S. Forbes-Spyratos, M. Kearney, M. Smart, and I. Jahn. “Trajectory design of a rocket-scramjet-rocket multi-stage launch system”. In: *21st AIAA International Space Planes and Hypersonics Technologies Conference, Hypersonics 2017*. Xiamen, China, 2017. ISBN: 9781624104633.
- [3] S. O. Forbes-Spyratos, M. P. Kearney, M. K. Smart, and I. H. Jahn. “Fly-back of a scramjet-powered accelerator”. In: *AIAA Scitech, 2018*. Orlando, FL, 2018. ISBN: 9781624105241. DOI: [10.2514/6.2018-2177](https://doi.org/10.2514/6.2018-2177).
- [4] J. Chai, M. Smart, S. Forbes-Spyratos, and M. Kearney. “Fly Back Booster Design for Mach 5 Scramjet Launch”. In: *68th International Astronautical Congress*. Aelade, Australia, 2017.
- [5] Federal Aviation Administration. *The Annual Compendium of Commercial Space Transportation: 2018*. Tech. rep. January. Washington, DC, 2018, p. 255. URL: https://www.faa.gov/about/office_org/headquarters_offices/ast/media/2018_AST_Compendium.pdf.
- [6] C. Niederstrasser and W. Frick. “Small Launch Vehicles A 2015 State of the Industry Survey”. In: *Proceedings of the 29th Annual AIAA/USU Conference on Small Satellites*. Logan, UT, 2015.
- [7] M. K. Smart and M. R. Tetlow. “Orbital Delivery of Small Payloads Using Hypersonic Air-breathing Propulsion”. In: *Journal of Spacecraft and Rockets* 46.1 (2009), pp. 117–125. ISSN: 0022-4650. DOI: [10.2514/1.38784](https://doi.org/10.2514/1.38784).

REFERENCES

- [8] A. D. Ketsdever, M. P. Young, J. B. Mossman, and A. P. Pancotti. “Overview of Advanced Concepts for Space Access”. In: *Journal of Spacecraft and Rockets* 47.2 (2010), pp. 238–250. ISSN: 0022-4650. DOI: [10.2514/1.46148](https://doi.org/10.2514/1.46148).
- [9] M. Smart. *Scramjet Inlets*. Tech. rep. 9. Defense Technical Information Center, 2010. DOI: [10.2514/5.9781600866609.0447.0511](https://doi.org/10.2514/5.9781600866609.0447.0511).
- [10] F. Curran, J. Hunt, N. Lovell, G. Maggio, and V. Bilardo. “The Benefits of Hypersonic Airbreathing Launch Systems for Access to Space”. In: *39th AIAA/ASME/SAE/ASEE Joint Propulsion Conference and Exhibit* July (2003), pp. 1–14. DOI: [10.2514/6.2003-5265](https://doi.org/10.2514/6.2003-5265). URL: <http://arc.aiaa.org/doi/10.2514/6.2003-5265>.
- [11] J. D. Shaughnessy, S. Z. Pinckney, and J. D. McMinn. “Hypersonic Vehicle Simulation Configuration Model : Winged-Cone Configuration”. In: (1990).
- [12] D. Preller and M. K. Smart. “Reusable Launch of Small Satellites Using Scramjets”. In: *Journal of Spacecraft and Rockets* 54.6 (2017), pp. 1–13. ISSN: 0022-4650. DOI: [10.2514/1.A33610](https://doi.org/10.2514/1.A33610). URL: <https://doi.org/10.2514/1.A33610>.
- [13] Heiser H. H. and D. T. Pratt. *Hypersonic Airbreathing Propulsion*. Washington, D.C: American Institute of Aeronautics and Astronautics, 1994, p. 11. ISBN: 1-56347-035-7. DOI: [10.2514/4.470356](https://doi.org/10.2514/4.470356).
- [14] D. L. Kors. “Combined cycle propulsion for hypersonic flight”. In: *Acta Astronautica* 18.C (1988), pp. 191–200. ISSN: 00945765. DOI: [10.1016/0094-5765\(88\)90099-9](https://doi.org/10.1016/0094-5765(88)90099-9).
- [15] J. R. Olds and P. X. Bellini. “AIAA 98-1557 Argus , a Highly Reusable SSTO Rocket- Based Combined Cycle Launch Vehicle with Maglifter Launch Assist Georgia Institute of Technology Atlanta , GA AIAA 8th International Space Planes and Hypersonic Systems and Technologies Conference April ”. In: (1998).
- [16] R. W. Powell, J. D. Shaughnessy, C. I. Cruz, and J. C. Naftel. “Ascent performance of an air-breathing horizontal-takeoff launch vehicle”. In: *Journal of Guidance, Control, and Dynamics* 14.4 (1991), pp. 834–839. ISSN: 0731-5090. DOI: [10.2514/3.20719](https://doi.org/10.2514/3.20719).
- [17] C. Trefny. “An Air-Breathing Concept Launch Vehicle for Single-Stage-to-Orbit”. In: *35th Joint Propulsion Conference and Exhibit*. May. Los Angeles, CA, 1999. DOI: [10.2514/6.1999-2730](https://doi.org/10.2514/6.1999-2730).
- [18] J. M. Roche and D. N. Kosareo. *Structural Sizing of a 25000-Lb Payload , Air-Breathing Launch Vehicle for Single-Stage-To-Orbit*. Tech. rep. January 2001. 2000.

- [19] F. Pescetelli, E. Minisci, C. Maddock, I. Taylor, and R. Brown. “Ascent Trajectory Optimisation for a Single-Stage-to-Orbit Vehicle with Hybrid Propulsion”. In: *18th AIAA/3AF International Space Planes and Hypersonic Systems and Technologies Conference*. September. 2012, pp. 1–18. ISBN: 978-1-60086-931-0. DOI: [10.2514/6.2012-5828](https://doi.org/10.2514/6.2012-5828). URL: <http://arc.aiaa.org/doi/abs/10.2514/6.2012-5828>.
- [20] D. Young, T. Kokan, C. Tanner, I. Clark, C. Tanner, and A. Wilhite. “Lazarus: A SSTO Hypersonic Vehicle Concept Utilizing RBCC and HEDM Propulsion Technologies”. In: *14th AIAA/AHI Space Planes and Hypersonic Systems and Technologies Conference*. 2006, pp. 1–15. ISBN: 978-1-62410-050-5. DOI: [10.2514/6.2006-8099](https://doi.org/10.2514/6.2006-8099). URL: <http://arc.aiaa.org/doi/10.2514/6.2006-8099>.
- [21] J. Bradford, J. Olds, R. Bechtel, T. Cormier, and D. Messitt. “Exploration of the design space for the ABLV-GT SSTO reusable launch vehicle”. In: *Space 2000 Conference and Exposition* September (2000). DOI: [doi:10.2514/6.2000-5136](https://doi.org/10.2514/6.2000-5136). URL: <http://dx.doi.org/10.2514/6.2000-5136>.
- [22] J. Olds, J. Bradford, A. Charania, L. Ledsinger, D. McCormick, and K. Sorensen. “Hyperion - An SSTO vision vehicle concept utilizing rocket-based combined cycle propulsion”. In: (2013). DOI: [10.2514/6.1999-4944](https://doi.org/10.2514/6.1999-4944).
- [23] A. W. Wilhite, W. C. Engelund, D. O. Stanley, and J. C. Naftel. “Technology and staging effects on two-stage-to-orbit systems”. In: *Journal of Spacecraft and Rockets* 31.1 (1991), pp. 31–39. ISSN: 0022-4650. DOI: [10.2514/3.26399](https://doi.org/10.2514/3.26399).
- [24] T. Fujikawa, T. Tsuchiya, and S. Tomioka. “Multidisciplinary Design Optimization of a Two-Stage-to-Orbit Reusable Launch Vehicle with Ethanol-Fueled Rocket-Based Combined Cycle Engines”. In: *Transactions of the Japan Society for Aeronautical and Space Sciences* 60.5 (2017), pp. 265–275. ISSN: 0549-3811. DOI: [10.2322/tjsass.60.265](https://doi.org/10.2322/tjsass.60.265).
- [25] U. B. Mehta and J. V. Bowles. “Two-Stage-to-Orbit Spaceplane Concept with Growth Potential”. In: *Journal of Propulsion and Power* 17.6 (2001), pp. 1149–1161. ISSN: 0748-4658. DOI: [10.2514/2.5886](https://doi.org/10.2514/2.5886).
- [26] S. Takahashi, K. Mizobata, and K. Sawada. “Conceptual Study of a Two-Stage, Air-Breathing Reusable Launch Vehicle”. In: *Journal of Spacecraft and Rockets* 34.5 (1997), pp. 628–635. ISSN: 0022-4650. DOI: [10.2514/2.3280](https://doi.org/10.2514/2.3280).
- [27] L. van den Aberleen. *Spaceplane HERMES: Europe's Dream of Independent Manned Spaceflight Luc van den Abeelen*. Cham, Switzerland: Springer, 2017, pp. 176–179. ISBN: 9783319444703.

REFERENCES

- [28] B. S. Germain, J. R. Olds, J McIntire, D Nelson, J Weglian, and L Ledsinger. “AIAA 2001-3516 Starsaber : A Small Payload-Class TSTO Vehicle Concept Utilizing Rocket-Based Combined Cycle Propulsion Georgia Institute of Technology 37 th AIAA / ASME / SAE / ASEE Joint Propulsion Conference And Exhibit Salt Lake City , Utah”. In: *Earth* July (2001).
- [29] D Eklund. “Quicksat: A Two Stage to Orbit Reusable Launch Vehicle Utilizing Air Breathing Propulsion for Responsive Space Access”. In: September (2012), pp. 1–20. DOI: [10.2514/6.2004-5950](https://doi.org/10.2514/6.2004-5950).
- [30] J. E. Bradford, a Charania, J. R. Olds, M Graham, S. Engineering, and U. S. a. Ga. “XCAL-IBUR : A VERTICAL TAKEOFF TSTO RLV CONCEPT WITH A HEDM UPPERSTAGE AND A SCRAM-ROCKET BOOSTER 53rd International Astronautical Congress The World Space Congress - 2002 10-19 Oct 2002 / Houston , Texas”. In: *Director* (2002).
- [31] T Kimura and K Sawada. “Three-Stage Launch System with Scramjets”. In: *Journal of Spacecraft and Rockets* 36.5 (1999), pp. 675–680. ISSN: 00224650. DOI: [10.2514/2.3500](https://doi.org/10.2514/2.3500).
- [32] D. Preller. “Multidisciplinary Design and Optimisation of a Pitch Trimmed Hypersonic Air-breathing Accelerating Vehicle”. Ph.D Dissertation. The University of Queensland, 2018.
- [33] C. R. Mcclinton. “High Speed / Hypersonic Aircraft Propulsion Technology Development”. In: *Advances on Propulsion Technology for High-Speed Aircraft* (2008), pp. 1–1–1–32.
- [34] R Bulirsch and K Chudej. “Combined optimization of trajectory and stage separation of a hypersonic two-stage space vehicle”. In: *Zeitschrift für Flugwissenschaften und Weltraumforschung* 19.1 (1995), pp. 55–60. ISSN: 0342-068X.
- [35] Australia’s hypersonic plane for a new space race. URL: <http://www.bbc.com/future/story/20161117-australias-hypersonic-spaceplane-for-a-new-space-race> (visited on 06/21/2018).
- [36] J. T. Betts. “Survey of Numerical Methods for Trajectory Optimization”. In: *Journal of Guidance, Control, and Dynamics* 21.2 (1998), pp. 193–207. ISSN: 0731-5090. DOI: [10.2514/2.4231](https://doi.org/10.2514/2.4231).
- [37] R. Kendall and P. Portanova. *Launch Vehicles Then and Now: 50 Years of Evolution*. 2010. URL: <http://www.aerospace.org/crosslinkmag/spring-2010/launch-vehicles-then-and-now-50-years-of-evolution/> (visited on 06/21/2018).
- [38] S. Lewin. *Blue Origin Announces Big 'New Glenn' Rocket for Satellite & Crew Launches*. 2016. URL: <https://www.space.com/34034-blue-origin-new-glenn-rocket-for-satellites-people.html> (visited on 06/21/2018).

- [39] H. Pettit. *The galaxy's fastest car*. 2018. URL: <http://www.dailymail.co.uk/sciencetech/article-5361789/Ride-Elon-Musks-Starman-travels-space.html> (visited on 06/21/2018).
- [40] R. D. Launius. "Assessing the legacy of the Space Shuttle". In: *Space Policy* 22.4 (2006), pp. 226–234. ISSN: 02659646. DOI: [10.1016/j.spacepol.2006.08.008](https://doi.org/10.1016/j.spacepol.2006.08.008).
- [41] J. Foust. *SpaceX achievements generate growing interest in reusable launchers*. 2018. URL: <http://spacenews.com/spacex-achievements-generate-growing-interest-in-reusable-launchers/> (visited on 06/21/2018).
- [42] D. Mosher. *SpaceX faces a growing list of competitors in the new space race*. 2018. URL: <https://www.businessinsider.com.au/spacex-elon-musk-competition-companies-rockets-2018-3> (visited on 06/21/2018).
- [43] S. Clark. *Ariane 6 Rocket Holding to Schedule for 2020 Maiden Flight*. 2016. URL: <https://spaceflightnow.com/2016/08/13/ariane-6-rocket-holding-to-schedule-for-2020-maiden-flight/> (visited on 10/06/2018).
- [44] To Challenge SpaceX, Rockets Get Wings. 2016. URL: <http://www.spacesafetymagazine.com/news/to-challenge-spacex-rockets-get-wings/> (visited on 06/21/2018).
- [45] Richard Webb. "Is It Worth It? The Economics of Reusable Space Transportation". In: *ICEAA 2016 International Training Symposium, Bristol, UK* (2016), pp. 1–19.
- [46] S. Clark. *Falcon 9 rocket launching Sunday sports fin upgrade*. 2018. URL: <https://spaceflightnow.com/2017/06/25/falcon-9-rocket-launching-sunday-sports-fin-upgrade/> (visited on 06/21/2018).
- [47] M. Sarigul-Klijn and N. Sarigul-Klijn. "Flight Mechanics of Manned Sub-Orbital Reusable Launch Vehicles with Recommendations for Launch and Recovery". In: *41st Aerospace Sciences Meeting and Exhibit, Aerospace Sciences Meetings*. Reno, NV, 2003.
- [48] M. Gilmour. *Gilmour Space Secures AUD 19 Million to Launch Next-Generation Hybrid Rockets to Space*. 2018. URL: <https://www.gspacetech.com/single-post/2018/09/28/Gilmour-Space-secures-AUD-19-million-to-launch-next-gen-hybrid-rockets> (visited on 10/06/2018).
- [49] Rocket Lab. *Electron*. 2016. URL: <https://www.rocketlabusa.com/electron/> (visited on 11/30/2017).
- [50] Zero2Infinity. *Bloostar*. 2016. URL: <http://www.zero2infinity.space/bloostar/> (visited on 11/30/2017).
- [51] RocketCrafters. *Intrepid-1*. 2017. URL: <http://rocketcrafters.space/products-services/intrepid-launcher-family/intrepid-1/> (visited on 12/01/2017).

REFERENCES

- [52] *China Launches New Rocket*. 2018. URL: <http://www.spacelaunchreport.com/kz.html> (visited on 10/06/2018).
- [53] Vector Space. *Vector Launch Vehicle Family*. 2017. URL: <https://vectorspacesystems.com/technology/> (visited on 12/01/2017).
- [54] M. Kuhn, I. Müller, I. Petkov, B. Oving, A. J. van Kleef, C. J. Verberne, B. Haemmerli, and A. Boiron. “Innovative European Launcher Concept SMILE”. In: *21st AIAA International Space Planes and Hypersonics Technologies Conference* March (2017), pp. 1–14. DOI: [10.2514/6.2017-2441](https://arc.aiaa.org/doi/10.2514/6.2017-2441). URL: <https://arc.aiaa.org/doi/10.2514/6.2017-2441>.
- [55] Firefly. *Firefly*. 2017. URL: <http://www.fireflyspace.com/> (visited on 11/30/2017).
- [56] VirginOrbit. *LauncherOne*. 2017. URL: <https://virginorbit.com/> (visited on 11/30/2017).
- [57] D. Outreach. *DARPA Picks Design for Next-Generation Spaceplane*. 2017. URL: <https://www.darpa.mil/news-events/2017-05-24> (visited on 11/16/2017).
- [58] Orbital Access. *The Orbital 500R*. 2017. URL: <http://www.orbital-access.com/the-orbital-500/> (visited on 12/01/2017).
- [59] M. K. Smart and M. R. Tetlow. “Orbital Delivery of Small Payloads Using Hypersonic Air-breathing Propulsion”. In: *Journal of Spacecraft and Rockets* 46.1 (2009), pp. 117–125. ISSN: 0022-4650. DOI: [10.2514/1.38784](https://arc.aiaa.org/abs/10.2514/1.38784). URL: [http://arc.aiaa.org/doi/abs/10.2514/1.38784](https://arc.aiaa.org/doi/abs/10.2514/1.38784).
- [60] F. S. Billig. “Research on supersonic combustion”. In: *Journal of Propulsion and Power* 9.4 (1993), pp. 499–514. ISSN: 0748-4658. DOI: [10.2514/3.23652](https://arc.aiaa.org/doi/10.2514/3.23652).
- [61] S. Cook and U. Hueter. “NASA’s Integrated Space Transportation Plan 3rd generation reusable launch vehicle technology update”. In: *Acta Astronautica* 53.4-10 (2003), pp. 719–728. ISSN: 00945765. DOI: [10.1016/S0094-5765\(03\)00113-9](https://arc.aiaa.org/doi/10.1016/S0094-5765(03)00113-9).
- [62] E. T. Curran. “Scramjet Engines: The First Forty Years”. In: *Journal of Propulsion and Power* 17.6 (2001), pp. 1138–1148. ISSN: 0748-4658. DOI: [10.2514/2.5875](https://arc.aiaa.org/doi/10.2514/2.5875). URL: [http://arc.aiaa.org/doi/10.2514/2.5875](https://arc.aiaa.org/doi/10.2514/2.5875).
- [63] M. K. Smart. “How Much Compression Should a Scramjet Inlet Do?” In: *AIAA Journal* 50.3 (2012), pp. 610–619. ISSN: 0001-1452. DOI: [10.2514/1.J051281](https://arc.aiaa.org/doi/10.2514/1.J051281). URL: [http://arc.aiaa.org/doi/10.2514/1.J051281](https://arc.aiaa.org/doi/10.2514/1.J051281).
- [64] E. T. Curran. “Scramjet Engines: The First Forty Years”. In: *Journal of Propulsion and Power* 17.6 (2001), pp. 1138–1148. ISSN: 0748-4658. DOI: [10.2514/2.5875](https://arc.aiaa.org/doi/10.2514/2.5875).
- [65] A Paull, R. Stalker, and D Mee. “Thrust Measurements of a Complete Axisymmetric Scramjet in an Impulse Facility”. In: *5th International Space Planes and Hypersonics Conference*. Munich, Germany, 1993.

- [66] E. Curran. *Scramjet Propulsion*. Progress in Astronautics and Aeronautics, 2001. ISBN: 978-1-60086-660-9.
- [67] W. Heiser, D. Pratt, D. Daley, and U. Mehta. *Hypersonic Airbreathing Propulsion*. the American Institute of Aeronautics and Astronautics, 1994. ISBN: 978-1-56347-035-6.
- [68] R. S. Fry. “A Century of Ramjet Propulsion Technology Evolution”. In: *Journal of Propulsion and Power* 20.1 (2004), pp. 27–58. ISSN: 0748-4658. DOI: [10.2514/1.9178](https://doi.org/10.2514/1.9178). URL: <http://arc.aiaa.org/doi/10.2514/1.9178>.
- [69] M Smart. “Scramjets”. In: 3219 (2007).
- [70] D. J. Dalle, S. M. Torrez, J. F. Driscoll, M. a. Bolender, and K. G. Bowcutt. “Minimum-Fuel Ascent of a Hypersonic Vehicle Using Surrogate Optimization”. In: *Journal of Aircraft* 51.6 (2014), pp. 1973–1986. ISSN: 0021-8669. DOI: [10.2514/1.C032617](https://doi.org/10.2514/1.C032617). URL: <http://arc.aiaa.org/doi/10.2514/1.C032617>.
- [71] D. Dalle, S. Torrez, and J. Driscoll. “Turn Performance of an Air-Breathing Hypersonic Vehicle”. In: *AIAA Atmospheric Flight Mechanics Conference* August (2011). DOI: [10.2514/6.2011-6300](https://doi.org/10.2514/6.2011-6300). URL: <http://arc.aiaa.org/doi/10.2514/6.2011-6300>.
- [72] J. C. Blair, R. S. Ryan, L. a. Schutzenhofer, and W. R. Humphries. *Launch Vehicle Design Process : Integration , Technical and Lessons Learned*. Tech. rep. May. NASA STI Program Office, 2001.
- [73] R. W. Staufenbiel. “Second-Stage Trajectories of Air-Breathing Space Planes”. In: 27.6 (2000), pp. 618–622.
- [74] M. R. Tetlow, U. M. Schograve, Ttle, and G. M. Schneider. “Comparison of Glideback and Flyback Boosters”. In: *Journal of Spacecraft and Rockets* 38.5 (1992), pp. 752–758. ISSN: 0022-4650. DOI: [10.2514/2.3742](https://doi.org/10.2514/2.3742). URL: <http://dx.doi.org/10.2514/2.3742>.
- [75] B. M. Hellman. *Comparison of Return to Launch Site Options for a Reusable Booster Stage*. Tech. rep. Space Sytems Design Lab, Georgia Institute of technology, 2005, pp. 1–18.
- [76] N. A.-s. Plane. “The National Aero-Space Plane”. In: () .
- [77] J. Olds and I. Budianto. “Constant Dynamic Pressure Trajectory Simulation with POST”. In: *Aerospace Sciences Meeting & Exhibit*. Reno, NV, 1998, pp. 1–13. DOI: [10.2514/6.1998-302](https://doi.org/10.2514/6.1998-302). URL: <http://citeserx.ist.psu.edu/viewdoc/download?doi=10.1.1.25.6506&rep=rep1&type=pdf>.
- [78] E. Mooij. *Modeling and Optimization in Space Engineering*. Springer, 2019.
- [79] P. Lu. “Inverse dynamics approach to trajectory optimization for an aerospace plane”. In: *Journal of Guidance, Control, and Dynamics* 16.4 (1993), pp. 726–732. ISSN: 0731-5090. DOI: [10.2514/3.21073](https://doi.org/10.2514/3.21073). URL: <http://arc.aiaa.org/doi/abs/10.2514/3.21073>.

REFERENCES

- [80] J. D. Shaughnessy, S. Z. Pinckney, and J. D. McMinn. “NASA Technical Memorandum Hypersonic Vehicle Simulation Configuration Model :” in: *Simulation* (1990).
- [81] C. R. McClinton, V. L. Rausch, R. J. Shaw, U. Metha, and C. Naftel. “Hyper-X: Foundation for future hypersonic launch vehicles”. In: *Acta Astronautica* 57.2-8 (2005), pp. 614–622. ISSN: 00945765. DOI: [10.1016/j.actaastro.2005.03.061](https://doi.org/10.1016/j.actaastro.2005.03.061).
- [82] T. Tsuchiya and T. Mori. “Optimal Design of Two-Stage-To-Orbit Space Planes with Air-breathing Engines”. In: *Journal of Spacecraft and Rockets* 42.1 (2005), pp. 90–97. ISSN: 0022-4650. DOI: [10.2514/1.8012](https://doi.org/10.2514/1.8012).
- [83] T. Jazra, D. Preller, and M. K. Smart. “Design of an Airbreathing Second Stage for a Rocket-Scramjet-Rocket Launch Vehicle”. In: *Journal of Spacecraft and Rockets* 50.2 (2013), pp. 411–422. ISSN: 0022-4650. DOI: [10.2514/1.A32381](https://doi.org/10.2514/1.A32381). URL: <http://arc.aiaa.org/doi/abs/10.2514/1.A32381>.
- [84] Hypersonix. URL: <https://hypersonix.space/>.
- [85] N. D. Moshman and R. J. Proulx. “Range Improvements in Gliding Reentry Vehicles from Thrust Capability”. In: *Journal of Spacecraft and Rockets* 51.5 (2014), pp. 1681–1694. ISSN: 0022-4650. DOI: [10.2514/1.A32764](https://doi.org/10.2514/1.A32764). URL: <http://arc.aiaa.org/doi/10.2514/1.A32764>.
- [86] C. L. Darby, W. W. Hager, and A. V. Rao. “Direct Trajectory Optimization Using a Variable Low-Order Adaptive Pseudospectral Method”. In: *Journal of Spacecraft and Rockets* 48.3 (2011), pp. 433–445. ISSN: 0022-4650. DOI: [10.2514/1.52136](https://doi.org/10.2514/1.52136).
- [87] F. Toso, A. Riccardi, E. Minisci, C. Maddock, and Ristie. “Optimisation of ascent and descent trajectories for lifting body space access vehicles”. In: *66th International Astronautical Congress*. Jerusalem, 2015.
- [88] D. Chai, Y. W. Fang, Y. L. Wu, and S. H. Xu. “Boost-skipping trajectory optimization for air-breathing hypersonic missile”. In: *Aerospace Science and Technology* 46 (2015), pp. 506–513. ISSN: 12709638. DOI: [10.1016/j.ast.2015.09.004](https://doi.org/10.1016/j.ast.2015.09.004). URL: <http://dx.doi.org/10.1016/j.ast.2015.09.004>.
- [89] H. J. Pesch. “Neighboring Optimum Guidance of a Space-Shuttle-Orbiter-Type Vehicle”. In: *Journal of Guidance, Control, and Dynamics* 3.5 (1980), pp. 386–391. ISSN: 0731-5090. DOI: [10.2514/3.56011](https://doi.org/10.2514/3.56011). URL: <http://arc.aiaa.org/doi/abs/10.2514/3.56011>.
- [90] B. A. J. Eggers, H. J. Allen, and S. E. Neice. *A Comparative Analysis of the Performance of Long-Range Hypervelocity Vehicles*. Tech. rep. October. Ames Aeronautical Society, 1957.

- [91] T. Kanda and T. Hiraiwa. “Evaluation of Effectiveness of Periodic Flight by a Hypersonic Vehicle”. In: *Journal of Aircraft* 44.6 (2007), pp. 2076–2077. ISSN: 0021-8669. DOI: [10.2514/1.31143](https://doi.org/10.2514/1.31143).
- [92] T. Jazra. “Optimisation of Hypersonic Vehicles for Airbreathing Propulsion”. In: November (2010).
- [93] R Bulirsch, E Nerz, H. J. Pesch, and O von Stryk. “Combining direct and indirect methods in optimal control: Range maximization of a hang glider”. In: *Optimal Control (Calculus of Variations, Optimal Control Theory and Numerical Methods)* 111 (1993), pp. 273–288.
- [94] O. Stryk and R. Bulirsch. “Direct and indirect methods for trajectory optimization”. In: *Annals of Operations Research* 37 (1992), pp. 357–373. ISSN: 0254-5330. DOI: [10.1007/BF02071065](https://doi.org/10.1007/BF02071065).
- [95] M. S. Bazaraa, H. D. Sherali, and C. M. Shetty. *Nonlinear Programming: Theory and Algorithms*. John Wiley & Sons, 2013.
- [96] P. Boggs and J. Tolle. “Sequential quadratic programming for large-scale nonlinear optimization”. In: *Journal of Computational and Applied Mathematics* 124.1-2 (2000), pp. 123–137. ISSN: 03770427. DOI: [10.1016/S0377-0427\(00\)00429-5](https://doi.org/10.1016/S0377-0427(00)00429-5). URL: <http://linkinghub.elsevier.com/retrieve/pii/S0377042700004295> \$ \backslash \$ <http://www.sciencedirect.com/science/article/pii/S0377042700004295>.
- [97] M. P. Kelly. “Transcription Methods for Trajectory Optimization A beginners tutorial”. In: *Arxiv* (2015), pp. 1–14.
- [98] A. Rao. “A survey of numerical methods for optimal control”. In: *Advances in the Astronautical Sciences* 135 (2009), pp. 497–528. URL: <http://vdol.mae.ufl.edu/ConferencePublications/trajectorySurveyAAS.pdf>.
- [99] G. Fasano and J. Pinter. *Modelling and Optimisation in Space Engineering*. New York, NY: Springer, 2013. DOI: [10.1007/978-1-4614-4469-5](https://doi.org/10.1007/978-1-4614-4469-5).
- [100] D. Jezewski. “An Optimal, Analytic Solution to the Linear-Gravity, Constant-Thrust Trajectory Problem”. In: *Journal of Spacecraft and Rockets* July (1971), pp. 793–796.
- [101] C. A. Maddock, L. Ricciardi, M. West, J. West, K. Kontis, S. Rengarajan, D. Evans, A. Milne, and S. McIntyre. “Conceptual design analysis for a two-stage-to-orbit semi-reusable launch system for small satellites”. In: *Acta Astronautica* 152.August (2018), pp. 782–792. ISSN: 00945765. DOI: [10.1016/j.actaastro.2018.08.021](https://doi.org/10.1016/j.actaastro.2018.08.021). URL: <https://doi.org/10.1016/j.actaastro.2018.08.021>.

REFERENCES

- [102] I. M. Ross and F. Fahroo. “Pseudospectral Knotting Methods for Solving Nonsmooth Optimal Control Problems”. In: *Journal of Guidance, Control, and Dynamics* 27.3 (2004), pp. 397–405. ISSN: 0731-5090. DOI: [10.2514/1.3426](https://doi.org/10.2514/1.3426).
- [103] F. Fahroo and I. Ross. “Direct trajectory optimization by a Chebyshev pseudospectral method”. In: *Proceedings of the 2000 American Control Conference*. Chicago, IL, 2000, pp. 3860–3864. ISBN: 0-7803-5519-9. DOI: [10.1109/ACC.2000.876945](https://doi.org/10.1109/ACC.2000.876945).
- [104] H.-O. Kreiss and J. Oliger. “Comparison of accurate methods for the integration of hyperbolic equations”. In: *Tellus A* 1971 (1972). ISSN: 0280-6495. DOI: [10.3402/tellusa.v24i3.10634](https://doi.org/10.3402/tellusa.v24i3.10634).
- [105] C. L. Darby, W. W. Hager, and A. V. Rao. “An hp-adaptive pseudospectral method for solving optimal control problems”. In: *Optimal Control Applications and Methods* 32.3 (2011), pp. 476–502. DOI: [10.1002/oca.957](https://doi.wiley.com/10.1002/oca.957). URL: <http://doi.wiley.com/10.1002/oca.957>.
- [106] G. Huntington, D. Benson, and A. Rao. “A Comparison of Accuracy and Computational Efficiency of Three Pseudospectral Methods”. In: *AIAA Guidance, Navigation and Control Conference and Exhibit* (2007), pp. 1–43. DOI: [10.2514/6.2007-6405](https://doi.org/10.2514/6.2007-6405). URL: <http://arc.aiaa.org/doi/abs/10.2514/6.2007-6405> <http://arc.aiaa.org/doi/pdf/10.2514/6.2007-6405>.
- [107] D. Garg, W. W. Hager, and A. V. Rao. “Pseudospectral Methods for Solving Infnite-Horizon Optimal Control Problems”. In: *Automatica* 47.4 (2011), pp. 829–837.
- [108] D. Garg, M. Patterson, and W. Hager. “An Overview of Three Pseudospectral Methods for the Numerical Solution of Optimal Control Problems”. In: *Advances in thAstronautical Sciences* 135 (2009), pp. 1–17. URL: <http://vdol.mae.ufl.edu/ConferencePublications/unifiedFrameworkAAS.pdf>.
- [109] Q. Gong, I. M. Ross, and F. Fahroo. “Costate Computation by a Chebyshev Pseudospectral Method”. In: *Journal of Guidance, Control, and Dynamics* 33.2 (2010), pp. 623–628. ISSN: 0731-5090. DOI: [10.2514/1.45154](https://doi.org/10.2514/1.45154).
- [110] F. Fahroo and I. M. Ross. “Costate Estimation by a Legendre Pseudospectral Method”. In: *Journal of Guidance, Control, and Dynamics* 24.2 (2001), pp. 270–277. ISSN: 0731-5090. DOI: [10.2514/2.4709](https://doi.org/10.2514/2.4709).
- [111] N. Bedrossian, B. Technologies, and L. N. Nasa. “Zero Propellant Maneuvre Flight Results For 180 Degree ISS Rotation”. In: *20th International Symposium on Space Flight Dynamics*. Annapolis, MD, 2007.

- [112] H. Li, R. Zhang, Z. Li, and R. Zhang. “Footprint problem with angle of attack optimization for high lifting reentry vehicle”. In: *Chinese Journal of Aeronautics* 25.2 (2012), pp. 243–251. ISSN: 10009361. DOI: [10.1016/S1000-9361\(11\)60384-1](https://doi.org/10.1016/S1000-9361(11)60384-1). URL: [http://dx.doi.org/10.1016/S1000-9361\(11\)60384-1](http://dx.doi.org/10.1016/S1000-9361(11)60384-1).
- [113] S. Josselyn and I. M. Ross. “Rapid Verification Method for the Trajectory Optimization of Reentry Vehicles”. In: *Notes* 26.3 (2002), pp. 505–508. ISSN: 0731-5090. DOI: [10.2514/2.5074](https://doi.org/10.2514/2.5074).
- [114] J. Zhao and R. Zhou. “Reentry trajectory optimization for hypersonic vehicle satisfying complex constraints”. In: *Chinese Journal of Aeronautics* 26.6 (2013), pp. 1544–1553. ISSN: 10009361. DOI: [10.1016/j.cja.2013.10.009](https://doi.org/10.1016/j.cja.2013.10.009). URL: <http://dx.doi.org/10.1016/j.cja.2013.10.009>.
- [115] B. Tian and Q. Zong. “Optimal guidance for reentry vehicles based on indirect Legendre pseudospectral method”. In: *Acta Astronautica* 68.7-8 (2011), pp. 1176–1184. ISSN: 00945765. DOI: [10.1016/j.actaastro.2010.10.010](https://doi.org/10.1016/j.actaastro.2010.10.010). URL: <http://linkinghub.elsevier.com/retrieve/pii/S0094576510003899>.
- [116] S. T.U. I. Rizvi, L. S. He, and D. J. Xu. “Optimal trajectory and heat load analysis of different shape lifting reentry vehicles for medium range application”. In: *Defence Technology* 11.4 (2015), pp. 350–361. ISSN: 22149147. DOI: [10.1016/j.dt.2015.06.003](https://doi.org/10.1016/j.dt.2015.06.003). URL: <http://dx.doi.org/10.1016/j.dt.2015.06.003>.
- [117] S. Yang, T. Cui, X. Hao, and D. Yu. “Trajectory optimization for a ramjet-powered vehicle in ascent phase via the Gauss pseudospectral method”. In: *Aerospace Science and Technology* 67 (2017), pp. 88–95. ISSN: 12709638. DOI: [10.1016/j.ast.2017.04.001](https://doi.org/10.1016/j.ast.2017.04.001). URL: <http://dx.doi.org/10.1016/j.ast.2017.04.001>.
- [118] M. Kodera, H. Ogawa, S. Tomioka, and S. Ueda. “Multi-Objective Design and Trajectory Optimization of Space Transport Systems with RBCC Propulsion via Evolutionary Algorithms and Pseudospectral Methods”. In: *52nd Aerospace Sciences Meeting January* (2014), pp. 1–14. DOI: [10.2514/6.2014-0629](https://doi.org/10.2514/6.2014-0629). URL: <http://arc.aiaa.org/doi/10.2514/6.2014-0629>.
- [119] Astos Solutions. *Astos Solutions*. 2018. URL: <https://www.astos.de/> (visited on 07/24/2018).
- [120] A. V. Rao, D. a. Benson, C. Darby, M. a. Patterson, C. Francolin, I. Sanders, and G. T. Huntington. “Algorithm 902”. In: *ACM Transactions on Mathematical Software* 37.2 (2010), pp. 1–39. ISSN: 00983500. DOI: [10.1145/1731022.1731032](https://doi.org/10.1145/1731022.1731032).
- [121] Y. Nie, O. Faqir, and E. Kerrigan. *ICLOCS2*. 2018. URL: <http://www.ee.ic.ac.uk/ICLOCS/> (visited on 07/24/2018).

REFERENCES

- [122] a Wächter and L. T. Biegler. *On the Implementation of a Primal-Dual Interior Point Filter Line Search Algorithm for Large-Scale Nonlinear Programming*. Vol. 106. 1. 2006, pp. 25–57. ISBN: 1010700405.
- [123] T. Lipp and S. Boyd. “Minimum-time speed optimisation over a fixed path”. In: *International Journal of Control* 87.January 2015 (2014), pp. 1297–1311. ISSN: 0020-7179. DOI: [10.1080/00207179.2013.875224](https://doi.org/10.1080/00207179.2013.875224). URL: <http://www.tandfonline.com/doi/abs/10.1080/00207179.2013.875224>.
- [124] I. M. Ross and F Fahroo. “A direct method for solving nonsmooth optimal control problems”. In: *Proceedings of the 2002 {IFAC World Congress}* (2002).
- [125] P. E. Rutquist and M. M. Edvall. “PROPT - Matlab Optimal Control Software”. In: *Tomlab Optimization Inc* 260 (2010), pp. –.
- [126] W. Colson. *Program to Optimize Simulated Trajectories 2*. 2017. URL: <https://post2.larc.nasa.gov/> (visited on 07/24/2018).
- [127] R. Falck. *OTIS*. 2016. URL: <https://otis.grc.nasa.gov/index.html> (visited on 07/24/2018).
- [128] D. Wassel, F. Wolff, J. Vogelsang, and C. Büskens. “the Esa Nlp-Solver Worhp Recent Developments and Applications”. In: *Modeling and Optimization in Space Engineering* (2013).
- [129] B Houska, H. Ferrau, and M. Diehl. “ACADO Toolkit – An Open Source Framework for Automatic Control and Dynamic Optimization”. In: *Optimal Control Applications and Methods* 32.3 (2011), pp. 298–312.
- [130] *JModelica.org*. URL: <https://jmodelica.org/> (visited on 07/24/2018).
- [131] C. Rosema, J. Doyle, L. Auman, M. Underwood, and W. B. Blake. *Missile DATCOM User’s Manual - 2011 Revision*. Tech. rep. Army Aviation and Missile Research Development, 2011. DOI: [10.21236/ad1000581](https://doi.org/10.21236/ad1000581).
- [132] D. Kinney. “Aero-Thermodynamics for Conceptual Design”. In: *42nd AIAA Aerospace Sciences Meeting and Exhibit*. January. Reno, NV, 2004, pp. 1–11. ISBN: 978-1-62410-078-9. DOI: [10.2514/6.2004-31](https://doi.org/10.2514/6.2004-31). URL: <http://www.aric.or.kr/treatise/journal/content.asp?idx=53932>.
- [133] U Reisch and Y Anseaume. *Validation of the Approximate Calculation Procedure HOTSOSE For Aerodynamic and Thermal Loads in Hypersonic Flow with Existing Experimental and Numerical Results*. Tech. rep. DLR-Forschungsbericht, 1998.
- [134] T. Eggers. “Aerodynamic Analysis of the Dual-Mode Ramjet Vehicle JAPHAR”. In: *Notes on Numerical Fluid Mechanics and Multidisciplinary Design*. Vol. 115. 2011, pp. 137–140. ISBN: 9783642177699.

- [135] M. J. Aftosmis, M. J., Berger and G. Adomavicius. “A Parallel Multilevel Method for Adaptively Refined Cartesian Grids with Embedded Boundaries”. In: *38th Aerospace Sciences Meeting and Exhibit*. Reno NV, 2000. DOI: [10.2514/6.2000-808](https://doi.org/10.2514/6.2000-808).
- [136] F. Manual, R. T. Biedron, J. M. Derlaga, P. A. Gnoffo, D. P. Hammond, W. T. Jones, B. Kleb, E. M. Lee-rausch, E. J. Nielsen, M. A. Park, C. L. Rumsey, J. L. Thomas, and W. A. Wood. *FUN3D Manual: 13.3*. Tech. rep. February. Langley Research Center, Hampton, Virginia: NASA, 2018.
- [137] NASA Glenn Research Center. *Euler Equations*. URL: <https://www.grc.nasa.gov/WWW/k-12/airplane/eulereqs.html> (visited on 07/24/2018).
- [138] D. Almosnino. “A Low Subsonic Study of the NASA N2A Hybrid Wing-Body Using an Inviscid Euler-Adjoint Solver”. In: *34th AIAA Applied Aerodynamics Conference* June (2016), pp. 1–18. DOI: [doi:10.2514/6.2016-3267](https://doi.org/10.2514/6.2016-3267). URL: <http://dx.doi.org/10.2514/6.2016-3267>.
- [139] A. D. Ward, M. K. Smart, and R. J. Gollan. “Development of a Rapid Inviscid/Boundary-Layer Aerodynamics Tool”. In: *22nd AIAA International Space Planes and Hypersonics Systems and Technologies Conference*. September. Orlando, FL, 2018, pp. 1–14. ISBN: 978-1-62410-577-7. DOI: [10.2514/6.2018-5270](https://doi.org/10.2514/6.2018-5270). URL: <https://arc.aiaa.org/doi/10.2514/6.2018-5270>.
- [140] R Gollan and P Jacobs. “About the formulation, verification and validation of the hypersonic flow solver Eilmser”. In: *International Journal for Numerical Methods in Fluids* 73 (2013). ISSN: 02712091. DOI: [10.1002/fld](https://doi.org/10.1002/fld). arXiv: [fld.1 \[DOI: 10.1002\]](https://arxiv.org/abs/1307.4003).
- [141] Ansys. *Fluent Bruchure*. Tech. rep. Ansys, 2014, p. 2. URL: <http://ansys.com/staticassets/ANSYS/staticassets/resourcelibrary/brochure/ansys-fluent-brochure-14.0.pdf>.
- [142] AEA Technology. *Itroduction to CFX-TASCflow*. URL: <http://hmf.enseeiht.fr/travaux/CD0102/travaux/optmfn/micp/reports/s19cfx2/pages/frame2.htm> (visited on 10/05/2018).
- [143] COMSOL. *Product: CFD Module*. URL: <https://www.comsol.com/cfd-module\#cfds-software> (visited on 10/05/2018).
- [144] D. Schwamborn, T. Gerhold, and R. Heinrich. “The DLR TAU-Code: Recent Applications in Research and Industry”. In: *European Conference on Computational Fluid Dynamics, EC-COMAS CFD 2006* (2006), pp. 1–25.
- [145] The OpenFOAM Foundation. *OpenFOAM*. URL: <https://openfoam.org/> (visited on 10/06/2018).

REFERENCES

- [146] D. Abeynayake and A. Agon. “Comparison of computational and semi-empirical aerodynamics tools for making fit-for-purpose modelling decisions”. In: December (2013), pp. 1–6.
- [147] C. Kiris, J. Housman, M. Gusman, D. Schauerhamer, K. Deere, A. Elmiligui, K. Abdol-Hamid, E. Parlette, M. Andrews, and J. Blevins. “Best practices for aero-database CFD simulations of ares V ascent”. In: *49th AIAA Aerospace Sciences Meeting Including the New Horizons Forum and Aerospace Exposition* (2011), pp. 1–21. DOI: [10.2514/6.2011-16](https://doi.org/10.2514/6.2011-16).
- [148] U. Mehta, M. Aftosmis, J. Bowles, and S. Pandya. “Skylon Aerospace Plane and Its Aerodynamics and Plumes”. In: *Journal of Spacecraft and Rockets* 53.2 (2016), pp. 340–353. ISSN: 0022-4650. DOI: [10.2514/1.A33408](https://doi.org/10.2514/1.A33408). URL: <http://arc.aiaa.org/doi/10.2514/1.A33408>.
- [149] R. Kimmel, D. Adamczak, K Berger, and M Choudhari. “HIFiRE-5 flight vehicle design”. In: *AIAA paper* July (2010), pp. 1–17. DOI: [10.2514/6.2010-4985](https://doi.org/10.2514/6.2010-4985). URL: <http://arc.aiaa.org/doi/pdf/10.2514/6.2010-4985>.
- [150] M. J. Aftosmis, M. Nemec, and S. E. Cliff. “Adjoint-based low-boom design with Cart3D”. In: *29th AIAA Applied Aerodynamics Conference 2011*. June. 2011, pp. 1–17. ISBN: 9781624101458. DOI: [doi:10.2514/6.2011-3500](https://doi.org/10.2514/6.2011-3500). URL: <http://www.scopus.com/inward/record.url?eid=2-s2.0-84872373928&partnerID=tZ0tx3y1>.
- [151] M Suraweera and M. K. Smart. “Shock Tunnel Experiments with a Mach 12 {REST} Scramjet at Off-Design Conditions”. In: *Journal of Propulsion and Power* 25.3 (2009), pp. 555–564. ISSN: 0748-4658. DOI: [10.2514/1.37946](https://doi.org/10.2514/1.37946).
- [152] M. K. Smart and E. G. Ruf. “Free-jet testing of a {REST} scramjet at off-design conditions”. In: *Collection of Technical Papers - 25th AIAA Aerodynamic Measurement Technology and Ground Testing Conference* AIAA 2006-2955 (2006), pp. 190–201. DOI: [doi:10.2514/6.2006-2955](https://doi.org/10.2514/6.2006-2955).
- [153] M. V. Suraweera and M. K. Smart. “Shock-Tunnel Experiments with a Mach 12 Rectangular-to-Elliptical Shape-Transition Scramjet at Offdesign Conditions”. In: *Journal of Propulsion and Power* 25.3 (2009), pp. 555–564. ISSN: 0748-4658. DOI: [10.2514/1.37946](https://doi.org/10.2514/1.37946). URL: <http://arc.aiaa.org/doi/10.2514/1.37946>.
- [154] NASA. *U.S. Standard Atmosphere, 1976*. U.S. Government Printing Office, Washington, D.C., 1976, pp. 1–243. URL: <http://ntrs.nasa.gov/archive/nasa/casi.ntrs.nasa.gov/19770009539.pdf>.
- [155] J. W. MacColl. “The Conical Shock Wave Formed by a Cone Moving at a High Speed”. In: *Proceedings of the Royal Society A: Mathematical, Physical and Engineering Sciences* 159.898 (1937), pp. 459–472. ISSN: 1364-5021. DOI: [10.1098/rspa.1937.0083](https://doi.org/10.1098/rspa.1937.0083). URL: <http://rspa.royalsocietypublishing.org/cgi/doi/10.1098/rspa.1937.0083>.

- [156] Pointwise. [www.pointwise.com.](http://www.pointwise.com/) 2017. URL: <http://www.pointwise.com/> (visited on 02/01/2017).
- [157] D. G. Sagerman, M. P. Rumpfkeil, B. M. Hellman, and N. Dasque. “Comparisons of Measured and Modeled Aero-thermal Distributions for Complex Hypersonic Configurations”. In: *55th AIAA Aerospace Sciences Meeting January* (2017), pp. 1–22. DOI: [10.2514/6.2017-0264](https://doi.org/10.2514/6.2017-0264). URL: <http://arc.aiaa.org/doi/10.2514/6.2017-0264>.
- [158] D. Abeynayake and A. Agon. “Comparison of computational and semi-empirical aerodynamics tools for making fit-for-purpose modelling decisions”. In: *20th International Congress on Modelling and Simulation*. Adelaide, Australia, 2013, pp. 1–6.
- [159] D Almosnino. “Assessment of an inviscid euler-adjoint solver for prediction of aerodynamic characteristics of the NASA HL-20 lifting body”. In: *34th AIAA Applied Aerodynamics Conference, 2016 June* (2016). DOI: [10.2514/6.2016-3266](https://doi.org/10.2514/6.2016-3266). URL: <https://www.scopus.com/inward/record.uri?eid=2-s2.0-84980371959&partnerID=40&md5=1b304aabaad2976daf4d0742d5bdc6ba>.
- [160] R. Gomez, D. Vicker, S. Rogers, M. Aftosmis, W. Chan, R. Meakin, S. Murman, and S. Murman. “STS-107 Investigation Ascent CFD Support”. In: *34th AIAA Fluid Dynamics Conference and Exhibit* (2004), pp. 1–15. DOI: [10.2514/6.2004-2226](https://doi.org/10.2514/6.2004-2226). URL: <http://arc.aiaa.org/doi/10.2514/6.2004-2226>.
- [161] S. Pandya, S. Murman, and M. Aftosmis. “Validation of Inlet and Exhaust Boundary Conditions for a Cartesian Method”. In: *22nd Applied Aerodynamics Conference and Exhibit January* (2004), pp. 1–16. ISSN: 10485953. DOI: [10.2514/6.2004-4837](https://doi.org/10.2514/6.2004-4837). URL: <http://arc.aiaa.org/doi/10.2514/6.2004-4837>.
- [162] Desktop Aeronautics. *Specifying Power BCs for Rocket Plumes*. Tech. rep. NASA, pp. 9–11. URL: https://www.nas.nasa.gov/publications/software/docs/cart3d/pages/howto/howTo_RocketPlumes_08.11.pdf.
- [163] U. Mehta, M. Aftosmis, J. Bowles, and S. Pandya. “Skylon Aerodynamics and SABRE Plumes”. In: *20th AIAA International Space Planes and Hypersonic Systems and Technologies Conference*. July. Glasgow, Scotland, 2015, pp. 1–21. ISBN: 9781624103209. DOI: [10.2514/6.2015-3605](https://doi.org/10.2514/6.2015-3605).
- [164] Space Exploration technologies. *Falcon 1 Launch Vehicle Payload Users Guide*. Tech. rep. Hawthorne, CA: Space Exploration Technologies, 2008, p. 65.
- [165] M. Wade. *Encyclopedia Astronautica*. 2017. URL: <http://www.astronautix.com/> (visited on 07/24/2018).

REFERENCES

- [166] G. Norris. *SpaceX Unveils Plans To Be Worlds Top Rocket Maker*. 2011. URL: <https://web.archive.org/web/20150621134912/http://aviationweek.com/awin/spacex-unveils-plans-be-world-s-top-rocket-maker> (visited on 03/17/2019).
- [167] G. Sutton and O. Biblarz. *Rocket propulsion Elements*. 8th. John Wiley & Sons, 2010, p. 67. ISBN: 978-0470080245. DOI: [10.1017/S0001924000034308](https://doi.org/10.1017/S0001924000034308).
- [168] J. W. Magee Bruno, T.J., Friend, D. G., Huber, M.L., Laesecke, A., Lemmon, E.W., McLinden, M.O., Perkins, R.A., Baranski, J., Widegren, J.A. *Thermophysical Properties Measurements and Models for Rocket Propellant RP-1: Phase I, NIST- IR 6644, National Institute of Standards and Technology (U.S.)* Tech. rep. 2006.
- [169] International Tungsten Industry Association. *Tungsten Properties*. URL: <https://www.itia.info/tungsten-properties.html> (visited on 10/05/2018).
- [170] E. Fitzer and L. Manocha. *Carbon Reinforcements and Carbon/Carbon Composites*. Berlin, Heidelberg: Springer Berlin Heidelberg, 1998. ISBN: 3-642-58745-3.
- [171] Amorim. *Reinventing Thermal Protection*. Tech. rep. Regency Park SA: Amorim Cork Composites, 2018. URL: <http://pdf.nauticexpo.com/pdf/amorim-cork-composites/tps/39162-105388.html>.
- [172] Rocket lab USA. *Rocket Lab reaches 500 Rutherford engine test fires*. 2018. URL: <https://www.rocketlabusa.com/news/updates/rocket-lab-reaches-500-rutherford-engine-test-fires/> (visited on 08/12/2019).
- [173] D Huzel and D Huang. *Design of Liquid Propellant Rocket Engines*. American Institute of Aeronautics and Astronautics, 1992, pp. 1–472. ISBN: 1563470136.
- [174] M. Marini. “Analysis of hypersonic compression ramp laminar flows under sharp leading edge conditions”. In: *Aerospace Science and Technology* 5.4 (2001), pp. 257–271. ISSN: 12709638. DOI: [10.1016/S1270-9638\(01\)01109-9](https://doi.org/10.1016/S1270-9638(01)01109-9).
- [175] M. Agoes Moelyadi. “Stage Separation Aerodynamics of Future Space Transport Systems”. PhD thesis. Technischen Universität München, 2006.
- [176] K. Kudo and T. Kanda. “Staging of Two-Stage-to-Orbit Aerospace Plane”. In: *Transactions of the Japan Society for Aeronautical and Space Sciences* 48.161 (2005), pp. 129–134. ISSN: 0549-3811. DOI: [10.2322/tjsass.48.129](https://doi.org/10.2322/tjsass.48.129).
- [177] C. Gong, B. Chen, and L. Gu. “Design and Optimization of RBCC Powered Suborbital Reusable Launch Vehicle”. In: *19th AIAA International Space Planes and Hypersonic Systems and Technologies Conference* June (2014), pp. 1–20. DOI: [10.2514/6.2014-2361](https://arc.aiaa.org/doi/abs/10.2514/6.2014-2361). URL: <http://arc.aiaa.org/doi/abs/10.2514/6.2014-2361>.

- [178] D. Preller. “Multidisciplinary Design and Optimisation of a Pitch Trimmed Hypersonic Air-breathing Accelerating Vehicle”. PhD thesis. University of Queensland, 2018.
- [179] M. a. Patterson, D Ph, A. V. Rao, and D Ph. *GPOPS-II manul: A General-Purpose MATLAB Software for Solving Multiple-Phase Optimal Control Problems Version 2 . 1.* Tech. rep. October. 2015, pp. 1–72.
- [180] R. J. Boain. “A-B-Cs of Sun-Synchronous Orbit Mission Design 14 AAS / AIAA Space Flight Mechanics Conference”. In: *14th AAS/AIAA Space Flight Mechanics Conference* (2004), pp. 1–19.
- [181] R. Simmon. *Three Classes of Orbit*. 2009. URL: <https://earthobservatory.nasa.gov/Features/OrbitsCatalog/page2.php> (visited on 08/22/2018).
- [182] M. Palin. *Australias first commercial space base to launch rockets within a year*. 2017. URL: <https://www.news.com/technology/science/space/australias-first-commercial-space-base-to-launch-rockets-within-a-year/news-story/eb7841c5b39e04fd31302e8b1056e3ab> (visited on 10/05/2018).
- [183] Icao. “World Geodetic System - 1984 (WGS-84) Manual”. In: 1984 (2002), pp. 21–23.
- [184] C. Maddock, F. Toso, L. Ricciardi, A. Mogavero, K. H. Lo, S. Rengarajan, K. Kontis, A. Milne, D. Evans, M. West, and S. McIntyre. “Vehicle and Mission Design of a Future Small Payload Launcher”. In: *21st AIAA International Space Planes and Hypersonics Technologies Conference* March (2017), pp. 1–20. DOI: [10.2514/6.2017-2224](https://arc.aiaa.org/doi/10.2514/6.2017-2224). URL: <https://arc.aiaa.org/doi/10.2514/6.2017-2224>.
- [185] A. Tewari. *Atmospheric and Space Flight Dynamics*. 2007. ISBN: 978-0-8176-4437-6. DOI: [10.1007/978-0-8176-4438-3](https://doi.org/10.1007/978-0-8176-4438-3). URL: <http://link.springer.com/10.1007/978-0-8176-4438-3>.
- [186] J. T. Betts. *Practical Methods for Optimal Control and Estimation Using Nonlinear Programming*. 2nd. New York, NY: Cambridge University Press, 2009. ISBN: 0898716888 9780898716887.
- [187] B Barrar. *An Analytic Proof That the Hohmann-Type Transfer is the True Minimum Tro-Impulse Transfer*. Tech. rep. Fort Belvoir, VA: Defense Technical Information Center, 1962.
- [188] Y. Kawajir, C. D. Laird, and A. Waechter. “Introduction to IPOPT: A tutorial for downloading, installing, and using IPOPT .” In: *Most* (2010), pp. 1–68. ISSN: 00981354. DOI: <http://web.mit.edu/ipopt_v3.8/doc/documentation.pdf>. arXiv: [arXiv:1011.1669v3](https://arxiv.org/abs/1011.1669v3).
- [189] H. Hindi. “A tutorial on convex optimization II: duality and interior point methods”. In: *2006 American Control Conference* 1 (2006), 11 pp. ISSN: 07431619. DOI: [10.1109/ACC.2006.1655436](https://doi.org/10.1109/ACC.2006.1655436). URL: <http://ieeexplore.ieee.org/document/1655436/>.

REFERENCES

- [190] P. Pucci and J. B. Serrin. *The maximum principle*. Vol. 73. Springer, 2007, pp. 80–104. ISBN: 978-3-7643-8145-5.
- [191] A. Gilbert, B. Mesmer, and M. D. Watson. “Exergy analysis of rocket systems”. In: *9th Annual IEEE International Systems Conference, SysCon 2015*. Vancouver, British Columbia, Canada, 2015, pp. 283–288. ISBN: 9781479959273. DOI: [10.1109/SYSCON.2015.7116765](https://doi.org/10.1109/SYSCON.2015.7116765).
- [192] D. W. Riggins, M. Abbas, M. Wainwright, and U. S. A. Force. “Analysis of Energy Utilization for Chemical Rockets”. In: *Journal of Spacecraft and Rockets* 56.3 (2019). DOI: [10.2514/1.A34296](https://doi.org/10.2514/1.A34296).
- [193] D. W. Riggins, J. Camberos, M. Wolff, T. B. Company, and H. Beach. “Mission-Integrated Exergy Analysis for Hypersonic Vehicles : Methodology and Application”. In: *Journal of Propulsion and Power* 29.3 (2013). DOI: [10.2514/1.B34733](https://doi.org/10.2514/1.B34733).
- [194] J. Anderson. *Hypersonic and high Temperature Gas Dynamics: Second Edition*. American Institute of Aeronautics and Astronautics, 2000.
- [195] D. Dirkx and E. Mooj. *Conceptual Shape Optimization of Entry Vehicles Applied to Capsules and Winged Fuselage Vehicles*. 1st ed. Cham, Switzerland: Springer, 2017, pp. 65–67.
- [196] M. E. Tauber, G. P. Menees, and H. G. Adelman. “Aerothermodynamics of transatmospheric vehicles”. In: *Journal of Aircraft* 24.9 (2008), pp. 594–602. ISSN: 0021-8669. DOI: [10.2514/3.45483](https://doi.org/10.2514/3.45483).
- [197] I. H. Jahn. *HTDT Code Repository*. URL: <https://bitbucket.org/uqturbine/htdt/src>.
- [198] D. a. Kourtides, W. C. Pitts, M. Araujo, and R. S. Zimmerman. “High-Temperature Properties of Ceramic Fibers and Insulations for Thermal Protection of Atmospheric Entry and Hypersonic Cruise Vehicles”. In: *Journal of Fire Sciences* 6.5 (1988), pp. 313–332. ISSN: 15308049. DOI: [10.1177/073490418800600501](https://doi.org/10.1177/073490418800600501).
- [199] Y. Zhu, W. Peng, R. Xu, and P. Jiang. “Review on active thermal protection and its heat transfer for airbreathing hypersonic vehicles”. In: *Chinese Journal of Aeronautics* 31.10 (2018), pp. 1929–1953. ISSN: 1000-9361. DOI: [10.1016/j.cja.2018.06.011](https://doi.org/10.1016/j.cja.2018.06.011). URL: <https://doi.org/10.1016/j.cja.2018.06.011>.
- [200] K. J. Davidian, R. H. Dieck, and I. Chuang. “A detailed description of the uncertainty analysis for high area ratio rocket nozzle tests at the NASA Lewis Research Center”. In: *NASA Technical Memorandum* (1987). ISSN: 04999320.
- [201] N. W. Hale, N. Lamotte, and T. Garner. “Operational Experience with Hypersonic Entry of the Space Shuttle”. In: *11th International Space Planes and Hypersonic Systems and Technologies Conference*. Orleans, France, 2002.

- [202] H. W. Carlson and D. J. Maglieri. “Review of Sonic Boom Generation Theory and Prediction Methods”. In: *The Journal of the Acoustical Society of America* 51.2C (1972), pp. 675–685. ISSN: 0001-4966. DOI: [10.1121/1.1912901](https://doi.org/10.1121/1.1912901). URL: <http://asa.scitation.org/doi/10.1121/1.1912901>.
- [203] R. L. Hershey and T. H. Higgins. *Statistical Model of Sonic Boom Structural Damage*. Tech. rep. July. U.S. Department of Transportation, 1976.
- [204] J. Hentschke. *Ordinary Meeting Agenda*. Streaky Bay, SA, Australia, 2017. URL: <https://www.streakybay.sa.gov.au/webdata/resources/minutesAgendas/CouncilAgenda-Report-October2017.pdf> (visited on 10/06/2018).

GLOSSARY OF KEY TERMS

ABLS A launch system containing one or more airbreathing engines or stages.

Aerodynamic Loads The forces on an aircraft due to the pressure of the incoming air.

Aerothermal Loading The heating of an aircraft due to the compression and friction of incoming air.

Aileron A mechanically deflected surface used to control a vehicle aerodynamically.

Airbreathing Engines An engine that uses atmospheric air as oxidiser.

Angle of Attack The incidence angle of an aircraft relative to oncoming air.

Apogee The point of an orbit that is farthest from the centre of the Earth.

Boost-Skip A supersonic or hypersonic trajectory involving repeated periodic altitude raising manoeuvres (skips), with periods of interspersed thrust from an airbreathing engine (boosts). Generally used to maximise range for minimum fuel.

C-REST Engine Rectangular-to-elliptical shape transition scramjet engines, configured to a conical forebody.

Carbon-Carbon Carbon fibre in a matrix of graphite, used for high temperature structural applications and heat shielding.

Centre of Gravity The location within a body at which the force due to gravity appears to act. Generally equated (with the assumption of a uniform gravity field) to the centre of mass, the averaged mass location within a body at which all uniform forces may be approximated to act.

Circularisation A burn that raises the perigee of an orbit so that the orbit is circular.

Glossary of Key Terms

Collocation Method A type of optimal control determination that approximates states and controls as polynomials, and constrains the dynamics of the system at distinct collocation points. Includes the pseudospectral methods of collocation.

Combustion chamber The section of an engine where fuel and oxidiser are combined and burned.

Computational Fluid Dynamics Numerical models used to calculate the flow of a fluid to produce quantitative analysis. Involves discretising a mesh of points or elements and time-marching the numerical solution.

Constraints The limitations on the states or controls of a system. May be functions of states and controls.

Control The time varying parameters of a system that are directly controlled.

Cruise Flight at relatively constant speed and altitude.

Downrange A horizontal distance from the launch site.

Dynamic Pressure An expression of the increase in a fluids pressure due to velocity.

Empirical Values or trends derived from experiment and experience rather than, or in addition to, theoretical calculations.

Exergy The available work that may be extracted from a system.

Fidelity The degree of accuracy of reproduction or representation.

Fly-back The process of returning part of a launch system to its original launch location.

Glide Flight without propulsion.

Hohmann Transfer Generally the most fuel efficient manoeuvre to get from one circular orbit to another. Two burns are utilised, the first into an elliptical orbit with apogee equal to the final desired orbital radius, and the second to circularise at apogee.

Hypersonic Much greater than the speed of sound, usually denoted as speeds greater than Mach 5.

Inlet The section of an airbreathing engine where air is drawn in.

Launch The process of flight to space.

Launch System A system of propulsion systems and vehicles designed for launching to space.

Mach Number A dimensionless value representing air speed as a multiple of the local speed of sound.

Mesh The discrete set of points or elements used for computational fluid dynamics.

Nonlinear Programming The process of solving an optimisation problem subject to a nonlinear objective value and/or nonlinear constraints. Computing an optimal trajectory is generally a nonlinear optimisation problem.

Nozzle The section of an engine that is used to expand and accelerate the gases from the combustion chamber to produce propulsive force.

Objective Function The function that describes the metric to which a given system is to be optimised.

On-Orbit Manoeuvres or services performed while orbiting.

Operational Regime The range of Mach numbers over which an engine or vehicle is capable of functioning.

Optimal Control Theory A set of mathematical techniques that find a control law over a period of time in order to maximise a given objective function.

Orbit A repeating, curved trajectory path that a satellite takes around the Earth.

Payload The object or entity that is carried by a launch system for delivery to a particular location or orbit.

Performance The measured degree to which a system accomplishes its objectives.

Perigee The point of an orbit that is closest to the centre of the Earth.

Pull-Up The raising of altitude using aerodynamic lift.

Ramjet A supersonic airbreathing engine that uses forward motion to compress air before combustion at subsonic speeds.

Reentry The entry of a spacecraft into the atmosphere from space.

Reusable Launch System A launch system capable of being used for launch more than once.

Robustness The degree to which a solver is able to converge from various initial guesses.

Rocket Engine A reaction engine that uses stored propellant.

Glossary of Key Terms

Rocket Propellant The reaction mass used by a rocket engine for propulsion, usually a combination of fuel and oxidiser.

Roll Angle Also known as roll angle. The angle at which an aircraft has been turned about its centre axis (nose-to-tail) relative to the horizontal.

Satellite An man-made object that has been placed into orbit.

Scramjet A supersonic airbreathing engine that uses forward motion to compress air before combustion at supersonic speeds.

Shock Wave A sharp pressure, temperaure and density gradient caused by a vehicle moving faster than the speed of sound.

Shooting Method A type of optimal control determination that involves forward time simulations using a varied set of controls. Includes the single and multiple shooting methods.

Space The expansive region that exists outside of Earth's atmosphere. The Karman line at 100km altitude above the Earth's surface is commonly represented as the border to space.

Space Sector The companies, government entities, and private individuals involved in space launch, satellite manufacturing, and space and ground operations.

Space-Plane An aerospace vehicle with aeroplane-like aerodynamic surfaces that is also designed to be operated exoatmospherically.

Specific Impulse A measure of the fuel usage efficiency of an engine, thrust produced divided by flow rate.

Stage A distinct section of a launch system, containing its own engine and propellant.

State The time varying parameters of a system that are not directly controlled.

Subsonic Less than the speed of sound.

Sun Synchronous Orbit A slightly retrograde, near-polar orbit with a precession rate that matches the orbit of the Earth around the Sun (ie 360° per year).

Supersonic Greater than the speed of sound.

Thermal Protection System The system that protects a vehicle from the aerothermal heating it generates during flight.

Throttle The system that controls the flow of fuel to an engine.

Thrust The propulsive force generated by an engine.

Thrust Vectoring The manipulation of the direction of thrust of a vehicle, generally through gimballing of a nozzle, flow injector manipulation, or the manipulation of the shape of a nozzle or flow path.

Trajectory The flight path of a launch vehicle.

Transonic Speeds transitioning between subsonic and supersonic, close to Mach 1.

Trim The deflection of control ailerons in order to counteract the moment generated by an aircraft, to maintain attitude.

Turbojet An airbreathing engine that uses a compressor to compress air before combustion.

Viscous Effects The aerodynamic effects of the viscosity (resistance to deformation or flow) of the air, generally significant near the body of the vehicle where a boundary layer results.

Wingspan The maximum distance between the two wing-tips of a vehicle.

APPENDIX A

THERMAL ANALYSIS

The thermal protection of a hypersonic launch system is essential to its operation, and managing the aerothermal loading produced during flight is one of the most significant challenges that must be overcome before airbreathing launch systems can become a reality. The representative launch system in this study uses nearly the same thermal protection that is used in studies of the SPARTAN[32]. However, no detailed thermal analysis of the SPARTAN has been carried out to date, and as such, it is necessary to analyse the heat shielding of the representative launch system in order to quantify the temperatures on the surface of the vehicles during flight. This section aims to provide a preliminary analysis of the heat shielding of the representative launch vehicle, in order to determine whether it is sufficient for operation to a first approximation. In this section, the heat flux over the trajectory is modelled at various locations on the scramjet accelerator and third stage, and analysed transiently for the duration of the flight using 1-D heat conduction analysis to determine the efficacy of the heat shielding of the representative launch system. The temperatures on both sides of the external heat shield are analysed, to determine if the temperatures will exceed the maximum operable temperatures of the external heat shielding material, and also if the internal temperature will exceed the maximum operable temperature of the multilayer internal insulation. In addition, some aspects of the design of the representative launch system's thermal protection system (TPS) are investigated to provide an indication of the sensitivity of the temperatures produced during flight to critical TPS design parameters.

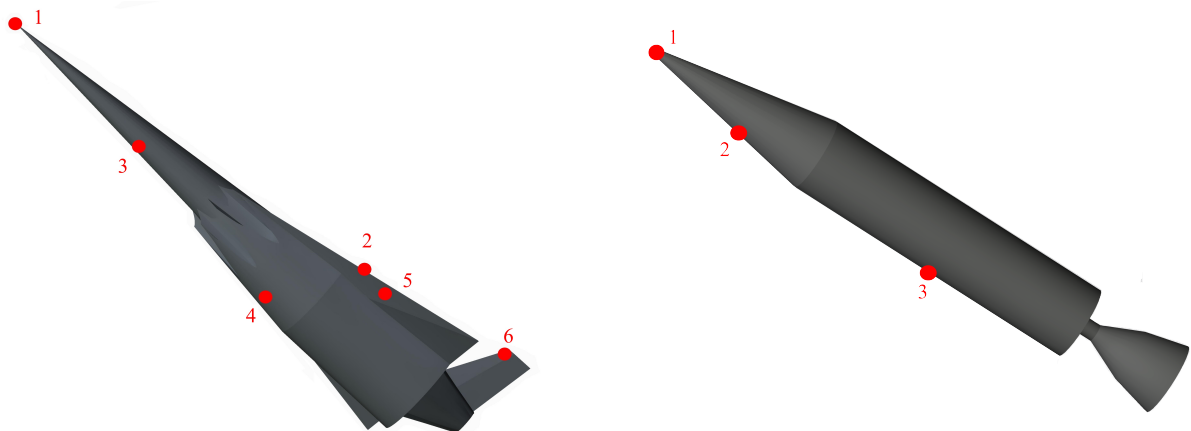
A.1 Heat Transfer Calculation

The heat transfer coefficients on the body of the vehicle are computed using Reynolds analogy:

$$c_h = \frac{c_f}{2s}, \quad (\text{A.1})$$

APPENDIX A. THERMAL ANALYSIS

where c_f is the coefficient of friction and s is the Reynold's analogy factor, assumed to be 1.16[139]. The value of c_f is determined using the viscous solver VC3D, at specific locations around the body of the scramjet accelerator and third stage, as shown in Figure A.1. On the scramjet accelerator, the nose stagnation point (1) and wing leading edges (2) are examined, along with a point midway along the nose (3), as well as midway along the cowl front (4), one-quarter of the length along the wing (5), and on the tip of the tail (6) on the windward side. On the third stage, the stagnation point on the nose (1) is examined, along with a point half way along the nose cone (2), and a point half way along the cylindrical cowl (3) on the windward side. These points are judged to be locations of potential high heat loads on the vehicles, and are examined as likely worst-case examples for thermal analysis.



(a) The locations examined on the scramjet accelerator.

(b) The locations examined on the third stage rocket.

Figure A.1: The locations chosen for thermal analysis, selected for the potential of high heat loading.

The heat transfer at the stagnation point and leading edge of the wings, where Reynold's analogy is not valid due to large pressure gradients in the flow[194], is estimated using semi-empirical correlations[195]. At the stagnation point, the heat transfer is given by[195]:

$$q_s = k_1 \rho^{N_1} V^{N_2}, \quad (\text{A.2})$$

where $N_1 = 0.5$ and $N_2 = 3$, and the constant k is[195]:

$$k_1 = \frac{1.83 \times 10^{-4}}{\sqrt{R_n}} \left(1 - \frac{T_w}{T_{aw}}\right), \quad (\text{A.3})$$

where R_n is the nose radius, T_w is the wall temperature, and T_{aw} is the adiabatic wall temperature.

The heating at the leading edge is given by a weighted average correlation between a stagnation point and a flat plate[195, 196]:

$$q_{LE} = \left(\frac{1}{2} q_s^2 \cos^2(\Lambda) + q_{FP}^2 \sin^2(\Lambda)\right)^{1/2}, \quad (\text{A.4})$$

where Λ is the wing sweep angle, and the heat flux for a flat plate is calculated using the correlation:

$$q_{FP} = k_2 \rho^{N_3} V^{N_4}, \quad (\text{A.5})$$

where $N_3 = 3.37$, $N_4 = 0.8$ for turbulent flow (2963m/s) [195, 196], and

$$k_2 = 3.35 \times 10^{-4} \cos^{1.78}(\theta) \sin^{1.6}(\theta) x_T^{-1/5} \left(\frac{T_w}{556} \right)^{-1/4} \left(1 - 1.11 \frac{T_w}{T_{aw}} \right), \quad (\text{A.6})$$

where θ is the flow incidence angle and x_T is the distance along the body from the transition point [195, 196]. For the purposes of the leading edge heating the transition point is assumed to be half the distance along the nose cone, and the transitional boundary layer length is assumed to be equal to the preceding laminar flow distance. Along with this assumption, in this study the aeroheating is calculated at the start of the wing, providing a worst case scenario for the heating rate on the leading edge.

A.2 Transient Thermal Analysis and Boundary Conditions

In order to determine the temperature that the heat shielding of the representative launch system reaches during launch, the outer heat shielding layer is analysed using the one-dimensional transient heat equation. Utilising the time varying heat flux on the outside of the vehicle and the thermal boundary conditions, the evolution of the temperature profile of the vehicle skin is calculated. This one-dimensional thermal analysis is performed using a modified version of the code *SurfaceTemp* distributed as part of the *htdt* code repository [197]. *SurfaceTemp* uses time-marching to solve the transient heat equation, with Heat flux boundary conditions for the outside surface calculated using the instantaneous wall temperatures and the correlations described in section A1, with inside heat flux conditions set as adiabatic. For flat plate locations this results in:

$$\frac{\delta T^2}{\delta x^2} = \frac{\rho c}{k} \frac{\delta T}{\delta t} \quad (\text{A.7})$$

with

$$q_{outside} = \text{Calculated using Eqn. A1.} \quad (\text{A.8})$$

$$q_{inside} = 0. \quad (\text{A.9})$$

Corresponding equations in spherical and cylindrical one-dimensional coordinates are solved for the nose stagnation and leading edge regions respectively.

Setting the inner boundary conditions as adiabatic results in somewhat of a worst case scenario,

because the heat load needs to be sustained using the latent heat capacity of the material. This results in the highest temperatures in the heat shielding material, which is particularly relevant to the survivability of the material. If more sophisticated cooling systems are implemented, more detailed analysis is essential as the reduced temperatures will increase heat transfer.

Table ??, summarises the parameters and modelling assumptions used for the analysis points shown in Figure A1. For all cases the standard optimised trajectory with fly-back is used (Case 11, Section 7.1).

The goal of this analysis is to show that the outside surface temperature does not exceed the temperature limit of the respective material and that the inside temperature is reduced sufficiently so that the external heat shielding material can interface with the internal multi-layer insulation.

A.3 Thermal Analysis of the Optimised Trajectory With Fly-Back

To determine the effectiveness of the heat shielding of the representative launch system, a 1-D heat analysis is conducted using the method described in the preceding sections. This analysis gives an indication of the temperature at the specified points around the representative launch system and third stage throughout their trajectories. Figures A.2 shows the heat responses at the specified locations on the scramjet accelerator over the ascent and return trajectories. The temperature on the outside of the scramjet accelerator raises throughout the acceleration, as expected, peaking just before third stage release. The temperature then generally decreases during descent, with smaller peaks during the 'skipping' manoeuvres, when velocity and dynamic pressure are raised.

On the scramjet accelerator, the tungsten nose reaches 2015.1K, and the Carbon-Carbon wing leading edge reaches 1665.8K. At the nose and leading edge it is assumed that there is no direct thermal connection to the internal insulation by the structure or heat shielding at the regions of maximum heat loads. The maximum heating in these areas are therefore assumed to be limited by the properties of the heat shielding itself. The temperatures that have been observed are within the operational regimes of the external heat shielding materials, and for the purposes of this study are considered sufficient for shielding during flight.

On the body of the scramjet accelerator, the interior of the nose cone reaches a maximum of 1363.1K, the cowl 1384.9K, the wing 1326.4K, and the tail 1142.3K on the inner surface of the heat shielding. These temperatures are well within the operational regime of the heat shielding material, although the internal temperatures are at the limits of the operational regime of the internal multilayer insulation, which is nominally designed for operation in the 900-1100°C (1173-1373K) range. These high temperatures will begin to reduce the mechanical strength of the internal insulation[198], and must be accounted for in the detailed internal design, so that the internal insulation does not fail when peak temperatures are reached.

In addition to the high temperatures possibly approaching the limits of the multilayer insulation,

A.3. THERMAL ANALYSIS OF THE OPTIMISED TRAJECTORY WITH FLY-BACK

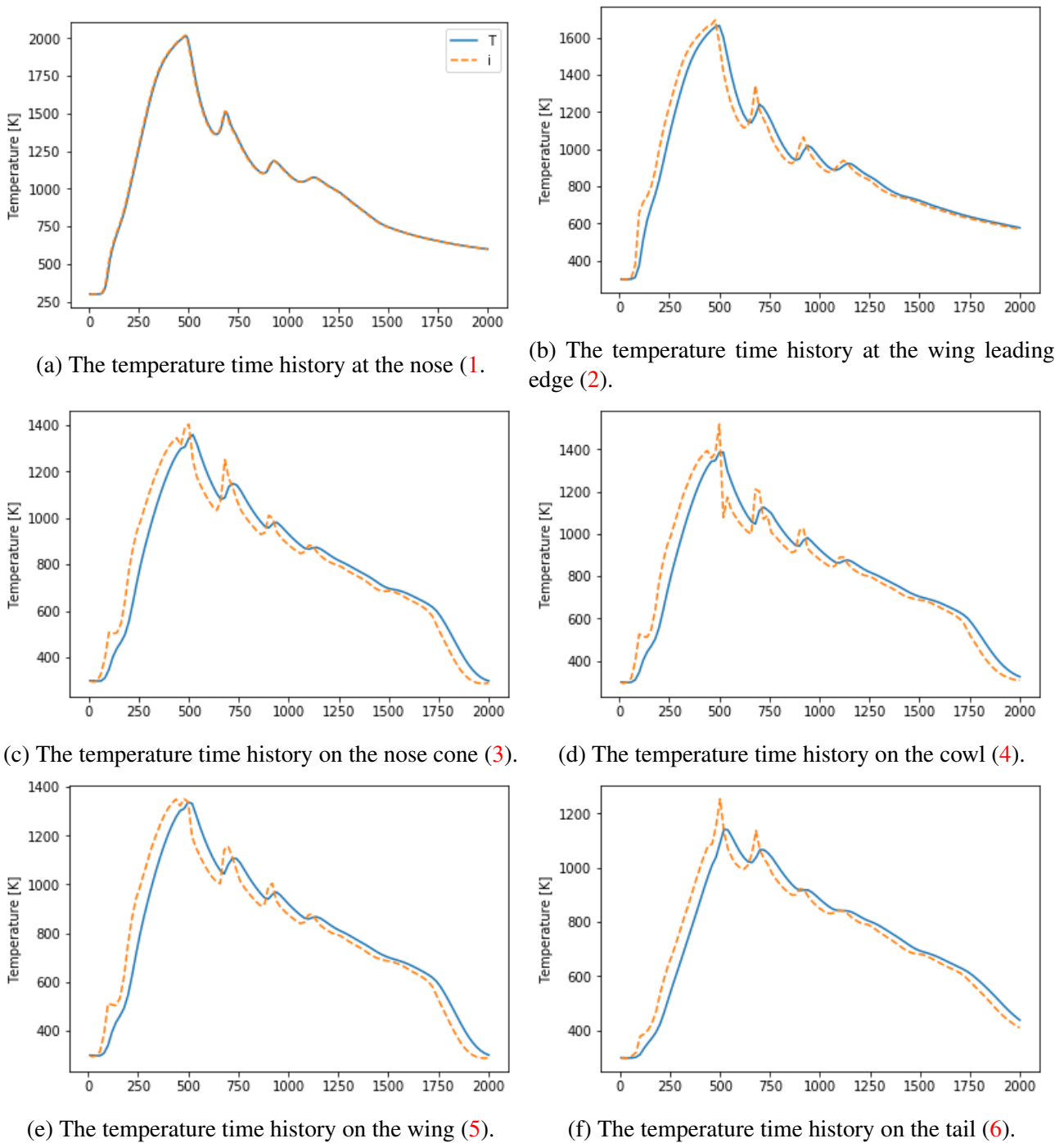
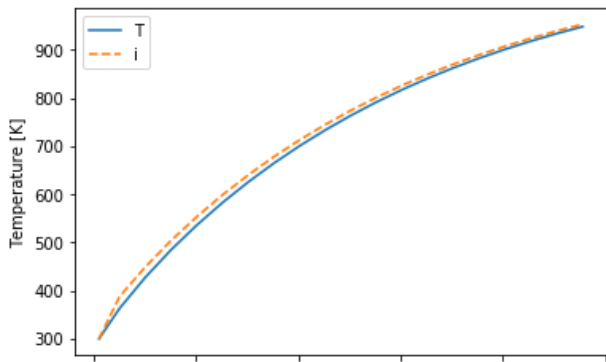


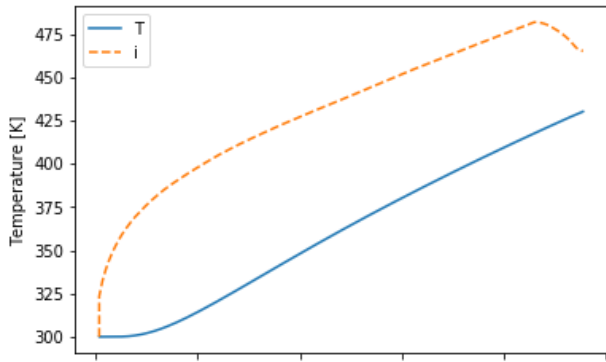
Figure A.2: Temperature time histories on the scramjet accelerator.

the high temperatures produced will influence the material used for the internal structure. In analytical studies based on experimental tests of the internal multilayer insulation at 1273K (1000°C) approximate surface temperature, the innermost surface of the insulation has been shown to keep temperatures below 546K (273°C)[198] when the multilayer insulation with best performance (silica felt insulation[198]) is used. Because the internal temperatures are above the experimentally tested

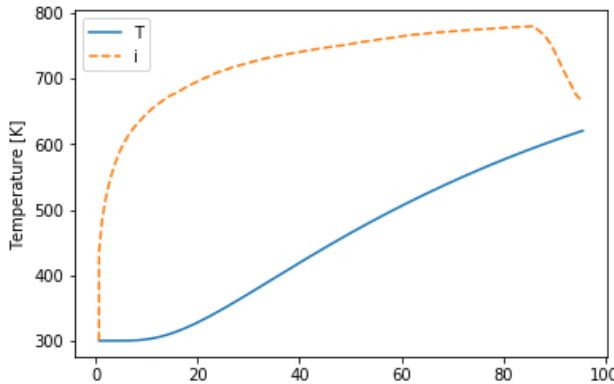
APPENDIX A. THERMAL ANALYSIS



(a) The temperature time history at the nose (1).



(b) The temperature time history on the nose cone (2).



(c) The temperature time history on the cylindrical body (3).

Figure A.3: Temperature time histories on the third stage rocket with time.

A.3. THERMAL ANALYSIS OF THE OPTIMISED TRAJECTORY WITH FLY-BACK

Point	Material	Thermal Conductivity	Specific Heat	Density (kg/m ³)	Geometry	Boundary Conditions
Scramjet Accelerator Point 1	Tungsten	237	134	19250	100mm diameter, 40mm thick hemispherical tip	Outer: Stagnation Inner: Adiabatic
Scramjet Accelerator Point 2	Carbon-Carbon	3.55	1829	1593	11.3mm thick, conical (modelled as cylindrical) on nose, flat on body	Outer: Swept Leading Edge Inner: Adiabatic
Scramjet Accelerator Points 3-6	Carbon-Carbon	3.55	1829	1593	11.3mm thick, conical (modelled as cylindrical) on nose, flat on body	Outer: Reynolds Analogy Inner: Adiabatic
Third Stage Point 1	Tungsten	237	134	19250	142mm diameter, 20mm thick hemispherical tip	Outer: Stagnation Inner: Adiabatic
Third Stage Point 2	Carbon-Carbon	3.55	1829	1593	10.8mm thick, conical (modelled as cylindrical)	Outer: Reynolds Analogy Inner: Adiabatic
Third Stage Point 3	Phenolic Cork	0.07	2100	512	3.1mm thick, cylindrical	Outer: Reynolds Analogy Inner: Adiabatic

temperature, the innermost surface temperature of the insulation is likely to be above 546K, and are likely to be within the range where conventional aluminium alloys begin to lose their mechanical strength. Because of this, it is likely that a high temperature aluminium alloy would be required for the internal structure, at least in the regions of the internal structure that are close to the interface with the external insulation.

Figure A.3 shows the temperature response at the specified locations over the third stage rocket, while the rocket is accelerating with the heat shield attached. The temperatures on the outside of the third stage rocket increase for most of its acceleration, reducing only at the very end, when the angle of attack is reduced, and the atmosphere is extremely thin. The temperatures on the third stage rocket are significantly lower than those experienced by the scramjet accelerator. The nose tip of the third stage reached a maximum inner surface temperature of 953.5K, while the nose cone and body reach maximum temperatures of 475.9K and 779.8K respectively. These relatively low temperatures indicate that the current heat shielding design is appropriate for resisting the thermal loading experienced by the third stage rocket. In fact, the heat shielding may be over-engineered, and it may be possible to reduce the mass of the heat shield by reducing the thickness of the tungsten and C-C protection on the nose, or by changing the material entirely.

A.4 Thermal Protection Exploration

The design of the thermal protection systems of the vehicles within an airbreathing launch system is critical to the successful operation of the system. While this work assumes that the TPS is sufficient for operation, the scramjet accelerator stage is flying close to its thermal limits, while the heat loading on the third stage rocket is significantly lower. As the modelling of the launch system improves, it is likely that the TPS will be redesigned and heat shielding redistributed to optimise the weight of each vehicle while accounting for heating distribution. The following sections explore the effect of changing the physical properties of the external heat shielding, applying active cooling, and the impact of imposing peak heat load limits on vehicle performance.

A.4.1 Scramjet Accelerator TPS Design Exploration

The simplest method of modifying the TPS of the launch system is to modify the properties of the external heat shielding. To illustrate the effects of these variations, the thickness, density, thermal conductivity and specific heat of the C-C heat shield on the scramjet engine shroud (Position 4) are varied by $\pm 10\%$. The shroud is chosen in order to measure the effect of the heat shielding properties and design at the region of highest heating with direct connection to the internal insulation. The maximum inner surface temperature recorded is shown in Table A.1. These variations indicate an inner surface temperature sensitivity of $-2.7\text{K}/\%$ to variation in thickness, $-1.9\text{K}/\%$ to variation in

density, and 0.6 K/% to variation in thermal conductivity when varied from the standard CCAT T-300 properties. The effects of a 10% variation in any of these properties is not particularly large. This indicates that if the maximum inner surface temperature is to be reduced in an area of high heating through modification of the heat shield, the heat shield design or properties in that area must be modified significantly to produce a significant effect.

	-10%	-5%	Standard	+5%	+10%
Thickness	1418.0	1401.4	1384.9	1375.6	1363.6
Density	1408.6	1396.3	1384.9	1378.0	1369.9
Thermal Conductivity	1380.4	1382.9	1384.9	1388.9	1393.6

Table A.1: Inner surface temperatures in kelvin on the shroud of the scramjet accelerator with variations in heat shielding properties.

If passive TPS is not sufficient, active cooling may be introduced in areas of high heat loads. This active cooling can take many forms, such as regenerative, film, and transpiration cooling[199], all of which are currently being actively studied for applications to hypersonic vehicles. For the most critical areas of high heating on the scramjet body, regenerative cooling is assumed to be the most practical method of active cooling, and the complex effects of this cooling are approximated as a set rate of heat transfer away from the inner face that directly reduces the temperature of the inner face of the heat shielding. Inner face temperatures on the shroud with heat transfer rates from 0 to 20kW away from the inner face are compared in Table A.2. The inner face temperature shows a sensitivity of -5.2 K/kW to a constant rate of heat transfer applied to the inner face.

Heat Transfer Rate	Standard (0kW/m ²)	5kW/m ²	10kW/m ²	15kW/m ²	20kW/m ²
Maximum T (K)	1384.9	1359.3	1333.4	1307.4	1281.2

Table A.2: Maximum inner surface temperature with a constant rate of heat transfer away from the inner surface of the shroud.

A.4.2 Heating limited Trajectory

The aerothermal effects on a launch vehicle may also be reduced by limiting the aeroheating of the vehicle during flight. However, performing a 1-D heat transfer analysis within a trajectory optimisation loop is prohibitively computationally expensive. As such, to investigate the effects of limiting the maximum aerothermal heating on the scramjet accelerator in a computationally efficient manner, the stagnation point heat flux is calculated in-loop using a cold wall approximation where the wall temperature is much smaller than the adiabatic wall temperature ($T_W/T_{AW} \approx 0$)[195]. This calculation of the heat flux is conservative, however it is useful for applying limits to the heat loading for optimal trajectory investigation. Stagnation point heat flux limits of 1700, 1600, 1500 and 1400kW/m² are

APPENDIX A. THERMAL ANALYSIS

Trajectory Condition q ₂ Lim:	Standard	1700kW	1600kW	1500kW	1400kW
Payload to Orbit (kg)	132.1	127.4	119.3	78.4	73.6
Total η_{exergy} (%)	1.576	1.510	1.402	1.042	1.010
1st Stage η_{exergy} (%)	6.925	6.902	6.825	6.917	6.902
Separation Alt, 1→2 (km)	24.58	26.09	25.83	24.57	24.55
Separation v, 1→2 (m/s)	1539	1526	1517	1538	1536
Separation γ, 1→2 (deg)	11.3	11.3	10.9	11.1	11.0
2nd Stage η_{exergy} (%)	3.758	3.631	3.428	4.303	4.185
Separation Alt, 2→3 (km)	42.52	43.21	43.34	34.45	34.92
Separation v, 2→3 (m/s)	2507	2474	2420	2657	2629
Separation γ, 2→3 (deg)	12.7	12.9	13.2	1.6	1.5
2nd Stage Flight Time (s)	508.8	545.6	579.2	544.7	551.4
2nd Stage Distance Flown (km)	872.3	909.2	943.7	970.3	981.5
2nd Stage Return Fuel (kg)	252.4	210.3	138.5	230.0	276.2
2nd Stage Return Distance (km)	1520.4	1358.8	1074.8	1285.0	1368.3
3rd Stage η_{exergy} (%)	13.142	12.676	11.888	7.617	7.158
3rd Stage t, q > 5kpa (s)	9.1	7.7	5.7	138.7	138.1
3rd Stage Fuel Mass (kg)	2853.1	2857.9	2865.9	2906.8	2911.6

Table A.3: Scramjet stage stagnation point heating limited trajectories, optimised for maximum payload-to-orbit with stagnation point heating calculated using a cold wall approximation.

applied, based on the maximum non-limited stagnation point heat flux of 1770kW/m², calculated using a cold-wall approximation in an optimised trajectory with return (Case 11). Optimised trajectories calculated with these heat flux limits applied to the scramjet accelerator stage are presented in Table A.3, and the trajectories of the scramjet stages are shown in Figure A.4.

From Table A.3 and Figure A.4 it can be observed that limiting the stagnation point heat flux has a significant effect on the optimised trajectory. However, it is also evident that the effects of the 1700kW/m² and 1600kW/m² limits are small, compared to the effects of 1500kW/m² and 1400kW/m² limits. This sharp change in trajectory shapes is caused by a distinct cut-off point at which the scramjet stage is no longer able to perform the manoeuvres necessary for a pull-up. When stagnation point heat flux is limited to 1700 or 1600kW/m², the scramjet stage compensates by flying a slower, higher trajectory after release from the first stage rocket, reaching maximum dynamic pressure later, and performing a larger pull-up. This flight path limits the speed of the scramjet stage and manoeuvres into a favourable position, while still performing a pull-up manoeuvre. In these cases, maximum heat flux is only reached at the start of the pull-up manoeuvre. However, when the stagnation point heating rate is limited to 1500kW/m² or 1400kW/m², the trajectory changes significantly. For these limits, the beginning of the scramjet stage trajectory conforms with the non-limited optimal flight path, but the stagnation point heating limit causes the scramjet stage to leave maximum dynamic pressure and climb in the middle of the trajectory, reducing efficiency and manoeuvrability, and removing the ability of the scramjet accelerator stage to perform a pull-up manoeuvre. This cut-

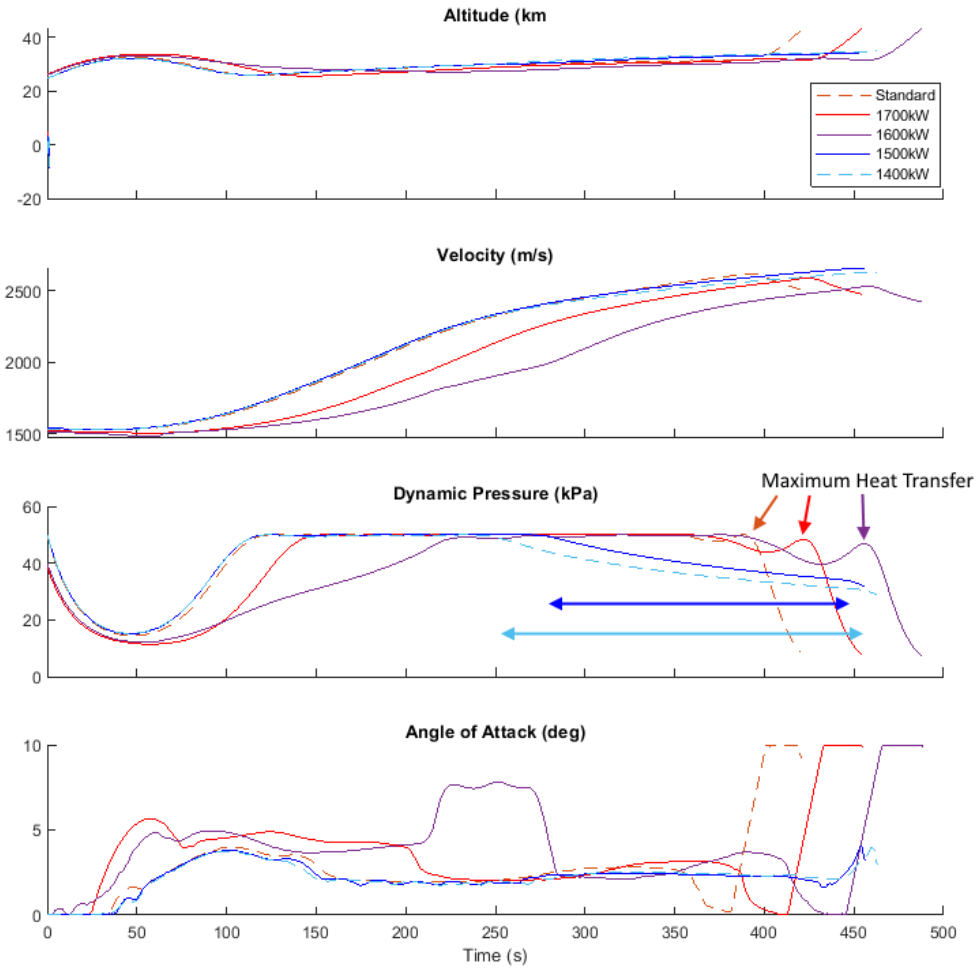


Figure A.4: Comparison of scramjet accelerator trajectories with varying stagnation point heating limits.

off point is primarily driven by the lower limit on the speed of the scramjet accelerator during flight, which limits the start-of-trajectory manoeuvres performed to enable the pull-up in the 1700kW/m^2 and 1600kW/m^2 heating limited trajectories.

Generally, these optimised trajectory results indicate that heating limits imposed on the trajectory of the scramjet accelerator vehicle result in the vehicle flying a significantly less efficient trajectory in order to reduce heat loads. For small heating limitations this may be suitable, however, in general, it is important to design an efficient airbreathing vehicle to be able to tolerate the heat loads required for an optimal payload-to-orbit flight path.

Property	-10%	-5%	Standard	+5%	+10%
Thickness	486.4	480.7	475.9	471.7	468.1
Density	489.9	482.6	475.9	469.6	464.3
Thermal Conductivity	480.0	477.9	475.9	474.1	472.5

Table A.4: Inner face temperatures in kelvin with variations in third stage heat shielding properties.

A.4.3 Third Stage Heat Shielding Design Exploration

To explore the design of the third stage heat shielding, various properties of the C-C on the conical nose cone are varied by $\pm 10\%$, and the temperature time histories along the optimised payload-to-orbit trajectory with return (Case 11) are calculated. The maximum temperatures observed on the inner surface at the centreline of the nose cone heat shielding are shown in Table A.4. These variations show an inner surface temperature sensitivity of -0.9 K/% to variation in thickness, -1.3 K/% to variation in density, and -0.4 K/% to variation in thermal conductivity when varied from the standard CCAT T-300 properties. These variations are relatively small, however, part of the reason for this is that the heat transfer, and the temperatures, are relatively low.

A.4.4 The Effects of a Pull-Up on the Third Stage Heat Shield Design

Payload to Orbit (kg)	147.4
Total η_{exergy} (%)	1.723
1st Stage η_{exergy} (%)	6.996
Separation Alt, 1→2 (km)	24.65
Separation v, 1→2 (m/s)	1548
Separation γ, 1→2 (deg)	10.9
2nd Stage η_{exergy} (%)	3.810
Separation Alt, 2→3 (km)	41.09
Separation v, 2→3 (m/s)	2531
Separation γ, 2→3 (deg)	12.3
2nd Stage Flight Time (s)	500.6
2nd Stage Distance Flown (km)	861.2
2nd Stage Return Fuel (kg)	262.9
2nd Stage Return Distance (km)	1515.2
3rd Stage η_{exergy} (%)	14.759
3rd Stage $t, q > 5\text{kpa}$ (s)	11.6
3rd Stage Fuel Mass (kg)	2831.7

Table A.5: Summary of a payload-to-orbit optimised trajectory with a 46.2kg third stage heat shield.

The third stage rocket used as part of the representational launch system in this study has been designed to be released from the end of a constant dynamic pressure trajectory[32]. This third stage

rocket has a heat shield mass of 124.6kg. However, a pull-up at the end of the scramjet stage acceleration has been shown in Section 3.1 to be an integral part of the payload optimal trajectory for a rocket-scramjet-rocket launch system. In addition to maximising payload, this pull-up also has significant aerothermal benefits for the third stage rocket, reducing the heat loading on the third stage significantly, and potentially allowing for the heat shielding of the third stage to be reduced. When separated from a scramjet stage constrained to constant dynamic pressure (presented in Section E.3), the third stage rocket exhibits temperatures of 2254.8K on the nose tip, 1511.7K on the nose cone, and 1415.8K on the body, much larger than the temperatures generated by a third stage separated after a pull-up manoeuvre, of 953.5K on the nose tip, 475.9K on the nose cone, and 779.8K on the body. It is likely that the temperatures generated after release from a constant dynamic pressure trajectory would be at the limits of the multilayer insulation, however when released after a pull-up, the temperatures are much lower. While it is desirable to have lower temperatures on the third stage, and lower temperatures may be required for payload survivability, it may also be desirable to redesign the heat shielding of the third stage specifically to take into account the conditions after release from a scramjet stage flying a pull-up.

To illustrate the effects of redesigning the heat shielding of the third stage rocket, the third stage heat shield thickness is reduced. The effects of the pull-up on the heat shield temperatures are too large to apply the linear sensitivity relationship developed in Section A.4.3. Because of this, the thicknesses of the nose tip, nose cone and cylindrical body are all reduced proportionally to the comparative reduction in temperature when the third stage is released after a pull-up, when compared to a third stage released without a pull-up. This resulted in a heat shield weighing 46.2kg. An optimised trajectory was produced using this heat shield mass, with results summarised in Table A.5. The payload-to-orbit increases to 147.4, an increase of 15.3kg (11.6%) when compared to an optimised trajectory with the full heat shield mass. This increase illustrates the potential payload-to-orbit benefits of a pull-up manoeuvre beyond simply increasing the operational performance of the launch system, by reducing the thermal loading on the third stage, and thus decreasing the necessary heat shielding mass.

A.5 Summary

A 1-D heat conduction analysis has been conducted to investigate the aerothermal effects of flying a payload-to-orbit optimised trajectory on the representative launch system. Various points around the scramjet stage and third stage were investigated, either using stagnation point heat transfer correlations for the nose and leading edges, or Stanton numbers computed using Reynold's analogy for points on the body. It was found that the maximum external temperatures on the nose and leading edges of the scramjet stage were very large, at 2015.1K and 1665.8K respectively. On the body of the scramjet accelerator, the interior of the nose cone was found to reach a maximum of 1363.1K,

APPENDIX A. THERMAL ANALYSIS

the cowl 1384.9K, the wing 1326.4K, and the tail 1142.3K on the inner surface of the heat shielding. These temperatures are close to the limits of the multilayer internal insulation, and will produce temperatures on the inside surface of the multilayer insulation that approach the limits of typical high temperature aerospace materials. It may be necessary to introduce further methods of mitigating this heating in future designs of this launch system or other airbreathing launch vehicles. To investigate possible mitigation strategies, key properties of the heat shielding of the scramjet-powered stage were varied by $\pm 10\%$ indicate an inner surface temperature sensitivity of $-2.7\text{K}/\%$ to variation in thickness, $-1.9\text{K}/\%$ to variation in density, and $0.6 \text{ K}/\%$ to variation in thermal conductivity. Next, active cooling was approximated by a constant rate of heat transfer away from the inner surface, exhibiting a sensitivity of $-5.2 \text{ K}/(\text{kW/m}^2)$. Lastly, heating limitations were imposed on the optimal trajectory, which had only a small effect at limits of 1700 and 1600kW/m^2 , requiring manoeuvring of the scramjet accelerator at the beginning of the trajectory. However, heating rate limits of 1500 and 1400kW/m^2 produced a distinct cutoff point at which the scramjet accelerator could no longer manoeuvre sufficiently at the beginning of the trajectory, so that the trajectory shape followed closely to the dynamic pressure and heating limits, and the performance of the launch system degraded significantly.

The maximum temperatures of the third stage rocket were determined to be much lower, with the nose tip of the third stage reaching a maximum inner surface temperature of 953.5K, the nose cone 475.9K, and the body 779.8K on the inner surface of the heat shielding. These relatively low temperatures indicate that it may be possible to reduce the thickness of the heat shield, or change material properties if so desired. A sensitivity study was conducted on key heat shielding design parameters on the nose cone section of the heat shield, and it was found that the third stage has a nose cone inner surface temperature sensitivity of $-0.9 \text{ K}/\%$ to variations in thickness, $-1.3 \text{ K}/\%$ to variations in density, and $-0.4 \text{ K}/\%$ to variations in thermal conductivity when varied $\pm 10\%$ from the standard CCAT T-300 properties.

To illustrate the possible design benefits of the decreased heat loading experienced when the third stage is released from the end of a pull-up manoeuvre, the third stage heat shielding was modified. The third stage heat shielding was reduced in thickness on each segment proportionally to the reduction in temperature caused by a pull-up manoeuvre, resulting in a heat shield weighing 46.2kg. A trajectory optimised for payload-to-orbit with this heat shield mass increased in payload mass to 147.4kg, a $+15.3$ ($+11.6\%$) increase over a trajectory optimised with the standard heat shield mass.

These results provide a preliminary heat shielding evaluation and TPS analysis of the representative launch system. Initial results indicate that the heat shielding may be assumed to be sufficient for operation, however, more detailed analysis and design is necessary. A thorough design study is necessary to determine the efficacy of a passive TPS, along with a design optimisation taking into account the trade-offs between the heat shielding, the internal multilayer insulation, and internal structure.

APPENDIX B

MODELLING UNCERTAINTIES

This thesis aims to provide new insight into the operability and feasibility of multi-stage launch systems incorporating an air-breathing stage. No such launch systems currently exist, and several of the technologies necessary for the successful operation of their systems and subsystems are in the research stage of development. This means that reliable performance data is not available, and while every effort has been made to apply accurate vehicle and subsystem models, it is acknowledged that the designs of several subsystems are simplified during the modelling process. These simplifications in the design and modelling are necessary because of the preliminary nature of this analysis, however, it is acknowledged that they will have an impact on the vehicle simulations. This work addresses simplifications and uncertainties in two distinct parts; the simplifications that arise during vehicle design that are investigated in Section 4.4; and the uncertainties that arise from the modelling of the launch system performance that are studied in this section.

The design uncertainties that arise from simplifications during the design process are investigated in Section 4.4, and affect the vehicle’s geometry, structure and internal layout, and mass and mass-distribution. In this work the design process is necessarily simplified, and it is assumed that by making appropriate design choices the nominal vehicle can be constructed (i.e. it is assumed that the designer can achieve the representative design by selecting appropriate materials and layouts), and that the nominal vehicle is capable of flying an appropriate launch trajectory. These simplifications account for the assumptions that lead to this nominal launch system, and in this stage of design it is primarily important for the designer to be aware of the sensitivities and trade-offs between the design choices and performance.

This section studies the uncertainties that arise during the modelling of the performance of the launch system, that introduce differences between the actual launch system and the “as-designed” nominal launch system. As the designer has no direct control over these uncertainties (which are both aleatory and epistemic), we need to rely on a-priori experience and a stochastic approach to quantify

how the ultimate performance of the vehicle will be different to the “as designed” simulations. The aim of this chapter is to apply a systematic approach to develop an understanding of how these uncertainties may affect the performance of the launch system. To consider this we first estimate the modelling uncertainties associated with the representative launch vehicle, and then conduct a reduced Monte-Carlo simulation (using Latin Hypercube sampling) to characterise how the modelling errors and simplifications affect the performance of an otherwise “known” vehicle.

B.1 Aerodynamic and Propulsion Simulation Uncertainties

To estimate the modelling uncertainties that are present in the simulation of the representative launch vehicle in this study, the methods by which it has been analysed must be put under scrutiny. The calculation of an optimal flight path in a preliminary design analysis requires a large number of aerodynamic and propulsive simulations in order to cover the possible flight regimes of the launch system. In addition, the analysis of an optimal trajectory does not require high fidelity modelling techniques for useful information to be generated, because it is the general performance of the system that is of interest, rather than the specific performance of the design. Because of these factors, the launch system in this study is analysed using medium and low fidelity modelling techniques chosen for their fitness-for-purpose for optimal trajectory analysis, with an emphasis on computational efficiency as well as accuracy. The uncertainties in the propulsive and aerodynamic properties of the launch system modelled in this work must be estimated, as there are no flight test or experimental results available for the representative launch system analysed in this study. In this section an estimate of the aerodynamic and propulsive uncertainties associated with the trajectory optimisations in this work is provided, and a Latin hypercube analysis is carried out to determine the variance in a sample trajectory optimisation and to assess the validity of the optimal trajectory results.

B.1.1 Aerodynamic Uncertainty

The aerodynamic coefficients of the representative launch system in this work are calculated using an inviscid Euler solver, Cart3D, with a flat plate correction for the viscous forces as outlined in Section 4.1.4. This is a medium fidelity method, which brings with it a significant associated uncertainty in the aerodynamics of the vehicle, particularly at subsonic and transonic conditions. Although the aerodynamics of the vehicle in this work are not experimentally validated, studies have previously compared Cart3D with experimental data for a number of geometries at various flight conditions. These experimental comparisons are utilised to estimate the uncertainty arising in the aerodynamic coefficients calculated by Cart3D. The first two of these comparison studies do not correct for viscous forces, and so underpredict drag in almost all cases in the supersonic and hypersonic regimes.

Abeynayake & Agon

Abeynayake & Agon assess two missile geometries; a conventional missile at transonic and supersonic speeds, and a non-conventional missile that has a cruise missile profile and includes small wings at subsonic speeds[146]. Abenayake and Agon estimate the magnitude of the uncertainty of Cart3D in a comparison to experimental results. The uncertainty magnitudes are estimated in relative error, normalised by the average value of data points between 0° and 10° angle of attack for drag, or the value at 10° angle of attack in the case of the lift and pitching moment coefficients[146]. Because of this normalisation, and because experimental data is not shown[146], the mean error values reported are used in this study, and it is noted that these relative errors only give an indication of the accuracy of a specific tool[146]. It is found that when compared to experimental results, Cart3D has a mean error in drag of 31.3% for subsonic, 23.5% for supersonic, and 18.0% for transonic cases[146] when compared to wind tunnel data for the non-conventional missile at angle of attack values between -10° and 10° in the subsonic regime, and the conventional missile at angles of attack of 0° to 10° in the transonic and supersonic regimes. The mean relative error in lift was found to be 16.5% for subsonic, 1.3% for supersonic, and 28.7% for transonic cases[146], and the error in pitching moment 22.0% for supersonic and 67.1% for transonic cases, with no subsonic error given[146]. In this comparison study Cart3D was not able to match experimental trends closely in the subsonic and transonic regimes. Errors of up to 80.2% in drag are observed in the subsonic regime for an unconventional missile geometry[146], although is is likely that the drag error in Cart3D likely diminishes significantly at angle of attack values between -5° and 5° . In the supersonic regime, Cart3D appears to closely match the experimental lift and drag trends, with an underprediction in the magnitude of the drag forces due to the absence of viscous forces. Cart3D had poor results when computing pitching moment, although it was occasionally able to match the magnitude of the pitching moment well Cart3D was not able to match the experimental pitching moment trends for either vehicle[146]. The work by Abeynayake & Agon indicates that the uncertainties associated with Cart3D are significant, particularly at angle of attack values greater than 5 in the subsonic and transonic regimes, and that it does not estimate pitching moment trends well. However, a portion of the uncertainty magnitudes are associated with the inviscid nature of Cart3D, particularly in the drag forces in the supersonic and hypersonic regimes.

Kiris et al.

Kiris et al. compare experimental data and CFD codes to assess their performance on the Ares V[147]. Cart3D is compared to the Overflow and USM3D RANS solvers, on a full scale Ares V model with conditions matching those expected during flight. In this comparison an axial force difference of maximum 10% was found, present in the supersonic regime due to the inviscid nature of Cart3D[147]. Cart3D, USM3D and Overflow were then compared against three wind tunnel tests with scaled vehicles, each with slightly different shroud or base shapes. Only one vehicle configuration produced

results good enough for comparison[147], showing high Cart3D error in the subsonic and transonic regimes. Cart3D was reported to exhibit maximums of 33% error in axial force and a 17% error in normal force in the subsonic regimes, 20% error in axial force and 21% error in normal force in the transonic regime, and 19% error in axial force and 12% error in normal force in the supersonic regime, when compared to experimental results. In the supersonic regime, the axial force under-predicts consistently, and much of the axial force error is likely due to a lack of viscous effects in Cart3D.

Ward et al.

A study by Ward et al.[139] compares Cart3D results to experimental results for a blunt body at hypersonic speeds, a lifting body vehicle at subsonic and supersonic speeds, and a hypersonic accelerator test geometry at hypersonic speeds. Ward et al. provide a method for viscous correction of the Cart3D results, and also compare this with experimental results, focusing on the amount that drag error is able to be corrected. In this study Cart3D was found to predict trends in drag coefficients well for all tested cases both subsonic and supersonic, although when uncorrected for viscous effects a consistent underprediction of 15-25% in drag coefficient was observed[139]. When corrected for viscous effects, the drag coefficient was found to agree closely with the experimental results at supersonic and hypersonic speeds, with error reducing to less than 10% for the hypersonic accelerator test vehicle, and less than 11% for the lifting body at supersonic speed[139]. Drag error at high angles of attack at subsonic speeds was still found to be large, at 38%, however, at angles of attack under 5° the error reduced significantly, matching the experimental results to within 16%.

Summary

The three studies investigated here are used to assign uncertainties to the aerodynamic coefficients computed by Cart3D. These uncertainties are separated by subsonic, transonic and supersonic/hypersonic regimes, because it is evident that Cart3D shows significantly varied and uncorrelated errors in each regime. Generally, the maximum error values reported are used as an approximation of the upper uncertainty bound for a given coefficient and regime. Note that while the values reported by Abeynayake & Agon[146] are non-dimensionalised relative accuracies, it is assumed here that the mean values reported are indicative of the accuracy of Cart3D.

The uncertainty values that have been assigned to each coefficient across regimes are summarised in Table B.1. In the subsonic and transonic regimes Abeynayake & Agon and Kiris et al. find that Cart3D is not capable of predicting the trends of the aerodynamic data well[146, 147], and as such the uncertainty values for coefficients in these regimes are set to the maximum error values observed within the operable regions across the investigated works, when data is available. The subsonic drag uncertainty is set as 33%, and lift uncertainty is set to 17%, matching the maximum error observed

by Kiris et al.[147] in the axial and normal forces in this regime. The pitching moment error in the subsonic regime is not stated in any of the works analysed, so the average relative error for all Cart3D coefficients at subsonic speeds reported by Abeynayake & Agon[146], 23%, is used. The drag uncertainty in the transonic regime is set to 21%, to match the axial force error reported by Kiris et al.[147], and the lift and pitching moment uncertainties in this regime are set to 28.7% and 67.1% respectively, to match the mean relative error reported by Abeynayake & Agon[146]. The lift coefficient uncertainty in the supersonic regime is set to 12%, to match the error reported by Kiris et al.[147], and the pitching moment uncertainty is set as 22.0%, to match the mean relative error reported by Abeynayake & Agon[146]. In the supersonic regime the ability of Cart3D to predict drag trends improves, with the lack of viscous effects causing a consistent underprediction in axial force while still matching experimental trends when uncorrected[139, 146, 147]. The uncertainty in drag in the supersonic regime is set to 11%, to match the maximum error observed after viscous correction by Ward et al.[139], due to the observations that the consistent underpredictions observed by Abeynayake & Agon[146] and Kiris et al.[147] are primarily due to a lack of viscous effects. The Euclidean correction method outlined by A. Ward was utilised to correct the inviscid aerodynamic coefficients in this study, with viscous aerodynamics provided by A. Ward for this work, warranting the use of the error value for axial force reported after viscous correction in the supersonic/hypersonic regime. These uncertainty values are summarised in Table B.1, along with the uncertainties in the propulsion systems.

B.1.2 Propulsion System Uncertainties

The Rocket Engines

The propulsive properties of the rocket engines that power the first and third stages of the launch system are taken from the Falcon 1 Launch Vehicle Payload User's Guide[164], a document released by SpaceX that does not contain detailed information as to how the engine properties are calculated. It is assumed that the properties of the engines presented by SpaceX have been measured experimentally, and that the primary uncertainties associated with the rocket engine properties are experimental uncertainties. With no knowledge of the experimental facilities or processes used, it is necessary to estimate the experimental uncertainty through analysis of other experimental facilities, information that is generally sparse. Davidian, Diek and Chuang[200] assess the specific impulse uncertainty associated with high area ratio rocket tests at NASA Lewis Research centre, by propagating an "exhaustive" list of possible error sources. The test facility was found to be capable of measuring specific impulse to within 1.30%, thrust to within 1.12%, and mass flow rate to within 0.72%. These propagated uncertainty values assumed that there was no bias errors, and that calibration had no error prior to testing. The uncertainty in the specific impulse of 1.30% is used as the rocket engine performance uncertainty for the purposes of this study, assuming that the testing that has been carried out on the

Merlin 1-C and Kestrel engines has the same error margins as the NASA Lewis Research Centre facilities.

The Scramjet Engine

The C-REST engines are modelled in this work using a dataset developed using a combination of high-fidelity CFD, and quasi 1-D analysis, tuned using experimental results[92]. Estimating the error in this model in comparison to a realistic, flight capable scramjet is not feasible, due to the lack of flight test data or full-scale engine ground testing for scramjet engines in the public domain. For the purposes of this study a nominal uncertainty of 25% is associated with the specific impulse of the scramjet engines based on the experience of the Author's colleagues and supervisors at The University of Queensland's Centre for Hypersonics. This is an estimated uncertainty margin, and it is possible that the uncertainty margin may be higher than this estimated value. However it is probable that if there are errors larger than 25% in the performance modelling of the scramjet engines, then the design of the system may have to change considerably to be feasible. For this reason, the uncertainty margin of the scramjet specific impulse is kept at 25% for payload-to-orbit uncertainty margin calculations, and this work is considered to be applicable to airbreathing engines with a performance close to those modelled.

B.1.3 Quantification of Aerodynamic and Propulsion Uncertainty Effects

The uncertainty margins of the aerodynamic and propulsive data for the representative launch system analysed in this study are shown in Table B.1. These uncertainty margins have been developed in Sections B.1 & B.1.2, based on studies comparing the modelling techniques used in this study to higher fidelity techniques and experimental data.

Uncertainty	Subsonic	Transonic	Supersonic/Hypersonic
1 st & 3 rd Stage I_{SP}	1.3%	1.3%	1.3%
Scramjet I_{SP}	-	-	25%
C_L	17%	28.7%	12%
C_D	33%	21%	11%
C_M	23%	67.1%	22.0%

Table B.1: The uncertainty margins associated with the aerodynamic and propulsive modelling of the representative launch system in this study. Values are shown to the significant figure accuracy reported by their source.

In order to quantify the effects of the modelling uncertainty in the aerodynamic and propulsion models, a Monte Carlo variation study is carried out using a Latin Hypercube Sampling technique to create a series of discrete points. A sample size of 100 runs was used, distributed using Matlab's

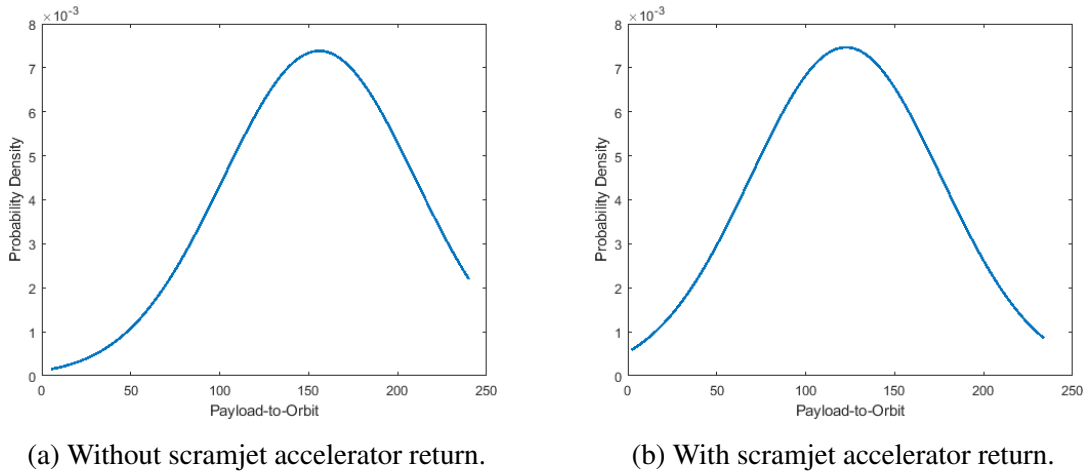


Figure B.1: The probability density distribution of optimised payload-to-orbit values over the range of LHC determined samples.

`lhsdesign` function. Figure B.1 shows the probability density function representations of the payloads-to-orbit for optimised trajectories with, and without return, with 97.5% confidence intervals of 8.8-238.8kg in payload-to-orbit with no scramjet accelerator return, and 6.8-233.6kg including scramjet accelerator return.

B.2 Atmospheric Variations

B.2.1 Seasonal and Solar Cycle Based Variations

The Earth's atmosphere varies significantly depending on location, and over time. Seasons, solar cycles, and general weather effects all contribute to these variations, which are numerous and difficult to predict. As such, the atmosphere into which the representative launch system is launched may be considerably different to the atmosphere that is being modelled in this work. Atmospheric variations may affect the aerodynamic and engine performance of the launch system significantly, for example changing the altitude at which the maximum dynamic pressure of the scramjet stage is reached. These variations may have significant impact on the aerodynamic and aerothermal performance of the launch system at a particular altitude, as well as the performance of the propulsion systems of the launch system, particularly the scramjet engines. This study uses the U.S Standard Atmosphere 1976 model[154] to calculate the properties of the atmosphere during simulations. The U.S Standard Atmosphere 1976 is based on a collection of data from sites across America, Brazil, Australia, and Russia, with values calculated for annual mean properties at an interpolated latitude of 45° [154]. The properties that are calculated using this atmosphere are subject to seasonal variability, as well as variability due to geographic position. Figure B.2 shows the variation in temperature and pressure in the 1976 U.S Standard Atmosphere model with altitude. In the higher latitudes maximum and minimum

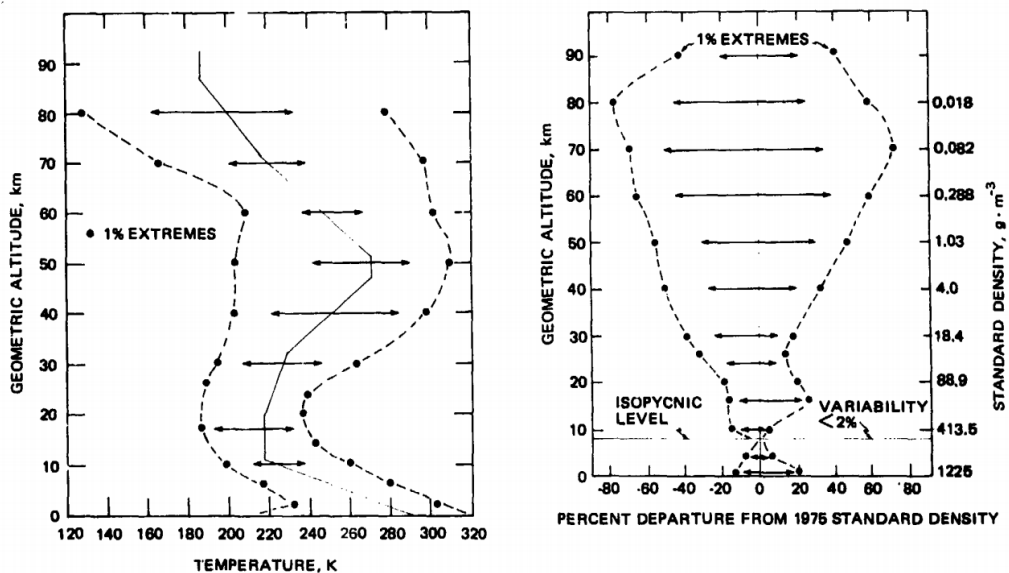


Figure B.2: Variation in temperature and density in the 1976 U.S Standard Atmosphere Model[154]. Arrows indicate lowest and highest mean monthly values obtained at any location, and dashed lines indicate one-percent extremes.

temperatures at altitudes below 25km are seasonal, however at higher altitudes semi-annual and biennial oscillations have a large influence[154]. The variations shown do not occur at the same time in the same envelopes of the atmosphere; warm temperatures at the surface are associated with cold temperatures near the tropopause, and temperatures near the stratopause are negatively correlated with temperatures near the mesopause[154]. These oscillations are particularly important in the equatorial regions, where the seasonal variation in temperature is smallest.

The effects of seasonal and solar cycle-based atmospheric variations are quantified by modelling the 1976 U.S Standard Atmosphere model to take into account the maximum and minimum mean monthly variations shown in Figure B.2. It is assumed that the conditions at the surface compared to the tropopause vary inversely, as well as the conditions of the stratopause compared to the mesopause, as indicated in Figure B.2. The conditions in the stratosphere are assumed to vary linearly between the conditions at the tropopause and stratopause. It is also assumed that density varies inversely to temperature, so that maximum temperature conditions correspond to minimum density. As such, there are two conditions at ground level, and two conditions at stratopause to be investigated, for a total of four combinations of atmospheric extrema. Optimised trajectories are developed for each combination of these conditions, with properties summarised in Table B.2. Large variations are observed in the cases where the ground and stratosphere properties are at different extremes, resulting in payload-to-orbit variations of +12.5kg when ground temperature is at a maximum and stratospheric temperature is at a minimum, and -16.8kg when ground temperature is at a minimum and stratospheric temperature is at a maximum. Maximum ground temperature (and minimum density) corresponds to minimum tropopause temperature (and maximum density). This causes the scramjet stage to be able to fly

Trajectory Condition	Standard	Min T_G	Max T_G	Min T_G	Max T_G
		Min T_S	Min T_S	Max T_S	Max T_S
Payload to Orbit (kg)	132.1	132.7	145.2	115.3	128.3
Total η_{exergy} (%)	1.578	1.592	1.713	1.357	1.539
1st Stage η_{exergy} (%)	6.923	6.785	6.888	6.943	6.872
Separation Alt, 1→2 (km)	24.57	23.92	25.01	24.95	25.54
Separation v, 1→2 (m/s)	1539	1524	1531	1539	1526
Separation γ, 1→2 (deg)	11.1	11.3	10.0	17.1	10.5
2nd Stage η_{exergy} (%)	3.758	3.730	4.092	3.276	3.757
Separation Alt, 2→3 (km)	42.87	43.93	44.46	40.89	40.24
Separation v, 2→3 (m/s)	2506	2484	2572	2404	2512
Separation γ, 2→3 (deg)	12.7	13.3	12.5	13.5	12.5
2nd Stage Flight Time (s)	506.9	508.6	477.1	674.0	502.2
2nd Stage Distance Flown (km)	869.6	862.7	827.1	1074.4	862.8
2nd Stage Return Fuel (kg)	257.8	273.2	266.4	121.0	252.5
2nd Stage Return Distance (km)	1522.3	1530.3	1559.0	1042.3	1486.3
3rd Stage η_{exergy} (%)	13.141	13.213	14.436	11.494	12.760
3rd Stage $t, q > 5\text{kpa}$ (s)	7.7	8.0	8.3	5.8	9.3
3rd Stage Fuel Mass (kg)	2853.1	2852.5	2840.0	2869.9	2856.9

Table B.2: Optimised trajectory properties with atmospheric uncertainty variations.

higher, and burn fuel faster at higher altitude. Minimum stratopause temperature (and maximum density) causes the third stage rocket to pull up more rapidly, and spend less time in the atmosphere. The combination of these factors results in a more efficient overall trajectory for the maximum ground temperature, minimum stratosphere temperature case, while the opposite is true for the minimum ground temperature, maximum stratosphere temperature case. For the other two cases, where tropopause density and stratopause density are at alternating extrema (and ground and stratospheric conditions are at the same extrema), these effects counteract one another, and result in little performance variation. A payload-to-orbit variation of only +0.6kg is observed when both temperatures are at a minimum, and -3.8kg when both temperatures are at a maximum.

The deviations in payload mass-to-orbit due to seasonal and solar cycle atmospheric variations are considered 'on-the-day' variations, that must be considered in tandem with launch location, direction and date, as well as wind and weather. For the purposes of this study, these atmospheric variations are not included in the uncertainty magnitude of the calculated payload-to-orbit, but are considered variables that must be taken into account when planning a launch mission.

B.2.2 Localised Variability

In addition to the seasonal and solar cycle-based variations in atmospheric properties, there is localised variability in the atmosphere that may have significant effects on the flight of hypersonic

APPENDIX B. MODELLING UNCERTAINTIES

launch vehicles. For example, during space shuttle entry, the density of the air was observed to vary by up to 19% in only a few seconds[201]. During the entry of the space shuttle, the effects of these density shears were identified as being crucial to the understanding of future hypersonic aircraft, along with the effects of electrical charges at high altitudes, and the effects of very high altitude clouds. Localised atmospheric variability may have large effects on an airbreathing hypersonic launch system, due to the requirement of flying at maximum dynamic pressure for long periods of time. Rapid atmospheric variations may require significant control to compensate for, and may change the performance of the scramjet engines significantly in a short period of time. The effects of these localised variabilities in atmospheric properties are beyond the scope of this study to quantify, however, it must be acknowledged that the atmosphere may vary rapidly during flight, and taken into account during detailed vehicle and control system design.

APPENDIX C

EXAMPLES AND VERIFICATION

C.1 Example - Brachistochrone Problem

This section describes a short example of an optimal control problem solved in GPOPS-II. The purpose of this example is to demonstrate the effectiveness of the pseudospectral method and GPOPS-II, and to provide a simple example case to establish the terminology of an optimal control problem.

The brachistochrone (from the Greek for 'shortest time') problem is a simple optimal control problem, which describes a ball rolling in two dimensions under gravity. The objective is to find the curve of descent which will minimise the time from point a , where the ball is at rest, to point b . It is assumed that gravity is constant and that there is no forces other than gravity acting on the ball. The analytical solution of this problem can be computed using the Euler-Lagrange equation as the equations describing a cycloid:

$$x = A(\theta + \sin \theta),$$

$$y = A(1 - \cos \theta)$$

This problem is included within GPOPS-2 as an example problem, and has been solved to illustrate the GPOPS-2 solution set-up[120]. Table C.1 describes the set-up of the optimal control problem in GPOPS-2. The dynamic equations for the Brachistochrone problem are:

$$\dot{x} = v * \cos(u),$$

$$\dot{y} = v * \sin(u),$$

$$\dot{v} = g * \sin(u).$$

These equations are provided to GPOPS-2 as the time-variant system model in this form. The control variable is set to be the descent angle. The initial constraints are defined to initiate the ball at rest at the origin, and the terminal constraints are defined to terminate the problem at coordinates of [2,2]. The cost is set to minimum time, so that the solution will be the descent angle which minimises the

Primal Variables	x Position y Position Speed
Control Variables	Angle of Descent
Initial Constraints	Speed x Position y Position
Terminal Constraints	x Position y Position
Path Constraints	None
Target Cost	Minimum Time

Table C.1: Optimisation setup of the Brachistochrone problem.

time to get from the initial position, to the end position.

The GPOPS-2 solution to the Brachistochrone problem is shown in Figure C.1, matching the analytical solution almost exactly. This is expected in this case, as the dynamics of the basic Brachistochrone problem are very simple. As the dynamics become more complex, it is no longer possible to obtain an analytical solution.

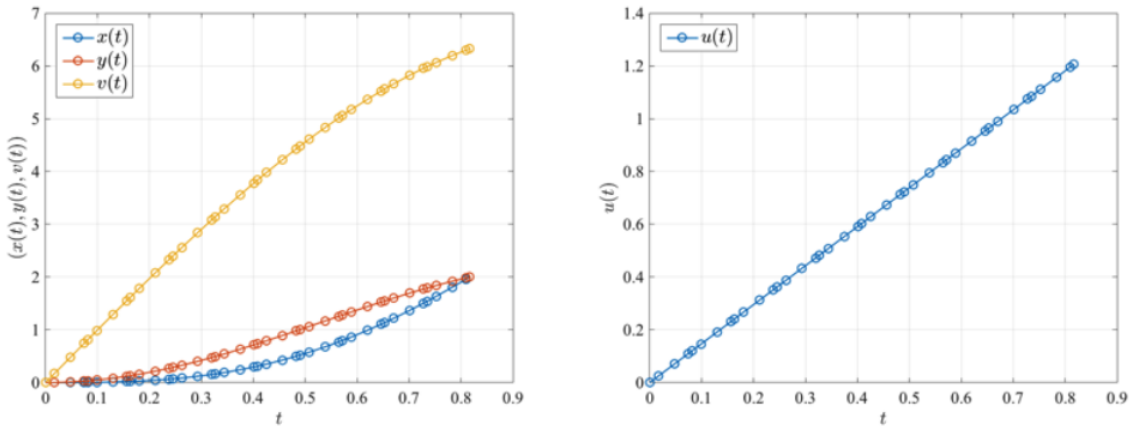


Figure C.1: The solution to the Brachistochrone problem, solved in GPOPS-2[120].

C.2 Example - Space Shuttle Reentry

This section describes an optimised shuttle reentry trajectory problem, taken from the textbook 'Practical Methods for Optimal Control and Estimation Using Nonlinear Programming' by Betts[186], which has been simulated in GPOPS-2 to illustrate the capabilities of GPOPS-2 when applied to a complex aerodynamic problem of an existing vehicle. The optimisation of the space shuttle reentry is

relevant due to the large flight regime and long time period being simulated, which leads to a complex, extremely sensitive optimal control problem[186], similar in a simplified manner to the problem being solved in this work. The shuttle reentry problem is highly nonlinear and intractable to simple optimisation methods[186], making it suitable for illustrating the robustness of GPOPS-2 for aerospace problems of this type. The space shuttle reentry problem aims to maximise crossrange during reentry, with two cases; unconstrained, and limited by a simple heating rate constraint. The example in this section uses the vehicle model exactly as defined by Betts[186] for comparison purposes, however the problem is formulated in a simplified version of the coordinate system that is used in the rest of this work.

C.2.1 Problem Formulation

The dynamics of the space shuttle are defined exactly similarly to those in the problem designed by Betts[186], using a simplified model that neglects the rotation of the Earth and the tangential component of gravity:

$$\dot{r} = v \sin \gamma, \quad (\text{C.1})$$

$$\dot{\xi} = \frac{v \cos \gamma \cos \zeta}{r \cos \phi}, \quad (\text{C.2})$$

$$\dot{\phi} = \frac{v \cos \gamma \sin \zeta}{r}, \quad (\text{C.3})$$

$$\dot{\gamma} = \frac{L \cos \eta}{mv} + \left(\frac{v}{r} - \frac{g}{v} \right) \cos \gamma, \quad (\text{C.4})$$

$$\dot{v} = \frac{D}{m} - g \sin \gamma, \quad (\text{C.5})$$

$$\dot{\zeta} = \frac{L \sin \eta}{mv \cos \gamma} - \frac{v}{r} \tan \phi \cos \gamma \cos \zeta. \quad (\text{C.6})$$

The aerodynamics of the vehicle are modelled using simple correlations, where $C_L = 0.20704 + 0.029244\alpha$, and $C_D = 0.07854 - 0.61592 \times 10^{-2}\alpha^2 + 0.621408 \times 10^{-3}\alpha^3$. The density is modelled as exponentially decaying, $\rho = 1.2255708354e^{-h/7254}$, and the gravity is modelled by an inverse square law, $g = \frac{\mu}{r^2}$. The space shuttle initial conditions are set as follows[186], to simulate the entry of the shuttle into the upper atmosphere:

$$\begin{aligned} h_0 &= 79248\text{m}, & v_0 &= 7803\text{m/s}, \\ \gamma_0 &= -1^\circ, & \phi_0 &= 0^\circ, \\ \xi_0 &= 0^\circ, & \zeta_0 &= 0^\circ, \end{aligned}$$

and the end conditions are set as follows[186], to match the terminal area energy management

interface:

$$h_f = 24384\text{m}, \quad v_f = 762\text{m/s}, \quad \gamma_f = -5^\circ.$$

The problem is set to maximise crossrange from the initial point, which in this case is equivalent to maximising latitude:

$$J = -\phi_f. \quad (\text{C.7})$$

C.2.2 Unconstrained Result

The shuttle reentry crossrange maximisation problem is optimised in GPOPS-2, with result time histories shown in Figures C.2 and C.3. The shuttle follows a 'skipping' trajectory, with an initially large bank angle that changes the heading of the vehicle rapidly in the early stages of reentry. The skips serve to maximise the range of the space shuttle's flight, and they are controlled by the angle of attack of the vehicle. The solution computed in GPOPS-2 matches the result computed by Betts[186], with the shape of the trajectories being close to identical. A maximum crossrange of 34.18° is achieved, a difference of 0.11% when compared to the solution computed by Betts[186]. This result is indicative of the ability of GPOPS-2 to compute highly sensitive optimal control problems for aerospace vehicles.

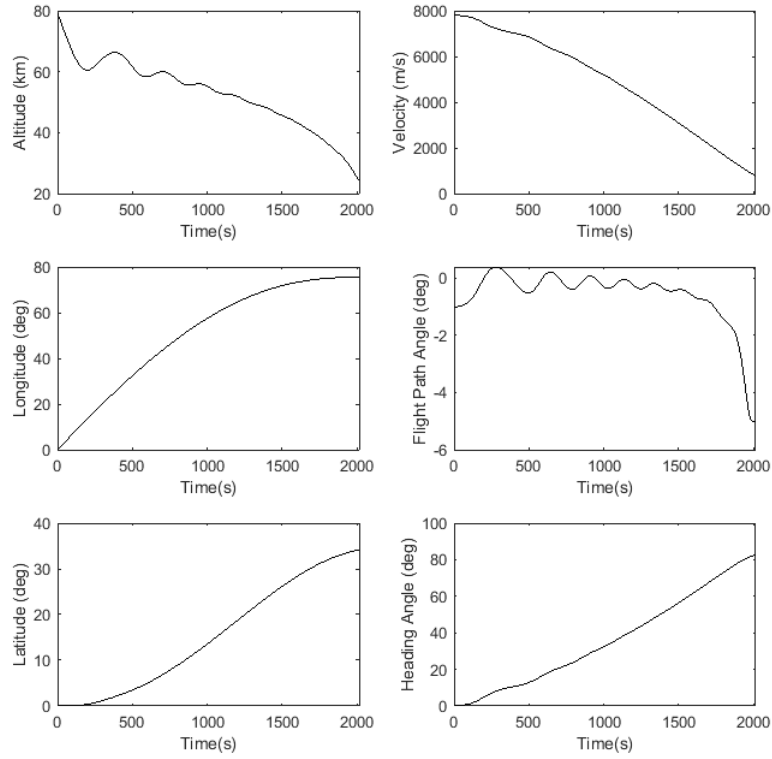


Figure C.2: The maximum crossrange trajectory solution of the unconstrained shuttle reentry problem.

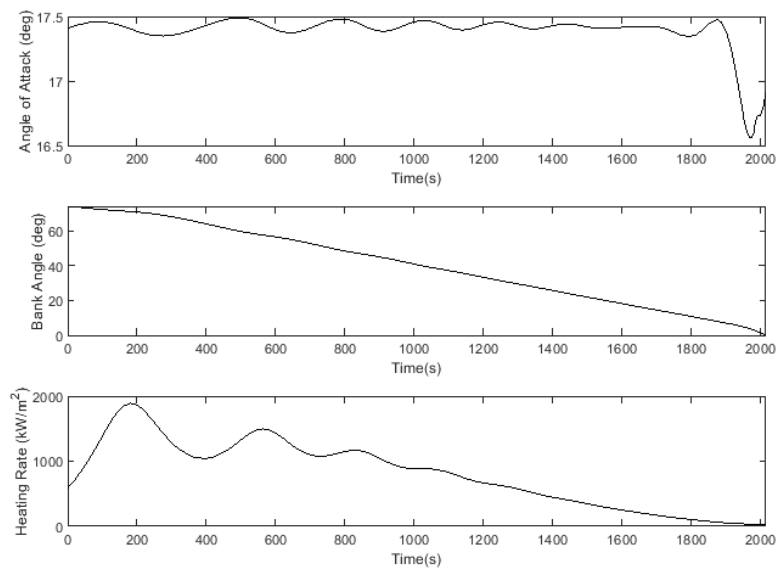


Figure C.3: The control and heating solution of the unconstrained shuttle reentry problem.

C.2.3 Heating Rate Limited Result

The heating rate of the space shuttle is limited during descent, to illustrate the ability of GPOPS-2 to deal with complex inequality constraints. The leading edge heating is approximated using a simplified empirical model, so that $q = q_a q_r$, where $q_r = 17700\sqrt{\rho}(0.0001v)^{3.07}$ and $q_a = 1.0672181 - 0.19213774 \times 10^{-1}\alpha + 0.21286289 \times 10^{-3}\alpha^2 - 0.10117249 \times 10^{-5}\alpha^3$. The trajectory is successfully optimised in the presence of this complex inequality, once again showing a near identical trajectory to the optimised solution calculated by Betts[186]. The maximum crossrange is reduced to 30.70° , a difference of 0.25% to the solution calculated by Betts[186].

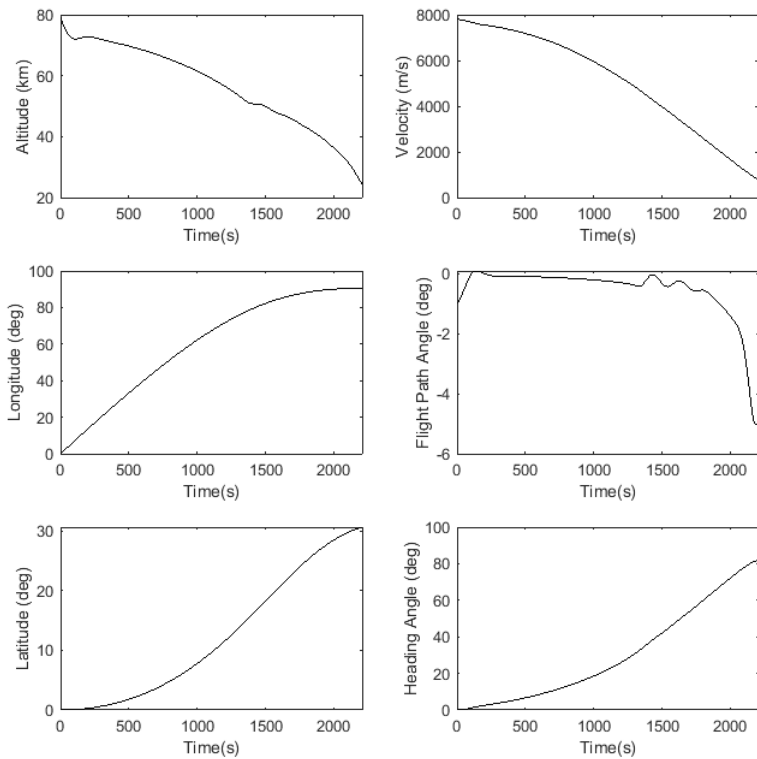


Figure C.4: The maximum crossrange trajectory solution of the constrained shuttle reentry problem.

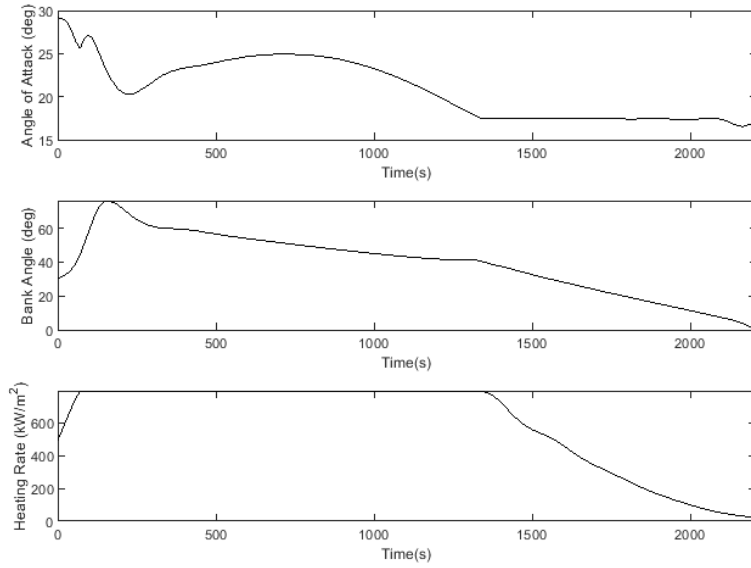


Figure C.5: The control and heating solution of the constrained shuttle reentry problem.

C.3 Optimised Trajectory Analysis

This section presents an example of the convergence and verification of a trajectory optimised using GPOPS-2, within LODESTAR. The convergence and verification of a maximum payload-to-orbit trajectory solution, with scramjet accelerator fly-back (Case 11) is shown.

C.3.1 Mesh History

The mesh history of the optimal trajectory solution is shown in Figure C.6. The mesh is updated by GPOPS-2 in each iteration of the optimal solution. It can be observed that the meshes of the first and third stage rockets contain significantly less node points at the final iteration than the meshes of the scramjet accelerator's acceleration and return. This is due to the relatively simple dynamics and shorter flight time of the first and third stages. The first stage shows a cluster of nodes at the beginning of its trajectory, in the subsonic, transonic and low Mach regimes. In this region, the aerodynamics are changing rapidly, and the nodes are clustered to accurately capture the dynamic behaviour of the vehicle. After transition occurs to supersonic flight, the aerodynamics and engine performance of the vehicle change more slowly, and the nodes become more widely spaced. In contrast, the acceleration of the scramjet accelerator shows significant node density throughout. The operation of the scramjet accelerator is complex, as the dynamics of the vehicle and the performance of the scramjet engines vary significantly, even during relatively level flight. For this reason, the nodes of the return flight show even greater density. The trajectory conditions change significantly as the scramjet accelerator

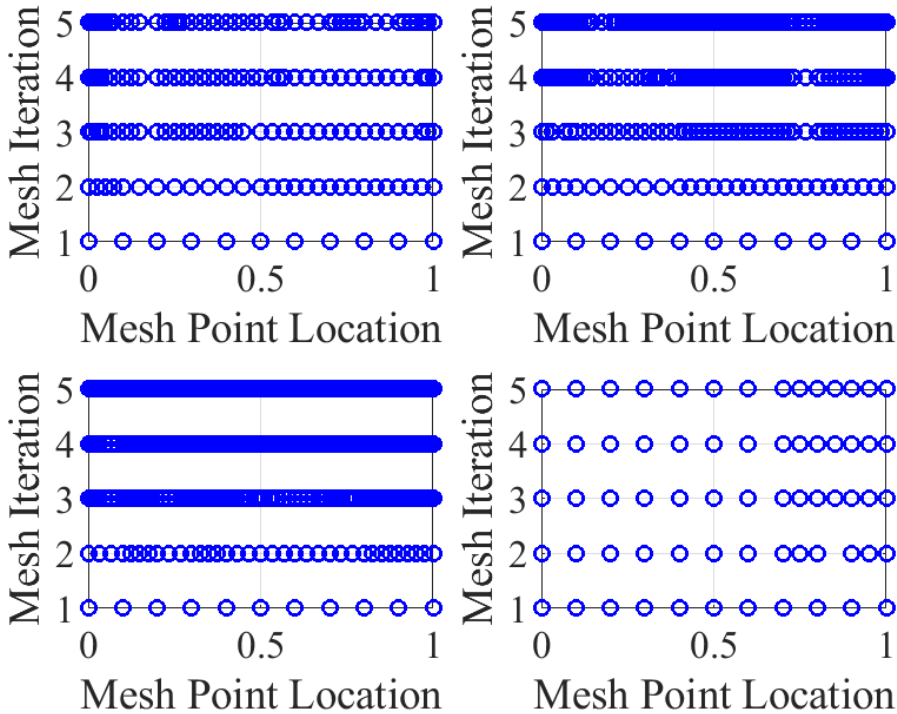


Figure C.6: The mesh history of each phase of the optimised, maximum payload-to-orbit trajectory with scramjet accelerator fly-back (Case 11). The phases are shown as follows: a) first stage rocket, b) scramjet accelerator acceleration, c) scramjet accelerator fly-back and d) third stage.

performs skipping manoeuvres, and transitions through the various return phases, necessitating high node density to capture the vehicle dynamics, particularly between powered and unpowered flight. The trajectories of the scramjet accelerator also last for a significantly longer time than the rocket trajectories, requiring more total nodes to accurately capture the vehicle dynamics. The third stage shows the least nodes at the final mesh iteration, as the dynamics of the third stage are relatively simple. Some node clustering is observed in the first part of the trajectory, where the atmospheric density is still significant.

C.3.2 Verification

After a trajectory has been calculated, it must be verified to ensure that the optimal control solver has converged correctly. Details on this verification are provided in Section 5.4. Figure C.7 shows the Hamiltonian time history for the optimised trajectory solution of Case 11. For an optimal solution to be found, the Hamiltonian should be equal to 0 at all points over every phase. In a practical solution, a Hamiltonian close to 0 is acceptable, which is observable over all phases in the optimised solution. The Hamiltonian is close to 0 at all points of the trajectory, indicating that an optimal solution has been found.

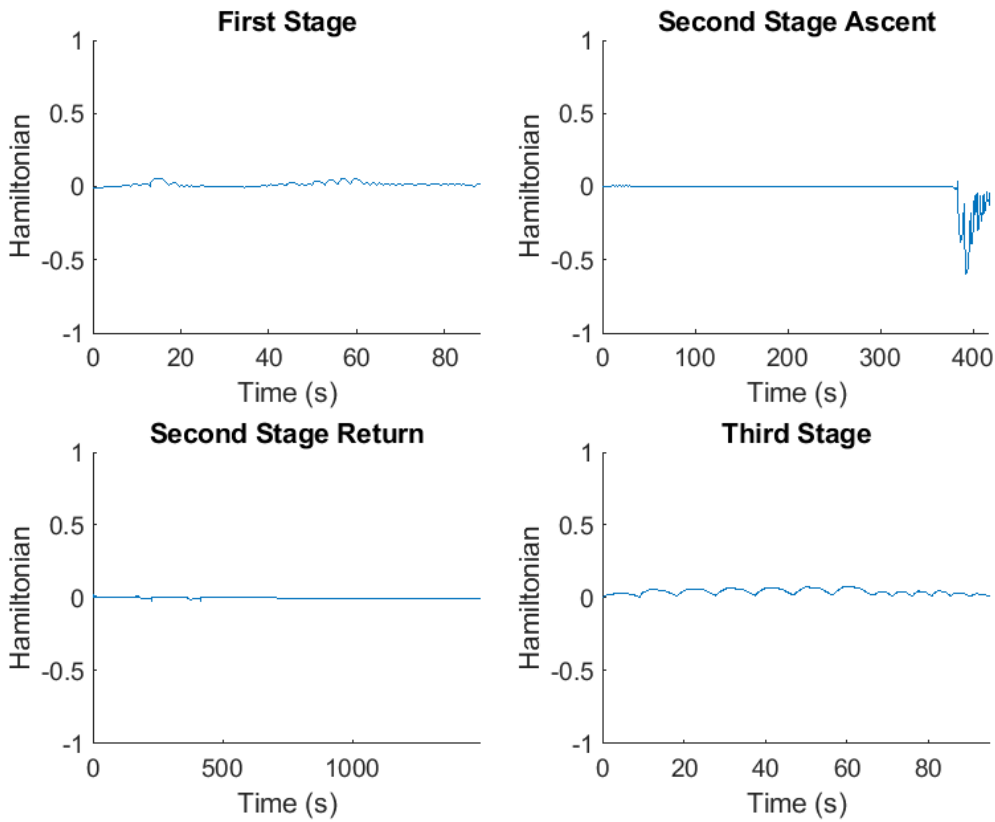


Figure C.7: The Hamiltonian time history of each phase of the maximum payload-to-orbit optimised trajectory, with scramjet accelerator fly-back (Case 11).

The next step in the verification process is to ensure that the dynamic constraints of the optimal control problem holds across the entire solution, ie. $\dot{\mathbf{x}}(t) = f[t, \mathbf{x}(t), \mathbf{u}(t)]$. This is the most important step in the verification process, which checks that the optimal control solver has converged correctly, so that the physical dynamics of the vehicle are being correctly represented by the polynomial approximations within GPOPS-2. The dynamic constraints are tested by first calculating the dynamics of each vehicle at every node of the solution, using the vehicle simulations. These dynamics are then integrated over time using trapezoidal integration, starting at the initial conditions of each phase. The integrated dynamics are then compared to the states of the optimised solution. If the dynamic constraints have been satisfied, then the integrated dynamics of the system will be equal to the state variables of the solution. The error in the dynamic constraints of each state are shown in Figure C.8, calculated as the difference between the integrated dynamics and each state variable, normalised to the range of the state variable. It can be observed that all errors in the dynamic constraints are very small. The error that is present is likely to be due to the inaccuracies of the trapezoidal method, which is significantly less accurate than the approximating polynomials of the pseudospectral method.

The final verification step is a forward simulation of each phase. This forward simulation com-

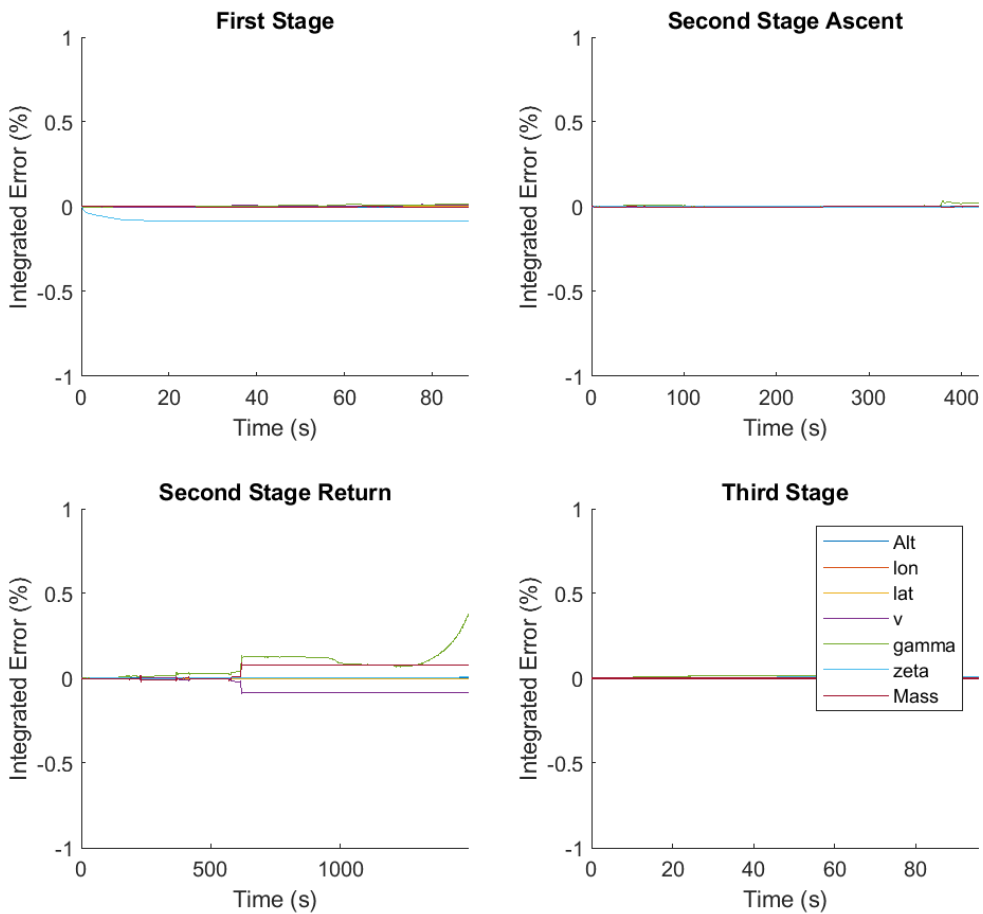


Figure C.8: The error between the integrated dynamics of the system, and the solution states of each phase of the maximum payload-to-orbit optimised trajectory, with scramjet accelerator fly-back (Case 11). Normalised to the range of each state.

pares the solution state with a simulation which is forward integrated using only the controls of each stage. This is the most stringent method of checking the validity of the solution dynamics. However, it is expected that this verification will have significantly higher errors than the check which verifies the dynamics of each state independently, as the interdependencies of each state come into play, and small errors are compounded. Figure C.9 shows the error between the forward simulation and the solution states. As described in Section 5.4, the forward simulation of the return flight is separated into three segments, at 1/6th and 1/3rd of the flight time. The errors in the forward simulation of each stage are observed to be acceptably small, significantly under 1% in all cases, and it is evident that compounding errors are the cause of the most extreme deviations.

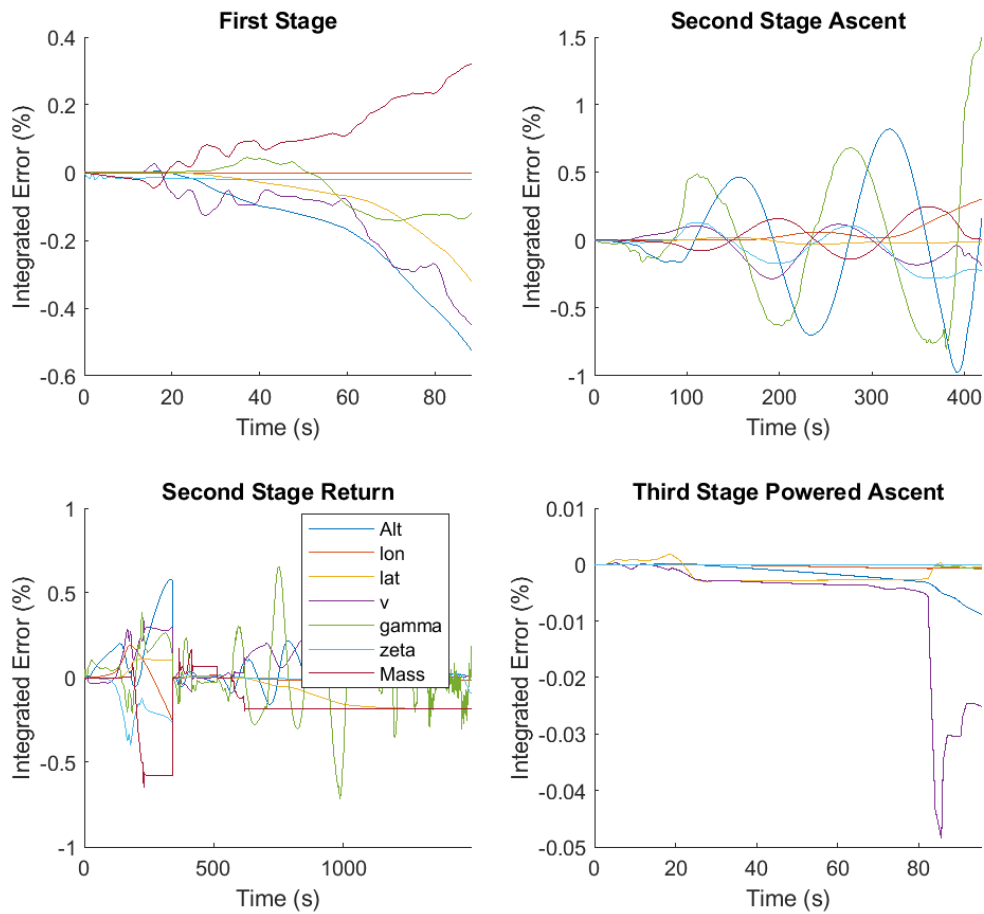


Figure C.9: The error between the forward simulated states, and the solution states of each phase of the maximum payload-to-orbit optimised trajectory, with scramjet accelerator fly-back (Case 11). Normalised to the range of each state.

APPENDIX D

MODELLING AND SIMULATION

D.1 Propulsion Interpolation Scheme

This section describes the interpolation scheme used for the C-RESTM10 database to determine

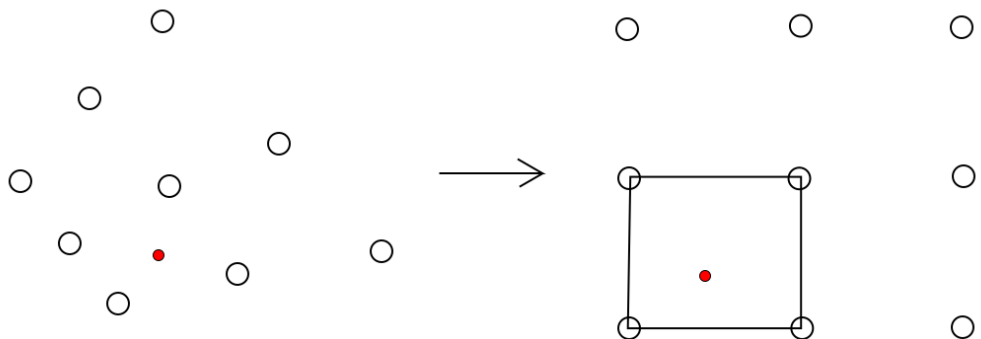


Figure D.1: The transformation to a normalised interpolation scheme.

specific impulse. The C-RESTM10 engine database consists of a set of engine conditions, including specific impulse, ordered by the inlet Mach number and temperature. This data set must be interpolated, to calculate the performance of the engine at each flight condition. However, no inlet Mach number and temperature values are repeated between any of the C-RESTM10 data points. This makes for a scattered data set which complicates the process of interpolating for specific impulse. It was observed that when interpolating for specific impulse, a scattered interpolation produces particularly poor results, and that fitting splines to the data set is the only way to produce an appropriate interpolation scheme. However, even when splines were fit, and the general trends of the specific impulse

were matched, minuscule oscillations were still present in the interpolated values. These oscillations do not significantly affect a forward simulation, however, when using the vehicle model as part of an optimal control calculation, they can affect the convergence process. Consequently, it was necessary to craft a bespoke interpolation scheme in order to accurately interpolate the specific impulse of the vehicle.

This interpolation begins by designating a new coordinate system, normalised to [0 1], running from data point with the lowest inlet temperature [0,0], to the data point with the highest inlet temperature [1,1]. Each data point is then given a set of normalised coordinates, and a cubic spline is fit to this set of normalised points using MATLAB's griddedInterpolant function. The normalised, ordered, data set ensures that this cubic spline is smooth, with no oscillations present. In order to interpolate at a specific location, each data point bounding the interpolation region is set as the corner of a square of data points in normalised coordinates. This is illustrated in Figure D.1. The distance to each of these bounding data points is calculated, and the location to be interpolated is assigned a set of normalised coordinates. This set of normalised coordinates is used to interpolate for specific impulse.

This process is accurate, but computationally time consuming, and would increase the computation time of the optimisation process significantly if implemented directly within the vehicle model. In order to expedite the interpolation process, interpolations are performed for the specific impulse for every combination of inlet Mach number and temperature present in the C-RESM10 database. This creates a grid of interpolated data points, which includes all of the data points present in the C-RESTM10 database. This grid of interpolated specific impulse values is then used as a new data set, which is now in meshgrid form, by which the specific impulse is interpolated. A bivariate spline is fitted to this grid of data points, using MATLAB's griddedInterpolant function, which is accessed by the vehicle model to determine specific impulse during flight.

D.2 Scramjet Accelerator Flow Results

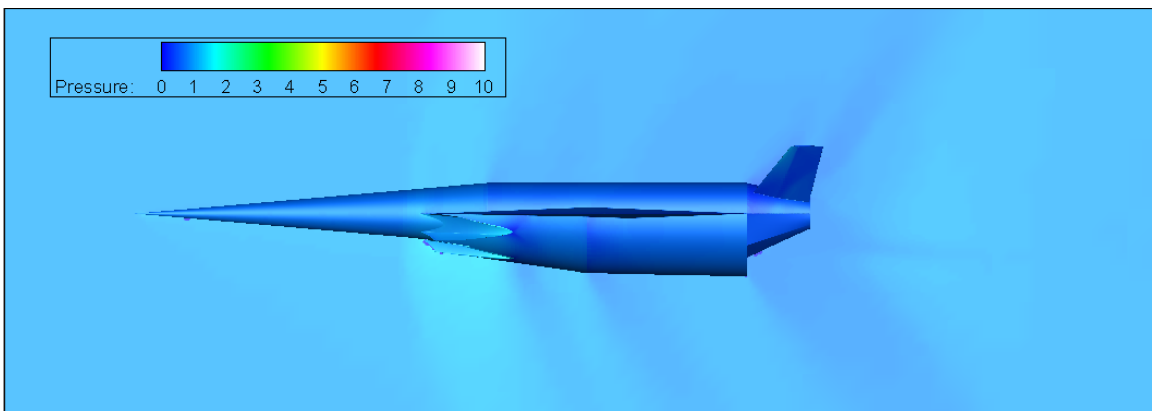


Figure D.2: CART3D flow result for the scramjet accelerator, at Mach 1.1, 6° angle of attack.

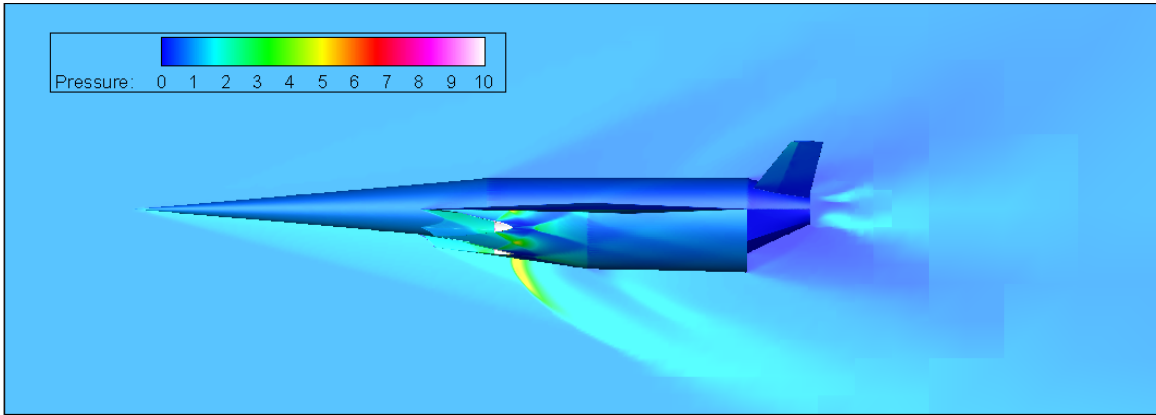


Figure D.3: CART3D flow result for the scramjet accelerator, at Mach 3, 6° angle of attack.

This section shows additional flow results for the scramjet accelerator, calculated using Cart3D. Figures D.2 and D.3 show flow results for the scramjet accelerator, at Mach numbers of 1.1 and 3 respectively. It can be observed that at Mach 1.1, the bow shock is not significant, and the shock structure that is evident at higher speeds has not yet formed. At Mach 3, the unstarted C-REST engines are evident, causing significant amounts of the air entering the inlet to be expelled. Shock-shock interaction structures are evident on the cowl of the engines, causing areas of localised high pressure.

D.3 Cart3D Mesh

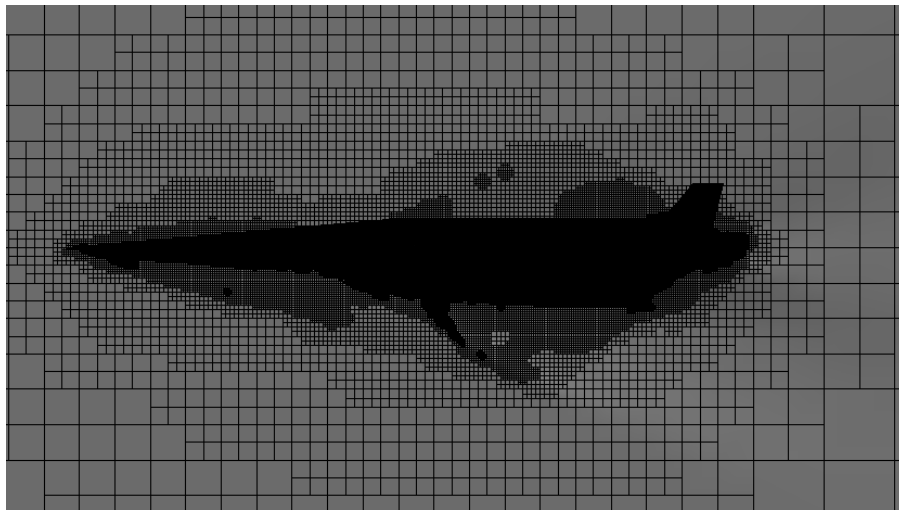


Figure D.4: Adapted mesh of the scramjet accelerator at Mach 6 3° angle of attack.

This section illustrates the converged meshes used by Cart3D. Figures D.4 and D.5 show adapted meshes for Cart3D solutions of the scramjet accelerator, and the scramjet accelerator and first stage.

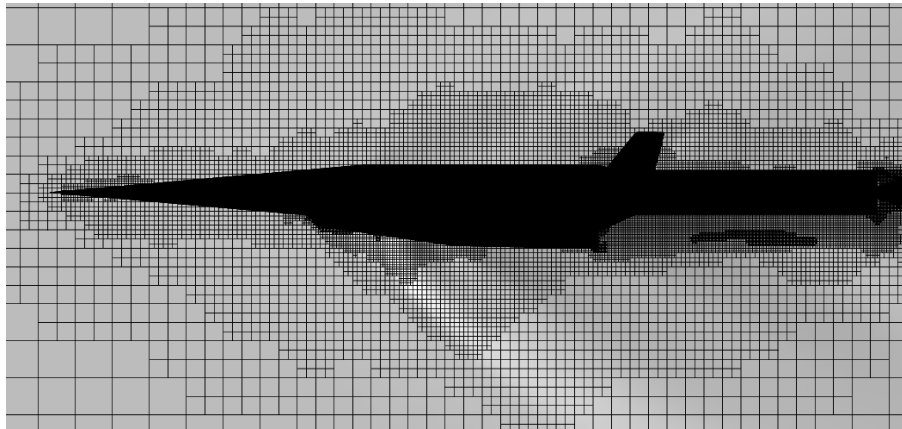


Figure D.5: Adapted mesh around the scramjet accelerator and first stage vehicles, flying at Mach 2, -1° angle of attack.

These meshes have been generated adaptively by Cart3D during the solution process. It can be observed that the mesh clusters around the vehicle, particularly in regions where strong shocks are present, where the mesh clusters at the shock front.

D.4 Performance of the Scramjet Accelerator During Fly-Back

Figure D.6 shows the performance of the scramjet accelerator during the boost phase, described in Section 7.3.

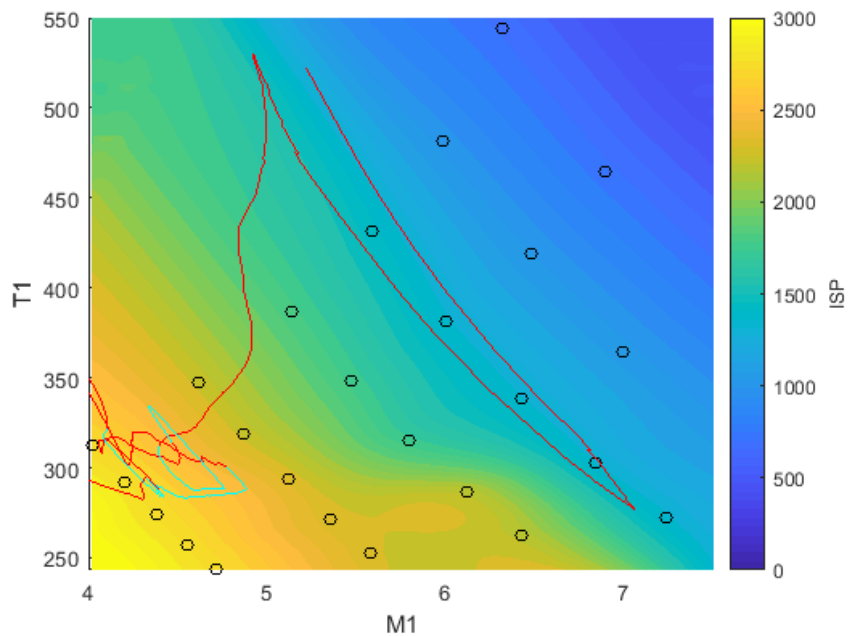


Figure D.6: The performance of the scramjet accelerator during the boost phase. Light blue indicates that the scramjet engines are turned on.

APPENDIX E

ALTERNATE TRAJECTORY CASES

E.1 Trajectory With Variation in Return Drag

I should maybe do a variation of just the return drag - "the performance of the launch system may be significantly different on the ascent and return trajectories (in addition to the engine flowpaths)"

E.2 Maximum Payload-To-Orbit Trajectory With Dynamic Pressure Constraint

The maximum payload-to-orbit trajectory of the launch system with no scramjet accelerator fly-back (Case 2) was found to involve a significant altitude raising manoeuvre in the middle of the acceleration trajectory of the scramjet accelerator. Discerning the benefits of this altitude raising manoeuvre proved complex, requiring a trajectory to be calculated in which the altitude raising manoeuvre is prevented from occurring. This section describes an optimised trajectory in which the middle section of the scramjet accelerator's acceleration is constrained to flight at maximum dynamic pressure.

This trajectory was optimised for maximum payload-to-orbit, with a 50kPa dynamic constraint between Mach numbers of 6 and 8, the region in which the altitude raising manoeuvre was observed to occur. This constraint successfully removed the altitude raising manoeuvre from the maximum payload-to-orbit optimised trajectory, allowing for a comparison to be made to quantify the benefits of the altitude raising manoeuvre. This comparison is made in Section 6.2. Figures E.1, E.2 and E.3 show the maximum payload-to-orbit trajectory constrained to 50kPa between Mach numbers 6 to 8, and Table E.1 details key parameters of the trajectory.

Trajectory Condition	Value
Payload to Orbit (kg)	155.9
Total η_{exergy} (%)	1.680
1st Stage η_{exergy} (%)	6.853
Separation Alt, 1→2 (km)	24.50
Separation v, 1→2 (m/s)	1530
Separation γ, 1→2 (deg)	11.3
2nd Stage η_{exergy} (%)	4.397
Separation Alt, 2→3 (km)	43.79
Separation v, 2→3 (m/s)	2638
Separation γ, 2→3 (deg)	12.3
2nd Stage Flight Time (s)	626.5
2nd Stage Distance Flown (km)	1182.6
3rd Stage η_{exergy} (%)	15.477
3rd Stage $t, q > 5\text{kpa}$ (s)	6.9
3rd Stage Fuel Mass (kg)	2829.3

Table E.1: A summary of key results from the maximum payload-to-orbit trajectory, constrained to 50kPa between Mach numbers 6 to 8.

E.3 Constant Dynamic Pressure Trajectory with Fly-Back

A payload-to-orbit optimised trajectory is calculated including scramjet accelerator return, and with the scramjet accelerator constrained to 50kPa dynamic pressure during ascent. This is calculated for the third stage heating comparison performed in Section A.4.4.

E.3. CONSTANT DYNAMIC PRESSURE TRAJECTORY WITH FLY-BACK

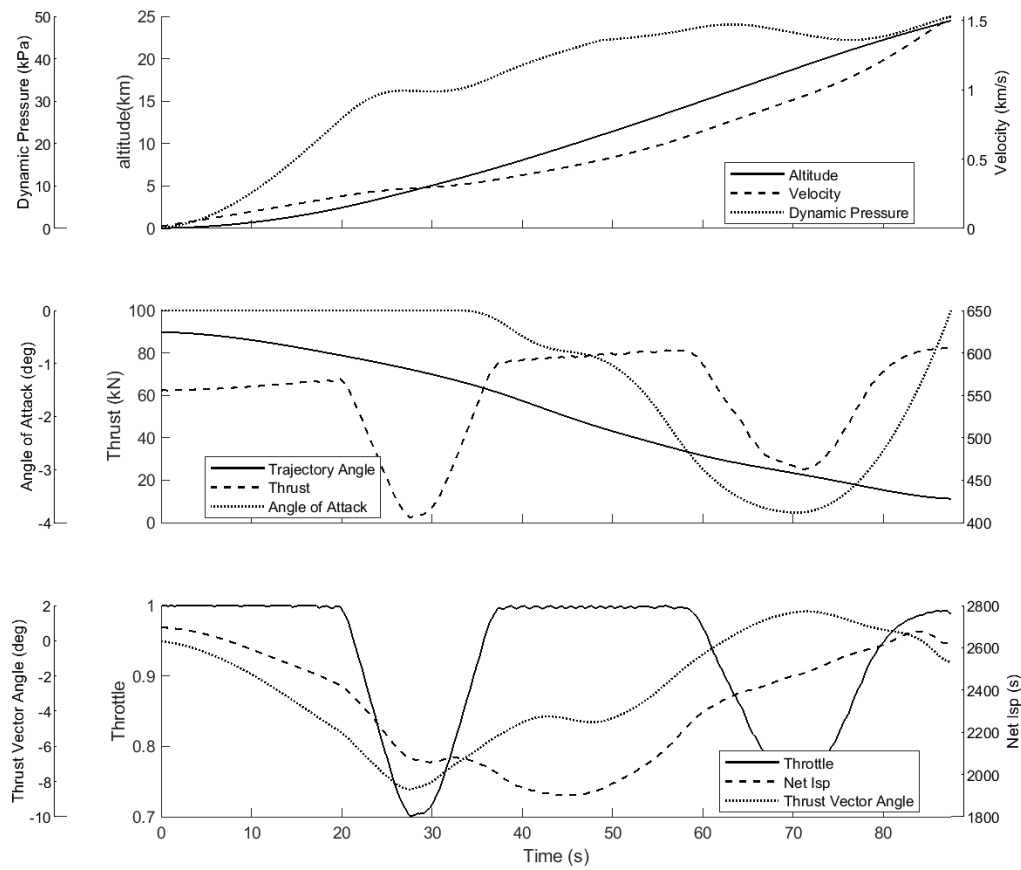
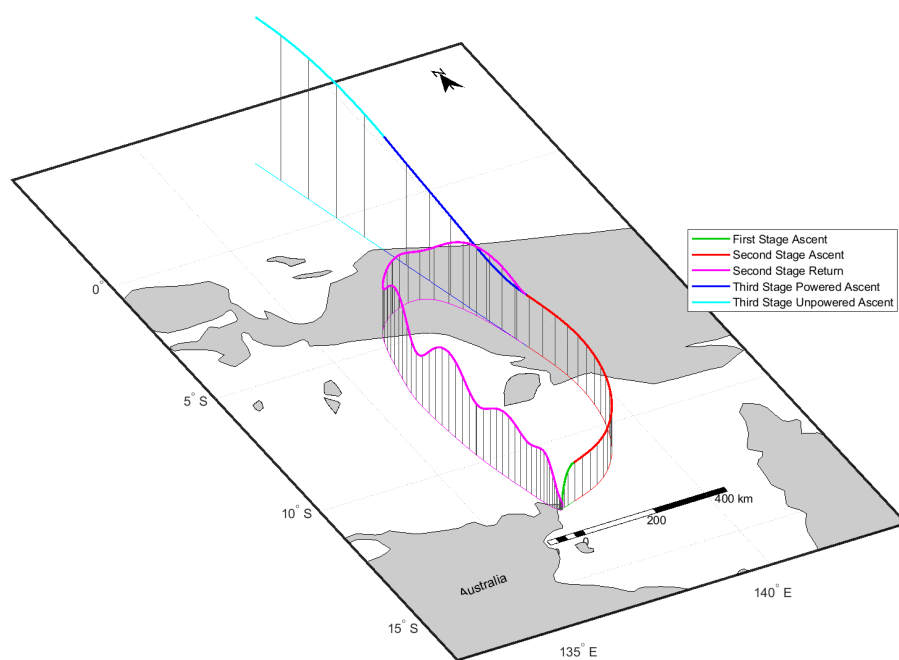


Figure E.1: The first stage trajectory of the representative launch system flying a maximum payload-to-orbit trajectory, constrained to 50kPa between Mach numbers 6 to 8.



APPENDIX E. ALTERNATE TRAJECTORY CASES

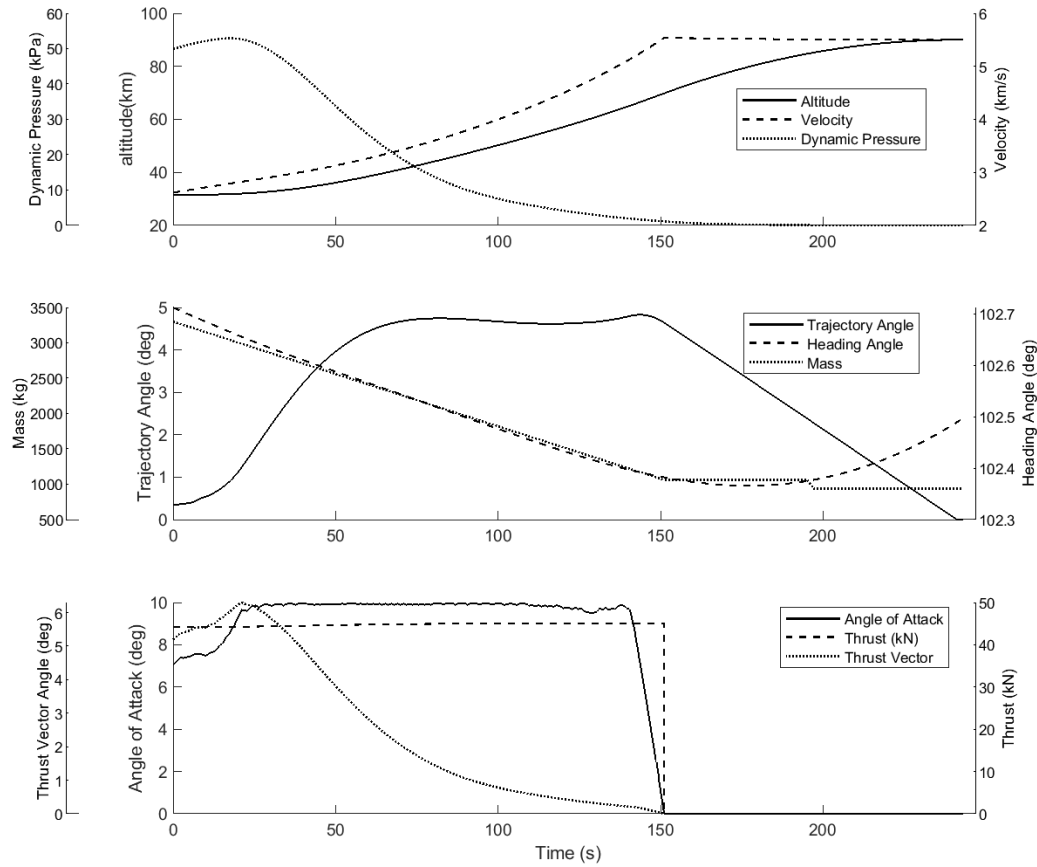


Figure E.5: The payload-to-orbit optimised third stage trajectory including scramjet accelerator return flight, with the scramjet accelerator constrained to 50kPa dynamic pressure during ascent.

Trajectory Condition	Constant q
Payload to Orbit (kg)	72.0
Total η_{exergy} (%)	1.010
1st Stage η_{exergy} (%)	6.341
Separation Alt, 1→2 (km)	23.94
Separation v, 1→2 (m/s)	1463
Separation γ, 1→2 (deg)	0.7
2nd Stage η_{exergy} (%)	4.284
Separation Alt, 2→3 (km)	31.38
Separation v, 2→3 (m/s)	2619
Separation γ, 2→3 (deg)	0.4
2nd Stage Flight Time (s)	463.8
2nd Stage Distance Flown (km)	757.8
2nd Stage Return Fuel (kg)	328.7
2nd Stage Return Distance (km)	1446.2
3rd Stage η_{exergy} (%)	7.005
3rd Stage $t, q > 5\text{kpa}$ (s)	115.0
3rd Stage Fuel Mass (kg)	2913.2

E.4 Sonic Boom Ground Effects

The flight of a hypersonic vehicle has the potential to create significant overpressures on the ground due to sonic booms. This section describes the effects of the sonic booms generated by the representative launch system.

Even when a hypersonic vehicle is flying at high altitudes, the overpressures on the ground may still be large enough to have detrimental effects on any populated areas being overflown. The overpressure from sonic booms can cause significant annoyance to the populace, or in more extreme cases, long term damage to building structures or peoples health. When the representative launch system is launched to a sun synchronous orbit from the Equatorial Launch Australia launch site, it flies over a significant portion of Papua. Fortunately, Papua is sparsely populated, and the number of towns flown over by the representative launch system will be low. However the effects on these population centres may still be significant. In order to assess the impact of the representative launch system's flight, the magnitude of the overpressure from its sonic booms must be calculated.

The sonic boom overpressures are estimated using the 'first cut' estimation technique [202]. This estimation technique can approximate sonic boom overpressures moderately well, and is useful as a first approximation to the sonic boom overpressures generated by an aerospace vehicle. The overpres-

sures generated by the representative launch system are calculated over its trajectory, shown in Figure E.7. It is found that overpressures of up to 385.1Pa occur during flight over land during the maximum payload-to-orbit trajectory of the representative launch system. These overpressures have a low but significant probability of causing cosmetic damage to structures (1.5% for plaster and 0.4% for glass)[203]. In addition, overpressures of these magnitudes have been rated as unacceptably annoying to the majority populace being overflowed, as shown in Figure E.6. These overpressures indicate that overflight of populated areas may not be reasonable for the representative launch system flying its maximum payload-to-orbit trajectory path, with fly-back (Case 11).

E.5 Alternate Launch Location

In this section, an alternate southerly launch is investigated for the rocket-scramjet-rocket launch system, in the case that flight over Papua is not possible. This launch occurs from Streaky Bay, the possible location of a launch site being developed by Southern Launch Australia[204]. The maximum payload-to-orbit has been calculated from this launch site using LODESTAR. Figure E.8 shows the ground track of this optimised trajectory, and Table E.2 details a summary of the key trajectory parameters. The shape of this optimised trajectory is very similar to the optimal trajectory of the launch system launched from the Northern Territory (Case 11). The first stage initially pitches towards the west, separating the scramjet accelerator in a westerly direction. the scramjet accelerator then performs a banking manoeuvre to the south, and a pull-up before third stage release. After separation, the scramjet accelerator exhibits initial turn, boost-skip and approach phases during fly-back, with the scramjet engine igniting three times at the troughs of the first three skips, in the same manner as when launching northerly. A higher payload to orbit is achieved when launching from a southerly location, attaining a total of 134.9kg of payload-to-orbit, an increase of +2.1% compared to northerly launch. This payload increase is caused by the rotation of the Earth hindering, rather than assisting, when launching into a retrograde orbit, making launch from a more southerly point desirable.

Trajectory Condition	Value
Payload to Orbit (kg)	134.9
Total η_{exergy} (%)	1.600
1st Stage η_{exergy} (%)	6.818
Separation Alt, 1→2 (km)	24.46
Separation v, 1→2 (m/s)	1525
Separation γ , 1→2 (deg)	11.6
2nd Stage η_{exergy} (%)	3.781
Separation Alt, 2→3 (km)	42.57
Separation v, 2→3 (m/s)	2504
Separation γ , 2→3 (deg)	12.8
2nd Stage Flight Time (s)	509.5
2nd Stage Distance Flown (km)	873.7
2nd Stage Return Fuel (kg)	245.1
2nd Stage Return Distance (km)	1503.8
3rd Stage η_{exergy} (%)	13.395
3rd Stage $t, q > 5\text{kpa}$ (s)	8.7
3rd Stage Fuel Mass (kg)	2850.3

Table E.2: A summary of key trajectory parameters of the maximum payload-to-orbit trajectory launched in a southerly direction.

APPENDIX E. ALTERNATE TRAJECTORY CASES

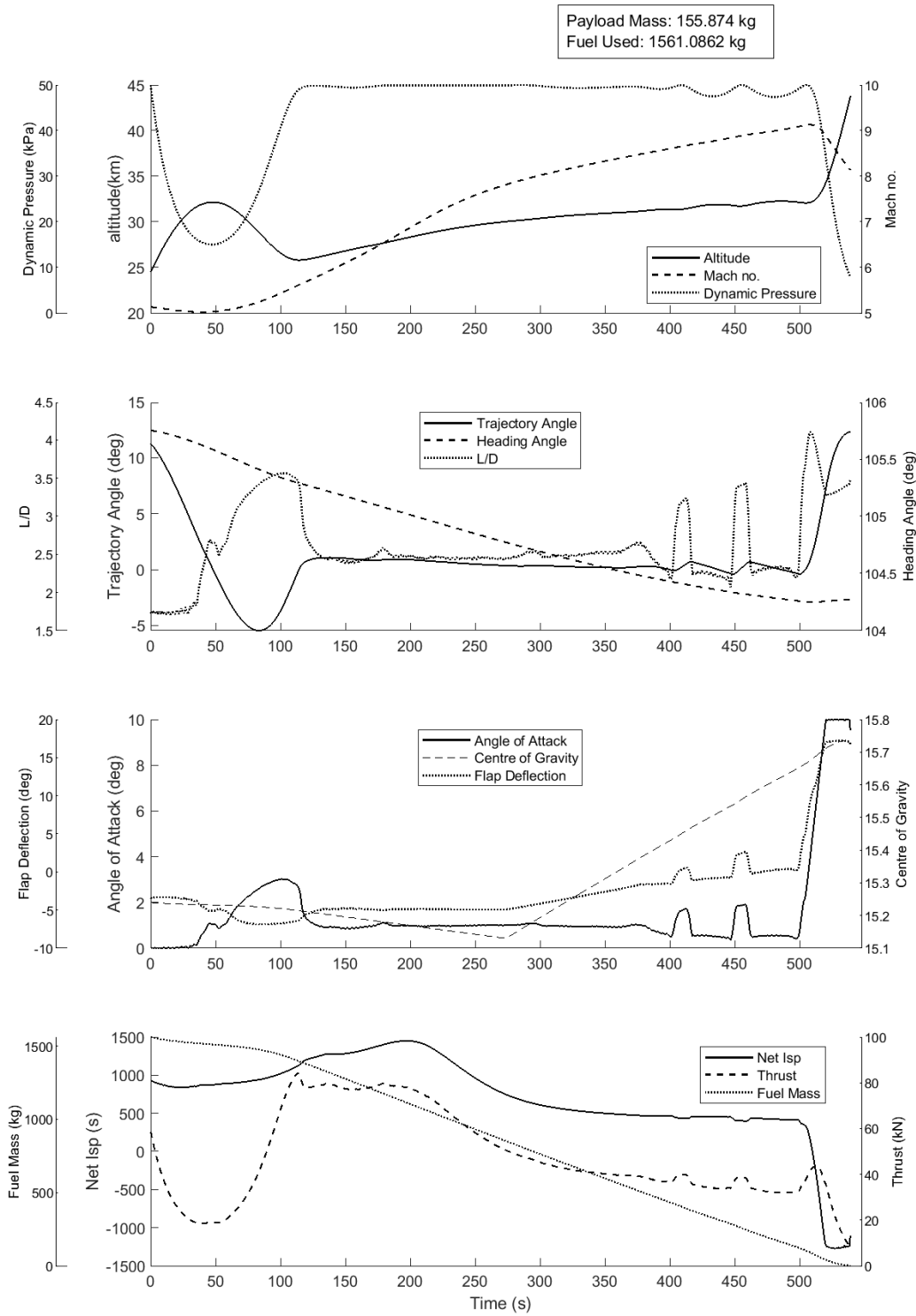


Figure E.2: The scramjet accelerator trajectory of the representative launch system flying a maximum payload-to-orbit trajectory, constrained to 50kPa between Mach numbers 6 to 8.

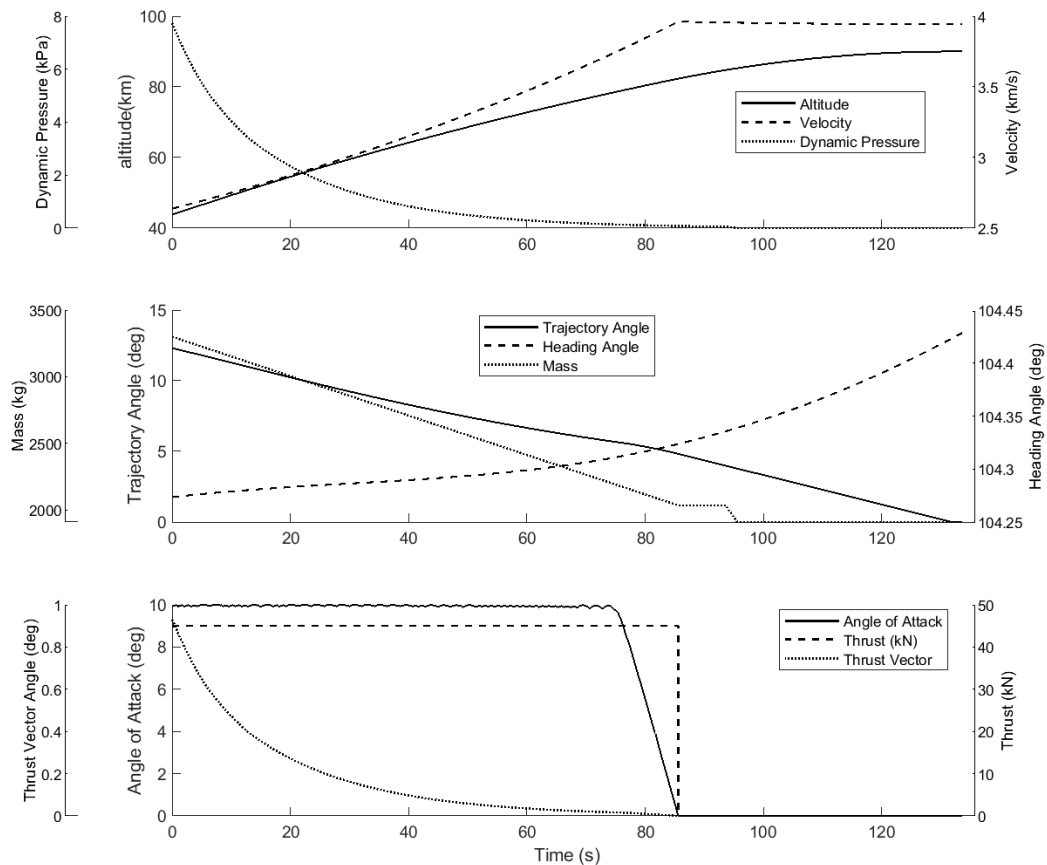


Figure E.3: The third stage trajectory of the launch system flying a maximum payload-to-orbit trajectory, constrained to 50kPa between Mach numbers 6 to 8.

APPENDIX E. ALTERNATE TRAJECTORY CASES

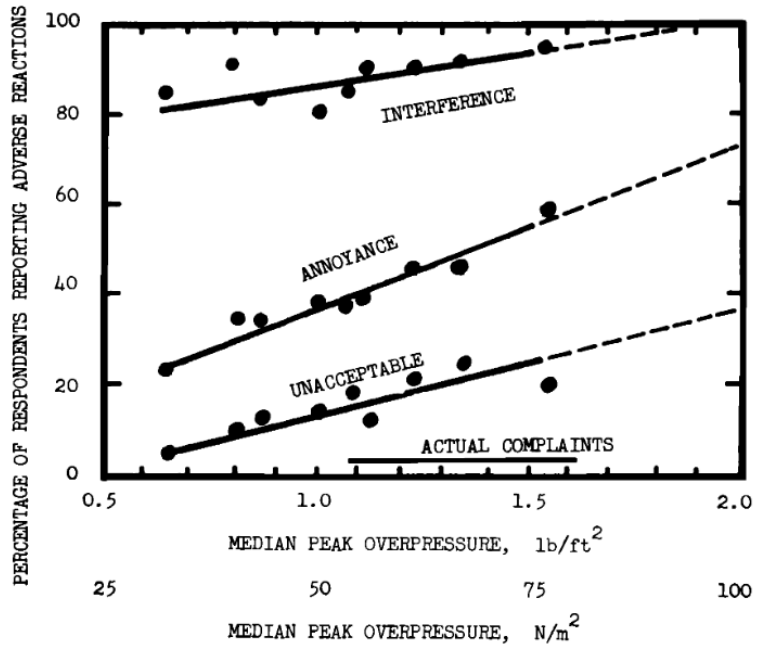


Figure E.6: The level of population annoyance with increasing overpressure.

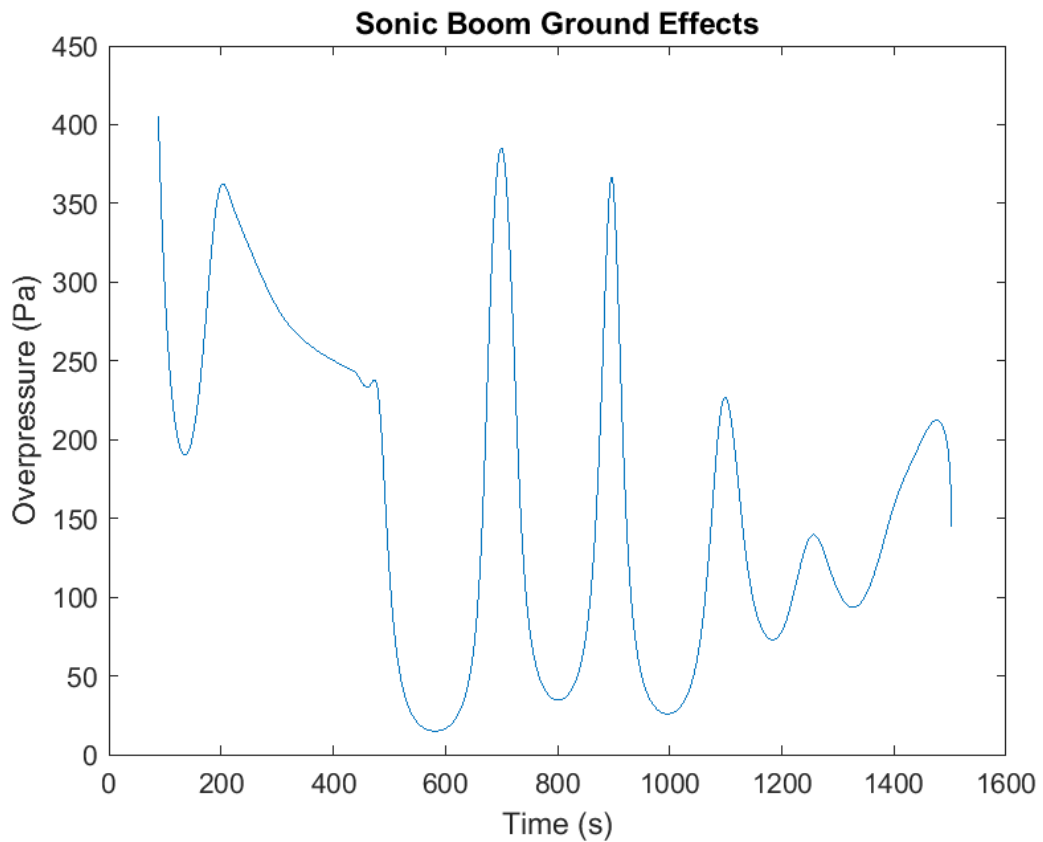


Figure E.7: The sonic boom overpressure on the ground, for the optimised trajectory path (Case 11).

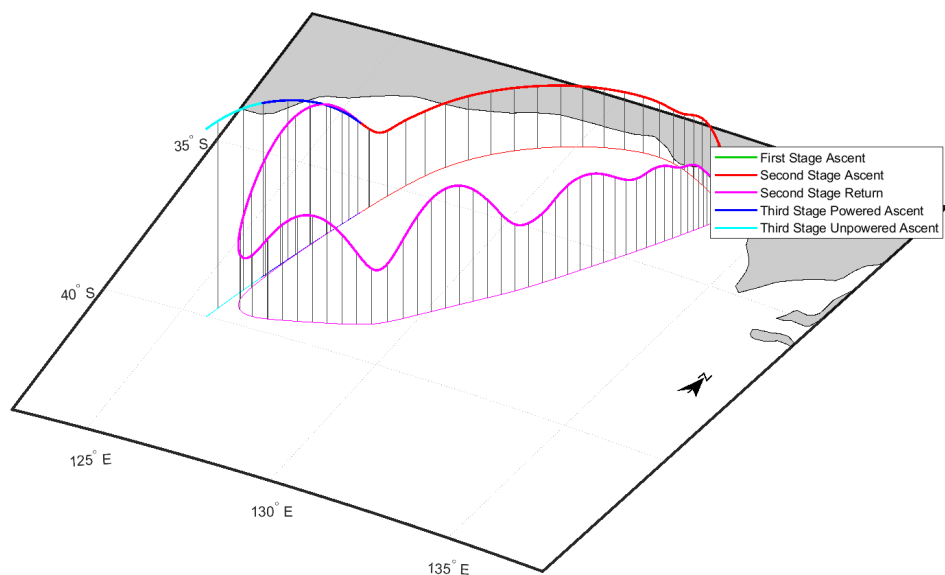


Figure E.8: The optimised maximum payload-to-orbit trajectory of the launch system launching onto a southerly orbit, from Streaky Bay.

APPENDIX F

TRAJECTORY PLOT COMPARISONS

This section contains trajectory plot comparisons for the sensitivity studies performed in Section 6.5 and 7.7. Comparisons and analyses between these trajectories are performed in the relevant sections.

F.1 Optimised Ascent Trajectory Comparisons With No Fly-Back

F.1.1 Case 3: Maximum Dynamic Pressure Sensitivity Comparison

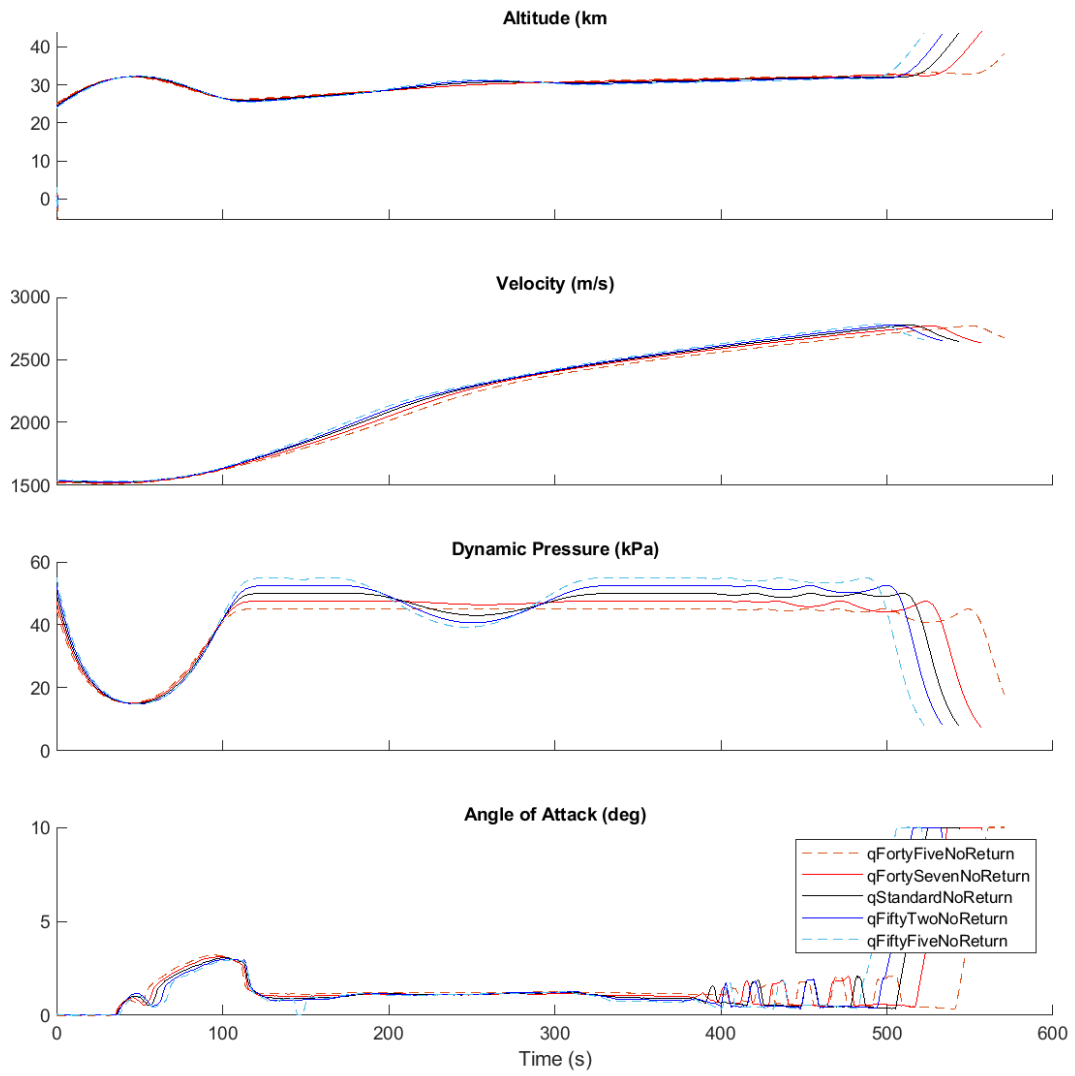


Figure F.1: Comparison of scramjet stage ascent trajectories with variation in the maximum dynamic pressure of the representative launch system.

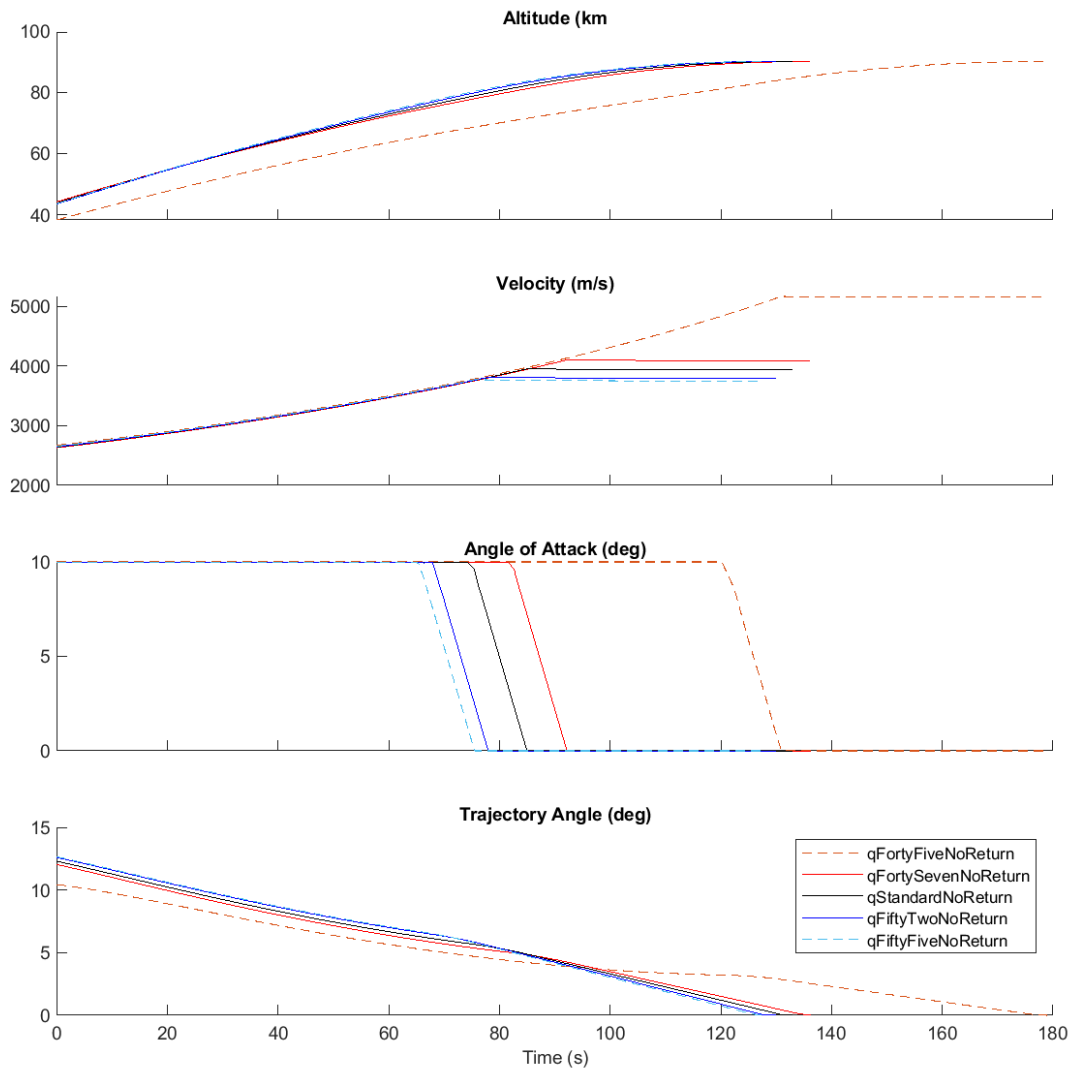


Figure F.2: Comparison of third stage rocket ascent trajectories with variation in the maximum dynamic pressure of the representative launch system.

F.1.2 Case 4: Scramjet Accelerator Drag Sensitivity Comparison

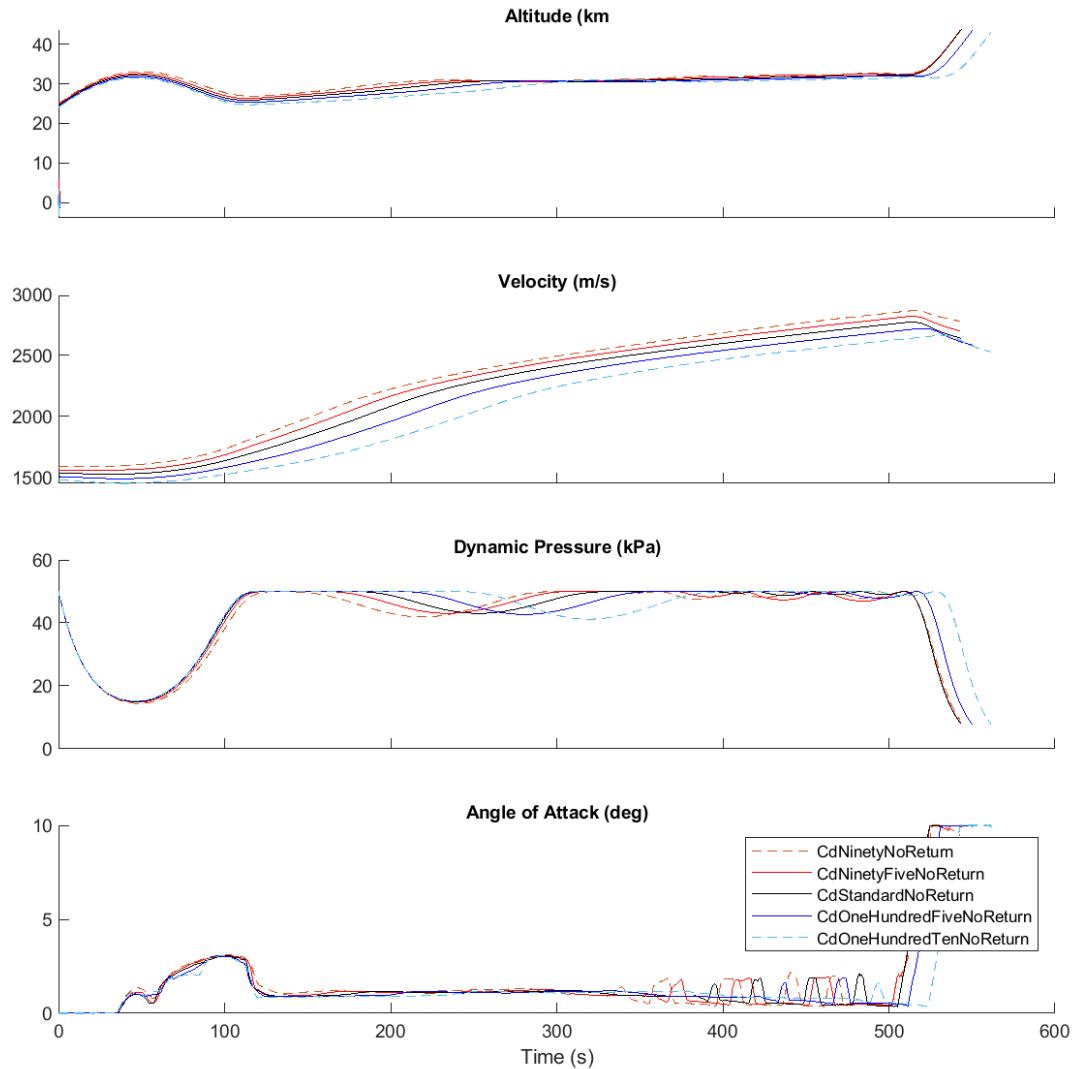


Figure F.3: Comparison of scramjet stage ascent trajectories with variation in the drag of the scramjet accelerator.

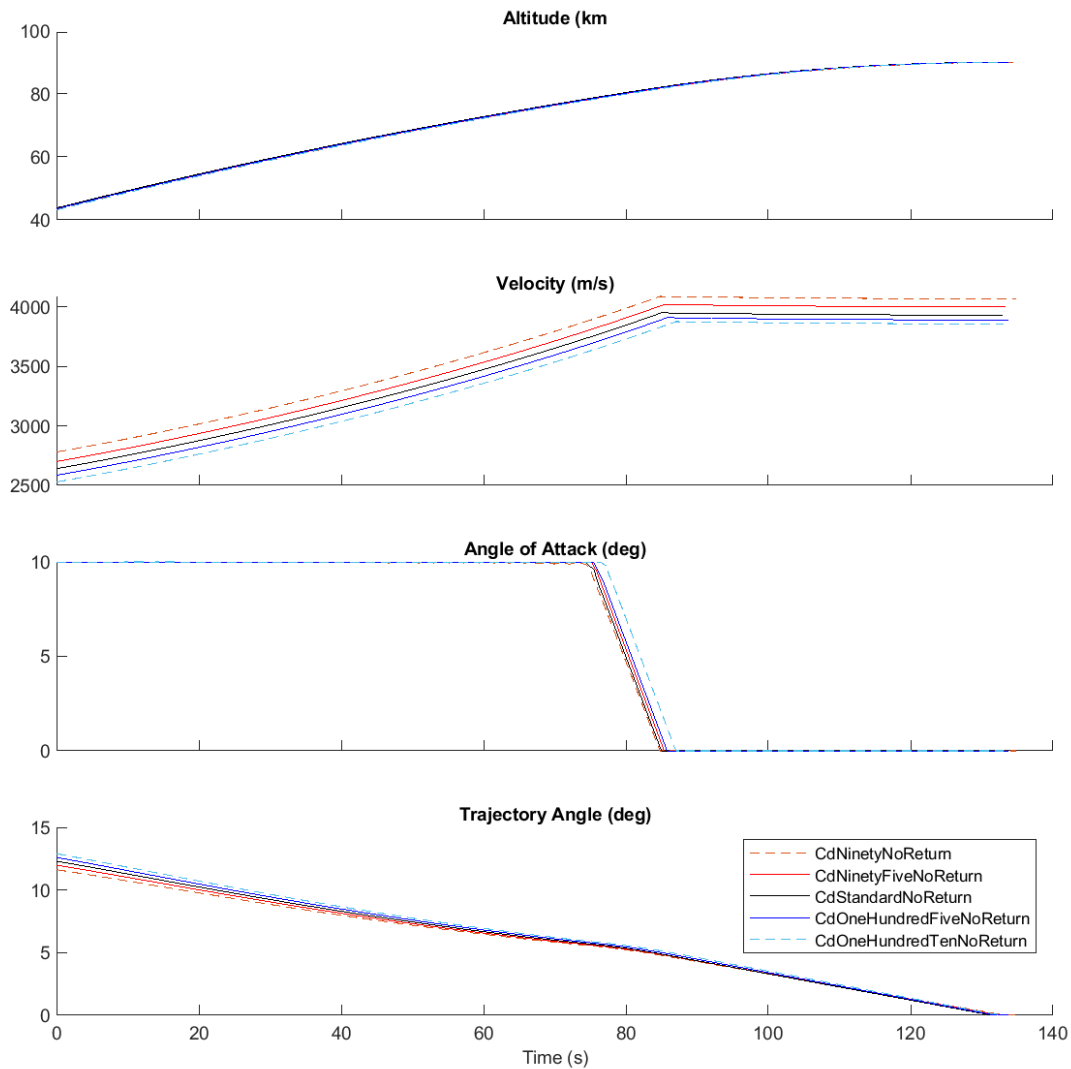


Figure F.4: Comparison of third stage rocket ascent trajectories with variation in the drag of the Scramjet Accelerator.

F.1.3 Case 5: Scramjet Accelerator Specific Impulse Sensitivity Comparison

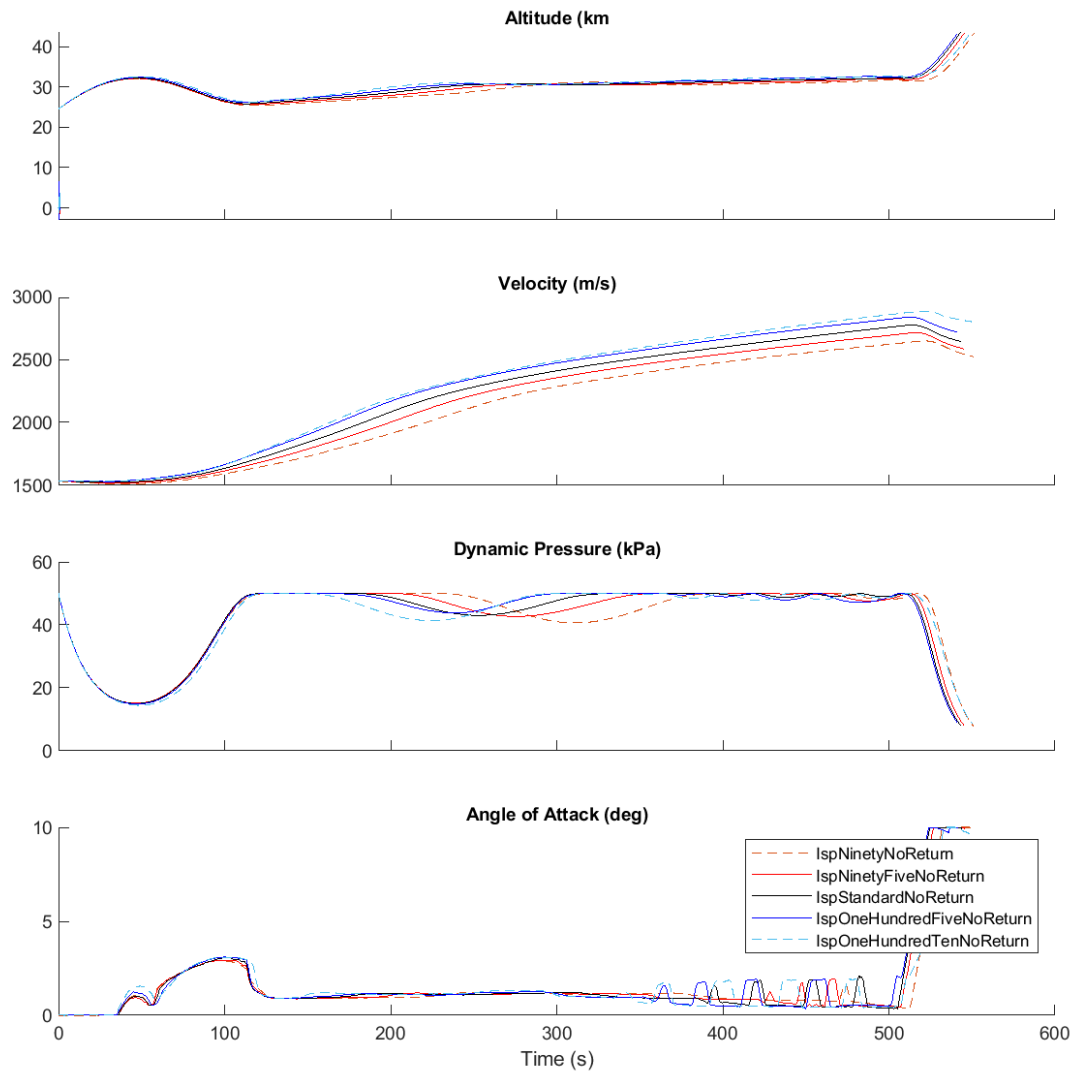


Figure F.5: Comparison of scramjet accelerator ascent trajectories with variation in the specific impulse of the scramjet accelerator.

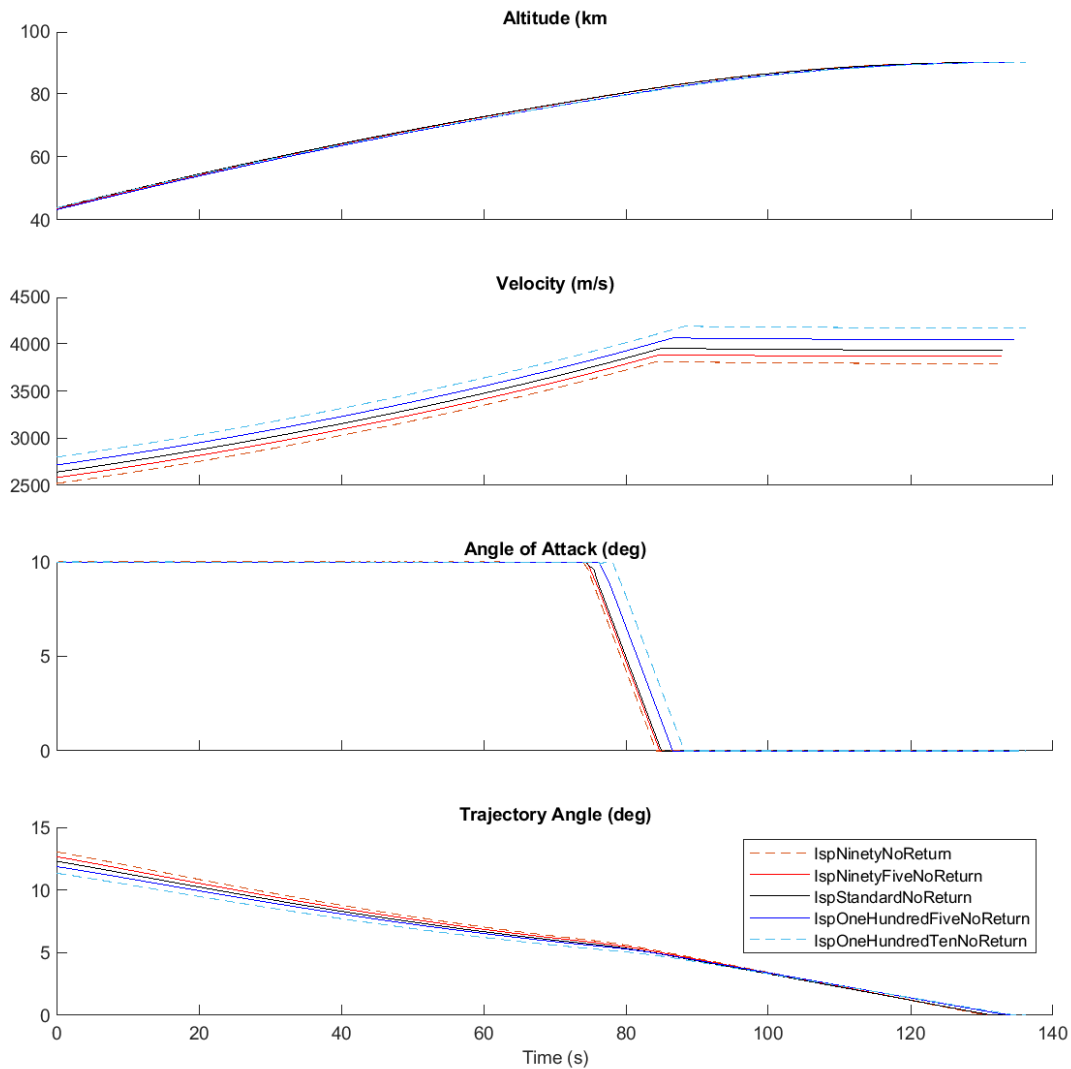


Figure F.6: Comparison of third stage rocket ascent trajectories with variation in the specific impulse of the scramjet accelerator.

F.1.4 Case 6: Scramjet Accelerator Mass Sensitivity Comparison

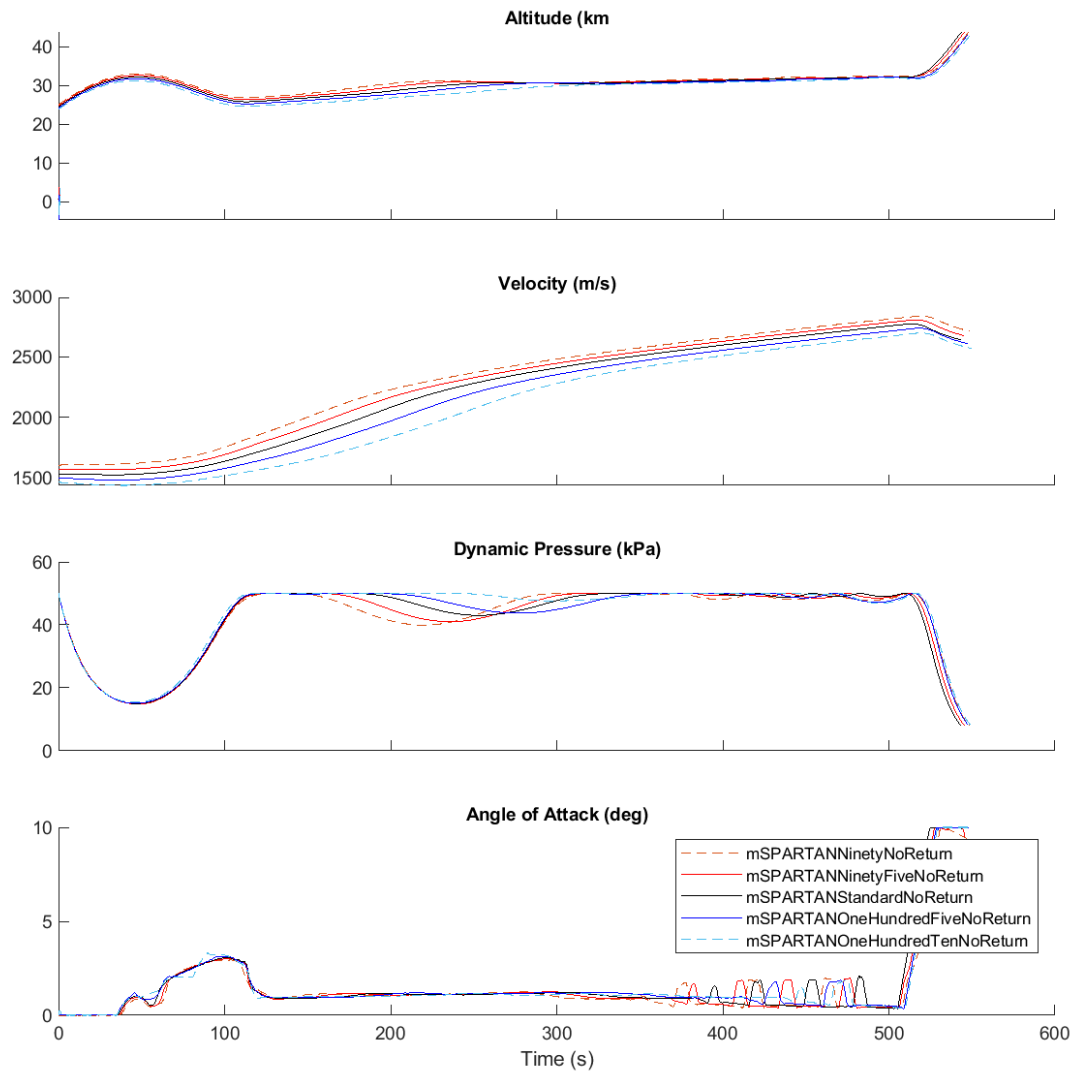


Figure F.7: Comparison of scramjet accelerator ascent trajectories with variation in the mass of the scramjet accelerator.

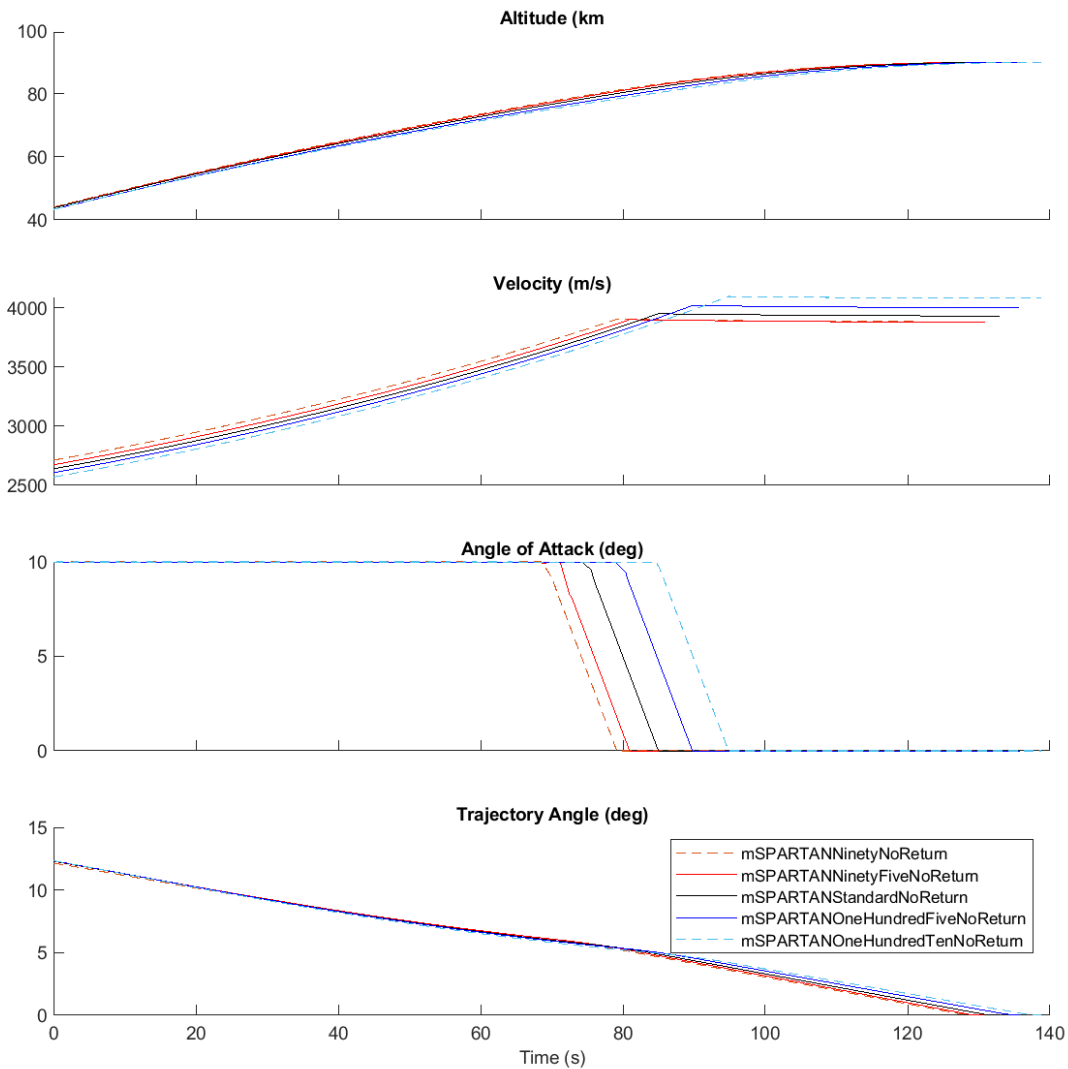


Figure F.8: Comparison of third stage rocket ascent trajectories with variation in the mass of the scramjet accelerator.

F.1.5 Case 7: Scramjet Accelerator Fuel Mass Sensitivity Comparison

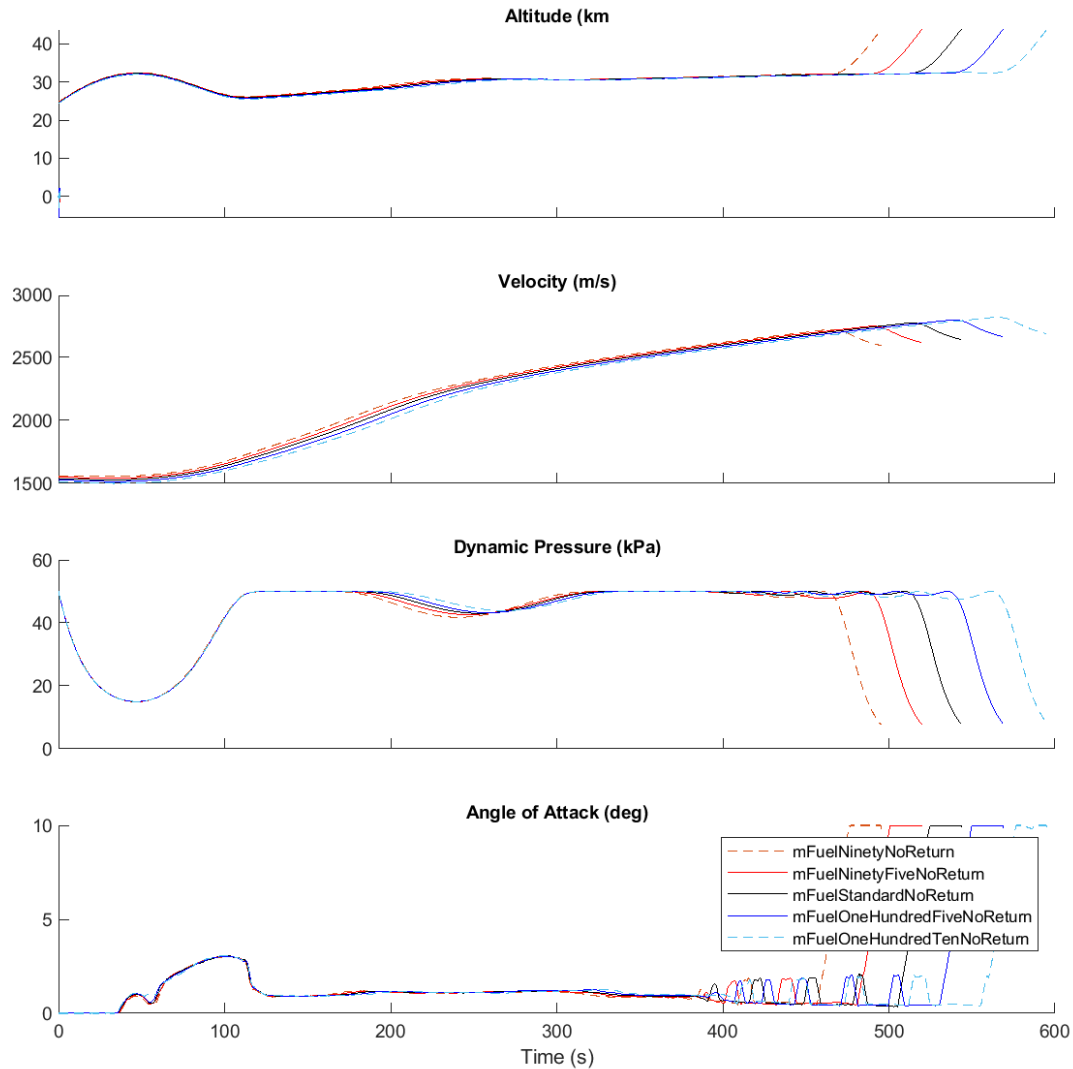


Figure F.9: Comparison of scramjet accelerator ascent trajectories with variation in the fuel mass of the scramjet accelerator.

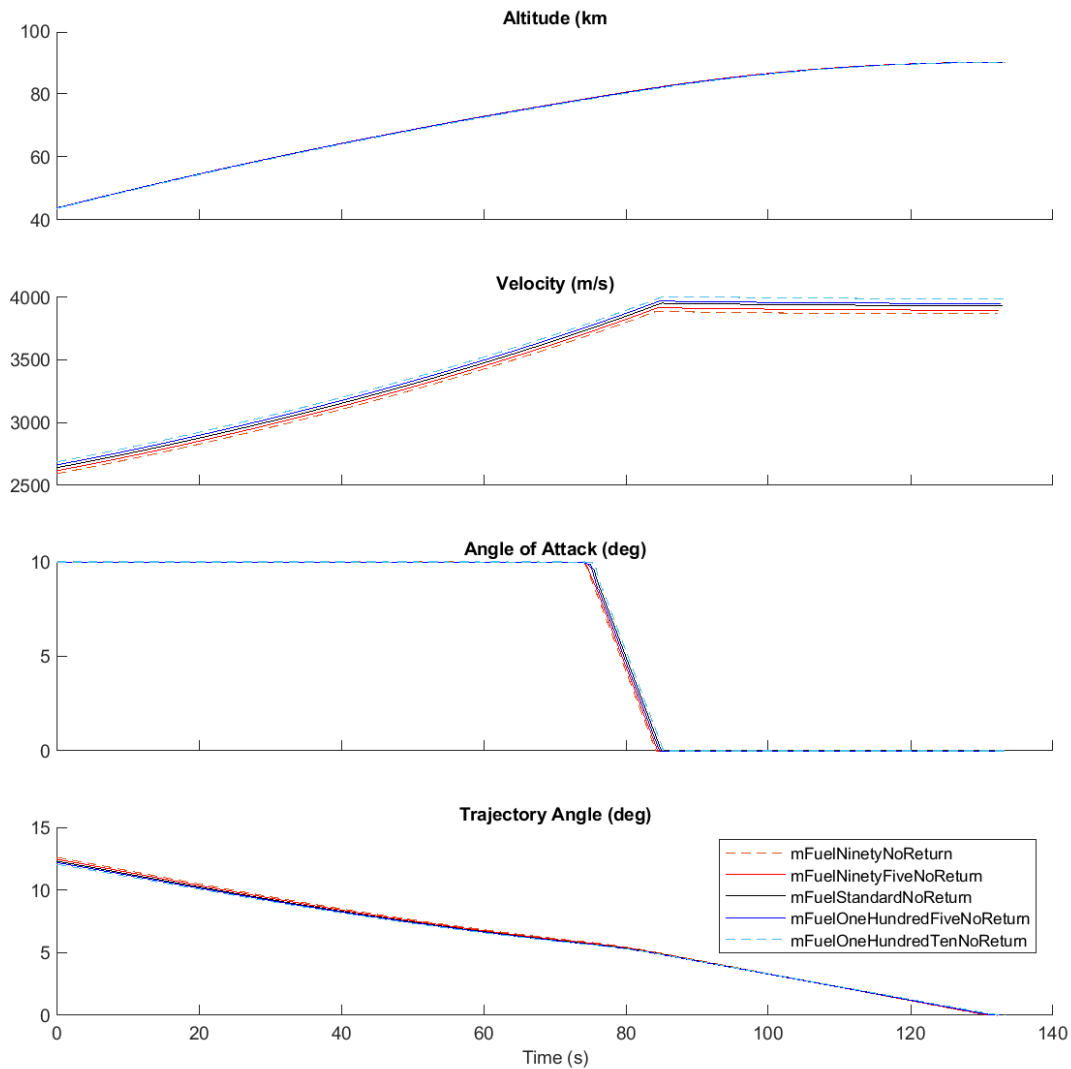


Figure F.10: Comparison of third stage rocket ascent trajectories with variation in the fuel mass of the scramjet accelerator.

F.1.6 Case 8: Third Stage Mass Sensitivity Comparison

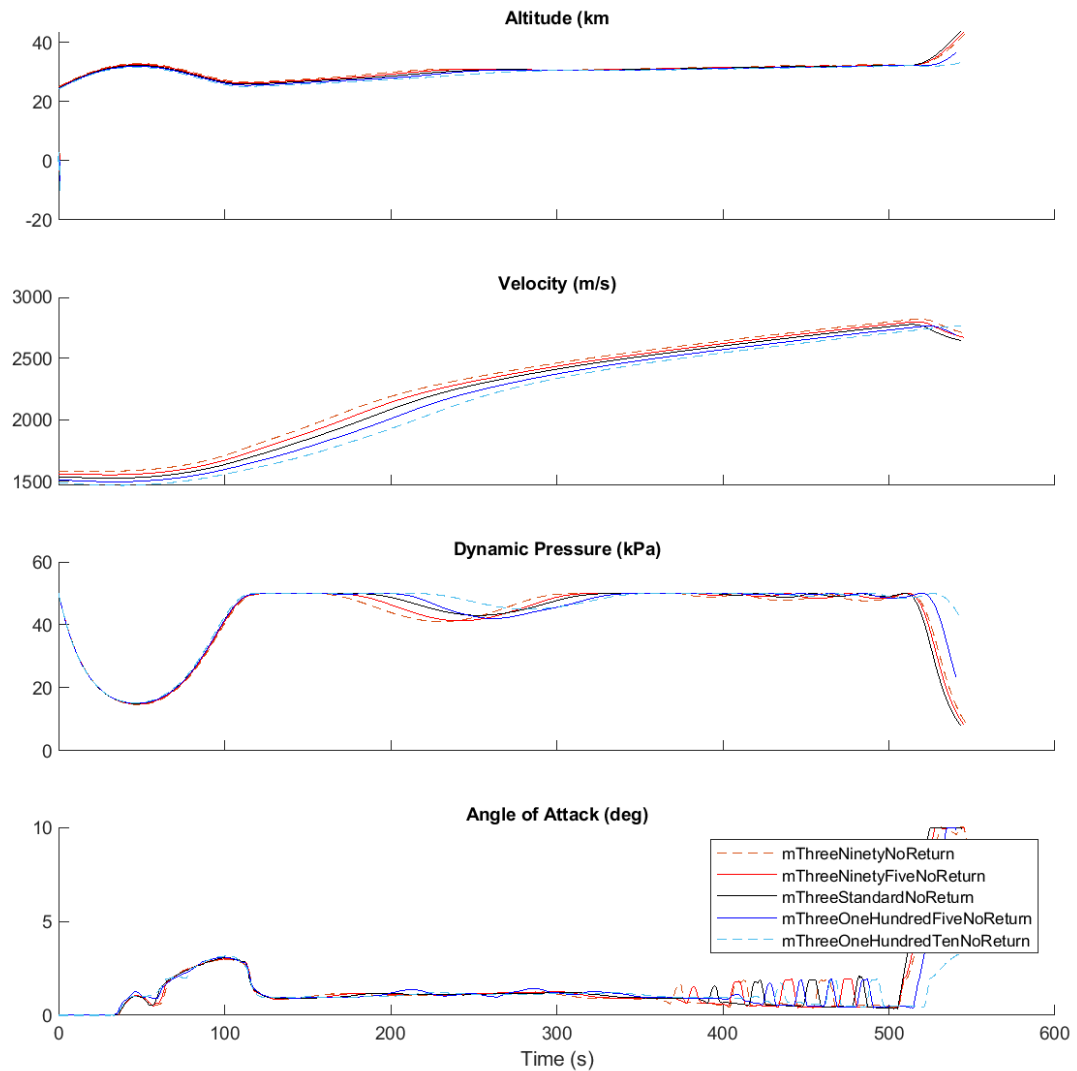


Figure F.11: Comparison of scramjet accelerator ascent trajectories with variation in the mass of the third stage.

F.1. OPTIMISED ASCENT TRAJECTORY COMPARISONS WITH NO FLY-BACK

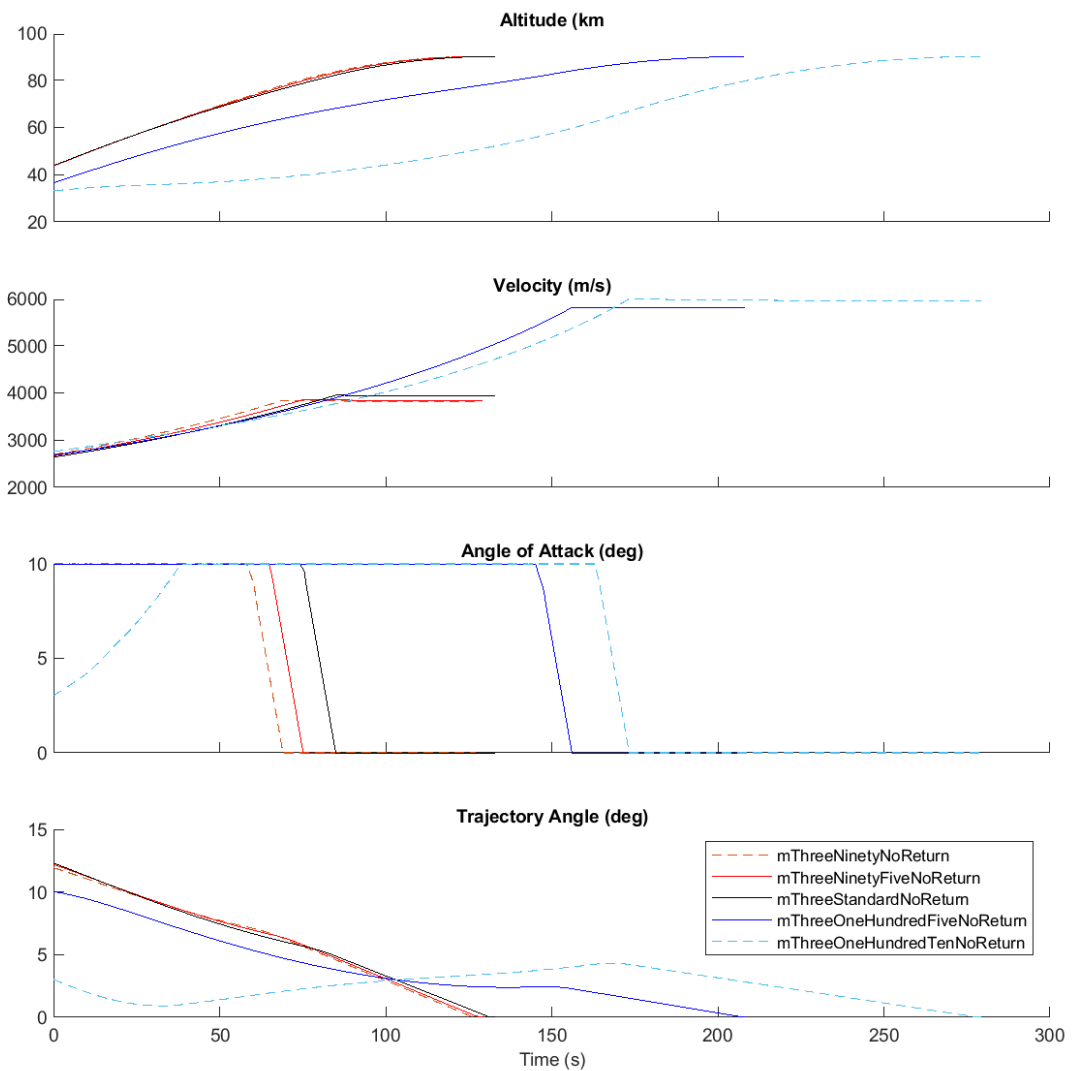


Figure F.12: Comparison of third stage rocket ascent trajectories with variation in the mass of the third stage.

F.1.7 Case 9: Third Stage Specific Impulse Sensitivity Comparison

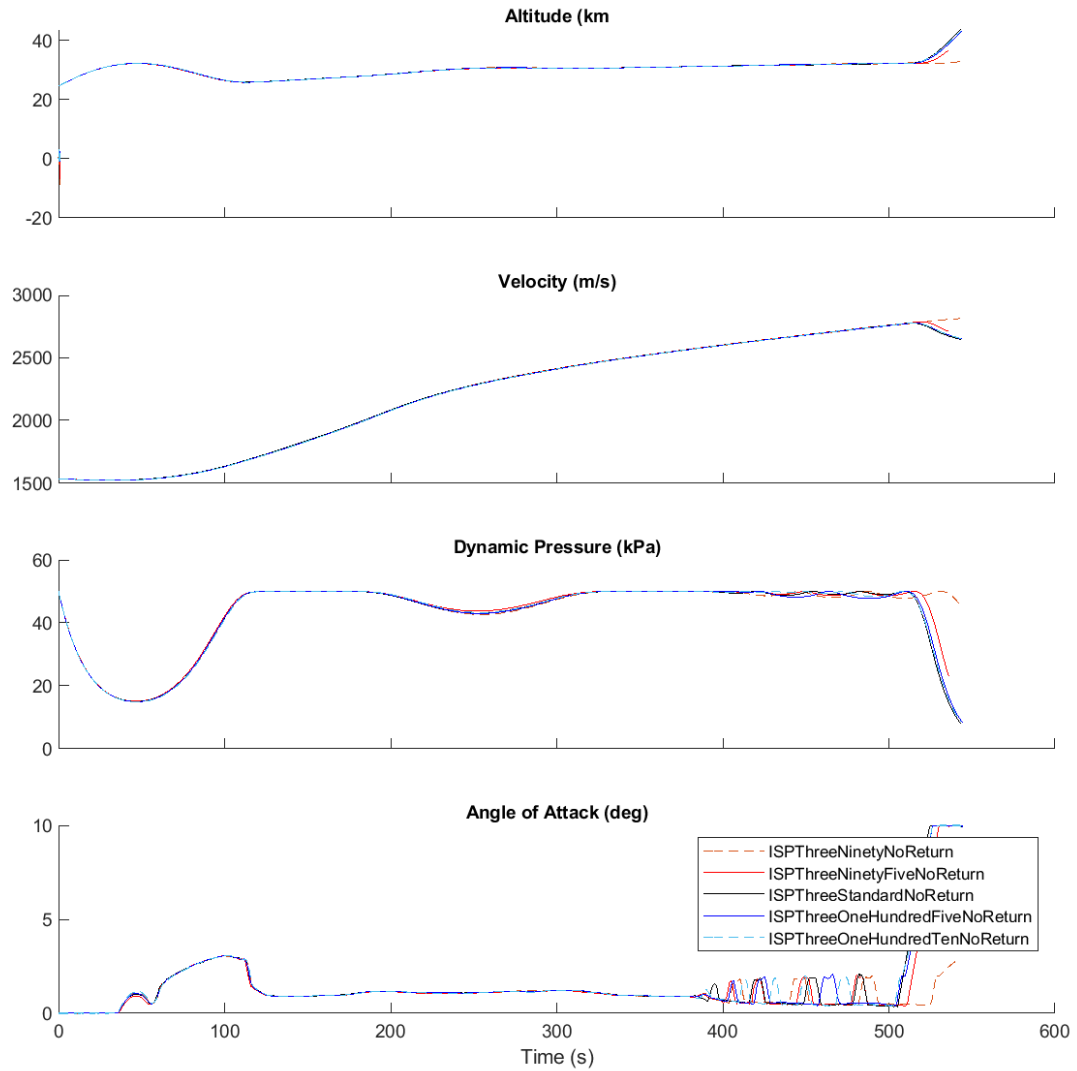


Figure F.13: Comparison of scramjet accelerator ascent trajectories with variation in the specific impulse of the third stage.

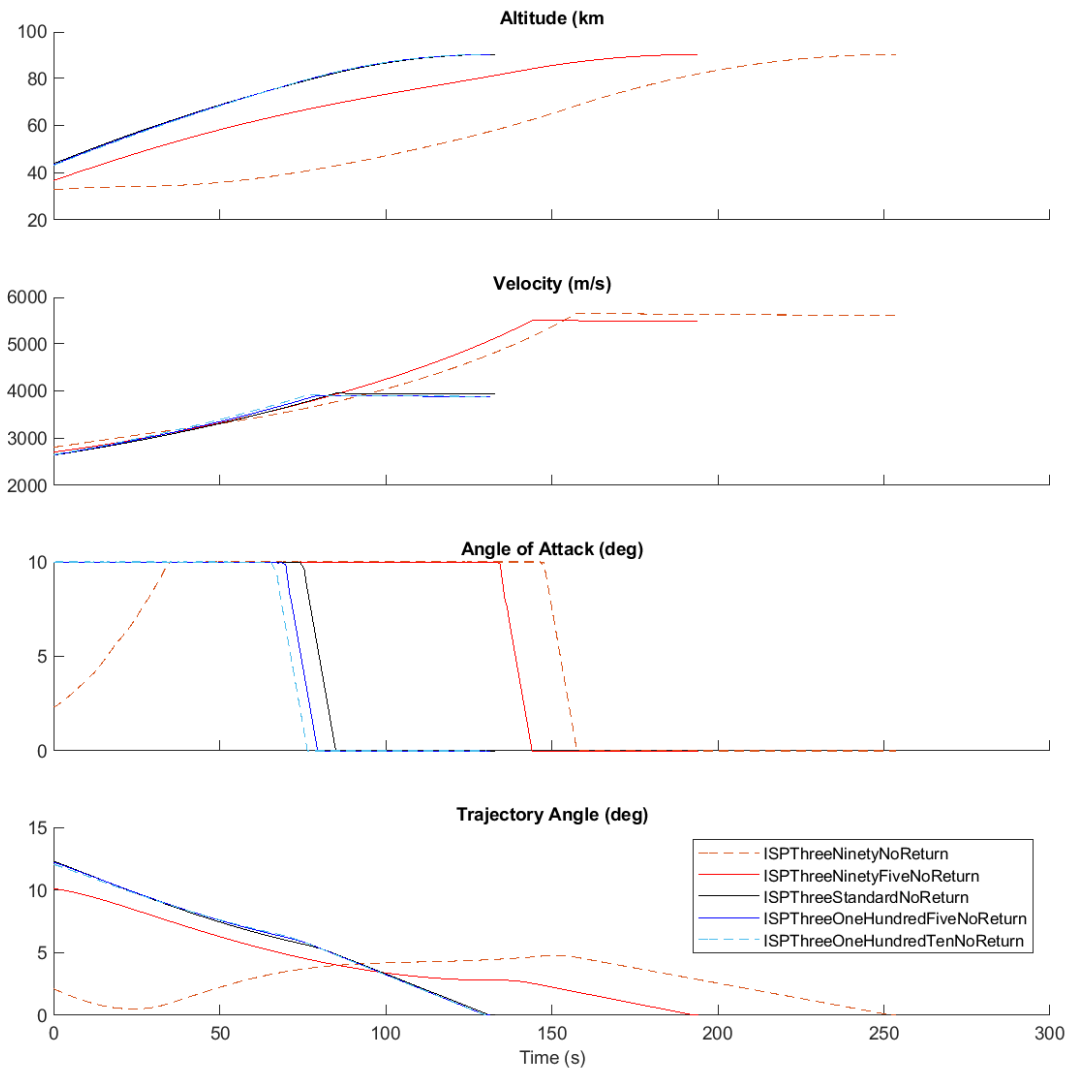


Figure F.14: Comparison of third stage rocket ascent trajectories with variation in the specific impulse of the third stage.

F.1.8 Case 10: Third Stage Drag Sensitivity Comparison

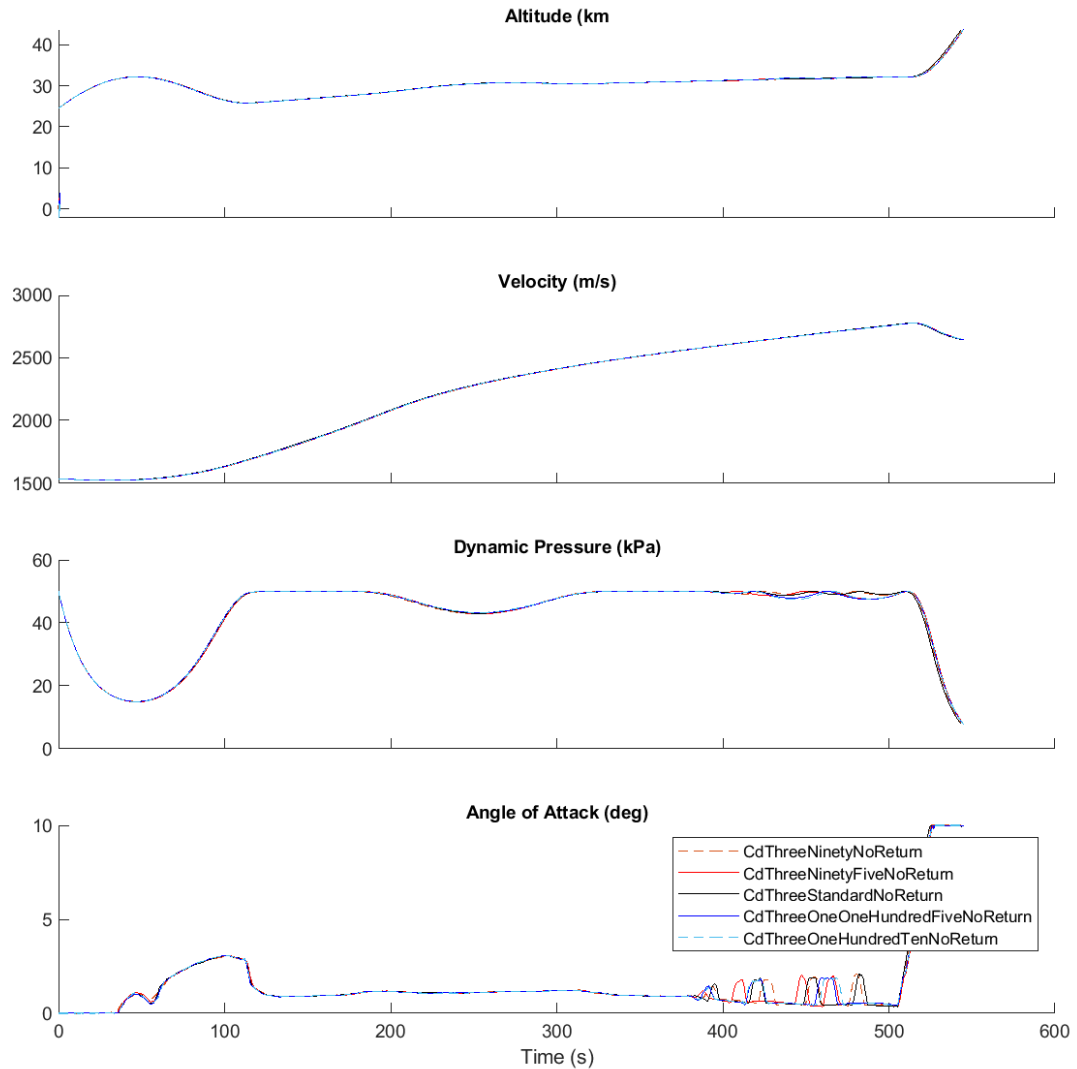


Figure F.15: Comparison of scramjet accelerator ascent trajectories with variation in the drag of the third stage.

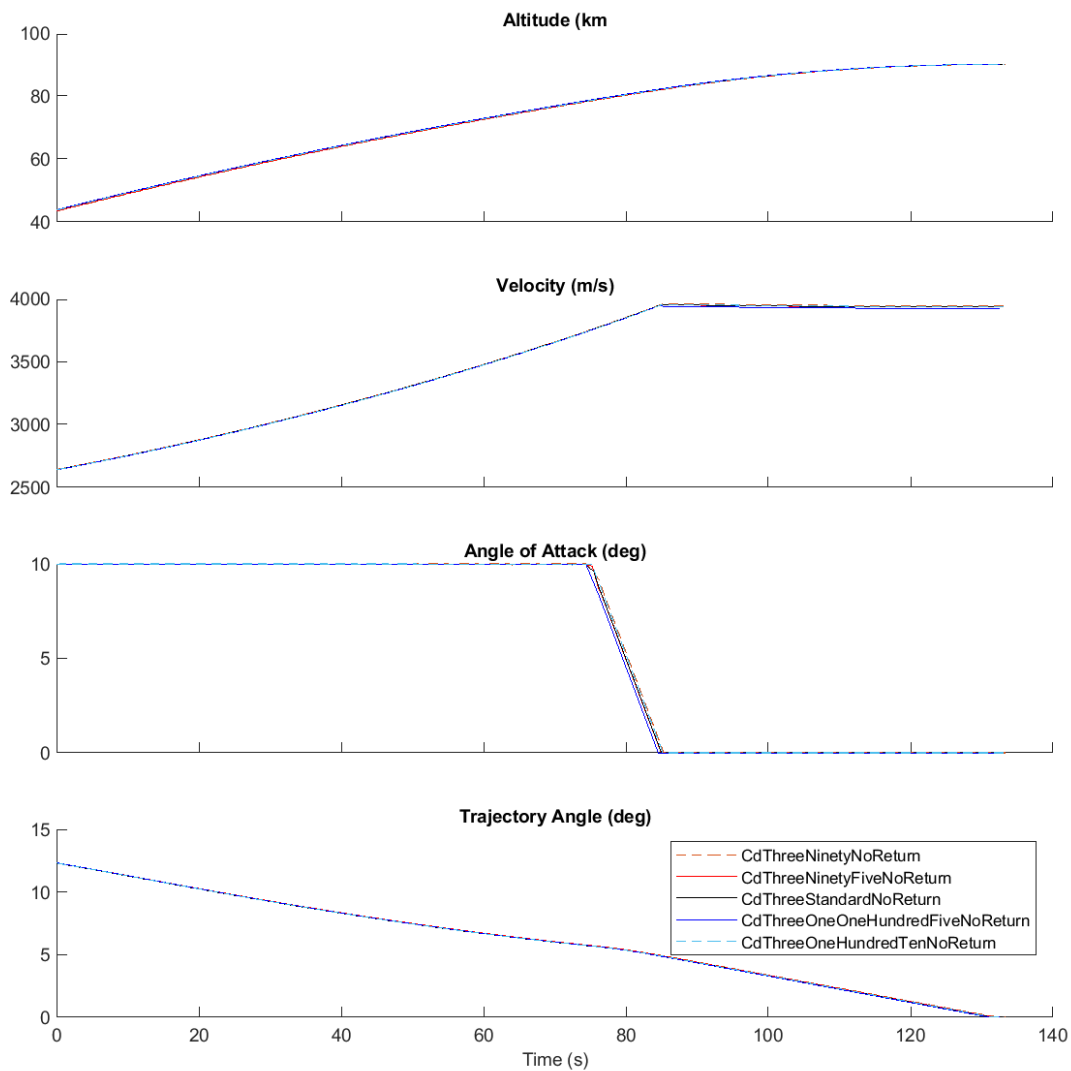


Figure F.16: Comparison of third stage rocket ascent trajectories with variation in the drag of the third stage.

F.2 Optimised Ascent Trajectory Comparisons With Fly-Back

F.2.1 Case 12: Dynamic Pressure Sensitivity Comparison

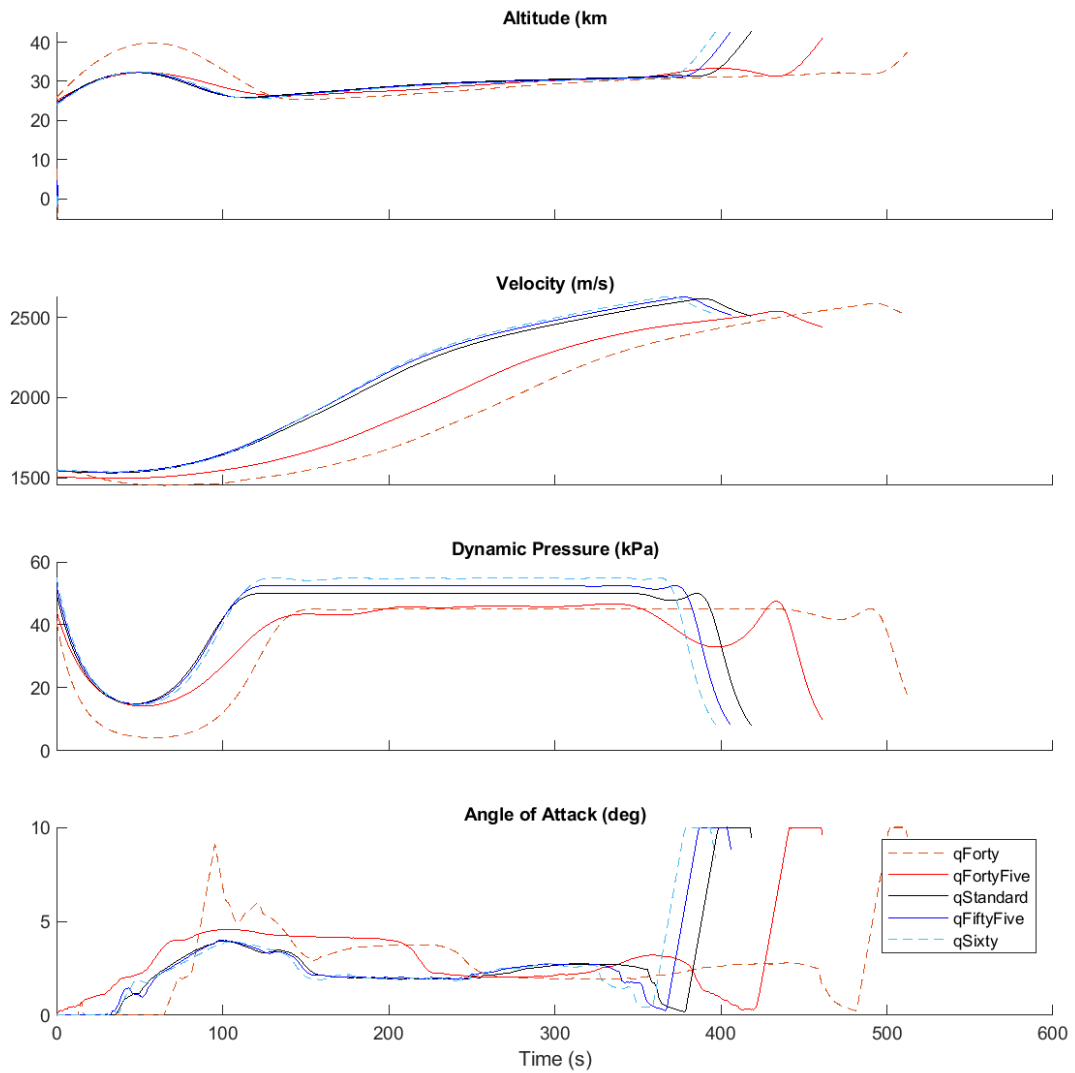


Figure F.17: Comparison of scramjet accelerator ascent trajectories with variation in the maximum dynamic pressure of the scramjet accelerator.

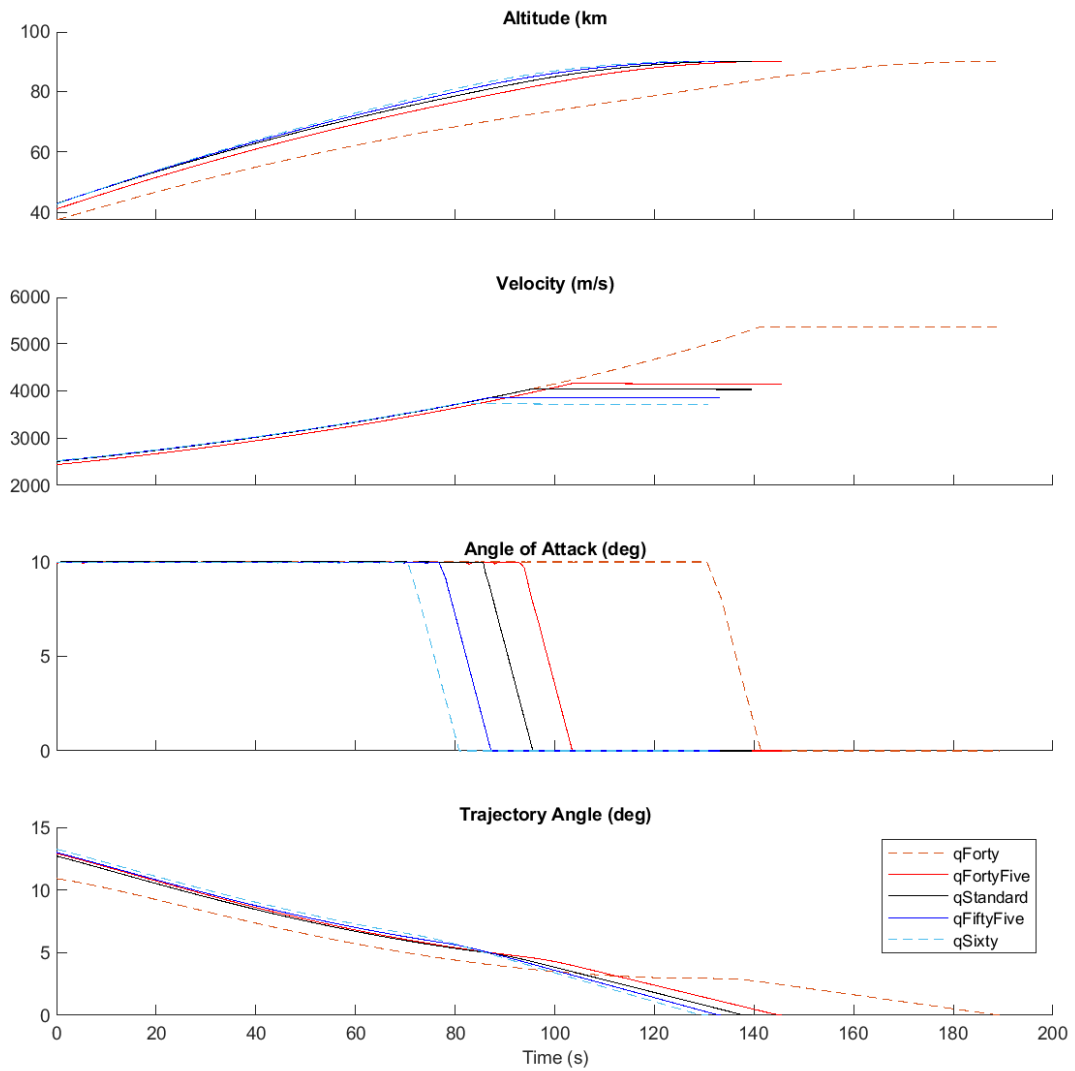


Figure F.18: Comparison of third stage rocket ascent trajectories with variation in the maximum dynamic pressure of the scramjet accelerator.

APPENDIX F. TRAJECTORY PLOT COMPARISONS

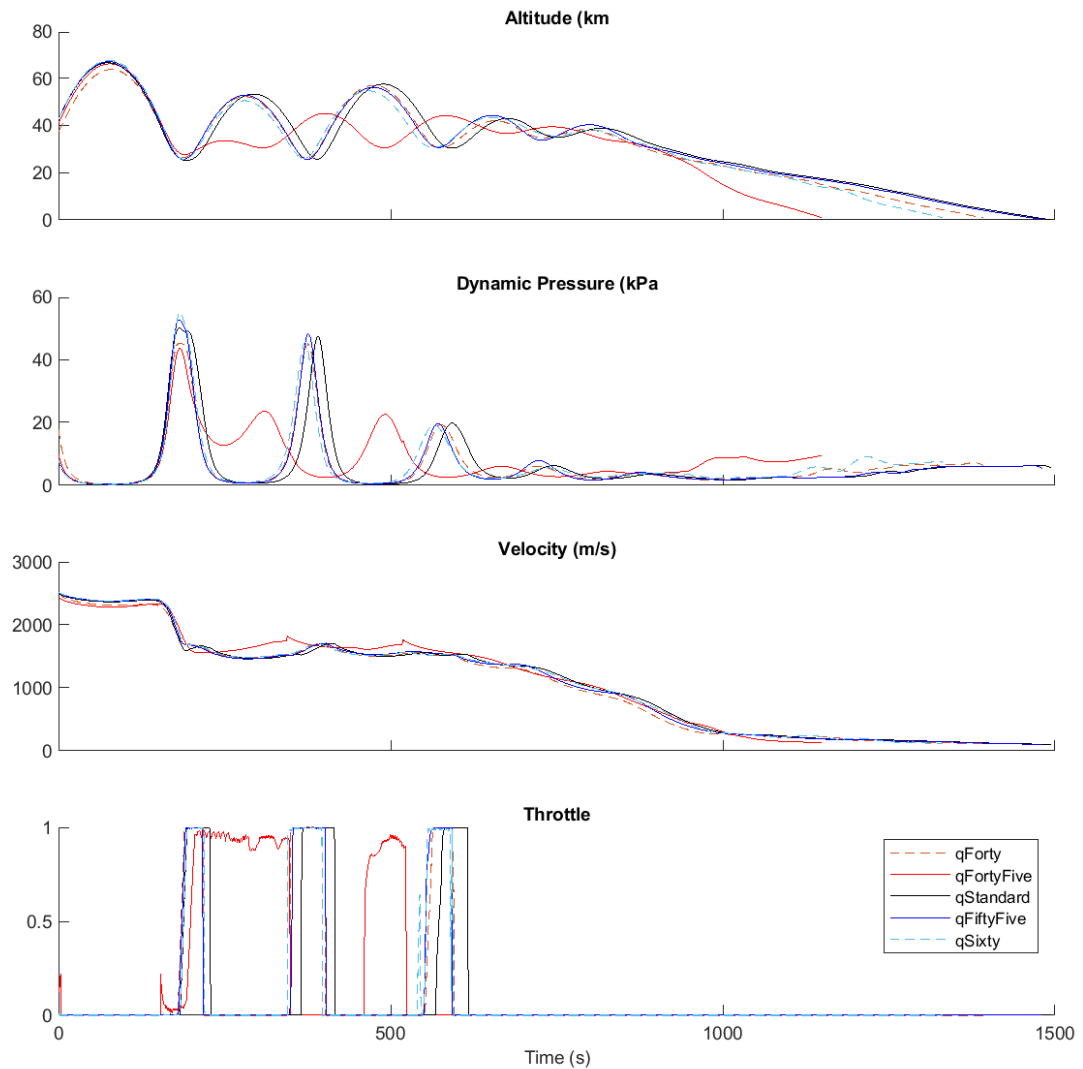


Figure F.19: Comparison of scramjet accelerator return trajectories with variation in the maximum dynamic pressure of the scramjet accelerator.

F.2.2 Case 13: Scramjet Accelerator Drag Sensitivity Comparison

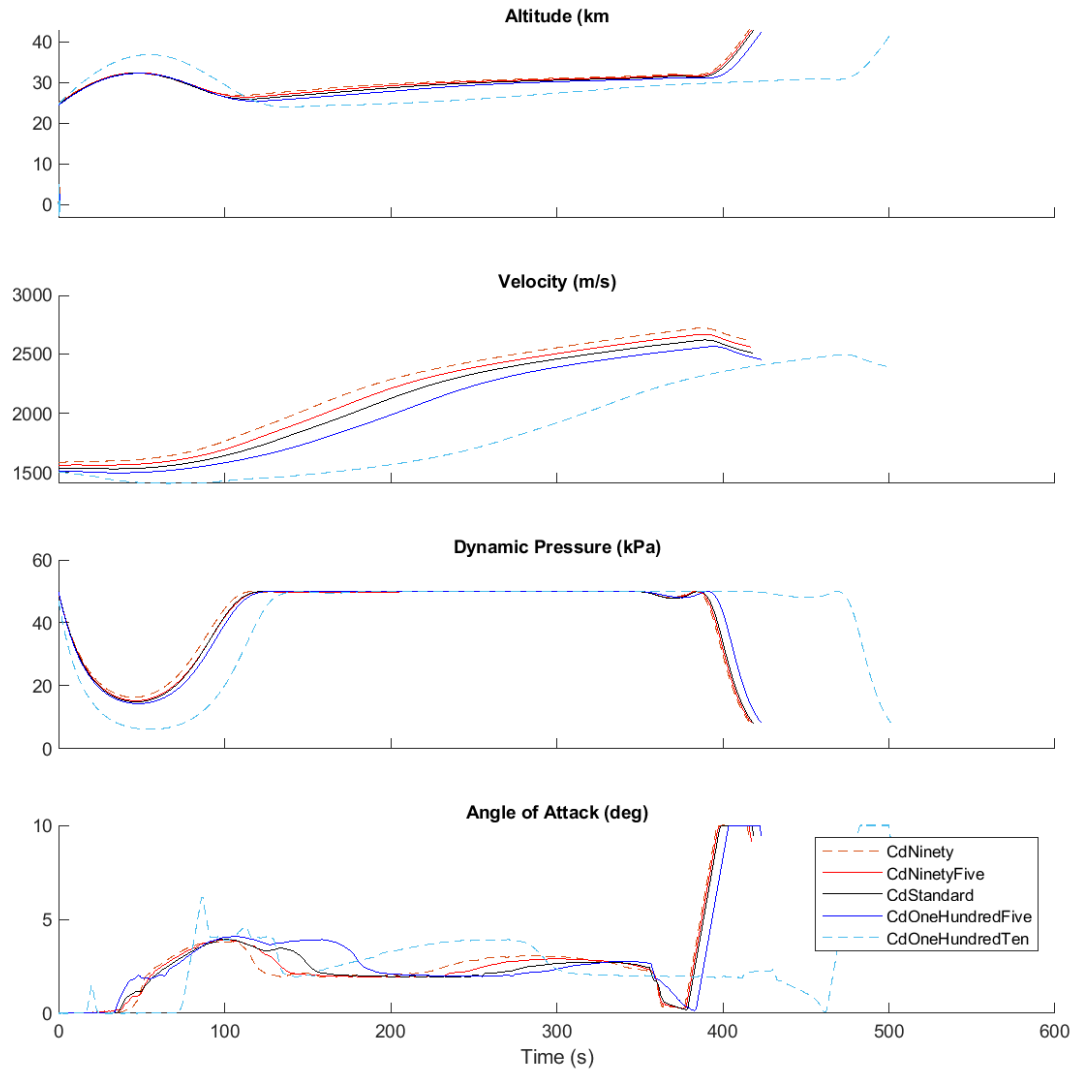


Figure F.20: Comparison of scramjet accelerator ascent trajectories with variation in the drag of the scramjet accelerator.

APPENDIX F. TRAJECTORY PLOT COMPARISONS

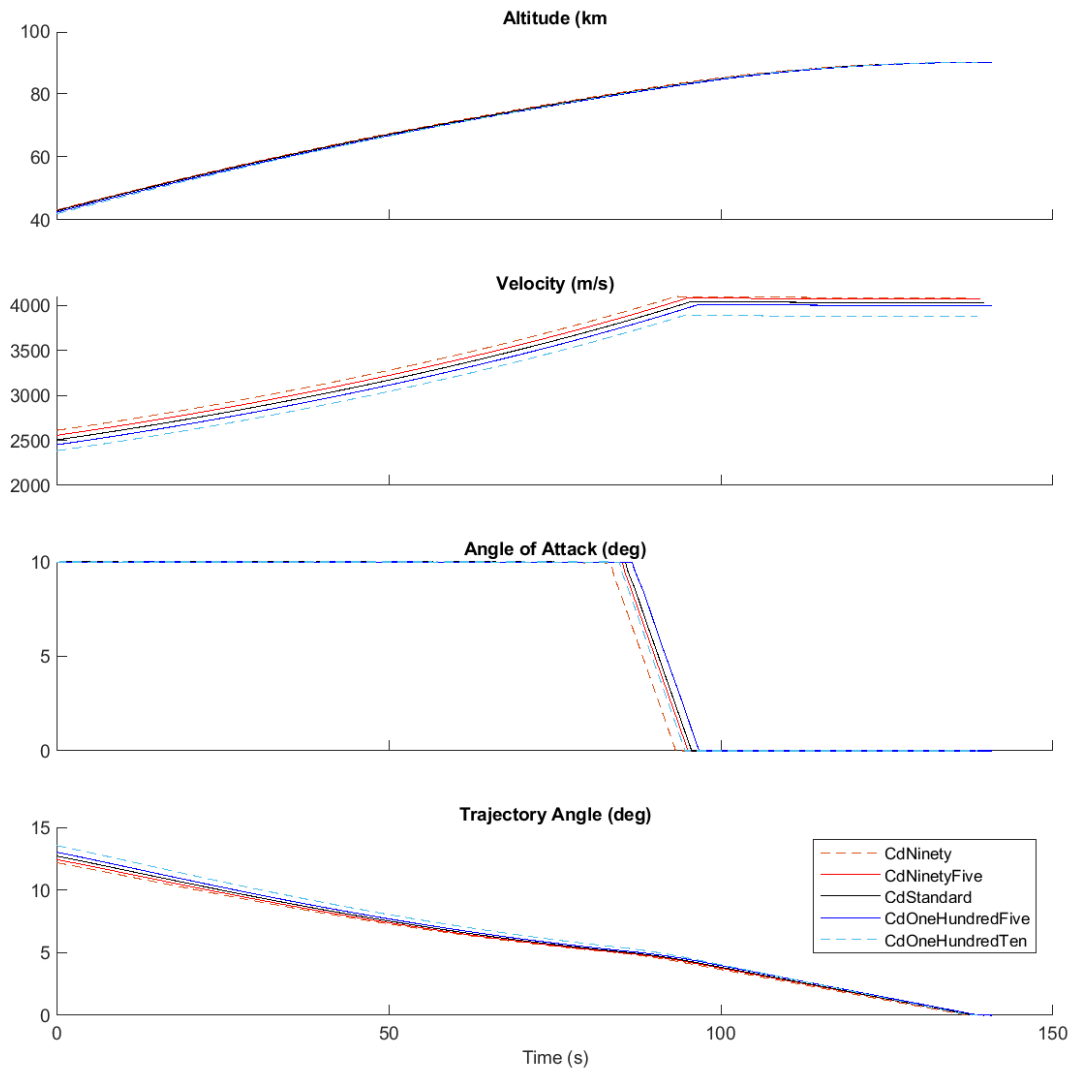


Figure F.21: Comparison of third stage rocket ascent trajectories with variation in the drag of the scramjet accelerator.

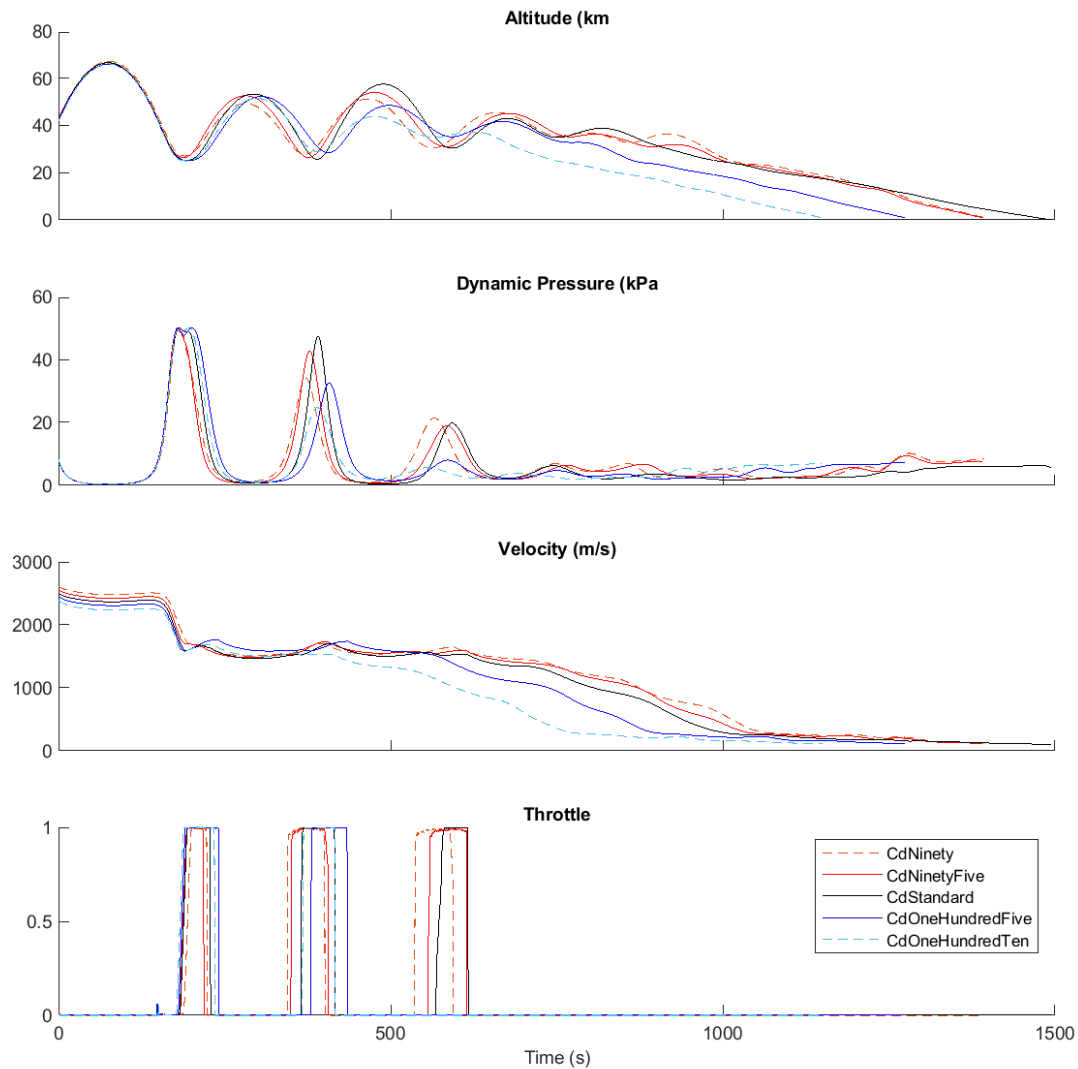


Figure F.22: Comparison of scramjet accelerator return trajectories with variation in the drag of the scramjet accelerator.

F.2.3 Case 14: scramjet accelerator Specific Impulse Sensitivity Comparison

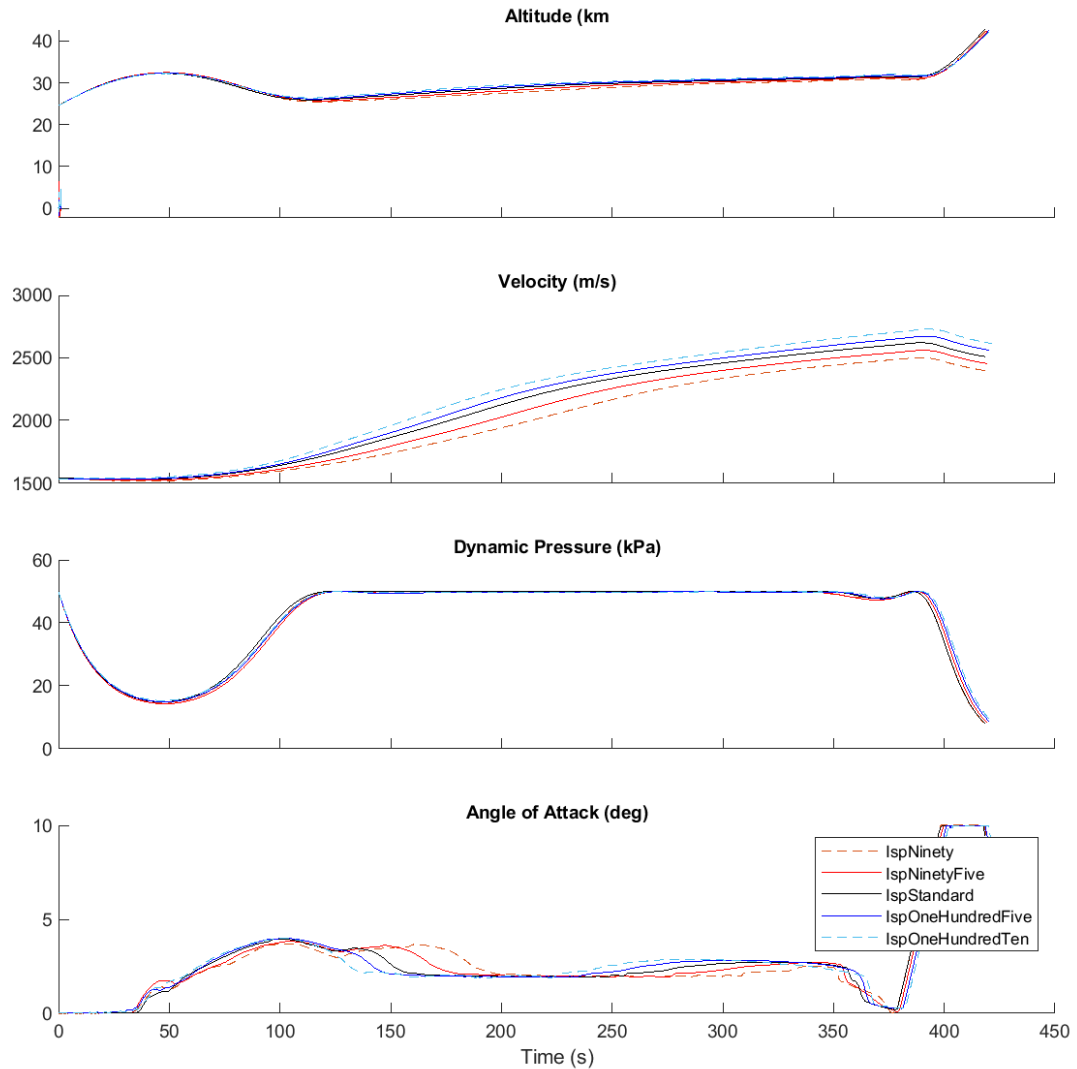


Figure F.23: Comparison of scramjet accelerator ascent trajectories with variation in the specific impulse of the scramjet accelerator.

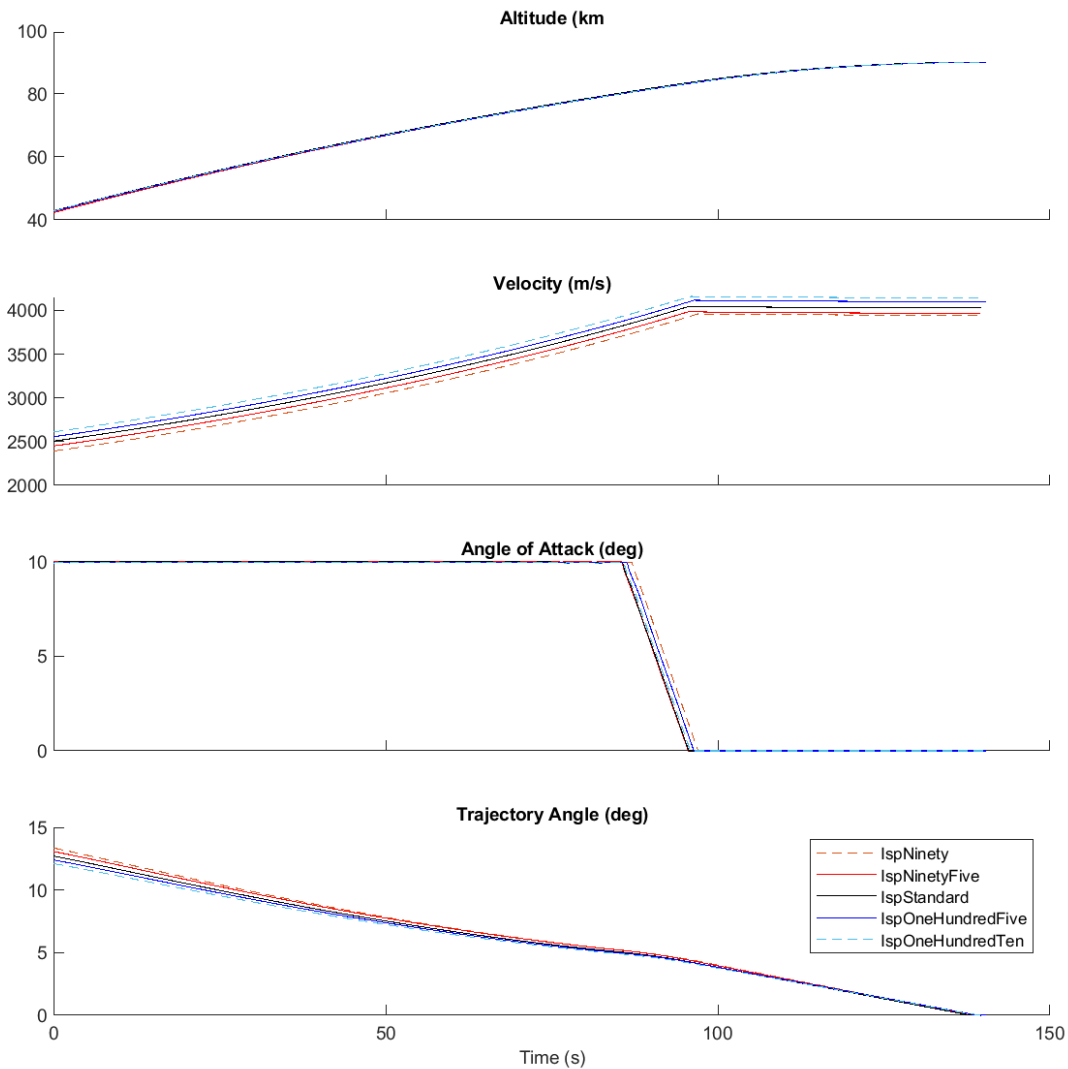


Figure F.24: Comparison of third stage rocket ascent trajectories with variation in the specific impulse of the scramjet accelerator.

APPENDIX F. TRAJECTORY PLOT COMPARISONS

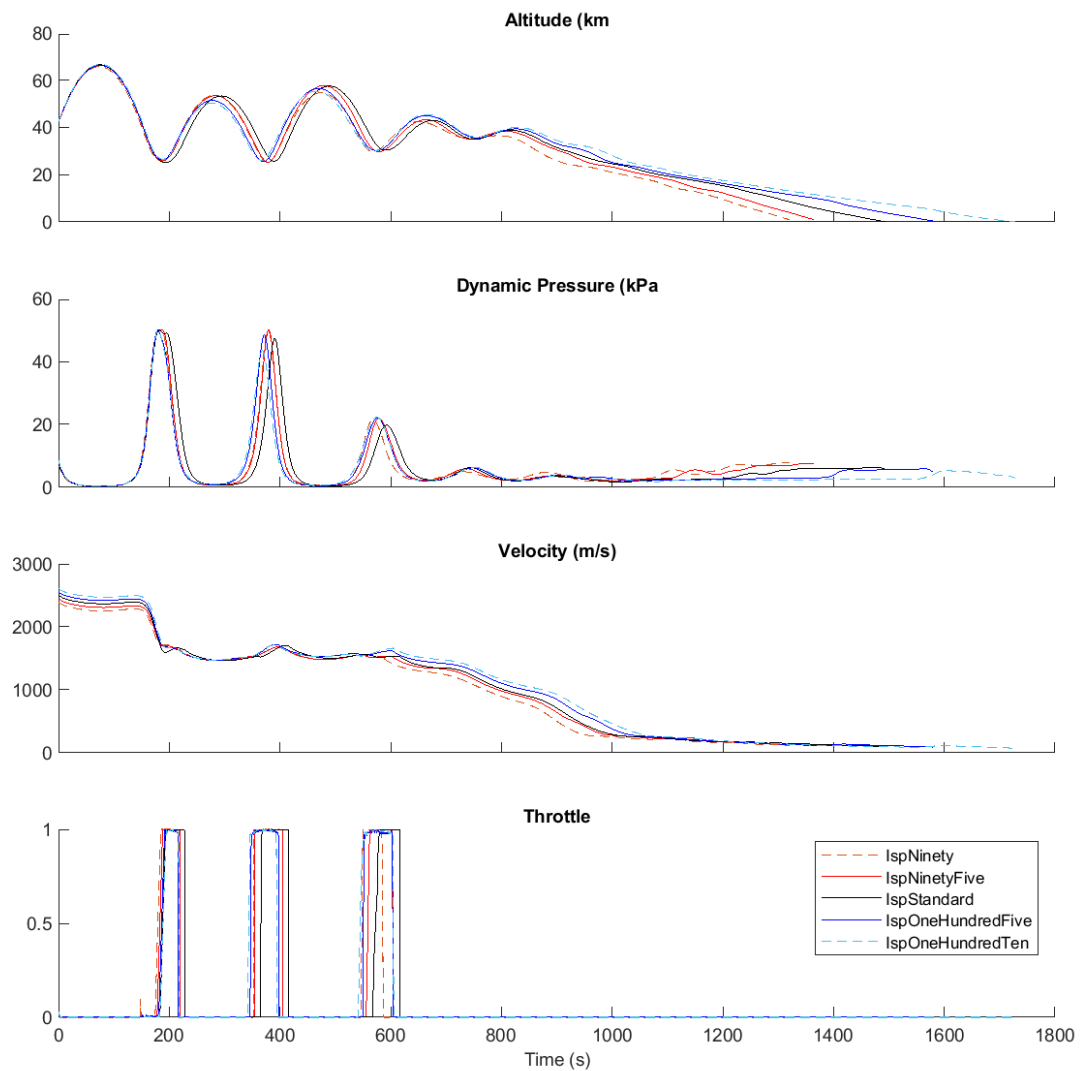


Figure F.25: Comparison of scramjet accelerator return trajectories with variation in the specific impulse of the scramjet accelerator.

F.2.4 Case 15: Scramjet Accelerator Mass Sensitivity Comparison

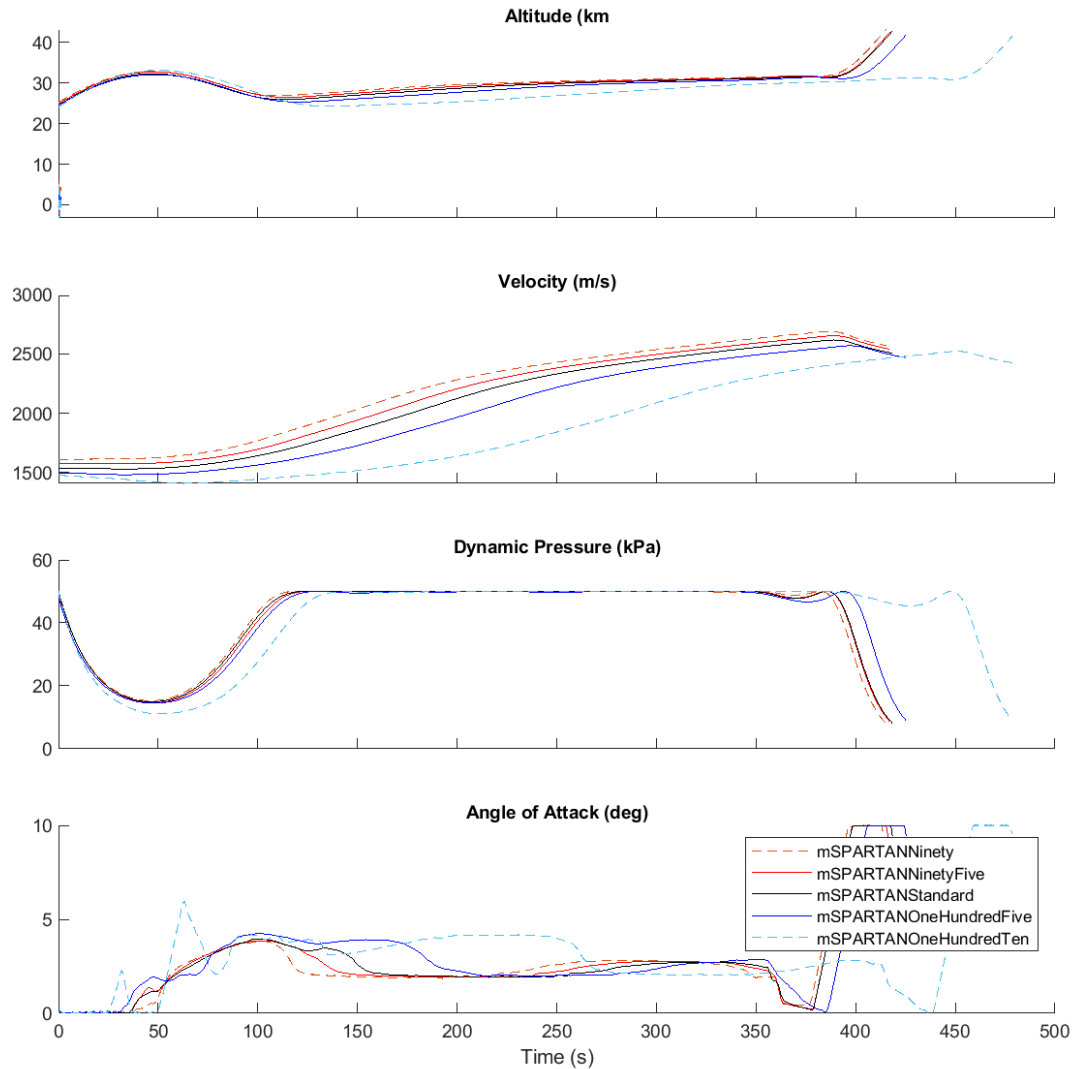


Figure F.26: Comparison of scramjet accelerator ascent trajectories with variation in the mass of the scramjet accelerator.

APPENDIX F. TRAJECTORY PLOT COMPARISONS

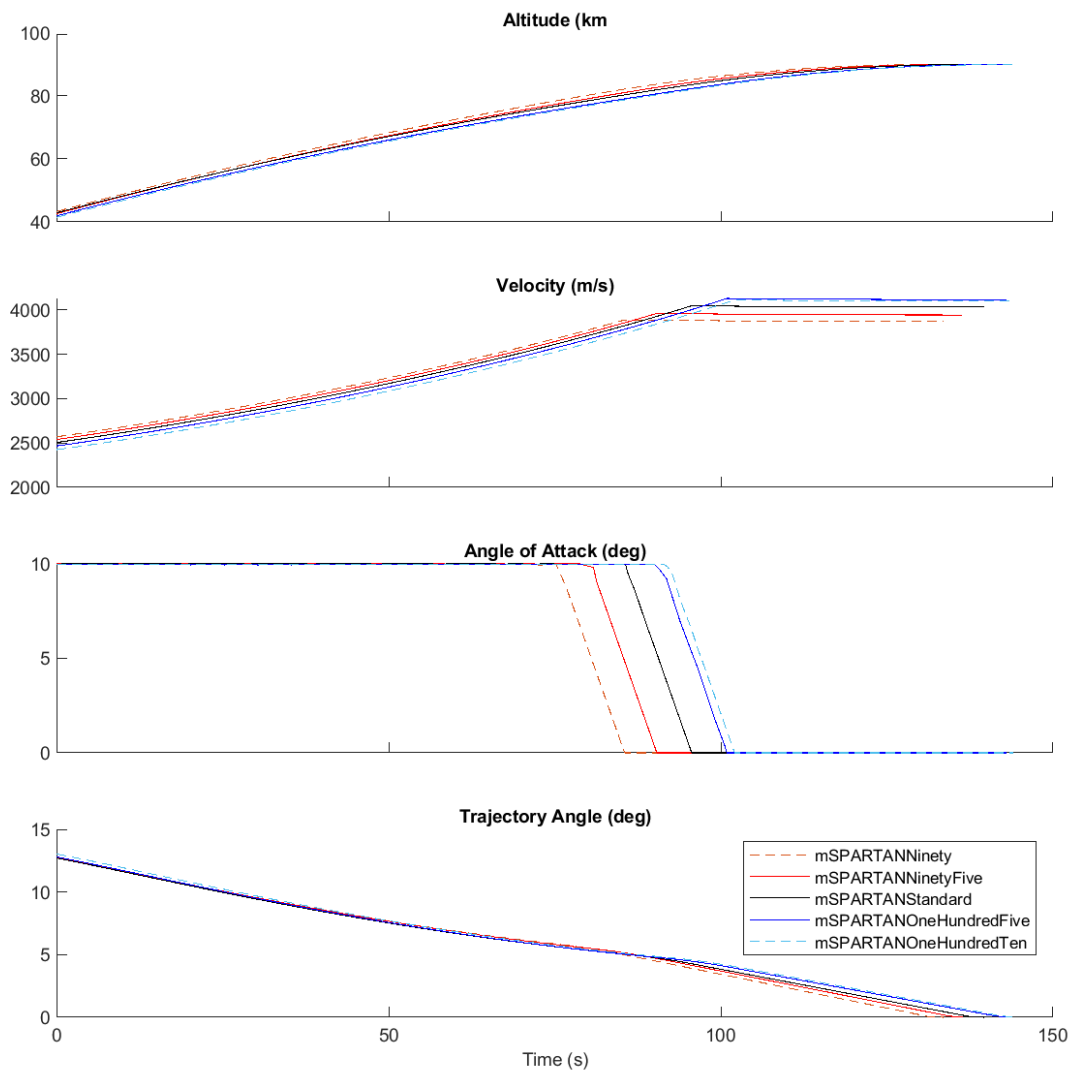


Figure F.27: Comparison of third stage rocket ascent trajectories with variation in the mass of the scramjet accelerator.

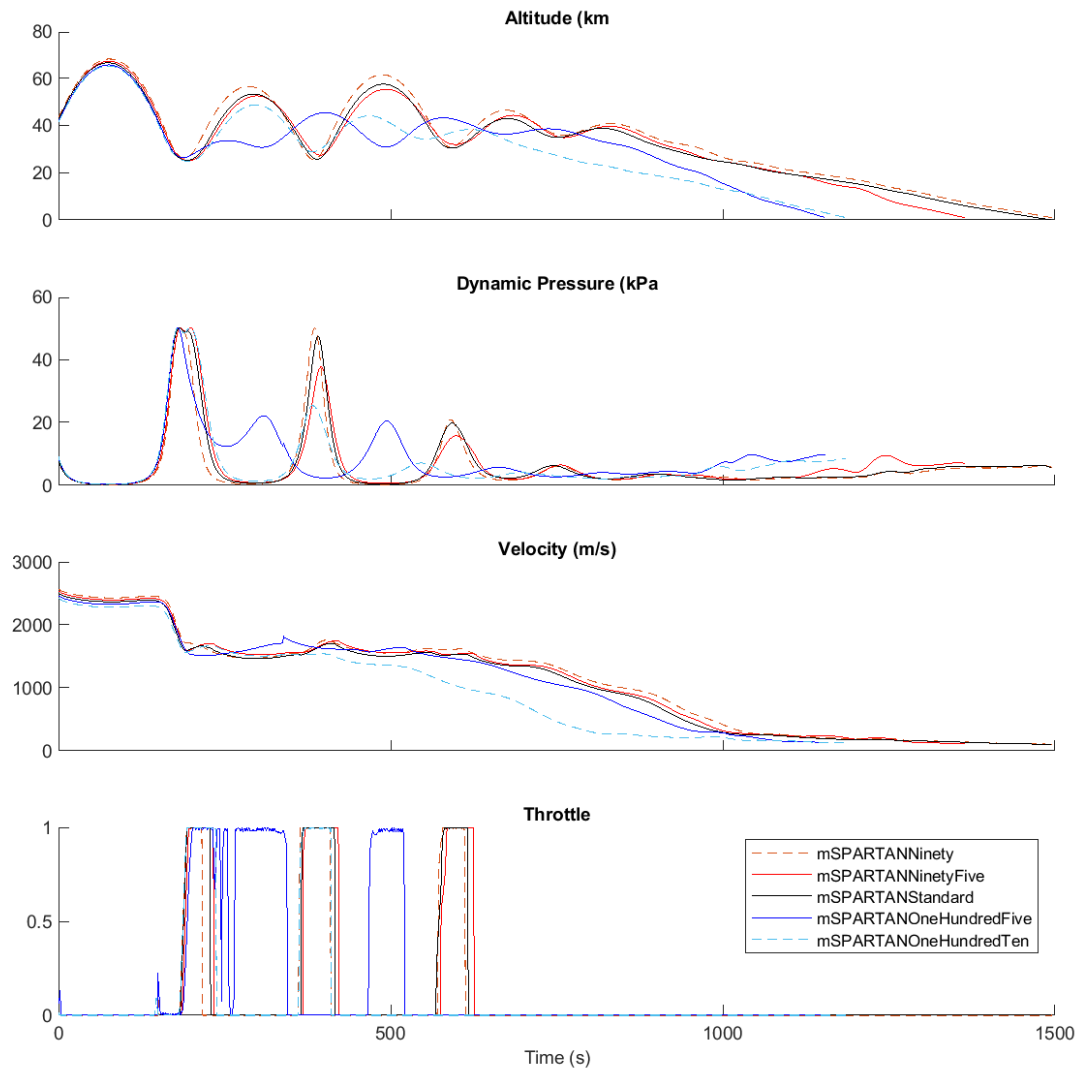


Figure F.28: Comparison of scramjet accelerator return trajectories with variation in the mass of the scramjet accelerator.

F.2.5 Case 16: Scramjet Accelerator Fuel Mass Sensitivity Comparison

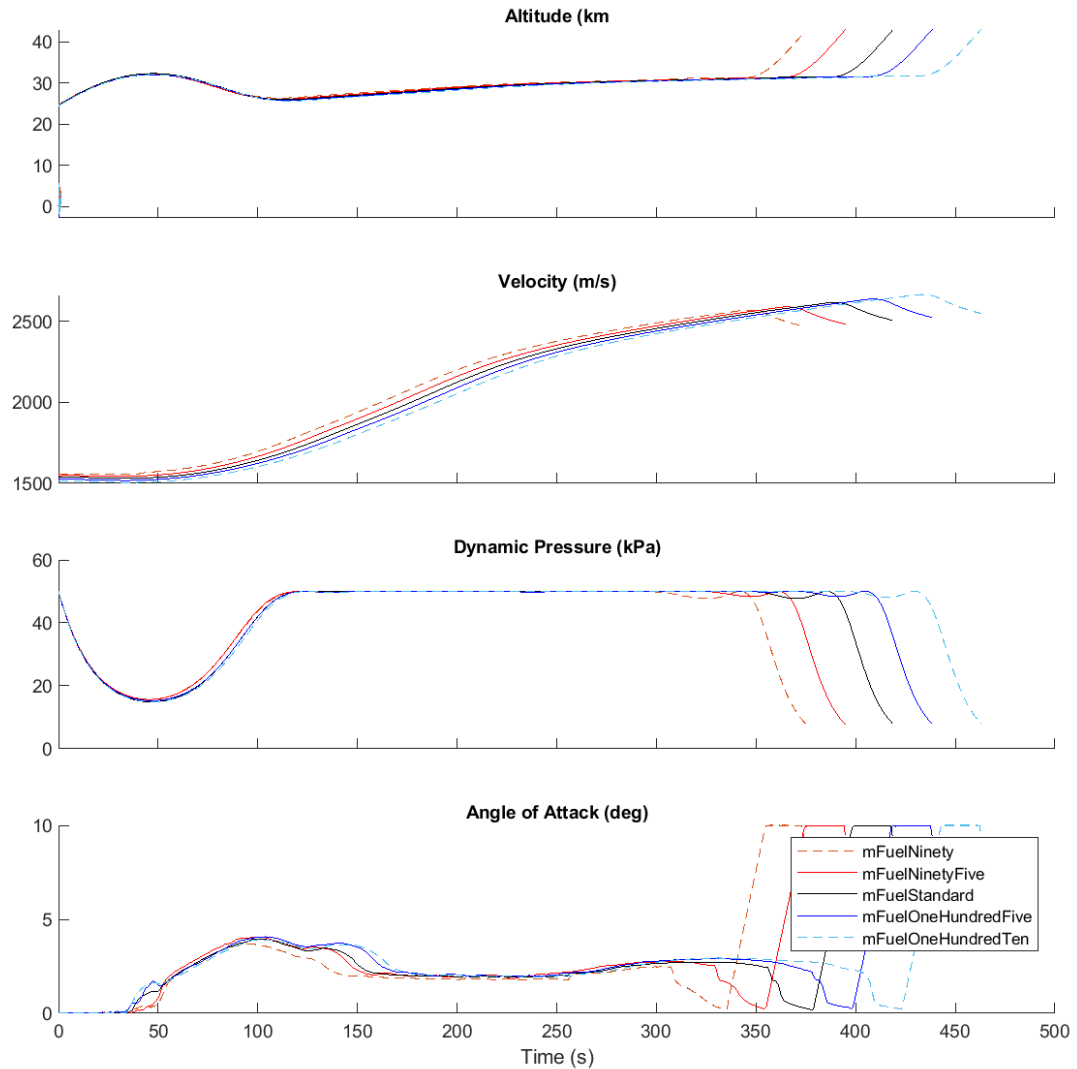


Figure F.29: Comparison of scramjet accelerator ascent trajectories with variation in the fuel mass of the scramjet accelerator.

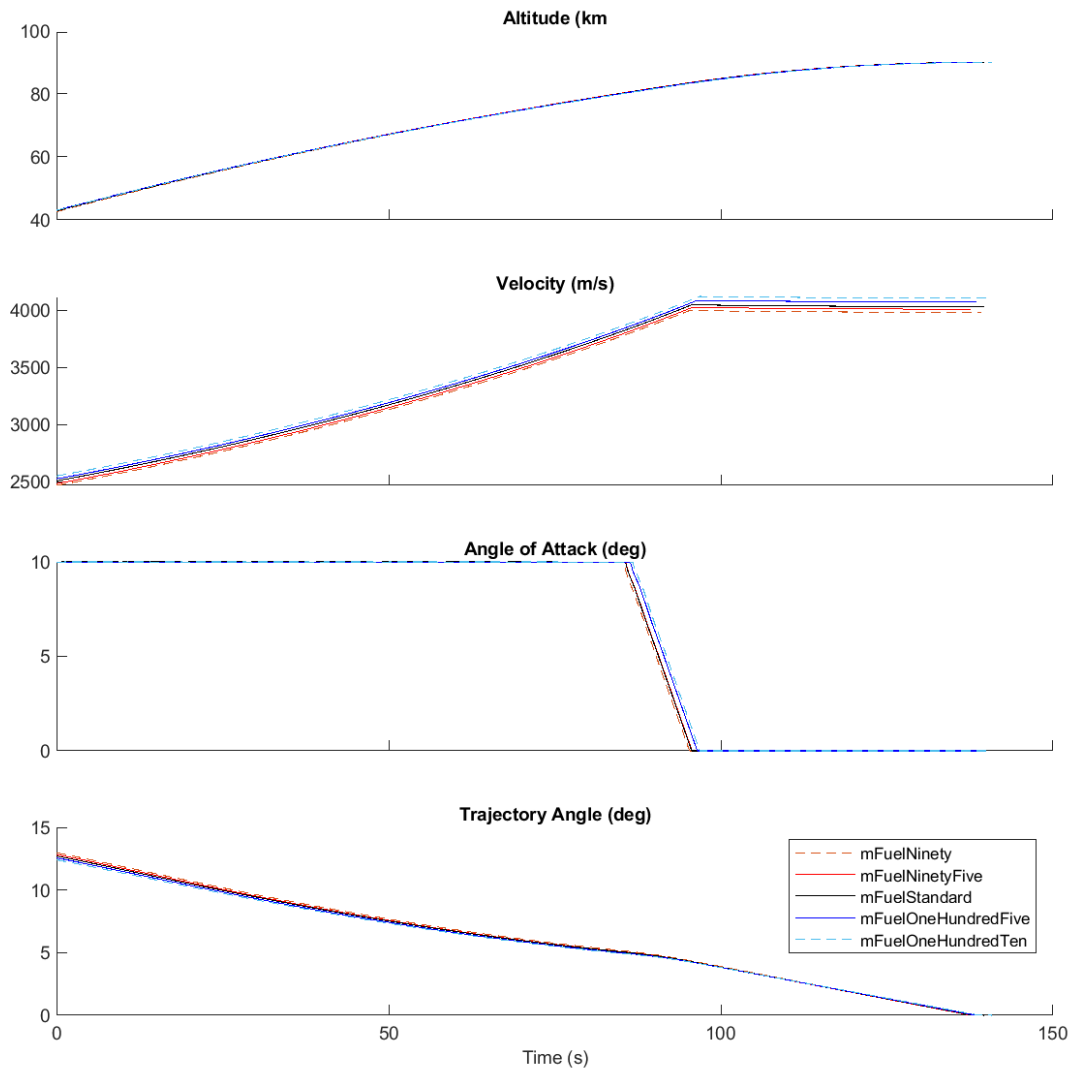


Figure F.30: Comparison of third stage rocket ascent trajectories with variation in the fuel mass of the scramjet accelerator.

APPENDIX F. TRAJECTORY PLOT COMPARISONS

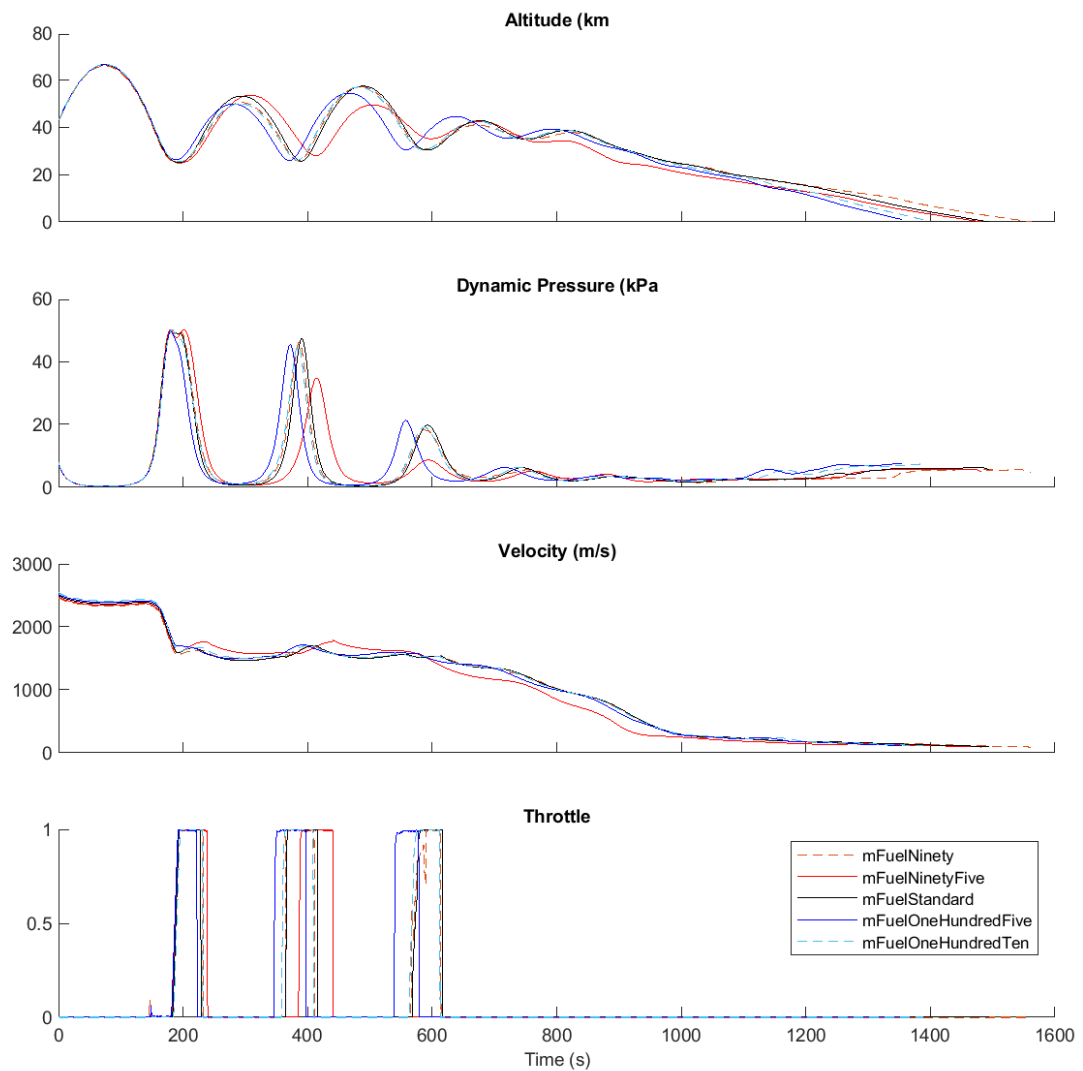


Figure F.31: Comparison of scramjet accelerator return trajectories with variation in the fuel mass of the scramjet accelerator.

F.2.6 Case 17: Third Stage Mass Sensitivity Comparison

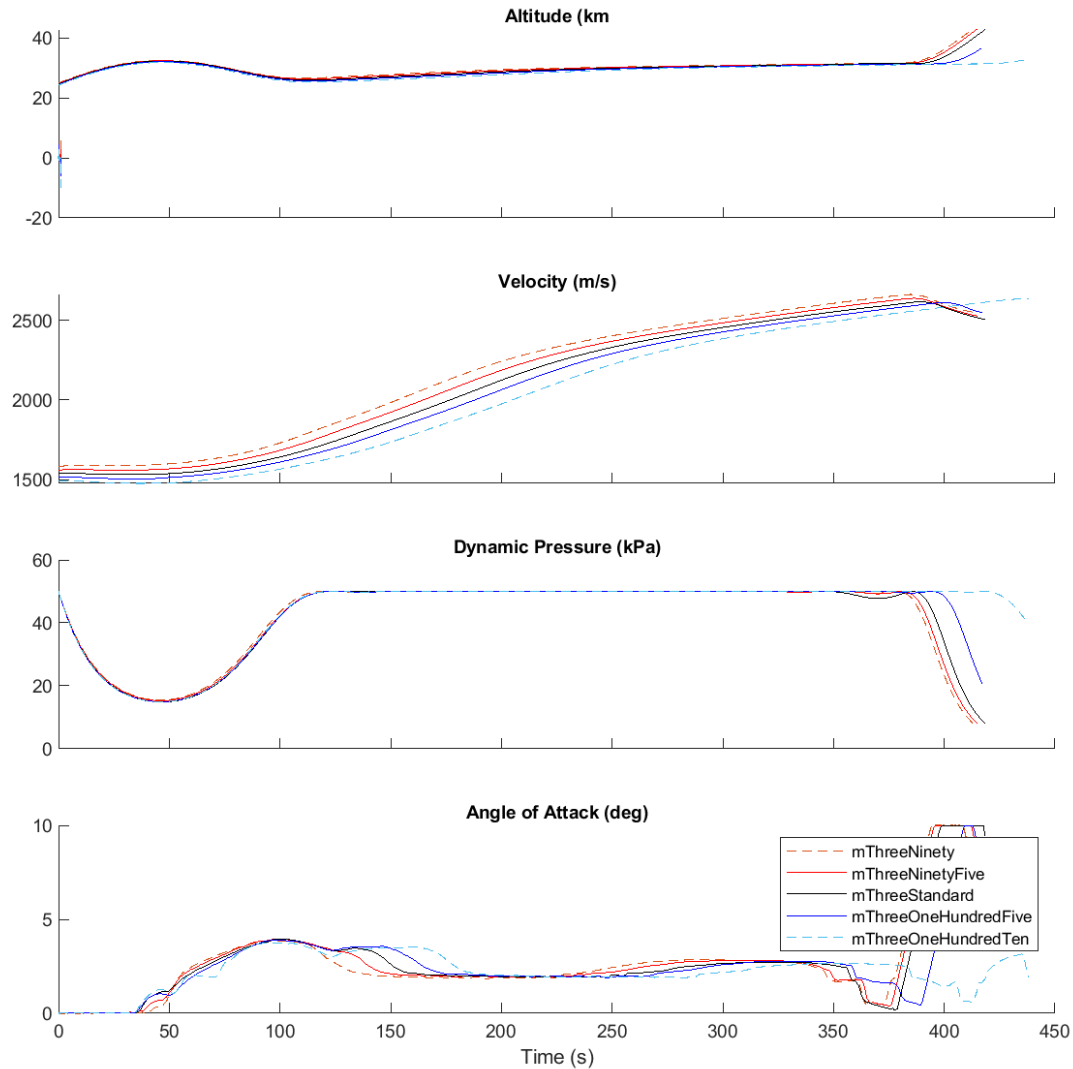


Figure F.32: Comparison of scramjet accelerator ascent trajectories with variation in the mass of the third stage.

APPENDIX F. TRAJECTORY PLOT COMPARISONS

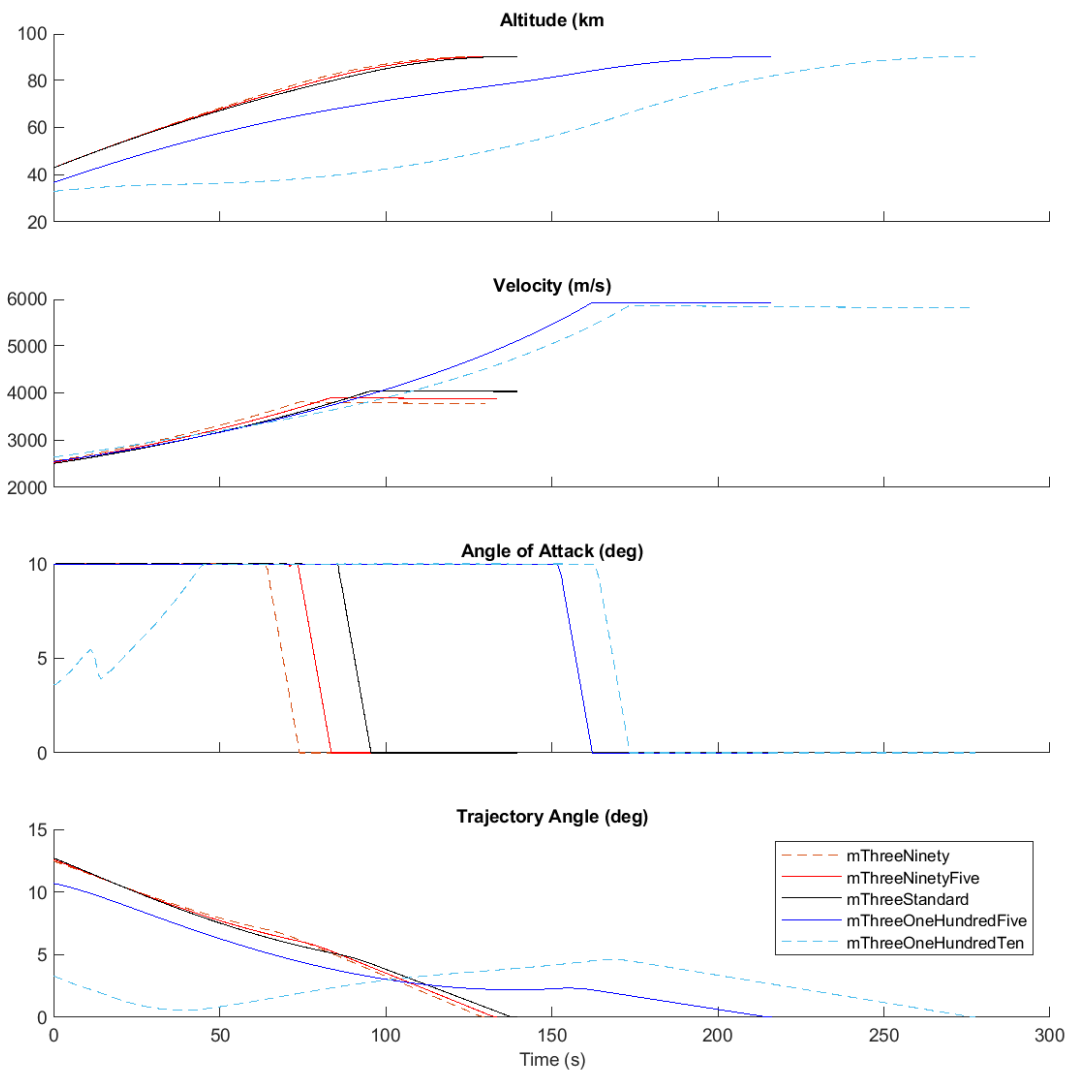


Figure F.33: Comparison of third stage rocket ascent trajectories with variation in the mass of the third stage.

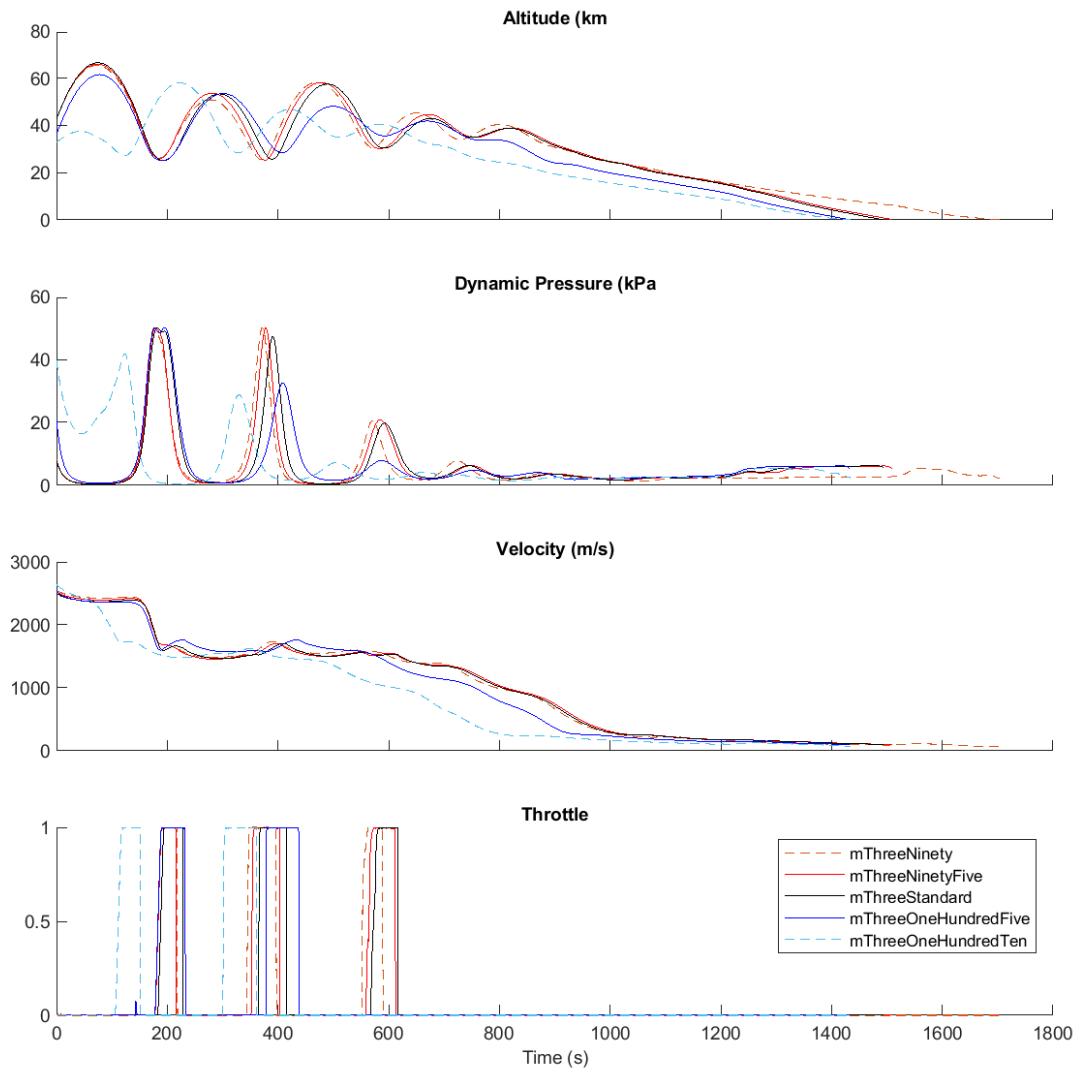


Figure F.34: Comparison of scramjet accelerator return trajectories with variation in the mass of the third stage.

F.2.7 Case 18: Third Stage Specific Impulse Sensitivity Comparison

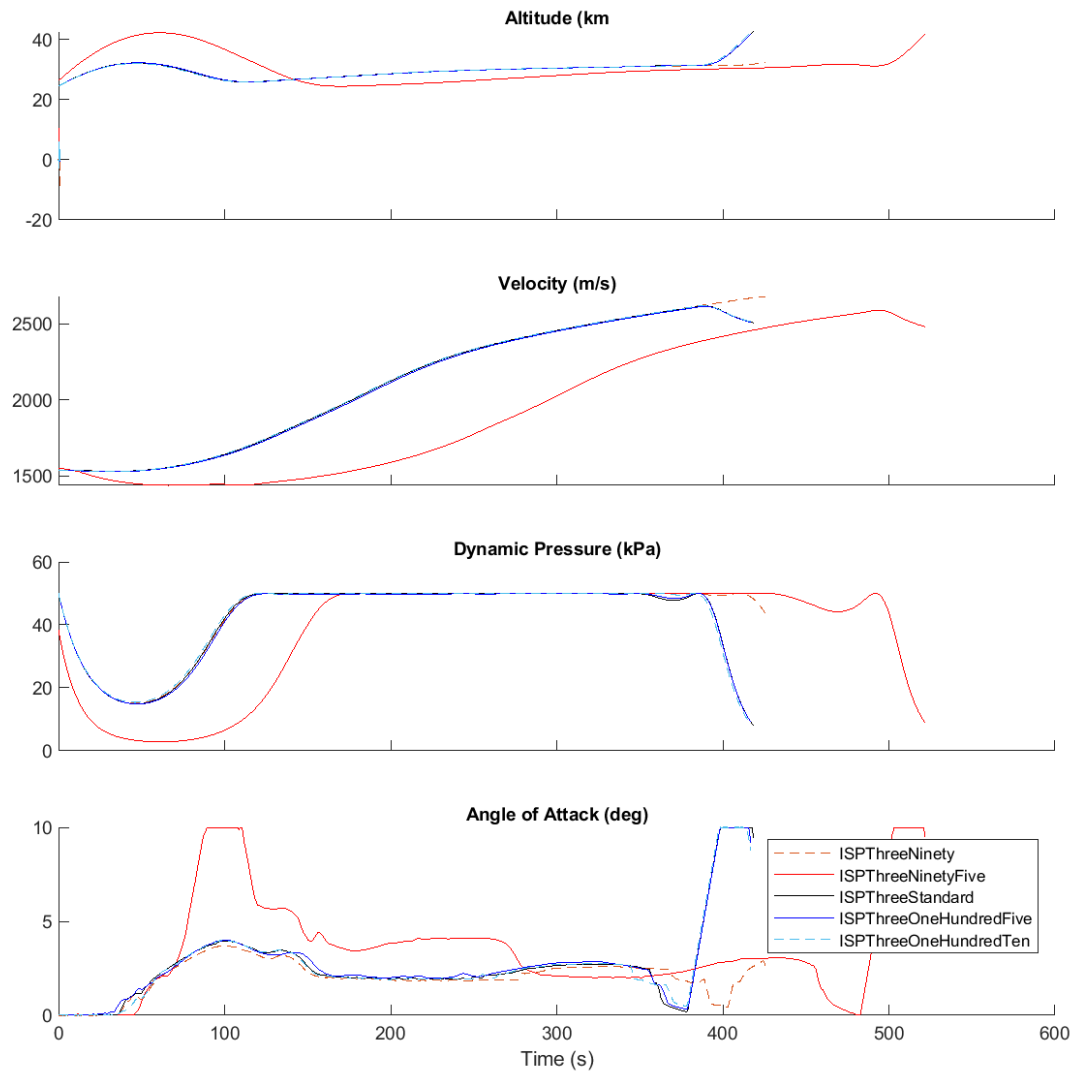


Figure F.35: Comparison of scramjet accelerator ascent trajectories with variation in the specific impulse of the third stage.

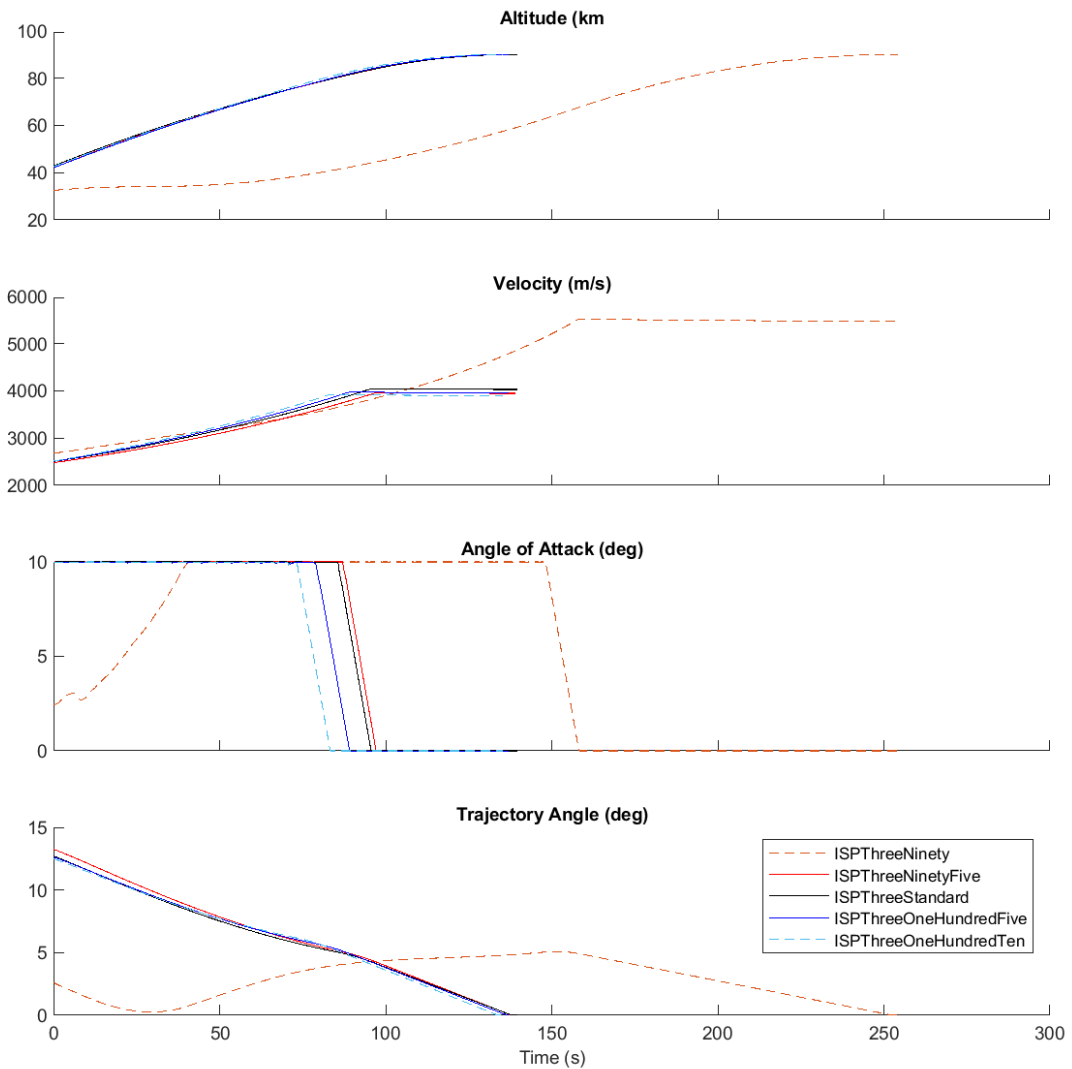


Figure F.36: Comparison of third stage rocket ascent trajectories with variation in the specific impulse of the third stage.

APPENDIX F. TRAJECTORY PLOT COMPARISONS

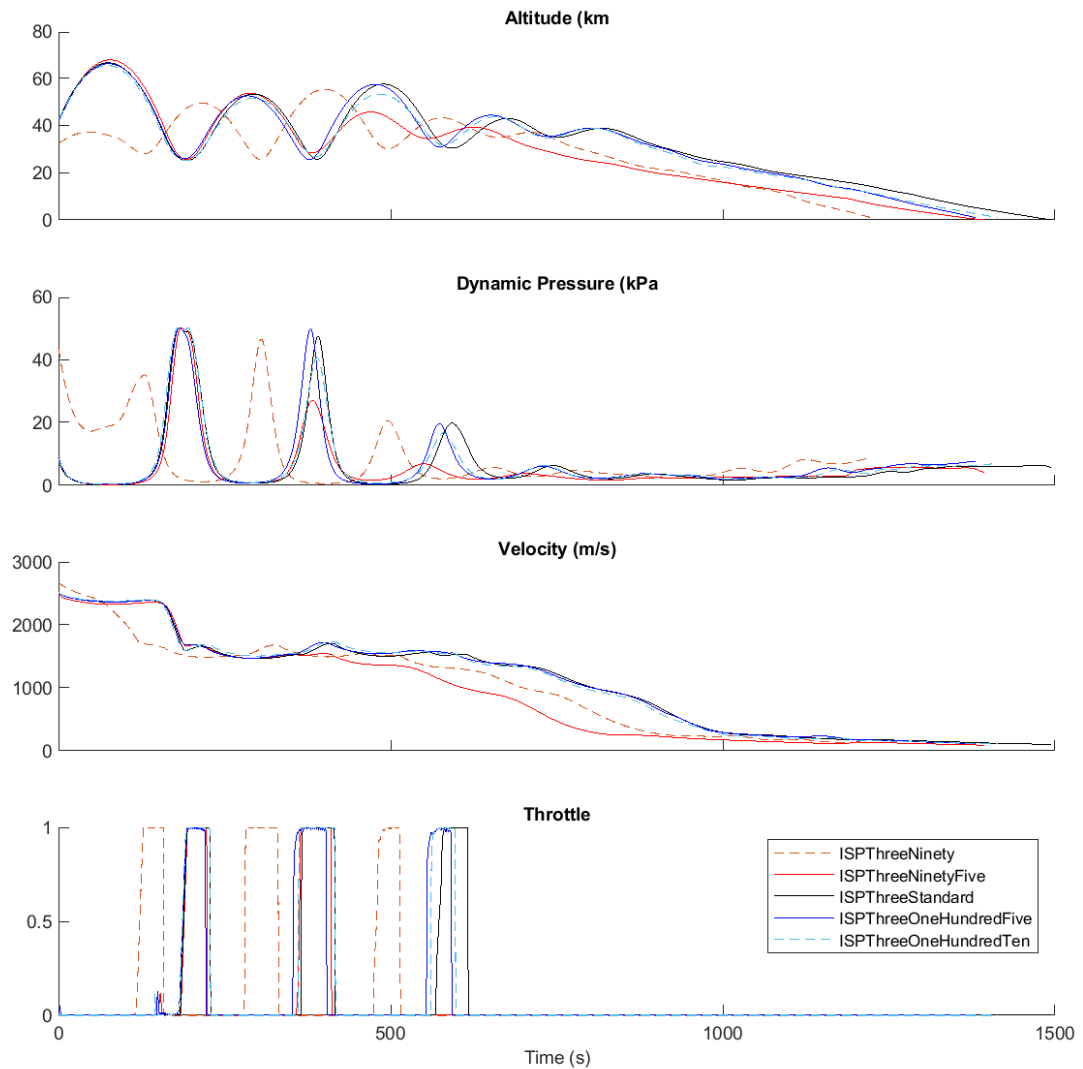


Figure F.37: Comparison of scramjet accelerator return trajectories with variation in the specific impulse of the third stage.

APPENDIX G

VISCOUS DRAG VARIATION

This section presents the sensitivity of the launch system performance to variations in the viscous drag of the scramjet accelerator. This sensitivity analysis is intended as a reference, to indicate the magnitude of variations in the viscous drag of the scramjet accelerator due to variations in modelling methods, and is unlikely to be indicative of any physical design variations. The viscous drag component of the scramjet accelerator's aerodynamics is calculated using flat plate correlations, which require an estimation of the laminar to turbulent transition point on the body of the scramjet accelerator[139]. This transition point is difficult to estimate to a high degree of accuracy, and can have a significant effect on the viscous drag of an aircraft[139]. The viscous drag component of the scramjet accelerator's aerodynamics is varied, in order to assess the impact of the viscous drag model used. Optimal trajectories are calculated with the viscous drag set at levels of 20%, 50%, 107% and 115% of the baseline, which correspond to the possible viscous drag range due to transition point variation. Table G.1 details key trajectory parameters of the optimised trajectories, and Figures G.1, G.2 and G.3 show comparison plots of the optimised trajectories. The sensitivity of the launch system to the viscous drag of the scramjet accelerator is shown to be relatively low, as the deviations in the viscous drag model are expected to be small, relative to the range tested. This low sensitivity indicating that the modelling process of the viscous drag is unlikely to have a large effect on the accuracy of the maximum payload-to-orbit solution.

Trajectory Condition	vC _D :	20%	50%	100%	107%	115%	$\Delta/\Delta\%vC_D$
Payload to Orbit (kg)	171.7	153.2	132.1	128.7	126.1	-	-2.3
Total η_{exergy} (%)	1.962	1.782	1.576	1.548	1.521	-	-0.00022
1st Stage η_{exergy} (%)	6.837	6.891	6.925	6.918	6.929	-	
Separation Alt, 1→2 (km)	24.50	24.54	24.58	24.57	24.58	-	
Separation v, 1→2 (m/s)	1528	1535	1539	1538	1540	-	
Separation γ, 1→2 (deg)	9.9	10.9	11.3	11.1	11.3	-	
2nd Stage η_{exergy} (%)	4.954	4.387	3.758	3.667	3.582	-	-0.069
Separation Alt, 2→3 (km)	43.25	42.83	42.52	42.66	42.35	-	
Separation v, 2→3 (m/s)	2756	2642	2507	2486	2468	-	-14.63
Separation γ, 2→3 (deg)	11.3	11.9	12.7	12.8	13.0	0.09	
2nd Stage Flight Time (s)	508.9	508.1	508.8	505.2	507.4	-	
2nd Stage Distance Flown (km)	934.5	907.8	872.3	858.7	857.6	-	-4.06
2nd Stage Return Fuel (kg)	245.9	248.6	252.4	265.3	261.8	-	
2nd Stage Return Distance (km)	1865.0	1671.8	1520.4	1492.3	1485.4	-	-18.78
3rd Stage η_{exergy} (%)	16.997	15.208	13.142	12.804	12.549	-	-0.226
3rd Stage $t, q > 5\text{kpa}$ (s)	9.7	9.2	9.1	7.7	7.6	-	-0.11
3rd Stage Fuel Mass (kg)	2813.5	2832.0	2853.1	2856.5	2859.1	-	2.32

Table G.1: Summary of key trajectory parameters with scramjet accelerator viscous drag variation.

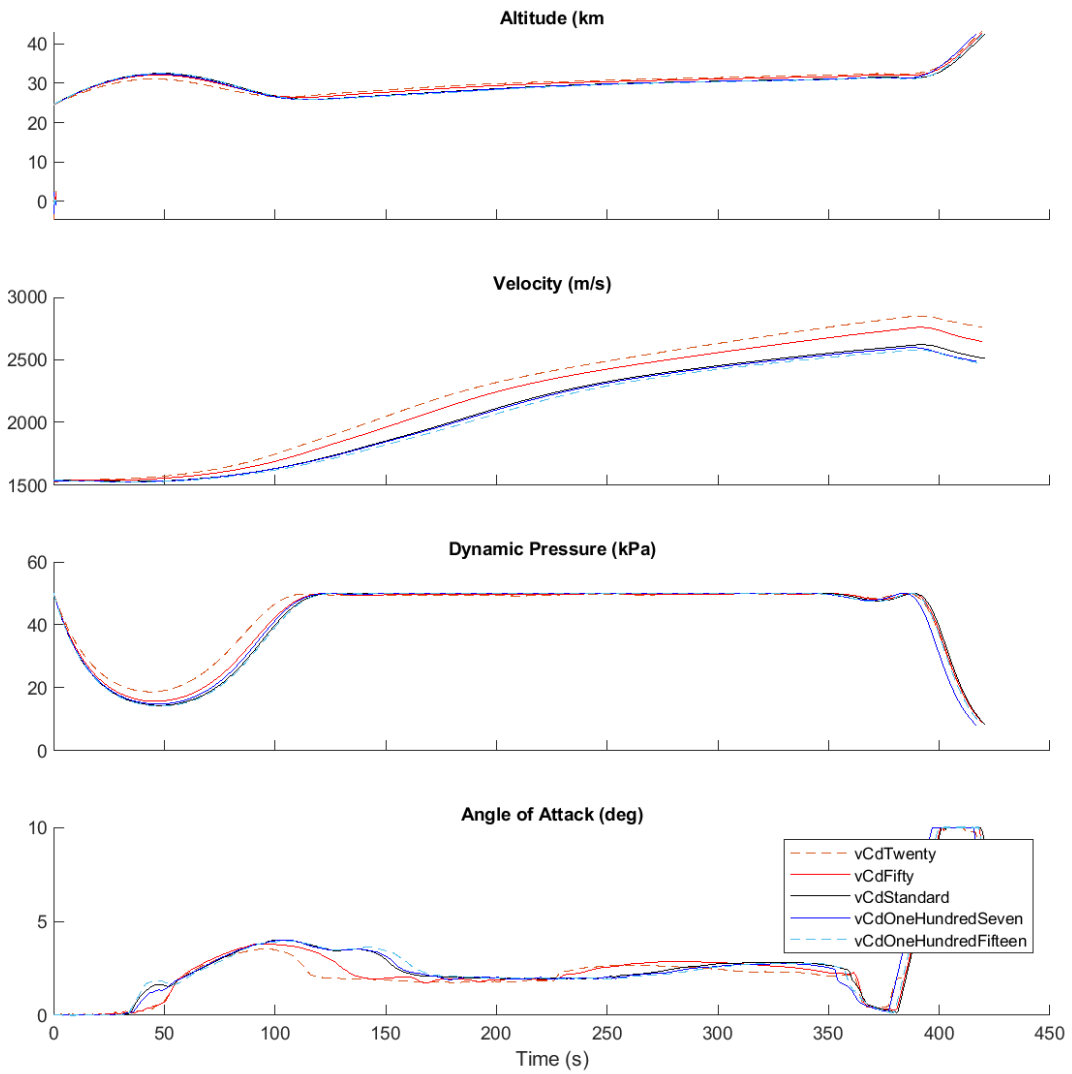


Figure G.1: Comparison of scramjet accelerator ascent trajectories with variation in the viscous drag of the scramjet accelerator.

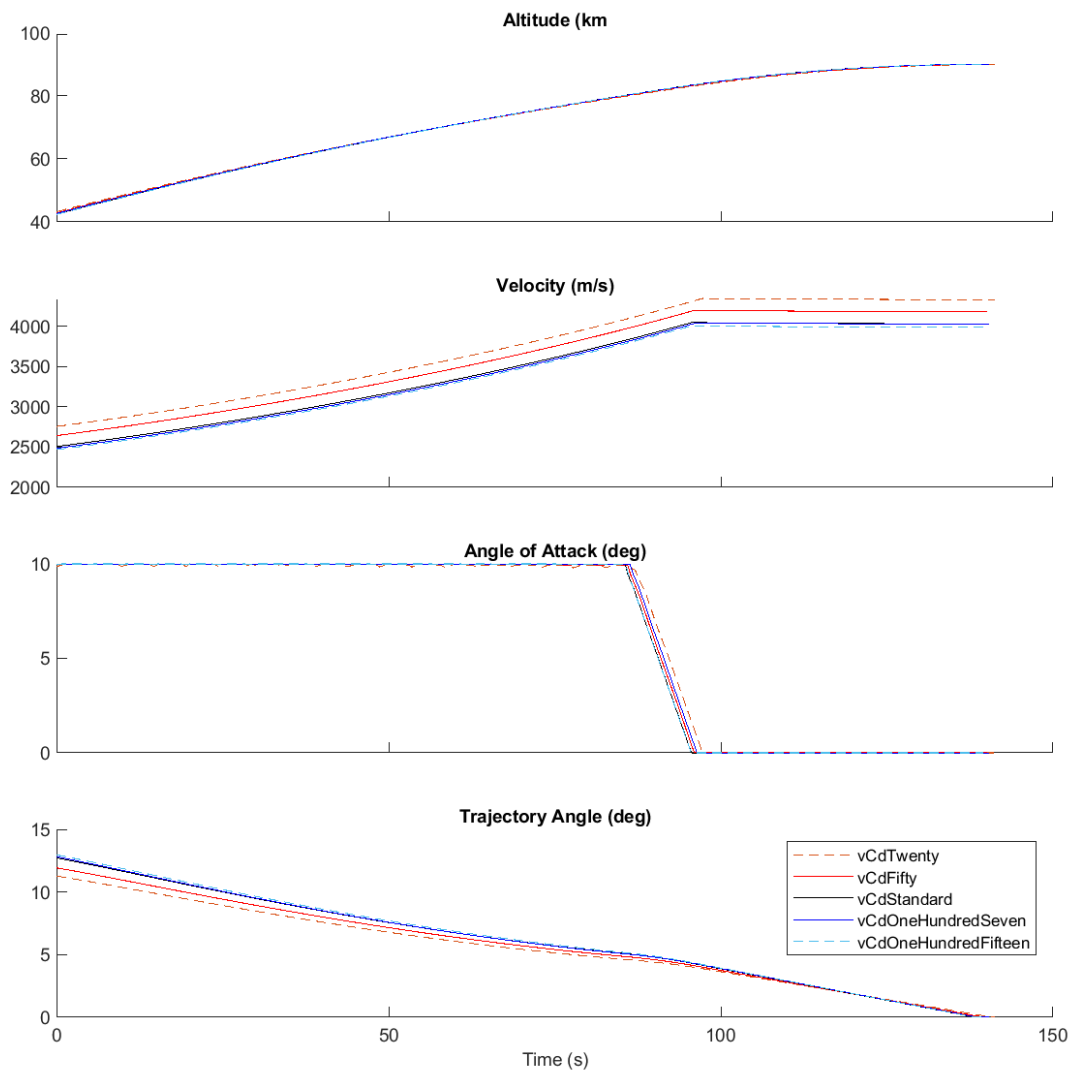


Figure G.2: Comparison of third stage ascent trajectories with variation in the viscous drag of the scramjet accelerator.

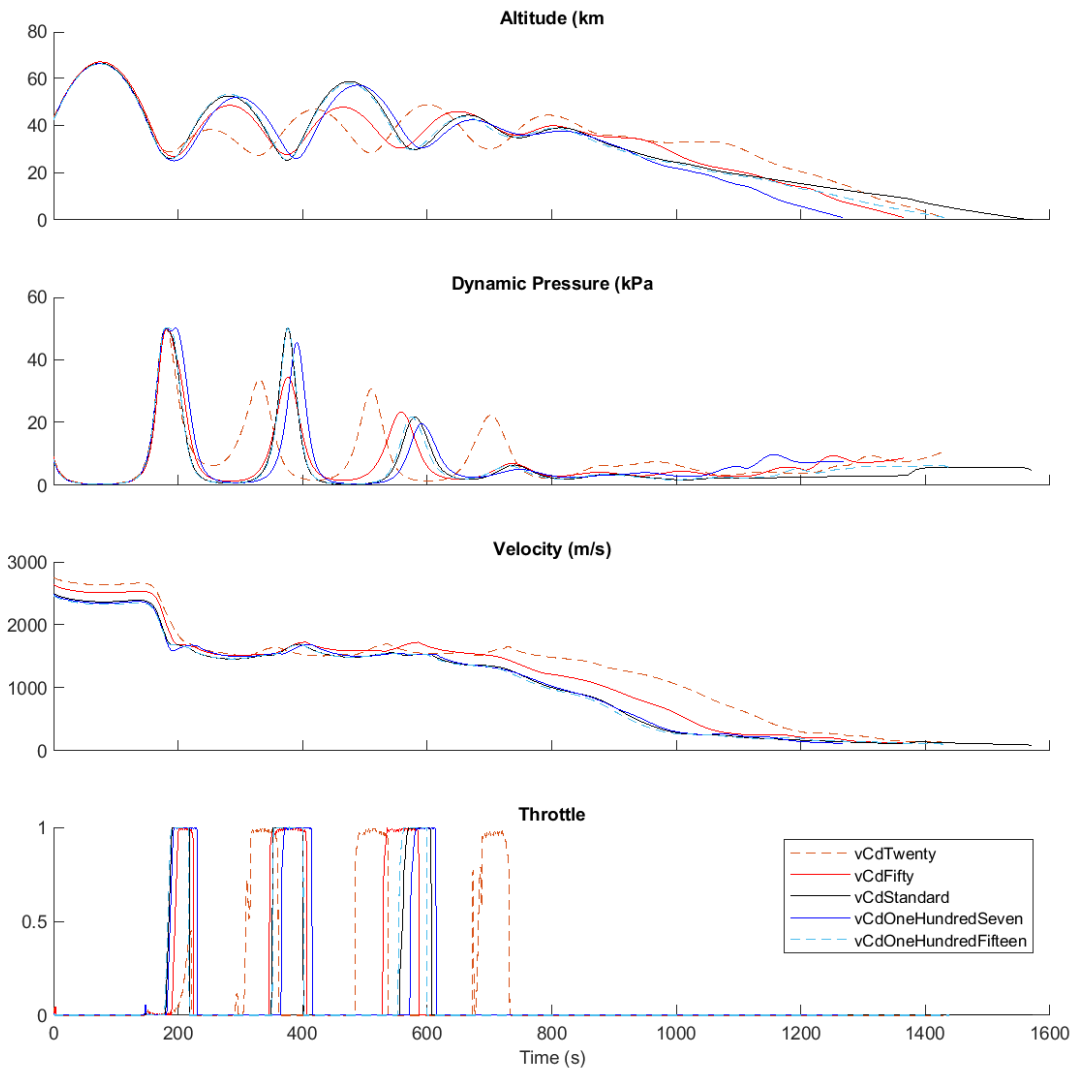


Figure G.3: Comparison of scramjet accelerator return trajectories with variation in the viscous drag of the scramjet accelerator.